

IAEA-TECDOC-1688

***Comparison of Heavy Water Reactor
Thermalhydraulic Code Predictions
with Small Break LOCA
Experimental Data***



IAEA

International Atomic Energy Agency

Comparison of Heavy Water Reactor
Thermalhydraulic Code Predictions with
Small Break LOCA Experimental Data

The following States are Members of the International Atomic Energy Agency:

AFGHANISTAN	GHANA	NIGERIA
ALBANIA	GREECE	NORWAY
ALGERIA	GUATEMALA	OMAN
ANGOLA	HAITI	PAKISTAN
ARGENTINA	HOLY SEE	PALAU
ARMENIA	HONDURAS	PANAMA
AUSTRALIA	HUNGARY	PAPUA NEW GUINEA
AUSTRIA	ICELAND	PARAGUAY
AZERBAIJAN	INDIA	PERU
BAHRAIN	INDONESIA	PHILIPPINES
BANGLADESH	IRAN, ISLAMIC REPUBLIC OF	POLAND
BELARUS	IRAQ	PORTUGAL
BELGIUM	IRELAND	QATAR
BELIZE	ISRAEL	REPUBLIC OF MOLDOVA
BENIN	ITALY	ROMANIA
BOLIVIA	JAMAICA	RUSSIAN FEDERATION
BOSNIA AND HERZEGOVINA	JAPAN	SAUDI ARABIA
BOTSWANA	JORDAN	SENEGAL
BRAZIL	KAZAKHSTAN	SERBIA
BULGARIA	KENYA	SEYCHELLES
BURKINA FASO	KOREA, REPUBLIC OF	SIERRA LEONE
BURUNDI	KUWAIT	SINGAPORE
CAMBODIA	KYRGYZSTAN	SLOVAKIA
CAMEROON	LAO PEOPLE'S DEMOCRATIC REPUBLIC	SLOVENIA
CANADA	LATVIA	SOUTH AFRICA
CENTRAL AFRICAN REPUBLIC	LEBANON	SPAIN
CHAD	LESOTHO	SRI LANKA
CHILE	LIBERIA	SUDAN
CHINA	LIBYA	SWEDEN
COLOMBIA	LIECHTENSTEIN	SWITZERLAND
CONGO	LITHUANIA	SYRIAN ARAB REPUBLIC
COSTA RICA	LUXEMBOURG	TAJIKISTAN
CÔTE D'IVOIRE	MADAGASCAR	THAILAND
CROATIA	MALAWI	THE FORMER YUGOSLAV REPUBLIC OF MACEDONIA
CUBA	MALAYSIA	TUNISIA
CYPRUS	MALI	TURKEY
CZECH REPUBLIC	MALTA	UGANDA
DEMOCRATIC REPUBLIC OF THE CONGO	MARSHALL ISLANDS	UKRAINE
DENMARK	MAURITANIA	UNITED ARAB EMIRATES
DOMINICA	MAURITIUS	UNITED KINGDOM OF GREAT BRITAIN AND NORTHERN IRELAND
DOMINICAN REPUBLIC	MEXICO	UNITED REPUBLIC OF TANZANIA
ECUADOR	MONACO	UNITED STATES OF AMERICA
EGYPT	MONGOLIA	URUGUAY
EL SALVADOR	MONTENEGRO	UZBEKISTAN
ERITREA	MOROCCO	VENEZUELA
ESTONIA	MOZAMBIQUE	VIETNAM
ETHIOPIA	MYANMAR	YEMEN
FINLAND	NAMIBIA	ZAMBIA
FRANCE	NEPAL	ZIMBABWE
GABON	NETHERLANDS	
GEORGIA	NEW ZEALAND	
GERMANY	NICARAGUA	
	NIGER	

The Agency's Statute was approved on 23 October 1956 by the Conference on the Statute of the IAEA held at United Nations Headquarters, New York; it entered into force on 29 July 1957. The Headquarters of the Agency are situated in Vienna. Its principal objective is "to accelerate and enlarge the contribution of atomic energy to peace, health and prosperity throughout the world".

IAEA-TECDOC-1688

COMPARISON OF HEAVY WATER
REACTOR THERMALHYDRAULIC
CODE PREDICTIONS WITH SMALL
BREAK LOCA EXPERIMENTAL DATA

INTERNATIONAL ATOMIC ENERGY AGENCY
VIENNA, 2012

COPYRIGHT NOTICE

All IAEA scientific and technical publications are protected by the terms of the Universal Copyright Convention as adopted in 1952 (Berne) and as revised in 1972 (Paris). The copyright has since been extended by the World Intellectual Property Organization (Geneva) to include electronic and virtual intellectual property. Permission to use whole or parts of texts contained in IAEA publications in printed or electronic form must be obtained and is usually subject to royalty agreements. Proposals for non-commercial reproductions and translations are welcomed and considered on a case-by-case basis. Enquiries should be addressed to the IAEA Publishing Section at:

Marketing and Sales Unit, Publishing Section
International Atomic Energy Agency
Vienna International Centre
PO Box 100
1400 Vienna, Austria
fax: +43 1 2600 29302
tel.: +43 1 2600 22417
email: sales.publications@iaea.org
<http://www.iaea.org/books>

For further information on this publication, please contact:

Nuclear Power Technology Development Section
International Atomic Energy Agency
Vienna International Centre
PO Box 100
1400 Vienna, Austria
email: Official.Mail@iaea.org

© IAEA, 2012
Printed by the IAEA in Austria
August 2012

IAEA Library Cataloguing in Publication Data

Comparison of heavy water reactor thermalhydraulic code
predictions with small break LOCA experimental
data. – Vienna : International Atomic Energy Agency,
2012.

p. ; 30 cm. – (IAEA-TECDOC series, ISSN
1011-4289 ; no. 1688)
ISBN 978-92-0-133710-8
Includes bibliographical references.

1. Heavy water reactors -- Safety measures.
2. Thermodynamics -- Computer simulation. 3.
Hydraulics -- Computer simulation. I. International
Atomic Energy Agency. II. Series.

IAEAL

12-00762

FOREWORD

Activities within the frame of the IAEA's Technical Working Group on Advanced Technologies for HWRs (TWG-HWR) are conducted in a project within the IAEA's subprogramme on nuclear power reactor technology development. The objective of the activities on HWRs is to foster, within the frame of the TWG-HWR, information exchange and cooperative research on technology development for current and future HWRs, with an emphasis on safety, economics and fuel resource sustainability. One of the activities recommended by the TWG-HWR was an international standard problem exercise entitled Intercomparison and Validation of Computer Codes for Thermalhydraulics Safety Analyses.

Intercomparison and validation of computer codes used in different countries for thermalhydraulics safety analyses will enhance the confidence in the predictions made by these codes. However, the intercomparison and validation exercise needs a set of reliable experimental data. Two RD-14M small break loss of coolant accident (SBLOCA) tests, simulating HWR LOCA behaviour, conducted by Atomic Energy of Canada Ltd (AECL), were selected for this validation project. This report provides a comparison of the results obtained from eight participating organizations from six countries (Argentina, Canada, China, India, Republic of Korea, and Romania), utilizing four different computer codes (ATMIKA, CATHENA, MARS-KS, and RELAP5). General conclusions are reached and recommendations made.

The IAEA expresses its appreciation to the CANDU Owners Group (COG) for releasing the experimental data to the international community, and to M. Krause of AECL, Canada for leading the activity. The IAEA officer responsible for this publication was J.H. Choi of the Division of Nuclear Power.

EDITORIAL NOTE

The use of particular designations of countries or territories does not imply any judgement by the publisher, the IAEA, as to the legal status of such countries or territories, of their authorities and institutions or of the delimitation of their boundaries.

The mention of names of specific companies or products (whether or not indicated as registered) does not imply any intention to infringe proprietary rights, nor should it be construed as an endorsement or recommendation on the part of the IAEA.

CONTENTS

1.	INTRODUCTION.....	1
1.1.	BACKGROUND AND MEETING SUMMARY	1
1.2.	OBJECTIVE AND SCOPE.....	2
1.3.	STRUCTURE OF THE REPORT	2
2.	RD-14M FACILITY	3
2.1.	DESCRIPTION	3
2.2.	INSTRUMENTATION.....	7
2.3.	INSTRUMENTATION UNCERTAINTY	7
2.4.	SUMMARY OF EXPERIMENTS.....	9
2.5.	TEST B9006.....	9
2.5.1.	Initial conditions	9
2.5.2.	Test procedure.....	10
2.5.3.	Measurements	11
2.6.	TEST B9802.....	11
2.6.1.	Initial conditions	11
2.6.2.	Test procedure.....	12
2.6.3.	Measurements	12
3.	PARTICIPANTS, CODES AND MODELS	13
3.1.	COMPUTER CODES	14
3.1.1.	ATMIKA.....	14
3.1.2.	CATHENA.....	15
3.1.3.	MARS-KS.....	17
3.1.4.	RELAP5	19
3.2.	GROUND RULES FOR BLIND AND OPEN CALCULATIONS	20
3.3.	PARTICIPANTS' IDEALIZATIONS AND ASSUMPTIONS FOR STEADY STATE AND TRANSIENT CALCULATIONS	23
3.3.1.	Atomic Energy of Canada Ltd — Canada	23
3.3.2.	Atomic Energy Regulatory Board — India	28
3.3.3.	Centrala Nucleara Electrica — Romania	35
3.3.4.	Comisión Nacional de Energía Atómica — Argentina.....	42
3.3.5.	Korea Atomic Energy Research Institute — Republic of Korea.....	47
3.3.6.	Korea Institute of Nuclear Safety — Republic of Korea.....	52
3.3.7.	Nuclear Power Corporation of India Ltd — India	55
3.3.8.	TsingHua University — China	60
3.4.	BLIND AND OPEN STEADY STATE CALCULATION RESULTS.....	68
4.	CODE COMPARISON WITH EXPERIMENTS.....	73
4.1.	DESCRIPTION OF TEST B9006.....	73
4.2.	BLIND CALCULATION RESULTS FOR TEST B9006.....	75
4.2.1.	Sequence of major events	75
4.2.2.	Pump differential pressures and flow rates	75
4.2.3.	Header differential pressure	79
4.2.4.	Header pressures	79
4.2.5.	Header ECI flow rates.....	81

4.2.6	Integral ECI flow	85
4.2.7	Void fractions in boiler plenums and primary pumps.....	86
4.2.8	Boiler thermal power and steaming rates.....	86
4.2.9	Boiler inlet and outlet temperatures	94
4.2.10	FES sheath temperatures in heated sections HS8 and HS13	96
4.2.11	Flow rates in heated sections HS5, 8, 10, and 13.....	99
4.2.12	Heated sections HS5, 8, 10, and 13 inlet and outlet void	102
4.2.13	Differential pressure along outlet feeder from HS13 to HDR5	106
4.3	OPEN CALCULATION RESULTS FOR TEST B9006.....	106
4.3.1	Sequence of major events	107
4.3.2	Primary pump differential pressures	107
4.3.3	Header differential pressures	111
4.3.4	Header pressures	111
4.3.5	Header ECI flow rates.....	113
4.3.6	Integral ECI flow, qint and sum of Q3 to Q6.....	116
4.3.7	Void fractions in boiler plenums and primary pumps.....	120
4.3.8	Boiler thermal power and steaming rates.....	123
4.3.9	Boiler inlet and outlet fluid temperatures	126
4.3.10	FES Sheath temperatures in heated sections HS8 and HS13	128
4.3.11	Flow rates in heated section HS 5, 8, 10 and 13	131
4.3.12	Inlet and outlet void in heated section HS 5, 8, 10 and 13.....	134
4.3.13	Differential pressure along outlet feeder from HS13 to HDR5	138
4.3.14	Snapshot of pressure, temperature and void fraction.....	138
4.4	DESCRIPTION OF TEST B9802.....	139
4.5	BLIND CALCULATION RESULTS FOR TEST B9802	142
4.5.1	Sequence of major events	142
4.5.2	Pump differential pressures and flow rates	143
4.5.3	Integral break flow and loop inventory	146
4.5.4	Void fractions in boiler plenums and primary pumps.....	148
4.5.5	Boiler inlet and outlet fluid temperatures	152
4.5.6	FES sheath temperatures in heated sections HS8 and HS13	154
4.5.7	Heated sections HS 5, 8, 10 and 13 inlet and outlet void	157
4.5.8	Pressure drop along the outlet feeder from HS13 to HDR5	162
4.6	OPEN CALCULATION RESULTS FOR TEST B9802.....	162
4.6.1	Sequence of major events	163
4.6.2	Primary pump differential pressures, ΔP_{P1} and ΔP_{P2} , and flow rates	163
4.6.3	Header differential pressures, ΔP_{HD8-5} and ΔP_{HD6-7}	166
4.6.4	Header pressures, P(HD8), P(HD7) and P(HD6)	167
4.6.5	Integral break flow and loop inventory	169
4.6.6	Void fractions in boiler plenums and primary pumps.....	169
4.6.7	Boiler inlet and outlet fluid temperatures	174
4.6.8	FES sheath temperatures in heated sections HS8 and HS13	177
4.6.9	Flow rates in heated section HS 5, 8, 10 and 13	180
4.6.10	Inlet and outlet void in heated section HS 5, 8, 10 and 13.....	180
4.6.11	Pressure drop along the outlet feeder from HS13 to HDR5	187
4.6.12	Snapshot of pressure, temperature and void fraction.....	187
5	LESSONS LEARNED FROM ICSP	189
5.1	USER EFFECTS	189
5.2	CODE DEFICIENCIES AND NEED FOR CAPABILITY IMPROVEMENT	190
5.3	EXPERIMENTAL CONSIDERATIONS AND ICSP SPECIFICATION	191

6	CONCLUSIONS AND RECOMMENDATIONS.....	192
	REFERENCES.....	197
	APPENDIX I: SENSITIVITY CASES.....	199
	APPENDIX II: SNAP SHOT GRAPHS.....	216
	CONTRIBUTORS TO DRAFTING AND REVIEW	243

1. INTRODUCTION

Intercomparison and Validation of Computer Codes for Thermalhydraulics Safety Analyses is an International Atomic Energy Agency (IAEA) activity designed to facilitate international cooperative research and promote information exchange on computer codes for thermalhydraulic safety analyses. The objective is to enhance the safety analysis capabilities of the participants and the effective use of their resources through this international co-operation.

In 1999, a IAEA Coordinated Research Programme (CRP) was started entitled The Intercomparison and Validation of Computer Codes for Thermalhydraulic Safety Analysis, which was led by AECL. The first International Collaborative Standard Problem (ICSP) was completed in 2003 using data from AECL's RD-14M Large-Break Loss-of-Coolant-Accident (LBLOCA) experiment B9401. The RD-14M facility is a full vertical-scale representation of a CANDU primary heat transport system. The comparison of results obtained from six participating countries, using four different computer codes, is documented in IAEA-TECDOC-1395 [1].

A second ICSP was discussed and endorsed in December 2005 by the TWG-HWR (Technical Working Group on Heavy Water Reactors) to conduct a code comparison using a Small-Break LOCA (SBLOCA) experiment from the RD-14M facility. Specific SBLOCA-relevant tests were presented to the TWG-HWR in 2007 June and two tests, B9006 and B9802, were selected by the group. This report documents the results of eight participants from six countries using four different computer codes for this second ICSP.

1.1. BACKGROUND AND MEETING SUMMARY

This ICSP, Comparison of HWR Code Predictions with SBLOCA Experimental Data, started with the first meeting of the participants in Vienna in November 2007.

During this meeting the lesson learned from the previous IAEA ICSP on LBLOCA prediction for RD-14M test were discussed and several SBLOCA tests and important phenomenology during a SBLOCA in a CANDU plant were presented. Two tests were selected for this activity, test B9006, a 7-mm inlet header break experiment with pressurized accumulator emergency coolant injection, performed in 1990, and test B9802, a 3-mm inlet header break experiment, performed in 1998, to provide data on the influence of condensation rates in the steam generators on primary loop response under conditions where such a sensitivity is expected. The participants agreed on a subset of 52 measurements (plus several additional code-to-code comparison variables), out of the available experimental data of almost 600 measurements, as a basis for the code comparison, and that both blind and open calculations would be performed. The facility description [2], test summary [3] and electronic boundary and initial conditions were distributed to participants in early 2008.

The second meeting was held in Winnipeg, Canada, in August 2008 and included a visit to the RD-14M facility, located in AECL's Whiteshell Laboratories. The meeting objectives were to discuss results of steady state calculations for initial conditions of RD-14M Tests B9006 and B9802 and to develop ground rules and common assumptions for blind transient calculations. The facility visit and discussion with operations staff proved very useful for the participants in resolving questions related to the facility configuration, operations, and code input models and nodalization.

All participating institutes provided the results of blind transient simulation for RD-14M tests B9006 and B9802 by mid-2009, which were discussed at the third meeting in Vienna in August 2009. Individual participants presented their model assumptions, nodalizations and sensitivities, and AECL presented the transient measurements. Several significant discrepancies between code predictions of the test behaviour and test observations were noted, and attributed to input errors, or incorrect assumptions, in particular related to the ECI system. Therefore, a second round of blind calculations was started (the test data was not distributed yet) to allow correction of obvious errors. This second round was completed in late 2009 and all transient test data was subsequently made available for the open calculations.

The fourth and final meeting was held in Daejeon, Republic of Korea, in November 2010. The purpose of the meeting was to discuss all calculation results, formulate conclusions and recommendations, and review and finalize the draft report.

1.2. OBJECTIVE AND SCOPE

One of the objectives of the TWG-HWR is an international standard problem exercise entitled Intercomparison and validation of computer codes for thermalhydraulics safety analyses to foster information exchange and cooperative research on technology development for current and future HWRs. Intercomparison and validation of computer codes used in different countries for thermalhydraulics safety analyses will enhance the confidence in the predictions made by these codes if it is based on a set of reliable experimental data. Two RD-14M Small-Loss of Coolant Accident (LOCA) tests, simulating HWR LOCA behaviour, that were conducted by Atomic Energy of Canada Ltd (AECL) were selected for this validation project.

The specific objectives of this ICSP are for the participants to:

- Improve understanding of important phenomena expected to occur in SBLOCA transients;
- Evaluate code capabilities to predict these important phenomena, their practicality and efficiency, by simulating integrated experiments;
- Suggest necessary code improvements or new experiments to reduce uncertainties.

1.3. STRUCTURE OF THE REPORT

This report provides a comparison of the results obtained from eight participating organizations from six countries, utilizing four different computer codes. General conclusions are reached and recommendations made.

Section 2 provides a description of the RD-14M facility and instrumentation, as it was configured for the SBLOCA experiments, and a detailed description of the two tests subject to this exercise. Section 3 summarizes the participants' codes, methodologies, nodalizations and assumptions, along with results obtained for the initial steady-state conditions prior to the transients. Sections 4 and 5 present the results of blind and open simulations, respectively, and comparison against experimental measurements for selected transient variables. Finally, Section 6 summarizes lessons learned from the ICSP, with conclusions and recommendations given in Section 7.

Insights gained from various sensitivity studies are summarized in Appendix I, while a novel way of presenting the simulation results, so called 'snapshots' are shown and discussed in Appendix II.

2. RD-14M FACILITY

2.1. DESCRIPTION

RD-14M is an 11 MW, full-elevation-scaled thermalhydraulic test facility possessing most of the key components of a CANDU® (CANada Deuterium Uranium) PHTS (primary heat transport system) [2]. While the loop configuration is similar to a figure-of-eight geometry of a typical CANDU circuit, it is not intended to be a scale model of any particular reactor. The intent is to reproduce the important geometric features of a reactor primary heat transport system and the appropriate operating conditions (e.g. fluid pressure, temperature). Figure 2–1 shows a simplified schematic of the RD-14M facility and Fig. 2–2 shows an isometric view of the loop layout. The facility is arranged in the standard CANDU two-pass, figure-of-eight configuration. The reactor core is simulated by ten, 6 m-long horizontal channels (test sections). Each test section has simulated end-fittings and seven electrical heaters, or fuel element simulators, designed to have many of the characteristics of the CANDU fuel bundle. The RD-14M fuel element simulators are designed to model CANDU natural uranium fuel in power density or heat flux, and in heat capacity or heat-up rate. Figure 2-3 is a cross-section of a heated test section.

Test sections are connected to headers via full-length feeders. Above header piping is also CANDU-typical including two full-heights, U-tube steam generators or boilers and two bottom-suction centrifugal pumps. Steam generated in the secondary, or shell side of the steam generators is condensed in a jet condenser and returned as feedwater to the boilers. The primary side pressure is controlled by a pressurizer/surge tank (TK1) using a 100-kW electric heater (HR1).

The facility operates at typical CANDU primary system pressures (up to 11 MPa) and temperatures (up to 310°C) and is designed to produce the same fluid mass flux, transit time, pressure, and enthalpy distributions in the primary system as those in a typical CANDU reactor under both forced and natural circulation conditions.

The RD-14M loop is extensively instrumented. Approximately 600 instruments are used to scan and record various thermalhydraulic parameters using a dedicated data acquisition system during RD-14M experiments. In addition to above-header pressures, temperatures, volumetric flows, and void fraction measurements, the test sections are extensively instrumented. Inlet and outlet temperature, pressure, volumetric flow and void fraction are measured for each test section. Fuel element sheath temperatures are measured around the inside circumference of the test bundle and along the length of the test section.

Experiments are conducted in RD-14M to gain an improved understanding of the thermalhydraulic behaviour of a CANDU during loss-of-coolant accidents, under forced and natural circulation conditions, and during shutdown scenarios. The data collected from this facility are used to identify and examine phenomena observed in the heat transport system and forms a database for use in developing and validating computer models used to predict CANDU behaviour.

Integral experiments have been performed in loops of increasing size starting with RD-4 (1974), then progressing to RD-12 (1976 to 1983), to the full-height single-channel-per-pass RD-14 loop (1984–1987), and finally to the current RD-14M loop (commissioned in 1988). Each of these pressurized-water loops contains the essential geometric and physical characteristics of a CANDU heat transport system. Table 2-1 compares the characteristics of this facility and those of a typical CANDU reactor.

TABLE 2-1. COMPARISON OF RD-14M LOOP CHARACTERISTICS WITH A TYPICAL CANDU REACTOR

Characteristic	RD-14M	CANDU-600
Operating pressure (MPa)	10	10
Loop volume (m ³)	1.01	60
Heated sections/Fuel channels	1 indirectly heated 7-rod bundle	12 Nuclear fuel 37-Rod bundles
Number per pass	5	95
Length (m)	6	6
Rod Diameter (mm)	13.1	13.1
Flow Tube ID (mm)	44.8	103.4
Power (kW/channel)	3x750 and 2x950	5410 *
Pumps:	Single stage	Single stage
Impeller diameter (mm)	381	813
Rated flow (kg/s)	24	24 *
Rated head (m)	224	215
Rated speed (rpm)	3560	1790
Specific speed	565	2000
Steam generators:	Recirculating U-tube	Recirculating U-tube
Tube bundle height (m)	9.42	9.42
Number of tubes	44**	37 *
Tube ID (mm)	13.6	13.6
Tube OD (mm)	15.9	15.9
Secondary heat transfer area (m ²)	41**	32.9 *
Secondary volume (m ³)	0.9	0.13 *
Recirculation ratio at full Power	6:1	5.7:1
Elevation difference (m) (bottom heated section to top of boiler U-tubes)	21.9	21.9

* average per channel

** For B9006, each SG had 2 tubes plugged (net 42). For B9802 BO1 had 5 tubes plugged (net 39) and BO2 had 4 tubes plugged (net 40). The secondary heat transfer area is thus reduced accordingly.

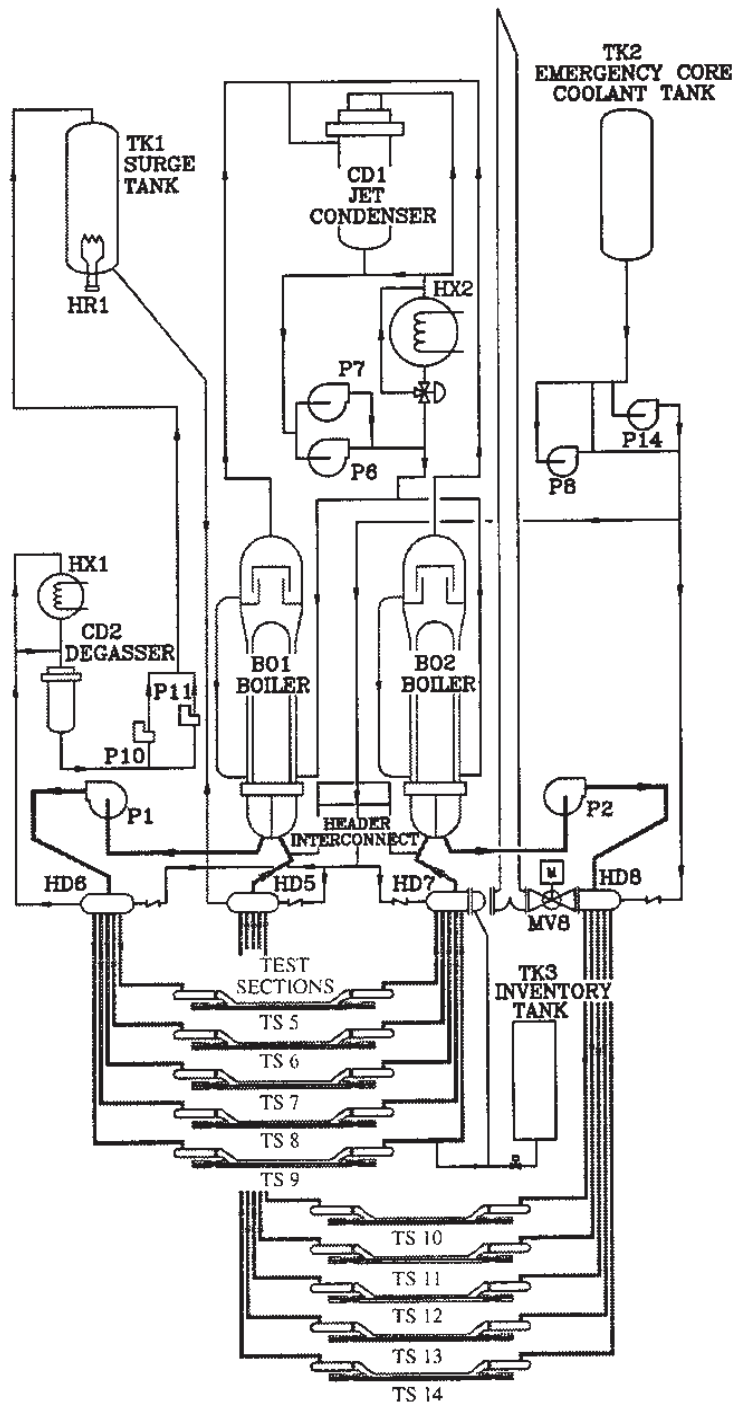


FIG. 2-1. RD-14M loop schematic.

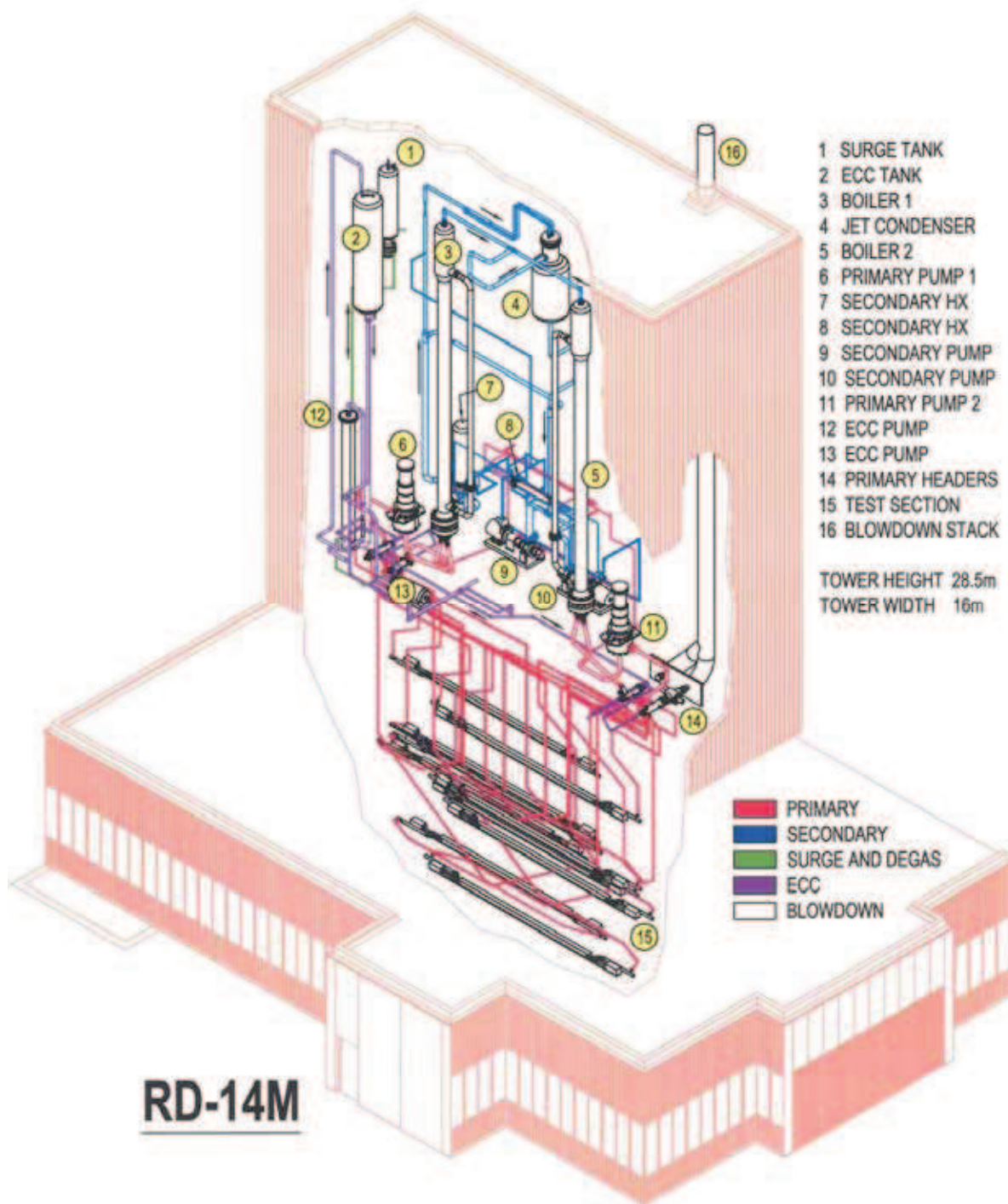


FIG. 2-2. RD-14M loop layout.

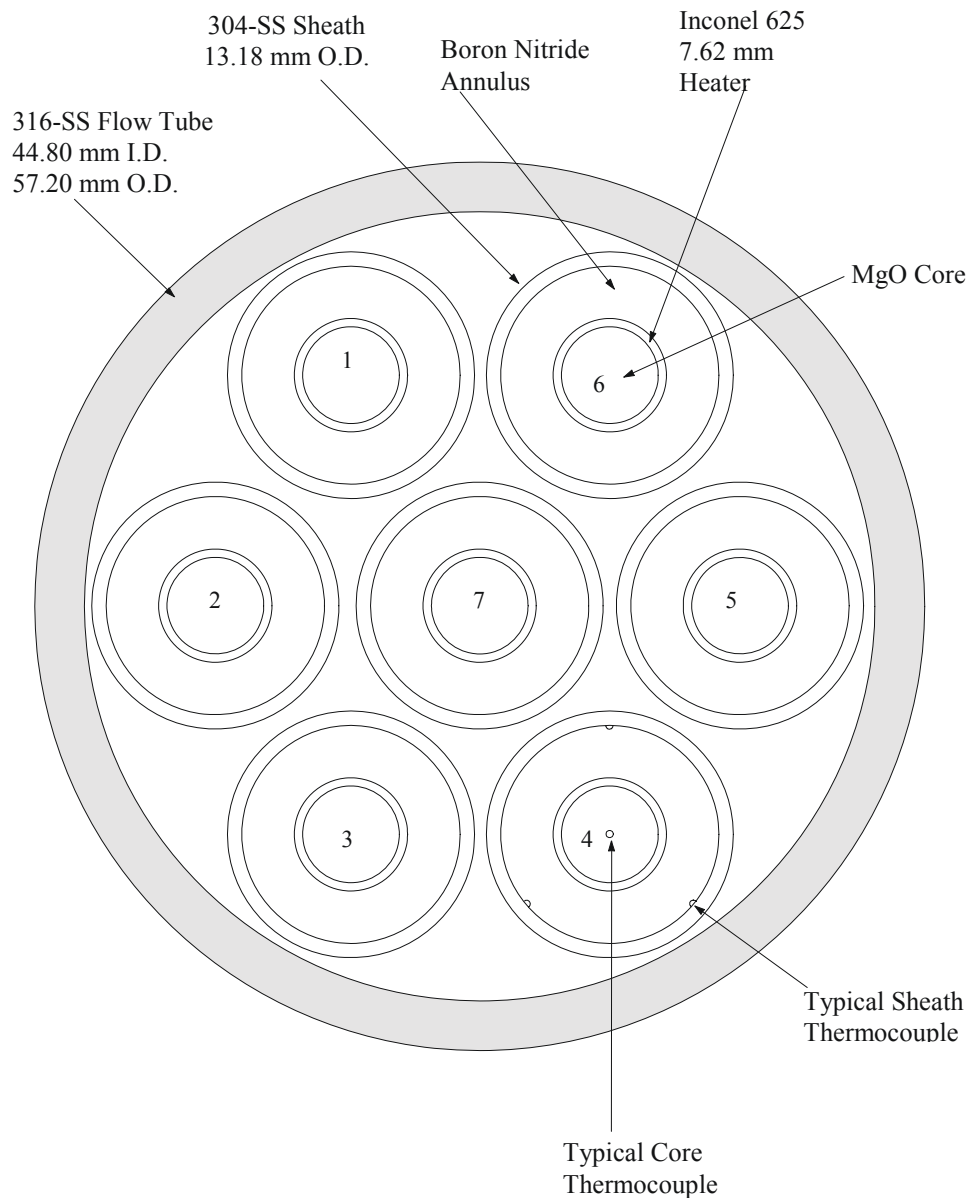


FIG. 2-3. Cross-section of an RD-14M heated section and FES numbering.

2.2. INSTRUMENTATION

RD-14M is extensively instrumented to measure parameters such as temperatures, pressures, flows, levels, and voids (gamma densitometers and conductivity probes). Each instrument in RD-14M is hard-wired into a panel near the data-acquisition system. A subset of available instruments is sampled during an experiment. The experimenter can choose the instruments to be recorded by the data-acquisition system for a particular experiment. This is done in software by providing a scan list of instruments to be sampled. There are a few instruments used for alarm, control, and trip functions that are recorded for all experiments. The facility description Swartz, 2003 [2] provides a detailed description of all instruments.

2.3. INSTRUMENTATION UNCERTAINTY

A detailed error analysis of RD-14M primary instrumentation was performed using a generic computer program that process RD-14M experimental data, and provides the experimental uncertainty of each recorded instrument. The program utilizes an existing comprehensive

calibration database. As part of standard RD-14M quality assurance procedures, each instrument in RD-14M is calibrated to traceable standards on an annual basis, at minimum. The uncertainty analysis program uses the calibration database to obtain pre- and post-test calibrations, as well as historical calibration performance, in calculating the actual instrument calibration uncertainties, as opposed to relying on instrument manufacturers specifications. Depending on the instrument type, additional uncertainty sources are then added to the calibration uncertainty to obtain the overall measurement uncertainty. The procedures used in the uncertainty analysis adhere to an ANSI standard (ANSI/NCSL Z540-2-1997) for uncertainty analysis, and are consistent with a similar ISO specification. The availability of this instrumentation uncertainty analysis will aid in the quantification of uncertainties associated with two fluid system hydraulic codes used for safety and licensing and analysis.

The present error analysis does not cover instrument types that do not have calibration entries in the calibration database. This includes gamma densitometers and conductivity probes, which both provide a voltage output that is not calibrated against a standard. It also does not include flow measurements made by orifices and venturis, since these flows are calculated values based on differential pressure measurements. Instrument uncertainties are available as an excel spreadsheet.

An error is defined as the true difference between the true value of a measured parameter and the measured value. Since the true value is never known, the error is also never known. The uncertainty is an estimate, or best guess, of the limits to which the error is expected to lie. All error sources are divided into two types: systematic (or bias) and precision (or random). Random errors are values that affect the test data in a random fashion from one reading to the next, thereby causing scatter in the results. Any errors that do not cause scatter in the test results are systematic errors. Both random and systematic errors are unknown, and have to be estimated as uncertainty intervals. Systematic uncertainty is an estimate, at some confidence level, of the limits in which the systematic error is expected to lie. Similarly, random uncertainty is an estimate, at some confidence level, of the limits in which the random error is expected to lie.

The ANSI uncertainty-analysis standard provides a methodology for combining systematic (bias) and random uncertainties. In general, the errors associated with an instrument measurement can be categorised into three types:

- Instrumentation errors: This source includes uncertainties associated with the calibration accuracy, including non-linearity and calibration drift. The instrument errors also include uncertainties associated with changes in ambient conditions and loop process conditions. For example, all instruments are influenced to some extent by changes in ambient temperature;
- Dynamic response error: All instruments have a particular response time to changes in the process being measured. For experiments with rapid changes in conditions, such as the initial depressurisation during a blowdown test, a non-symmetric bias error may occur due to the limited response time of an instrument;
- Application errors: This source includes errors arising from the nature of the environment in which the instrument is used. These are not instrument errors, but are errors associated with system-sensor interaction, or system disturbance errors. Quantification of these errors typically involves theoretical analysis.

Dynamic response errors are not included in the present uncertainty analysis, due to limited information currently available to quantify this error source. The application errors discussed above are also not included in the present uncertainty analysis. These error sources are assumed to be negligible compared with the other error sources.

2.4. SUMMARY OF EXPERIMENTS

Both tests begin from CANDU-typical initial conditions (10 MPa(g) outlet header, representative, scaled flows and heat fluxes) and involve multiple channels. Single-channel tests in RD-14 were not considered for this ICSP.

The loop initially depressurizes very rapidly, until the pressure in the hot leg regions reaches saturation. After less than 1 s, the depressurization rate reduces due to the formation of steam in the heated sections, outlet feeders and outlet headers. When the loop pressure reached a predetermined value, the power to the heated sections was reduced to represent a reactor trip, and a pump ramp was also started to represent a coincident loss of Class-IV power in test B9006, while in B9802 the heater power and pump speeds remained constant. When the loop pressure falls below the high-pressure ECC tank pressure of 4.2 MPa(g), ECC flow starts (test B9006 only, no ECC injection occurred in B9802). During the blowdown period (prior to the start of ECI), the pumps maintained coolant flow through the system, removing the heat generated in the heated sections via liquid convection and nucleate boiling heat transfer. Steam generated from boiling and flashing was condensed in the steam generators as long as the secondary pressure was less than the primary pressure.

The terms "broken pass" and "intact pass" are used to distinguish the two halves of the RD-14M "figure-of-eight" primary circuit. For an inlet header break test, like B9006 and B9802, the broken pass is that portion of the primary loop between the outlet of pump P2 and the inlet of pump P1, including the associated heated sections (HS10 through 14). The intact pass is that portion of the primary loop between the outlet of pump P1 and the inlet of pump P2, including the associated heated sections (HS5 through 9).

2.5. TEST B9006

Test B9006 was a 7-mm inlet header break experiment with pressurized accumulator emergency coolant injection, performed in 1990 May. The break was represented by a fast-opening valve connected to an inlet header, and an orifice plate, scaled by the ratio of break area to loop volume to represent a feeder-sized break. Once the break valve was opened, single-phase liquid was discharged through the orifice, changing to two-phase flow when the inlet header pressure reached saturation. The break discharge flow was not measured directly.

This is the most complete SBLOCA test conducted in RD-14M in terms of including all the phases of the transient (blowdown, exponential pump ramp, secondary pressure ramp (crash cool), high-pressure ECC, refill, low pressure ECC, and natural circulation) and had the fewest problems during test execution. The break was represented by a 7-mm orifice connected to the inlet header, and power was reduced to decay power.

2.5.1. Initial conditions

The nominal initial conditions for test B9006 are given in Table 2-2 Krause, 2008 [3] actual conditions may differ slightly.

TABLE 2-2. NOMINAL TEST CONDITIONS OF TEST B9006

Primary system	Outlet header pressure	10.0 MPa(g) @ Header HD5
	Nominal input power	4.0 MW per pass
	Power in each heated section	
	Sections 5, 6, 7 ¹ , 8, 9:	748.0, 748.0, 811.0, 944.0, 757.0 kW
	Sections 10, 11, 12 ² , 13, 14:	749.0, 760.0, 822.0, 961.0, 760.0 kW
	Flow in each heated section	
	Sections 5, 6, 7, 8, 9:	3.92, 4.00, 4.80, 5.03, 3.92 kg/s
Sections 10, 11, 12, 13, 14:	3.80, 3.95, 5.22, 4.82, 3.88 kg/s	
Pump Flow	27.5 l/s or 21.7 kg/s (full speed)	
Break size (circular orifice)	7.0 mm @ Header 8	
Secondary system	Steam drum pressure	4.5 MPa(g)
	Steam separator level	55%
	Feedwater temperature	180°C
ECC	Pressurized accumulator	4.2 MPa(g)
	Low pressure pumped	1.5 MPa(g)
Notes:		
¹ FES#5 in heated section 7 was disconnected		
² FES#3 in heated section 12 was disconnected		

2.5.2. Test procedure

Before the experiment, the loop was evacuated, filled and degassed, all instrument lines vented, and instrument readings verified. The loop was warmed using low power and reduced pump speed. Input power and pump speed were then increased to reach the desired single-phase initial conditions for the experiment. All channels were scanned for 20 s to obtain initial conditions. Finally, the ECI accumulator was pressurized. Data gathering started at $t = 0$ s.

The surge tank is isolated prior to the break opening (important as the surge tank in RD-14M represents a significant volume of water). The blowdown valve was opened at inlet header 8 to simulate the break approximately 10 s after data sampling started. About two seconds after break initiation, the FES power was decreased to represent decay power levels and the primary loop pump speeds were exponentially decreased to simulate the loss of class IV power. Event or action timings were not recorded at the time of this test, and the actual timings were extracted from the data. The ECC isolation valves were opened on a pressure signal from header HD7 and the low pressure pumped ECI started when the ECC tank inventory dropped to 10% of the initial volume. The test was terminated at 2284 s.

The following Table 2-3 shows the sequence of events during test B9006. Valve positions and actual event times were not monitored at the time, and the actual start times of pump, power, and secondary pressure ramps could be delayed by up to 0.5 s, while the ECC valves could have a delay of up to 1.5 s.

TABLE 2-3. NOMINAL EVENT TIMINGS DURING TEST B9006

Time (s) or condition	Event/action
0.0 s	Data gathering started
6.0 s	Surge tank isolated
11.0 s	Break valve opened
8.8 MPa(g) @ HD7	Primary pump ramp and power ramp down to 200 kW/pass started
6.0 MPa(g) @ HD7	Individual header ECC valves opened and secondary pressure ramp started
4.2 MPa(g)	High-pressure ECC flow started (each header independent)
TK2 @ 10% level	Stopped high pressure ECC, started low-pressure pumped ECC
2284 s	Data gathering stopped

2.5.3. Measurements

Four hundred forty two (442) data channels were scanned at a scan rate of between 0.15 and 1.0 s and collected during test B9006.

Actual measurements of pump speed and torque, heated section power, secondary pressure, feedwater flow and temperature from the test were supplied electronically as boundary conditions for the blind simulation of this ICSP. The transient ECC tank pressure was also provided, although not used by most participants. ECC gas space temperature was not measured. The entire test data was available electronically following the blind simulations of this ICSP.

2.6. TEST B9802

Test B9802 was a 3-mm inlet header break experiment, performed in 1998 January, to provide data on the influence of condensation rates in the steam generators on primary loop response under conditions where such a sensitivity is expected. The break was represented by a 3-mm orifice installed in the drain line from header HD8 to an inventory tank. Once the break valve was opened, single-phase liquid was discharged through the orifice, changing to two-phase flow when the inlet header pressure reached saturation. The break discharge flow was condensed and measured.

Test B9802 had a smaller break (3 mm) than B9006, no ECC injection, no pump ramp, and no secondary pressure ramp. Channel power remained at full power during most of the transient, and pump speed was slightly reduced from nominal in order to achieve higher initial enthalpy in the channels and thus more boiling. This test was intended to study boiling in channels and condensation in steam generators in a slowly depressurizing loop rather than a blowdown.

2.6.1. Initial conditions

The nominal initial conditions for test B9802 are given in Table 2-4 [3]; actual conditions may differ slightly.

TABLE 2-4. NOMINAL TEST CONDITIONS OF TEST B9802

Primary system	Outlet header pressure	9.98 MPa(g) @ Header HD5
	Nominal input power	4.0 MW per pass
	Power in each heated section Sections 5, 6, 7 ¹ , 8, 9: Sections 10, 11, 12 ² , 13 ³ , 14:	745.0, 748.5, 796.5, 951.0, 753.7 kW 749.3, 761.1, 890.3, 907.9, 756.9 kW
	Flow in each heated section Sections 5, 6, 7, 8, 9: Sections 10, 11, 12, 13, 14:	3.38, 3.39, 4.10, 4.24, 3.38 kg/s 3.32, 3.17, 4.48, 4.17, 3.35 kg/s
	Pump flow	23.4 l/s or 18.5 kg/s @ 3000 rpm (83% of full speed)
	Break size (circular orifice)	3.0 mm @ Header 8, discharged through a condenser
Secondary system	Steam drum pressure	4.5 MPa(g)
	Steam separator level	55%
	Feedwater temperature	186°C
ECC	Pressurized accumulator	none
	Low pressure pumped	none

Notes:

¹ FES#5 in heated section 7 was disconnected.

² FES#7 in heated section 12 was disconnected.

³ FES#7 in heated section 13 was disconnected.

2.6.2. Test procedure

Before the experiment, the loop was evacuated, filled and degassed, all instrument lines vented, and instrument readings verified. The loop was warmed using low power and reduced pump speed. Input power and pump speed were then increased to reach the desired single-phase initial conditions for the experiment. All channels were scanned for 60 s to obtain initial conditions. Data gathering started at $t = 0$ s.

Table 2-5 shows the sequence of events during test B9802.

2.6.3. Measurements

Five hundred sixty five (565) data channels were scanned at a 0.2-s scan rate and collected during test B9802. Actual measurements of pump speed and torque, heated section power, secondary pressure, feedwater flow and temperature from the test were supplied electronically as boundary conditions for the blind simulation of this ICSP. The entire test data was available electronically following the blind simulations of this ICSP.

TABLE 2-5. NOMINAL EVENT TIMINGS DURING TEST B9802

Time (s)	Event/action
0.0	Data gathering started
8.2	Surge tank isolated
11.2	Break valve MV17 opened
449.6	Scans stopped and restarted *
901.6	Scans stopped and restarted *
1191.8	Pump 1 tripped on over-voltage process protection trip
1336.3	Power supplies tripped on high FES sheath temperature process protection trip (>600°C) **
1362.7	Break valve MV17 closed
1362.7	Data gathering stopped

* Scanning 565 channels @ 0.2 s/scan filled up the memory of the data logger in about 450 s, so the data logging had to be stopped momentarily to back up the data and restart the scans. The data set has small gaps at about 450 and 900 s.

** The actual process trip logic is as follows: Each channel has 9 pairs of thermocouples and if any pair reaches 600°C, the power supply that is connected to that channel is tripped. Thus, the maximum temperature actually recorded in this test was 640°C. For simplicity, it was agreed to use the first occurrence of 600°C in any location as the trip parameter in the simulations.

3. PARTICIPANTS, CODES AND MODELS

A list of participants, along with the computer code and version used, is provided in the following Table 3-1.

TABLE 3-1. PARTICIPANTS ORGANIZATION, COUNTRY AND CODE

Participant organization	Country	Code and version
AECL, Atomic Energy of Canada Ltd.	Canada	CATHENA MOD-3.5d/Rev 2
AERB, Atomic Energy Regulatory Board	India	RELAP5/MOD3.2
CNE, Centrala Nucleara Electrica (Cernavoda)	Romania	CATHENA MOD-3.5d/Rev 1
CNEA, Comisión Nacional de Energía Atómica	Argentina	CATHENA MOD-3.5c/Rev 0
KAERI, Korea Atomic Energy Research Institute	Republic of Korea	CATHENA MOD-3.5d/Rev 2
KINS, Korea Institute of Nuclear Safety	Republic of Korea	MARS-KS
NPCIL, Nuclear Power Corporation of India Ltd.	India	ATMIKA
THU, TsingHua University	China	CATHENA MOD-3.5d/Rev 2

All participants submitted blind calculations for test B9006, all except CNEA for B9802. Revised open calculations were submitted for both tests by all participants, except CNE (who submitted more sensitivity cases) and CNEA (only for B9006).

The following sections summarize first the four codes used, followed by each participant's idealizations, assumptions, and steady-state results.

3.1. COMPUTER CODES

3.1.1. ATMIKA

NPCIL participated with the system thermal hydraulic neutronic computer code 'ATMIKA' [4] developed in NPCIL for the analysis of Loss-of-Coolant Accident (LOCA) scenarios in Indian Pressurized Heavy Water Reactors (IPHWRs) [5].

ATMIKA is based on Unequal Velocity Equal Temperature (UVET) model using three conservation equations with a drift flux model. A staggered mesh arrangement is adopted where pressure, density and enthalpy are defined at the node, flow is defined along the flow path at the junction of two control volumes. Mass and energy conservation equations are applied on lumped control volume and momentum equation is applied on flow paths. A semi-implicit scheme has been adopted for solving the set of differential equations. Thermal hydraulics of a system is simulated by nodalising the entire system into a number of lumped control volumes (Nodes). Nodes are connected by means of flow paths. A flow path can be defined along with a valve or pump or both. Nodalization is done keeping in view the requirement of analysis and physical configuration of piping network. Usually control volume is chosen such that its boundaries coincide with the junctions of the flow paths, where there is a change in the geometry of the pipe or a valve/pump exists. In some cases, a piping of same geometry throughout may have to be divided into two or more control volumes as per the requirement of the analysis. A multiple connection or a network of piping is modelled by considering the junction of two or more pipes as a nodal point.

Some of the important models that ATMIKA utilizes are wall heat transfer model for estimation of heat transfer from fuel to coolant and coolant to heat exchanger tube including various transition boundaries. Critical Heat Flux (CHF) is estimated based on Groeneveld's Look-up table. AECL Look-up table is used for post dry out heat transfer coefficients [6]. Critical discharge through break is estimated using options from several available correlations e.g. Burnell's (for single-phase liquid), Moody, Homogeneous Equilibrium Model, frozen slip model. Friction Model is used to calculate pressure drop across pipes; among various options, model suggested by Chisholm based on Lockhart-Martinelli and Friedel correlation is used to evaluate two-phase frictional pressure drop. Pump Model is used for evaluating pump behavior under single phase and two-phase conditions. Heat Conduction model is used for estimation of radial temperature profile in fuel rod and pipes. Neutron Point Kinetics Model is used for small reactor for estimation of reactor power. To deal with space-time effects of large size reactor which behave in loosely coupled manner, the 3-D reactor kinetics model based on improved quasi-static scheme is adopted.

A model has been incorporated for simulation of indirectly heated Fuel Element Simulator (FES). Initial temperature distribution in conduction medium (FES) is determined by solving a steady state conduction equation. The radiative heat transfer and zirconium steam reaction rates can also be calculated. Two phase flow at low velocity in a horizontal pipe can be stratified as a result of buoyancy forces caused by density difference between the vapor and the liquid. Computer code identifies the stratified flow regime in horizontal channel based on

Taitel and Duckler model. The ability to calculate the heat transfer from individual groups of pins in a fuel bundle subjected to stratified flow is incorporated into code [5]. Under these conditions, the top pins in a bundle are exposed to steam, while the bottom pins are exposed to liquid. In exposed fuel pin, non-thermal equilibrium is considered. Code also predicts the velocity of both phases and simulates the counter current flow limitation in vertical feeders. Thermodynamic properties of the coolant have been simulated in all range of subcooled, two phase and superheated conditions. In general, a control volume is assumed to have homogeneous mixture of vapor and liquid. In some special cases such as accumulator, steam drum, bleed condenser, etc. the two phases are assumed to be separated with vapour occupying the top portion of control volume and liquid occupying bottom portion. In case of vapour and liquid, it is assumed that both the phases are in thermal equilibrium. In case of accumulators, the gas is assumed to expand according to $PV^k=c$ where P is pressure; V is the volume of gas and k is user specified. Steam generator modeling with homogeneous and non-homogeneous control volume has been adopted.

There is a provision to simulate Atmosphere Steam Discharge Valves (ASDV's) to simulate the crash cooldown during LOCA condition. PHT pressure control through feed and bleed system is modelled in a simplified manner. The appropriate selection of various empirical correlations makes this code suitable to the use for large and small break LOCA analysis.

During steady state analysis, input parameters e.g. pressure and enthalpy are read and other thermodynamic fluid properties such as temperature, void, density etc. are calculated. Based on flow distribution in the circuit, loss coefficient at each junction is fixed by using steady state momentum equation.

During the development of computer code, the behaviour of individual models representing different phenomena such as critical discharge, heat transfer, flow quality, frictional pressure drop, fuel conduction and models representing components like pump, etc. were verified against expected result. The computer code ATMIKA as an integration of all the above individual models, assessed with respect to published results in open literature on Canadian experimental facilities. It is observed that overall predictions of ATMIKA match reasonably well with the experimental results and is able to predict overall trend/ transient accurately. In addition, comparison against 'RELAP-4' was also carried out for Main Steam Line Break, and simulation of wide range of break sizes and locations on these facilities demonstrate the predicting capability of computer code ATMIKA, as documented in Indian PHWR safety reports.

Computer code ATMIKA is used for licensing calculations with conservative inputs. Some of the models and modeling technique used for analysis yield conservative results. For estimation of critical discharge, Burnell model is used for single phase liquid and Moody correlation is used for two phase mixture and vapor phase. Maximum rated fuel pin at each node is considered for heat flux considerations. However, in the present validation exercise for system modeling and simulation, best estimate/ realistic approach is used to the extent possible.

3.1.2. CATHENA

Five participants used the CATHENA code [7]; CNEA used Version 3.5c/Rev.0, CNE used Version 3.5d/Rev.1, while AECL, THU and KAERI used Version 3.5d/Rev.2. The acronym CATHENA stands for Canadian Algorithm for *Thermalhydraulic Network Analysis*. It was developed primarily for the analysis of postulated upset conditions in CANDU reactors; but is also used to model research reactors and thermalhydraulic test facilities.

CATHENA uses a transient, one-dimensional, two-fluid representation of two-phase flow in piping networks. In the thermalhydraulic model, the liquid and vapour phases may have different pressures, velocities, and temperatures. The thermalhydraulic model consists of solving six partial differential equations for the conservation of mass, momentum and energy for each phase. Interface mass, energy and momentum transfer between the liquid and vapour phases are specified using constitutive relations.

The thermal-hydraulic model in CATHENA includes pipe, volume, reservoir and tank components. The pipe component is the main thermalhydraulic component and consists of one or more “nodes” where volume-related dependent variables (void fraction, pressure, phase enthalpy and non-condensable mass fractions) are calculated. These nodes are connected by “links” where the phase velocities are calculated. Volume components are used at junctions of multiple pipe components to more accurately calculate the pressure and flow distributions through the junctions. Reservoir components are used to establish boundary conditions for a simulation. Tank components are used to model volumes in which liquid and vapour may co-exist in lower and upper regions of the volumes.

The Generalized Heat Transfer Package (GENHTP) in CATHENA is used to calculate radial and circumferential conduction, wall-to-fluid heat transfer, solid-solid contact, thermal radiation, pressure tube deformation and the zirconium-steam reaction. This heat transfer package allows the connection of multiple wall surfaces to one or more thermalhydraulic nodes.

The CATHENA code includes system models for components such as tanks, pumps, valves, emergency coolant injection accumulator, user definable junction resistances, and separators. Also included are a point-reactor kinetics model, a break-discharge model and a heat-balance calculation. An extensive control system modelling capability is provided for complete loop simulations (*i.e.*, regulation and safety shutdown systems).

The code uses a staggered-mesh, one-step, semi-implicit, finite-difference solution method, that is not transit time limited. A system of finite-difference equations is constructed from the linearization of the partial differential mass, momentum and energy conservation equations, after integration over finite time steps and finite space (nodes or links). The time step is automatically selected based on the rates of changes of a set of parameters including pressure and void fraction.

A number of new modelling capabilities have been incorporated into the CATHENA MOD-3.5d code version to address identified deficiencies and limitations observed during MOD-3.5c validation exercises. The primary new modelling additions or revisions in the MOD-3.5d code version compared to the MOD-3.5c version include:

- Revised post-dryout (PDO) modelling for bundles and tubes;
- Hydraulic area feedback effects;
- Solid-solid heat transfer feedback (emissivity and geometry changes);
- CANFLEX fuel-bundle modelling capabilities;
- Aging effect modelling (crept pressure-tube pressure drop and CHF);
- Break and tank modeling in thermalhydraulic and GENHTP models;
- Updated CHF look-up table (for MOD-3.5d/Rev 1 and Rev 2).

The revised post dry-out (PDO) modelling addition (fully developed and developing flow post-dryout heat transfer) is expected to improve the post-dryout fuel sheath temperature predictions as a result of better-estimate heat transfer between fuel surface and vapour phase. The revised break-discharge modeling is expected to significantly improve the code robustness in predicting the break discharge for low pressure-drop gas flow conditions and for cases where multiple break nodes are defined. All of the new modelling changes listed above are expected to have no or negligible impact on the predictions of the nucleate boiling heat transfer, condensation heat transfer, and coolant voiding phenomena, which govern the behaviour in the two tests B9006 and B9802.

3.1.3. MARS-KS

A multi-dimensional thermal-hydraulic system code MARS-KS has been developed for a realistic analysis of thermal-hydraulics transients in pressurized water reactors, by consolidating and restructuring the RELAP5/MOD3.2 and COBRA-TF codes.

The RELAP5 code is a versatile and robust code based on a one-dimensional two-fluid model for two-phase flows. The code includes many generic component models and special process models. The COBRA-TF code employs a three-dimensional two-fluid, three-field model for two-phase flows. The three-dimensional feature permits extremely flexible noding of the reactor vessel and, thus, more realistic simulations.

The two codes were adopted to take advantage of the very general, versatile features of RELAP5 and the realistic three-dimensional hydrodynamic module of COBRA-TF. Moreover, the MARS code was coupled with a three-dimensional reactor kinetics code, MASTER. This coupled calculation feature, in conjunction with the existing hot channel analysis capabilities of the MARS and MASTER codes, allows for more realistic simulations of nuclear system transients.

The objective of the code development program in Korea was to develop a best-estimate system code that has a coupled capability of multi-dimensional thermal-hydraulics, three-dimensional neutron kinetics, containment analysis, and critical heat flux calculation. To improve the code portability, two codes were completely merged into a single code, running in a serial computation mode, and the programming language was converted into standard Fortran 90. The resulting consolidated code was named MARS (Multi-dimensional Analysis of Reactor Safety). Further unification of code models, code restructuring and modernization, and new feature development has been carried out. MARS has evolved into the current version, MARS-KS with one-dimensional and three-dimensional modules, respectively. The MARS code has been generalized for widening its application to both nuclear and non-nuclear field, horizontal and vertical type of reactor, light and heavy water reactors. Its nuclear specific applications include the simulations of transients such as loss of coolant accidents, anticipated transients without scram and operational transients such as loss of feedwater, loss of offsite power etc. The V&V of the MARS multi-D model including its update is one of the main topics to be focused in the ongoing project. After the project will be finished, KINS will assign MARS codes as an official code for audit calculation.

The MARS code is based on a nonhomogeneous and nonequilibrium model for the two-phase system. It solves unsteady and one-dimensional mass, energy and momentum equations for each phase based on a fast and partially implicit finite-difference numerical scheme. The code includes many generic component models such as pumps, valves, pipes, heat releasing or absorbing structures, reactor point kinetics, electric heaters, jet pumps, turbines, separators, accumulators, and control system components. In addition, special process models are

included such as form loss, flow at an abrupt area change, branching, choked flow, boron tracking, and noncondensable gas transport.

The differential equations are based on the concept of a control volume in which mass and energy are conserved. Thus, the scalar properties of the volume are defined at cell centres, and vector quantities are defined on cell boundaries. Heat structures represent the solid structures bounding hydrodynamic volumes structures internal to the volumes. One dimensional heat conduction equation is used to compute temperature distributions within heat structures. Thermal boundary conditions of hydrodynamic volumes are coupled with heat structure conditions.

The constitutive correlations are used for defining flow regimes and heat transfer regimes models such as interphase drag and shear, the coefficient of virtual mass, wall friction, wall heat transfer, and interphase heat and mass transfer. The basic approach to pump modelling is to superimpose a quasi-static model for pump performance on the volume-junction flow path representation. The pump is a volume-oriented component, and the head developed by the pump is apportioned equally between the suction and discharge junctions of a pump component.

Early assessments performed in Korea of RELAP5 against RD-14 tests showed some deficiencies in the prediction of the heated section sheath temperatures. Therefore, the development of RELAP5/CANDU code was initiated by KINS in cooperation with KAERI to reduce the identified deficiencies. Thereafter the important models for CANDU characteristic have been applied to original MARS code. The major model modifications were performed in following areas:

- Critical Flow Model;
- Nuclear Kinetics Model;
- Critical Heat Flux Model;
- Valve and Spray Model;
- Improvement of Horizontal Flow Regime Map;
- Heat Transfer Model in Horizontal Channel.

The six items were improved not only for CANDU reactor but also for generic nuclear reactor system. The CANDU fuel channel heat transfer model and the flow regime model were improved to be suitable to a CANDU specific feature. The stratification criteria proper to CANDU fuel feature and the fuel element heatup process induced by stratification were newly implemented. The digital control model was mainly deduced from CANDU plant specific feature of digital control, but it could be also applied to the special processing feature of plants. By this improvement, the digitally processed signal can be simulated. Other four items, i.e. ANS94-4 decay heat model, Moody critical model, motor operative valve model and pressurizer spray model, were developed on generic base and could be applicable to PWR also. Especially, the plutonium contribution to decay heat can be considered by the ANS94-4 decay heat model. The Moody critical flow model using a heavy water property can provide an additional capability to evaluate the conservative break flow in CANDU system. Simulation of different rate of opening and closing the motor valve is now possible when calculating the liquid relief valve behaviour during transient. Moreover, the new pressurizer spray model can be used for evaluating the droplet size effect on the condensation. All of

those improvement were verified through some assessments with simple conceptual problems and Marviken critical flow test.

3.1.4. RELAP5

The light water reactor (LWR) transient analysis code, RELAP5, was developed at the Idaho National Engineering Laboratory (INEL) for the U.S. Nuclear Regulatory Commission (NRC). The RELAP5 code has been developed for best-estimate transient simulation of light water reactor coolant systems during postulated accidents. The code includes many generic component models from which general systems can be simulated. The component models include pumps, valves, pipes, heat releasing or absorbing structures, reactor point kinetics, electric heaters, jet pumps, turbines, separators, accumulators, and control system components. In addition, special process models are included for effects such as form loss, flow at an abrupt area change, branching, choked flow, boron tracking, and non-condensable gas transport.

The RELAP5 hydrodynamic model is a one-dimensional, transient, two-fluid model for flow of a two-phase steam-water mixture that can contain non-condensable components in the steam phase and/or a soluble component in the water phase. The numerical solution scheme used results in a system representation using control volumes connected by junctions. The difference equations are based on the concept of a control volume (or mesh cell) in which mass and energy are conserved. This results in defining mass and energy volume-average properties and requires knowledge of velocities at the volume boundaries. The velocities at boundaries are obtained through the use of momentum control volumes (cells) centered on the mass and energy cell boundaries. Therefore, the scalar properties (pressure, energies, and void fraction) of the flow are defined at cell centers, and vector quantities (velocities) are defined on cell boundaries. A physical system consisting of flow paths, volumes, areas, etc., is simulated by constructing a network of control volumes connected by junctions. The RELAP5 hydrodynamic model contains several options for invoking simpler hydrodynamic models. These include homogeneous flow, thermal equilibrium, and frictionless flow models. These options can be used independently or in combination. The RELAP5 thermal-hydraulic model solves eight field equations for eight primary dependent variables.

Heat structures represent the solid structures bounding hydrodynamic volumes (i.e. pipe walls) or structures internal to the volumes (fuel pins). The one dimensional heat conduction equation is used to compute temperature distributions within heat structures. Hydrodynamic volumes and heat structure conditions are coupled through heat structure boundary conditions. The constitutive relations include models for defining flow regimes and flow-regime-related models for interphase drag and shear, wall friction, wall heat transfer, and interphase heat and mass transfer. Heat transfer regimes are defined and used for wall heat transfer.

The basic approach to pump modeling is to superimpose a quasi-static model for pump performance on the RELAP5 volume-junction flow path representation. The pump is a volume-oriented component, and the head developed by the pump is apportioned equally between the suction and discharge junctions that connect the pump volume to the system. The pump model is interfaced with the two-fluid hydrodynamic model by assuming the head developed by the pump is similar to a body force. The pump head is coupled implicitly to the volumetric flow rate.

3.2. GROUND RULES FOR BLIND AND OPEN CALCULATIONS

Ground rules and common assumptions for blind transient calculations were agreed to at the second meeting in 2008 in Winnipeg, incorporating experiences gained during the preceding steady-state calculations. The ground rules basically consisted of agreed boundary conditions (BCs) and modeling assumptions to be used by all participants, a few additional variables for code comparison purposes, and output format of the results on MS Excel templates.

All participants are to use their steady-state models to start transient tests and a break opening time as given in the test description (B9006 – 11.0s, B9802 – 11.2s).

Start of ramped BCs (B9006), shown in Figs 3–1 to 3–7, should be applied according to the trip parameters, not according to the time when they occurred in the test. Data of primary heat transport system pump head versus void was provided to allow participants to implement an appropriate degraded pump performance model. Pump torque and ECC pump head vs. flow curve were also provided, although not necessarily used. At the end of the pump rundown the pumps are stopped.

While both the secondary side steam outflow rate and feedwater inflow rate were measured, the feedwater flowrate measurement is more accurate and used as a boundary condition. Boiler thermal power should be calculated as follows: Primary side heat flux multiplied by inner SG tube surface area.

While the ECC tank level was provided to the participants, it should not be used as a boundary condition. Instead the ECC system, including the tank, should be part of the model domain.

Averaged, constant BC values, listed in Table 3–2, were provided and applied to test B9802 transient simulation to allow a time-shift in the simulations, e.g. running for longer time than the available test data, if necessary. Pump P1 trip was kept as a function of time (1191.8s). Minimum simulation time is 1360s.

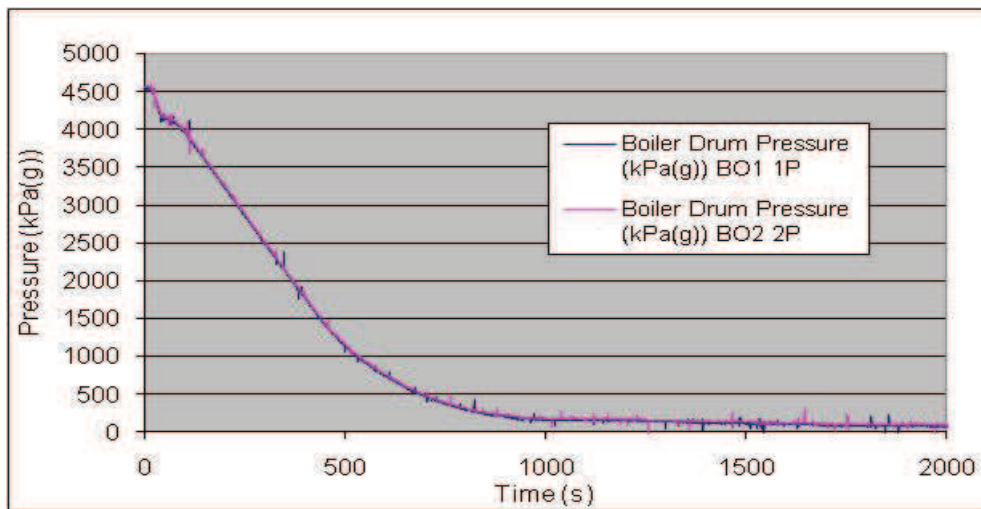


FIG.3-1. Boiler drum pressure boundary condition for test B9006.

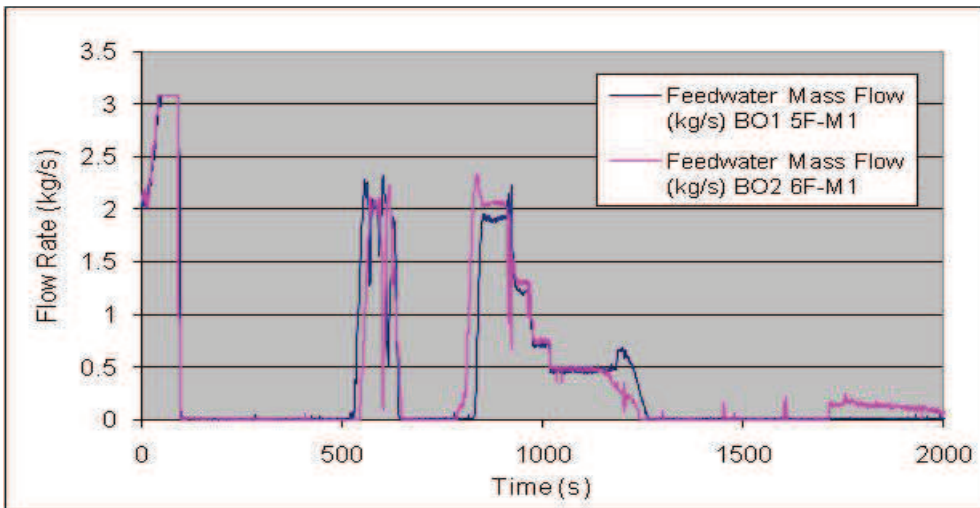


FIG. 3-2. Boiler feedwater flow rate boundary condition for test B9006.

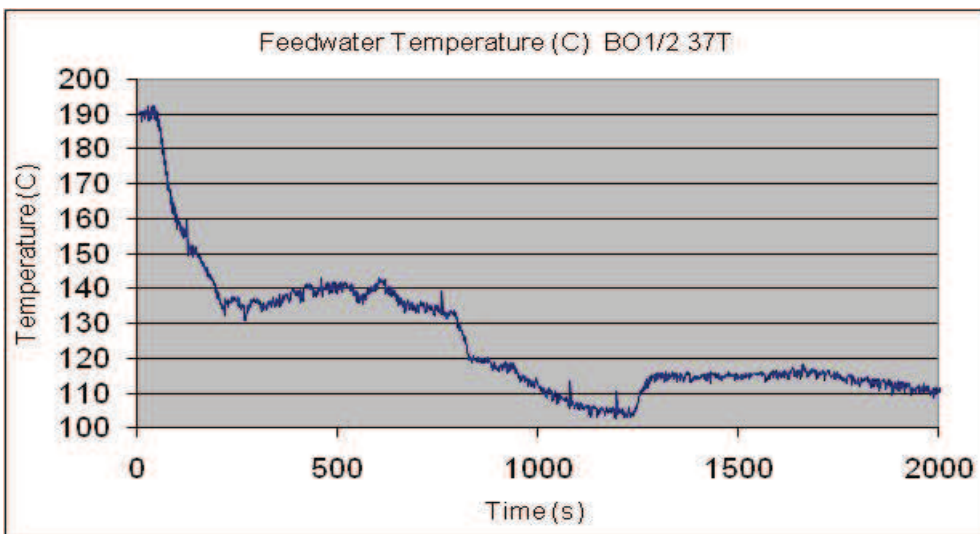


FIG 3-3. Boiler feedwater temperature boundary condition for test B9006.

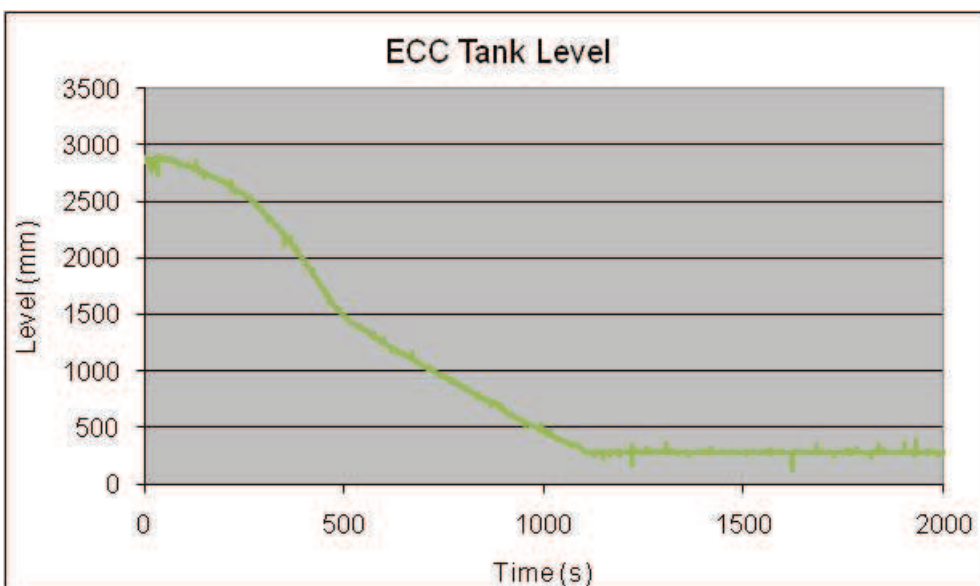


FIG.3-4. Measured ECC tank level for test B9006.

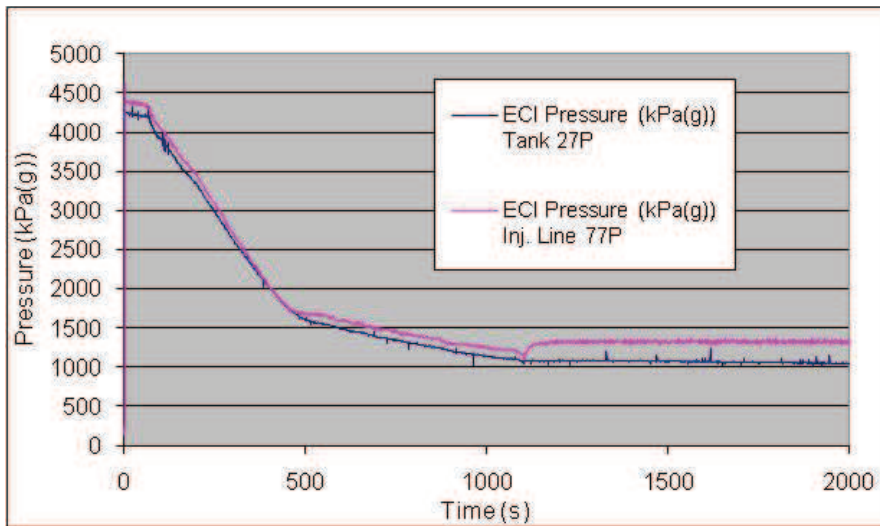


FIG. 3-5. ECC Tank pressure boundary condition for Test B9006.

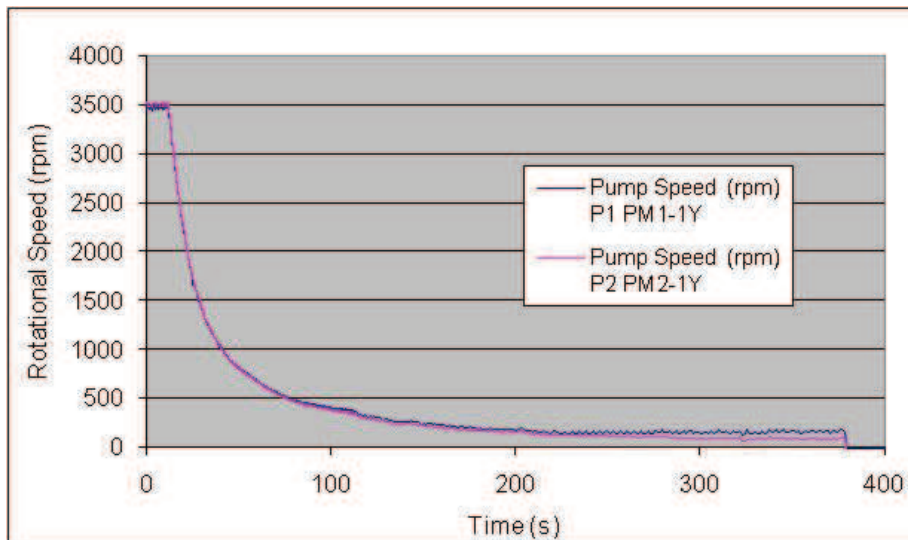


FIG 3-6. PHTS Pump speed boundary condition for Test B9006.

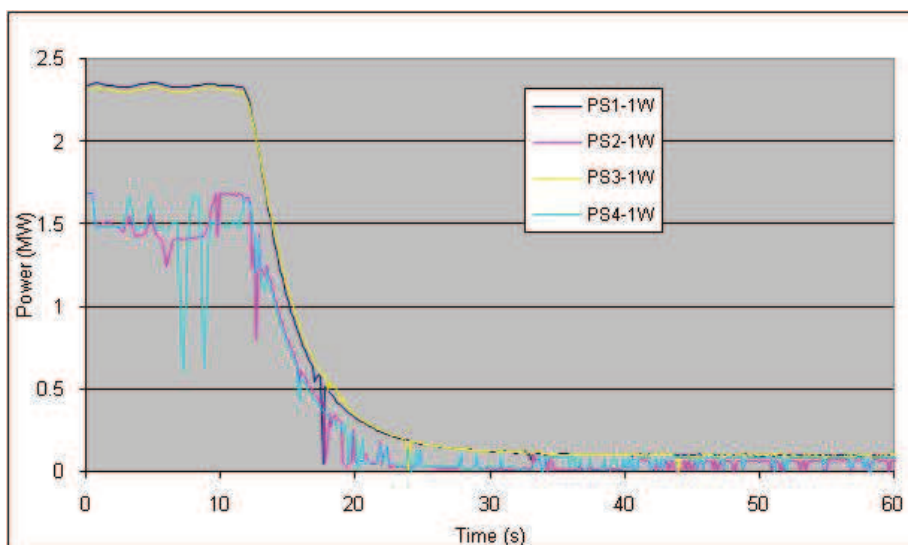


FIG. 3-7. Measured heated section power supply transient for Test B9006.

TABLE 3-2. CONSTANT BOUNDARY CONDITIONS FOR TEST B9802

Boiler drum pressure	kPa(g)	4508 (BO1)	4504 (BO2)
Feedwater flow rate	kg/s	2.10 (BO1)	2.00 (BO2)
Feedwater temperature	C	188.2	
PHTS pump speed	rpm	2987 (P1)	3002 (P2)

3.3. PARTICIPANTS' IDEALIZATIONS AND ASSUMPTIONS FOR STEADY STATE AND TRANSIENT CALCULATIONS

The following sections describe each participant's idealizations and assumptions. The idealization descriptions are based on the blind simulations (in most cases they were the same for the open calculation). Some individual discussions about steady state and transient results may be provided, and the steady state results are summarized at the end of this chapter in four tables (blind and open calculations for both tests). Note that the experimental values are slightly different for the blind and open calculation: The experimental values in the "blind calculation" tables are from the 60-s average pre-transient data files, given to the participants for the blind calculations, while the experimental values in the "open calculation" tables are taken from the first few seconds of the transient data file, provided to the participants for the open calculation. The differences are insignificant and give an indication of the actual variability in steady-state conditions prior to the transient.

CNE did not provide updated calculations for the open phase of this exercise, therefore, the "open calculation" tables show the same results as the "blind calculation" tables for CNE. Instead, they performed additional sensitivity cases, which are discussed in Appendix I. CNEA did not participate in the comparison for test B9802 in either the blind or open phase.

Most participant calculated acceptable values for all pressure, temperature and flow rate variables. Initial loop inventory was calculated within about 2% by all participants, except for KAERI, who calculated a high inventory by about 5%, because part of the surge-tank line was included in the calculation, and THU calculated a low inventory by about 8%, because their model did not include the "dead spaces" in the end-fitting simulators.

3.3.1 Atomic Energy of Canada Ltd — Canada

The primary circuit, secondary circuit, and ECI system (only for test B9006) were modelled in the simulations for RD-14M tests B9802 and B9006. All the simulations were performed using CATHENA 3.5d/Rev 2 on a Windows[®]-based PC cluster. The idealization of B9802 used 778 nodes, 790 links, 6 boundary conditions, 106 system models and 67 control models; the idealization of B9006 used 859 nodes, 873 links, 8 boundary conditions, 125 system models, 2 tank models, and 92 control models.

3.3.1.1 Primary system idealization

The RD-14M primary circuit consists of all piping connecting the headers, heated sections, steam generators, pumps, and pressurizer. The CATHENA idealization used to model the primary-side piping is shown in Fig. 3-8. Only one pass is shown for clarity.

In developing the primary-side idealization, the volume, length, flow area and elevation change of each CATHENA pipe component resembled, as closely as possible, the RD-14M

test facility. This ensured that the fluid transit time and hydrostatic pressure changes around the loop were represented accurately in the simulation.

The flow areas of complicated geometries, such as the end fittings, boiler plenums and primary pumps were determined by dividing the volume of the component by the flow path length. Loss coefficients used in this idealization were first derived from the geometry then adjusted appropriately using the flow and pressure-drop information from a number of RD-14M single-phase commissioning experiments as well as a recommended channel roughness.

The heat transfer models in the *GENeralized Heat Transfer Package* (GENHTP) were used to model all solid components in contact with the fluid. They were also used to account for heat transfer from the primary fluid to the pipe walls and from pipe walls to the environment, or in the case of the steam generator tubes, to the secondary side. Pipe radii (inner and outer) were used in defining the metal mass and heat transfer area in contact with the primary fluid.

Each heated section was modelled using a single pipe component divided into 12 equal length thermalhydraulic nodes. The 7-element FES bundle was represented by 3 "cylinder groups" to model heat transfer to the liquid and vapour phases under stratified flow conditions. The FES bundle was modelled using four radial regions (lower, middle, upper, and unheated FES) with a total of 12 radial nodes. This axial and radial nodalization is expected to provide adequate model convergence and is typical of the nodalizations applied in CANDU reactor calculations. The power distribution in the axial direction was assumed to be uniform in the CATHENA model.

3.3.1.2. Secondary system idealization

The secondary-side idealization used to simulate the RD-14M test facility is shown in FIG 3-9. This idealization includes the steam generators up to the steam nozzle and that part of the feed water line from the thermocouple location measuring the feed water temperature to the steam generator feed water inlets. The portion of the feed water lines upstream of this location was represented by flow and enthalpy boundary conditions. The secondary-side steam generator outlet pressures were modelled using pressure boundary conditions obtained from the boiler steam dome pressure measurements. Time-varying feed water flow rates, extracted from the experimental results, were imposed as flow boundary conditions.

Separator models were used to simulate liquid separation at the bottom of the steam drum, and steam separation in the spiral-arm separator at the top of the steam drum. Valve/orifice models were used to account for the orifice in the external downcomers and flow resistance through the hole in the longitudinal baffle box in the centre of the steam generators.

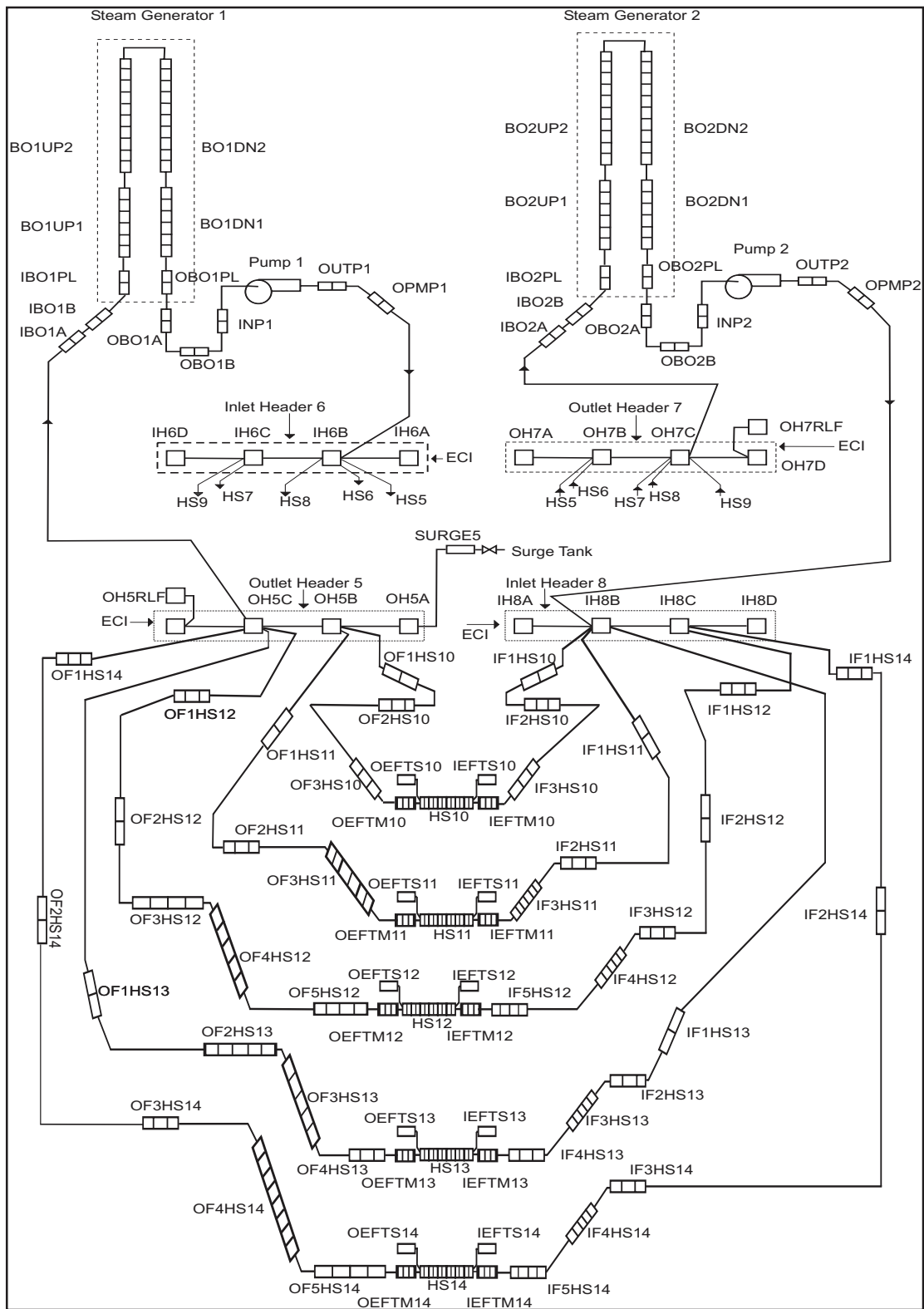


FIG. 3-8. CATHENA Idealization of primary side of the RD-14M facility.

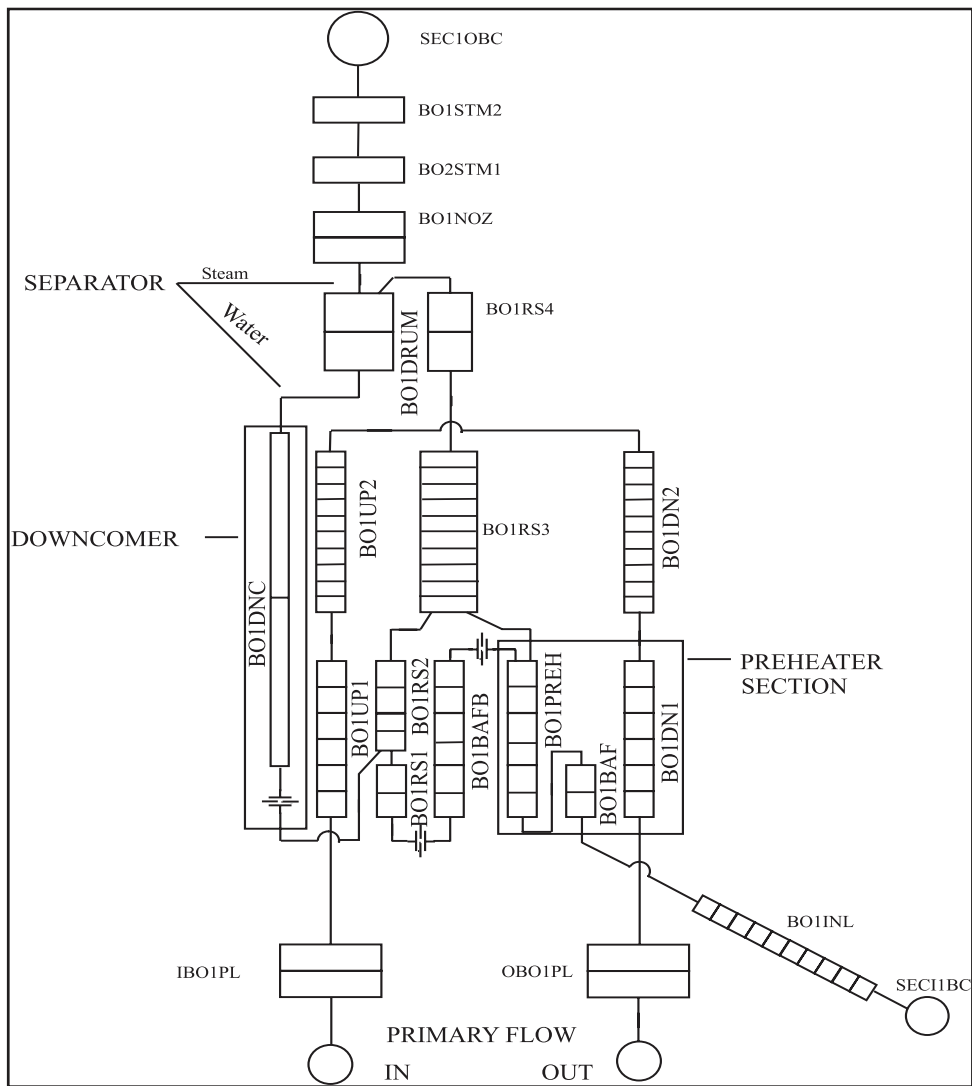


FIG. 3-9. CATHENA Idealization of secondary side of the RD-14M facility.

3.3.1.3. ECCS idealization

For RD-14M test B9006, both the high pressure ECC accumulator and low pressure ECC pumped system are modelled. The idealization for the ECC system is shown in FIG 3-10.

In the high pressure ECC phase, the tank model of CATHENA is used for the high pressure ECC tank TK2. The measured tank pressure is applied as a reservoir boundary condition connecting to the top of the tank model. The ECI tank isolation valves MV4-M7 opened when the loop pressure decreased below 6.1 MPa, while if the pressure of RD-14M test loop decreases below 4.3 Mpa, the ECC injection by the accumulator tank starts (this is controlled by a check valve model) and the water level in the accumulator tank begins to decrease. The high pressure injection valve (MV11) will later close automatically on indication of low level in the accumulator tank. This is modelled by tracking the cumulative water mass discharged from the accumulator tank. When the level in the accumulator tank reaches 10% of the initial level, the valve begins to close.

After the accumulator injection valve is closed, a low pressure ECC pump injection phase starts. The low pressure ECC pump (Pump 8) is modelled using user-defined pump characteristics.

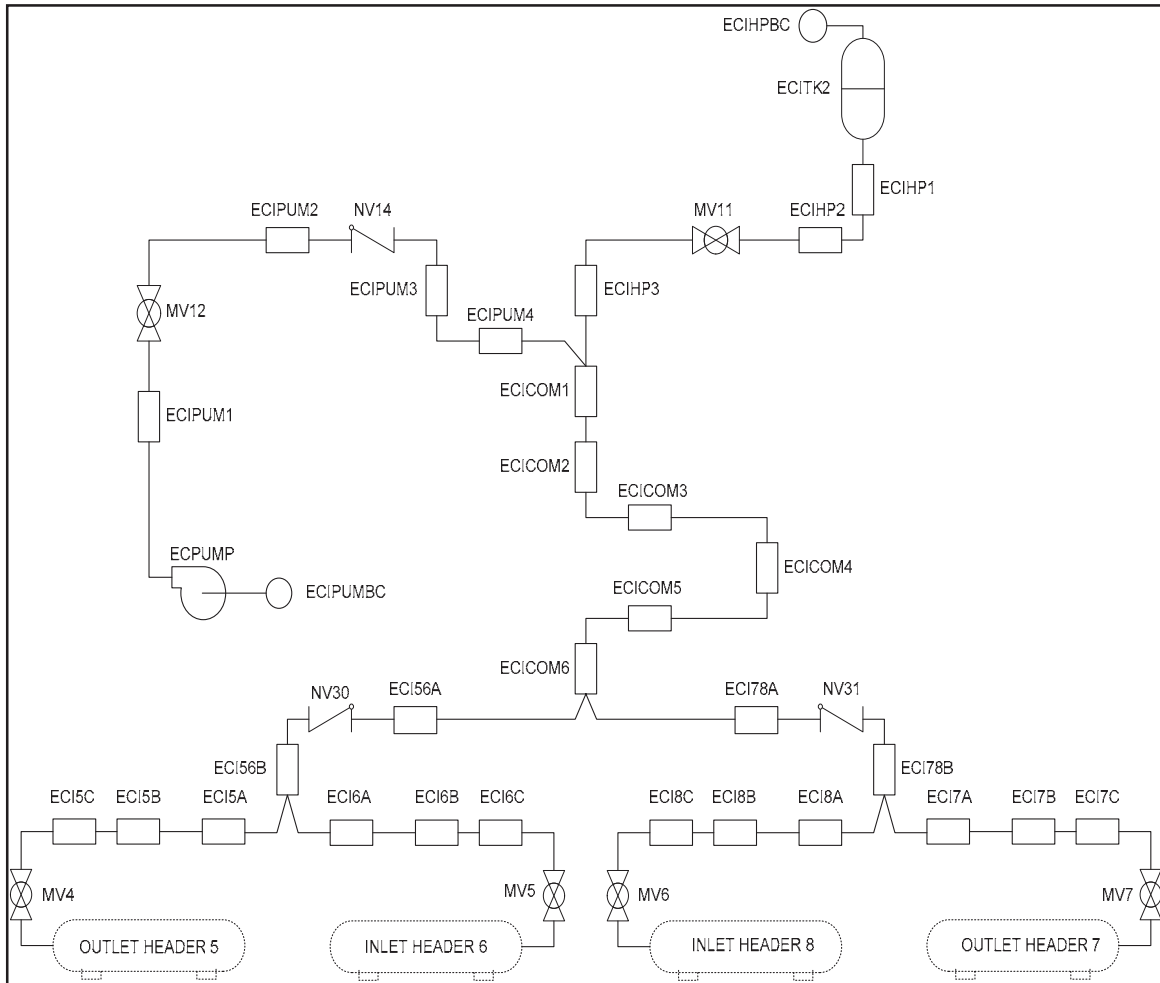


FIG 3-10. CATHENA idealization of ECC system for RD-14M facility.

3.3.1.4. Others

Some modelling specifications that are worth to note for test B9802 and/or B9006 simulations are summarized below:

- STM-GEN-CON' option is applied to the pipe components representing the steam generator primary side tubes to better predict condensation rates within the steam generators;
- In both steady state and transient runs, all known code biases in the code correlations were corrected. This is achieved through the use of an auxiliary file, which specifies all known code biases along with the methods to be used to correct them.

3.3.1.5. Steady state calculation

Steady state runs for all simulations were performed for a simulation time of 1000 s to establish steady-state conditions, and the steady-state conditions reached along the loop were carefully compared with the experimental data to ensure that the differences are acceptable.

3.3.1.6. *Modification from blind to open calculation*

The following changes were implemented between the blind and open calculations, mostly based on changes in the reference RD-14M idealization from 2004 to 2009 (AECL proprietary information):

- Changes to ECI piping, valve areas and discharge coefficients;
- Minor geometrical model, solid component properties, and nodalization changes;
- Changes in heat loss, piping sizes, and mixing options in pump inlet and outlets;
- Revised specification of two-phase multiplier in heated sections.

The following further changes were implemented to open calculations for sensitivity studies:

- For B9006 simulations, the heat transferred from the ECI tank wall to the upper region; noncondensable gas (N₂) during the ECI tank depressurization was modelled as a heat addition to tank top region (insignificant effect);
- The best estimate developing PDO option ‘DEV-PDO-2()’ was applied to the GENHTP models for 7-element FES pins (insignificant effect);
- Break discharge coefficients (for liquid and two-phase flow) was reduced by 15% from the default values (0.61 and 1.0) to 0.5185/0.85 to account for the fact that the pipe line downstream the break orifice bends down 90° in the RD-14M facility (significant effect, see Appendix I).

3.3.2 **Atomic Energy Regulatory Board — India**

The primary circuit, secondary circuit and ECI system are simulated using RELAP5/MOD 3.2. The total number of control volumes used in the model is 900 and total number junctions used are 973. The total number of control volumes considered in the primary, secondary and ECI are 684, 122 and 94 respectively.

3.3.2.1 *Primary system idealization*

The RD-14M primary side consists of all piping connecting the headers, heated sections, steam generators, pumps and Pressurizer. The idealization used to model the primary-side piping is shown in Figs 3–11 and 12.

In developing the primary-side idealization, the volume, length, flow area and elevation change of each RELAP5 pipe component resemble, as closely as possible, the RD-14M test facility. This ensures that the fluid transit time and hydrostatic pressure changes around the loop are accurately modelled. Frictional Losses were incorporated in the primary side as junction loss factors distributed over the entire loop. No loss data was available for the secondary side so standard ASTM Steel wall roughness values were used.

Each header was modelled as pipe component (PIPE) with five volumes except for Header 6 which has four volumes. The inlet header is connected to inlet feeders by single junctions (SNGLJUN). Header end cap was modelled for HDR 7 and break orifice was modelled on header 8 for both the tests B9006 and B9802.

Each feeder is modelled as pipe component (PIPE) having either thirteen or fourteen volumes. The orifices were modelled as junctions with abrupt area change and appropriate loss coefficients. All other junctions use the smooth area change model. The inlet feeders are connected to the corresponding inlet end fittings by single junction (SNGLJUN).

Each of the inlet and outlet end fitting is split into one pipe and one single volume component. In inlet end fitting, coolant enters the shield plug via holes on the liner tube, then either by the annulus outside the shield plug (stagnant volume) or through the shield-plug holes to the flow tube. The reverse flow path is followed in the outlet end fitting. A large volume of coolant in the dead space near the shield plug is normally stagnant. This dead space is represented by a single volume component whose volume is adjusted to match the total fluid volume of 5 L in the actual facility. The outlet end fitting is connected to outlet feeder by single junction component.

Each heated section is modelled as a pipe component of sixteen volumes with the middle twelve corresponding to the twelve segments of FES. The cross-sectional flow area was calculated by subtracting the cross-sectional area of the heater pins from the area of the channel.

The fuel element simulators are simulated as heat structure components having 23 axial heat structures and 5 radial node points (Figs 3-13 and 14). The heated (475mm long) and unheated (20 mm long) portions of FES are modelled alternately as shown in Fig. 3. Symmetric boundary condition is provided for the left boundary (fuel centerline). The right boundary of each heat structure is linked to the corresponding hydrodynamic volume of heated section. The thermo-physical data for each material used in the pin is provided in tabular format as a function of temperature (using general tables in RELAP5). Also the power of the heated section (HS) is provided in tabular format. Heat is generated in the second radial interval only (Inconel 625). The axial distribution of power in the heated section is uniform.

For test B9006, in HS7 and HS12 all seven FESs are modelled independently as heat structures and for other heated sections the pins are clubbed and modelled as a single heat structure with appropriate surface area. For input deck of test B9006, the data for HS7 (FES#5 disconnected) and HS 12 (FES#3 disconnected) are modified appropriately.

For test B9802, in HS7, HS12, HS 13 all seven FESs are modelled independently as heat structures and for other heated sections the pins are clubbed and modelled as a single heat structure with appropriate surface area. For input deck of test B9802, the data for HS7 (FES#5 disconnected), HS 12 (FES#7 disconnected) and HS13 (FES#7 disconnected) are modified appropriately.

The surge tank, its associated piping and heater of surge tank are modelled. The surge tank is protected from over pressure by connecting the tank to atmosphere (TMDPVOL) by a trip valve (TRPVLV) with required trip logic. The heater is turned on or off depending on the system pressure. The primary pressure is controlled at HDR5 with the desired value (10.129125 MPa for test B9006 and 10.129101 MPa for test B9802).

In each loop, the above header piping is modelled as three PIPE components. The first pipe connects the outlet header to SG inlet plenum; the second connects SG outlet plenum to the inlet of pump component, and the third pipe connects the pump outlet to inlet header.

The steam generator inlet and outlet plenum are modelled as BRANCH components. In test B9006, for each steam generator the 42 U-tubes (2 tubes are plugged) were modelled as one “average” pipe and one individual pipe to correctly reflect the geometry taking into account the position of measurement probes. In test B9802, the 39 U-tubes (5 tubes plugged) were modelled as one “average” pipe and one individual pipe in boiler1 and the 40 U-tubes (4 tubes plugged) are modelled as one “average” pipe and one individual pipe in boiler2. The height is equal to the length for vertical portions. U-bend part is modelled as volumes of the pipe, one

horizontal and other two making 18 degrees with vertical as shown in Fig 2. The tube walls are modelled as heat structures with left boundary as primary side hydrodynamic volume and right boundary as boiler secondary side hydrodynamic volumes. The plugged tube wall is also modelled as heat structure with the inner surface as insulated boundary condition and outer surface as convective boundary condition. The boiler inlet and outlet plenum are connected to SG tubes by single junctions.

The primary pumps are modelled as pump components in RELAP. The pump data is taken from RD-14M description report [2]. The rated speed, rated head, rated torque, initial pump speed, rated density, rated flow etc are provided in the pump model. The homologous head, torque and two phase head, torque difference and two phase degradation data for the pump is provided. For test B9006, pump coast down is simulated through a time vs. pump velocity lookup table as reported during the transient. For test B9802, the pump P1 trip logic is modelled as a function of time by use of RELAP specific trip parameters.

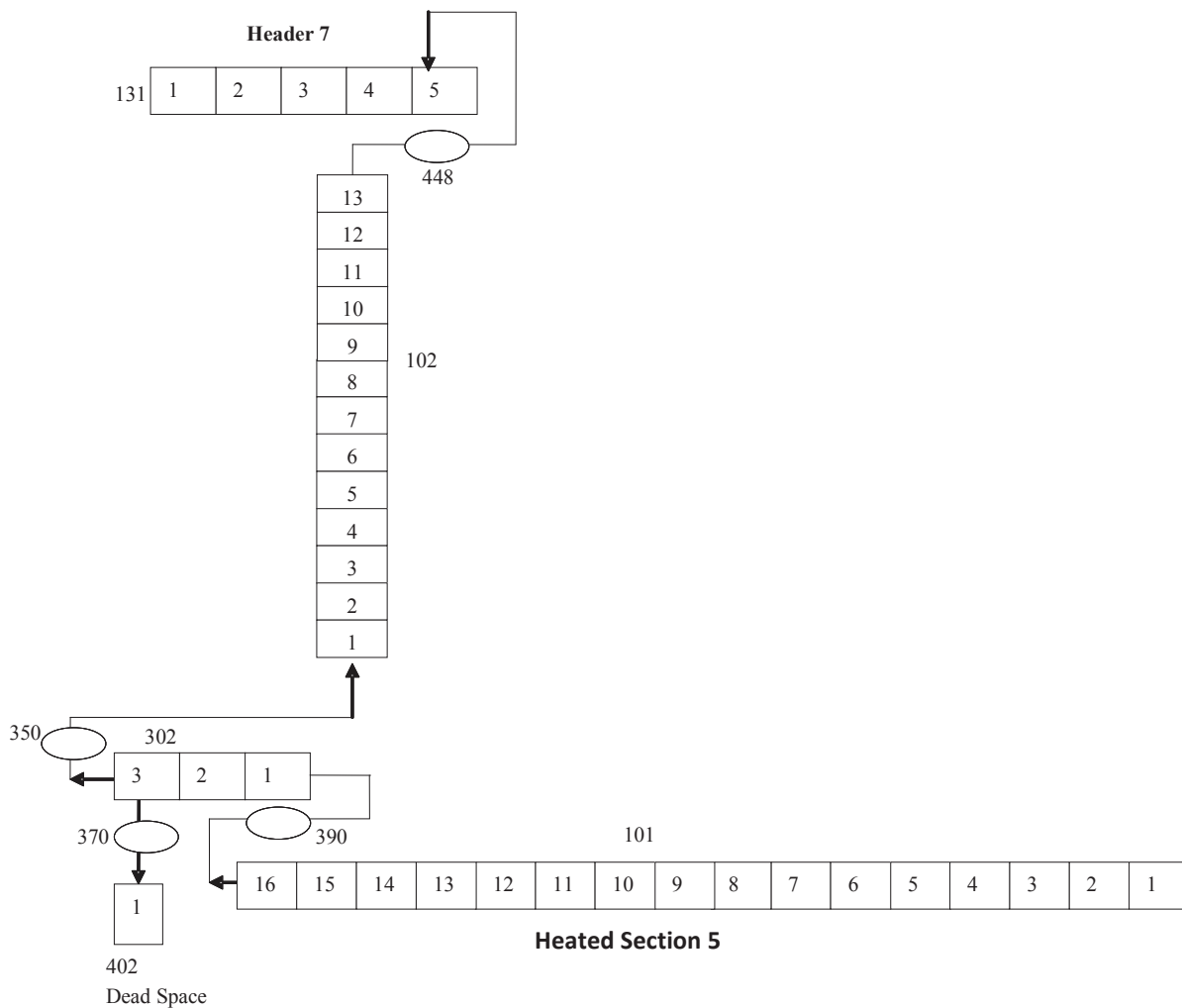


FIG.3-11. Nodalization of primary circuit (below header piping).

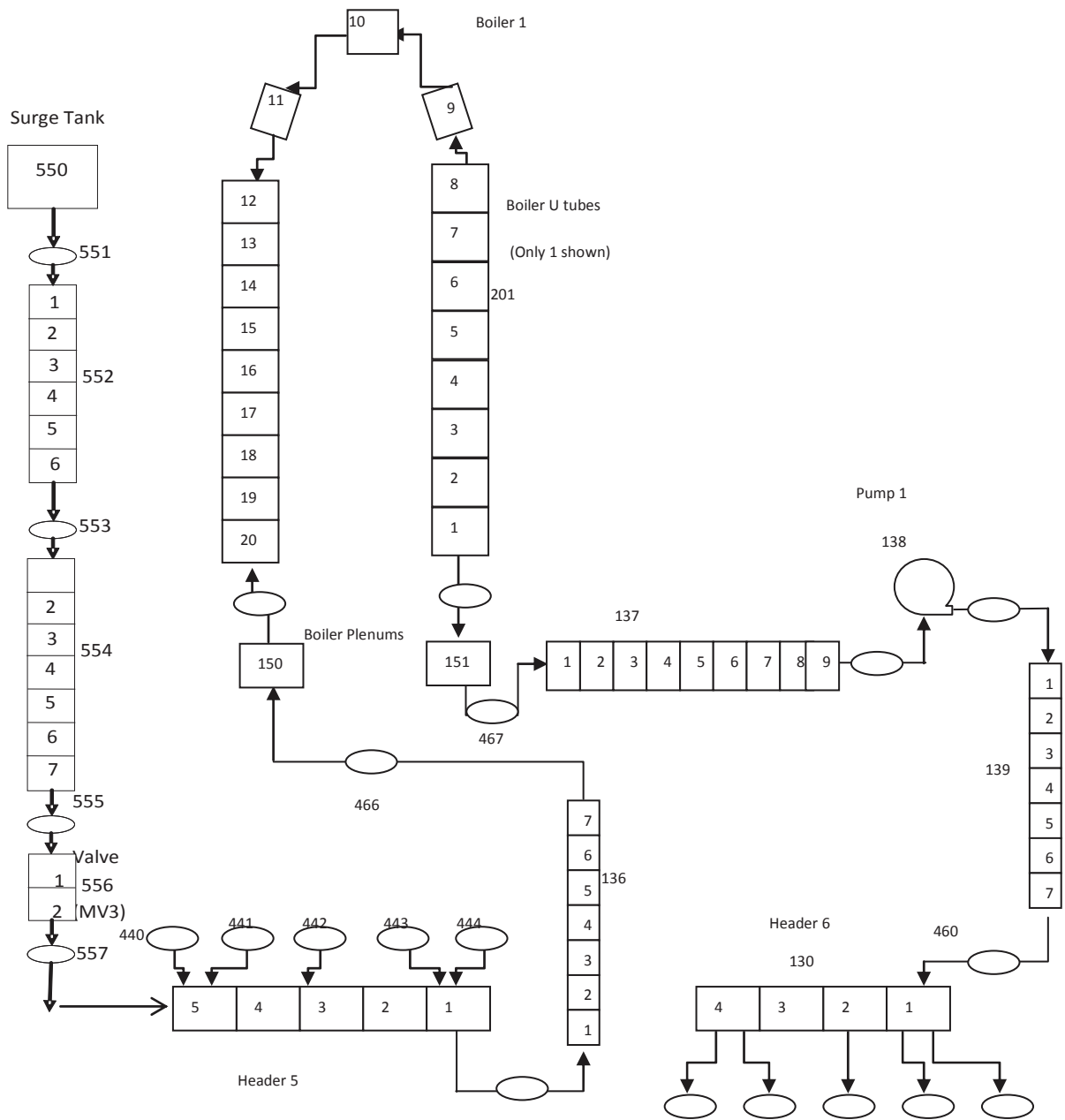


FIG 3-12. Nodalization of primary circuit (above header piping).

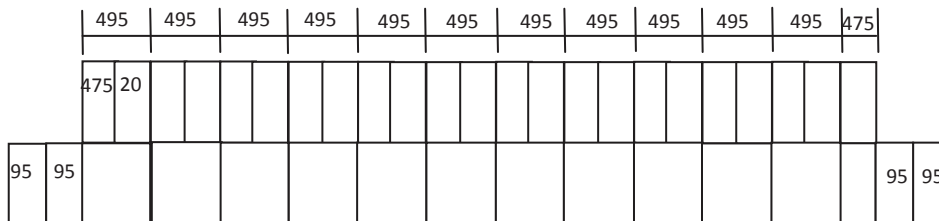
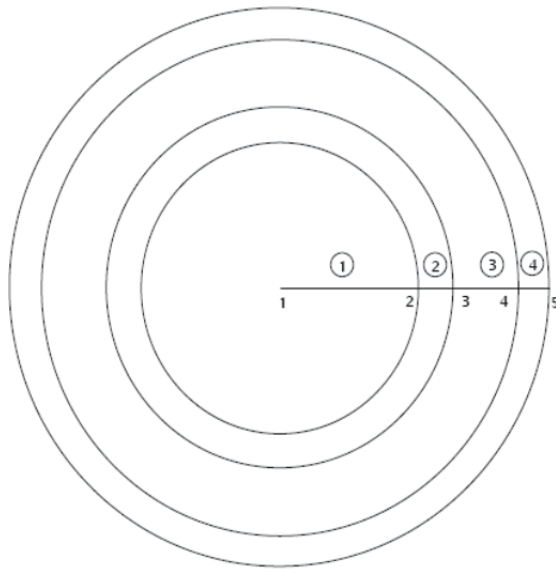


FIG.3-13. Heated section and FES.



Interval Number	Mat ID	Name
1	1	MgO
2	2	Inconel 625
3	3	Boron Nitrite
4	4	SS304
Node no	Radius (mm)	
1	0.0	
2	3.5159	
3	3.8241	
4	5.9795	
5	6.5740	

FIG. 3-14. Fuel element simulator (heat structure) radial nodes.

3.3.2.2. Secondary system idealization

The secondary parameters such as feed water flow, temperature and steam drum pressure are simulated using boundary conditions. The secondary side of the steam generators is simulated as follows:

Each steam generator is modelled as three vertical pipe components capped by a branch component (Fig. 3-15). A simple separator component is connected to the outlet of the branch via a pipe component. A single volume acting as the top of steam drum is connected to the top of the separator. A pipe with four control volumes, which served as the down comer, is attached to the water outlet junction of separator via a pipe having 2 control volumes.

One of the three vertical pipes represents the vertical baffle and the other two represent the feed-water side and down comer side of the steam generators. This nodalization is chosen so as to correctly model the large thermal inertia introduced by the vertical baffle on the secondary side of SG. Heat transfer area between the baffle and rest of the boiler is represented as rectangular heat structure having identical dimensions as the baffle wall.

The inter connections between baffle and feed water side and down comer side of boiler is modelled as single junctions. The interconnections between feed water (FW) and down comer (DC) side of SG are represented by single junctions also.

The source and sink for SG are modelled as time dependent volume (TDV) with temperature and pressure as boundary condition respectively. The source TDV is connected to boiler feed water side pipe component by time dependent junction. The sink TDV is connected to steam drum (SD) top by single junction. Feed water mass flow rate and temperature are considered as boundary condition.

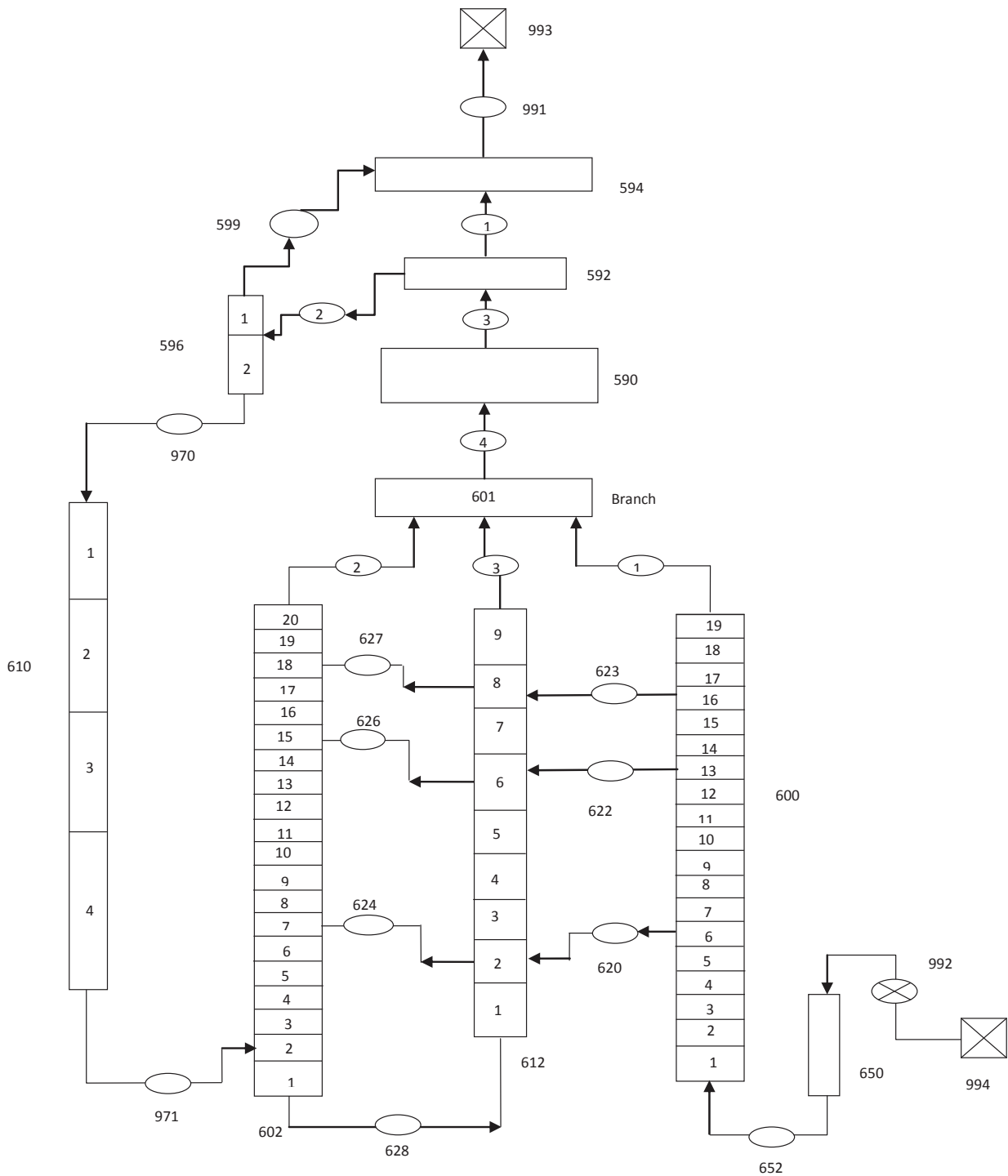


FIG. 3-15. Nodalization of secondary side of boiler 1 (boiler 2 is similar).

3.3.2.3 ECCS idealization

For test B9006, both the high pressure accumulator and low pressure pumped system are modelled. The nodalisation scheme for the ECI system is shown in Fig. 3-16.

The ECI tank (TK2) is modelled as RELAP specific accumulator (ACCUM) component. The tank volume, volume of water in the tank, volume of nitrogen, level of water, elevation of injection point, pressure, temperature, the elevation of tank etc are provided in the input deck.

The ECI piping is modelled as RELAP pipe (PIPE) and branch (BRANCH) components. The line from ECI tank to isolation valve MV11 is modelled as pipe component (502). MV 11 is modelled as valve component. Orifice (OR25) in the common line is modelled as junction of the pipe 504 with the required loss coefficient and junction area. The common line modelled as branch component (506) which divides the ECI flow to two paths. One path goes to header 7 and 8 and the other goes to header 5 and 6. The non-return valves (NV 30 and 31) in the two paths are modelled as check valve (507 and 509) to prevent reverse flows. The orifices in the ECI line connecting to different headers are modelled as junctions with required loss coefficients and flow area. The ECI valves (MV4, 5, 6 and 7) are modelled as trip valves. They open when ECI water needs to be injected to the system and get closed when ECI system needs isolation.

The distilled water tanks (TK 4 and 9) are modelled as time dependent volume (535) with required temperature as boundary condition. The line connecting pump P8 to main ECI line is modelled as pipe components. The flow resistance of line connecting from the outlet of P8 to OR-25 is also modelled by providing loss coefficients in the junctions of the pipes. The non-return valve NV14 is modelled as check valve. P8 is simulated using time-dependent junction (536) whose flow characteristic is given as functions of downstream discharge pressure.

3.3.2.4 *Others*

Heat loss in the primary as well as secondary system is modelled. The insulation thickness is taken from the RD14M design description report. Wherever the thickness is not available, 76 mm is assumed in the simulation. The RELAP5 inbuilt heat transfer package is used on both the inside and outside of the heat structure. The sink temperature is fixed at 296 K (230C).

The break orifice in both the tests is modelled as single junction (144) connecting header 8 to blowdown line (145). The junction area signifies the break area. The ball valve is modelled as trip valve (146) and connects the blow down line to atmosphere, which is modelled as time dependent volume (155).

3.3.2.5 *Steady state calculation*

Steady state calculations were carried out for both the tests separately. Steady state conditions were assumed for different component as initial conditions in performing the steady state calculations. Initial conditions for all the nodes of a particular component were assumed as constant. For B9802, the pump speed was reduced to achieve a reduction in the pump discharge flowrate and hence increase in the boiler inlet fluid temperature. The steady state calculations for both B9006 and B9802 tests were carried out up to 2000 seconds, however, it was found that the steady state conditions were achieved in first 1000 seconds. Steady state calculations for both the blind and open calculations were the same.

3.3.2.6 *Modification from blind to open calculation*

For the test B9006, the accumulator inventory has been adjusted based on the data provided in the open calculations. Accumulator isolation level also readjusted as per the available data. This has resulted in less amount of high pressure fluid injection in comparison with the blind calculations.

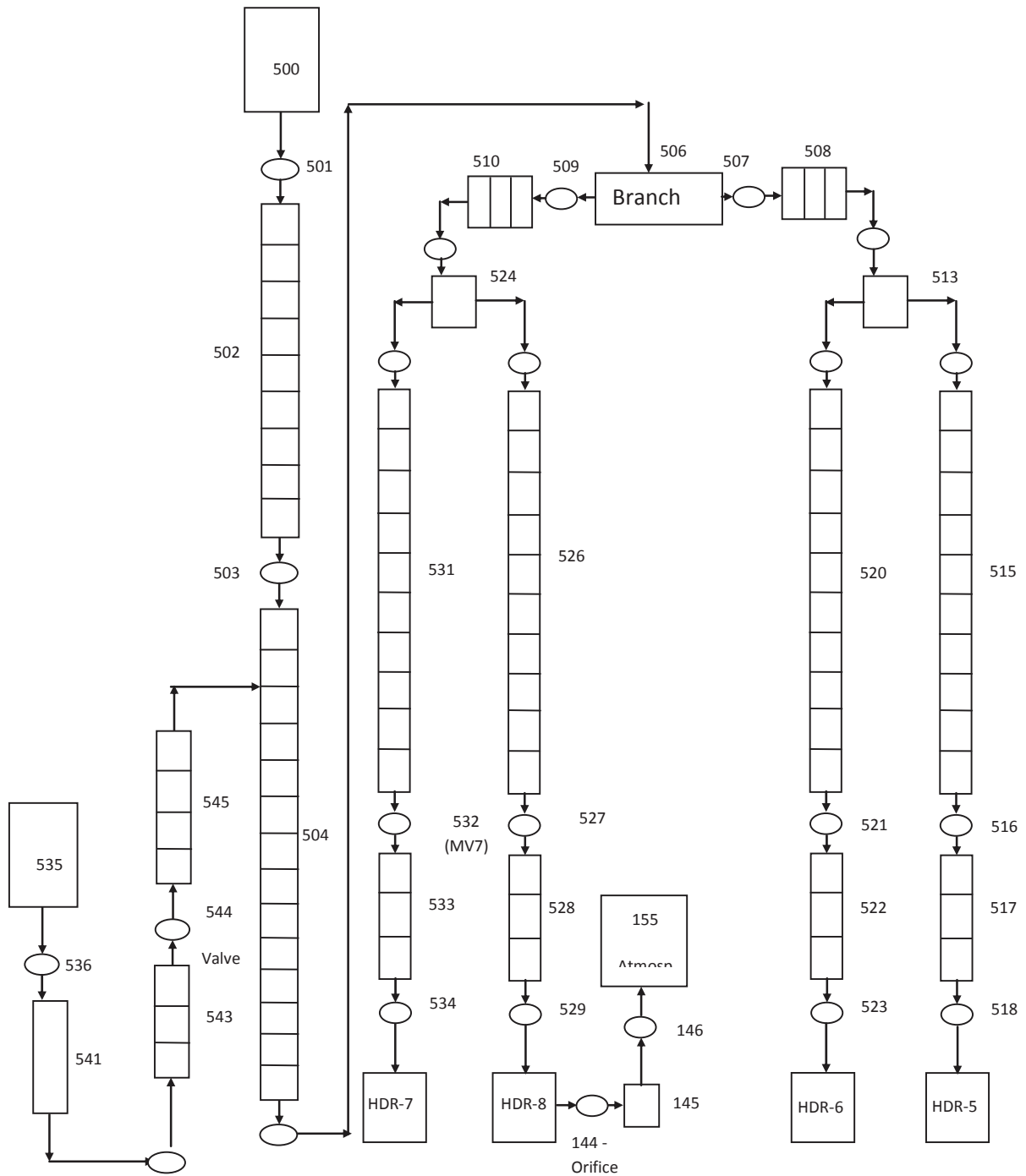


FIG. 3-16. Nodalization of ECI system and bowdown system.

For the test B9802, the break discharge rate is adjusted by modifying the break discharge coefficients. RELAP5 critical discharge model enables to input discharge coefficients for subcooled, saturated and superheated conditions separately. The discharge coefficients were adjusted to 0.7, 0.99 and 1.22 respectively instead of the default value.

3.3.3 Centrala Nucleara Electrica — Romania

The calculations were performed using the computer code CATHENA MOD 3.5d/Rev1 on an Intel IV (3GHz) Windows XP machine.

The CATHENA idealization used to simulate the RD-14M tests consisted of 802 nodes, 816 links and 173 wall heat transfer models, representing primary side, secondary side, ECC and control models. Even though the ECC was not requested for test B9802, the same model was included in the overall model but the ECC functionality was inhibited.

3.3.3.1 *Primary side idealization*

The idealization used to model the primary side piping is shown in Figures 3–17 to 3–19. The RD-14M primary side consists of all piping connecting the headers, heated sections, boilers, pumps and pressurizer (surge tank). The surge tank was included for the steady state calculations but it is isolated during the transients at the specified moments of time as presented by AECL in the event sequences.

Heated sections were simulated using a single pipe component with 12 equal length axial nodes. The internal capability of CATHENA code was used to simulate the fuel rods. The 7 elements bundle was represented through the ‘7ELMT’ option considering three cylinder groups. In each of the two experiments proposed to be simulated, two or three of the seven heated elements were disconnected in different heated sections. In experiment B9006, FES#5 in heated section 7 and FES#3 in heated section 12 were disconnected while in experiment B9802, FES#5 in heated section 7, FES#7 in heated section 12 and FES#7 in heated section 13 were disconnected. In the GENHTP heat transfer models for these heated sections, the cylinder group including the unpowered pin was divided into two cylinder groups. One cylinder group with zero power assigned was defined to model the unpowered pin. Another group was used to model the powered pins.

In developing the primary side idealization, the length, flow area and the elevation change of each component was calculated based on the available information.

Since CATHENA is a two fluid code, horizontal and vertical sections of piping were not combined as one inclined pipe component, unless the respective sections were very short. The main reason for this segregation was the fact that the flow regime in each is quite different. Sections of pipe that were inclined were combined to simplify the idealization. The feeder geometry for pass 1 is presented in Fig. 3–17. The idealization is similar for the other pass but it was not included for simplicity. Since the different pipes are differently inclined, this was also tried to be shown in the figure.

The reactor headers are large longitudinal manifolds, which connect the large pipes from/to the pumps, boilers and to five parallel fuel channels via feeders. There are four headers in the RD-14M loop. Each pair of inlet and outlet headers connects five channels. The headers idealization is presented in Fig. 3-18 showing all the connections for each individual header. The nodalization is similar for the other core pass but again it was not included for simplicity.

The “above header” idealization shows the primary side of the boilers and associated connections. Even the geometric characteristics of the boilers tubes are identical for both cases, because the real number of boiler tubes is different in the two tests (42 tubes for each boiler for test B9006 and 39 respectively 40 tubes for test B9802) the number has been changed accordingly for each model.

The inlet and outlet pumps nodalization and their connections are identically used in both tests and they are shown in the Fig. 3-18. The pumps were modelled considering the design pump speed and the test-measured speed that was introduced accordingly with the data provided during the simulated transients.

The heat transfer models in the GENeralized Heat Transfer Package (GENHTP) were used to model solid components that are in contact with the fluid (H₂O). They also account for the heat transfer from the primary fluid to the pipe walls, from primary side to the secondary side and from the pipes to the environment. The thermal properties used for the piping materials were obtained from the internally stored temperature-dependent properties of the CATHENA code except for the fuel properties that have been included based on the information provided. Heat losses to the environment were modelled by applying heat transfer coefficients based on the values presented in reference documentation. A reference temperature of 20°C to the outside components was considered in each model for the base case. The temperature was changed accordingly for the sensitivity cases.

A mixed flow regime was specified at the end fittings, the primary pumps and partially for the secondary side of the boilers using the 'FIX-MIXED' option. The 'STM-GEN-CON' option is applied to the pipe components representing the steam generator primary side tubes.

3.3.3.2 *Secondary side idealization*

The idealization of the secondary side is presented in Fig. 3-19 and includes part of the feedwater system, boilers and part of the steam line. The feedwater part of the circuit is represented by flow and enthalpy boundary conditions but also includes the line from the thermocouple location that is used to measure the feedwater temperature. The steam line includes the line up to the steam nozzle. The secondary side boilers outlet pressure were modelled using pressure boundary conditions obtained from the experimental data provided. Since the data presented for each boiler is different, separate conditions were imposed as presented.

3.3.3.3 *Emergency core cooling (ECC) idealization*

The idealization of the ECC system is presented in Fig. 3-20. The work done includes idealization of both high and low pressure stages. The high pressure stage was simulated by considering the gas tank depressurization. The switch from the high pressure to low pressure was simulated based on the high pressure tank water volume inventory depletion and closing respectively opening of a low pressure isolation valve. Based on the discussions during the meetings, the low pressure ECC stage was simulated by considering a pressure boundary condition instead of including effectively a pump model.

3.3.3.4 *System control models*

System control models have been used to control the opening of the break, surge tank isolation, heated section power rundown, pump speed rundown, feedwater flow control, feedwater temperature and boilers secondary side pressure.

In both tests, the power was reduced to low values at different moments during the transient. For test B9006, the data provided was included in the model and applied accordingly in order to simulate the power reduction. For test B9802, the power trip was determined by maximum fuel element simulator temperature. For this test, a supplementary model was included in order to evaluate the maximum fuel sheath temperature. Once this parameter increased over 600°C, the power reduction was initiated. Following high temperature trip initiation, the power reduction as per test data was imposed in the transient.

For each test, pump rundown, secondary side pressure and feedwater flow have been extracted from experimental data provided.

The Henry-Fauske discharge model was used to simulate the break. The default parameters available in CATHENA code have been considered for discharge coefficients.

The time interval to isolate the surge tank was assumed to be 0.1 seconds.

For test B9006, opening of the four ECC isolation valves and the switch from high pressure injection to low pressure injection have been simulated also using control models based on ECC tank inventory depletion. Opening and closing of the valves in the ECC part of the circuit was considered within 1.0 seconds time interval.

3.3.3.5 *Simulation procedure and steady state calculations*

For each test, the respective model was run as a transient consisting of two parts.

The first part was assimilated to the steady state condition. For this part of the run, all the data were imposed constant (power, pump speed, feedwater flow, boilers pressure) based on the steady state data provided. The same steady state conditions were maintained for at least 100 seconds before the transient condition were imposed. For the second part of the transient, the boundary conditions that have been provided were included as boundary conditions as it was mentioned above.

For the steady state part of each test, the CATHENA code was run for about 990 seconds, in such a way that the break opening to be assimilated with time 1000 seconds from the beginning of the run. During the time interval between about 990 seconds and 1000 seconds, the surge tank was also isolated according to the time data presented. For example, for test B9006, the break is initiated at 11.0 seconds from the start of the data acquisition. The surge tank was isolated at 6.0 seconds from the start of the data acquisition. Considering these moments, the test boundary conditions provided were included starting at 989 seconds for the run. Five seconds later (at 994 s from the beginning of the transient), the surge tank was isolated and at 1000 seconds, the break was initiated. However, the results have been presented considering as time zero the moment of time when the boundary conditions were started to be modified (i. e. time 989 seconds for the case presented).

As presented above, a separate set of steady state conditions were obtained for each test (base case). The conditions obtained at the end of the steady state imposed period (about 990 seconds for each simulation) are presented in separate tables.

3.3.3.6 *Modifications from blind to open calculations*

The same nodalization used in the blind calculation was also used for the open calculation tests (sensitivity cases).

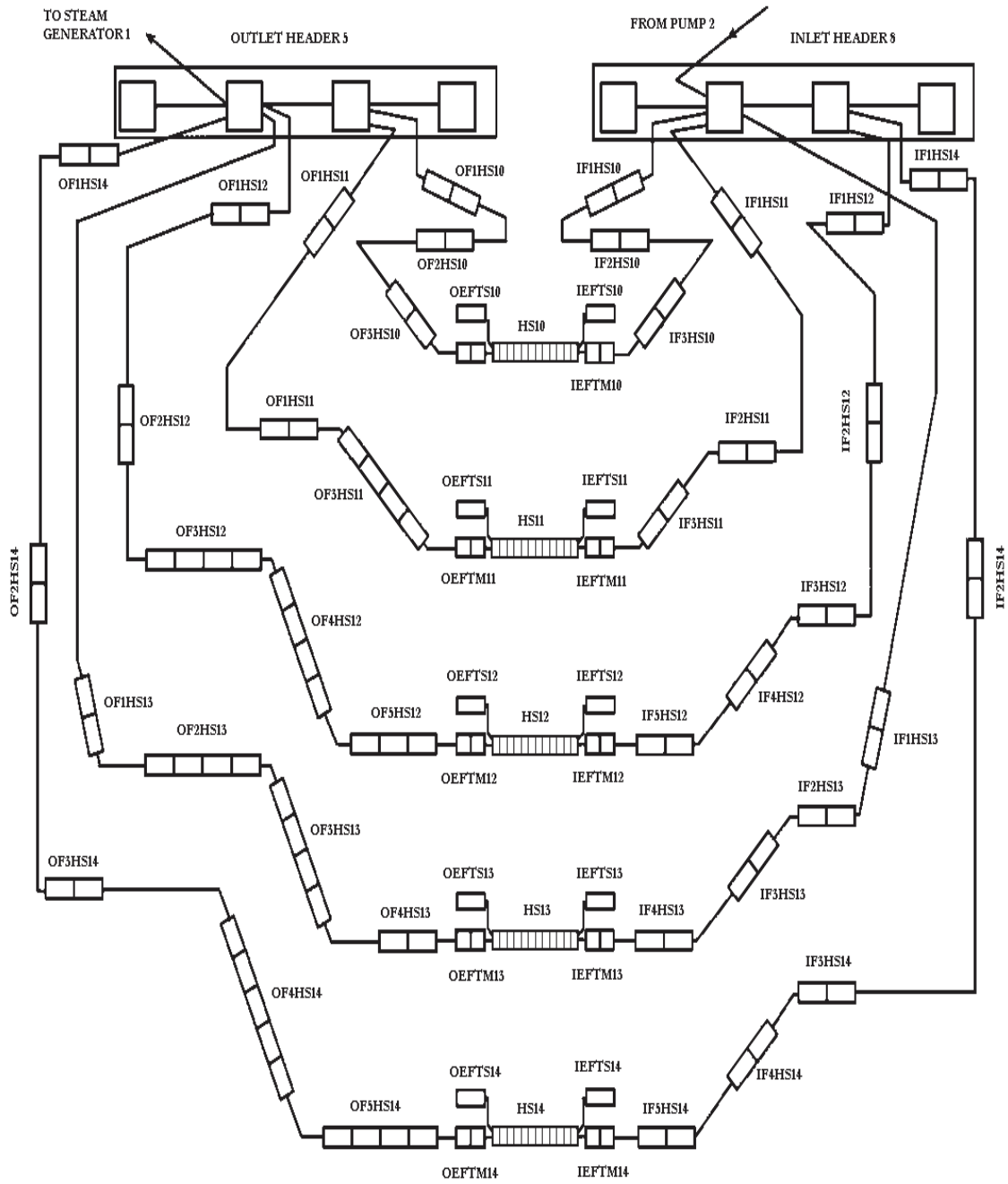


FIG. 3-17. CATHENA idealization – Primary system, below headers.

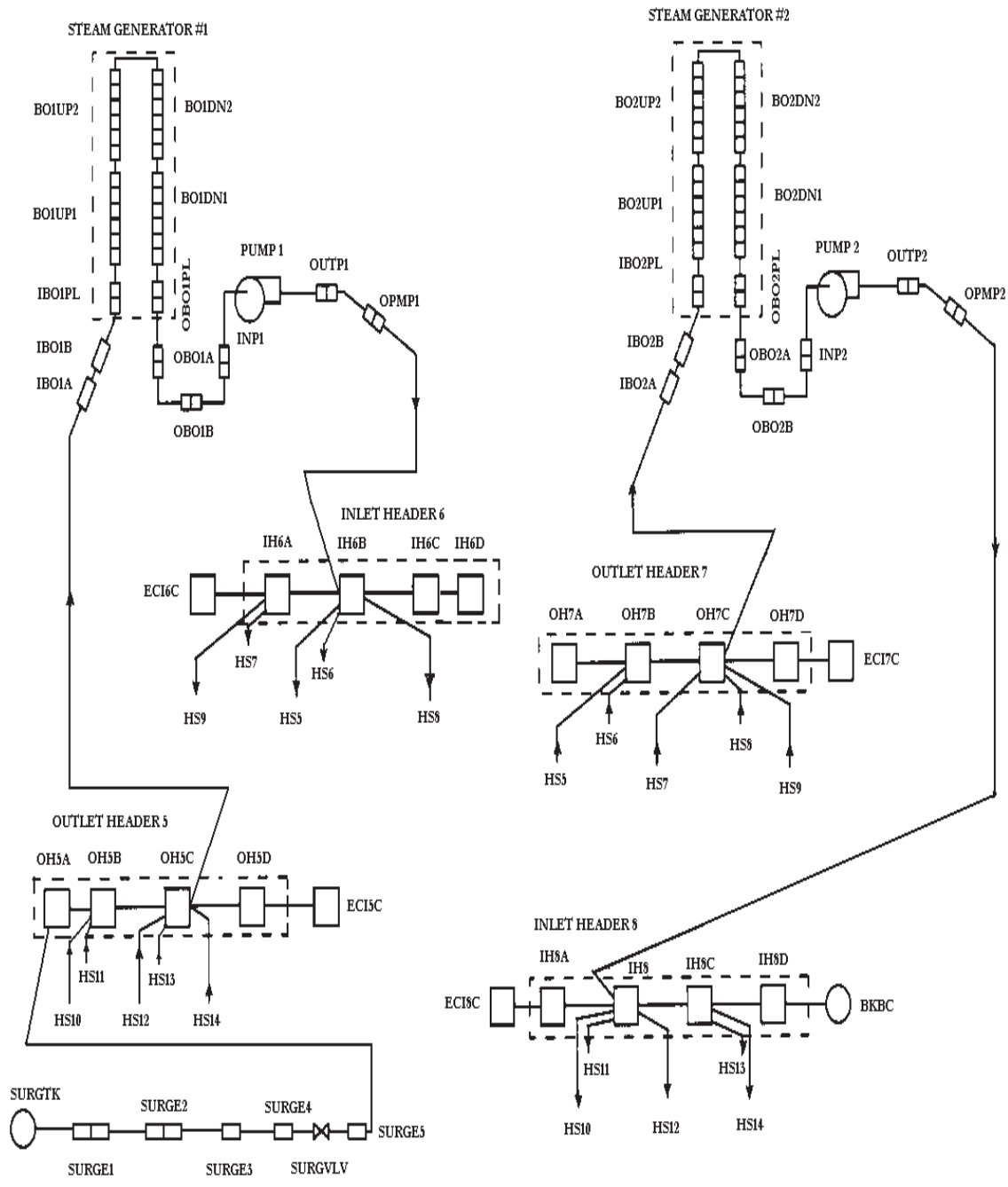


FIG. 3-18. CATHENA idealization – Primary system, above headers.

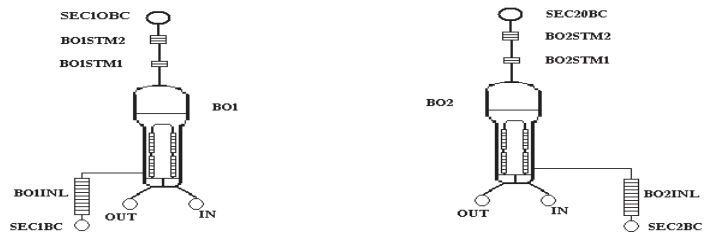


FIG. 3-19. CATHENA idealization – Secondary side and boilers.

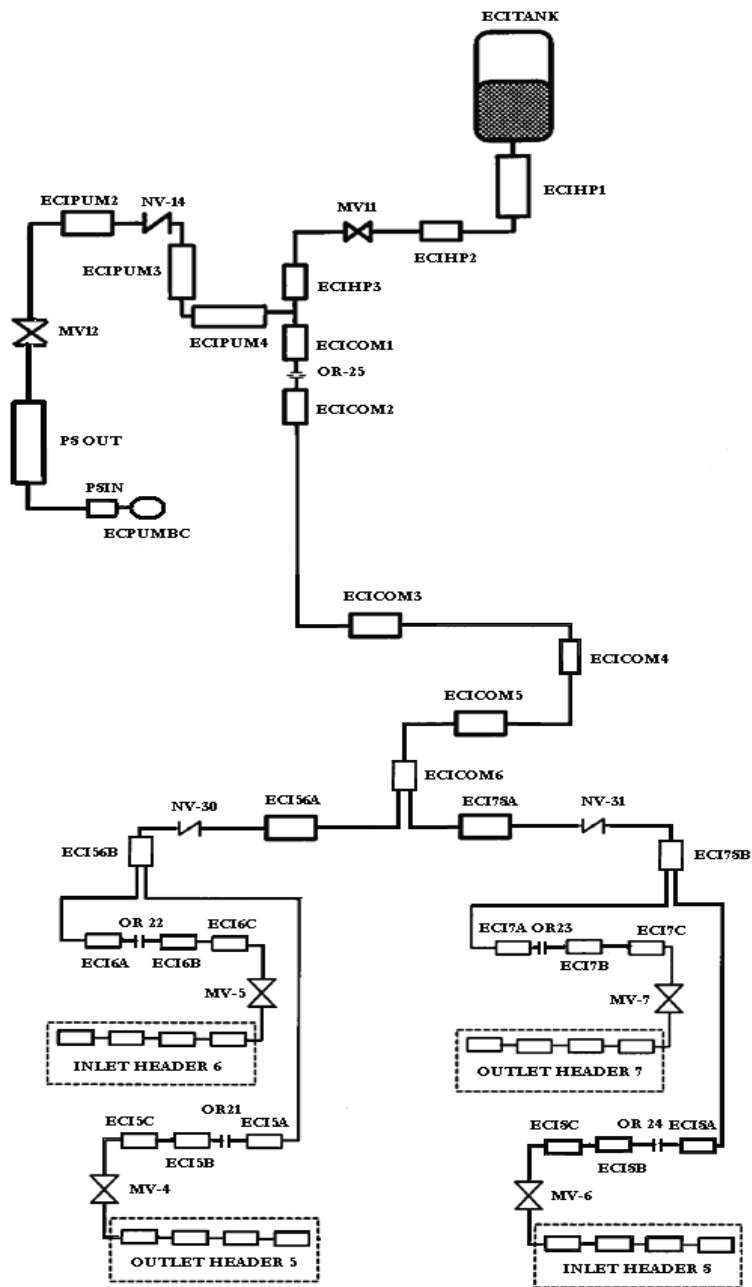


FIG. 3-20. CATHENA idealization – emergency core cooling.

3.3.4. Comisión Nacional de Energía Atómica — Argentina

Cathena code (Version WINDOWS/NT:- CATHENA (MOD-3.5c/Rev 0) - 16/06/1999) was used to simulate test B9006.

The CATHENA idealizations of the RD-14M facility (Primary and Secondary Side and Emergency Core Cooling System) are shown in Figures below and some of its relevant dimensions are summarized in the Table 3–3.

TABLE 3-3. MAIN DIMENSIONS OF CATHENA CODE NODALIZATION

No	Quantity	Value	Notes
1	Minimum time step [s]	0.0001	
2	Maximum time step [s]	0.1	
3	Total number of hydraulic nodes	481	
4	Total Number of links	496	
5	Numbers of axial nodes for each fuel elements simulator	12	
6	Numbers of nodes for each header	4	
7	Wall model	154	
8	Fluid-wall heat transfer surfaces	812	
9	Primary system volume. [m ³]	1.027	excluding the pressurizer

3.3.4.1 Primary system idealization

The RD-14M primary side consists of all piping connecting the headers, heated sections, steam generators, pumps and pressurizer (the idealization is shown in Fig. 3–21).

The volume, length, flow area, elevation, heat transfer areas, loss coefficients, etc. were taken from Reference [2] and modelled as close as possible to the loop.

The flow area of complicated geometries, such as the end fittings, boiler plenums and primary pumps were determined by dividing the volume of the component by the flow path length. The total volume of the primary-side idealization, excluding the pressurized, has been compared with the volume of the facility and found to be a difference of 1.66 %

The heat transfer models in the GENeralized Heat Transfer Package (GENHTP) were used to model solid components in contact with the fluid. They also account for the heat transfer from the primary fluid to the pipe walls and from pipe walls to the environment, or in the case of the steam generator tubes, to the secondary side. Pipe radii (inner and outer) were used in defining the metal mass and heat transfer area in contact with the primary fluid. The thermal properties used for the piping materials were obtained from CATHENA's internally stored temperature-dependent thermal properties and from reference [2]. Heat losses to the environment were modelled by applying heat transfer coefficients, and a reference temperature of 23°C to the outside of piping components.

The heated section was modelled using a single pipe component divided into 12 equal length thermalhydraulic nodes. The 7-element FES bundle was represented by 3 “cylinder groups” to model the heat transfer split between the liquid and vapour phases under stratified flow conditions. The power distribution in the axial direction was assumed to be constant in the CATHENA model and the values for the different heated sections were taken from [3].

3.3.4.2 *Secondary system idealization*

The secondary-side idealization is shown in Fig. 3-22. This idealization includes the steam generators up to the steam nozzle and that part of the feeder water line from the thermocouple location measuring the feedwater temperature to the steam generator feedwater inlets. The portion of the feedwater lines, upstream of this location was represented by flow and enthalpy boundary conditions. The secondary side steam generator outlet pressures were modelled using the pressure boundary conditions obtained from boiler steam dome pressures. Time varying feedwater flowrates, extracted from the experimental results, were imposed as the flow boundary conditions.

Junction resistance models were used to account for head losses in the contraction at the top of the riser section to the steam separator, expansion/contraction losses at the connection between the external downcomer and the hot leg of the steam generator, the expansion/contraction losses at the connection between the external downcomer and the steam drum and the resistance of the steam generator. At the exit of the riser separator models were used to simulate phase separation; vapour goes to the steam drum and the liquid flows to the downcomer.

3.3.4.3 *ECCS idealization*

High pressure and low pressure ECI system were considered in the idealization as can be seen in Fig. 3-23. In the high pressure phase, the pressure was used as a boundary condition.

In the low pressure phase a polynomial head relation was used to model P8 according to reference [2] chapter 8.532

3.3.4.4 *Others*

The CATHENA thermalhydraulic code provides a number of “system control” models that can be configured to perform the measurement and control functions of a reactor or the RD-14M test facility. System control models were used in these simulations to control the opening of the break, pressurizer isolation, heated section power rundown, primary pump speeds rundown and opening of the four ECC isolation valves.

Opening of the break and closing of the pressurizer and ECC isolation valves was assumed to occur over a 0.1 s time span. Heat section power and pumps speed were extracted from experimental data.

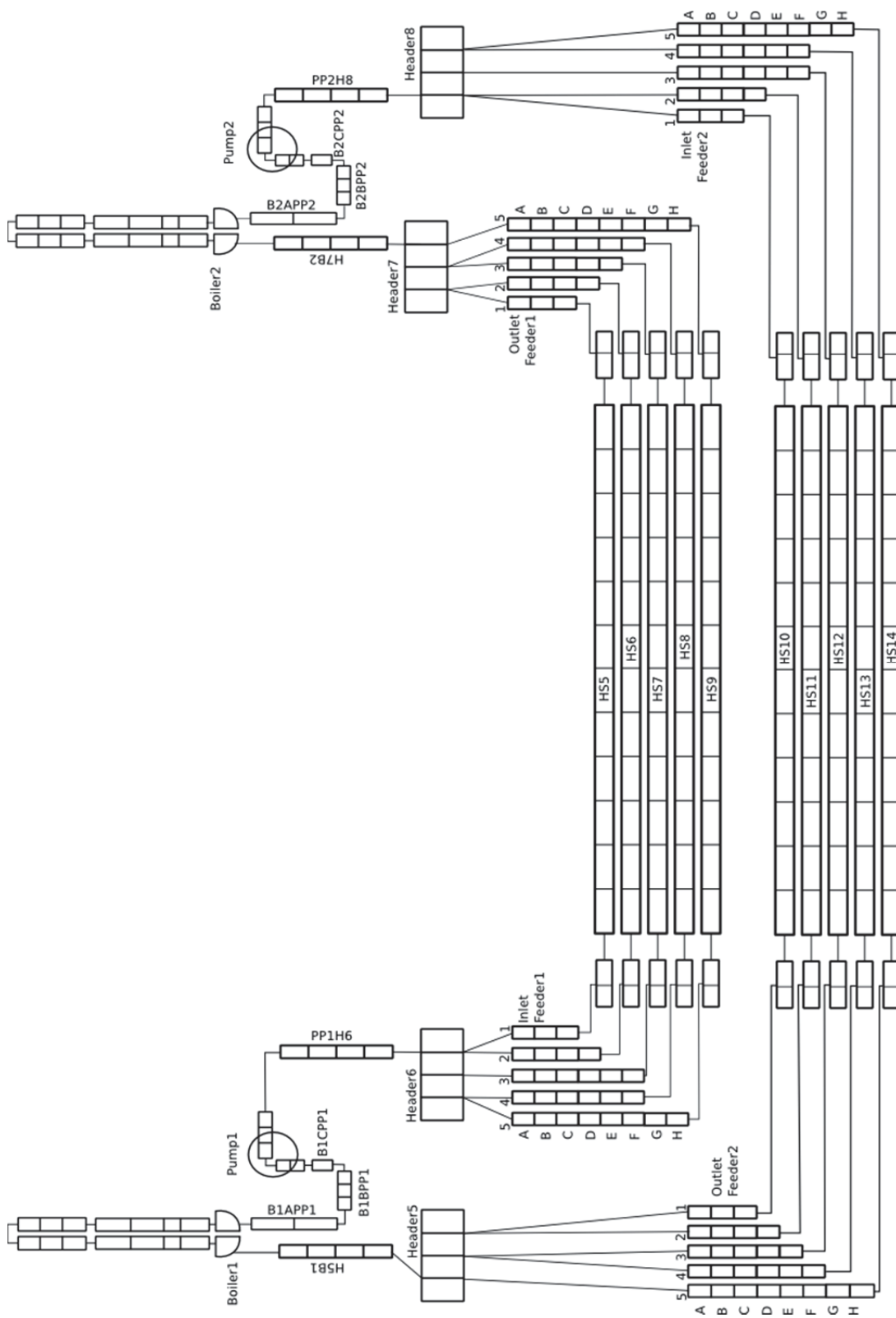


FIG.3-21. CATHENA idealization – primary side.

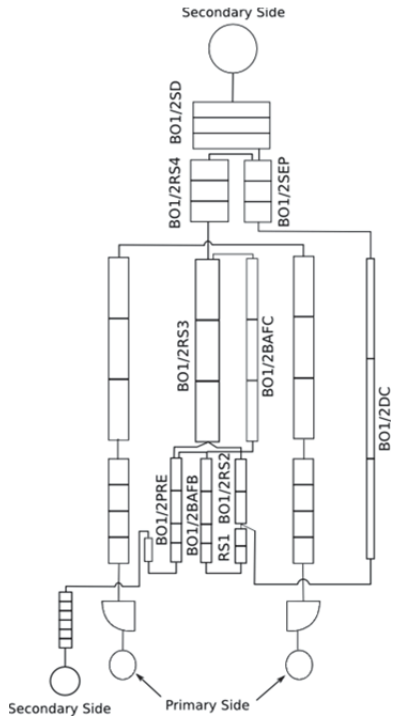


FIG. 3-22. Idealization of secondary side.

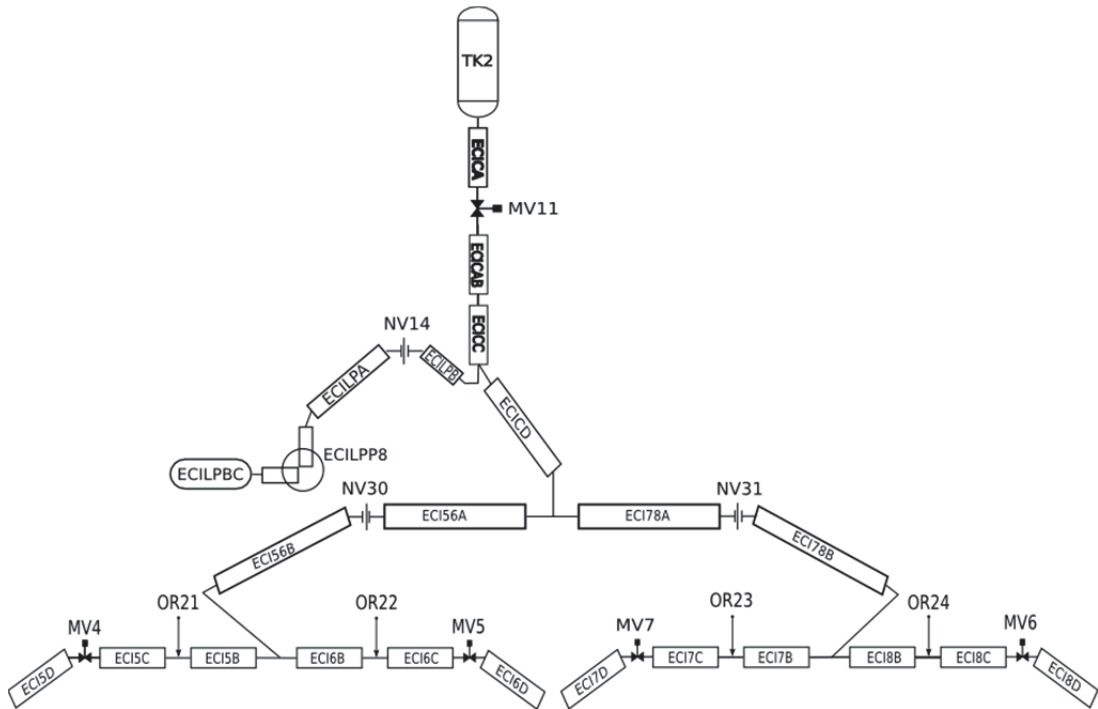


FIG. 3-23. Idealization of emergency core cooling system.

The Henry-Fauske (“HENFK-ORIF-GAS”) discharge model was selected for these simulations.

A trip model was used to switch from high pressure ECI to low pressure pumped ECI. This model isolates the high pressure ECI, opens the pumped ECI isolation valve and starts up the low-pressure ECI pump.

The heat transfer coefficients for the heat losses were calculated from Chapter 8–7 of Reference [2] using the values of Table 8–15.

3.3.4.5. Steady state calculation

The steady state was reached after 1000 seconds of calculation. Table 3–4 shows the calculated heat balance for the blind and open run.

TABLE 3-4. POWER BALANCE FOR STEADY STATE CALCULATIONS

Power	Blind run		Open run	
	MW	%	MW	%
Heat balance in Channels	7.974	99.68	7.974	99.68
Heat Out Boiler1	-3.998	-49.97	-4.036	-50.45
Heat Out Boiler2	-3.930	-49.13	-3.886	-48.58
Heat balance in Pumps	0.072	0.90	0.071	0.89
Heat Inlet Feeders Pass 1 ^(*)	-0.010	-0.13	-0.010	-0.18
Heat Inlet Feeders Pass 2 ^(*)	-0.015	-0.18	-0.015	-0.35
Heat Outlet Feeders Pass 1	-0.028	-0.35	-0.028	-0.31
Heat Outlet Feeders Pass 2	-0.025	-0.31	-0.025	-0.51
Heat Out Pipes Pass 1 and Pass 2	-0.040	-0.50	0.041	-0.05
Balance	0.000	0.01	0.001	0.01

^(*) Pass 1: Upstream the break – Pass 2: Downstream the break.

3.3.4.6 Modification from blind to open calculation

In the open run the main changes made in the model to match the experimental data were:

- additional flow resistance along the heated channels to get the initial flow values for the steady state;
- Partially closing of interconnection ECI valves (MV4/5/6/7);
- Partially closing high pressure injection valve (MV11);
- Small reduction of the low pressure ECI pump velocity.

3.3.5 Korea Atomic Energy Research Institute — Republic of Korea

3.3.5.1 *Primary system idealization*

The CATHENA nodalizations of the RD-14M facility with primary and secondary side loops are shown in Fig. 3–24. The CATHENA nodalization used to simulate B9006 experiment consists of 528 thermal-hydraulic nodes, 543 links and 150 wall heat transfer models. However, in case of B9802, the numbers of thermalhydraulic nodes and links are decreased to 483 and 494, respectively, because the modeling of ECCS is excluded in the B9802 simulation.

The RD-14M primary side consists of all piping connecting the headers, heated sections, steam generators, pumps and pressurizer.

In developing the primary side nodalization, the volume, length, flow area and elevation change of each CATHENA pipe component resembled, as closely as possible, those from the RD-14M test facility description [2].

The flow area of complicated geometries, such as the end fittings, boiler plenums and coolant pumps are determined by dividing the volume of the component by the flow path length.

The heat transfer models in the GENHTP are used to model all solid components in contact with the fluid. They also account for the heat transfer from the primary fluid to the pipe walls and from pipe walls to the environment, or in the case of the steam generator tubes, to the secondary side. Pipe radii (inner and outer) are calculated from the pipe schedules for each piping system, and these are used in defining the metal mass and heat transfer area in contact with the primary fluid. The thermal properties used for the piping materials are obtained from CATHENA's internally stored temperature-dependent thermal properties.

The heated section is modelled using a single pipe component divided into 12 equal length thermalhydraulic nodes. The standard 7-element FES bundle was represented by 3 “cylinder groups” to model the heat transfer split between the liquid and vapour phases under stratified flow conditions. However, one more cylinder group may be added for a heater rod disconnected from the power supply. The power distribution in the axial direction is assumed to be constant in the CATHENA model.

3.3.5.2 *Secondary system idealization*

This nodalization, also shown in Figure 3-24, includes the steam generators up to the steam nozzle and that part of the feeder water line from the thermocouple location measuring the feedwater temperature to the steam generator feedwater inlets. The portion of the feedwater lines, upstream of this location is represented by flow and enthalpy boundary conditions. The secondary side steam generator outlet pressures are modelled using the pressure boundary conditions obtained from boiler steam dome pressures. Time varying feedwater flow rates, extracted from the experimental results, are imposed as the flow boundary conditions.

Separator models are used to simulate the liquid separation at the bottom of the steam drum, and steam separation in the spiral-arm separator at the top of the steam drum.

3.3.5.3 *ECCS idealization*

The nodalization of the ECC system is included for both the high pressure ECC tank and low pressure ECC pump injection phases used in the B9006 experiment (Fig. 3–25).

In the high pressure ECC phase, accumulator tank model of CATHENA is used for the high pressure ECC tank. The accumulator tank pressure is calculated assuming isentropic expansion of the gas portion of the tank as the liquid is expelled. For the simulation of RD-14M, a more detailed model of the accumulator is represented as shown in Figure 3-26. This model describes an accumulator tank filled with 2.72 m³ of 21.4 °C water at an initial pressure of 4.3 MPa. If the pressure of RD-14M test loop decreases below 4.3 MPa, the ECC injection by the accumulator starts and the water level in the accumulator tank decreases. The high pressure injection valve (MV 11) will later close automatically on indication of low level in the accumulator tank. This is modelled by tracking cumulative water mass discharged from the accumulator tank. When the level in the accumulator tank reaches 10% of the initial level (modelled when the cumulative water mass discharged from the accumulator tank exceeds 1711.7 kg), the valve begins to close.

After the accumulator injection valve is closed, a low pressure ECC pump injection phase starts. A pressure boundary condition was used to simulate the low pressure pumped ECC phase since the break flow of test loop is smaller than the prediction of ECC injection flow by the low pressure pump (pump 8) performance curve. A constant pressure boundary condition (1.6 MPa) is applied to the location of pump discharge during the low pressure ECC phase.

3.3.5.4 *Others*

Heat loss

GENHTP accounts for the heat transfer from pipe walls of the primary loop to the environment. Heat losses to the environment are modelled by assuming the heat transfer coefficients of 5.0 W/m²/°C for the feeder pipes and 35.0 W/m²/°C for the pressure tubes, and a reference temperature of 20°C to the outside of piping components.

Simulation time steps

The simulation times for B9006 and B9802 are 2280 seconds and 1363 seconds, respectively. Using the CATHENA time step control algorithm, the time steps during the simulation time are calculated within the user specified minimum and maximum time steps. The minimum time step is 10⁻⁶ second, which is small enough to cover the rapid transient period. The maximum time step is specified as 10⁻¹ second.

Boundary conditions

The heater thermal powers, coolant pump speeds, feedwater temperatures and flow rates, and secondary side steam outlet pressures are given for the blind calculations of B9006 and B9802 tests. Instead of using the pressure history of the ECC tank in B9006 test, the high pressure ECC injection is simulated by the CATHENA accumulator model.

Discharge models

The CATHENA discharge model uses Bernoulli's equation for subcritical discharge and provides the option of selecting a choked flow model.

In the simulation of B9006 test Henry-Fauske critical flow model is used for two-phase and superheated steam, but choking is not considered for single-phase liquid.

In the simulation of B9802 test Henry-Fauske critical flow model is used for single-phase liquid discharge and homogeneous polynomial formulation is used for critical two-phase and superheated steam flow.

$3.8484 \times 10^{-5} \text{ m}^2$ break (7 mm break) and $7.0686 \times 10^{-6} \text{ m}^2$ break (3 mm break) are specified between the PIPE component IHD8D (inlet header) and the RESERVOIR component named BKBC (atmospheric pressure boundary) for B9006 and B9802 tests, respectively. A discharge coefficient of 0.61 is specified for single-phase liquid conditions.

CHF and Post-dryout heat transfer models

The default option for CHF calculations in CATHENA is the Groeneveld-Leung CHF table lookup method, as recommended in the CATHENA Mod3.5d Theory Manual. This option actually consist of 8 separate tables, including tables for both light water (H₂O) and heavy water (D₂O) in tubes, 37-element bundles, CANFLEX (43-element) Mk-IV and CANFLEX Mk-V bundles. The input parameters for the table lookup are pressure, mass flux, and equilibrium quality. CATHENA automatically selects the most appropriate table based on the channel geometry defined by the user.

The default correlation for fully developed post-dry out heat transfer is the Leung lookup table (based on wall superheat). The wall-superheat based lookup table provides a value of heat transfer coefficient from known pressure, equilibrium quality, mass flux and wall superheat.

3.3.5.5 Steady state calculation (cover both simulations)

The first part of the code run is to get the steady-state solutions. For this part of the run some parameters such as channel power, pump speed, feedwater flow, steam generators pressure are imposed as constant, which are based on the steady-state data provided. Instead of using the pressure history of the ECC tank in the test B9006, the high pressure ECC is simulated by the CATHENA accumulator model.

For the steady-state calculation, CATHENA code was run for 500 seconds to make the major output variables approach the constant values. Adjusting the flow resistance in the inlet feeder line of CATHENA input model, CATHENA calculates the nearly same flow distribution as the test data.

The differences between the measured data and the code prediction are considered acceptable and the steady-state results are used as the starting point for the transient calculation.

3.3.5.6 Modification from blind to open calculation

In addition to the fully-developed post-dry out heat transfer correlations, the best-estimate post-dryout heat transfer correlation is available for the developing post-dryout heat transfer model in the CATHENA code. In a tube or bundle with flow and enthalpy non-uniform distributions, the onset of dryout is reached in a non-uniform way on different surfaces. Close to CHF, the dry patch covers only a fraction of a tube or bundle. Without using the developing post-dryout heat transfer model in the one-dimensional code like CATHENA, the entire surface is assumed to experience fully-developed post-dryout heat transfer conditions

after the first occurrence of CHF in the tube or bundle. As a result, the net surface heat flux will be significantly underestimated. The best-estimate post-dryout heat transfer correlation is used for an “average” heat transfer calculation, based on interpolation of the heat transfer between CHF (i.e. nucleate boiling) and fully-developed film boiling conditions. An important consideration in the application of the best-estimate post-dryout calculations is that they are based on the average thermalhydraulic conditions for the entire surface of the tube or bundle.

In the blind calculations of RD-14M small break tests, the default options for CHF and the fully-developed post-dryout heat transfer models are used.

However, in the open calculation of B9802 test, the best-estimate 37-element developing post-dryout heat transfer model (Senaratne and Leung model, described in the CATHENA Mod3.5d Theory and User Manuals) is applied to the FES pin model to improve the bundle post-dryout heat transfer predictions during the oscillatory phase of the test B9802. This model requires that the user has specified either of the PDO look-up table methods. The best-estimate heat transfer correlation is defined through the form,

$$h^* = [a_1 \exp(a_2 T^*)] - [a_3 \exp(a_4 T^*)]$$

where
$$h^* = \frac{h_{b-e} - h_{fd}}{h_{nb} - h_{fd}} \text{ and } T^* = \frac{(T_w - T_{sat})}{(T_{CHF} - T_{sat})}$$

- with
- $h_{nb} = q_{CHF} / (T_{CHF} - T_{sat})$,
 - h_{fd} = fully-developed film boiling coefficient,
 - h_{b-e} = best-estimate heat transfer coefficient to be calculated
 - T^* = wall superheat ratio
 - T_w = wall temperature °C
 - T_{CHF} = critical heat flux temperature, °C, where $q_{nb} \equiv q_{CHF}$ and
 - T_{sat} = saturation temperature °C

This model requires four coefficients with the default values given by

$$a_1 = 1.6403, a_2 = -0.4442, a_3 = 0.0807, \text{ and } a_4 = -0.4437$$

However, the following two coefficients are changed as; $a_1 = 0.58$ and $a_2 = -0.1442$ (without changing other two coefficients) for the open calculation of the test B9802.

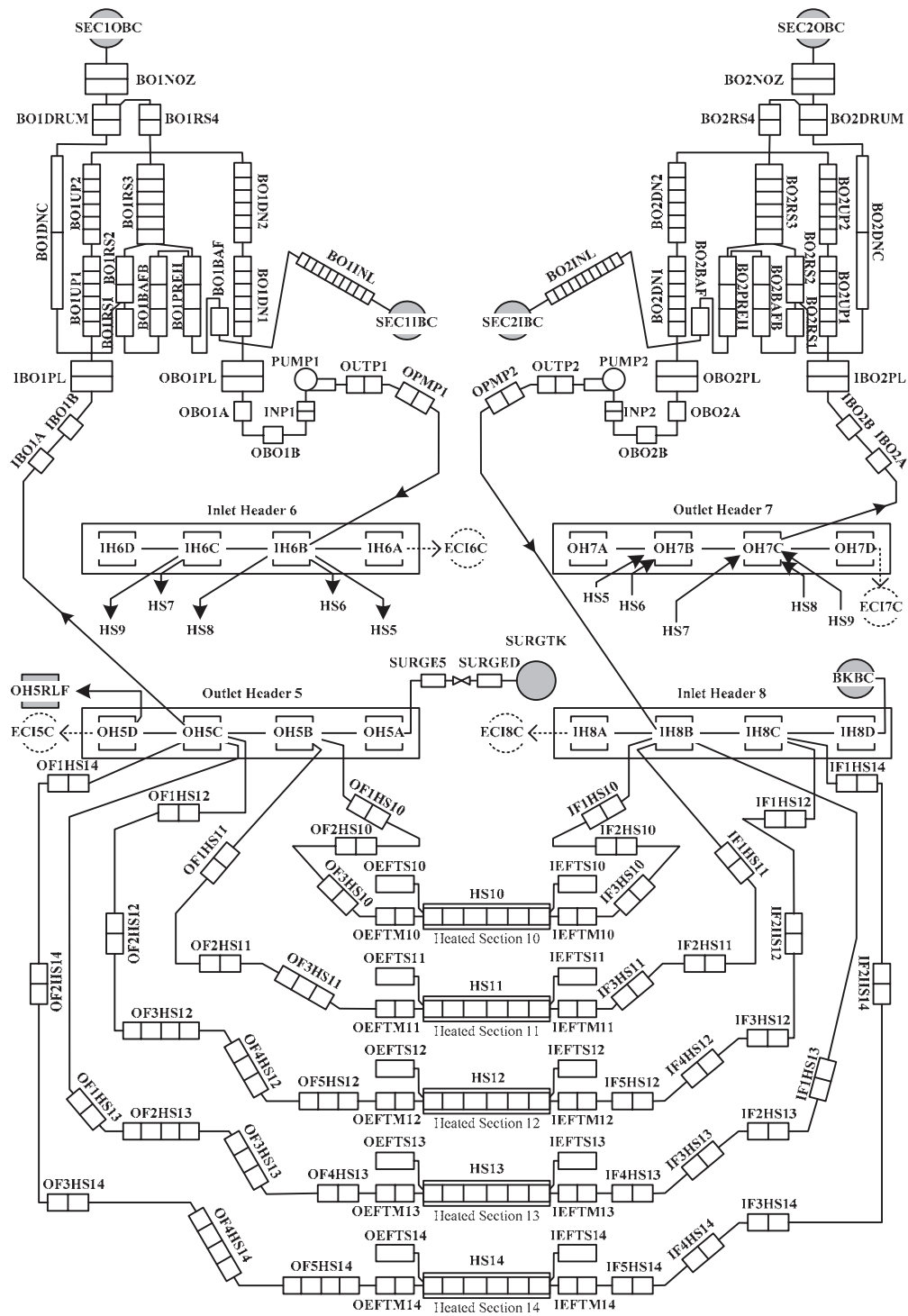


FIG. 3-24. CATHENA nodalization – RD-14M coolant loop.

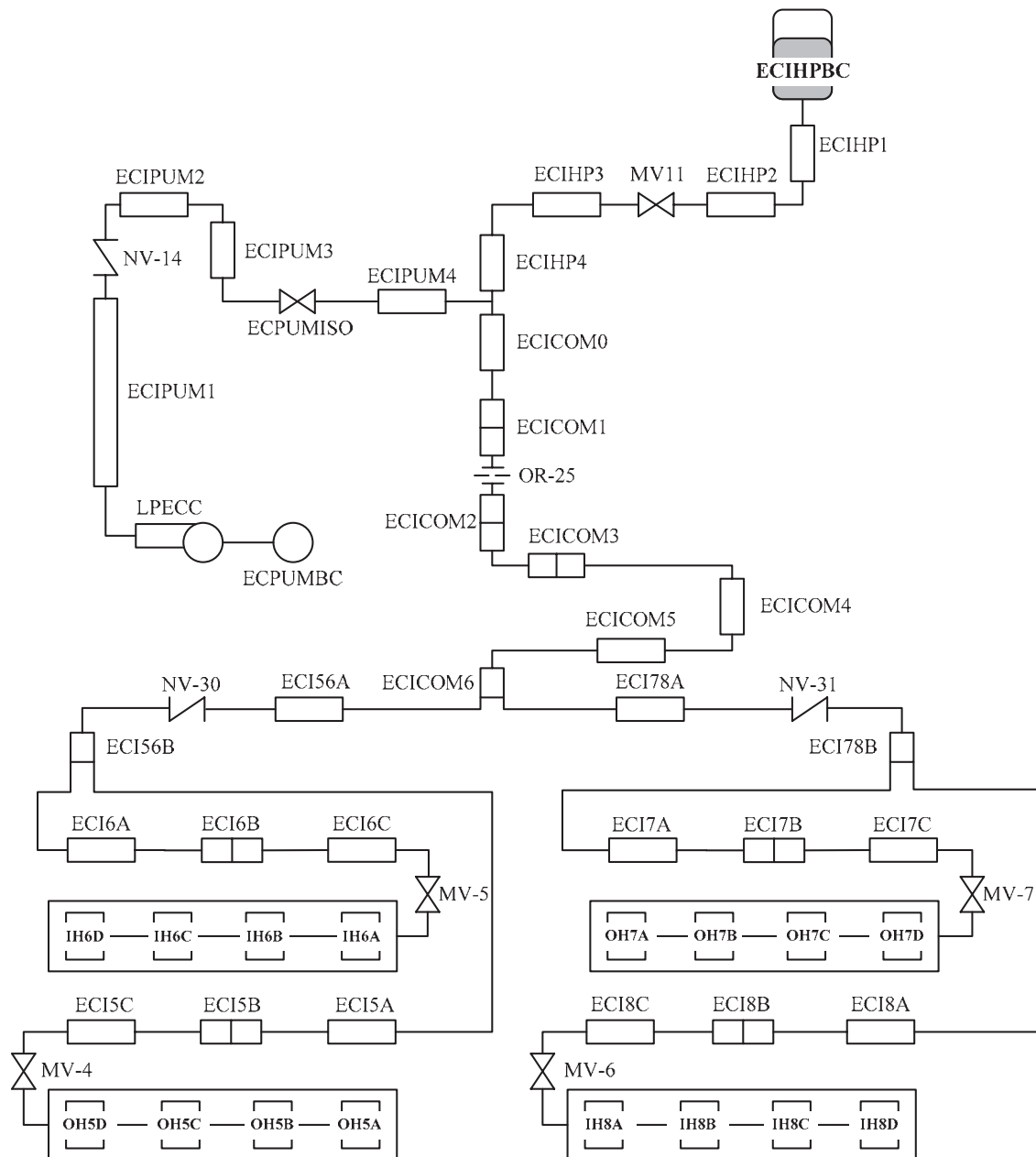


FIG. 3-25. CATHENA nodalization – RD-14M ECC system.

3.3.6 Korea Institute of Nuclear Safety — Republic of Korea

3.3.6.1 Primary system idealization

In modeling the primary-side nodalization, the volume, length, flow area and elevation change of each MARS-KS pipe component resembles the RD-14M test facility, as closely as possible. This ensures that the fluid transit time and hydrostatic pressure changes around the loop are represented accurately during the simulation. Since the system is modelled as one dimensional structures, horizontal and vertical sections of components are not combined as one inclined pipe component, unless the horizontal or vertical sections are very short. Another reason of the segregation between horizontal and inclined pipe sections is that the flow regime map used in each section is quite different. feeder lines are nodalized such that sections of the pipes having similar inclination and cross-sectional area are combined.

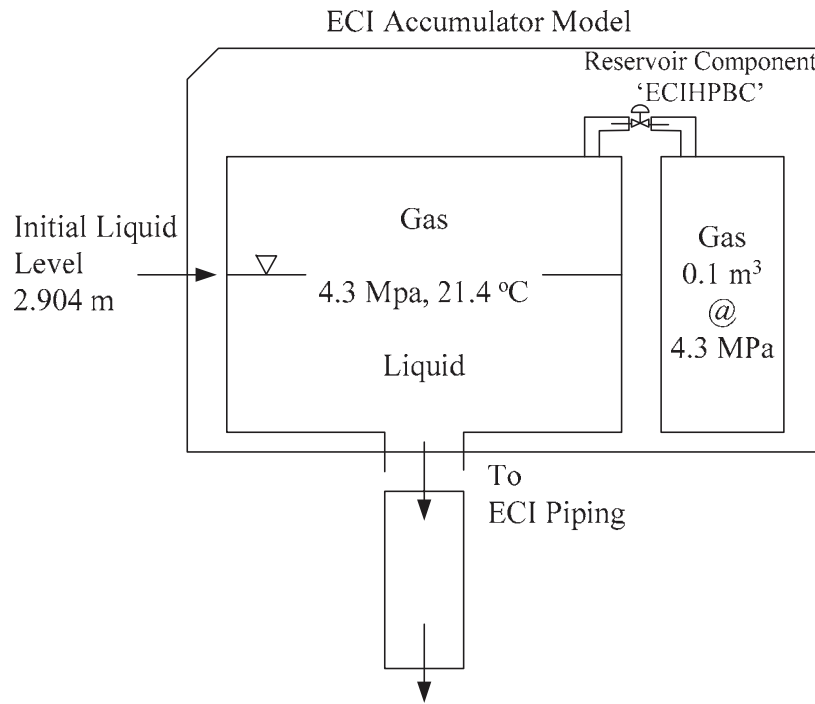


FIG. 3-26. RD-14M Accumulator model.

The forward/backward junction loss coefficients are used to simulate pressure loss, and junction abrupt area change model is used in the case of orifice. The total volume of the primary-side excluding the pressurizer and its surge line is compared with the volume of the RD-14M facility, and the error is minimized to be limited within 1%.

The heated sections are modelled using a single pipe component divided axially into six equal lengths in accordance with the number of thermal-hydraulic volumes. The seven fuel pins are combined into a single fuel pin heat structure maintaining the surface area, mass and equivalent heated perimeter, which are represented by 3 “groups” to model the heat transfer split between the liquid and vapor phases under stratified flow conditions. These fuel pins generate heat corresponding to each channel power. The power distribution in the axial direction is assumed to be uniform in the MARS-KS model. The power ramp down during the transient is given in a tabular form in the code as reported in the experiment. The convective boundary condition for the heat transfer coefficient is used from the heat transfer package for CANDU fuel bundle element.

3.3.6.2 Secondary system idealization

The secondary-side nodalization models the steam generator from the thermocouple location measuring the feedwater temperature of feedwater inlet up to the steam nozzle. Also, the secondary side of steam generator consists of riser, drum and downcomer volumes. The upstream of the thermocouple location in feedwater line are set as flow and enthalpy boundary conditions. The feedwater flowrate, extracted from the experimental results, is imposed as the flow boundary conditions. The pressure of steam nozzle is modelled using the pressure boundary conditions, obtained from boiler steam dome pressures. Junction resistance models are used to account for the head losses in the contraction at the top of the riser section to the steam separator, the expansion/contraction losses at the connection between the external downcomer and the bottom plenum of the steam generator, the expansion/contraction losses at

the connection between the external downcomer and the steam drum. The steam generator U-tubes are segregated into five volumes, which are attached with the heat slabs, forming the thermal linkage between the primary and secondary system. The U-tube heat slabs are connected to the two volumes of the riser portion. It picks up heat from the U-tubes, converts into a two-phase mixture and rises in the riser volume. One pipe volume downcomer connects the drum inlet to the secondary riser inlet. At the exit of the riser this two-phase mixture enters the separator volume. A MARS-KS specific separator component, attached with the drum volume, is used to separate out steam and water. Separator model simulates the moisture separation through the spiral-arm separator in the steam drum. Steam moves from the separator to the upper portion of the drum volume, and saturated liquid falls back into the lower portion of the drum volume. The bottom volume of the drum is connected to the downcomer. The feedwater from a time-dependent volume is injected into the downcomer portion and mixes with the saturated water in the riser. The turbine is modelled as a time dependent volume with constant pressure. In transient stage of test B9006, the feedwater flow and the steam flow to turbine are controlled according to a time-dependent values provided by ICSP project team. This may be helpful to simulate more precisely the phenomena in test B9006.

3.3.6.3 *ECCS idealization*

High pressure ECC system consists of an accumulator and the lines linked to 4 feeder headers, and it is actuated when the pressure primary system falls down its setpoint of 4.2 MPa. The accumulator contains the water pressurized on 4.2 MPa. If the water level of accumulator lowers below 10%, the injection from an accumulator is stopped to protect the entrainment of noncondensable gas into the system. In case of RD-14M experiment, the initial water level of accumulator is set as 2.855 m. Low ECC pumps are modelled as time dependent junctions which mass flow is controlled by discharge pressure. Especially, the ECC piping is modelled in order to simulate the ECC flow-splitting behaviour. In Test B9802, ECI is blocked, because ECC system was not used.

3.3.6.4 *Others*

The break is modelled by the trip valve attached at inlet header #8. And the break valve is connecting with the downstream pipe and a time dependent volume for discharge reservoir. The downstream pipe is modelled according to RD-14M facility description. It is anticipated that this modeling suppresses unnecessary fluctuation of header pressures during two phase stage. The improved critical flow model is adopted instead of original RELAP5 critical flow model developed by Ransom and Trapp.

3.3.6.5 *Steady state calculation*

At the early stage of the preparation for steady states, primary and secondary initialization was performed separately, after input preparation of RD-14M system had been finished. For primary system, the most important parameters for steady state are loop mass flow rate and differential pressures among the headers. Those parameters were adjusted using junction form loss coefficients. Secondary side initialization is performed using adjusting separator setting parameters and form loss coefficient settings. The calculated steady-state values of the major parameters are in good agreement with the experiment data.

3.3.6.6 *Modification from blind to open calculation*

The ECC isolation valves opening set points and logic are modified according to experimental facility. The accumulator discharge form loss coefficient is revised to similar high pressure ECC injection duration with experiment results. The break discharge coefficient is also

revised from 0.85 to 0.65 based on the sensitivity study results. Adopting the 0.65 discharge coefficient shows the better header pressure transient prediction.

3.3.7 Nuclear Power Corporation of India Ltd — India

The ATMIKA nodalisation of the RD-14M test facility for tests B9006 and B9802 consisting of primary, secondary and ECI system are shown in Figures 3–27 and 3–28 respectively. It consisted of 225 thermal hydraulic nodes, 240 links and 181 heat transfer structures for simulation of test B9006. For simulation of Test B9802, nodalisation (Fig. 3-28) consisted of 212 thermal hydraulic nodes, 224 links and 181 heat transfer structures. Following write up gives brief description of the nodalisation and salient aspects of the input modeling. A brief description of the primary, secondary side and the ECI systems are presented in the following sub-sections.

3.3.7.1 *Primary system idealization*

In developing the primary-side idealization, the volume, length, flow area and elevation change of each pipe component resembled, as closely as possible to the RD–14M test facility. This ensured that the fluid transit time and hydrostatic pressure changes around the loop were represented accurately in the simulation.

The total volume of the primary-side idealization, excluding the pressurizer and the line connecting it to the primary loop, has been compared with the volume of the facility. The flow area of complicated geometries, such as the end fittings, boiler plenums and primary pumps were determined by dividing the volume of the component by the flow path length.

The heat structures are used to model all solid components in contact with the hot fluid. They also account for the heat transfer from the primary fluid to the pipe walls and from pipe walls to the environment, or in the case of the steam generator tubes, to the secondary side. Pipe radii (inner and outer) were used in defining the metal mass and heat transfer area in contact with the primary fluid. Heat losses to the environment are modelled based on steady state energy balance through heat structure wall. Inside heat transfer coefficient (h) is calculated from normal heat transfer correlation based on fluid condition during the transient. Removal of primary loop heat by environment is modelled using heat transfer coefficient (h) which is estimated based on the initial steady state condition and is assumed to be constant during the transient. An ambient temperature of 23°C is considered.

The RD-14M primary side consists of all piping connecting the headers, heated sections, steam generators, pumps and pressurizer and is briefly described below covering in below header, above header piping, SG tubes and pressurizer.

Below header modeling

Each header was split in three nodes to take into account pump/boiler and feeders connection. All pipes connected to headers (feeders, pump discharge, ECI pipes, pressurizer line) were linked to the corresponding node.

Feeders connected to each heated section (total ten heated sections), inlet as well as outlet feeder are modelled separately with three nodes for each feeder.

TABLE 3-5. MAIN DIMENSIONS OF THE ATMIKA NODALISATION DEVELOPED FOR RD-14M

No.	Parameter	Test B9006	Test B9802	
1.	Total number of nodes	225	212	
2.	Total number of links	240	224	
3.	Total number of heat structures	181	181	
4.	Number of nodes for each feeder	3	3	
5.	Number of nodes for end-fitting simulators	2	2	
6.	Number of nodes for each heated section	6	6	
7.	Number of nodes for each header	3	3	
8.	Number of nodes for above header piping	Steam generator inlet	1	1
		Pump suction	1	1
		Pump discharge	1	1
9.	Number of nodes for steam generators (primary side)	Inlet plenum	1	1
		U-tubes	5	5
		Outlet plenum	1	1
10.	Number of nodes for steam generators (secondary side)	9	9	
11.	Number of nodes for emergency coolant injection system	13	NO ECI	

Geometrical parameters of end-fitting simulators were observed as far as possible. The model consisted of 2 nodes: one for the moving volume and one for the stagnant volume.

Each heated section is modelled with six equal length thermal hydraulic nodes axially. The power distribution in the axial direction was assumed to be constant.

Above header piping

Outlet header to steam generator inlet, steam generator outlet to pump suction and pump discharge to inlet header is represented by one node each.

The steam generators' primary side U-tubes are grouped together and axially are divided in 5 nodes, one of the nodes corresponding to the preheater zone.

Five of the U-tube volumes are attached with five heat slabs, forming the thermal linkage between the primary and secondary system. Additionally, two control volumes are considered, one for each inlet and outlet plenum volumes.

Pressurizer (PRZ) component gets isolated before the initiation of the transient. However, it has been modelled in steady state as a boundary condition for its interaction with the primary

system. A single node is used to model the pressurizer. The piping connecting the pressurizer to the RD-14M loop (pressurizer line) is modelled as one separate node.

3.3.7.2 *Secondary system idealization*

The secondary system consists of riser, drum and downcomer volumes. The U-Tube heat slabs are connected to the four volumes of the riser portion. Two volume downcomer connects the drum to the secondary riser inlet. The feed is injected into the riser portion and mixes with the saturated water from the downcomer. It picks up heat from the U-tubes, converts into a two-phase mixture and rises in the riser volume. At the exit of the riser, this two-phase mixture enters the separator volume. Steam from the separator moves to the upper portion of the drum volume and the saturated liquid falls back into the lower portion of the drum volume. The bottom volume of the drum is connected to the downcomer. Drum consists of one non-homogenous control volume and steam lines were modelled as two control volumes. The secondary side steam generator outlet pressures were modelled using the pressure boundary conditions obtained from boiler steam drum pressures. Time varying feed water (FW) flow rates and temperature, provided based on experimental data are imposed as the boundary conditions.

3.3.7.3 *ECC system idealization*

ECC system is modelled for the Test B9006. In Test B9802, ECC is not used, therefore it is not modelled.

The ATMIKA idealization of the ECC configurations is shown in Fig. 3–27. The idealization of the ECI system includes the high pressure ECI phase (high pressure ECI tank) and low pressure ECI phase (low pressure pump) injection modes. Thirteen nodes were used for representing the operation of both phases of the ECI system.

3.3.7.4 *Steady state calculation*

During steady state analysis, input parameters e.g. pressure and enthalpy are read and other thermodynamic fluid properties such as temperature, void, density etc. are calculated. Based on flow distribution in the circuit, loss coefficient at each junction is fixed up by using steady state momentum equation. Initial temperature distribution in FES is determined by solving a steady state conduction equation. Heat losses to the environment are modelled based on steady state energy balance through heat structure wall. Inside heat transfer coefficient (h) is calculated from normal heat transfer correlation based on fluid condition during the transient. Removal of primary loop heat by environment is modelled using heat transfer coefficient (h) which is estimated based on the initial steady state condition and is assumed to be constant during the transient. Based on this methodology, Computer code ATMIKA predicted steady state results consistent with the experimental data within the error band of instrumentation for both the tests apart from minor deviations that do not significantly affect the prediction of the transient scenario.

3.3.7.5 *Modification from blind to open calculation*

After the comparison of blind calculation results with the experimental results, input deck was revised in particular with regards to appropriately allocating flow resistances to obtain improved pressure distribution in the steady state. As modeling of pressure distribution in the entire circuit is important in the transient behavior, pressure distribution in the loop is refined which leads to improvement in the open results. MCP characteristics were also refined. Whole input was checked thoroughly and minor corrections were done.

3.3.7.6 *Transient calculation*

Time steps are used in the range of 0.2 to 0.4 ms for test B-9006 and 0.4 ms for test B-9802. Input data used in analysis has been taken from Reference [2–3]. These include the geometrical data of the system, process conditions and control logics etc. It was seen that during experiment some parameters (e.g. power and flow) was different from rated values. In analysis, these values have been taken from experimental measured initial values.

Assumptions made during analysis are as follows:

- Initial coolant flow rate in all channels has been used as measured during experiment at steady state;
- Heat generation is assumed uniform throughout the length of fuel element;
- Low pressure ECI injection through pump has been simulated as fill in ECI lines considering pump (P8) characteristics, with water temperature (21⁰C) as boundary condition. ECI tank temperature in Test B9006 is used as specified (21⁰C);
- Locked up inventory in ECI lines after first isolation valve is assumed at a temperature of 53⁰C;
- Power in each heated section has been used as measured during experiment at steady state as well as in transient condition. Further, power supply to heated sections is tripped following sheath temperature excursion $\geq 600^{\circ}\text{C}$ at any location in the core;
- Instrument uncertainty given for Test B9802 is also assumed for Test B9006 for estimation of error in initial conditions;
- Main coolant pump (MCP) characteristics as applicable to test facility are generated based on reference [McGee, 1993] and used;
- For all types of valves shown in Nodalisation, valve characteristics are assumed as existing in ATMIKA like valve type, area, zeta, opening/closing time, % opening and response time;
- For all DP measurement, response time of 0.25 s is used;
- Time varying SG drum pressure and feed water temperature was observed similar. Hence, SG-1 drum pressure and feed water temperature is imposed as boundary conditions for both SGs.

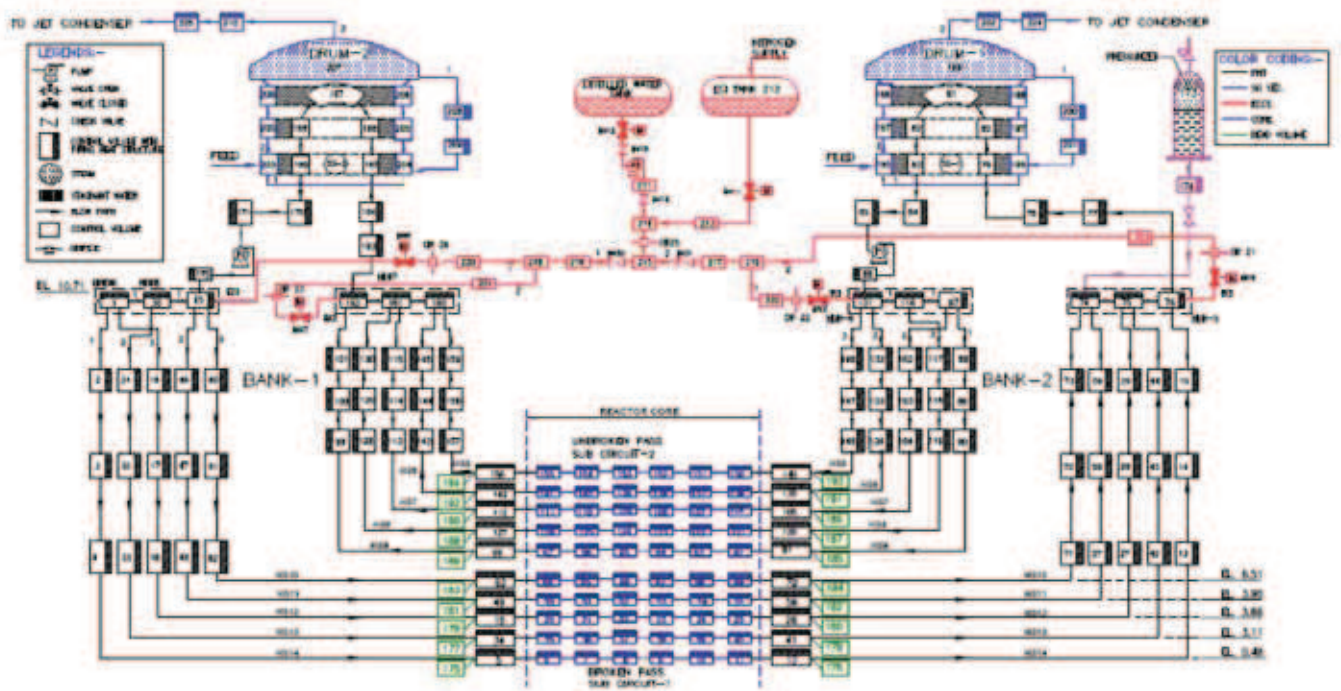


FIG. 3-27. Nodalization scheme for simulation of LOCA on RD-14M test facility (Test B9006).

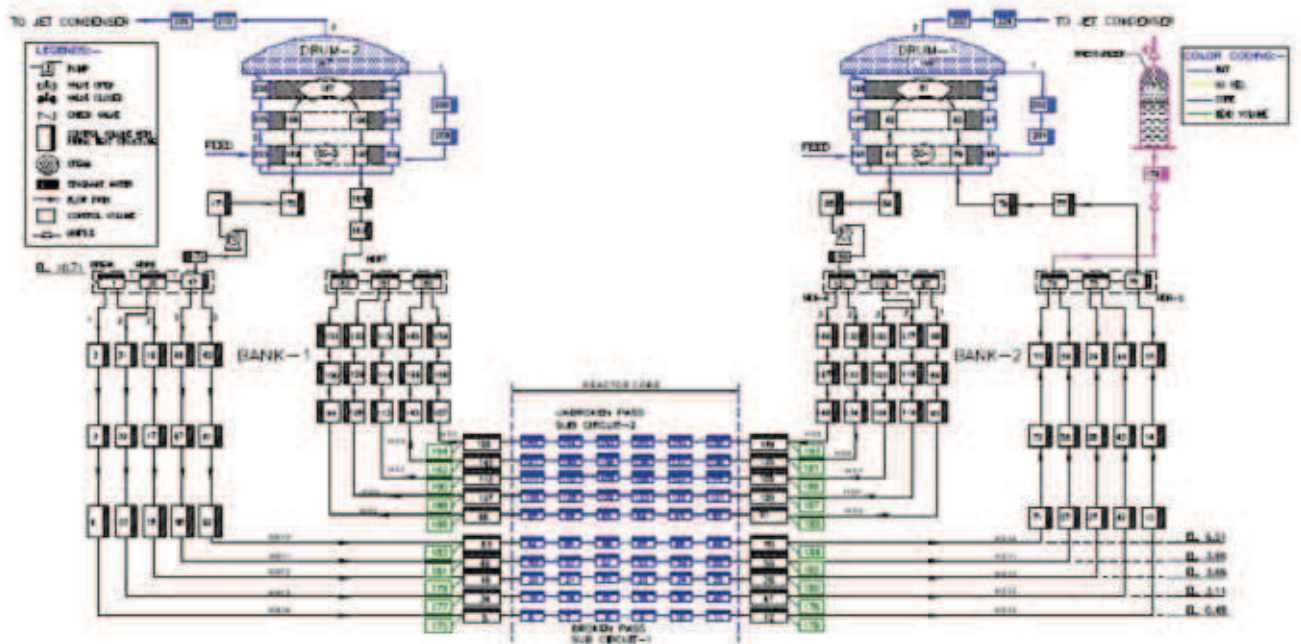


FIG. 3-28. Nodalization scheme for simulation of LOCA on RD-14M test facility (Test B9802).

3.3.8 TsingHua University — China

3.3.8.1 *Primary system idealization*

The whole primary system was built based on the simulation of each heat section. To get the steady state of the system, each channel (including feed pipes, heat sections and outlet pipes) is run separately. Figure 3–29 shows the nodalization of heat section 5/10. The red words in the figure are control volume names used in the CATHENA input deck.

There are totally 33 control volumes in HS5. HS5-TS is the heat section which contains 12 sub-control volumes (sub-CVs). HS5-7 contains 2 sub-CVs and HS5-26 contains 3 sub-CVs. The nodalization of HS6/HS11 to HS9/HS14 are essentially the same.

3.3.8.2 *Secondary system idealization*

Figure 3–30 shows the nodalization of BO1 primary side circuit (BO2 is the same). The primary side of BO1 has 34 control volumes while BO2 has 36 control volumes. The U-tube section of both boilers have 10 sub-CVs each for the control volumes of BO1-10, BO1-11, BO2-10 and BO2-11.

The secondary side of both boilers are nodalized as shown in Fig. 3–31. The turbine is simulated as a time dependant volume with constant pressure. Between the steam line and the turbine, a check valve is set to control the flow direction.

3.3.8.3 *ECCS idealization*

The ECCS system is nodalized as Fig. 3–32. There are 91 control volumes in the ECCS loop. The control volume name used in the input deck is ECI-xx, where xx is the number shown in red color in the Fig. 3–32. Between ECI-4 and ECI-5, ECI-37 and ECI-38, ECI-LP to ECI-1, there are three check valves.

Figure 3-33 shows the nodalization of the whole system. For the case of 9006, there are 748 nodes, 759-links, 366 wall models and 1178 fluid-wall heat transfer surfaces. The nodalization of the Case 9802 is same as that of 9006 but without the ECI circuit. The inlet header 8 is cut into 4 sub-volumes in the open calculation of both cases.

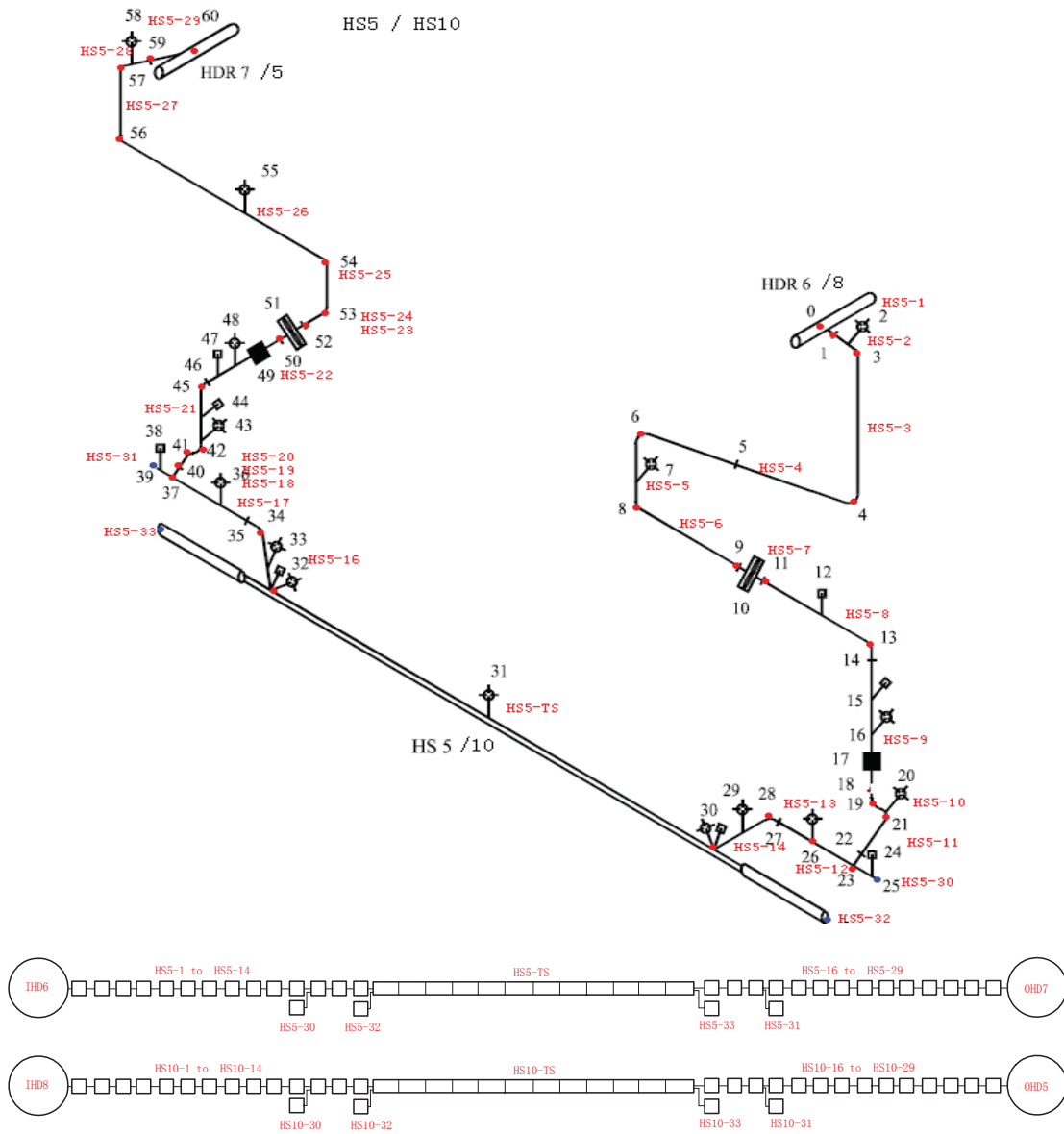


FIG 3-29. Nodalization of HS5 / HS10.

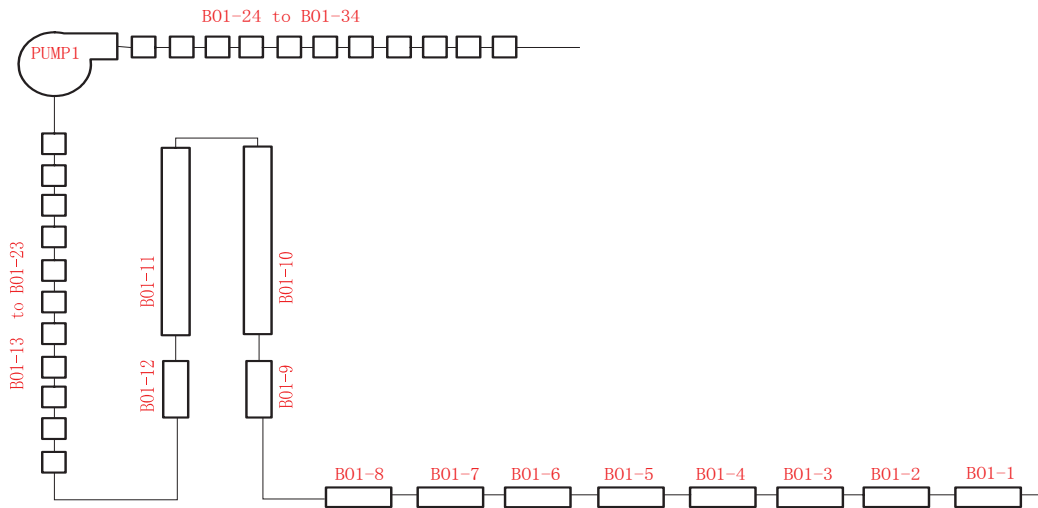
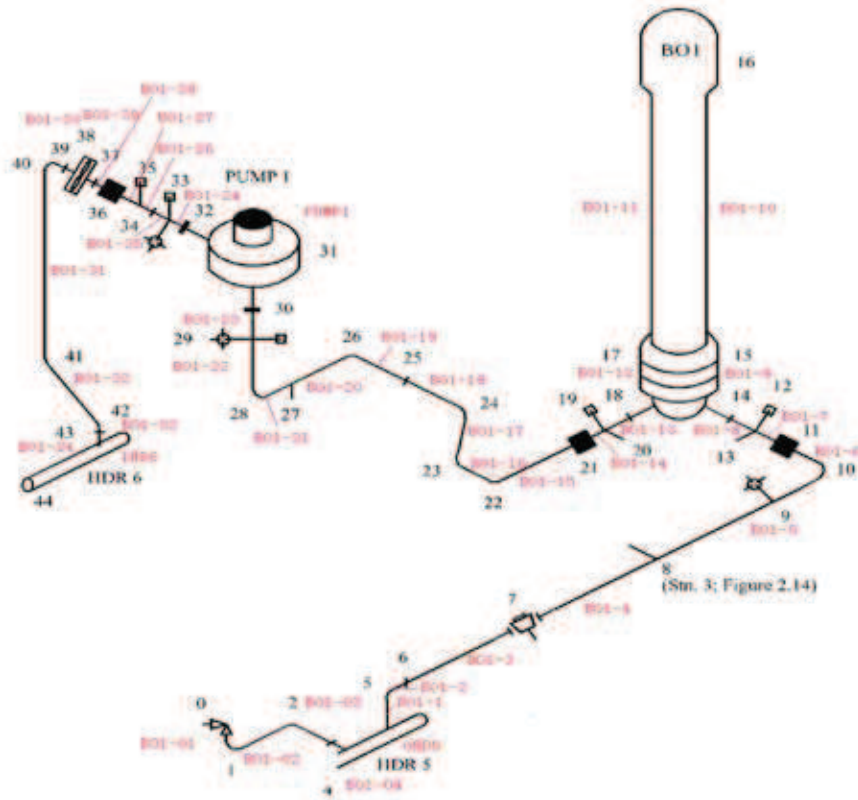


FIG 3-30. Nodalization of BO1 circuit.

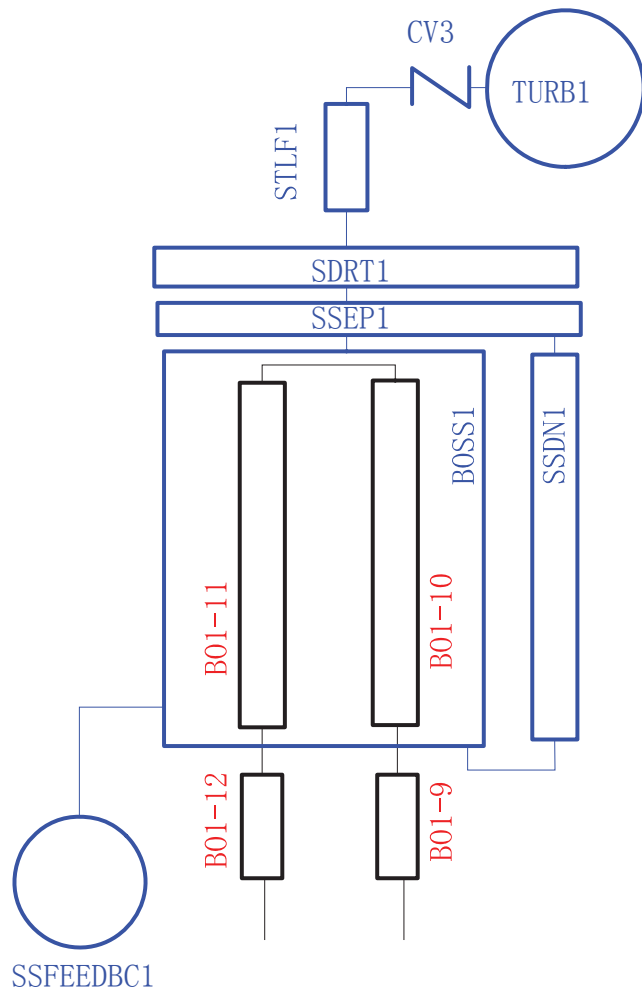


FIG. 3-31. Nodalization of secondary side of boiler.

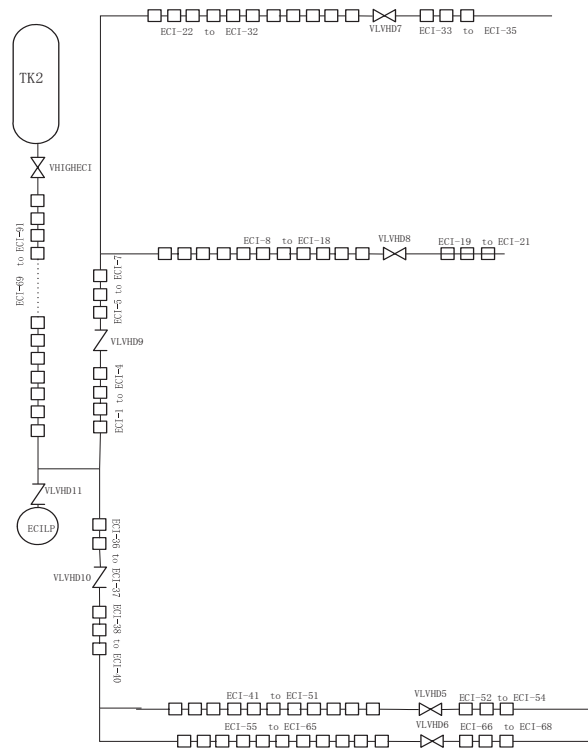
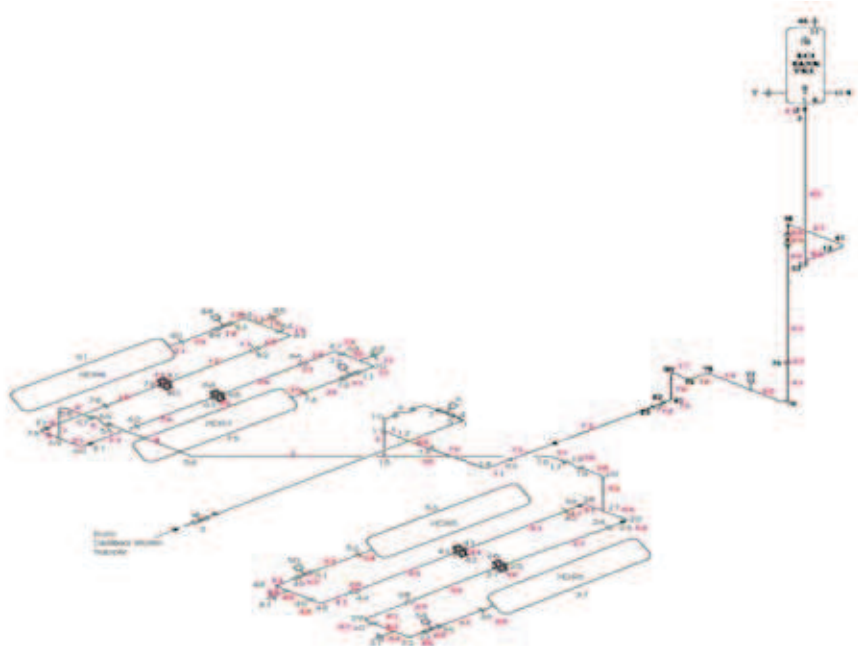


FIG.3-32. Nodalization of ECI circuit.

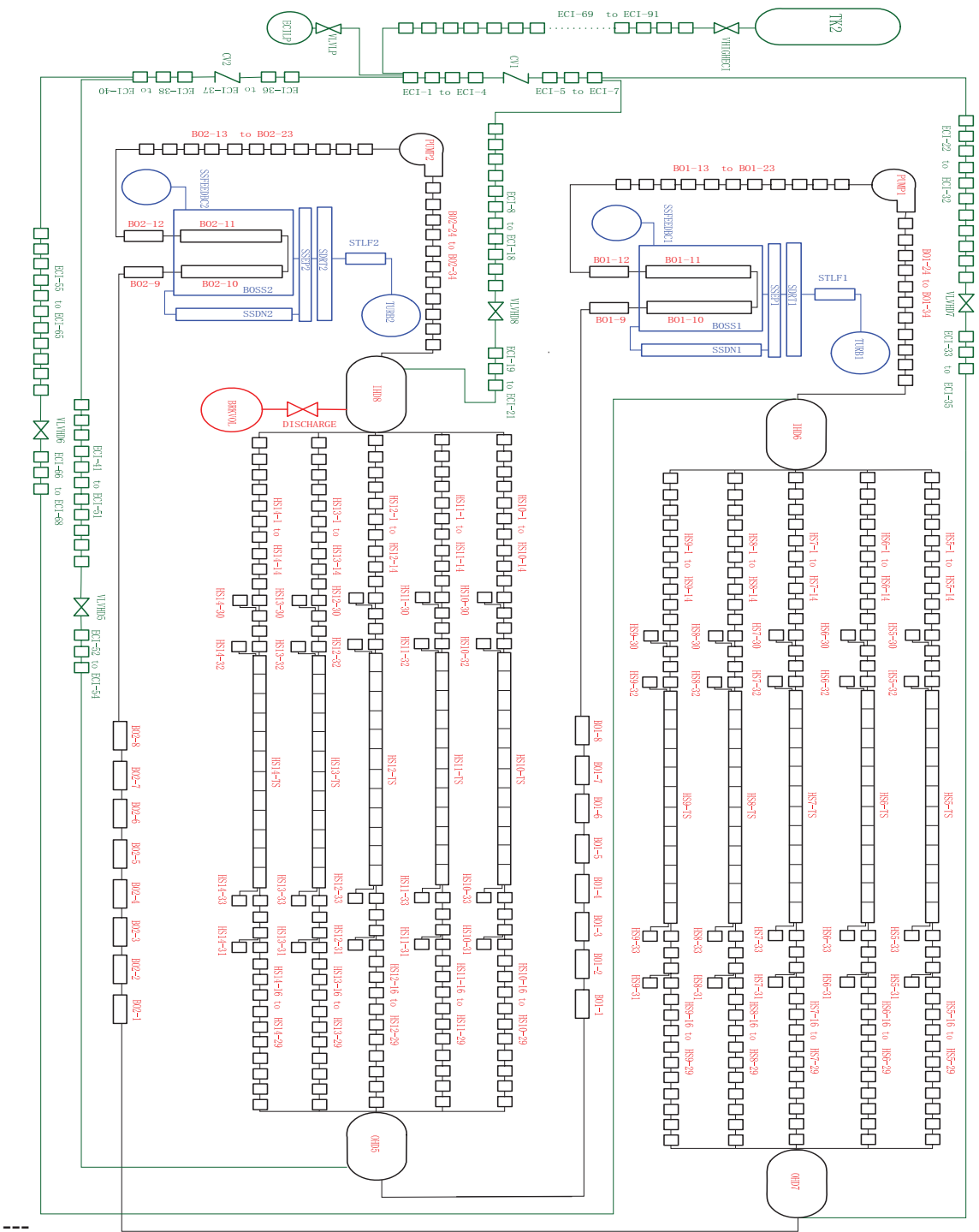


FIG. 3-33. Nodalization of the whole system.

3.3.8.4 Others

To get the steady state of the system, each channel (including feed pipes, heat sections and outlet pipes) is run separately by setting the pressure of inlet header, the inlet mass flow rate and temperature as boundary conditions. Given the correct power in the channel, one can get the pressure and temperature in the outlet header in the steady state for any single channel. By tuning the loss coefficient distribution, one can get the specified outlet pressure as needed. Then by tuning the heat transfer coefficient between walls to surroundings, one can get the temperature distribution needed.

After each channel is tuned, assemble them together with the whole loop. By setting the temperature and mass flow rate of the feed water of both boilers, the second side pressures, and the pressure of header 5 as boundary conditions, one can get the steady state of the whole system. The steady state is run about 200s to keep all parameters almost stable. Then the stable data is striped out to update the initial data in the input deck.

Heat loss is assumed as a constant heat transfer coefficient between the wall of pipes and surroundings. The temperature of surroundings is set to be 24.5°C while the heat transfer coefficient is set to be 15W/m²-°C. The total heat loss is about 7% of the total power.

Pump coast down is used for both cases. During coast down, both pump speed and pump motor torque are controlled by time dependant boundary conditions. The RD-14 ECI tank model shown as the fig. 3-34 is used for case 9006 in the blind calculation. All data for the ECI tank is set to be default as

```
'ECI SYSTEM','MECI'/
'ECITK'/
'RD-14', 2.72, 2.885, 5.5E+6, 21.4, 1.41, 0.173, 0.656, 0.2885,0.1E+6, 6.5E+6/
12.0E+6, 8.0, 1.36, 2.5E-5, 8.6E-2, 1.14E-3, 8.7E-5, 1.173, 20.0, 1.0/.
```

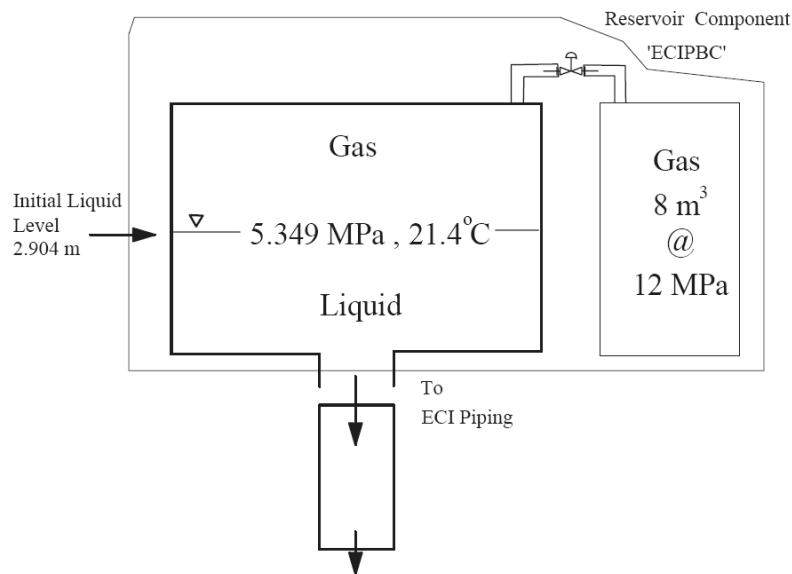


FIG. 3-34. ECI tank model.

Pump coast down is used for both cases. During coast down, both pump speed and pump motor torque are controlled by time dependant boundary conditions.

The discharge model used in the blind simulation of B9006 is DISCHARGE with coefficient 0.61. The discharge model used in the blind simulation of B9802 is DISCHARGE with coefficient 0.45.

In both cases, the data for the control volumes (such as HS5-30,HS5-31,HS5-32,HS5-33) of end fittings have some input error that cause less inventory in the primary side.

3.3.8.5 *Steady state calculation*

To get the steady state of the system, each channel (including feed pipes, heat sections and outlet pipes) is run separately by setting the pressure of inlet header, the inlet mass flow rate and temperature as boundary conditions. Given the correct power in the channel, one can get the pressure and temperature in the outlet header in the steady state for any single channel. By tuning the loss coefficient distribution, one can get the specified outlet pressure as needed. Then by tuning the heat transfer coefficient between walls to surroundings, one can get the temperature distribution needed.

After each channel is tuned, they are assembled together with the whole loop. By setting the temperature and mass flow rate of the feed water of both boilers, the second side pressures, and setting the pressure of header 5 as constant, one can get the steady state of the whole system. The steady state is run about 200s to keep all parameters almost stable. Then the stable data is striped out to update the initial data in the input deck.

Heat loss is assumed as a constant heat transfer coefficient between the wall of pipes and surroundings. The temperature of surroundings is set to be 24.5°C while the heat transfer coefficient is set to be 15W/m²-°C. The total heat loss is about 7% of the total power. The total heat loss is integrated as the total heat transferred from coolant to inside wall of pipes and heat transfer tubes inside boilers. That means if the inner wall temperature is higher than the temperature of coolant, the heat loss at this location will be negative.

3.3.8.6 *Modification from blind to open calculation*

In the open calculation, the heat transfer coefficient between wall to surroundings is set to be 8 W/m²°C. The total heat loss is about 3.7% of the total power for the case of 9006.

In the open calculation of the case of 9006, the RD-14M ECI tank model is tuned. The volume of accumulator is set to be 3.23 m³. The initial liquid level in accumulator is set to be 3.185 m. The initial pressure of the gas in the accumulator is set to be 4.3 MPa. The temperature of liquid in accumulator is set to be 21.4 °C. The level below which the accumulator is isolated is set to be 0.2885 m. The lower control pressure is set to be 0.32MPa and the upper control pressure is set to be 1.33MPa to keep the system pressure as the pressure boundary given. The initial pressure of gas reservoir is set to be 12MPa. The valve between the gas reservoir ant the ECI tank will not open in the case 9006. The initial temperature of pressurizing gas (assumed to be uniform) is set to be 21.4 °C. Other parameters are set to be default as shown follows.

```
'ECI SYSTEM','MECI'/  
'ECITK'/  
'RD-14M', 3.32, 3.185, 4.3E+6, 21.4, 1.41, 0.173, 0.656, 0.2885,0.32E+6, 1.33E+6/  
12.0E+6, 8.0, 1.36, 2.5E-5, 8.6E-2, 1.14E-3, 8.7E-5, 1.173, 21.4, 1.0/
```

In the open calculation of the case 9006, discharge model uses a VLALE model (with discharge coefficient of 0.4) as follows:

```
'VALVE','VLVBRK'/  
'R-IHD8-4','L-BRKPIPE'/  
3.848E-5, 0.4,0.0/
```

In the open calculation of the case 9802, only the discharge model is changed. The discharge model uses a VLALE model instead of DISCHARGE (with discharge coefficient of 0.23) as follows:

```
'VALVE','VLVBRK'/  
'R-IHD8','BRKVOL'/  
7.069E-6, 0.23,0.0/
```

3.4. BLIND AND OPEN STEADY-STATE CALCULATION RESULTS

The steady state results obtained by each participant as part of blind and open calculation phases are presented in Tables 3–6 to 3–9. For comparison the experimental values are also included in a separate column.

TABLE 3-6. SELECTED VARIABLES FOR STEADY STATE COMPARISON (B9006 BLIND CALCULATION)

Variable Name	Variable description	Unit	Desired Value (Exp.)	Steady state values from participants										Order*
				AECL	AERB	CNE	CNEA	KAERI	KINS	NPCIL	THU			
ΔP_{P1}	Pump 1 Differential Pressure (DP)	kPa(a)	1704.9	1770	1651.7	1615.6	1666.6	1703.2	1708.1	1731.8	1738.0	2		
ΔP_{P2}	Pump 2 DP	kPa(a)	1742.4	1740	1691.3	1679.7	1714.3	1742.4	1697.7	1734.3	1736.0	3		
ΔP_{HDR5}	DP from HDR8 to HDR5	kPa(a)	1466.4	1440	1449.9	1417.6	1446.6	1464.0	1472.1	1495.3	1463.0	4		
ΔP_{HDR7}	DP from HDR6 to HDR7	kPa(a)	1506.4	1500	1466.6	1462.3	1445.7	1549.0	1500.5	1441.0	1437.0	5		
P_{HDR8}	Header 8 Pressure	MPa(a)	11.537	11.47	11.570	11.609	11.60	11.62	11.555	11.523	11.926	6		
P_{HDR6}	Header 6 Pressure	MPa(a)	11.509	11.48	11.552	11.599	11.57	11.69	11.574	11.509	11.946	7		
P_{HDR7}	Header 7 Pressure	MPa(a)	10.075	9.98	10.085	10.137	10.13	10.14	10.073	10.069	10.509	8		
Q_{P1}	Pump 1 Discharge Flowrate	kg/s	21.7	21.5	21.8	20.3	21.72	21.7	24.0	21.67	21.5	9		
Q_{P2}	Pump 2 Discharge Flowrate	kg/s	21.5	21.5	21.8	20.3	21.72	21.7	24.0	21.67	21.4	10		
T_{B1-IN}	Boiler 1 Inlet Fluid Temp.	°C	293.9	297	299.6	296.1	295.9	296.0	297.1	294.6	297.9	22		
T_{B2-IN}	Boiler 2 Inlet Fluid Temp.	°C	295.2	296	299.2	295.5	294.5	295.4	297.1	294.4	297.1	23		
T_{B1-OUT}	Boiler 1 Outlet Fluid Temp.	°C	259.4	261	265.6	258.3	260.3	260.7	263.4	259.2	263.6	24		
T_{B2-OUT}	Boiler 2 Outlet Fluid Temp.	°C	260.2	262	265.6	258.5	260.5	261.0	263.3	259.0	264.0	25		
T_1	FES Temp.@top pin, middle HS13	°C	322.4	312	314.1	316.3	322.6	323.5	314.6	319.3	325.2	26		
T_2	FES Temp.@top pin, inlet HS13	°C	311.7	297	298.8	299.7	307.5	307.7	302.3	300.7	309.4	27		
T_3	FES Temp.@top pin, outlet HS13	°C	333.6	324	325.6	322.5	333.6	335.4	330.6	331.0	337.2	28		
T_4	FES Temp.@bottom pin, outlet HS13	°C	335.5	324	325.6	316.3	333.6	335.4	330.6	331.0	337.2	29		
T_5	FES Temp.@top pin, middle HS8	°C	321.7	311	313.1	315	321.5	321.7	314.3	317.2	322.6	30		
$\Delta P_{HS13-HDS}$	DP from HS13 to HDR5	kPa(a)	122.8	240	91.6	154.0	178.8	179.0	153.4	131.1	128.0	39		
ΔP_{HS13}	DP Across HS13	kPa(a)	1083	990	1018	1363	1150	1117	1072	1110	1006	40		
Q_7	HS5 inlet mass flow	kg/s	3.87	4.02	4.08	3.83	5.40 l/s	3.94	3.99	3.88	3.89	41		
Q_8	HS8 inlet mass flow	kg/s	4.98	4.83	4.97	4.50	6.15 l/s	4.93	4.91	5.03	4.99	42		
Q_9	HS10 inlet mass flow	kg/s	3.79	3.97	3.81	3.79	5.41 l/s	3.84	3.97	3.80	3.75	43		
Q_{10}	HS13 inlet mass flow	kg/s	4.82	4.82	4.93	4.49	6.15 l/s	4.86	4.95	4.82	4.75	44		
Q_{11}	Boiler 1 steam flow	kg/s	1.90	2.00	2.20	2.00	2.06	2.00	1.93	1.99	1.92	45		
Q_{12}	Boiler 2 steam flow	kg/s	1.90	1.96	2.21	1.95	2.08	1.96	1.93	1.99	2.08	46		
M	Mass Inventory in Primary Loop**	kg			790.2	786.6		840	810.2	793.1	767.1	49		
W_{TH1}	Thermal Power Across Boiler 1**	kW			3908	3950		3967	3936	3960	3850	50		
W_{TH2}	Thermal Power Across Boiler 2**	kW			3861	3870		3868	3903	3960	3689	51		
W_{loss}	Total loop heat loss	kW			367.4	238			263.7	238.3	696.2	52		
$B01DC$	Boiler 1 Downcomer Flow	kg/s			20.6					19.9	66.9	53		
$B02DC$	Boiler 2 Downcomer Flow	kg/s			21.4					19.9	66.4	54		

* The order number starts from 2 since the time is the first parameter

** These are variables that were not measured experimentally, but will aid in the code-to-code comparison.

TABLE 3-7. SELECTED VARIABLES FOR STEADY STATE COMPARISON (B9802 BLIND CALCULATION)

Variable name	Variable description	Unit	Desired value (Exp.)	Steady state value from code							Order
				AECL	AERB	CNE	KAERI	KINS	NPCIL	THU	
ΔP_{P1}	Pump 1 Differential pressure (DP)	kPa(a)	1295.6	1250	1215.0	1282.7	1259.0	1257.7	1320.2	1298.0	2
ΔP_{P2}	Pump 2 DP		1283.1	1250	1228.3	1289.5	1271.0	1259.0	1318.1	1297.0	3
ΔP_{HDR5}	DP from HDR8 to HDR5	kPa(a)	1084.0	1060	948.3	1088.9	1091.0	1075.7	1084.3	1095.0	4
ΔP_{HDR6-7}	DP from HDR6 to HDR7		1121.5	1100	965.1	1123.4	1127.0	1123.0	1148.8	1076.0	5
P_{HDR8}	Header 8 Pressure	MPa(a)	11.087	11.09	11.077	11.175	11.286	11.054	11.078	11.759	6
P_{HDR6}	Header 6 Pressure		11.106	11.09	11.071	11.184	11.299	11.077	11.111	11.774	7
P_{HDR7}	Header 7 Pressure		9.962	9.99	10.105	10.061	10.172	9.954	9.962	10.698	8
Q_{P1}	Pump 1 Discharge Flowrate	kg/s	18.5	18.2	18.5	17.5	18.5	18.3	18.5	18.6	9
Q_{P2}	Pump 2 Discharge Flowrate		18.4	18.2	18.5	17.5	18.5	18.5	18.5	18.5	10
T_{B1-IN}	Boiler 1 Inlet Fluid Temp.	°C	301.8	303	305.0	303.6	300.7	301.8	302.2	301.2	22
T_{B2-IN}	Boiler 2 Inlet Fluid Temp.		301.8	302	304.8	303.2	300.1	301.2	301.9	330.8	23
T_{B1-OUT}	Boiler 1 Outlet Fluid Temp.		260.9	262	266.0	261.1	259.7	263.0	261.5	262.3	24
T_{B2-OUT}	Boiler 2 Outlet Fluid Temp.		262.6	262	265.5	260.7	259.7	262.9	261.1	262.1	25
T_1	FES Temp.@top pin, middle HS13	°C	323.0	320	324.3	324.4	330.0	316.1	328.0	327.5	26
T_2	FES Temp.@top pin, inlet HS13		313.6	302	307.7	306.7	310.7	302.4	308.0	309.4	27
T_3	FES Temp.@top pin, outlet HS13		338.0	333	336.4	331.1	344.2	332.9	340.4	341.2	28
T_4	FES Temp.@bottom pin, outlet HS13		337.4	333	336.4	324.4	344.2	332.9	340.4	341.2	29
T_5	FES Temp.@top pin, middle HS8		326.7	316	317.3	323.0	326.6	318.7	324.9	325.1	30
$\Delta P_{HS13-HD5}$	DP from HS13 to HDR5	kPa(a)	58.8	180	81.7	134.6	146.0	125.8	63.2	110.0	39
ΔP_{HS13}	DP Across HS13		824.2	730	658.7	1037.4	837.0	787.7	815.5	756.0	40
Q_7	HS5 inlet mass flow	kg/s	3.40	3.42	3.42	3.30	3.39	3.44	3.36	3.36	41
Q_8	HS8 inlet mass flow		4.27	4.10	4.34	3.88	4.17	4.22	4.24	4.04	42
Q_9	HS10 inlet mass flow		3.29	3.38	3.55	3.26	3.30	3.38	3.32	3.24	43
Q_{10}	HS13 inlet mass flow		4.15	4.09	4.22	3.88	4.17	4.20	4.17	4.10	44
Q_{11}	Boiler 1 steam flow	kg/s	1.93	1.92	2.08	1.96	1.98	1.96	1.98	1.86	45
Q_{12}	Boiler 2 steam flow		1.91	2.00	1.99	1.96	1.91	1.96	1.98	1.86	46
M	Mass Inventory in Primary Loop*	kg			775.9	766.8	840	799.6	745.0	737.6	49
W_{TH1}	Thermal Power Across Boiler 1*	kW			3857	3910	3949	3903	3954	3783	50
W_{TH2}	Thermal Power Across Boiler 2*	kW			3877	3910	3883	3847	3945	3747	51
W_{loss}	Total loop heat loss*	kW			371.7	277		259.5	238.3	701.7	52
$B01DC$	Boiler 1 Downcomer Flow*	kg/s			20.5				19.8	27.2	53
$B02DC$	Boiler 2 Downcomer Flow*	kg/s			21.2				19.8	9.8	54

* These are variables that were not measured experimentally, but will aid in the code-to-code comparison.

TABLE 3-8. SELECTED VARIABLES FOR STEADY STATE COMPARISON (B9006 OPEN CALCULATION)

Variable name	Variable description	Unit	Desired value (Exp.)*	Steady state values from participants										Order
				AECL	AERB	CNE	CNEA	KAERI	KINS	NPCIL	THU			
ΔP_{P1}	Pump 1 Differential pressure (DP)	kPa(a)	1701.8	1684.4	1651.7	1615.6	1681.5	1703.2	1709.4	1731.8	1726.7	2		
ΔP_{P2}	Pump 2 DP	kPa(a)	1739.2	1739.0	1691.3	1679.7	1721.6	1742.4	1695.7	1734.3	1730.3	3		
ΔP_{HDR5}	DP from HDR8 to HDR5	kPa(a)	1471.4	1446.6	1449.9	1417.6	1464	1464	1472.9	1495.3	1463	4		
ΔP_{HDR6-7}	DP from HDR6 to HDR7	kPa(a)	1498.9	1491.4	1466.6	1462.3	1452	1549	1501.6	1440.0	1422	5		
P_{HDR8}	Header 8 pressure	MPa(a)	11.556	11.490	11.570	11.609	11.644	11.66	11.575	11.624	11.581	6		
P_{HDR6}	Header 6 pressure	MPa(a)	11.518	11.496	11.552	11.599	11.618	11.69	11.556	11.610	11.592	7		
P_{HDR7}	Header 7 pressure	MPa(a)	10.103	9.994	10.085	10.137	10.166	10.14	10.073	10.170	10.170	8		
Q_{P1}	Pump 1 Discharge flowrate	kg/s	21.7	21.2	21.8	20.3	21.3	21.7	24.0	21.7	21.4	9		
Q_{P2}	Pump 2 Discharge flowrate	kg/s	21.4	21.2	21.8	20.3	21.3	21.7	24.0	21.7	21.4	10		
T_{B1-IN}	Boiler 1 Inlet fluid temp.	°C	295.4	299.4	299.6	296.1	296.4	296.0	298.1	294.6	296.2	22		
T_{B2-IN}	Boiler 2 Inlet fluid temp.	°C	296.5	298.8	299.2	295.5	296.9	295.4	298.4	294.4	295.7	23		
T_{B1-OUT}	Boiler 1 Outlet fluid temp.	°C	260.7	263.5	265.6	258.3	261.1	260.7	263.6	259.2	261.8	24		
T_{B2-OUT}	Boiler 2 Outlet fluid temp.	°C	261.3	263.8	265.6	258.5	260.3	260.9	263.5	259.0	261.9	25		
T_1	FES Temp.@top pin, middle HS13	°C	324.2	314.6	314.1	316.3	322.8	323.5	314.8	319.3	323.1	26		
T_2	FES Temp.@top pin, inlet HS13	°C	313.6	298.8	298.8	299.7	307.5	307.7	302.6	300.7	307.2	27		
T_3	FES Temp.@top pin, outlet HS13	°C	335.5	323.5	325.6	322.5	333.9	335.5	331.2	331.0	335.0	28		
T_4	FES Temp.@bottom pin, outlet HS13	°C	337.4	326.4	325.6	316.3	333.9	335.5	331.2	331.0	335.0	29		
T_5	FES Temp.@top pin, middle HS8	°C	323.0	313.4	313.1	315	322.3	321.7	314.4	317.2	320.7	30		
$\Delta P_{HS13-HD5}$	DP from HS13 to HDR5	kPa(a)	123.9	186.6	91.6	154.0	176.6	179	153.4	131.1	53.0	39		
ΔP_{HS13}	DP Across HS13	kPa(a)	1087	1094	1018	1363	1172	1117	1073	1110	1006	40		
Q_7	HS5 inlet mass flow	kg/s	3.90	3.97	4.08	3.83	3.91	3.94	3.99	3.92	3.87	41		
Q_8	HS8 inlet mass flow	kg/s	4.95	4.76	4.97	4.50	4.87	4.93	4.91	5.03	4.97	42		
Q_9	HS10 inlet mass flow	kg/s	3.82	3.93	3.81	3.79	3.83	3.84	3.97	3.80	3.76	43		
Q_{10}	HS13 inlet mass flow	kg/s	4.80	4.75	4.93	4.49	4.81	4.87	4.95	4.82	4.76	44		
Q_{11}	Boiler 1 steam flow	kg/s	1.97	2.00	2.20	2.00	2.06	2.00	1.93	1.99	1.90	45		
Q_{12}	Boiler 2 steam flow	kg/s	1.94	1.98	2.21	1.95	2.08	1.96	1.94	1.99	1.85	46		
M	Mass inventory in primary loop**	kg		795.5	790.2	786.6	810.8	840.9	809.2	793.1	739.6	49		
W_{TH1}	Thermal power across boiler 1**	kW		3980	3908	3950	4035	3967	4047	3960	3823	50		
W_{TH2}	Thermal power across boiler 2**	kW		3892	3861	3870	3885	3868	4041	3960	3750	51		
W_{loss}	Total loop heat loss	kW		223.4	367.4	238	223.0	288.0	141.6	238	606.8	52		
B01DC	Boiler 1 Downcomer Flow	kg/s		18.5	20.62	10.98	10.98	13.43	19.9	19.9	36.5	53		
B02DC	Boiler 2 Downcomer Flow	kg/s		18.6	21.38	10.87	10.87	14.01	19.9	19.9	42.6	54		

* Slight variations in the experimental values between blind and open calculations are due to clarifications obtained during the exercise.

** These are variables that were not measured experimentally, but will aid in the code-to-code comparison.

TABLE 3-9. SELECTED VARIABLES FOR STEADY STATE COMPARISON (B9802 OPEN CALCULATION)

Variable Name	Variable description	Unit	Desired Value (Exp.)*	Steady state value from code								Order
				AECL	AERB	CNE	KAERI	KINS	NPCIL	THU		
ΔP_{P1}	Pump 1 Differential pressure (DP)	kPa(a)	1295.6	1317.7	1215.0	1282.7	1259.0	1258.9	1320.2	1298	2	
ΔP_{P2}	Pump 2 DP		1283.1	1318.8	1228.3	1289.5	1271.0	1259.9	1318.1	1297	3	
ΔP_{HDR5}	DP from HDR8 to HDR5	kPa(a)	1084.0	1098.1	948.3	1088.9	1091.0	1076.7	1084.3	1095	4	
ΔP_{HDR6-7}	DP from HDR6 to HDR7		1121.5	1133.5	965.1	1123.4	1127.0	1123.9	1148.8	1076	5	
P_{HDR8}	Header 8 Pressure	MPa(a)	11.087	11.211	11.077	11.175	11.29	11.055	11.179	11.759	6	
P_{HDR6}	Header 6 Pressure		11.106	11.224	11.071	11.184	11.30	11.079	11.212	11.774	7	
P_{HDR7}	Header 7 Pressure		9.962	10.091	10.105	10.061	10.17	9.955	10.064	10.698	8	
Q_{P1}	Pump 1 Discharge flowrate	kg/s	18.5	18.4	18.5	17.5	18.5	18.2	18.5	18.6	9	
Q_{P2}	Pump 2 Discharge flowrate		18.5	18.4	18.5	17.5	18.5	18.5	18.5	18.5	10	
T_{B1-IN}	Boiler 1 Inlet fluid temp.	°C	301.8	302.7	305.0	303.6	300.8	303.4	302.2	301.2	22	
T_{B2-IN}	Boiler 2 Inlet fluid temp.		301.8	302.4	304.8	303.2	300.1	303.0	301.9	330.8	23	
T_{B1-OUT}	Boiler 1 Outlet fluid temp.		261.1	262.1	266.0	261.1	259.7	263.3	261.5	262.3	24	
T_{B2-OUT}	Boiler 2 Outlet fluid temp.		262.6	261.8	265.5	260.7	259.7	263.2	261.1	262.1	25	
T_1	FES Temp.@top pin, middle HS13	°C	323.0	318.0	324.3	324.4	330.0	316.4	328.0	327.5	26	
T_2	FES Temp.@top pin, inlet HS13		313.6	301.5	307.7	306.7	310.7	302.7	308.0	309.4	27	
T_3	FES Temp.@top pin, outlet HS13		338.0	328.3	336.4	331.1	344.2	335.5	340.4	341.2	28	
T_4	FES Temp.@bottom pin, outlet HS13		338.0	299.8	336.4	324.4	344.2	335.5	340.4	341.2	29	
T_5	FES Temp.@top pin, middle HS8		326.7	316.7	317.3	323.0	326.6	319.0	324.9	325.1	30	
$\Delta P_{HS13-HDR5}$	DP from HS13 to HDR5	kPa(a)	58.5	153.7	81.7	134.6	146.0	125.9	63.2	110.0	39	
ΔP_{HS13}	DP Across HS13		824.2	834.6	658.7	1037.4	837.0	788.4	815.5	756.0	40	
Q_7	HS5 inlet mass flow	kg/s	3.40	3.45	3.42	3.30	3.39	3.44	3.38	3.356	41	
Q_8	HS8 inlet mass flow		4.27	4.12	4.34	3.88	4.17	4.22	4.24	4.308	42	
Q_9	HS10 inlet mass flow		3.29	3.41	3.55	3.26	3.30	3.38	3.32	3.240	43	
Q_{10}	HS13 inlet mass flow		4.15	4.12	4.22	3.88	4.17	4.21	4.17	4.098	44	
Q_{11}	Boiler 1 steam flow	kg/s	1.93	1.96	2.08	1.96	1.98	1.94	1.98	1.859	45	
Q_{12}	Boiler 2 steam flow		1.92	1.96	1.99	1.96	1.98	1.96	1.98	1.857	46	
M	Mass Inventory in primary loop**	kg		782.8	775.9	766.8	835.6	798.1	745.0	737.6	49	
W_{TH1}	Thermal power across boiler 1**	kW		3930	3857	3910	3950	4049	3953	3783.4	50	
W_{TH2}	Thermal power across boiler 2**	kW		3920	3877	3910	3883	4017	3953	3747.4	51	
W_{loss}	Total loop heat loss	kW		222.9	371.7	277	288.4	142.6	238.3	701.7	52	
$B01DC$	Boiler 1 Downcomer flow	kg/s		17.7	20.5		13.84		19.8	27.2	53	
$B02DC$	Boiler 2 Downcomer flow	kg/s		17.9	21.2		14.10		19.8	9.8	54	

* Slight variations in the experimental values between blind and open calculations are due to clarifications obtained during the exercise.

** These are variables that were not measured experimentally, but will aid in the code-to-code comparison.

4 CODE COMPARISON WITH EXPERIMENTS

As discussed previously, a subset of the almost 600 measurements in RD-14M was selected as the basis for a meaningful comparison between the experiment and code calculations. The list of variables to be compared against test measurements was developed by the participants during the second meeting. Table 4-1 lists these 48 selected variables for the code intercomparison, their experimental “device code” (instrument identifier), and their steady state values measured at the beginning of the transients (Note: The experimental measurements are also shown in Tables 3-6 and 3-7, where they are compared to blind calculation results, and Tables 3-8 and 3-9 against open calculation results). Exact locations of the measurement for these variables can be found in [Swartz, 2003] based on the “Device Code” given in Table 4-1. The uncertainties given are based on test B9802 and were calculated using the methodology described in Section 2.3). Variables 49 to 54 were not measured experimentally (and therefore are not included in Table 4-1), but were selected to aid in the code-to-code comparison.

Data were collected for 2284 s in B9006 and for 1363 s in B9802 experiment. However, only the first 1600 s of the transient for test B9006 is used for the intercomparison since all significant events occur during this time.

In the following sections explain the significance of these variables to the overall loop behaviour and certain details or local phenomena is given and discuss participant’s results compared to measurements. For each test, results from the blind calculations are discussed very briefly in terms of major differences to the experiment and, if warranted, differences to the later, open calculations. The sections on the open results include more detailed discussion on code-to-experiment comparison.

Test B9006 description, blind, and open results are presented in Sections 4.1 to 4.3.

Test B9802 description, blind, and open results are presented in Sections 4.4 to 4.6.

4.1 DESCRIPTION OF TEST B9006

In this test, following 7 mm inlet header break at 11 s (the break valve actually started to open at 10.8 s), the system pressure decreases rapidly till it reaches saturation pressure of the fluid at hottest locations. Once void appears in the system, depressurization becomes gradual. System pressure¹ falls to 8.8 MPa(g) in HDR-7 at 11.3 s triggering heater power reduction to decay level (5%) with a short delay in the test. Pump ramp boundary conditions are also imposed at the same time to represent a coincident loss of Class-IV power supply.

Pressure reduction in the primary system continues and pressure falls to 6.0 MPa(g), at 28s when a time varying secondary pressure (cool down) is imposed as a boundary condition representing the effect of opening of main steam safety valves. At this time, ECI valves are also signalled to open, allowing some inter-header flow, but no flow from the ECI tank. The actual ECI valve open time, extracted from flow rate measurements, was approximately 1.5s later, indicating a significant delay in the valves. Following the valves opening, due to pressure difference between the headers, there is flow in the header connection lines.

¹ Pressures are expressed as absolute pressure, unless otherwise indicated with (g) to denote gauge pressure.

TABLE 4-1. SELECTED VARIABLES AND THEIR EXPERIMENTAL DEVICE CODES (INITIAL STEADY-STATE VALUES ARE ALSO SHOWN TO INDICATE DIFFERENCES AND SIMILARITIES BETWEEN THE TWO TESTS)

Variable Name	Variable Description	Device Code	Experiment			Var. Unit	Order	
			B9006	B9802	Uncertainty			
	Time		0 - 2284	0 - 1363	± 0.075	s	1	
ΔP_{P1}	Pump 1 Differential Pressure (DP)	5Q-D1	1704.90	1295.60	+27.2/-32.3	kPa(a)	2	
ΔP_{P2}	Pump 2 DP	12Q-D1	1742.40	1283.11	+35.0/-22.7		3	
ΔP_{HDR8-5}	DP from HDR8 to HDR5	35Q-D1	1466.40	1083.97	+29.3/-20.8	kPa(a)	4	
ΔP_{HDR6-7}	DP from HDR6 to HDR7	36Q-D1	1506.40	1121.46	+30.3/-19.8		5	
P_{HDR8}	Header 8 Pressure	10P-D1	11.536	11.074	+0.085/-0.082		MPa(a)	6
P_{HDR6}	Header 6 Pressure	4P-D1	11.508	11.106	+0.032/-0.049	7		
P_{HDR7}	Header 7 Pressure	6P-D1	10.074	9.962	+0.043/-0.037	8		
Q_{P1}	Pump 1 Discharge Flow rate	1F	27.50	23.44	+0.14/-0.52	l/s	9	
Q_{P2}	Pump 2 Discharge Flow rate	2F	27.20	23.35	+0.06/-0.51		10	
Q_3	ECI to Header 5 Flow rate	231F-D1	0.00	n/a	n/a	kg/s	11	
Q_4	ECI to Header 6 Flow rate	232F-D1	0.00	n/a	n/a		12	
Q_5	ECI to Header 7 Flow rate	233F-D1	0.00	n/a	n/a		13	
Q_6	ECI to Header 8 Flow rate	234F-D1	0.00	n/a	n/a		14	
Q_{INT}	Integral of ECI Flows	1H	0.00	n/a	n/a	kg	15	
α_1	Boiler 1 Inlet Void Fraction	11VF-DT1	0.00	0.00	n/a	-	16	
		11VF-DT2	0.00	0.00	n/a			
α_2	Boiler 1 Outlet Void Fraction	11VF-DT3/4	0.00	0.00	n/a		17	
α_3	Boiler 2 Inlet Void Fraction	12VF-DT3	0.00	0.00	n/a		18	
α_4	Boiler 2 Outlet Void Fraction	12VF-DT4	0.00	0.00	n/a		19	
		12VF-DT1/2	0.00	0.00	n/a			
α_5	Pump 1 Outlet Void Fraction	21VF-DTZ	0.00	0.00	n/a	-	20	
α_6	Pump 2 Outlet Void Fraction	4VF-DTZ	0.00	0.00	n/a		21	
T_{B1-IN}	Boiler 1 Inlet Fluid Temp.	60T-D1	293.9	301.8	+1.5/-3.5	°C	22	
T_{B2-IN}	Boiler 2 Inlet Fluid Temp.	61T-D1	295.2	301.8	+1.7/-3.4		23	
T_{B1-OUT}	Boiler 1 Outlet Fluid Temp.	60T-D2	259.4	260.9	+1.5/-3.4		24	
T_{B2-OUT}	Boiler 2 Outlet Fluid Temp.	61T-D2	260.2	262.6	+1.6/-3.1		25	
T_1	FES Temp.@top pin, middle HS13	208T-D12	322.4	323.0	+6.1/-4.2	°C	26	
T_2	FES Temp.@top pin, inlet HS13	208T-D3	311.7	313.6	+4.7/-3.5		27	
T_3	FES Temp.@top pin, outlet HS13	208T-D14	333.6	338.0	+4.2/-5.4		28	
T_4	FES Temp.@bot pin, outlet HS13	208T-D18	335.5	337.4	+5.1/-4.8		29	
T_5	FES Temp.@top pin, middle HS8	203T-D12	321.7	334.9	+7.1/-2.1		30	
α_7	HS5 Inlet Void Fraction	15VF	0.00	0.00	n/a	-	31	
α_8	HS5 Outlet Void Fraction	16VF	0.00	0.00	n/a		32	
α_9	HS8 Inlet Void Fraction	21VF	0.00	0.00	n/a		33	
α_{10}	HS8 Outlet Void Fraction	22VF	0.00	0.00	n/a		34	
α_{11}	HS10 Inlet Void Fraction	25VF	0.00	0.00	n/a		35	
α_{12}	HS10 Outlet Void Fraction	26VF	0.00	0.00	n/a		36	
α_{13}	HS13 Inlet Void Fraction	31VF	0.00	0.00	n/a		37	
α_{14}	HS13 Outlet Void Fraction	32VF	0.00	0.00	n/a		38	
$\Delta P_{HS13-HD5}$	DP from HS13 to HDR5	45Q-D1	122.80	58.76	+4.5/-3.3		kPa(a)	39
ΔP_{HS13}	DP Across HS13	32Q-D1	1082.90	824.23	+24.9/-17.1			40
Q_7	HS5 inlet mass flow	177F-D1	4.9 (l/s)	4.30 (l/s)	n/a		kg/s (l/s)	41
Q_8	HS8 inlet mass flow	183F-D1	6.3 (l/s)	5.40 (l/s)	n/a			42
Q_9	HS10 inlet mass flow	187F-D1	4.8 (l/s)	4.17 (l/s)	+0.04/-0.10			43
Q_{10}	HS13 inlet mass flow	193F-D1	6.1 (l/s)	5.25 (l/s)	+0.05/-0.11			44
Q_{11}	Boiler 1 steam flow	3F-M1	1.90	1.93	n/a	kg/s	45	
Q_{12}	Boiler 2 steam flow	4F-M1	1.90	1.91	n/a		46	
Q_{BRK}	Break Discharge Mass Flow rate	237F-D1	n/a	0	n/a	kg/s	47	
$Q_{INT-BRK}$	Integrated Break Discharge	7H-D1	n/a	0	n/a	kg	48	

Because the circuit pressure is higher than the ECI pressure, the check valves that are present in the lines to the headers do not allow ECI flow injection. This allows flow between the inlet header from one pass and outlet headers of the other pass, i.e. between HD5 and 6 and

between HD7 and 8. This results in approximately 1/6 of the pump flow rate to bypass the heated sections.

No water from HP ECI system enters the loop at that time as tank pressure (4.2 MPa(g)) was lower than header pressure. Entry of relatively cold fluid from inlet header to outlet header reduced the coolant temperature of outlet header and thereby primary coolant pressure. Header pressures reached 4.2MPa in the timeframe from 78 to 80 s, however, significant net ECI inflow did not start until about 115 s in the experiment.

Forced convection flow provided by pump coast down brings the primary fluid temperature close to the secondary fluid temperature in the initial period of the transient. Following loss of forced circulation after pump coast down, intermittent flow stagnation is observed in some of the channels occasionally. This results in FES temperature excursion in those channels for very short duration. The duration of intermittent flow stagnation and corresponding FES temperature excursions are governing parameter to determine the flow reversal in the channels. On establishment of flows in the channels, coolant picks up heat and raises its temperature and boils resulting in increase in voids in the channels in the flow direction. Higher temperature fluid from channel exit gets mixed with cold ECI in the headers.

At 1110 s, High pressure ECI gets isolated on depletion of 1700 kg inventory in ECI tank and LPI is initiated maintaining the loop pressure at about 1.3MPa.

4.2 BLIND CALCULATION RESULTS FOR TEST B9006

All eight participants performed blind calculations, using ground rules and boundary conditions discussed in Section 3.2, and their results are presented below along with the corresponding experimental measurements.

4.2.1 Sequence of major events

The sequence of major events in Test B9006 is summarized in Table 4–2. Where two times are given in the Experiment column (the second one in parentheses), the first time refers to the time when the event was indicated through direct measurement and the second time refers to the time the trip parameter (which was used in the calculations to trigger the event) reached its setpoint. With a scan rate of 0.2s, the minimum experimental uncertainty is estimated to be $\pm 0.15s$. For times estimated from graphs (indicated by “~”) the estimated uncertainty in timing is $\pm 5s$.

4.2.2 Pump differential pressures and flow rates

Primary loop coolant circulation is provided by two high-head centrifugal pumps. In test B9006, the break occurred at inlet-header HD8 at 10.8 s, and the primary pumps were ramped down when header HD7 pressure reached 8.8 MPa(g) at the same time as the heater power was ramped down (in the test the ramp-downs actually occurred at 11.6 s). Header pressure was used in the simulations to initiate the exponential pump rundown, which curves were provided as a boundary condition from the experimental measurements.

TABLE 4-2 SEQUENCE OF EVENTS FOR TEST B9006 (BLIND CALCULATIONS)

Events	Experiment ± 0.15 (s) $\sim \pm 5$ (s)	Code predictions (s)							
		AECL	AERB	CNE	CNEA	KAERI	KINS	NPCIL	THU
Data gathering started/Calculation starts	0.0	0.0	0.0	0.0	0.0	0.0	0.0	0.0	0.0
Surge tank isolated	6.0	6.0	6.0	6.0	6.0	6.0	6.0	6.0	0.0
Blowdown valve (MV-8) opens	10.8	11.0	11.0	11.0	11.0	11.0	11.0	11.0	11.0
Primary pump run down Power run down (8.8 MPa(g) @ HD7)	11.6 (11.3)	11.3	11.4	11.4	11.5	11.6	11.4	11.6	11.8
Secondary pressure ramp ECI accumulator poised (6.0 MPa(g) @ HD7)	29.5 (28.0)	30.6	31.9	31	27.3	29.5	21.6	26.9	29.2
ECI Valve MV-11 Opens (4.2 MPa(g) @ HD7)	78.0 (78.5)	82	94.4	52	----	70.8	119.6	70.5	77
HP ECI flow into loop starts	~ 115	83	95	52	58	79.3	118	45	77
Channel reverse flow starts (HS _x , x = 5,8,10,13)	~ 180 (5,10)	97 (10)	150(5) 107(10)	139 (5,10)	---	115(10) 240(5)	190(5) 225(13)	200 (10,13)	~ 125 (5,10)
Initial Integral Loop Refill*	~ 480	~ 520	~ 440	~ 540	~ 90	~ 570	~ 400	~ 125	~ 510
HP ECI complete (10% of initial level) and LPI start	~ 1100	1157	1301	1087	999	1126	990	1070	1180
End of test	2284	2280	2300	2310	2400	2280	2284	2300	2285

* Experiment time is estimated from the time the last void measurement is observed to reach zero (except pump P2 outlet, which is suspect) and simulation times are taken from Figure 4–16 when the fast refill ends

The histories of ΔP_{P1} and ΔP_{P2} and the pump flow rates are a reflection of the pump rundown and are not affected by the small break, unlike in a LBLOCA.

Figures 4–1 to 4–4 provide the code comparison to experiment, in terms of pump differential pressure and mass flow rates. All calculations show the proper trends, with the correct initiation time and only slight variation in the rundown curve (KINS used an incorrect location for the pump differential pressure curves in their blind submission, thus showing an artificial offset from the other curves; this was corrected in the open calculation results). This indicates correct single-phase pump models by all participants. The trend that pump P1 flow becomes stagnant faster than P2 is reproduced by some code predictions, while others calculate a similar long-term low flow rate in the positive direction for both pumps. Note that the experimental flow rates, measured in l/s, have been converted to mass flow rates in kg/s using the liquid density calculated at the corresponding boiler outlet temperature (BO1 for P1, BO2 for P2) and header HD6 pressure (pressure effect is negligible).

Several participants submitted their blind calculation results with rather coarse time steps, hence showing an apparently decreasing differential pressure prior to the break.

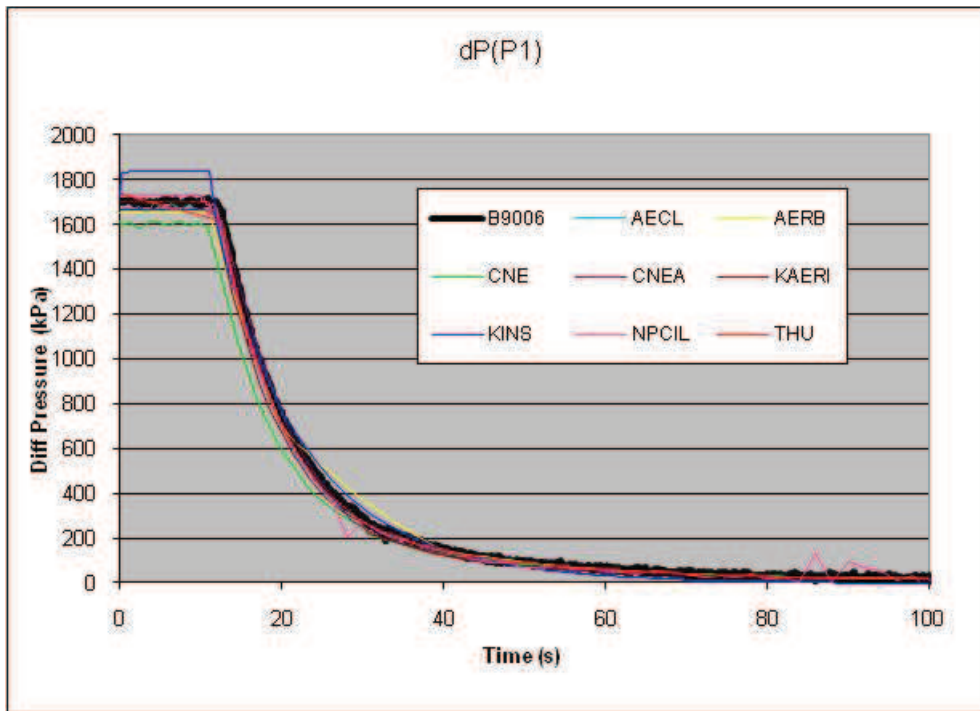


FIG. 4-1. Pump P1 differential pressure.

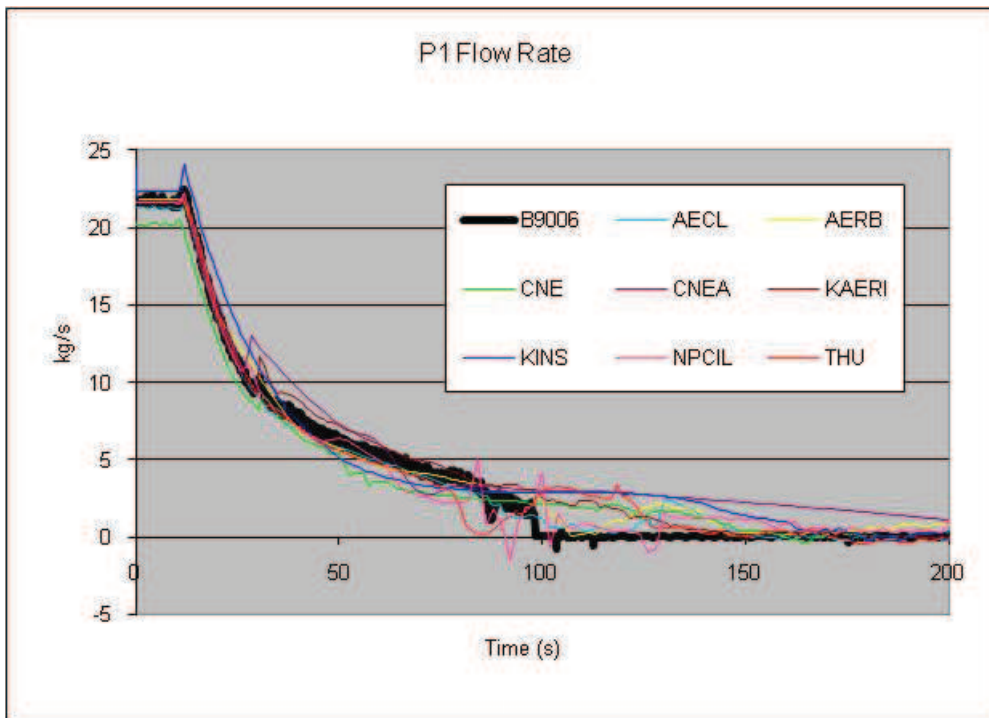


FIG. 4-2. Pump P1 flow rate.

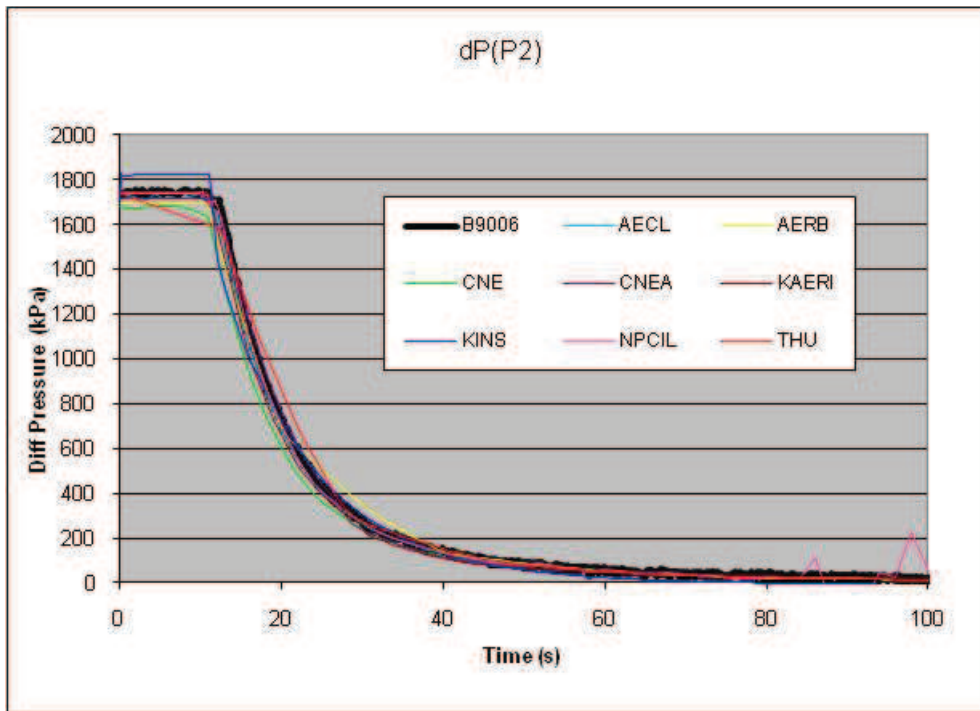


FIG. 4-3. Pump P2 differential pressure.

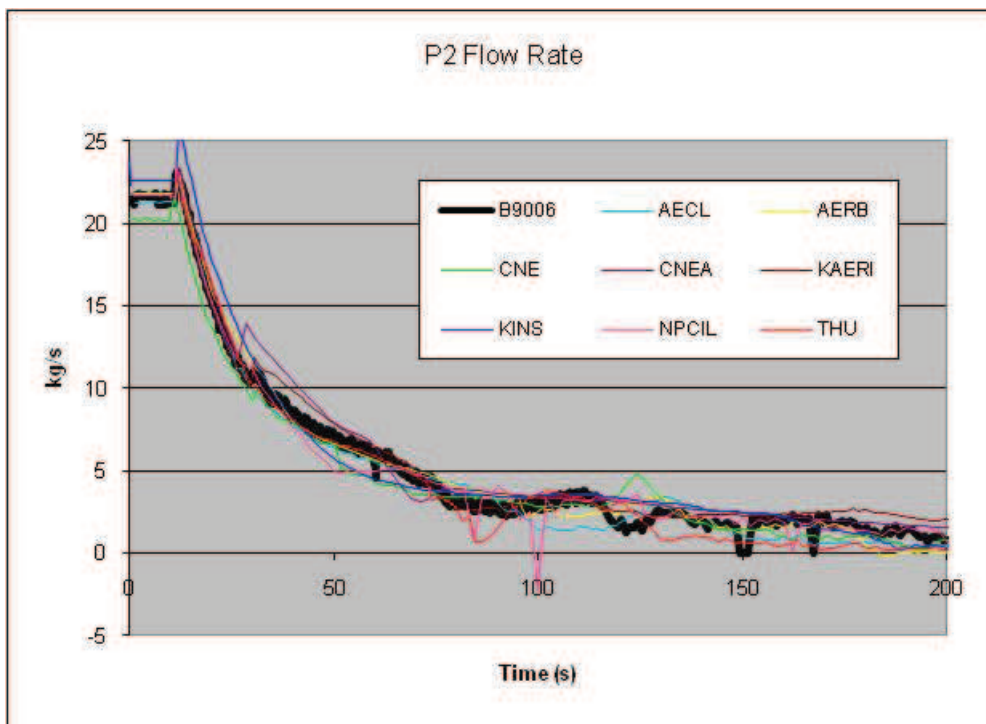


FIG. 4-4. Pump P2 flow rate

4.2.3 Header differential pressure

Since the break is relatively small, the pumps still determine the header pressure differences during the rundown period from 11s to 100 s, when they reach 10% of their initial speed. Therefore, the header-to-header differential pressures follow the same general trend as the pump differential pressures.

Figures 4–5 and 4–6 show the broken and unbroken-pass header-to-header differential pressures, respectively. This pressure drives the flow through below-header portion of the loop (inlet feeders, heated sections and outlet feeders) during the transient. At 100 s the pressure difference reaches values below 30 kPa and remains below for the remainder of the test, thus providing very little driving force for channel flow. As discussed later, there are some periods of stagnation and reverse flow in individual channels.

All calculations show the correct timing and overall trend, but only some of the participants correctly predict the small differential pressure increase in the intact loop immediately after the break opening. The differential pressures are slightly underpredicted by some participants and overpredicted by others in the 20-s to 40-s period.

KINS predicted higher differential pressures initially, similar to the pump differential pressures for the same reason as provided in the previous section. NPCIL shows some significant spikes in the header-to-header differential pressures during the later phase of the pump rundown while it showed smaller spikes in pump differential pressure at slightly different times. These spikes were avoided in their open calculations and are likely due to high-frequency header pressure oscillations (not visible because of the 2-s frequency of data presentation) calculated by them during the 80-100-s time period when cold water mixes with the hot two-phase mixture in the headers. For other simulations, the blind and open simulations are virtually the same.

4.2.4 Header pressures

The entire loop depressurized relatively uniformly during this SBLOCA, with differential pressures driven mainly by the pumps running down, as discussed in the previous section. Even during ECI injection, the header pressures are very close to the ECI tank pressure, thus ECI injection does not significantly affect header pressures. The initial depressurization to about 8 MPa in the outlet and 9.5 MPa in the inlet headers is the result of single-phase discharge from the break until saturation is reached and two-phase discharge starts. The depressurization is considerably slower during the two-phase discharge and slows down even further when flashing occurs in the heated channels.

Figures 4–7 and 4–8 show the early pressure transients in headers HD8 (the broken header) and HD7 (the outlet header of the intact pass). The initial depressurization behaviour is captured well by all simulations. From about 40 s, when voiding in the channels becomes significant but flow is still driven by the pumps, until 200 s, when pump flow is essentially zero (see pump P2 flow rate), some participants overpredict, while others underpredict, the header pressures by up to 0.5 MPa, with the occasional large spike in the NPCIL case.

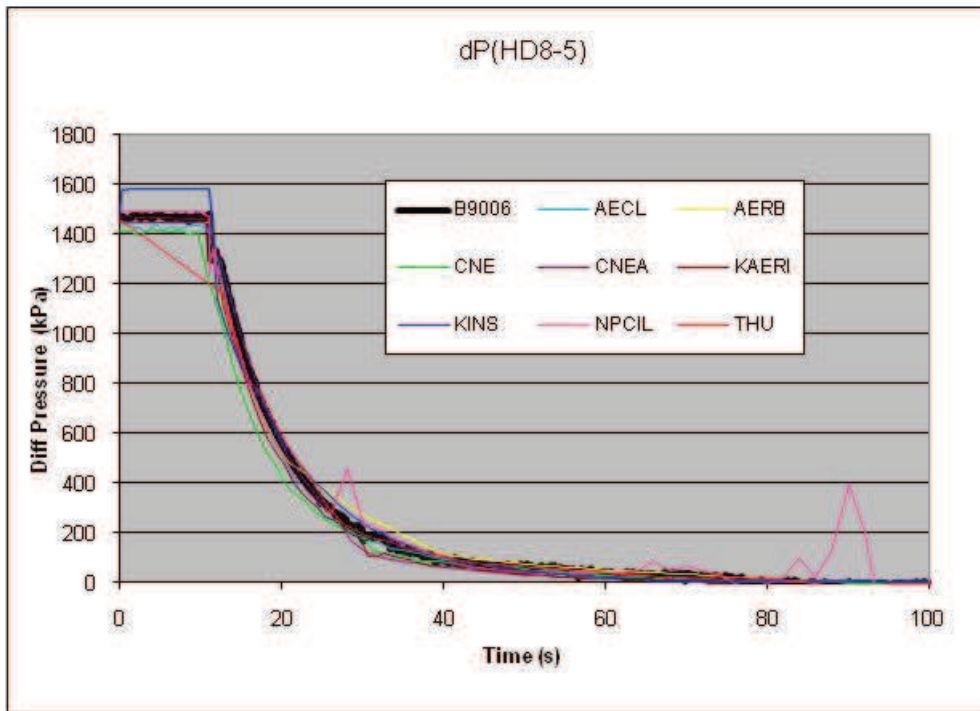


FIG. 4-5. Broken pass header-to-header differential pressure.

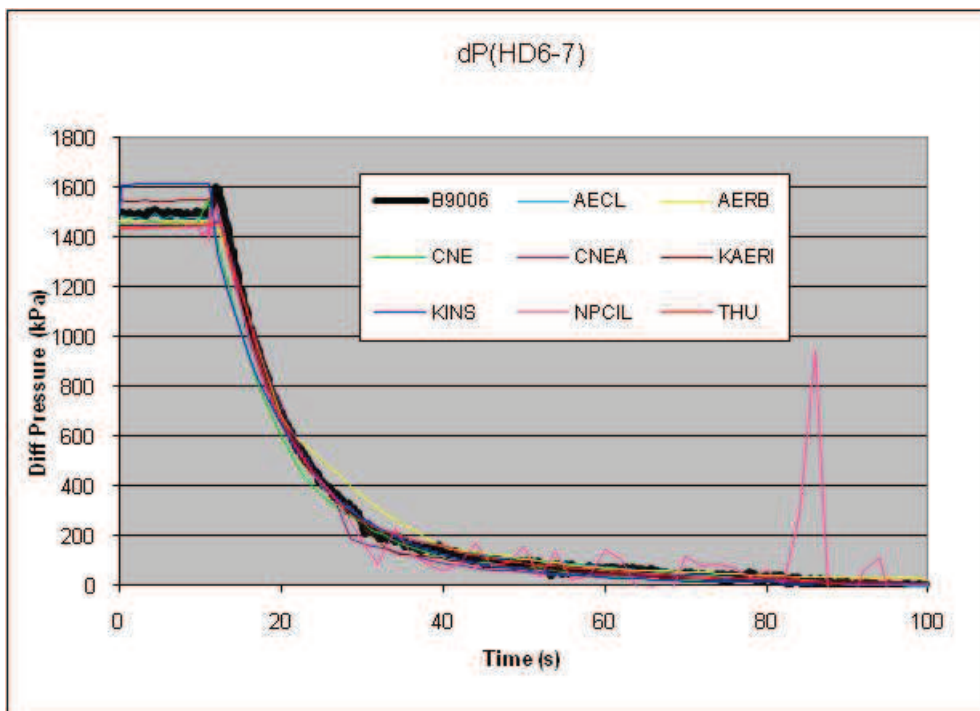


FIG. 4-6. Intact pass header-to-header differential pressure.

From 200 to 500s (see Figure 4-9), when the loop is being refilled by ECI water, all participants predict pressures close to the test measurements (only HD6 is shown, but others are qualitatively similar). KINS calculates a long, but temporary high-pressure plateau between 400 and 900 s, which was not observed in the experiment. The higher volume of non-condensable gas in the accumulator, which is a user mistake, might be the cause of this unreasonable pressure increase.

4.2.5 Header ECI flow rates

Following the small break, the primary pump speeds and heater powers are reduced (HD7 reaches 8.8 MPa(g)), ECI flow is poised when header HD7 reaches 6 MPa(g) and ECI flow into headers, shown in figs 4–10 to 4–13 for each header, starts when the particular header pressure drops below the ECI tank pressure of 4.2 MPa(g). In the test the ECI isolation valves to all headers opened at 29.5 s and the main ECI valve (MV-11) opened at 78 s (HD7 reaches 4.2 MPa(g)). Header pressures reached 4.2 MPa(g) in the timeframe from 78 to 80 s, however, significant net ECI inflow did not start until about 115 s in the experiment, when the pressure in all headers is approximately 4.0 MPa(a). Between 78 and 115 s the loop and ECI system depressurize in sync without any measured net inflow of ECI water into the loop.

The header depressurization behaviour is almost identical in all headers. Furthermore, when they reach the ECI pressure of about 4.2 MPa(g), the depressurization rate is slowed due to a near-balance in channel steaming and discharge from the small break. However, eventually the inflow from the ECI system will refill the loop and while the detailed flow rates into each header are considered of secondary importance, the overall ECI flow rate is important.

The main difference between blind and (better) open calculation of initial ECI flow rates were in the timing of the isolation valve opening. This difference resulted from various participants (AERB, KINS, THU) using an incorrect trip logic for the ECI isolation valves in the blind phase of the exercise and in the case of CNEA, inappropriate loss coefficients in the ECI piping and/or valves.

From the experimental measurements it is inferred that the loop initially refills around 400-500s.

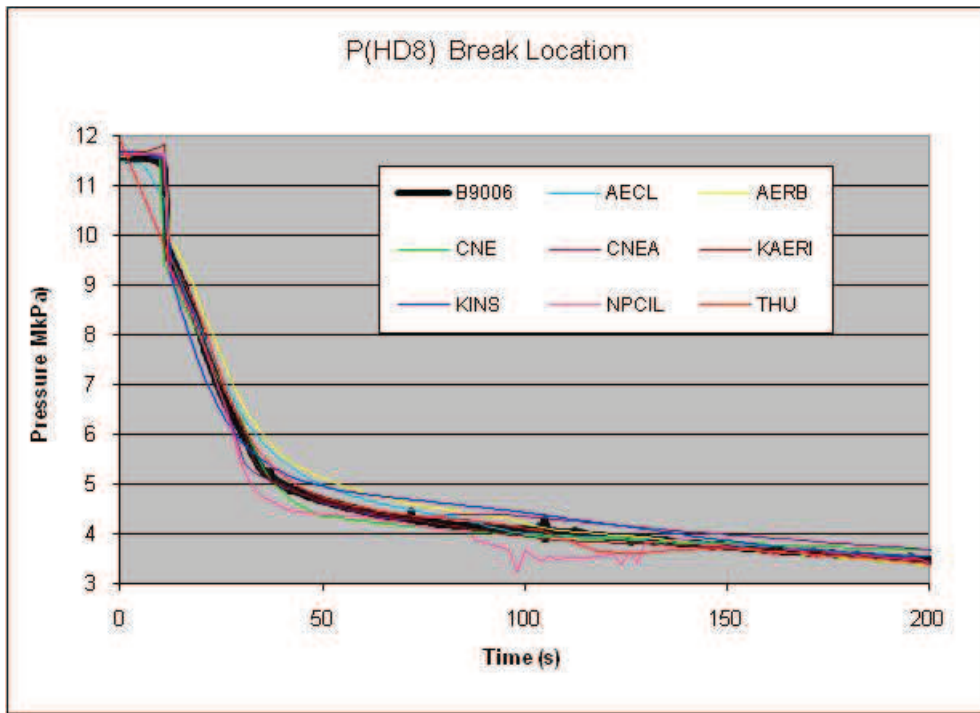


FIG. 4-7. Header HD8 pressure.

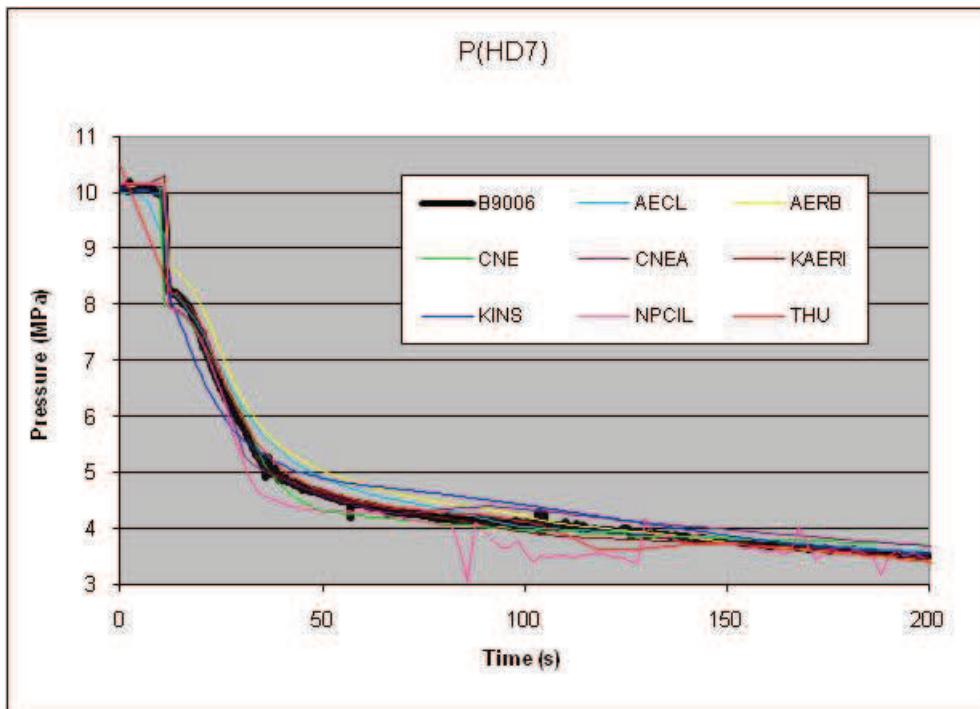


FIG. 4-8. Header HD7 pressure.

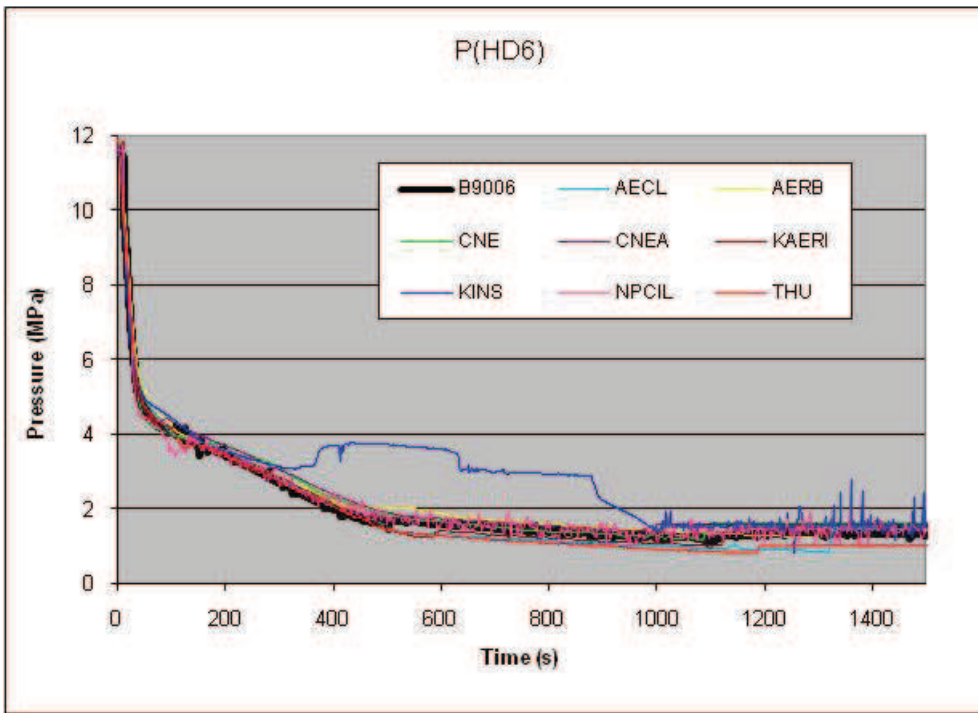


FIG. 4-9. Header HD6 pressure.

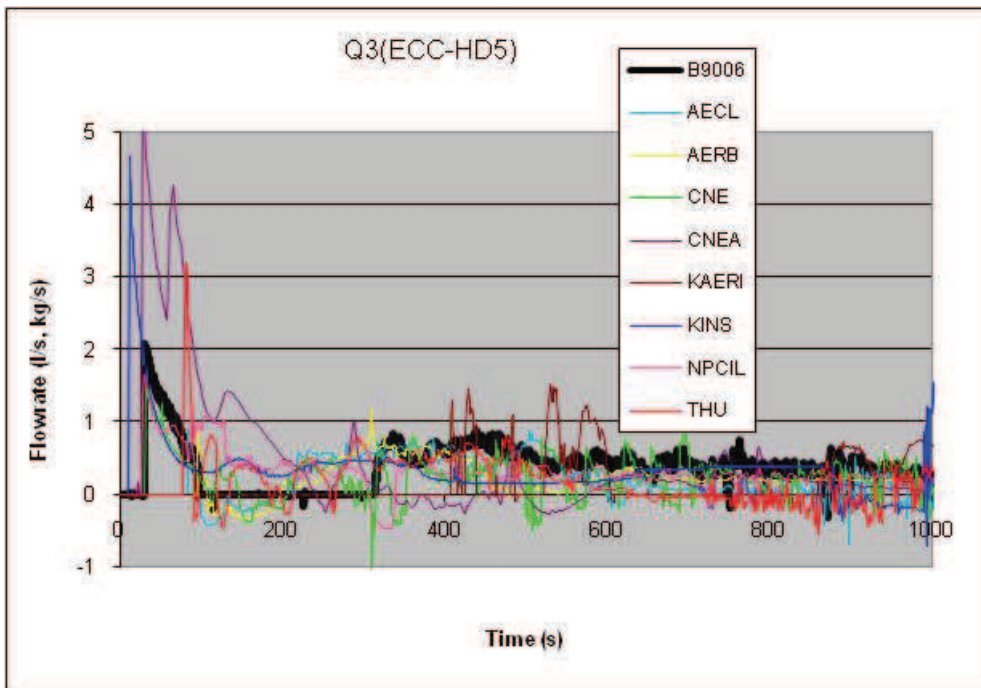


FIG. 4-10. ECI to Header HD5 flow rate.

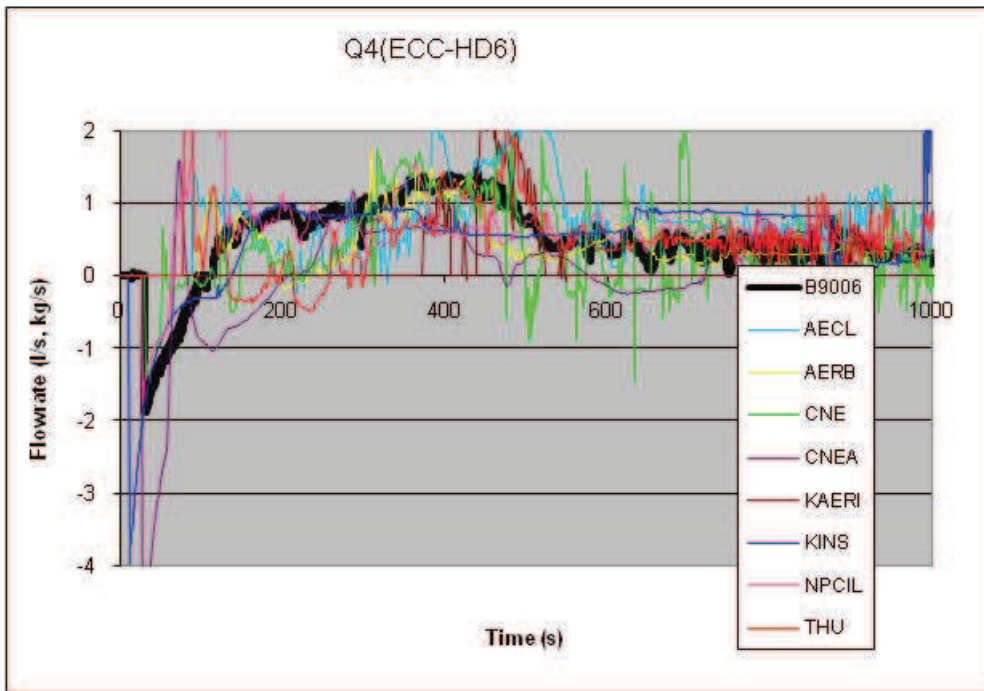


FIG. 4-11. ECI to Header HD6 flow rate.

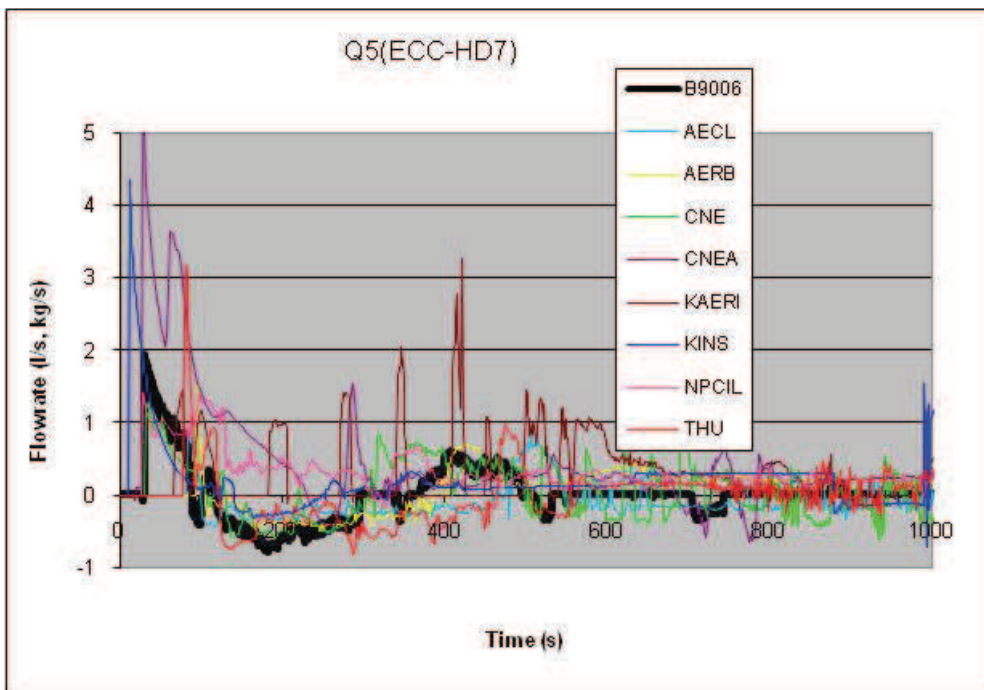


FIG. 4-12. ECI to Header HD7 flow rate.

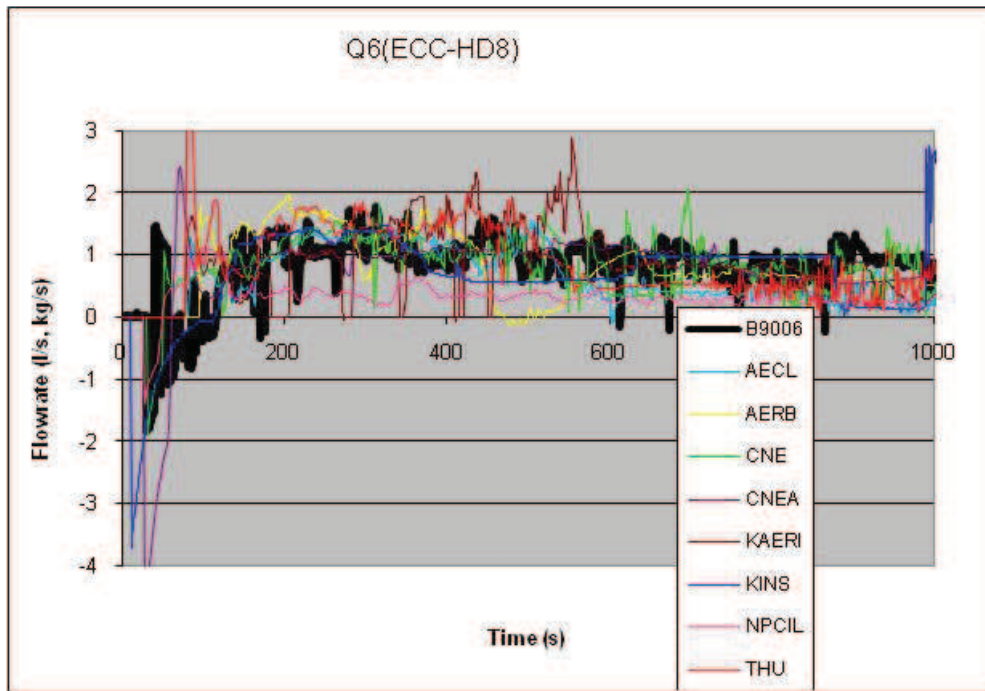


FIG. 4.13. ECI to Header HD8 flow rate.

4.2.6 Integral ECI flow

Figures 4–14 and 4–15 show the net total ECI flow rate and integral flow into the primary loop; Figure 4–16 shows the calculated total loop inventory, resulting from flow out the break and in from the ECCS. Integrated header ECI flow rates provides the total mass of water that comes from the ECI system to the primary loop. It is important since it has a direct impact on primary loop pressure, FES sheath temperatures and mass inventory of the primary system. Two derived measurements are shown in Fig. 4–15, Qint(HPECI) represents only the high-pressure ECI flow and is based on the ECI tank level measurement, and Qint(ECI) is the sum of all measured ECI-HDx flow rates, thus including both high- and low-pressure ECI. The calculated curves are the sum of the four individual ECI-to-header flow rates, presented in the previous section. The slight deviation between the two measurement-derived curves is due to accumulated measurement error. At 1110 s, the high-pressure ECI gets isolated on depletion of ~1700 kg inventory in the ECI tank and low-pressure injection is initiated.

Figure 4-16 shows the loop mass inventory. This is the total mass in the primary system excluding the ECI system and the Pressurizer. It is noted that the RD-14M loop volume is approximately 1.01 m³, and coupled with the density distribution in the loop, the mass inventory in primary loop at initial state (steady state) is about 800 kg. Variations in the initial calculated mass are explained in Section 3.

Several important timings should be noted for the experiment: Net ECI injection starts at ~115 s (Fig 4–15), loop refill occurs at ~480 s (indicated in Fig. 4–14 by a sharp decrease in ECC inflow rate), and ECI switches from high- to low-pressure injection at ~1100 s (Fig. 4–15, also shown in Fig.4–14 by a spike in ECC flow rate).

The high initial ECC flow rates from CNEA and NPCIL result in a large deviation of total ECC water into the loop (Fig. 4–15) and early refill times (Fig. 4–16). By the time each participant refills the loop, all curves converge to the experimental integral ECC flow, as

expected. The deviation in final total ECC mass injected (Fig. 4–15) is a reflection of the total break flow calculated, while the differences in final loop inventory reflect differences in initial loop inventory (Fig. 4–16).

Most participants predict similar blind and open results on the integrated ECI flows, except for KINS and THU. In both cases, the blind calculation results are closer to the experimental measurements than the open results, as can be seen by comparing Fig.4–15 with Fig. 4-66, although the timing of first net ECI injection into the loop is nearly identical for all participants when comparing their blind and open results.

Differences are also evident in the transient total loop inventory, shown in fig. 4–15 for the blind results, and in comparison in Fig. 4–64 for the open calculations. For example, KINS shows a significantly higher minimum loop inventory (700kg) in their blind calculation, when compared to the open simulations (600kg).

4.2.7 Void fractions in boiler plenums and primary pumps

Secondary side temperatures decreased after power and secondary side pressure reduction. Coolant boiling in the heated channels increases void fractions at inlets of boilers before the primary loop is fully refilled, as shown in Figs 4–17 and 4–20 for boilers BO1 and BO2, respectively. After refilling of the primary loop, void fractions at inlets of boilers are reduced to zero by ECI injection cooling. Following break initiation until $t \sim 200$ s, void appears in the boiler inlet and is collapsed in the outlet (Figs 4–18 and 4–21) due to heat transfer to the secondary side. During later times and before loop refill ($200\text{s} < t < 480\text{s}$), higher void at the pumps and boiler outlets than boiler inlets could be a result of either reverse loop flow or the boiler(s) acting as heat source(s) in the experiment and simulations. The periods of measured full void at the pump P1 from ~ 250 - 450 s and P2 from ~ 200 - 1150 s (Figs 4–19 and 4–22) is believed to be very localized to the high-elevation (and still relatively hot) piping near the pump exits. It is inconsistent with both the measured boiler outlet void (Figs 4–18 and 4–21) and the measured broken-loop heated section inlet voids, and thus is not “circulating void” but local void resulting from hot pipes, high elevation, and very low loop flow rates. A few participants, AECL and CNE for pump P2 and KINS and THU for pump P1, predict the same trend, but with various timing. This phenomenon is also illustrated in Appendix II snapshots at $t = 1050$ s, which show the temperature and void distributions throughout the loop (for open calculation results).

4.2.8 Boiler thermal power and steaming rates

The thermal power across the boilers represents the total net heat removed from the primary loop; negative values indicate that the boiler is adding heat to the primary side fluid.

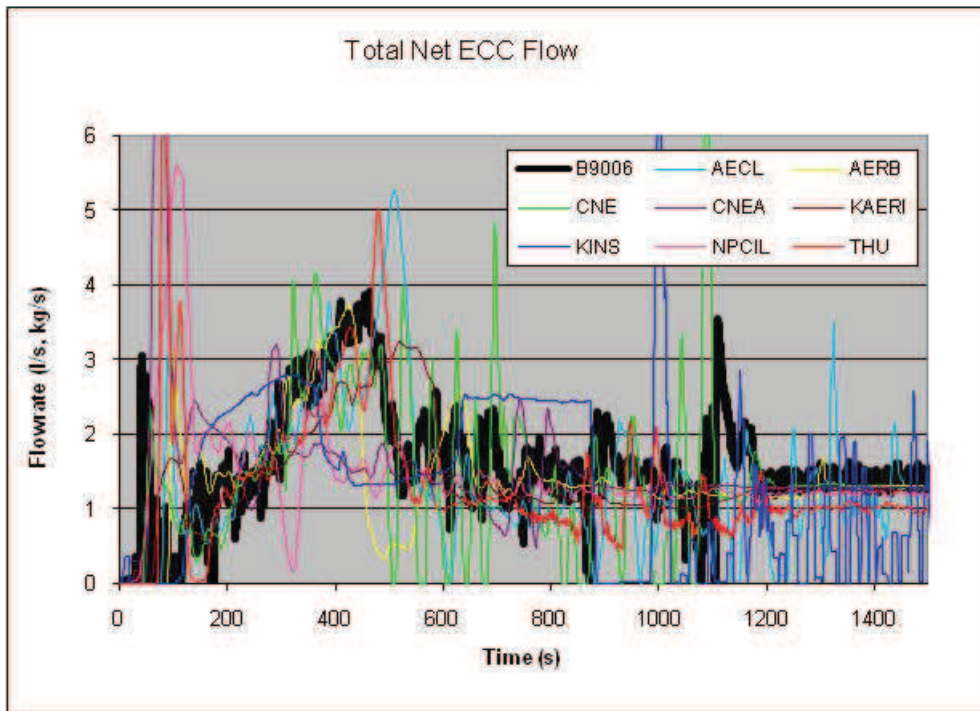


FIG. 4-14. Total net ECI Flow into loop

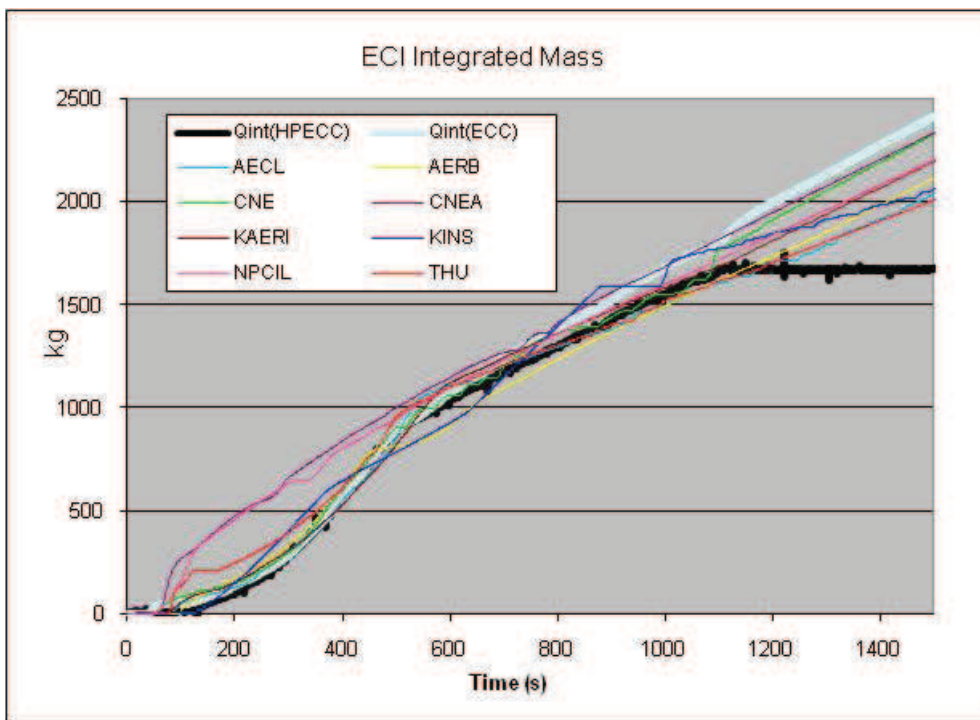


FIG. 4-15. Integral of ECI flows.

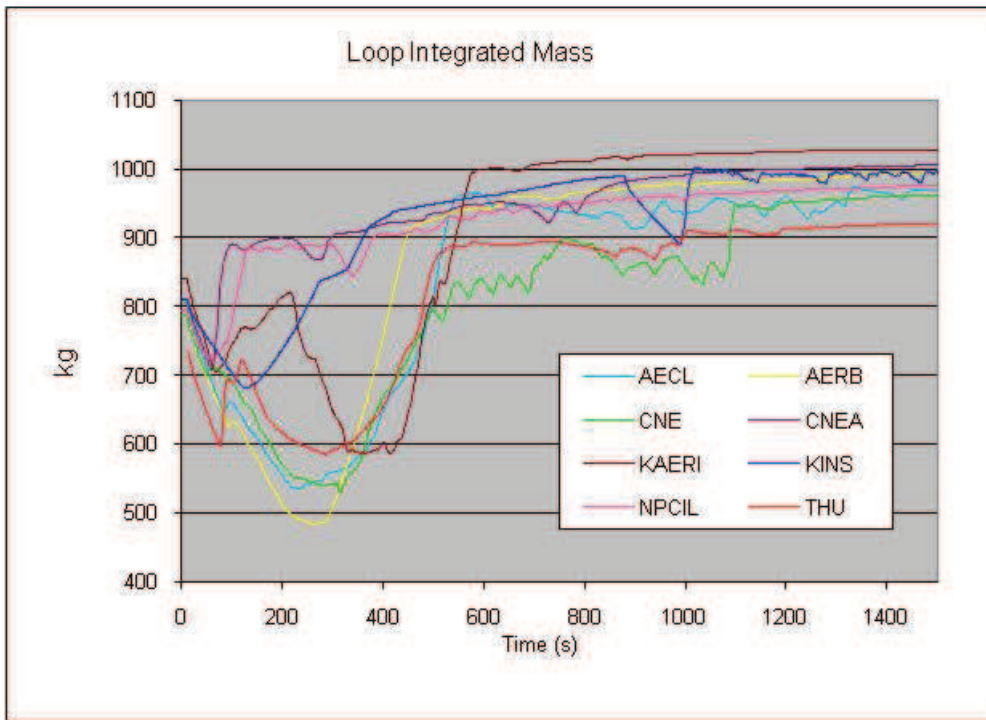


FIG. 4-16. Calculated loop mass.

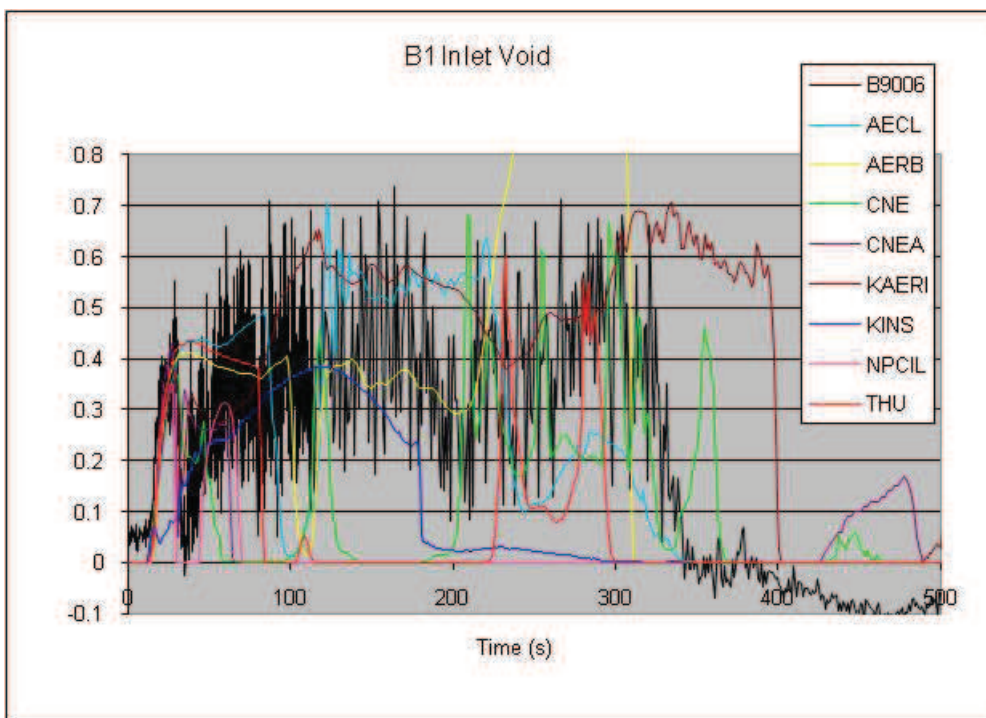


FIG. 4-17. Boiler BO1 inlet void.

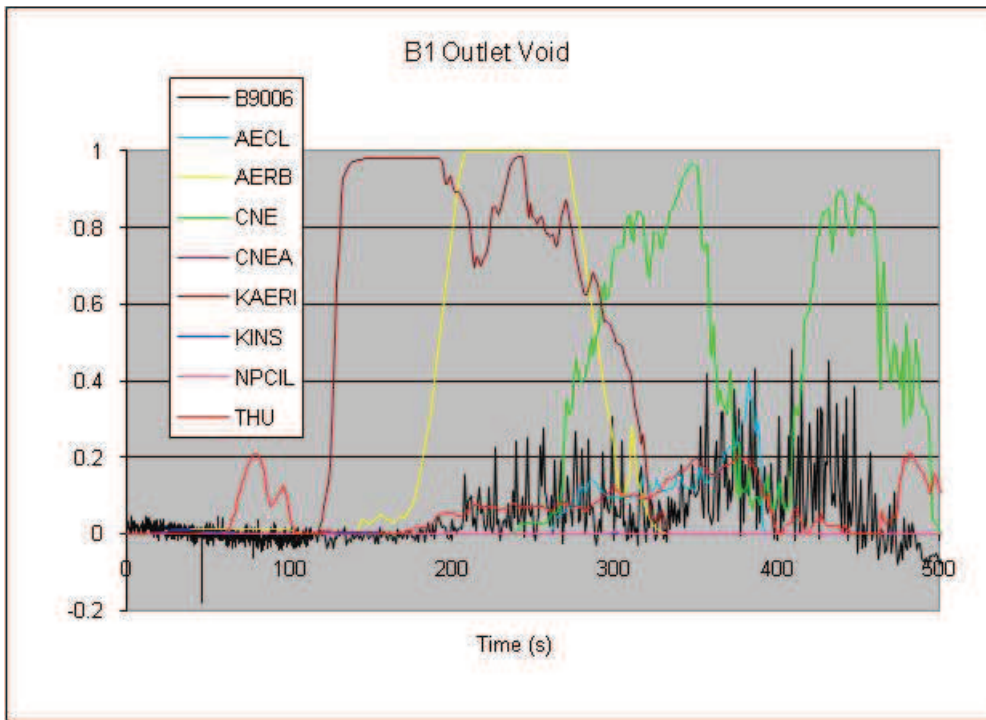


FIG. 4-18. Boiler B01 outlet void.

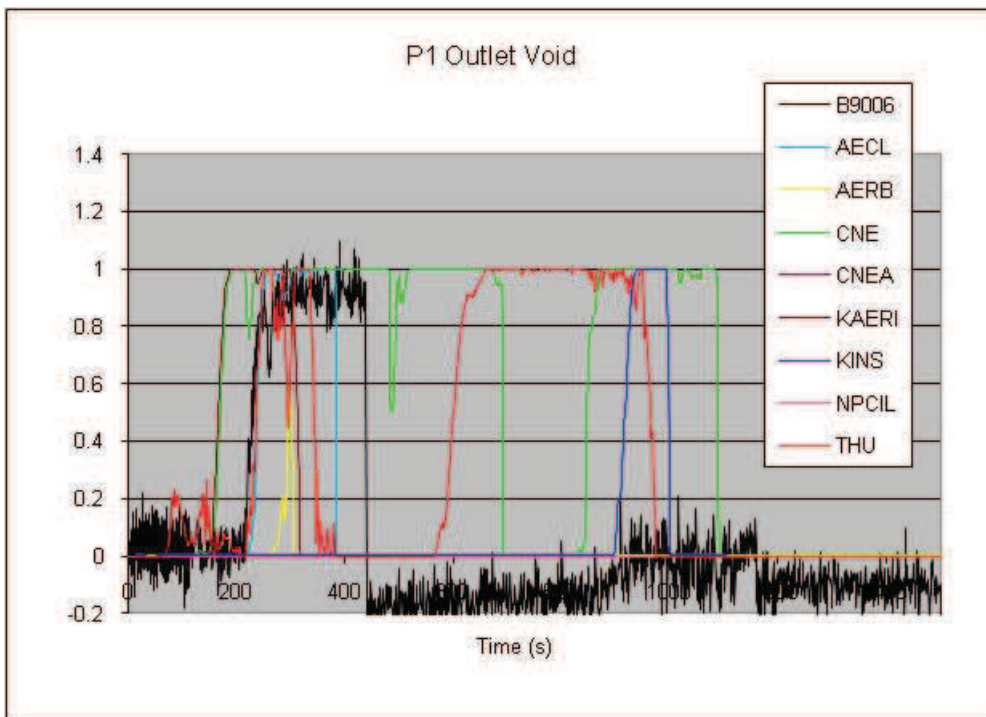


FIG. 4-19. Pump P1 outlet void.

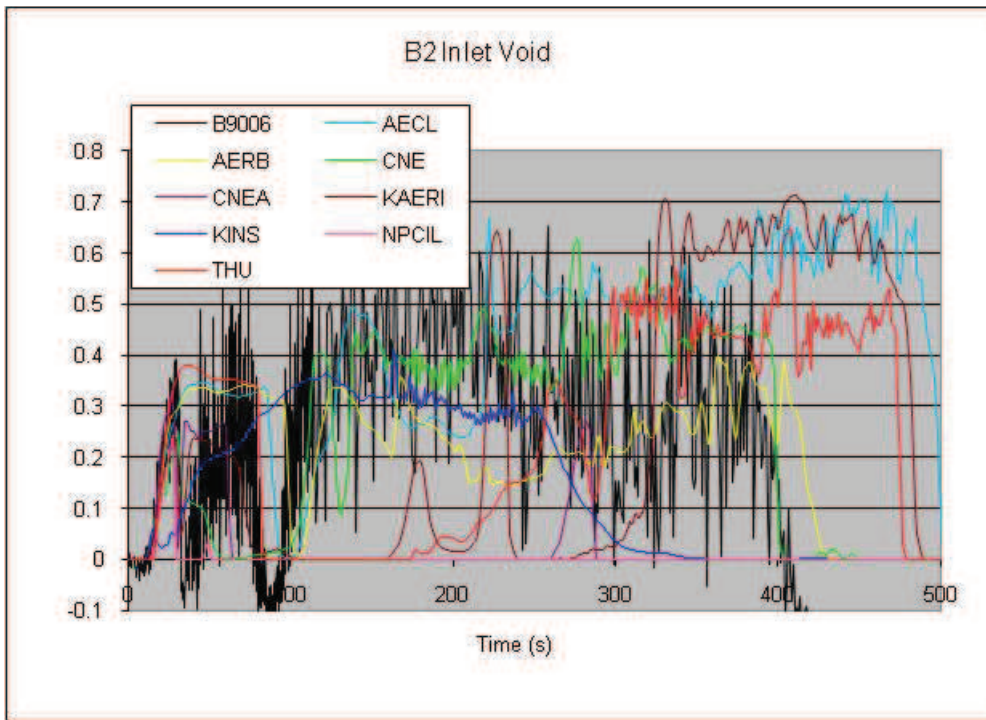


FIG. 4-20. Boiler BO2 inlet void.

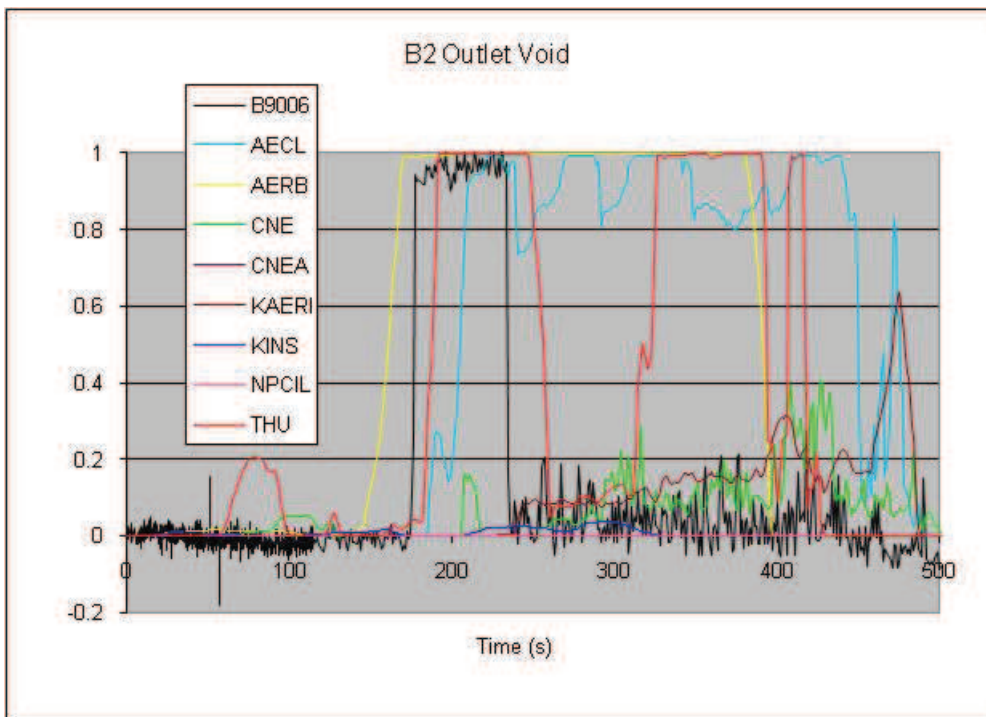


FIG 4-21. Boiler BO2 outlet void.

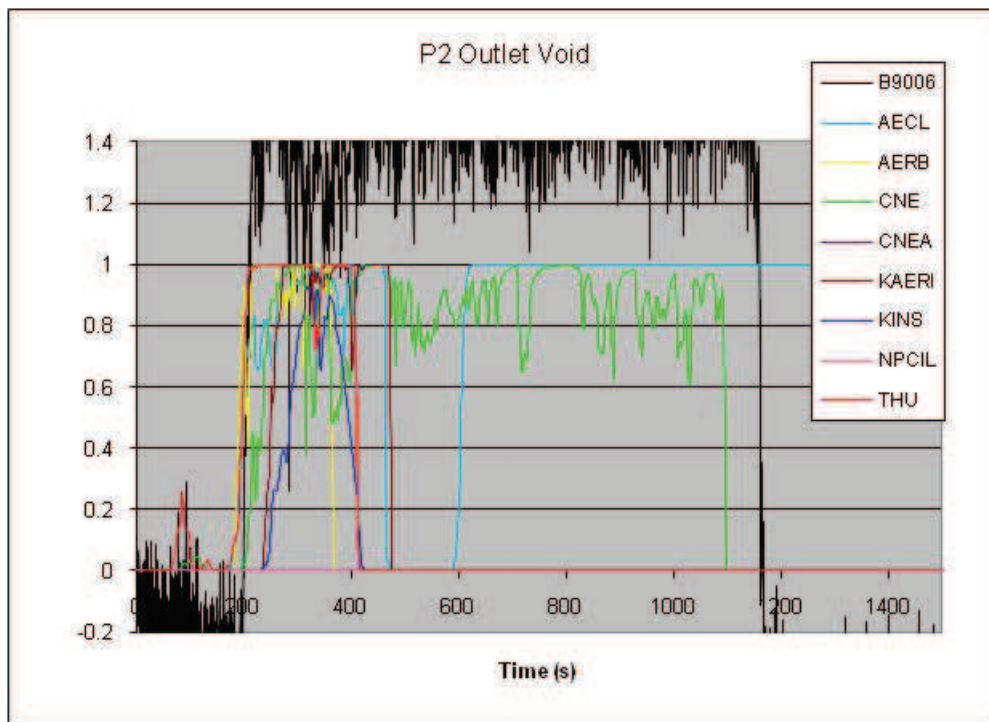


FIG. 4-22. Pump P2 outlet void.

Figures 4–23 and 4–24 show the calculated thermal power (or heat transfer rate, in kW) across the boiler tubes. This quantity was not measured in the experiment, but the secondary side feedwater flow rate is known and was controlled in the experiment to keep a constant secondary side collapsed water level in the boilers. Therefore, Figures 4–25 and 4–26 compare the experimentally measured steam drum exit steam mass flow rate with the calculated steaming rates (shown in the Figures as an 11-point average to smooth the oscillations) in the boilers BO1 and BO2, respectively. Note, that the feedwater rate was used as a boundary condition by all participants, therefore the deviations between the calculated and measured boiler steaming rates in these two figures indicate a higher or lower (than in the test) boiler thermal power. The steam drum pressure was applied as the secondary side outlet boundary condition.

While in the experiment the boiler steaming rates were relatively constant between 0.25 and 0.5 kg/s in boiler BO1 and between 0.35 and 0.7 kg/s in boiler BO2 after the initial depressurizations, participants calculated significantly higher or lower steaming rates for long time periods, indicating that the boilers are either larger or smaller heat sinks (or even heat sources), respectively, than in the experiment. This discrepancy would also lead to changes in calculated boiler secondary side levels and temperature, thus affecting the heat sink conditions for the primary side. Observations here are consistent with, and explain to a certain extent the boiler inlet and outlet temperatures, discussed in the following section. Possible overall loop flow reversal in some calculations complicates this interrelation. Unfortunately, boiler level and overall loop flow directions were not compared in this ICSP. Instead, the downcomer flow rate was added to the list of data to be compared (it was not measured in the test); however, examination of the results did not provide any insight into possible reasons for deviations of the various participants. Downcomer flow rates varied widely (with some even calculating negative recirculation rates during portions of the transient) and did not correlate with good or poor agreement of the steaming rates.

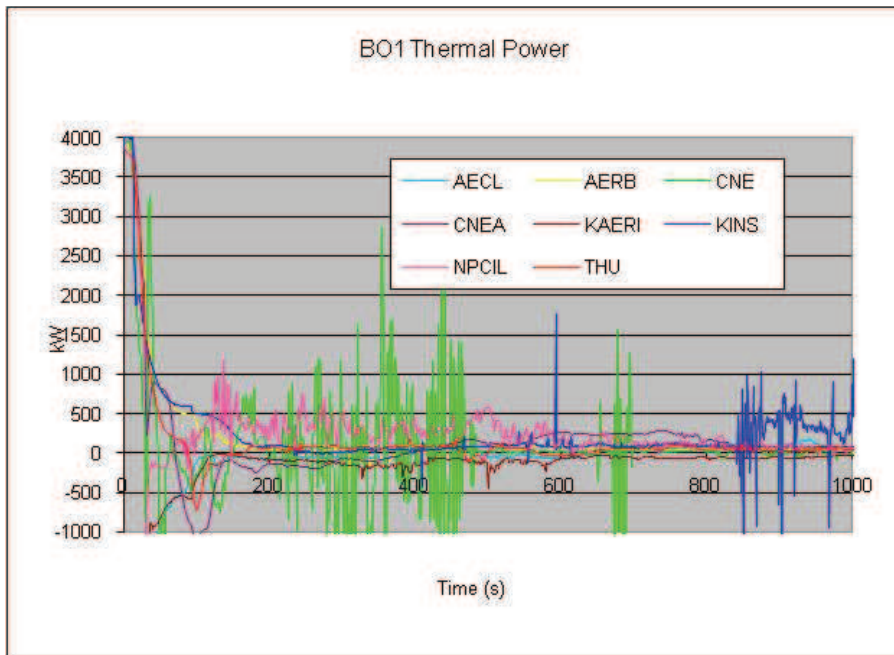


FIG. 4-23. Boiler BO1 thermal power.

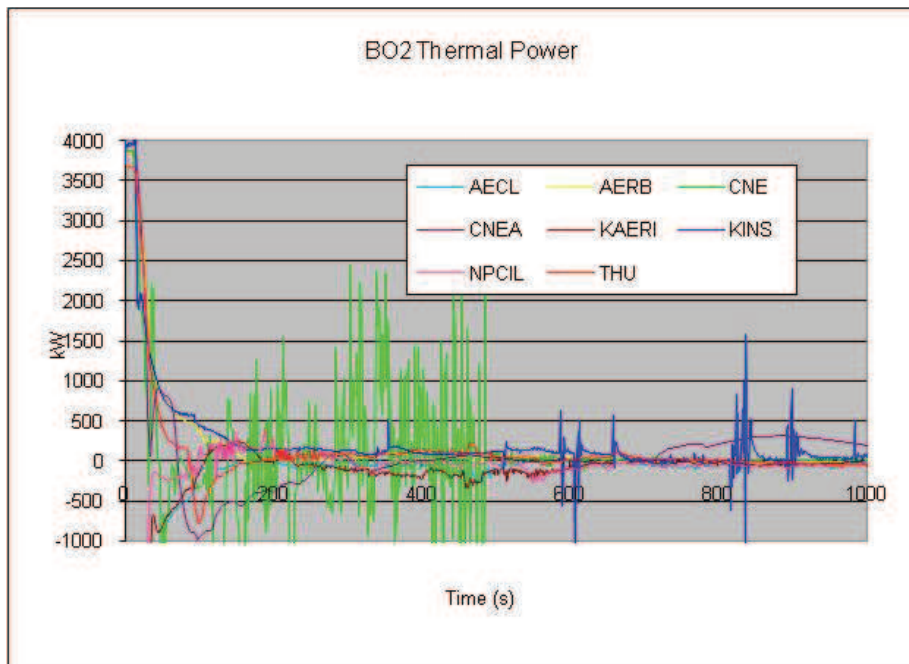


FIG. 4-24. Boiler BO2 tube thermal power.

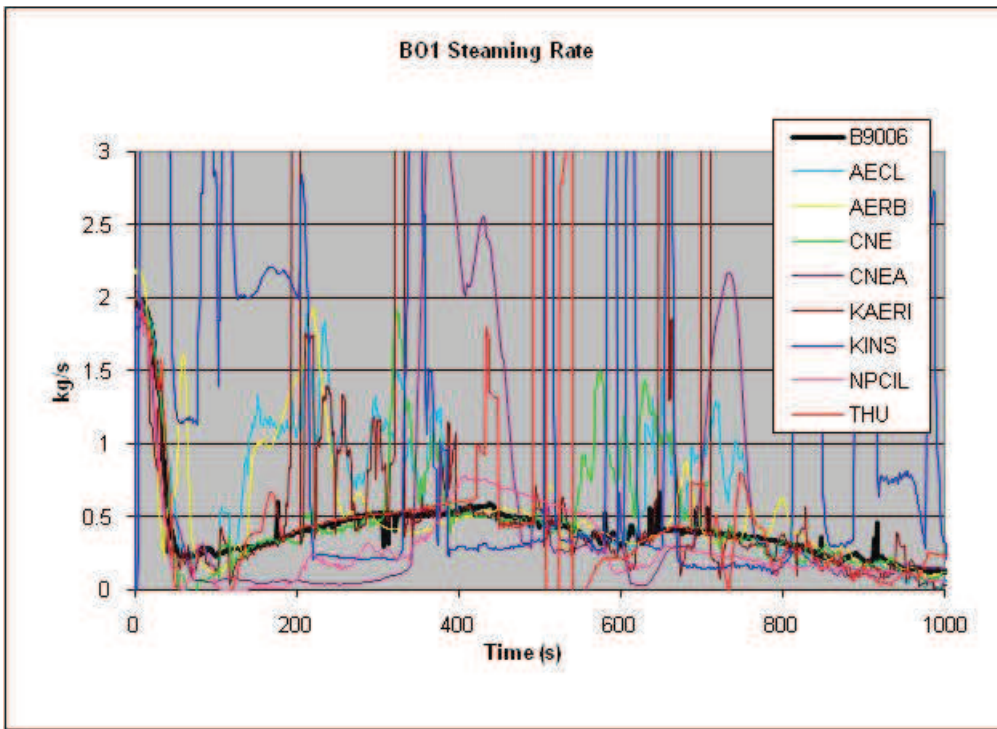


FIG. 4-25. Boiler BO1 steam flow rate.

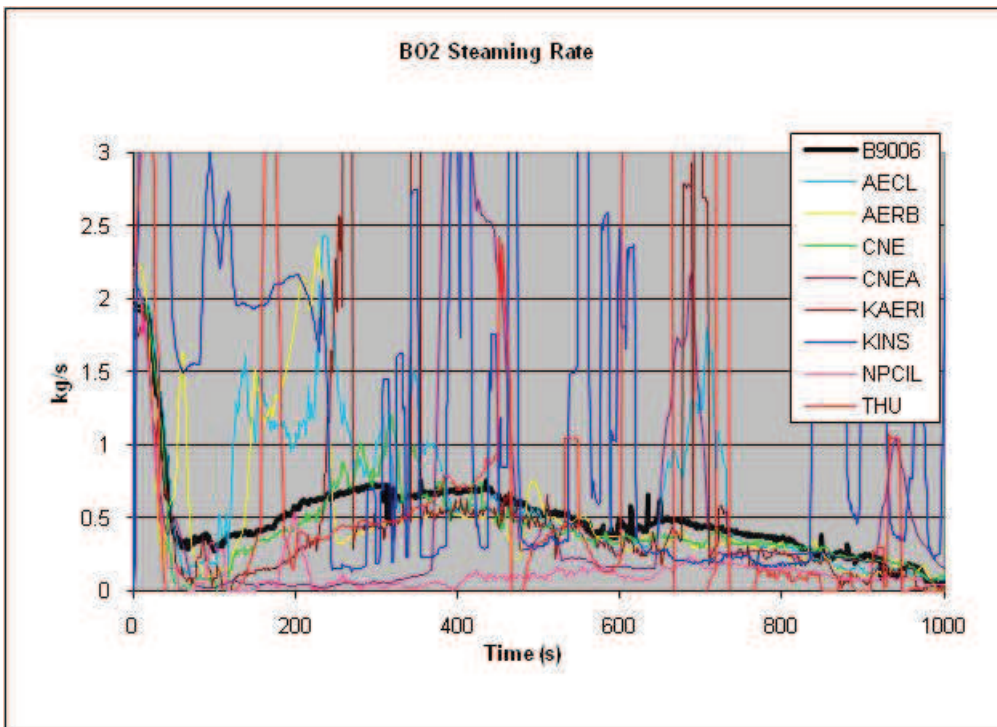


FIG. 4-26. Boiler BO2 steam flow rate.

4.2.9 Boiler inlet and outlet temperatures

Boiler inlet and outlet fluid temperatures provide local fluid temperature measurements in the primary loop and can be used as confirmatory data for simulations. They provide information about heat removal/addition capability of the boilers during the experiment (interpretation depends on calculated overall loop flow direction). Secondary side temperatures decreased following power and secondary side pressure reduction.

Figures 4–27 to 4–30 provide the code comparison to experiment. All calculations show the correct experimental trend and all agree well with experiment for about the first 80s of the transient, i.e. before ECI injection. After that point, significant differences are noted, with the lower temperatures in some calculations being due to the arrival of low-temperature ECI water, roughly corresponding to the loop refill times discussed previously.

In general, predictions for both boiler vary widely amongst participants, in particular the inlet-to-outlet temperature change (recall previous section discussion). However, since the loop flow direction is not obvious, and may be predicted different by different participants, no conclusion about the boilers acting as heat sink or source can be drawn, based only on these figures. Even the end of the experiment (1500 s) a relatively large variation remains.

In general, the accuracy of boiler temperatures improved from the blind to the open calculations, in large part due to improving the ECI injection rate and distribution into the headers.

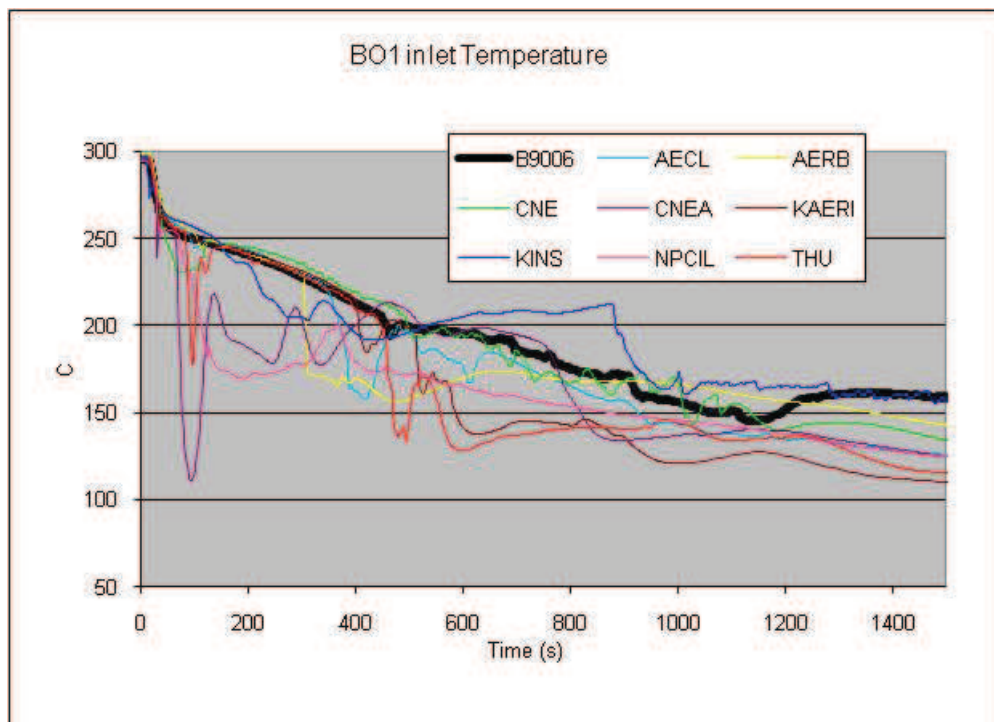


FIG. 4-27. BO1 inlet temperature.

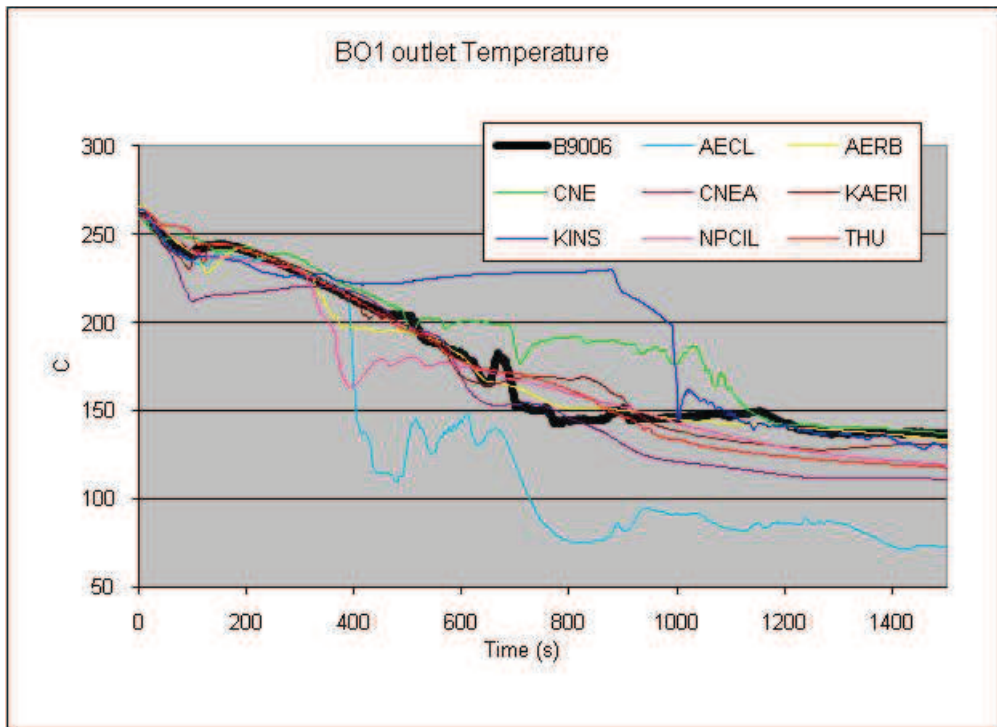


FIG. 4-28. BO1 outlet temperature.

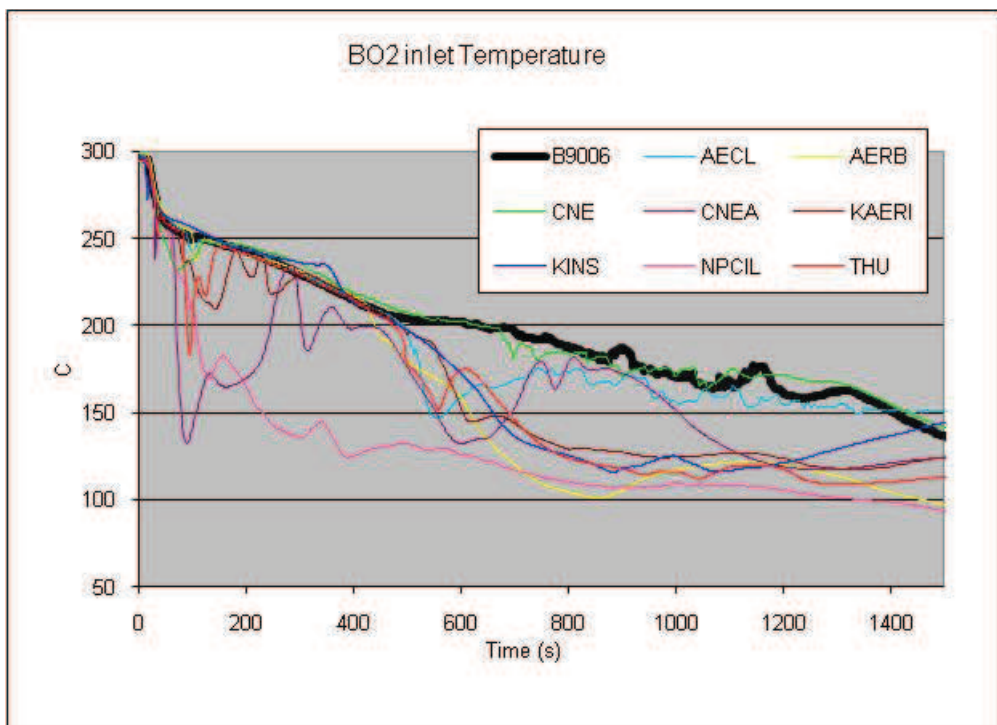


FIG. 4-29. Boiler BO2 inlet temperature.

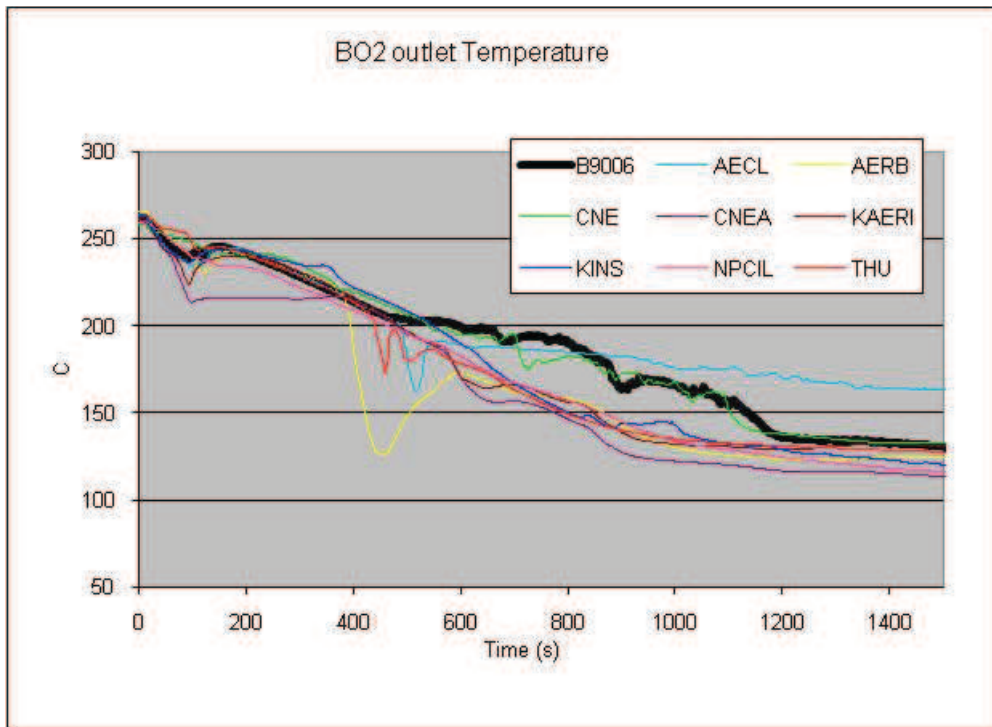


FIG. 4-30. Boiler BO2 outlet temperature.

4.2.10 FES sheath temperatures in heated sections HS8 and HS13

The maximum FES sheath temperature is often the most significant parameter in safety analyses, in particular SBLOCA. In test B9006, the highest FES sheath temperatures is expected in the high power channel of the broken pass, heated section 13 (HS13) and/or in the high-power channel of the intact pass (Fig. 4–31). While no significant temperature excursions were expected, or observed in the experiment, during the depressurization, some participants predict short heat-up periods during the quasi-steady pressure period after ~200 s. In particular, CNE and THU show brief temperature excursions to about 300-400°C on the top FES over the entire channel length in HS13 and also in HS8.

In the experiment the inlet, center and outlet temperatures of the top FES (Figs 4–32 to 4–34) generally have gradually increasing temperatures throughout the transient, indicating a continuous forward flow, with no flow reversal in this channel (HS13). Some participants predict a “reverse” temperature gradient, indicating reverse flow (see also next section).

In order to show if significant flow stratification is present during the transient, Figs 4-34 and 4-35 are compared. With the exception of a few short spikes both in the measurement and in some calculations, indicating periods of boiling, the top and bottom FES have nearly identical temperatures, indicating no significant or sustained stratification.

FES temperature predictions only improved slightly in the open calculations, and temperature spikes remained in the participant’s calculations.

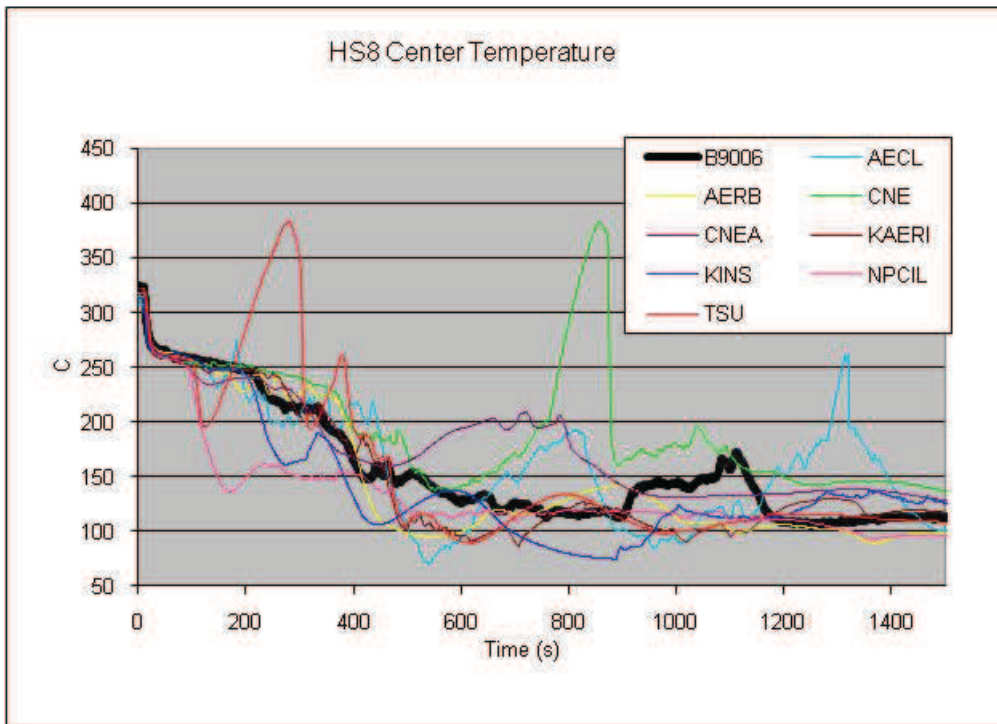


FIG. 4-31. Heated section HS8 center temperature.

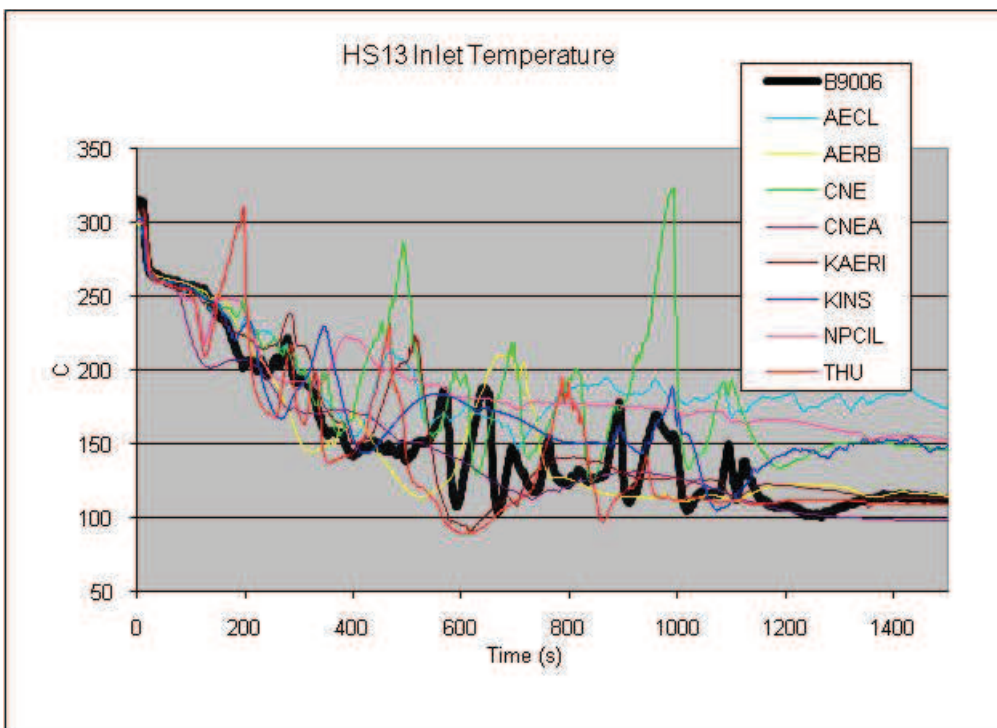


FIG. 4-32. Heated section HS13 inlet temperature.

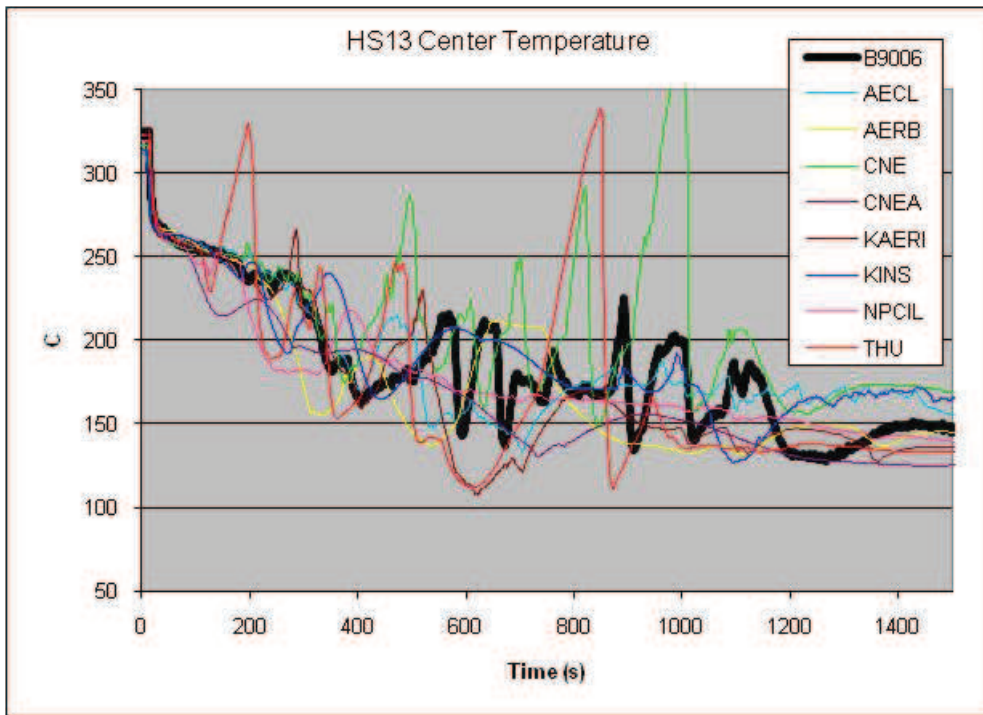


FIG. 4-33. Heated section HS13 center temperature.

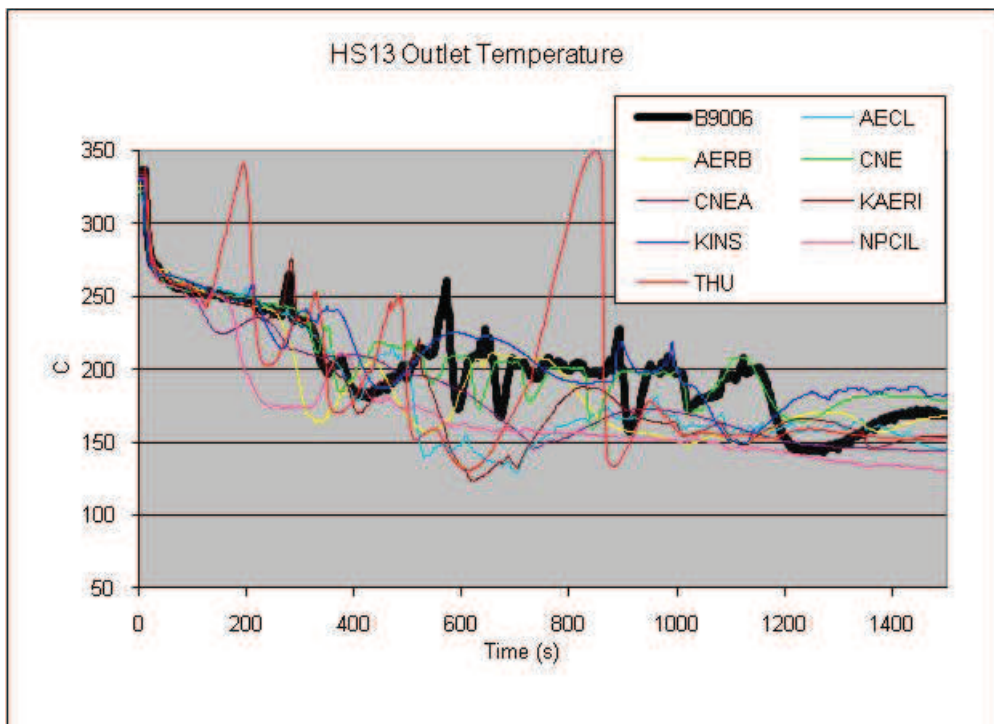


FIG. 4-34. Heated section HS13 outlet temperature.

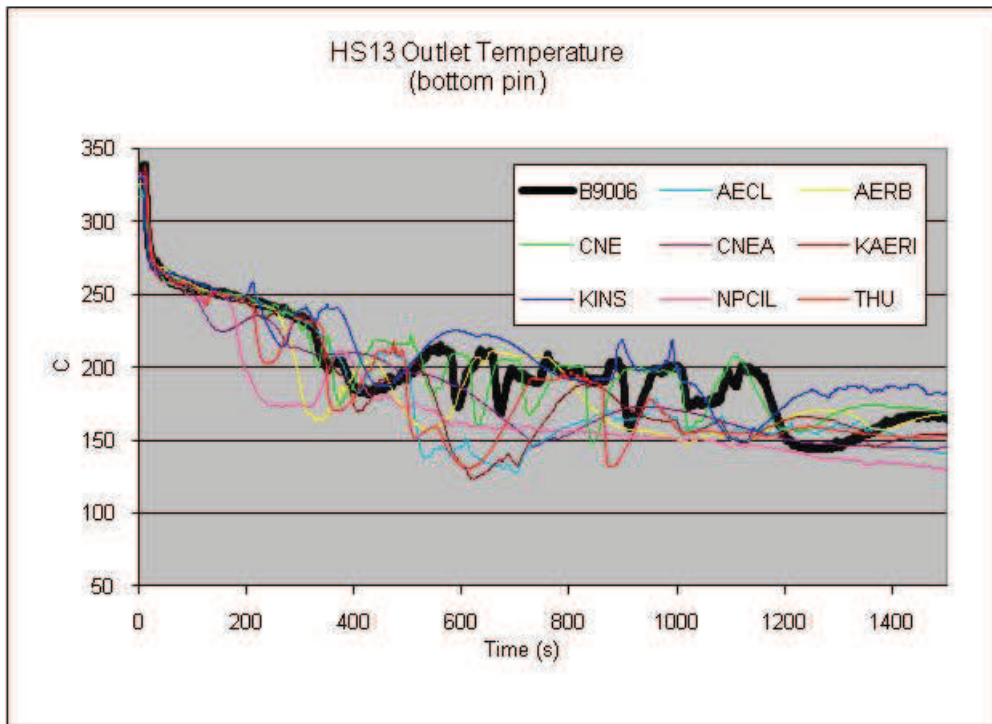


FIG. 4-35. Heated section HS13 outlet temperature (Bottom FES).

4.2.11 Flow rates in heated sections HS5, 8, 10, and 13

After the pumps have run down, the driving forces for flow through the heated channels are very low, as indicated in the low header-to-header differential pressures, discussed above. Therefore, four channels were selected to assess the code's capability to simulate potentially complex, low-flow patterns. HS5, 8, 10, and 13 are, respectively, low and high power channels in the intact and broken pass. The flow rates were measured in the inlet/outlet feeders for each channel (typically several meters from the end fittings) and are shown in Figs 4-36 to 4-39.

Channel flows are very low, but in the normal (forward) direction, for both high powered channels throughout the experiment, and are predicted to be such by all participants, except through HS13, by NPCIL (from ~120s) and AECL (from ~400s).

Both low-powered channels, HS5 and HS10, show clear flow reversal after ~200 to the end of the test, as shown in figs 4-36 and 4-38. Some participants capture this sustained flow reversal, while others predict forward flow throughout the transient. In general, once a particular flow direction is calculated, it is maintained throughout the simulation. In broken pass, flow reversal occurred in two channels (HS10 & HS12, HS 12 not shown) as compared to flow reversal occurred in only one channel (HS5) of unbroken pass. This also explains the elevated temperature at Header HD8 as compared to Header HD6 during the latter part of the transient.

It should be noted that measured flow rates below 0.2 l/s and during two-phase flows (as is the case during $\sim 200\text{s} < t < \sim 400\text{s}$ reverse-flow periods for HS5 and 10) are only to be taken as an indication of flow direction, not of the flow magnitude.

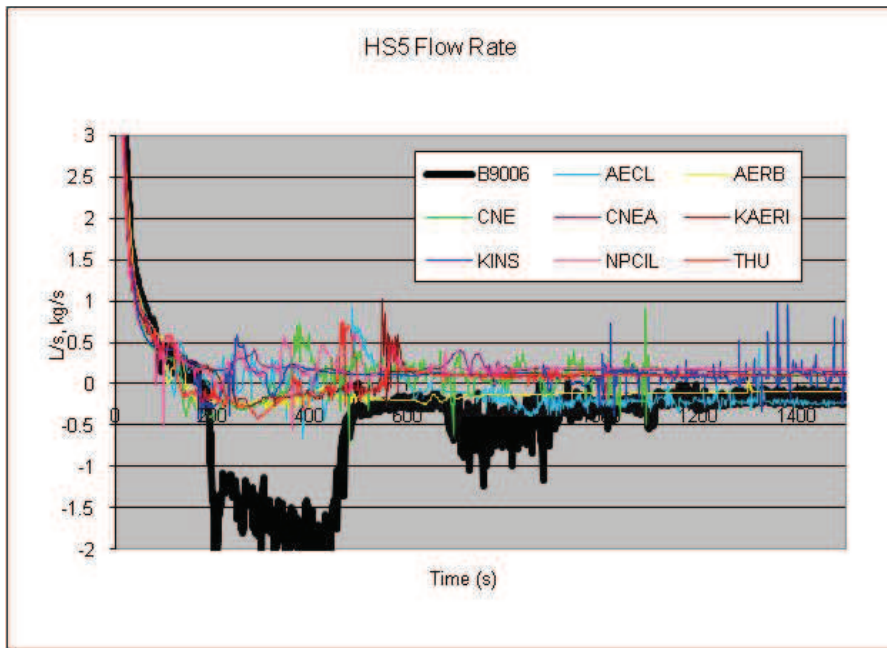


FIG. 4-36. Flow through heated section HS5.

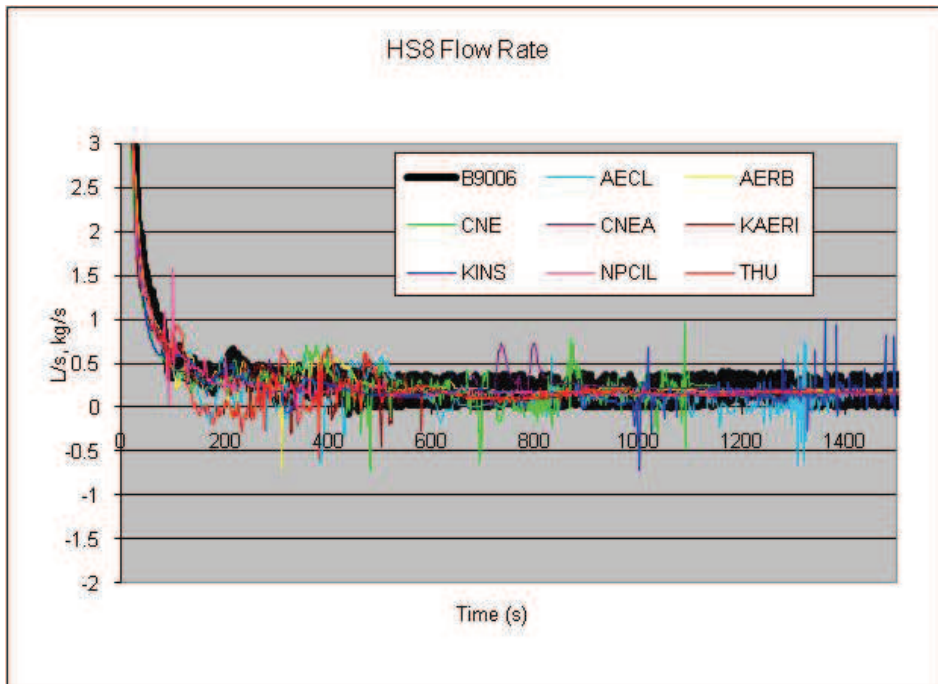


FIG. 4-37. Flow through heated section HS8.

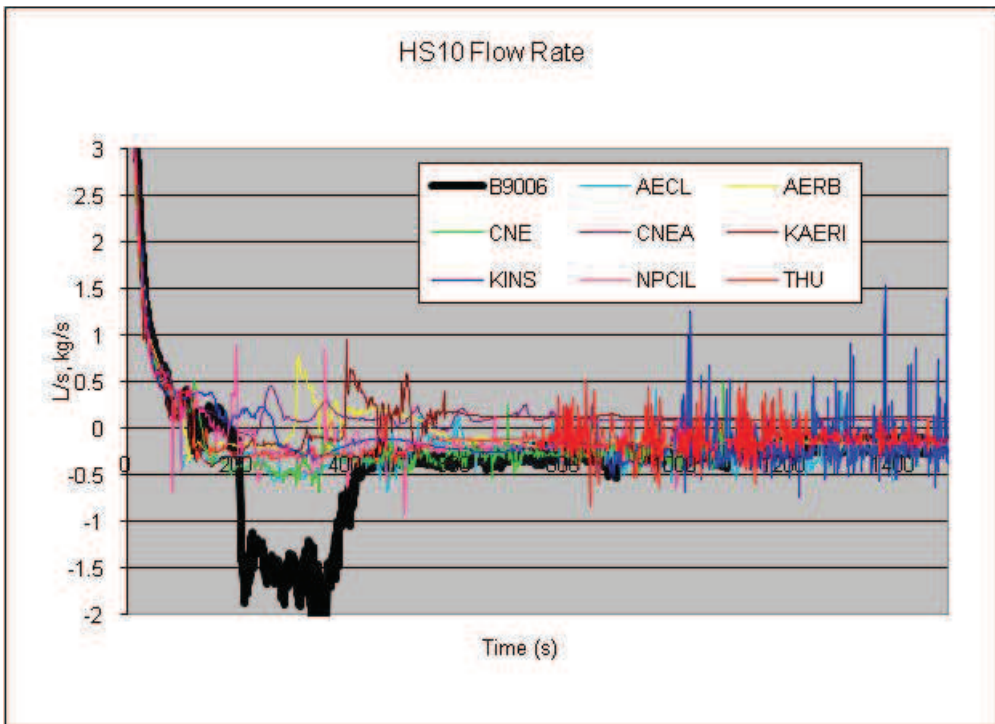


FIG. 4-38. Flow through heated section HS10.

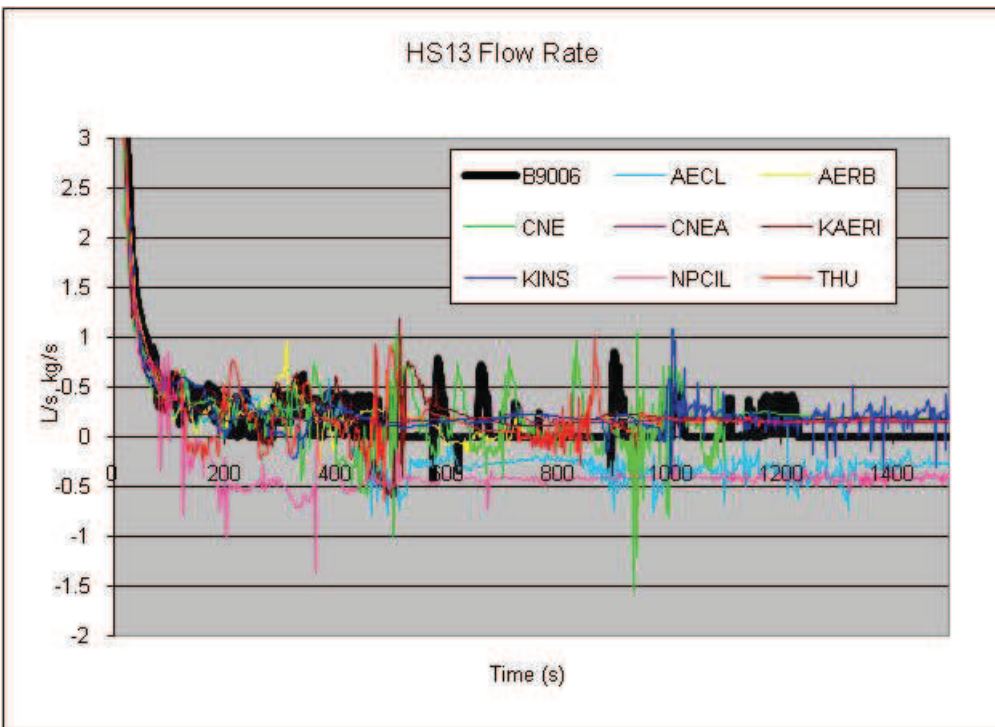


FIG. 4-39. Flow through heated section HS13.

4.2.12 Heated sections HS5, 8, 10, and 13 inlet and outlet void

Channel inlet and outlet void fractions were measured approximately 1–3 m upstream and downstream of the heated section end in the inlet and outlet feeders.

Voiding occurred in the outlet feeders approximately 30 s into the transient, quickly reaching 50-100% void and sustaining it until 200 to 400 s. The inlet feeders of both low-powered channels also voided around 200 s, while the high-powered channel inlet feeders remained filled. This can be attributed to the low-powered channels being located at significantly higher elevations, thus having less gravitational head and a lower saturation pressure. Intermittent void was also detected in the inlet of HS5 and outlet of HS13 at later times.

Figures 4–40 to 4–47 show the experimental measurements and code predictions. The experimental data shows negative void due to measurement error or instrument drift; these should be considered as zero void. Most simulations correctly show periods of various duration and timings and of significant void in the outlets before loop refill at ~480s, but also intermittent void during later times in various feeders of various channels, where the test did not show voiding.

Large differences in simulations are expected due to the interdependence of channel boiling, low flow, flashing in the feeders, flow direction, low header-to-header pressure differences, and the complexity of the end fittings.

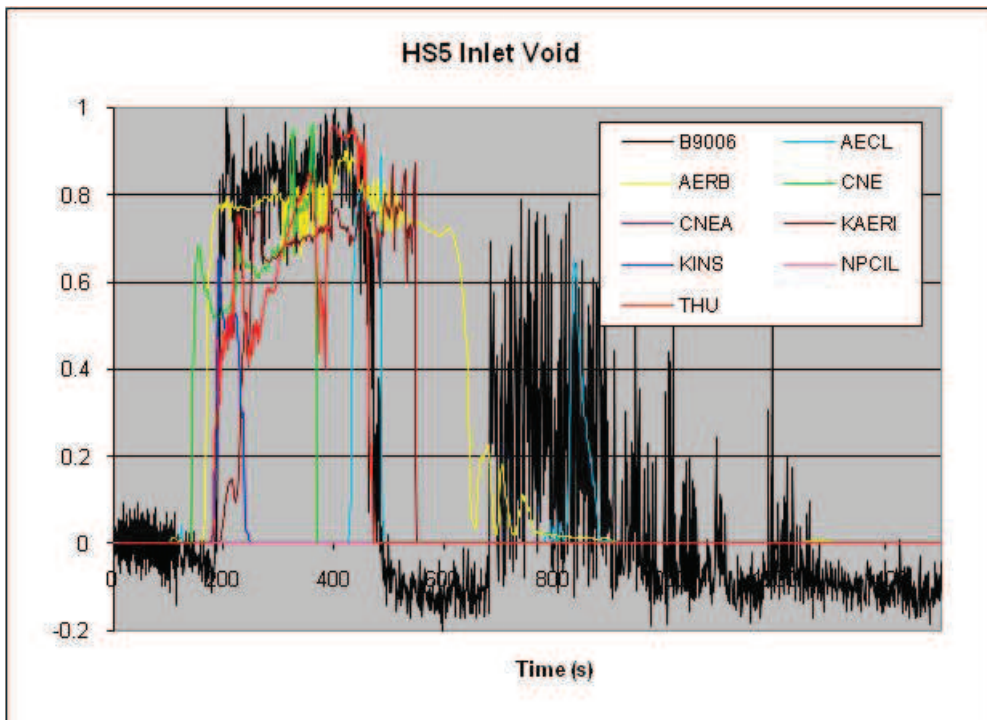


FIG. 4-40. Heated section HS5 inlet void.

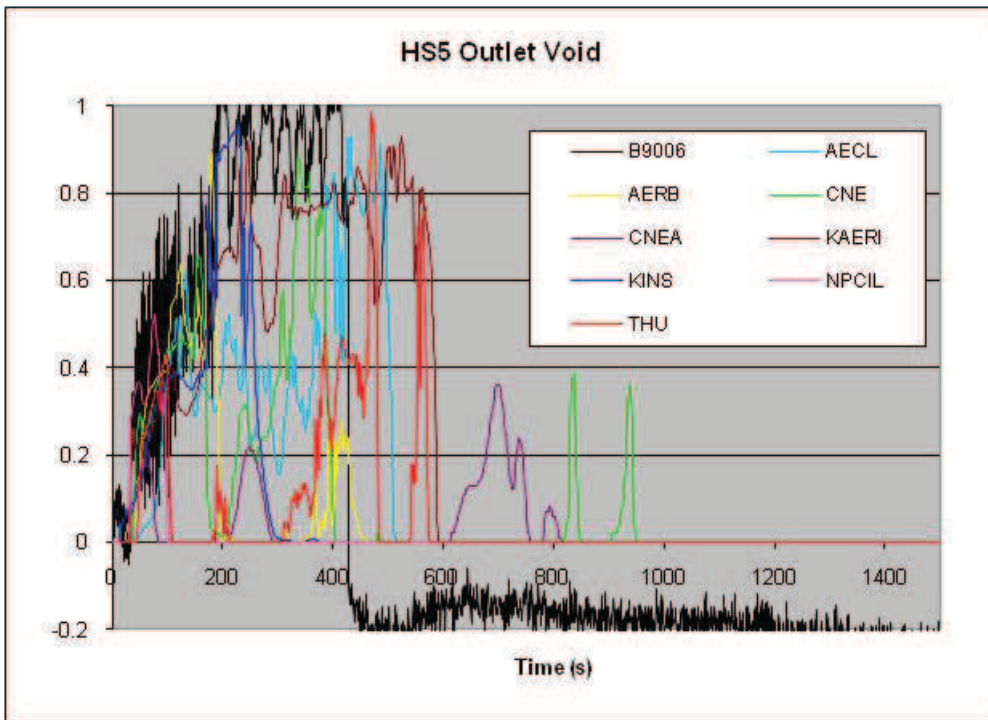


FIG. 4-41. Heated section HS5 outlet void.

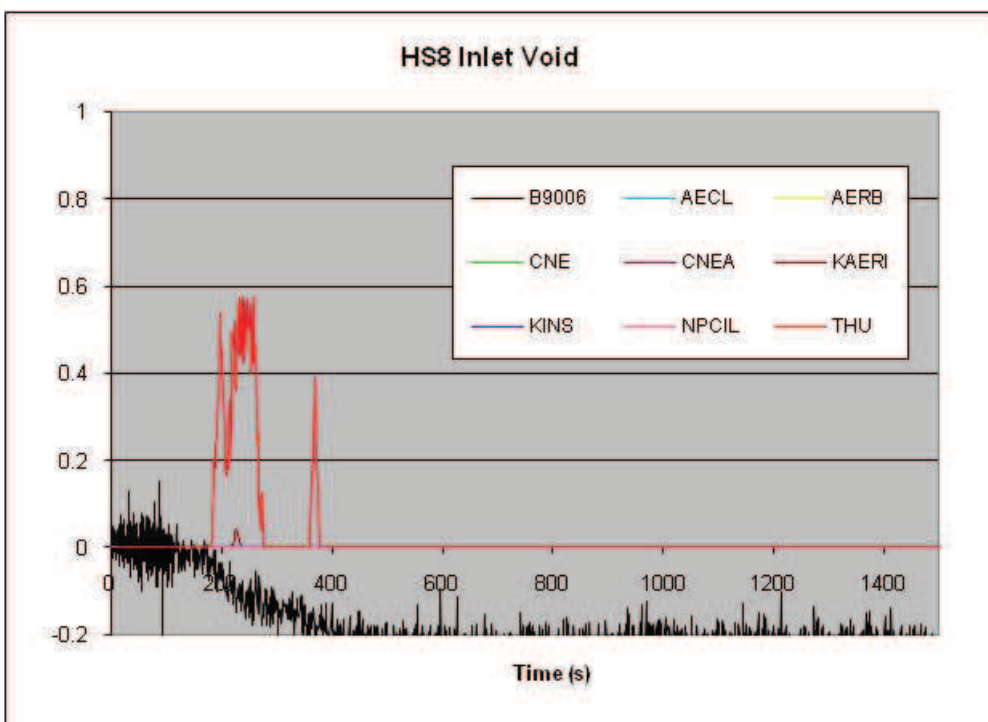


FIG. 4-42. Heated section HS8 inlet void.

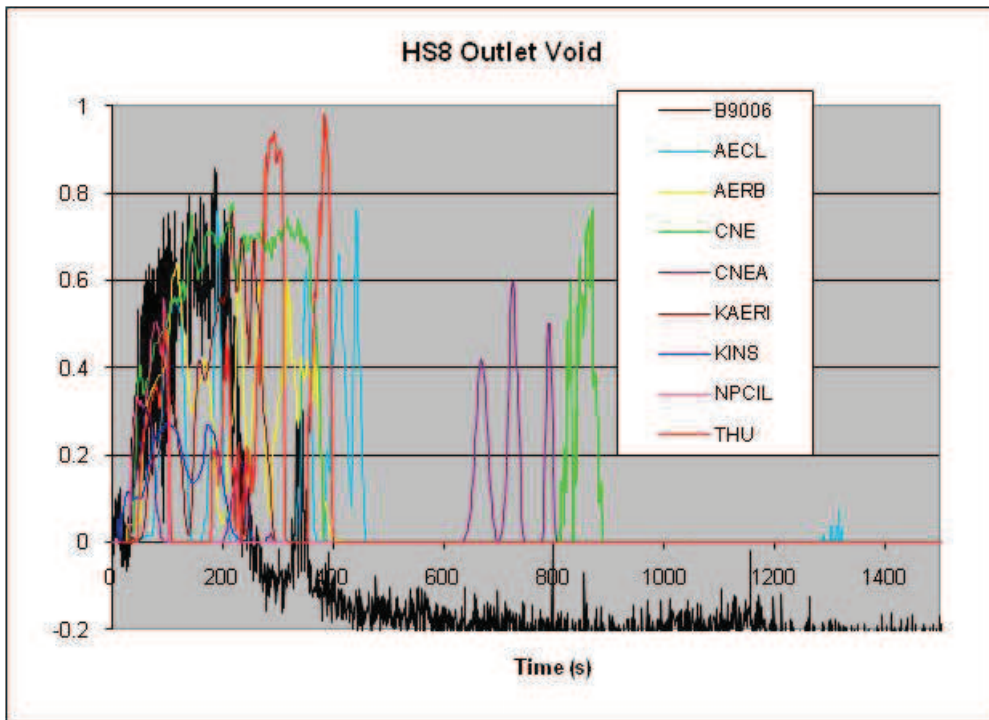


FIG. 4-43. Heated section HS8 outlet void.

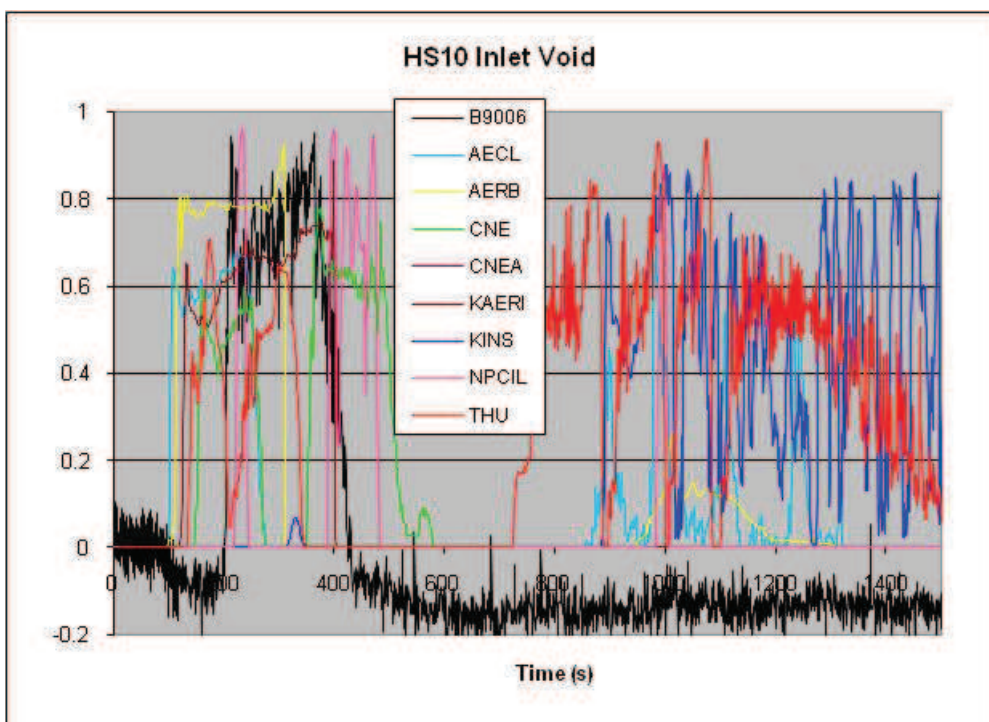


Figure 4-44. Heated section HS10 inlet void.

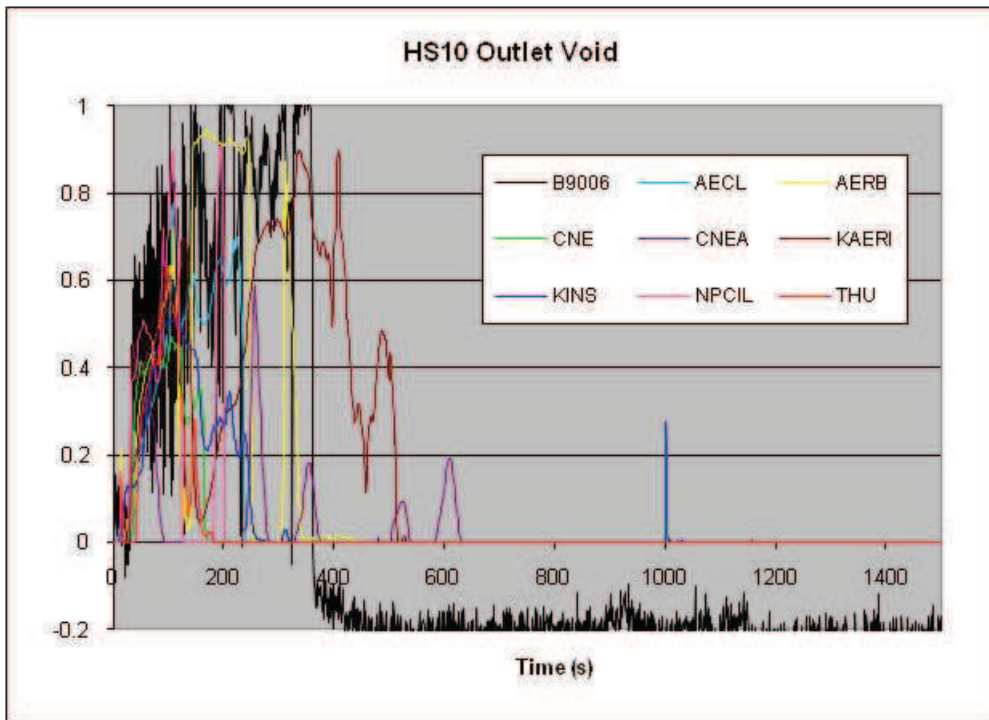


FIG. 4-45. Heated section HS10 outlet void.

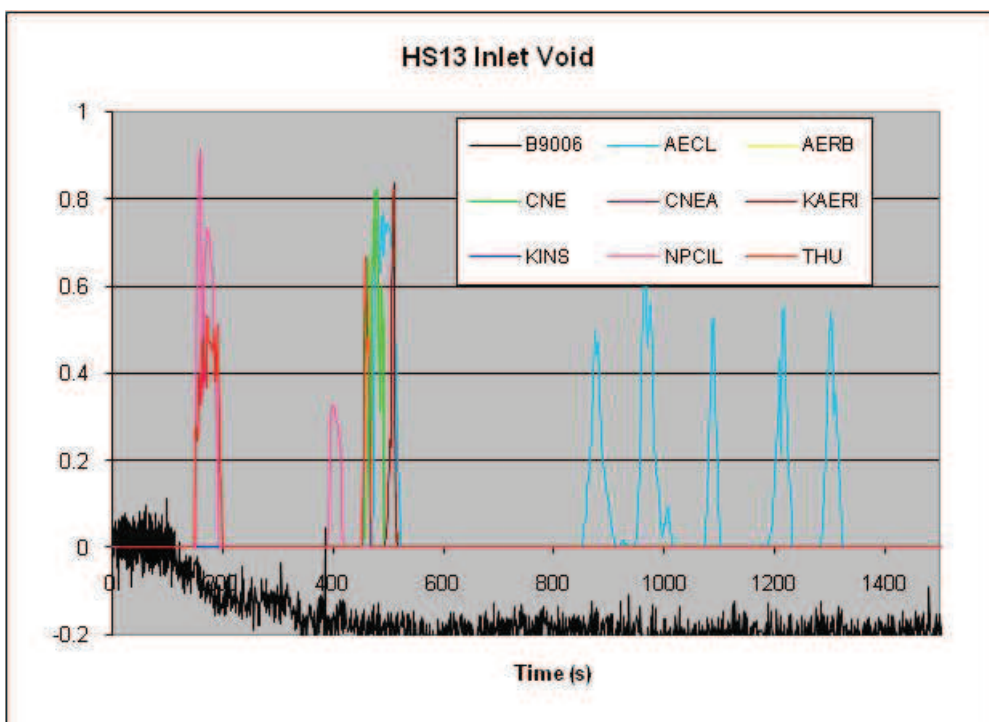


FIG. 4-46. Heated section HS13 inlet void.

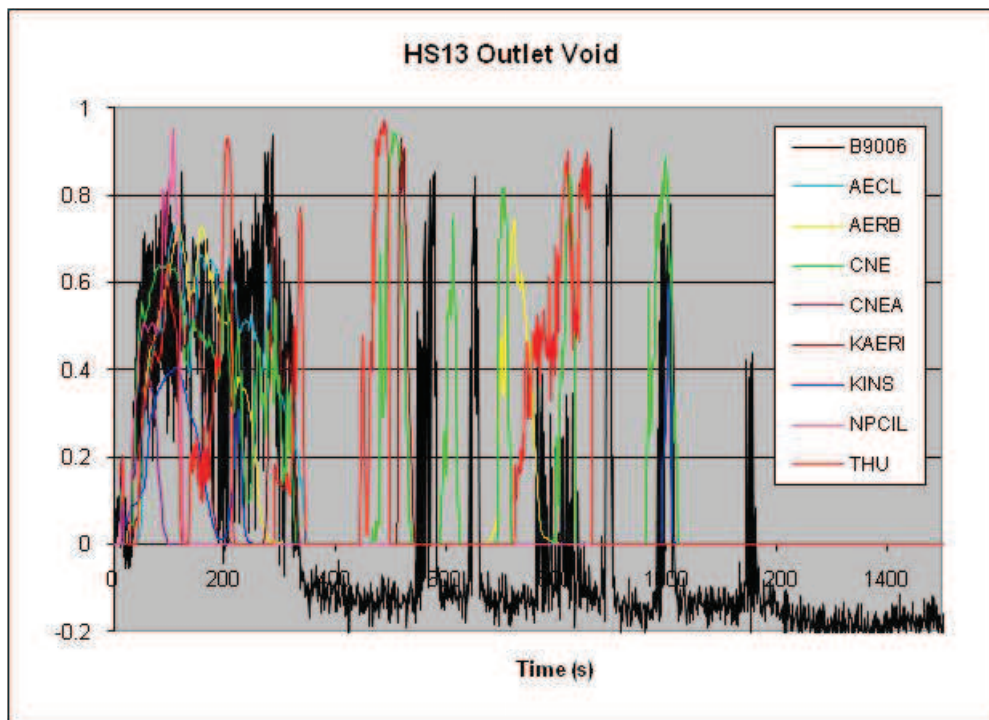


FIG. 4-47. Heated section HS13 outlet void.

4.2.13 Differential pressure along outlet feeder from HS13 to HDR5

Since flow rates are very low (nearly zero after ~400s) and predominantly single-phase, except for brief periods of time, the feeder pressure drop predictions follow experimental trends closely, as shown in fig. 4-48. One exception is NPCIL, who predicts large pressure variations and a rather low average pressure drop after ~300s, compared to the experiment and other calculations, because they predict reverse flow through HS13 (see Section 4-2.11). Note, that due to the elevation difference, negative flow does not necessarily result in a negative pressure drop (explained in detail in Section 4-5.8)

Pressure drop predictions in the 100-300-s timeframe are related to whether single- or two-phase flow is predicted and the amount of void, in this particular outlet feeder (see previous section). In general, lower pressure drops are associated with higher void, due to the reduced density gravity head.

4.3 OPEN CALCULATION RESULTS FOR TEST B9006

All participants, except CNE, submitted revised open calculations. These are presented in the following sections (CNE data shown is the same as their blind calculation results). CNEA submitted open calculations close to the time of the last meeting. Note that all the following figures contain results of blind calculations for CNE and CNEA.

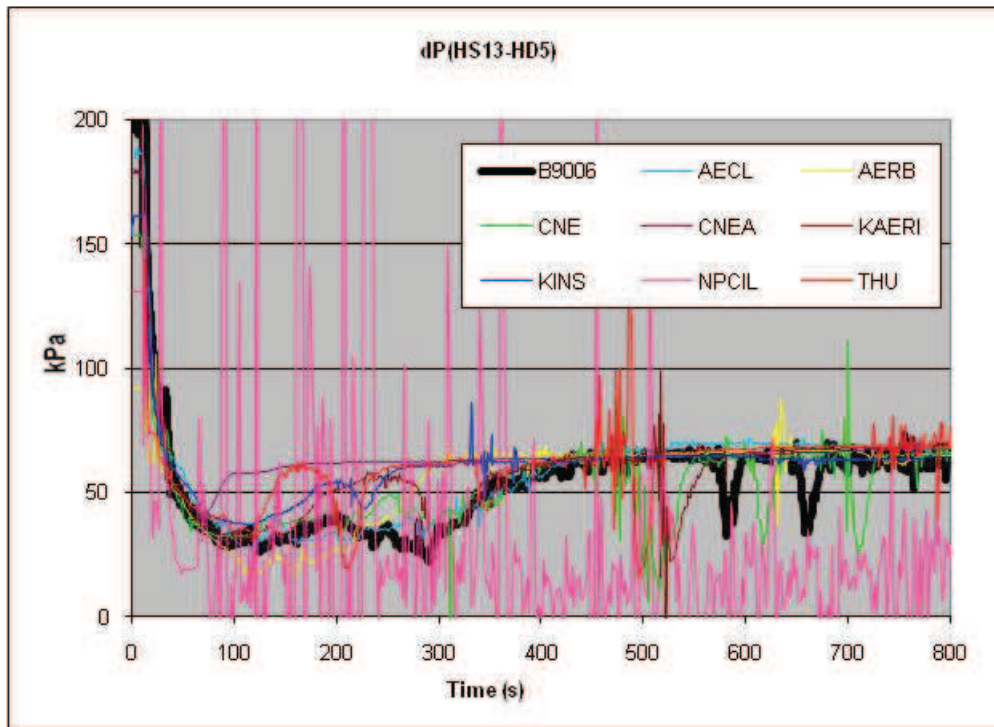


FIG. 4-48. Heated section HS13 to header HDR5 pressure drop.

4.3.1 Sequence of major events

The sequence of major events in Test B9006 is summarized in Table 4.3. Where two times are given in the experiment column (the second one in parentheses), the first time refers to the time when the event was indicated through direct measurement and the second time refers to the time the trip parameter (which was used in the calculations to trigger the event) reached its setpoint. With a scan rate of 0.2s, the minimum experimental uncertainty is estimated to be ± 0.15 s. For times estimated from graphs (indicated by “~”) the estimated uncertainty in timing is ± 5 s.

4.3.2 Primary pump differential pressures

Primary loop coolant circulation is provided by two high-head centrifugal pumps. In test B9006, the break occurred at inlet-header HD8 at 10.8 s, and the primary pumps were ramped down when header HD7 pressure reached 8.8 MPa(g) at the same time as the heater power was ramped down (in the test the ramp-downs actually occurred at 11.6 s).

Figures 4–49 to 4–53 provide the code comparison to experiment in terms of pump differential pressure and (liquid) mass flow rate, with fig. 4–51 showing in detail the start of the pump rundown, using P2 as an example. All calculations show the proper trends, with the correct initiation time and only slight variation in the rundown curve. Other than the correction by KINS in their output date, there were no substantial changes from the blind calculations. NPCIL was able to improve their pump model and reduce or eliminate pressure spikes predicted in their blind calculation.

TABLE 4-3. SEQUENCE OF EVENTS FOR TEST B9006 (OPEN CALCULATIONS)

Events	Experiment ± 0.15 (s) ~ ± 5 (s)	Code predictions (s)							
		AECL	AERB	CNE	CNEA	KAERI	KINS	NPCIL	THU
Data gathering started/calculation starts	0.0	0.0	0.0	0.0	0.0	0.0	0.0	0.0	0.0
Surge tank isolated	6.0	6.0	6.0	6.0	6.0	6.0	6.0	6.0	0.0
Blowdown valve (MV-8) opens	10.8	11.0	11.0	11.0	11.0	11.0	11.0	11.0	11.0
Primary pump run down Power run down (8.8 MPa(g) @ HD7)	11.6 (11.3)	11.3	11.4	11.4	11.5	11.6	11.3	11.6	12.5
Secondary pressure ramp ECI accumulator poised (6.0 MPa(g) @ HD7)	29.5 (28.0)	31	31.9	31	30	29.5	28.0	27.2	31.6
ECI Valve MV-11 Opens (4.2 MPa(g) @ HD7)	78.0 (78.5)	74	95	52	67	70.8	108	74.3	65
HP ECI flow into loop starts	~115	68	95	52	65	79.3	118	115	74
Channel reverse flow starts (HS _x , x = 5,8,10,13)	~180 (5,10)	112 (10) 149 (5)	159 (5) 238(10)	139 (5,10)	120(10) 126(5)	115 (10) 240 (5)	185 (5) 245(10)	200 (5,10)	130.6
Initial integral loop refill*	~480	550	500	540	570	570	640	160	430
HP ECI complete (10% of initial level) and LPI start	~1100	1157	977	1087	~1100	1126	1013	1063	1110
End of test	2284	2280	2300	2310	2400	2280	2284	2300	2285

* Experiment time is estimated from the time the last void measurement is observed to reach zero (except pump P2 outlet, which is suspect) and simulation times are taken from Fig. 4-68 when the fast refill ends.

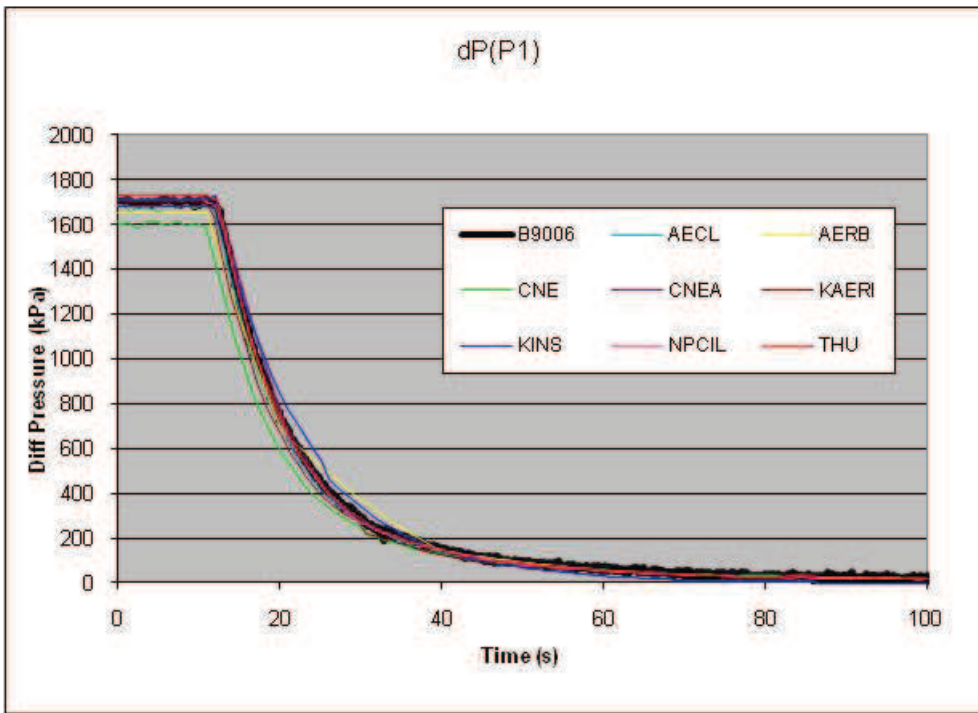


FIG. 4-49. Pump P1 differential pressure.

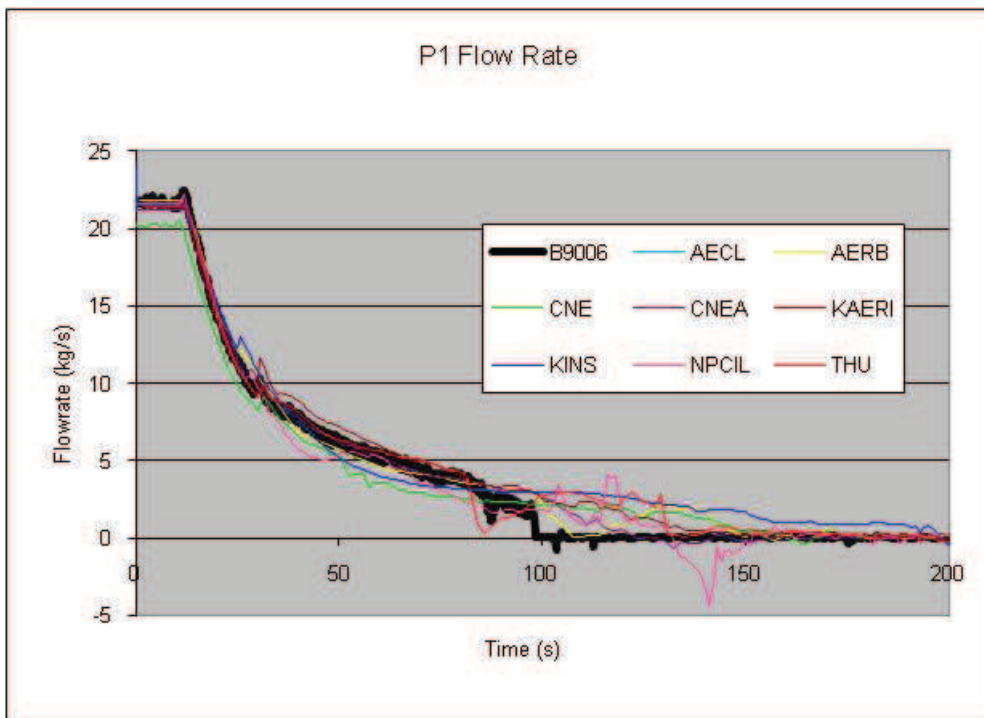


FIG. 4-50. Pump P1 flow rate.

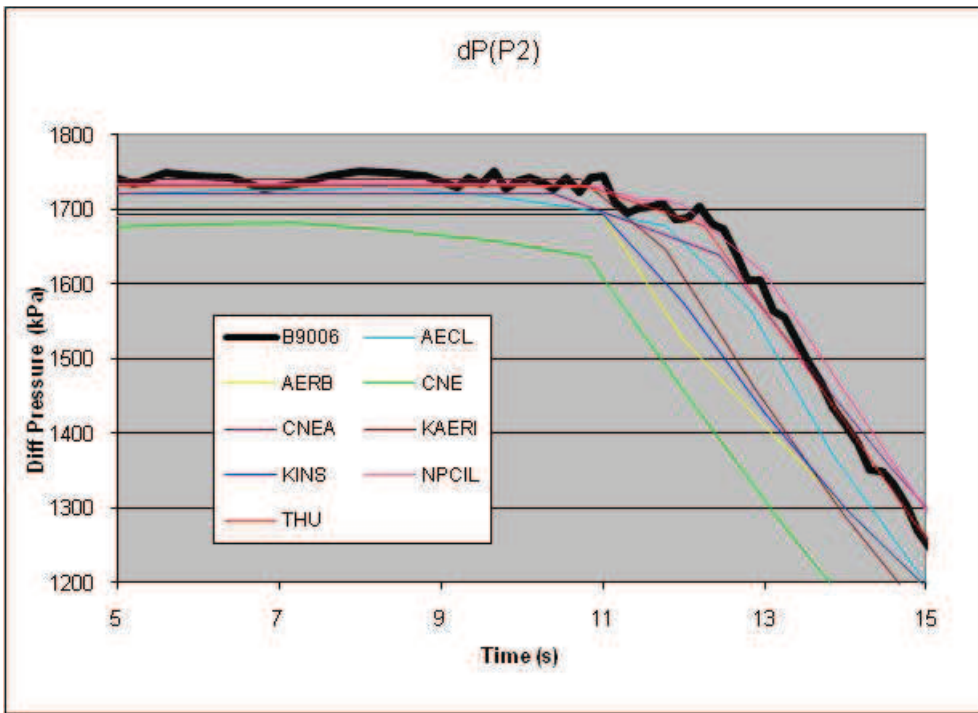


FIG. 4-51. Pump P2 differential pressure indicating start of pump rundown.

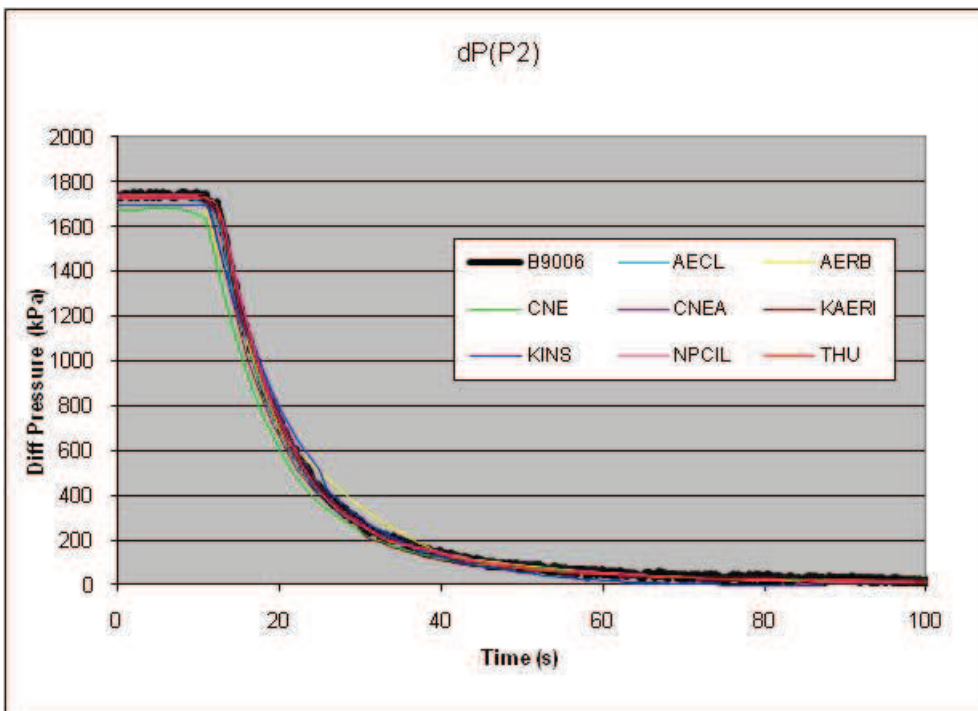


FIG. 4-52. Pump P2 differential pressure.

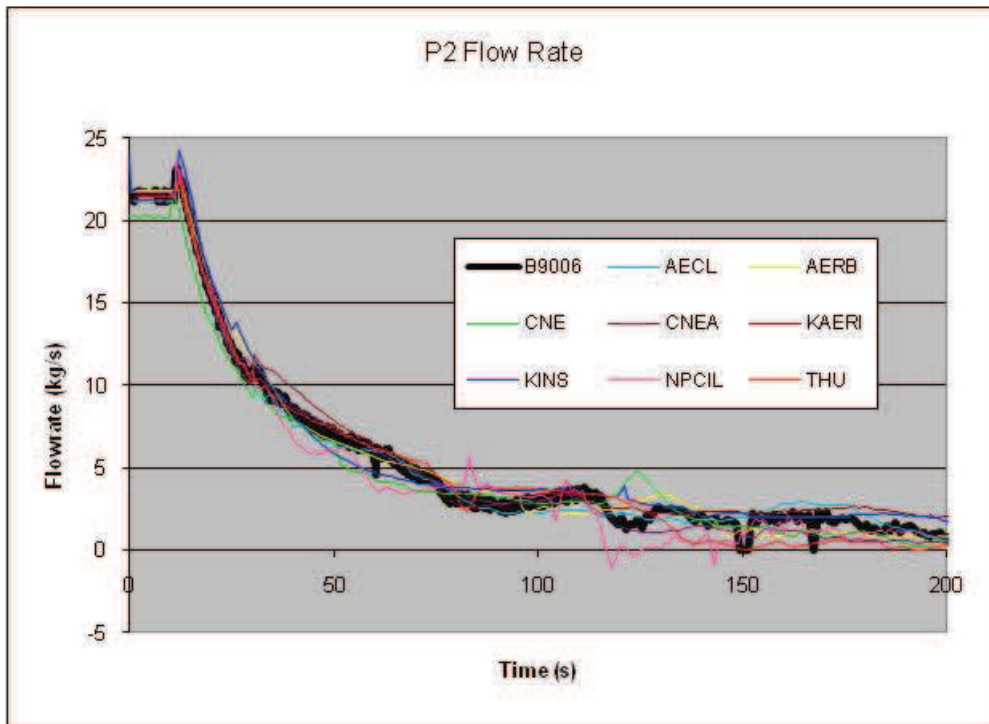


FIG. 4-53. Pump P2 flow rate.

4.3.3. Header differential pressures

The behaviour of the header-to-header differential pressures mirrors that of the pump differential pressure during the pump rundown, since the break is rather small.

Figures 4–54 and 4–55 show the broken and intact-pass header-to-header differential pressures, respectively. This pressure drives the flow through below-header portion of the loop (inlet feeders, heated sections and outlet feeders) during the transient. At 100 s the pressure difference reaches values below 30 kPa and remains below for the remainder of the test, thus providing very little driving force for channel flow. As discussed later, there are some periods of stagnation and reverse flow in individual channels.

All calculations show the correct timing and trend, including the slight differential pressure increase in the intact loop immediately after the break opening. The differential pressures are slightly underpredicted by some participants and over-predicted by others in the 20-s to 40-s period.

4.3.4 Header pressures

Following the small break, the primary pump speeds and heater powers are reduced (HD7 reaches 8.8 MPa(g)), ECI flow is poised when header HD7 reaches 6 MPa(g) and ECI flow into each header starts when the particular header pressure drops below the ECI tank pressure of 4.2 MPa(g). In the test the ECI isolation valves to all headers opened at 29.5 s and the main ECI valve (MV-11) opened at 78 s (HD7 reaches 4.2 MPa(g)).

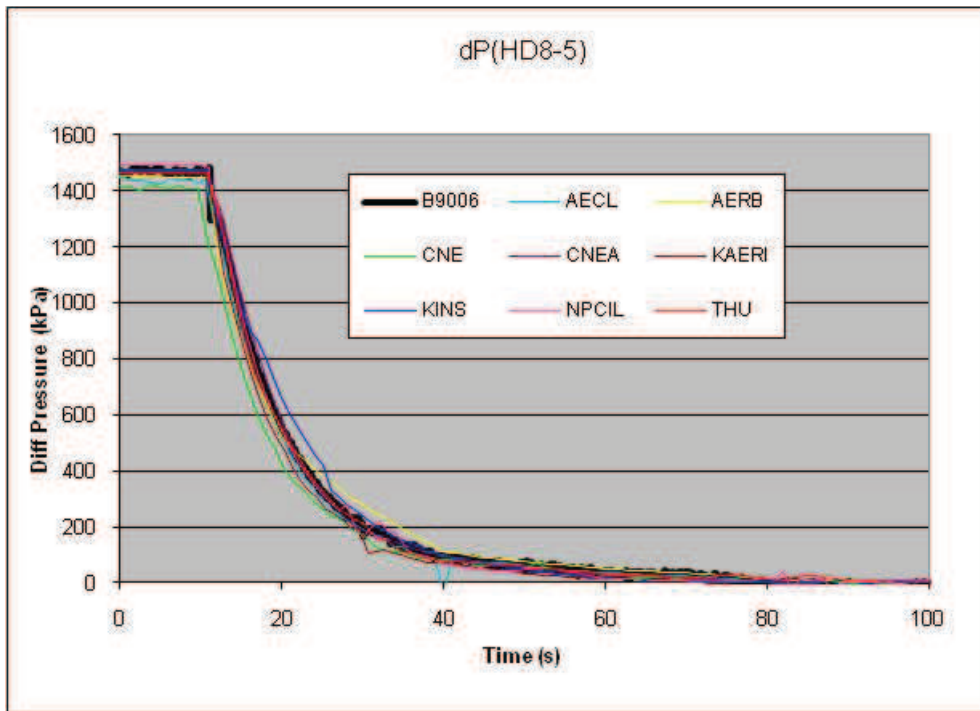


FIG. 4-54. Broken pass header-to-header differential pressure.

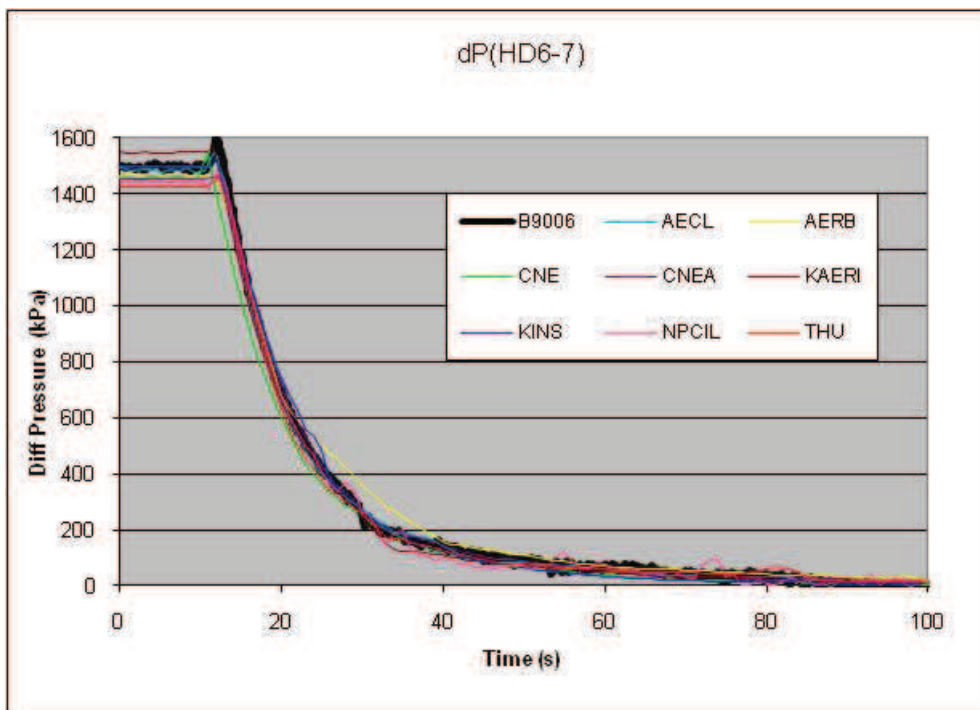


FIG. 4-55. Intact pass header-to-header differential pressure.

Header pressures reached 4.2 MPa(g) in the timeframe from 78 to 80 s, however, significant net ECI inflow did not start until about 115 s in the experiment, when the pressure in all headers is approximately 4.0 MPa(a). Between 78 and 115 s the loop and ECI system depressurize in sync without any measured net inflow of ECI water into the loop.

The entire loop depressurized relatively uniformly during this SBLOCA, with differential pressures driven mainly by the pumps running down, as discussed in the previous section. Even during ECI injection, the header pressures are very close to the ECI tank pressure, thus ECI injection does not significantly affect header pressures. The initial depressurization to about 8 MPa in the outlet and 9.5 MPa in the inlet headers is the result of single-phase discharge from the break until saturation is reached and two-phase discharge starts. The depressurization is considerably slower during the two-phase discharge and slows down even further when flashing occurs in the heated channels.

Figures 4–56 and 4–57 show the early pressure transient in headers HD8 (the broken header) and HD7 (the outlet header of the intact pass). While the initial depressurization behaviour is captured well by all simulations, AECL shows a pressure decrease and KAERI a pressure increase after the pressurizer (surge tank) is isolated at 6 s, before the break opening. AECL also predicts a significant “undershoot” of the header pressure at the end of the single-phase discharge.

From about 40 s, when voiding in the channels becomes significant but flow is still driven by the pumps, until 200 s, when pump flow is essentially zero (see pump P2 flow rate), some participants overpredict, while others underpredict, the header pressures by up to 0.5 MPa. From 200 to 500s, when the loop is being refilled by ECI water, all participants predict pressures close to the test measurements (only HD6 is shown in Fig. 4–58, but others are qualitatively similar). KINS calculates a temporary pressure increase between 650 (when they calculate complete refill) and 850 s, which was not observed in the experiment. The higher volume of non-condensable gas in the accumulator, which was a user input error, might be the cause of this unreasonable pressure increase.

From the experimental measurements it is inferred that the loop initially refills around 450-500s.

4.3.5 Header ECI flow rates

The header depressurization behaviour is almost identical in all headers. When they reach the ECI pressure of about 4.2 MPa(g), the depressurization rate is slowed due to a near-balance in channel steaming and discharge from the small break. However, eventually the inflow from the ECI system refills the loop and while the detailed flow rates into each header are considered of secondary importance, the overall ECI flow rate is important.

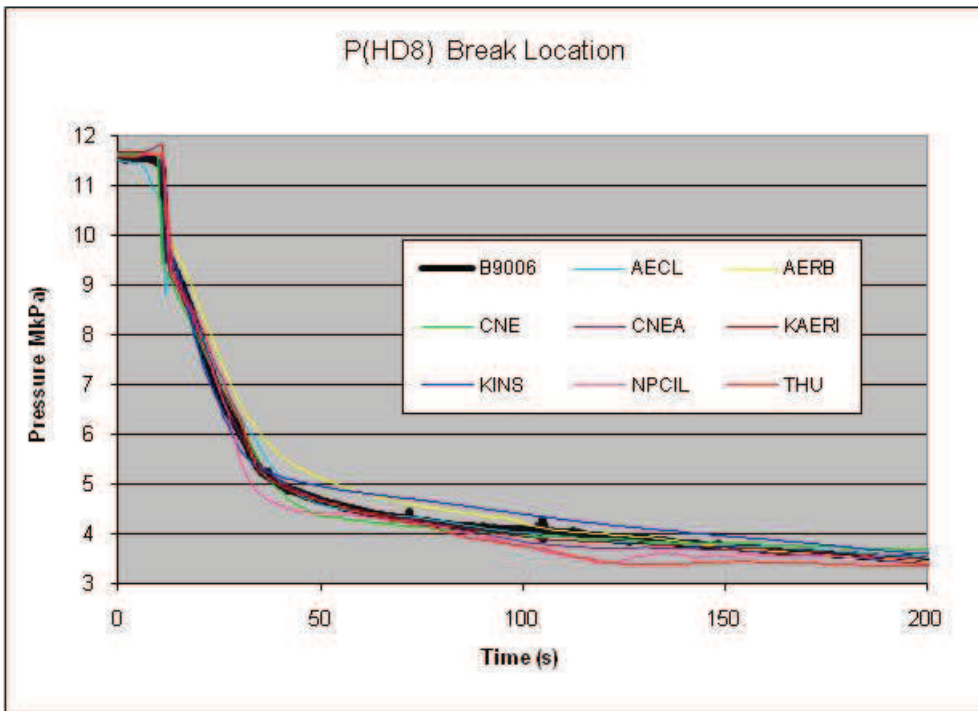


FIG. 4-56. Header HD8 pressure.

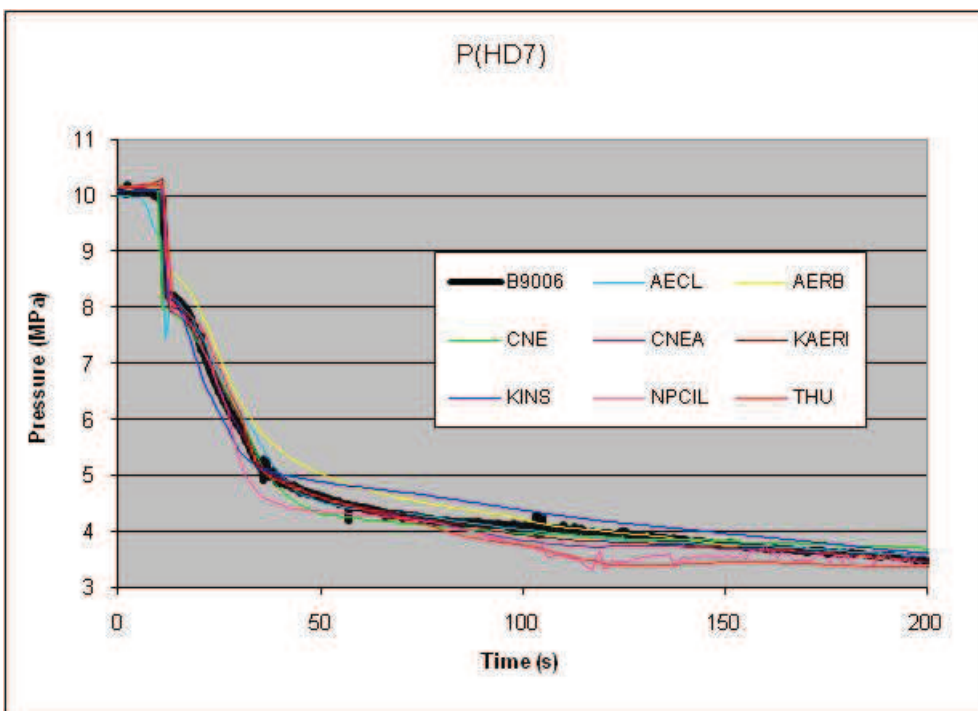


FIG. 4-57. Header HD7 pressure.

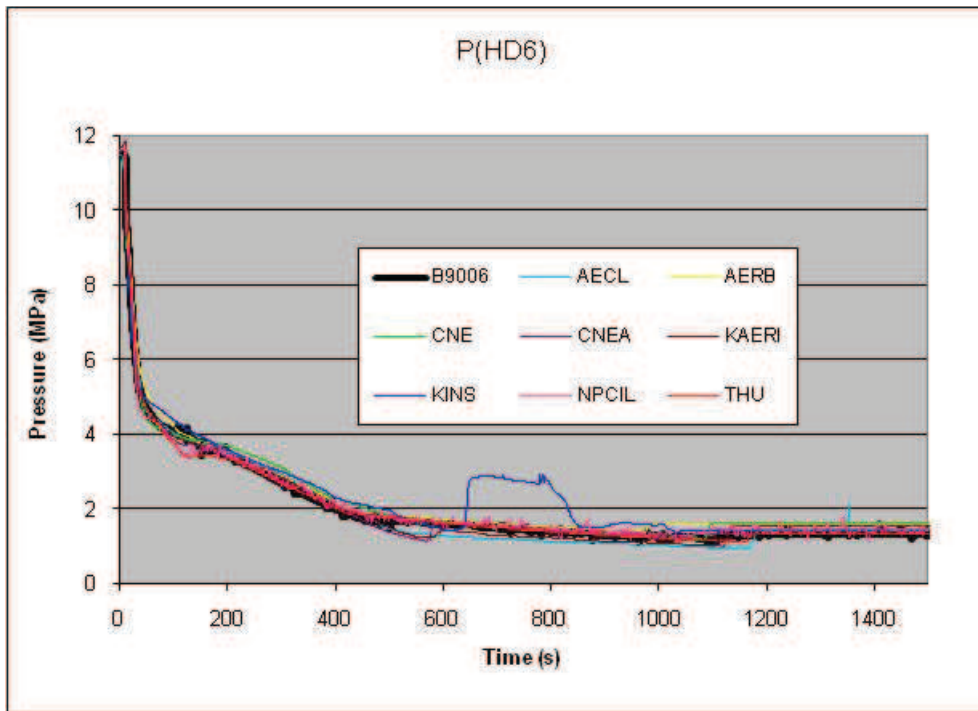


FIG. 4-58. Header HD6 pressure.

ECI flow is poised when Header HD7 reaches 6 MPa(g) and ECI flow into each header starts when the particular header pressure drops below the ECI tank pressure of 4.2 MPa(g). In the test HD7 reached 6 MPa(g) at 28 s, at which time the ECI isolation valves to all headers open. Following the valves opening, due to pressure difference between the headers, there is flow in the header connection lines. Because the circuit pressure is higher than the ECI pressure, the check valves that are present in the lines to the headers do not allow ECI flow injection. This allows flow between the inlet header from one pass and outlet headers of the other pass, i.e. between HD5 and 6 and between HD7 and 8. This results in approximately 1/6 of the pump flow rate to bypass the heated sections. Header pressures reached 4.2 MPa in the timeframe from 78 to 80 s, however, significant net ECI inflow did not start until about 115 s in the experiment. Since the break is relatively small, the pumps still determine the header pressures during the rundown period from 11 s to 100 s, when they reach 10% of their initial speed.

Figures 4-59 to 4-62 provide the code comparison to experimental measurements for each of the four headers. The flows are measured and calculated near the header entrances, thus during the period prior to net ECI flow ($< \sim 115$ s) the flow rates are not from the ECI to the headers, but reflect inter-header flows, as described in the previous paragraph. Most participants calculate this inter-header flow with the correct direction and magnitude, except for KAERI, who overpredict by about a factor of two and CNEA, who predict initially reverse flow as compared to the measured directions and the other participants. This could possibly indicate incorrect modeling of the ECI system pipe losses. This also adversely affects the ECI flow rate predictions once ECI flow into the loop and results in a significant overprediction of the early ECI injection rate and an early loop refill (see next section) by KAERI. AERB does not show any inter-header flow rates through the interconnecting ECI piping, due to header valve opening trip logic (less than 4.2 MPa(g) header pressure). Note that many of the participants made significant changes to ECC pipe losses between blind and open submissions.

Net ECI flow starts first into the (lower-pressure) outlet headers, HD5 and HD7, while the inlet headers show zero, or very low, flow (HD6) or outflow (HD8). After ~350 s ECI flows into all four headers at a rate of between 0.5 and 1 kg/s. All participants calculate approximately correct ECI flow rates. High-pressure ECI is exhausted in the experiment at 1110 s and code predictions vary between 977 and 1157s.

4.3.6 Integral ECI flow, qint and sum of Q3 to Q6

Figures 4–63 and 4–64 show the net total ECI flow rate and integral flow into the primary loop, with the start of net ECI flow into the loop shown in Fig. 4–67. Figure 4–68 shows the calculated total loop inventory, resulting from flow out the break and in from the ECCS.

Integrated header ECI flow rates represent the total volume of cold water that comes from the ECI system to the primary loop. It is important since it has a direct impact on primary loop pressure, FES sheath temperatures and mass inventory of the primary system. Figure 4–64 shows the entire test, while Figure 4–65 shows the early details. Two derived measurements are shown, Qint(HPECI) represents only the high-pressure ECI flow and is based on the ECI tank level measurement, and Qint(ECI) is the sum of all measured ECI-HDx flow rates, thus including both high- and low-pressure ECI. The calculated curves are also the sum of the four individual ECI-to-header flow rates, presented in the previous section. The slight deviation between the two measurement-derived curves is due to accumulated measurement error.

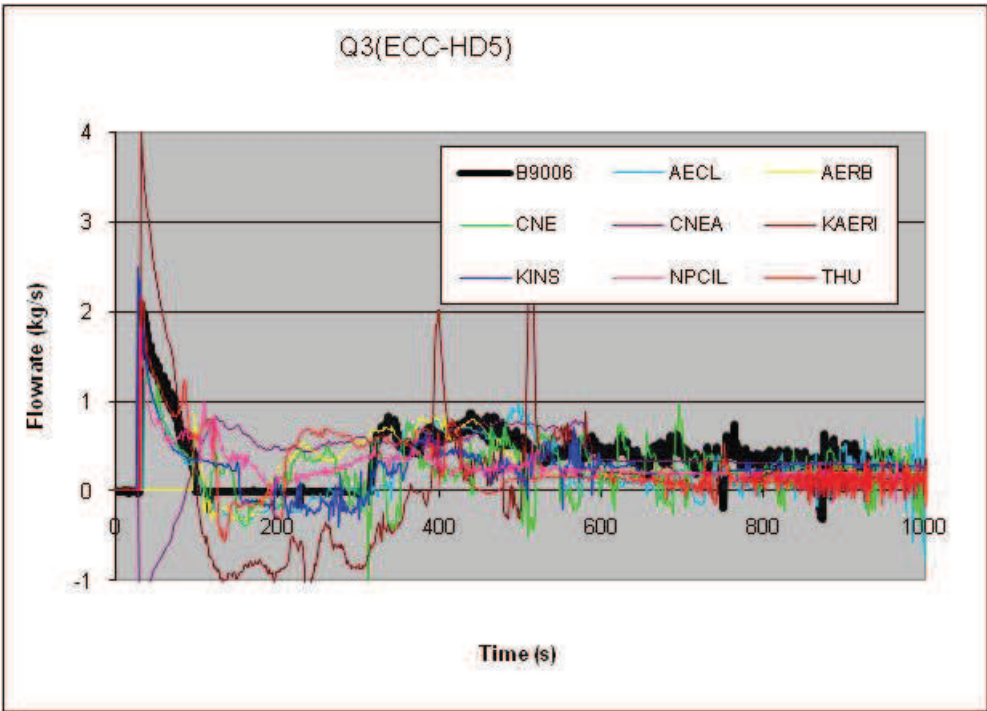


FIG. 4-59. ECI to header HD5 flow rate.

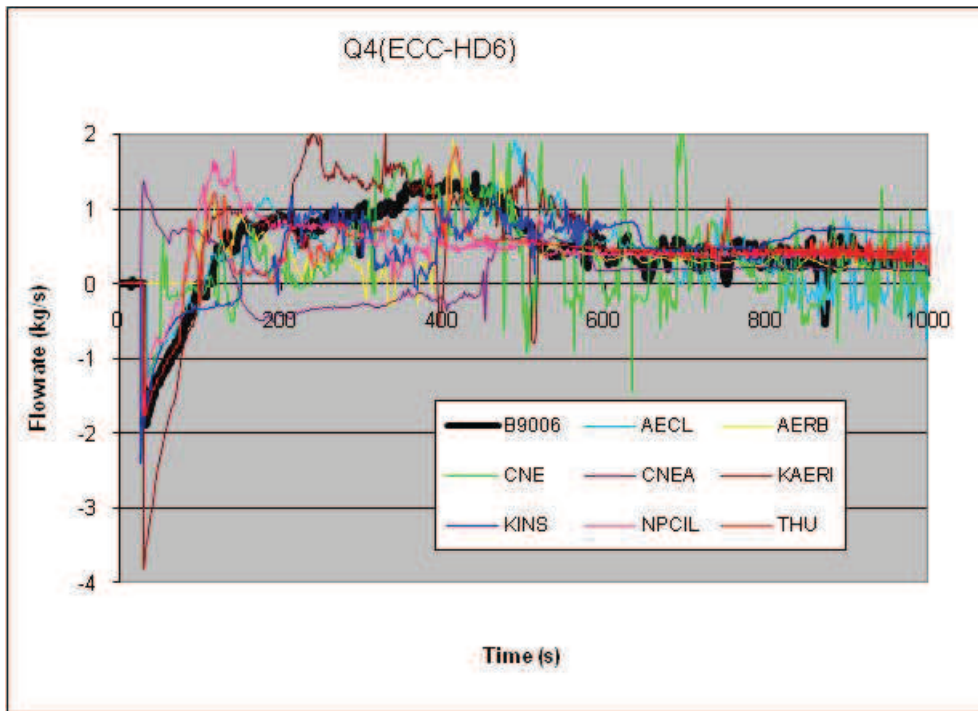


FIG. 4-60. ECI to header HD6 flow rate.

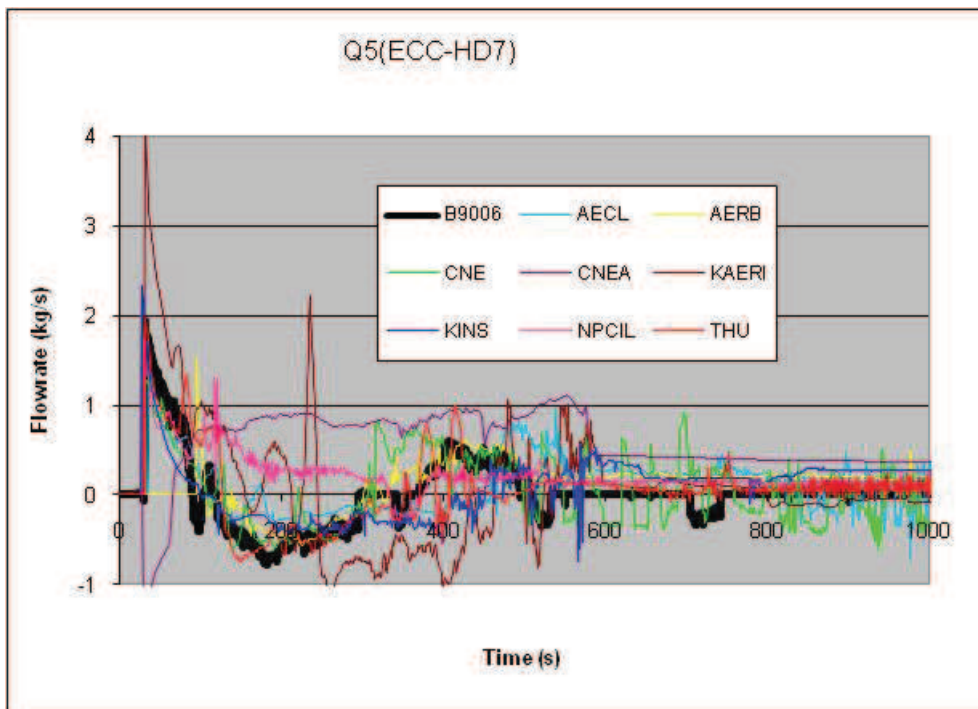


FIG.4-61. ECI to header HD7 flow rate.

At 1110 s, the high-pressure ECI gets isolated on depletion of ~1700 kg inventory in the ECI tank and low-pressure injection is initiated. The loop pressure at the end of high pressure ECI stage is around 1.2 MPa. The initiation of the low pressure pumped ECI phase slightly increases and maintains the loop pressure at about 1.3MPa. Spikes in Fig. 4-63 near ~1100s indicate this switch-over in the test and in the simulations.

Figure 4-66 shows the loop mass inventory. This is the total mass in the primary system excluding the ECI system and the Pressurizer. Predictions of ECC injection timings and loop inventory transients did not change significantly from the blind calculations.

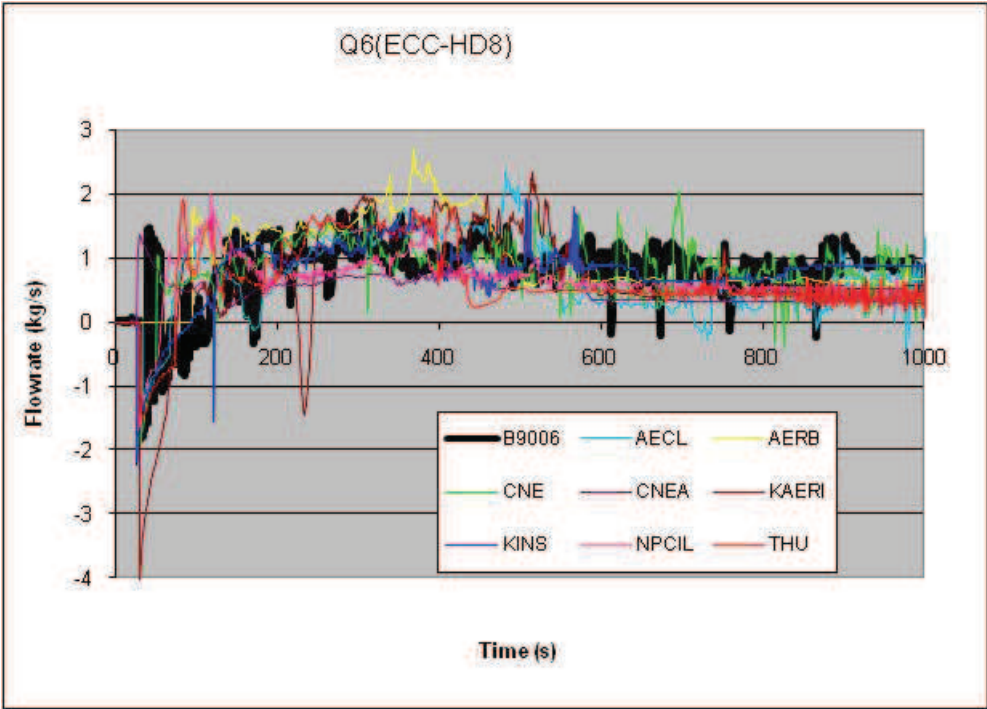


FIG. 4-62. ECI to Header HD8 flow rate.

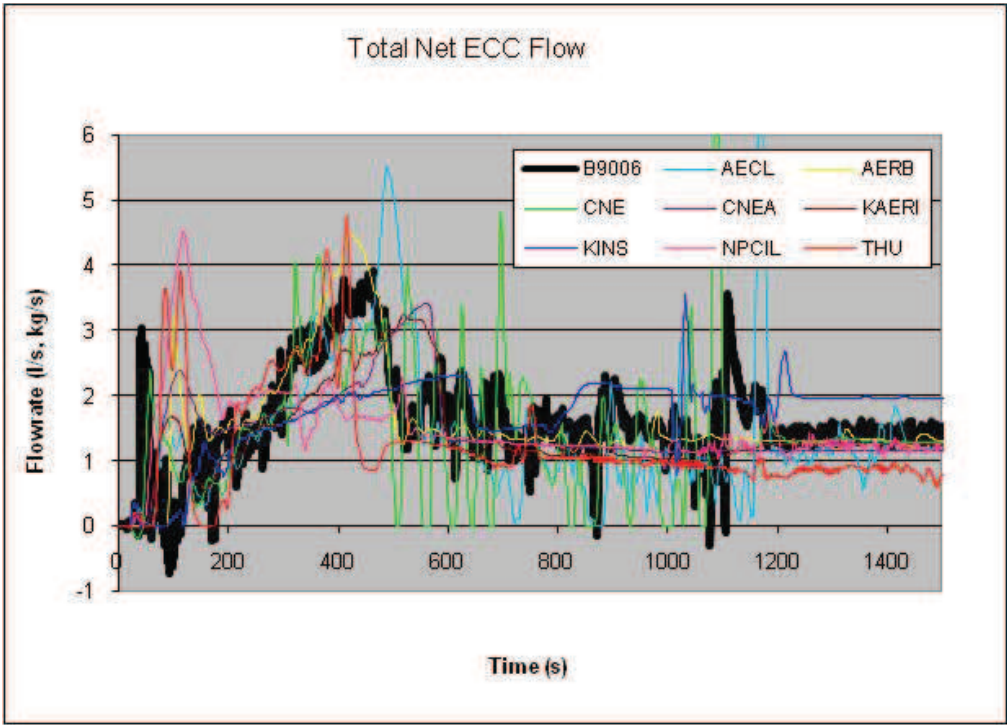


FIG. 4-63. Total net ECI flow into loop.

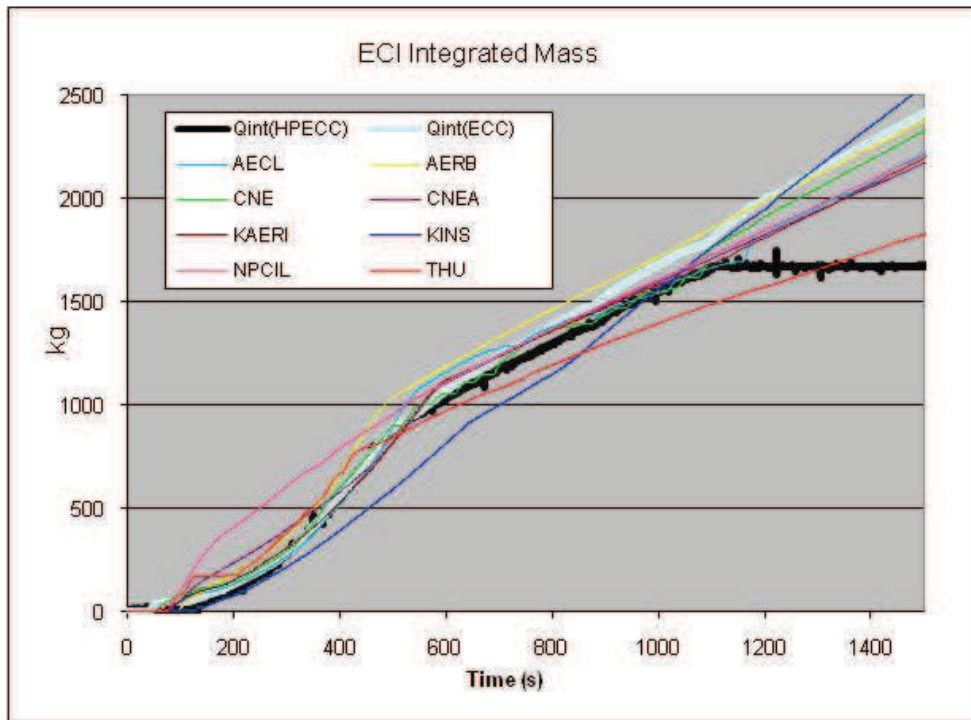


FIG. 4-64. Integral of ECI flows.

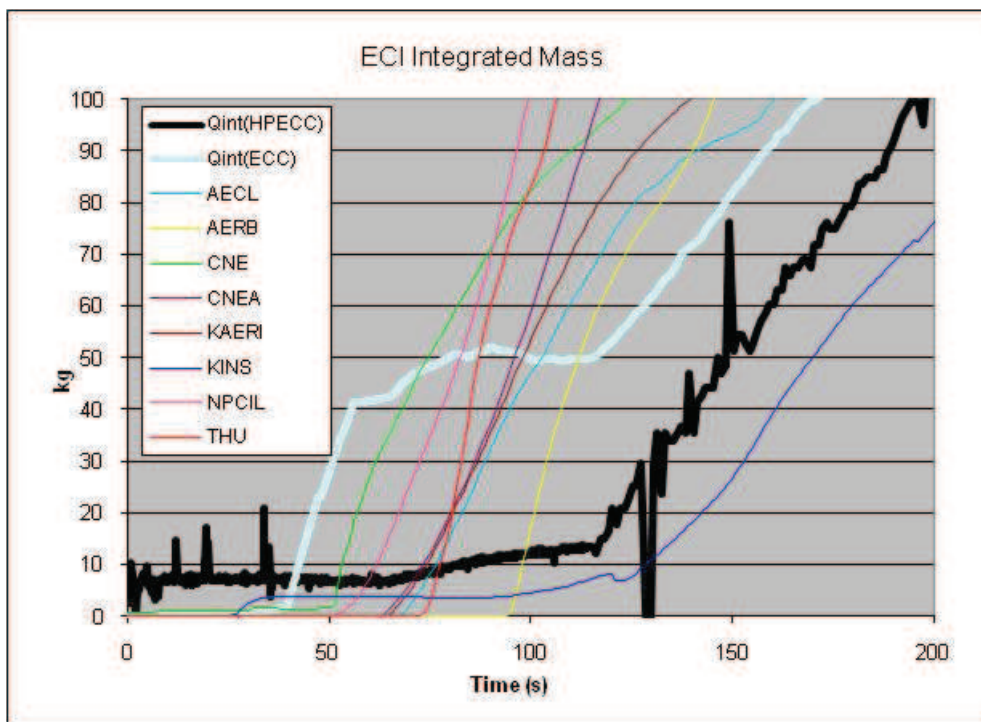


FIG. 4-65. Integral ECI flows during start of ECI injection.

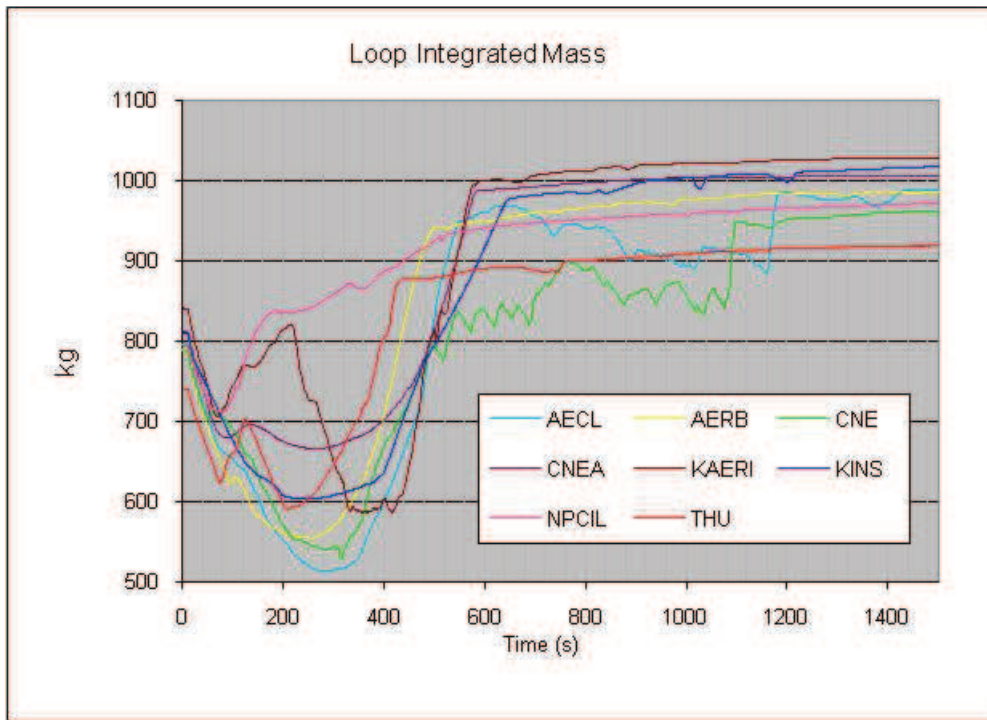


FIG. 4-66. Calculated loop mass.

4.3.7 Void fractions in boiler plenums and primary pumps

The complexity of interpreting boiler and pump voids was discussed in Section 4.2.7 for the blind calculations. While some open calculations showed a markedly different transient void in some or all of these locations, no definite conclusions (i.e. are they better or worse than the blind calculations?) could be drawn.

Figures 4-67 to 4-72 show calculated (blind) and measured voids in both boilers and pumps.

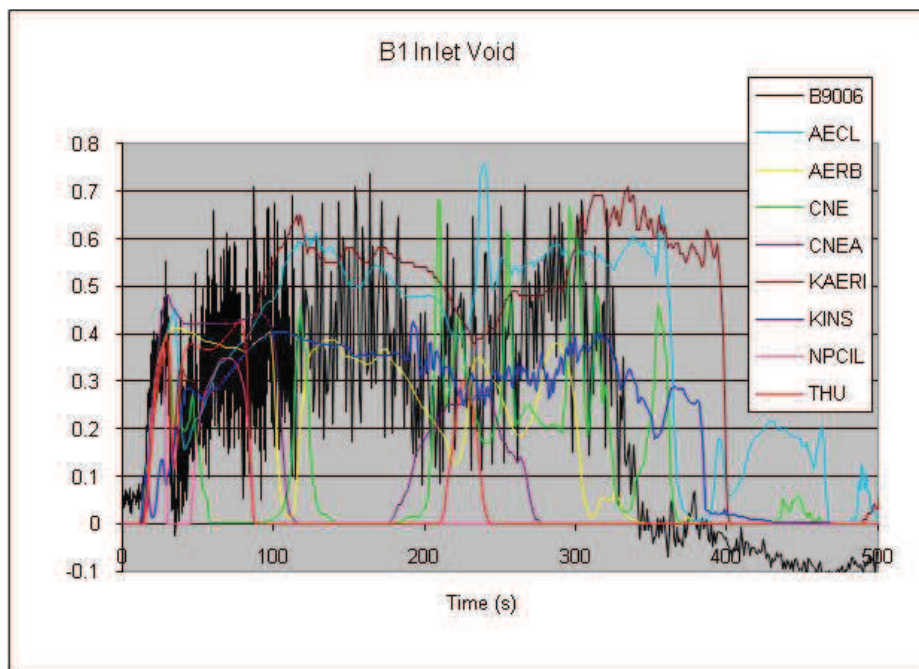


FIG. 4-67. Boiler BO1 inlet void.

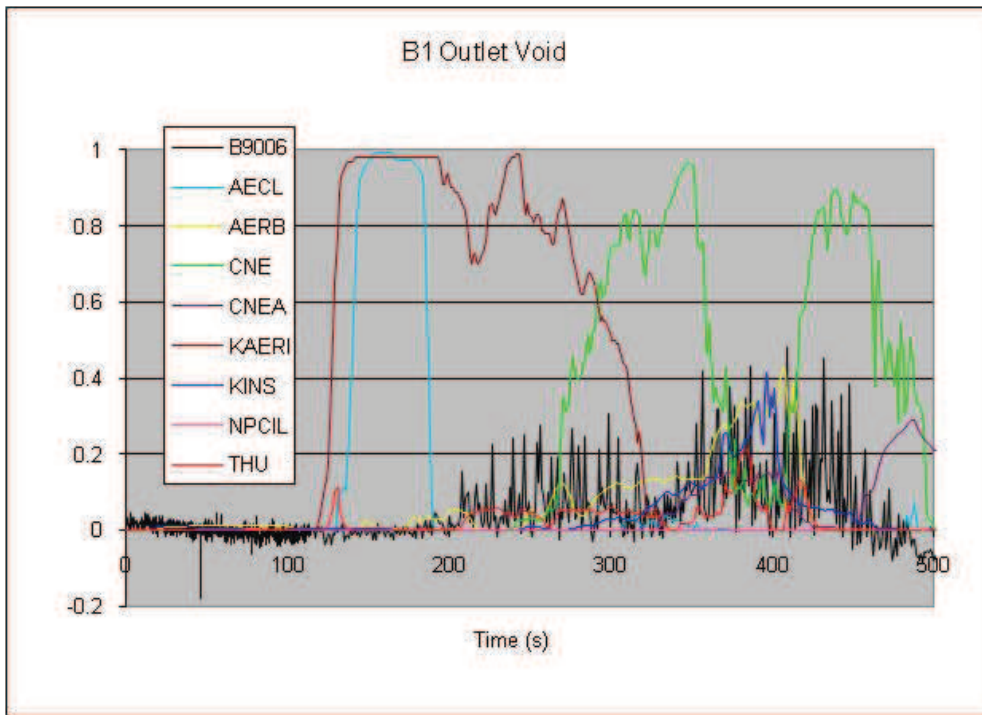


FIG. 4-68. Boiler BO1 outlet void

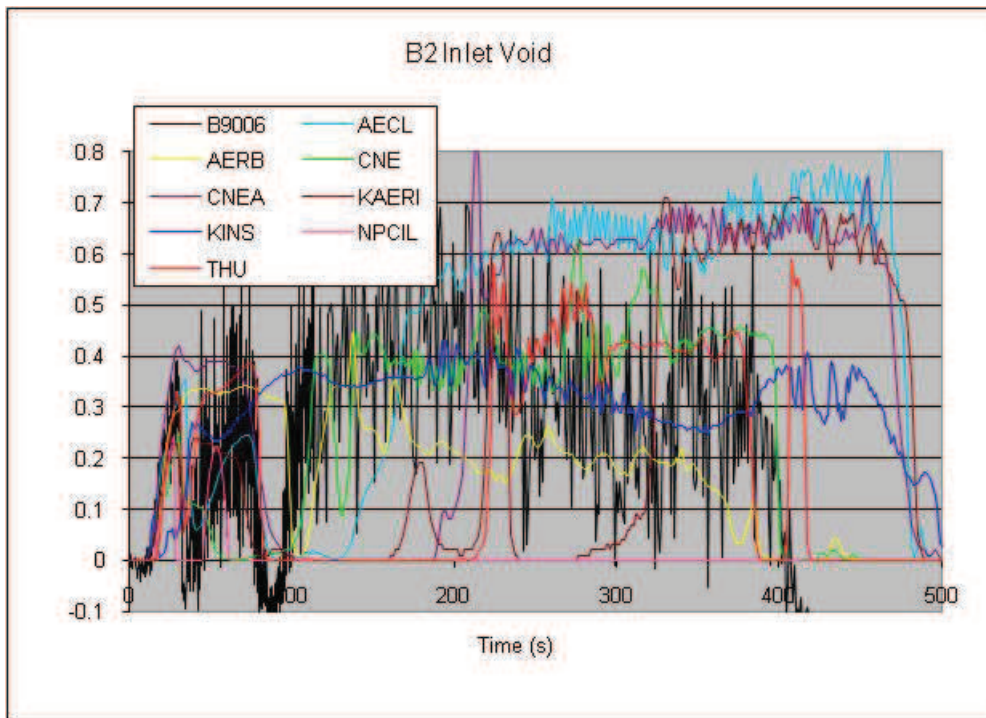


FIG. 4-69. Boiler BO2 inlet void.

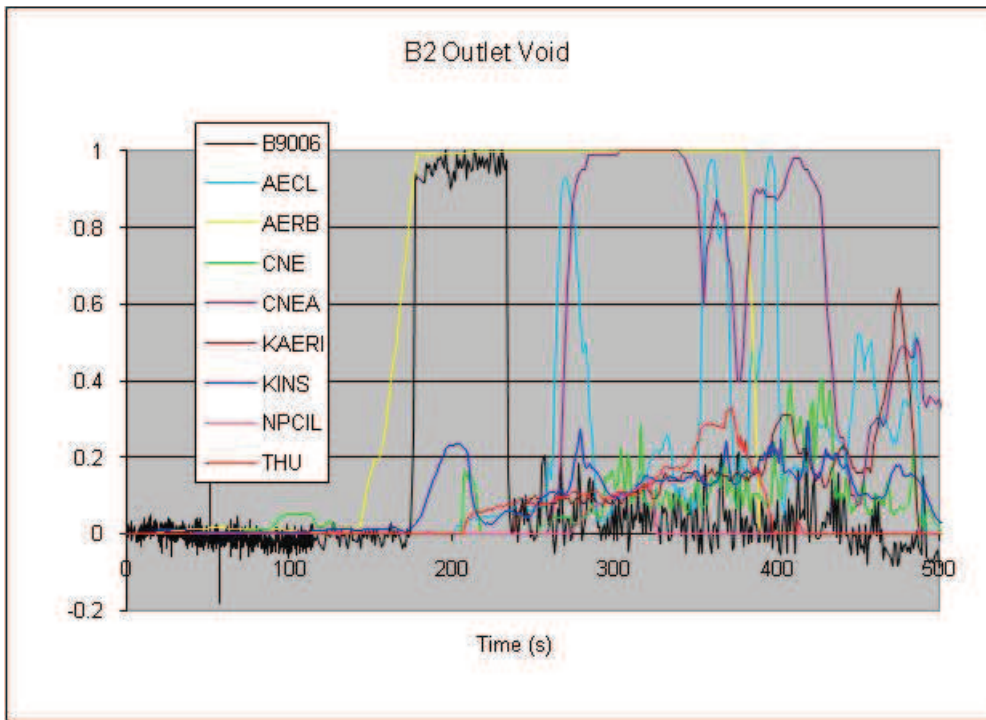


FIG. 4-70. Boiler BO2 outlet void.

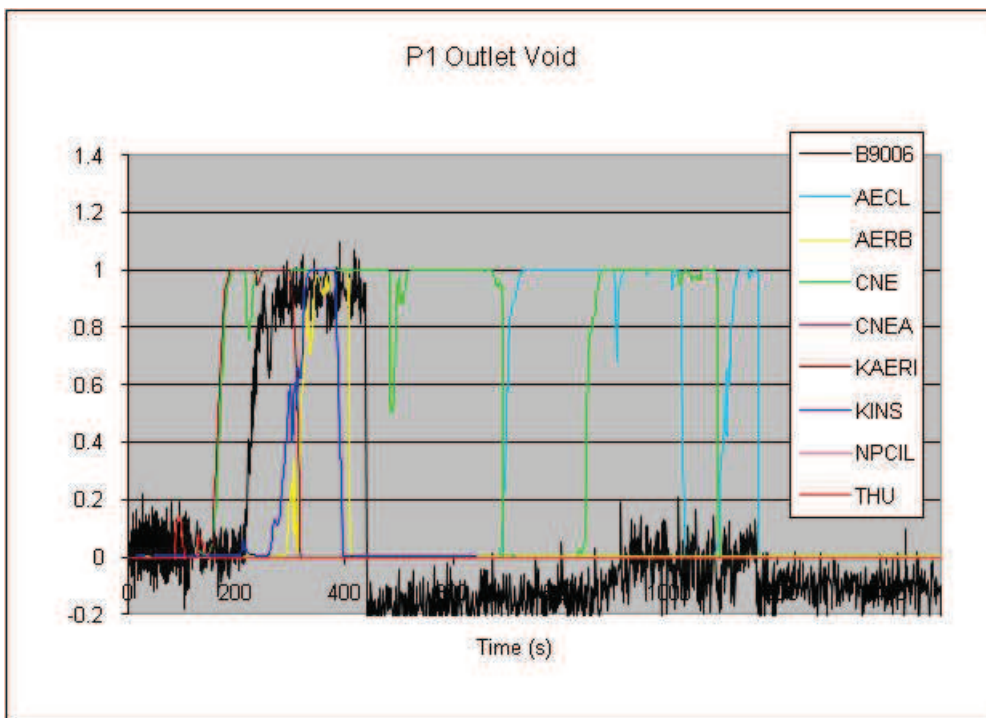


FIG. 4-71. Pump P1 outlet void.

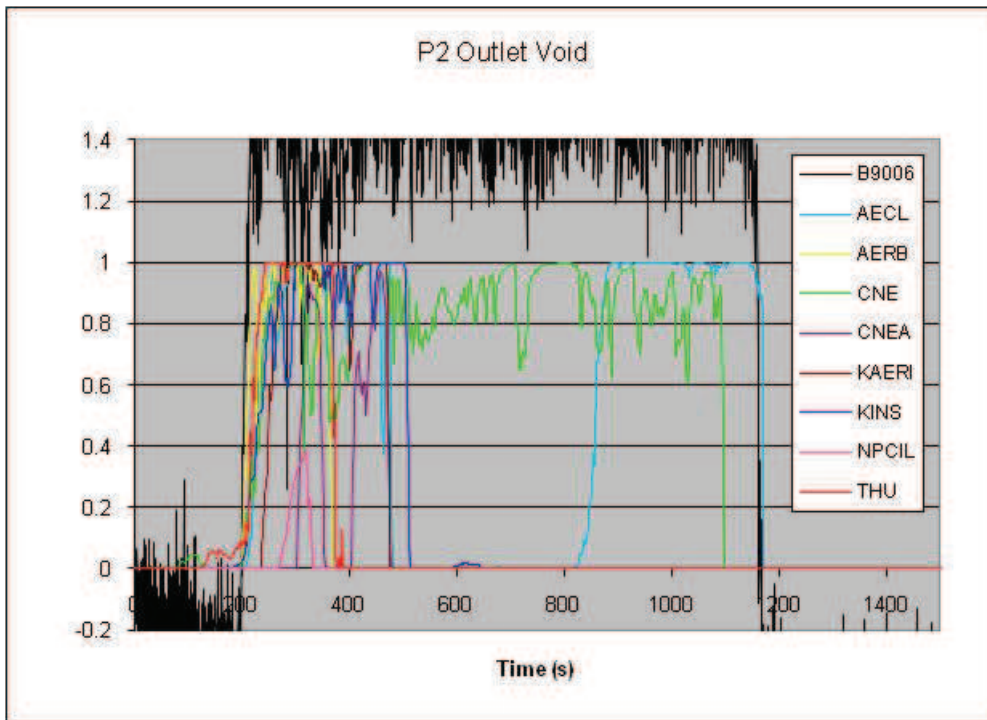


FIG. 4-72. Pump P2 outlet void.

4.3.8 Boiler thermal power and steaming rates

Figures 4-73 and 4-74 show the calculated thermal power (or heat transfer rate, in kW) across the boiler tubes. Figures 4-75 and 4-76 compare the experimentally measured steam drum exit steam mass flow rate with the calculated steaming rates (shown in the Figs as an 11-point average to smooth the oscillations) in the boilers BO1 and BO2, respectively. The deviations between the calculated and measured boiler steaming rates in these two figures indicate a higher or lower (than in the test) boiler thermal power.

While in the experiment the boiler steaming rates were relatively constant between 0.25 and 0.5 kg/s in boiler BO1 and between 0.35 and 0.7 kg/s in boiler BO2 after the initial depressurizations, participants still calculated significantly higher or lower steaming rates for long time periods, indicating that the boilers are either larger or smaller heat sinks (or even heat sources), respectively, than in the experiment. AECL and NPCIL improved their match with the experimental data somewhat, while other results remained qualitatively the same as in the blind calculations.

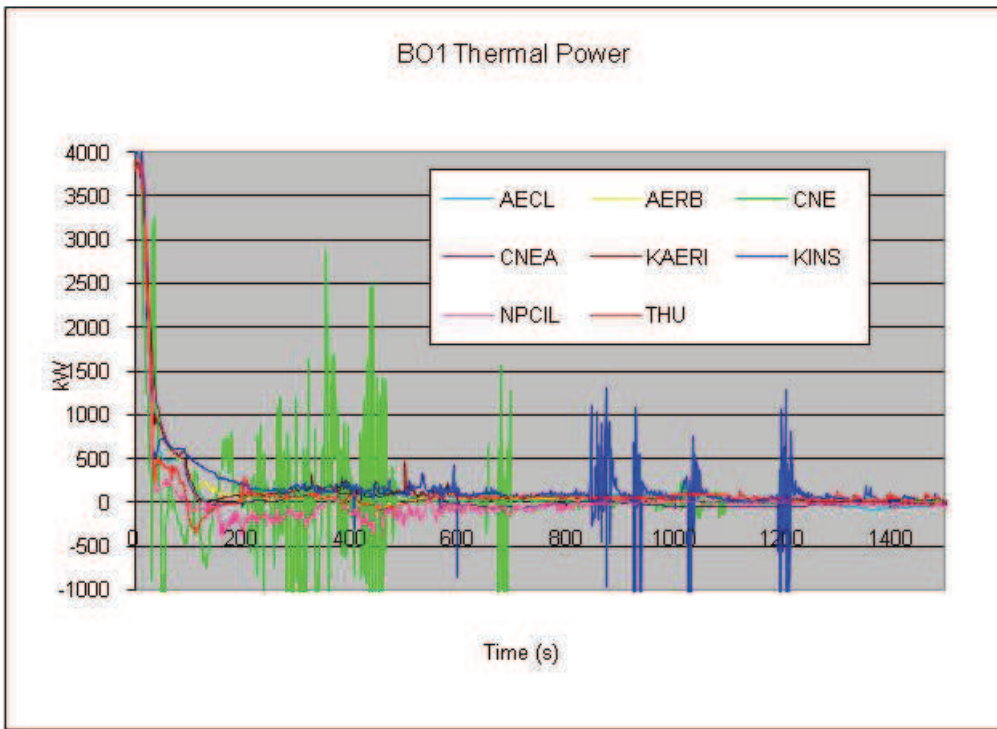


FIG. 4-73. Boiler BO1 thermal power.

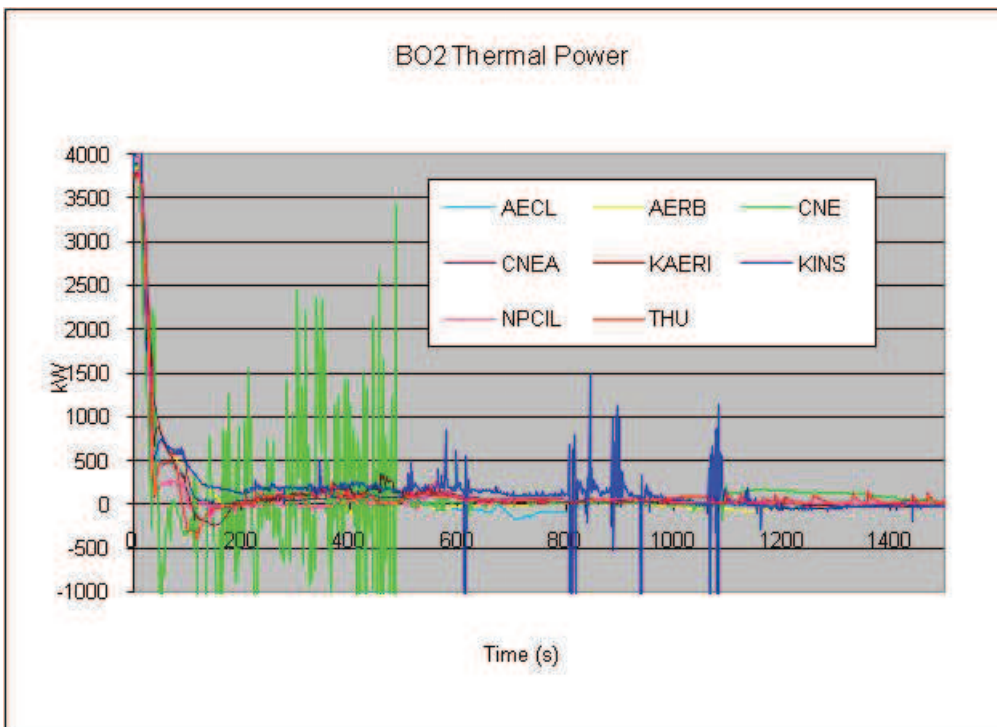


FIG 4-74. Boiler BO2 thermal power.

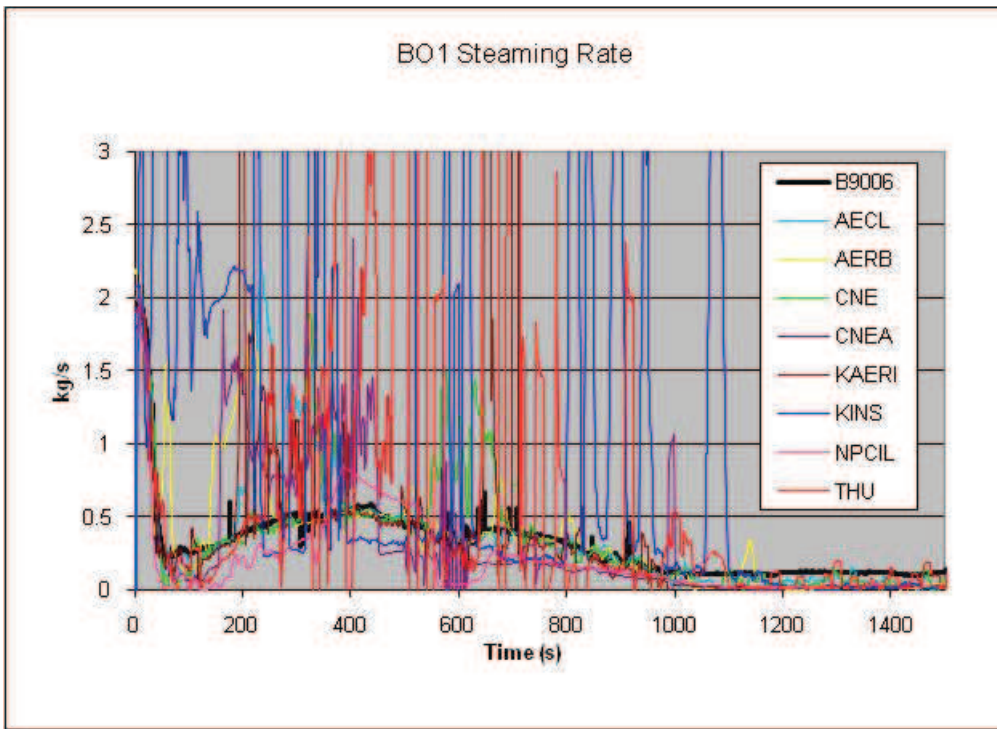


FIG. 4-75. Boiler BO1 steam flow rate.

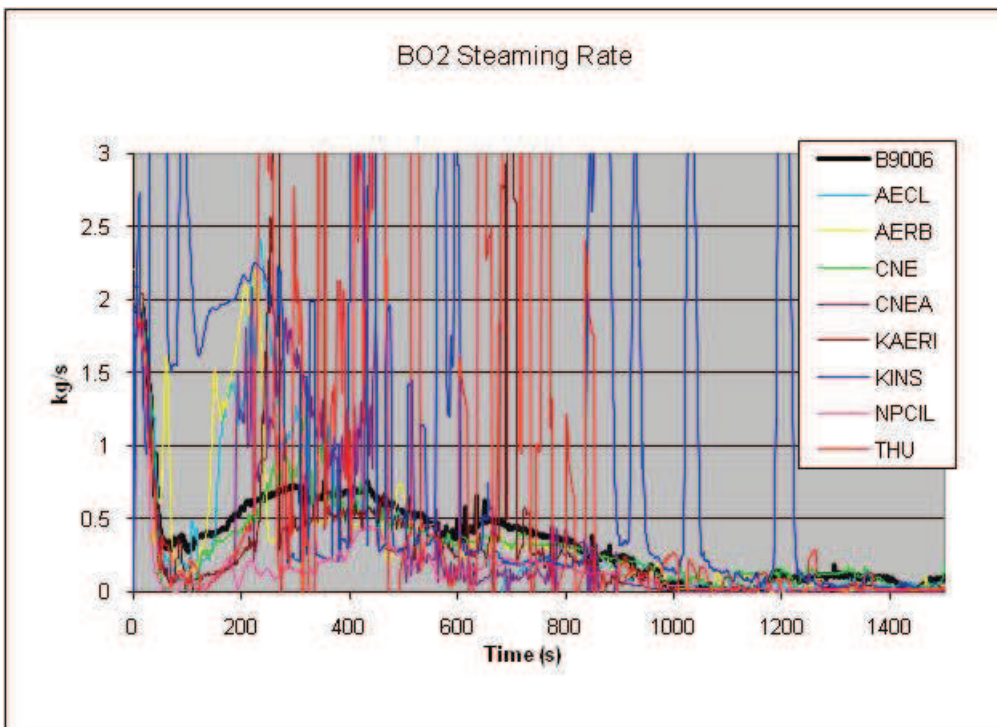


FIG. 4-76. Boiler BO2 steam flow rate.

4.3.9 Boiler inlet and outlet fluid temperatures

Figures 4–77 to 4–80 provide the code predictions of boiler plenum temperatures in comparison to the experiment. All calculations show the correct experimental trend and all agree well with experiment for about the first 80 s of the transient, i.e. before ECI injection. After that point, significant differences are noted, with the lower temperatures in some calculations being due to the arrival of low-temperature ECI flow, roughly corresponding to the loop refill times discussed previously.

In general, predictions for boiler BO1 are better than for BO2, in particular the inlet-to-outlet temperature change. However, since the loop flow direction is not obvious, and may be predicted different by different participants, no conclusion about the boilers acting as heat sink or source can be drawn, based only on these figures. At the end of the experiment (1500 s) all participants predict relatively uniform temperatures within a 50°C range.

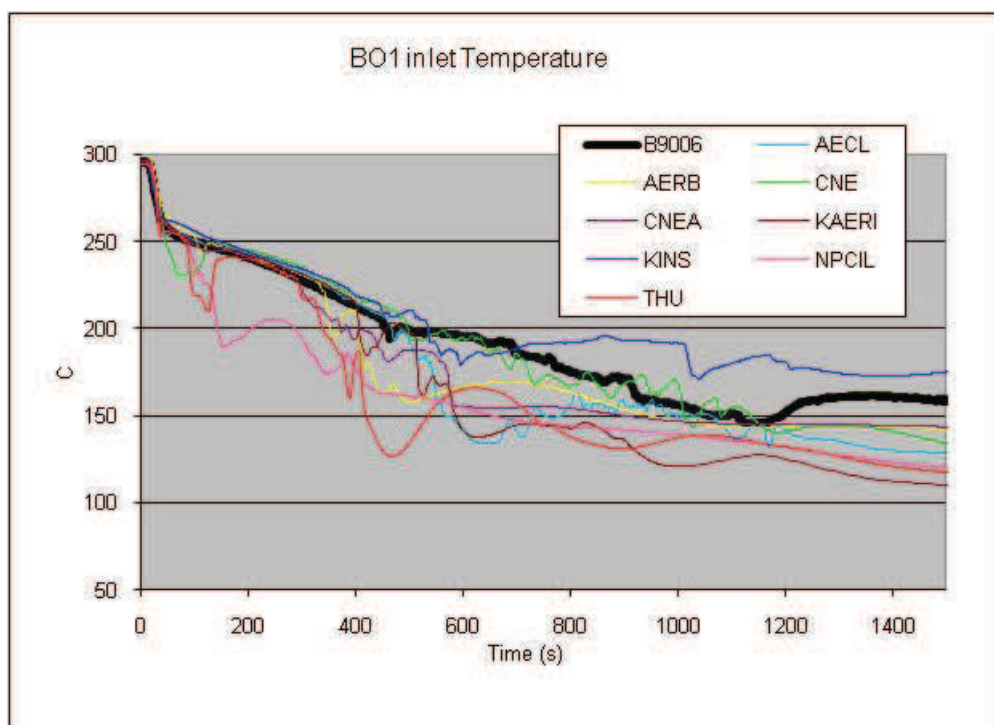


FIG. 4-77. Boiler BO1 inlet temperature.

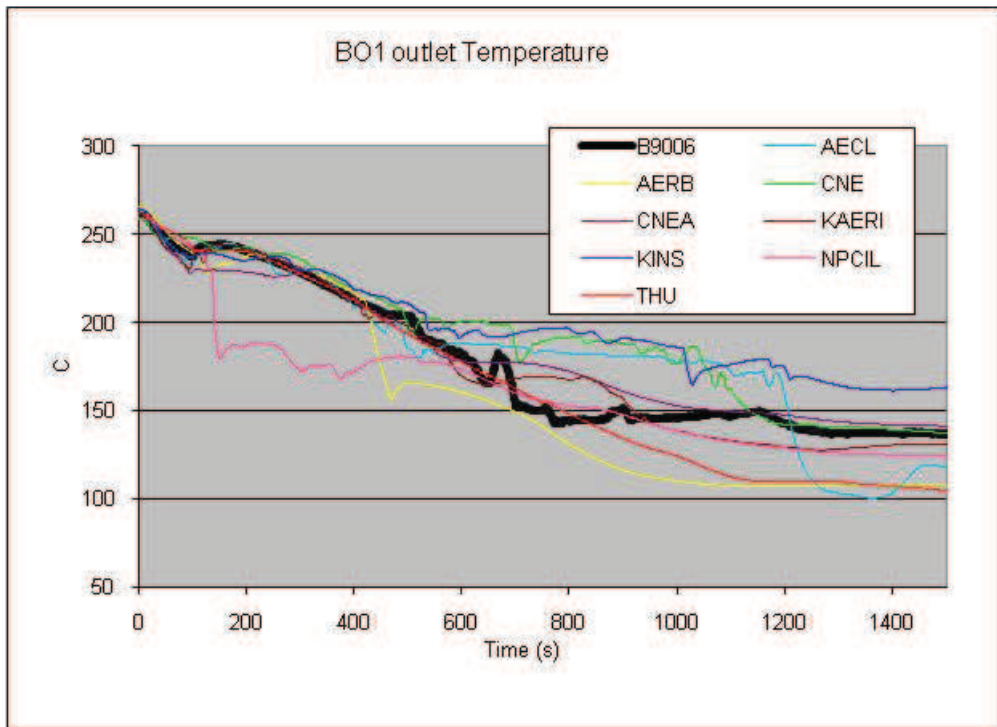


FIG. 4-78. Boiler BO1 outlet temperature.

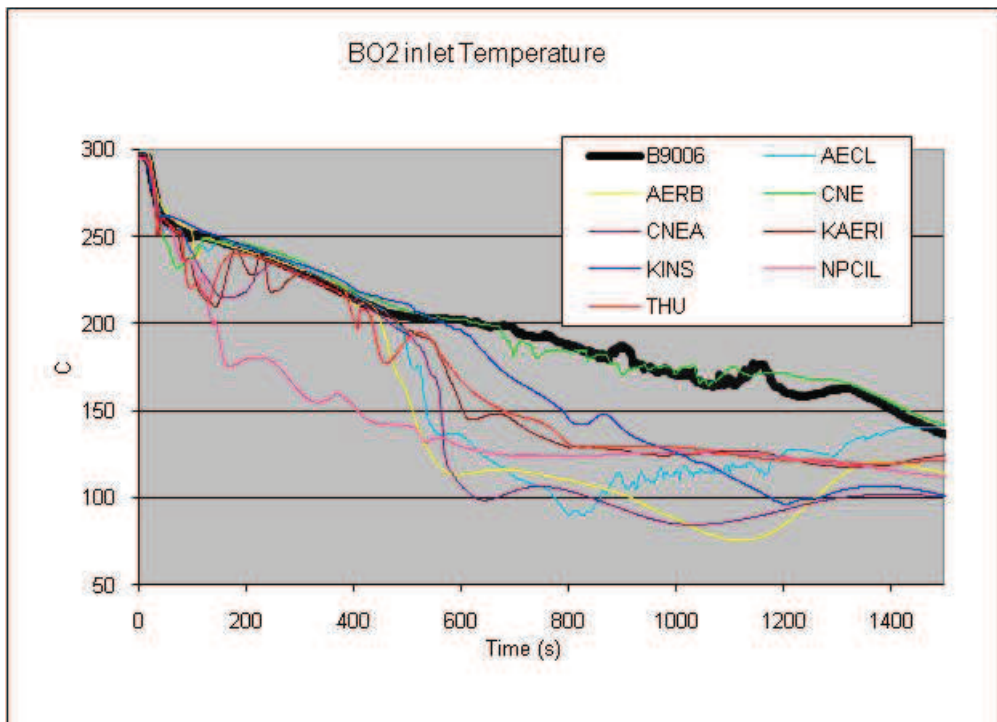


FIG. 4-79. Boiler BO2 inlet temperature.

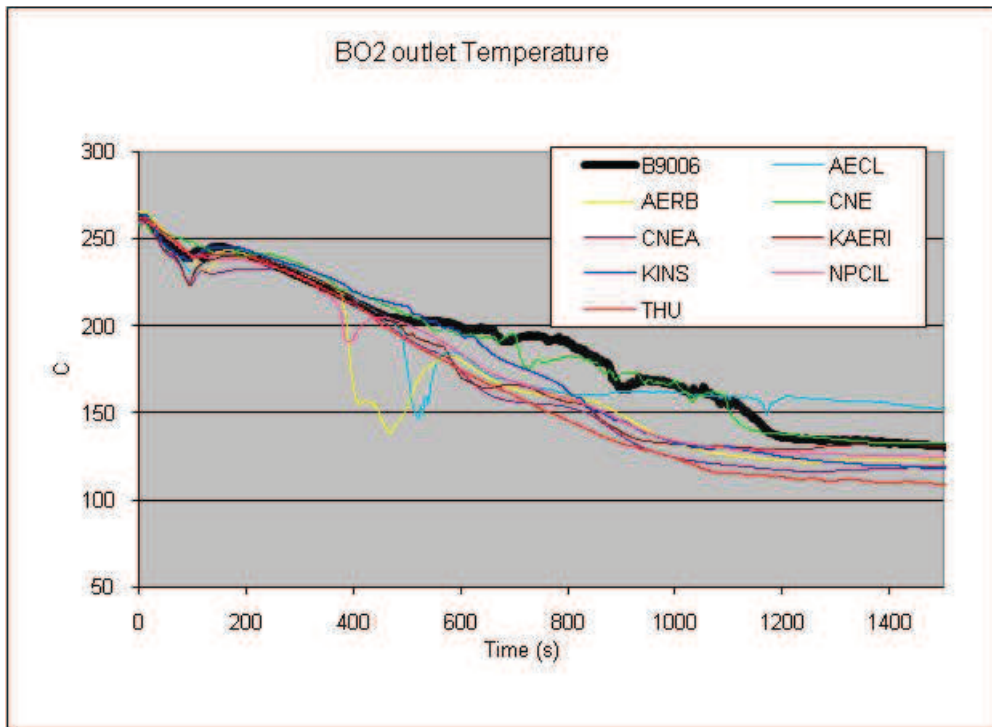


FIG. 4-80. Boiler BO2 outlet temperature.

4.3.10 FES sheath temperatures in heated sections HS8 and HS13

The maximum FES sheath temperature is often the most significant parameter in safety analyses. In test B9006, the highest FES sheath temperatures are most likely in the high power channel of the broken pass, heated section 13 (HS13), and possibly also in the high-powered channel of the intact pass (HS8, shown in Fig. 4–81). While no significant temperature excursions were expected, or observed in the experiment, during the depressurization, some participants predict short heat-up periods during the quasi-steady pressure period after ~200 s. In particular, AECL and THU show brief temperature excursions to about 300-350°C on the top FES over the entire channel length, slightly less than in the blind calculations. On the other hand, the temperature excursions predicted by some participants for HS8 are larger than in their blind calculations. It can be concluded that codes, in particular CATHENA, does have the tendency to calculate excessive FES temperature excursions in such SBLOCA simulations.

In the experiment and all calculations the inlet, center and outlet temperatures of the top FES (Figs 4–81 to 4–84) show similar behaviours of gradually increasing temperatures throughout the transient, indicating a continuous forward flow, with no flow reversal in these channels.

To show if significant flow stratification is present during the transient, Figs 4–84 and 4–85 are compared. With the exception of a few short spikes in the measurement and in some CATHENA calculations indicating periods of boiling, the top and bottom FES have nearly identical temperatures, indicating no significant or sustained stratification.

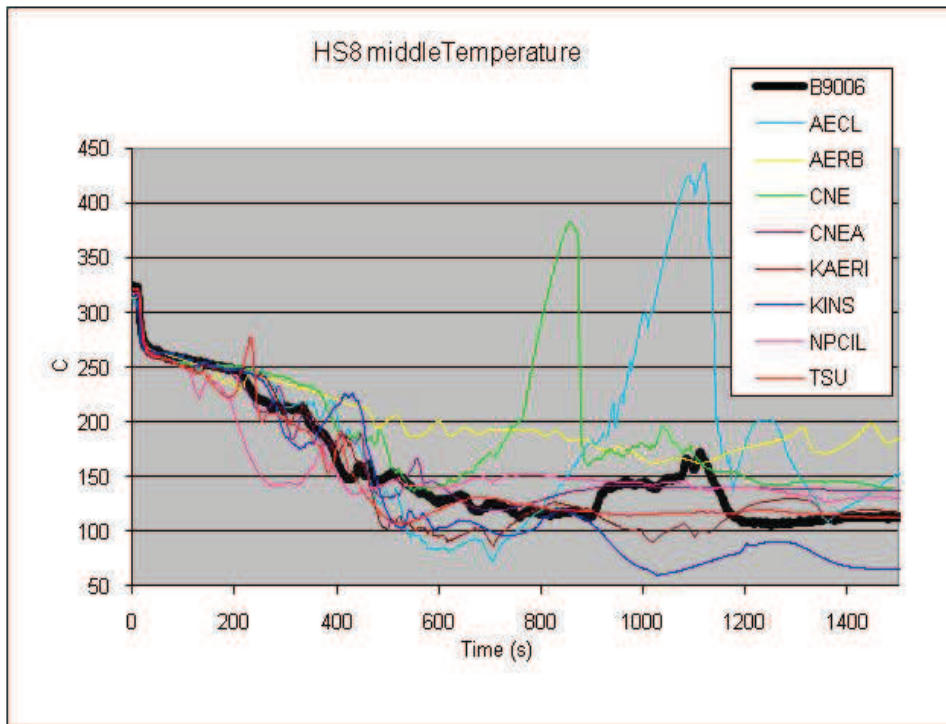


FIG. 4-81. Heated section HS8 center temperature.

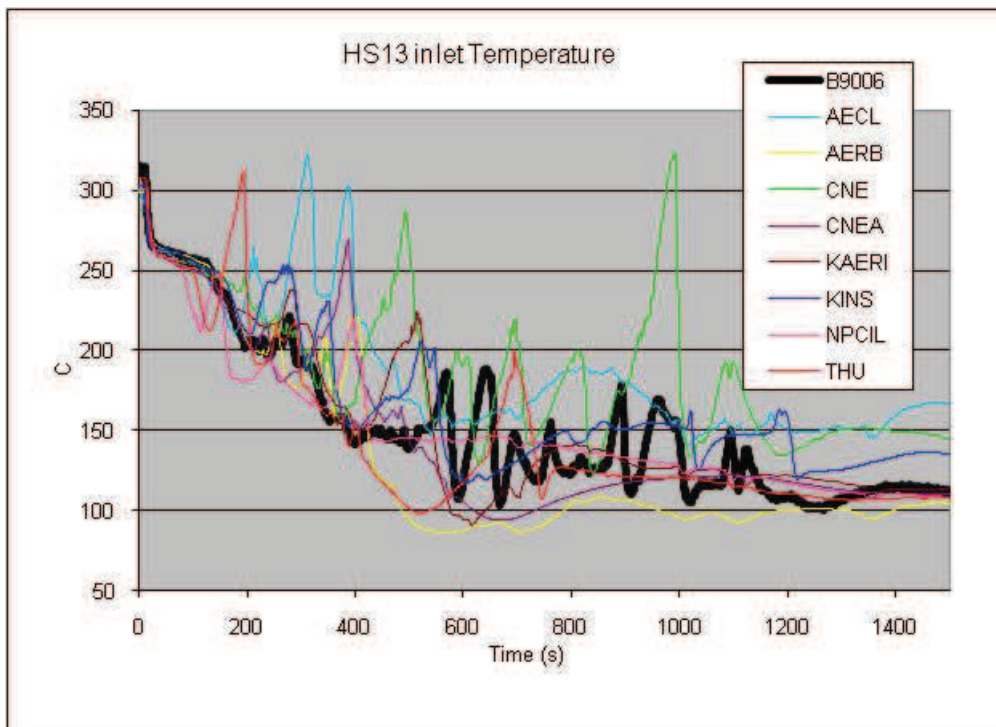


FIG. 4-82. Heated section HS13 Inlet temperature.

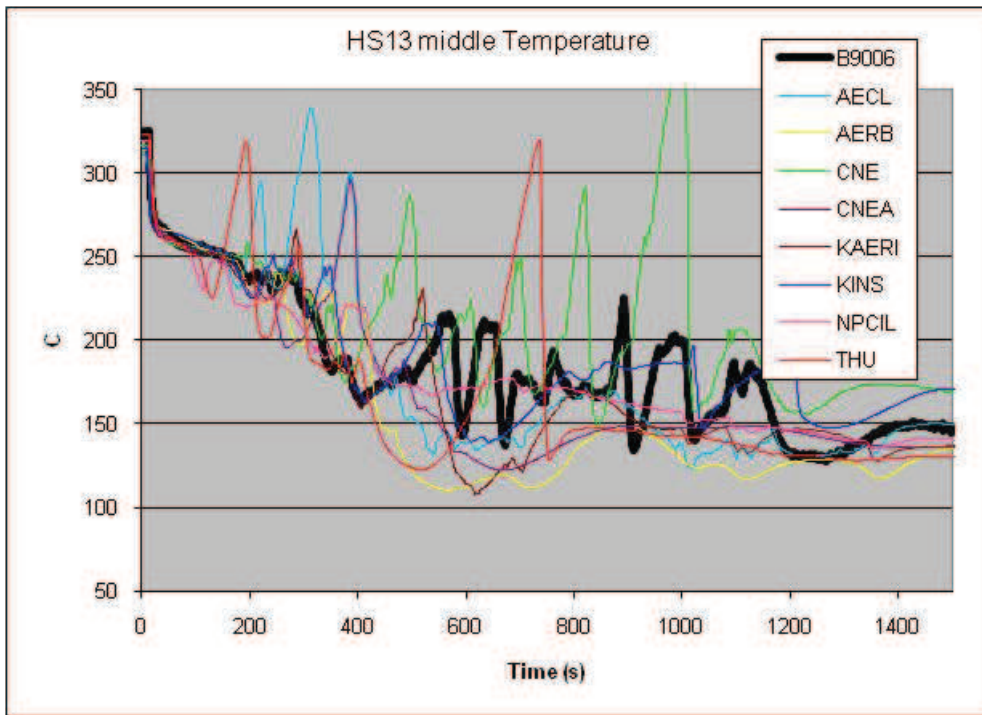


FIG. 4-83. Heated section HS13 center temperature.

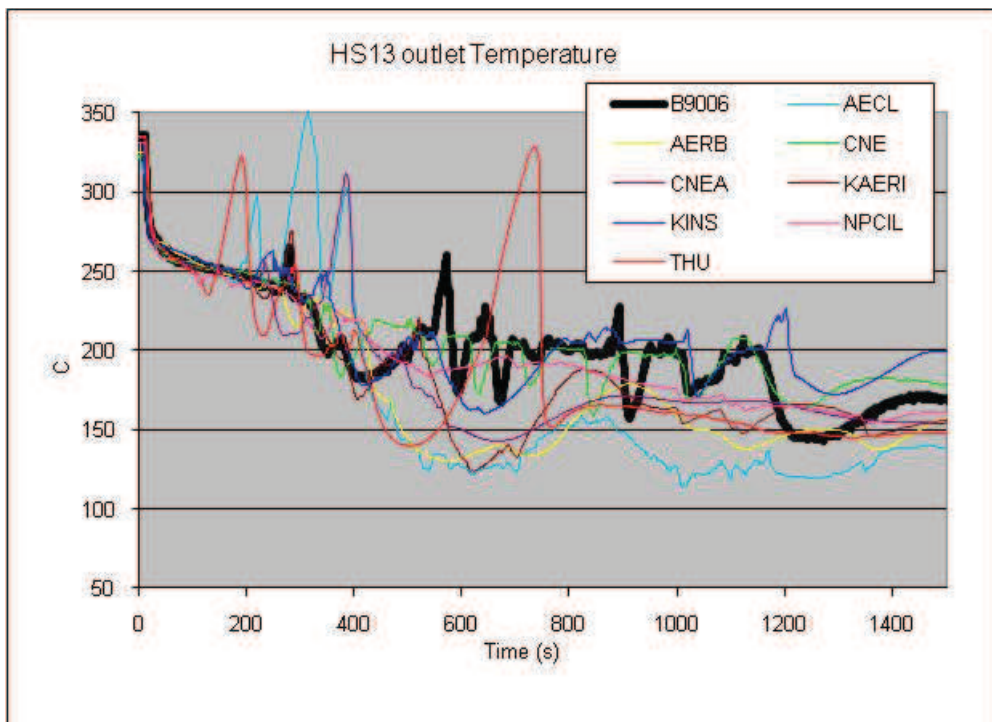


FIG. 4-84. Heated section HS13 outlet temperature.

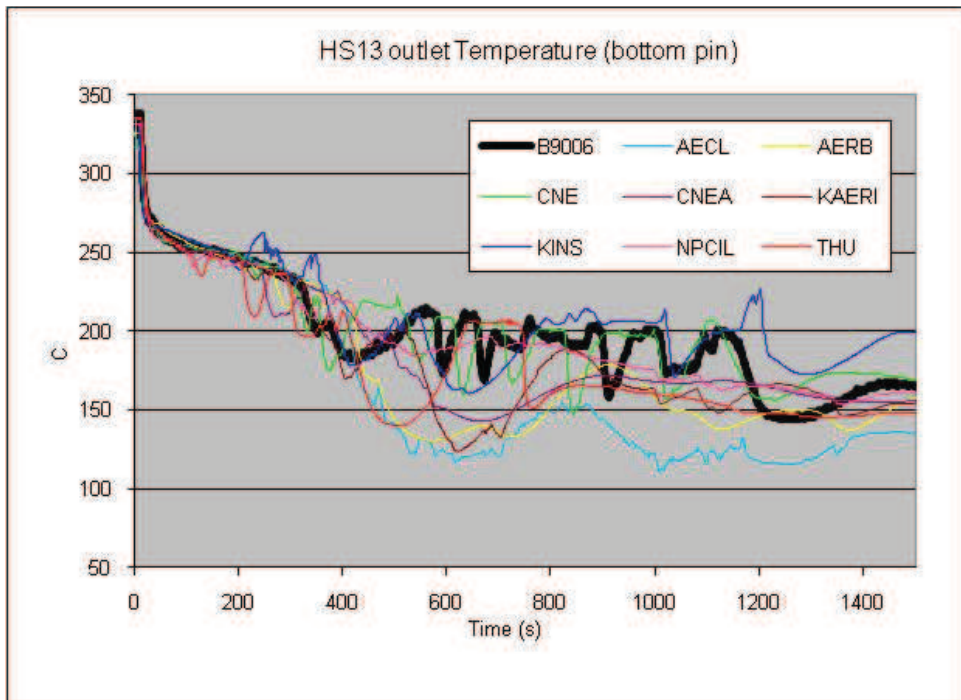


FIG. 4-85. Heated section HS13 outlet temperature (Bottom FES).

4.3.11 Flow rates in heated section HS 5, 8, 10 and 13

Heated section flow rates were measured in the inlet/outlet feeders for each channel and are shown in Figs 4–86 to 4–89 for the four channels (measured in inlet feeder) that were selected for code comparison.

Channel flows are in the normal (forward) direction for both high powered channels (HS 8 and 13) throughout the experiment, and are predicted to be such by all participants, except for AERB predicting sustained reverse flow through HS8 and AECL through HS13 (some other participants also predicted short periods of reverse flow).

It should be noted that measured flow rates below 0.2 l/s and during two-phase flows are only to be taken as an indication of flow direction, not of the flow magnitude.

Both low-powered channels, HS5 and HS10, show periods of clear flow reversal over a significant time period (~200 to 500s), as shown in Figs 4–86 and 4–88. Some participants capture this prolonged flow reversal, while others predict forward flow throughout the transient. In general, once a particular flow direction is calculated, it is maintained throughout the simulation. Note that the relatively high apparent magnitude of the reverse flow rate measured is likely an artefact of the turbine flow meters, which do not accurately measure mass flow in two-phase regime.

In the broken pass, flow reversal occurred in two channels (HS10 & HS12, HS 12 not shown) as compared to flow reversal occurring in only one channel (HS5) of the unbroken pass. This also explains the elevated temperature at Header HD8 as compared to Header HD6 during the latter part of the transient in the experiment.

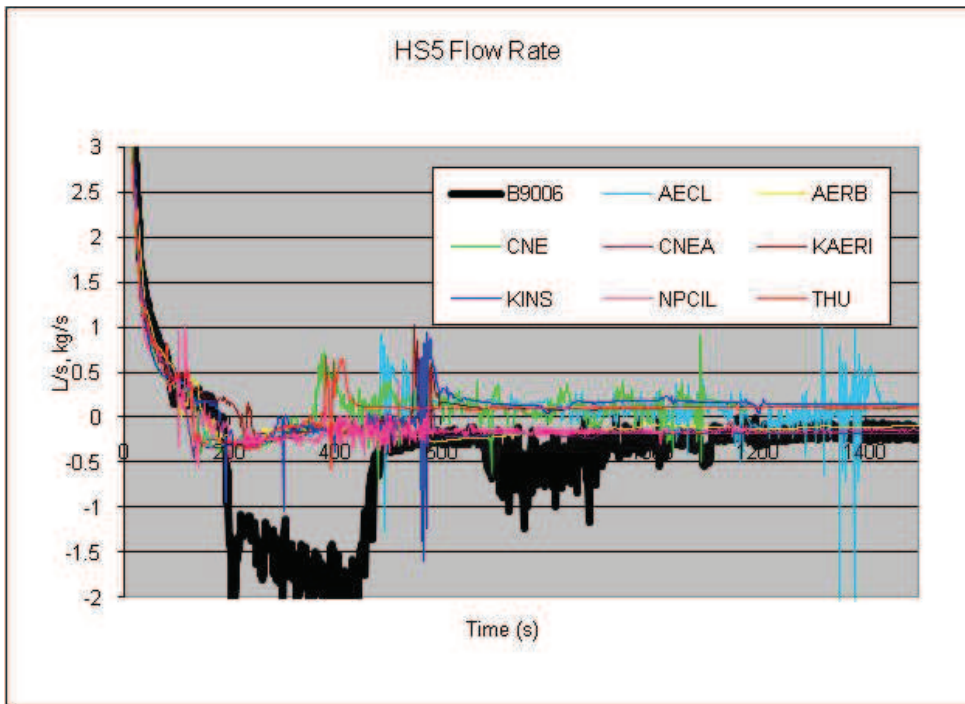


FIG. 4-86. Flow through heated section HS5 (low power, intact pass).

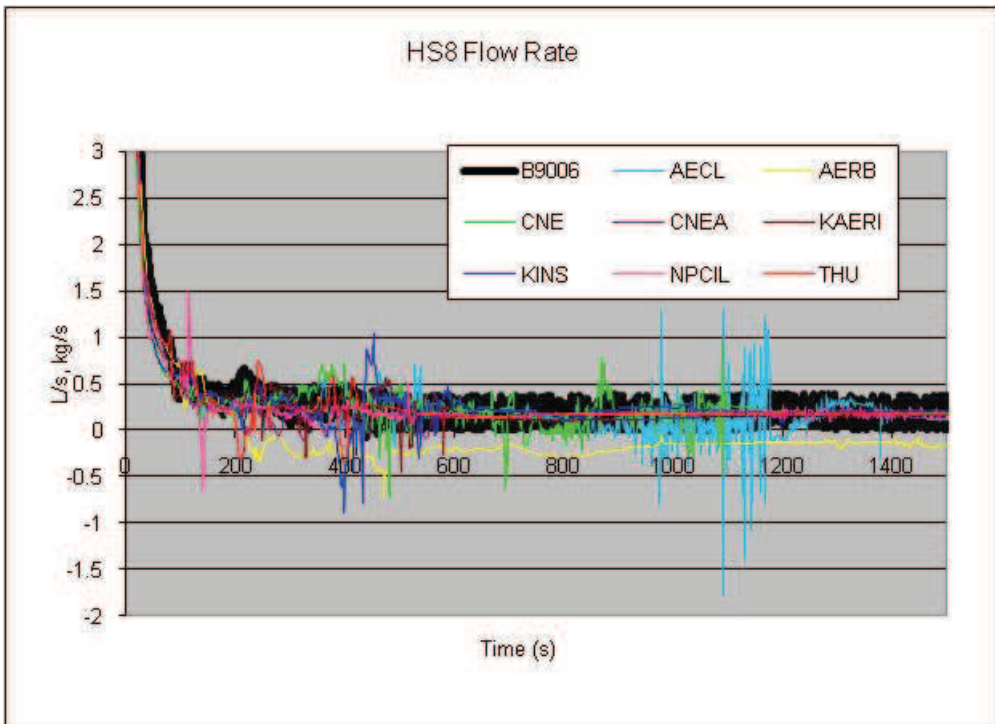


FIG. 4-87. Flow through heated section HS8 (high power, intact pass).

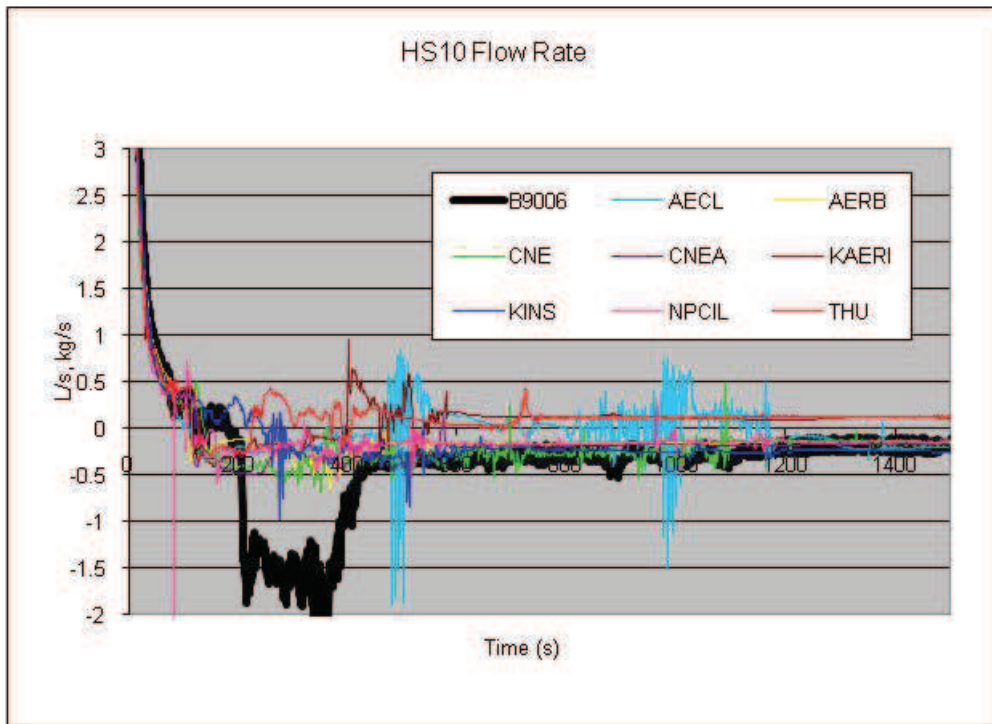


FIG. 4-88. Flow through heated section HS10 (low power, broken pass).

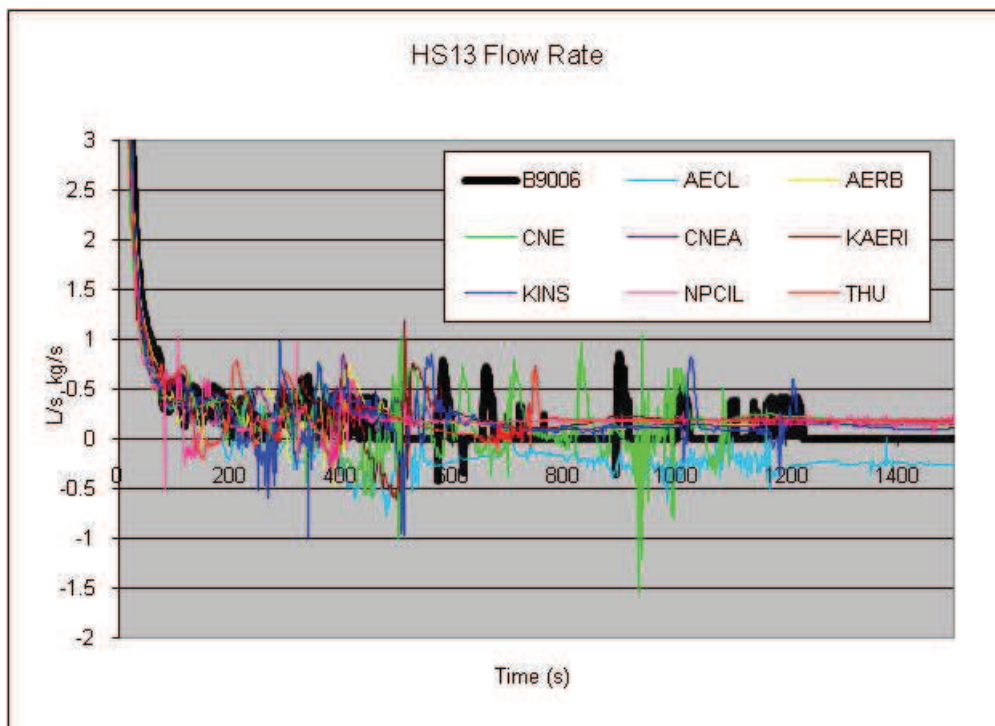


FIG. 4-89. Flow through heated section HS13 (high power, broken pass).

4.3.12 Inlet and outlet void in heated section HS 5, 8, 10 and 13

Channel inlet and outlet void fractions were measured approximately 2 m upstream and downstream of the heated section end in the inlet and outlet feeders.

Voiding occurred in the outlet feeders approximately 30 s into the transient, quickly reaching 50-100% void and sustaining it until 200 to 400 s. The inlet feeders of both low-powered channels also voided around 200 s, while the high-powered channel inlet feeders remained filled. This can be attributed to the low-powered channels being located at significantly higher elevations, thus having less gravitational head and a slightly lower saturation pressure.

Figures 4-90 to 4-97 show the experimental measurements and code predictions. The experimental data shows negative void due to measurement error or instrument drift; these should be considered as zero void. Most simulations correctly show periods of various duration and timings and of significant void in the outlets, but also sporadic void during later times, where the test did not show voiding. These spikes coincide with high FES temperatures.

Large differences in simulations are expected due to the interdependence of channel boiling, flow direction, low header-to-header pressure differences, and the complexity of the end fittings. While changes from blind calculations can be observed, there is no clear trend that the open results are improved.

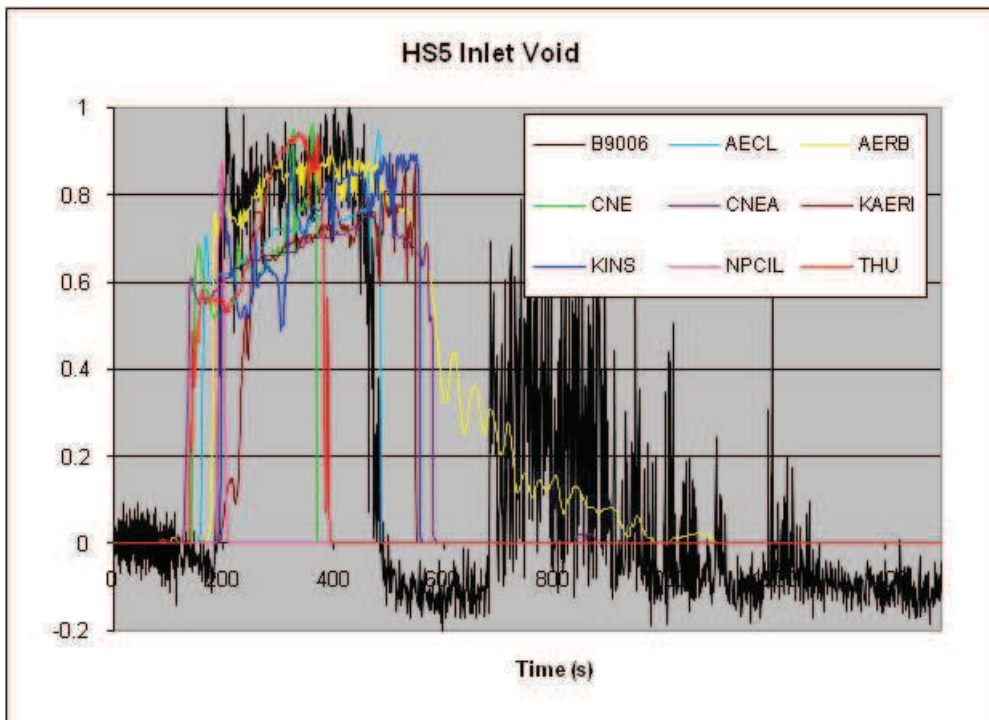


FIG. 4-90. Heated section HS5 inlet void.

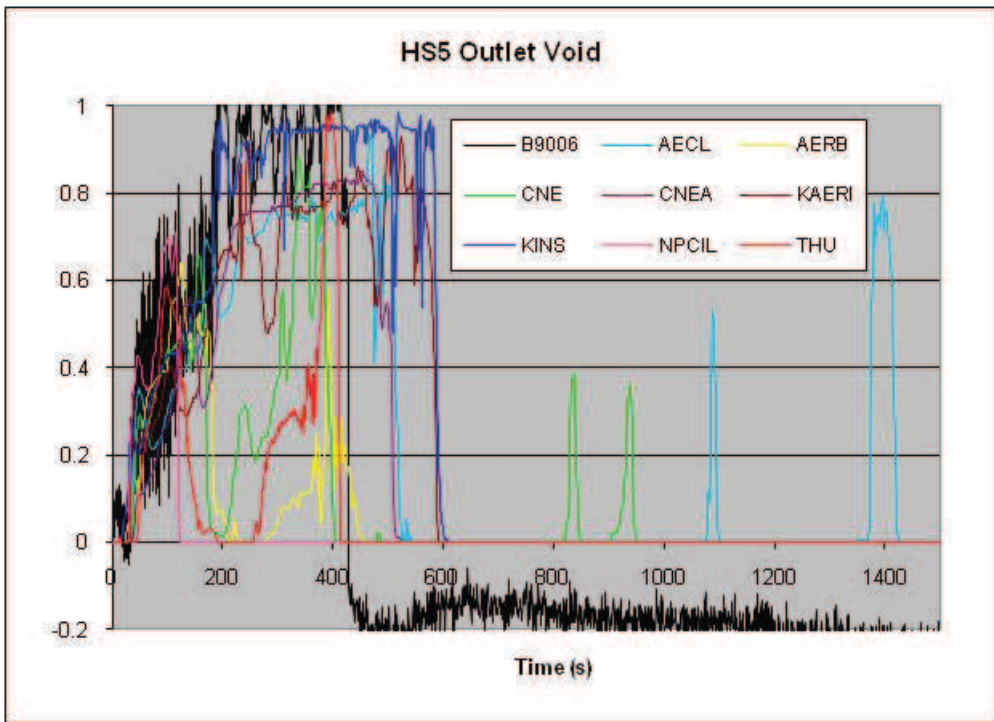


FIG.4-91. Heated section HS5 outlet void.

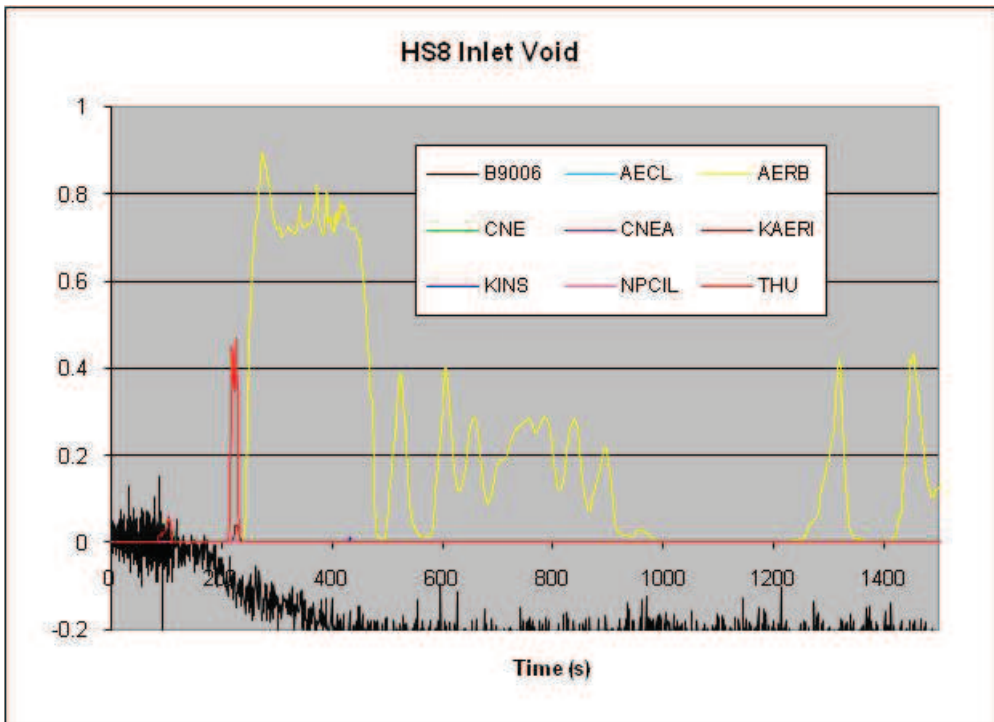


FIG. 4-92. Heated section HS8 inlet void.

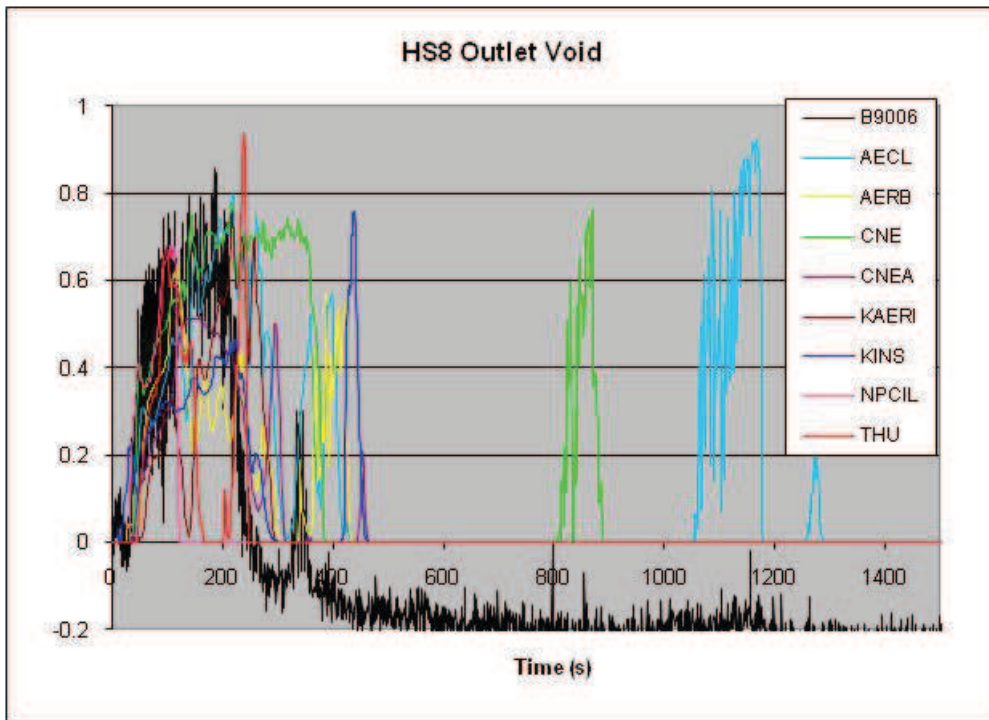


FIG. 4-93. Heated section HS8 outlet void.

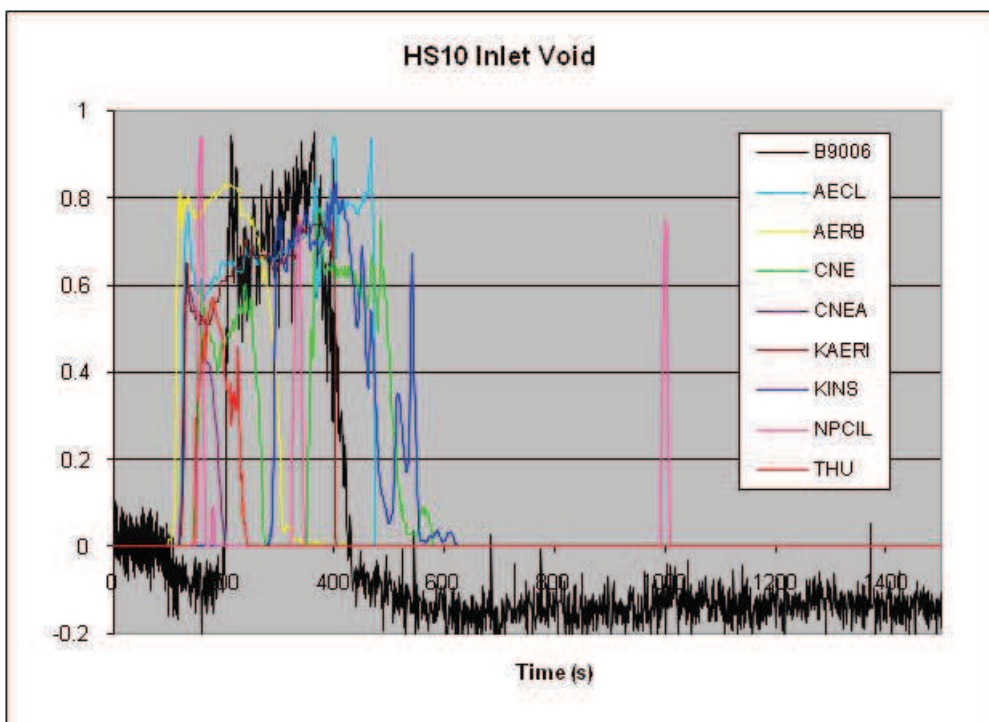


FIG. 4-94. Heated section HS10 inlet void.

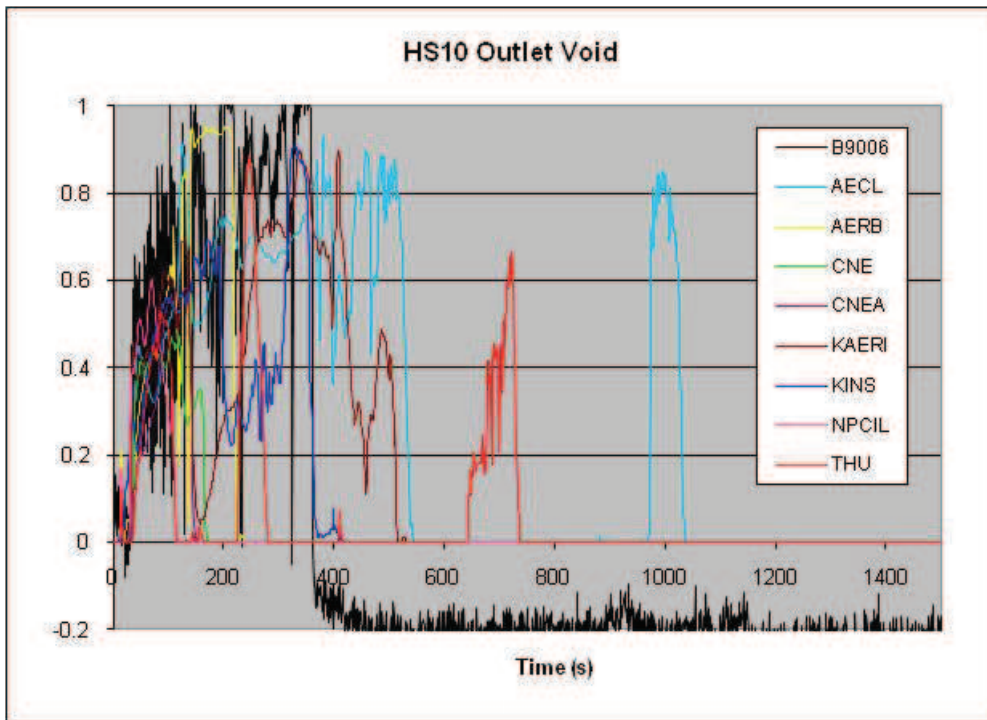


FIG.4-95. Heated section HS10 outlet void.

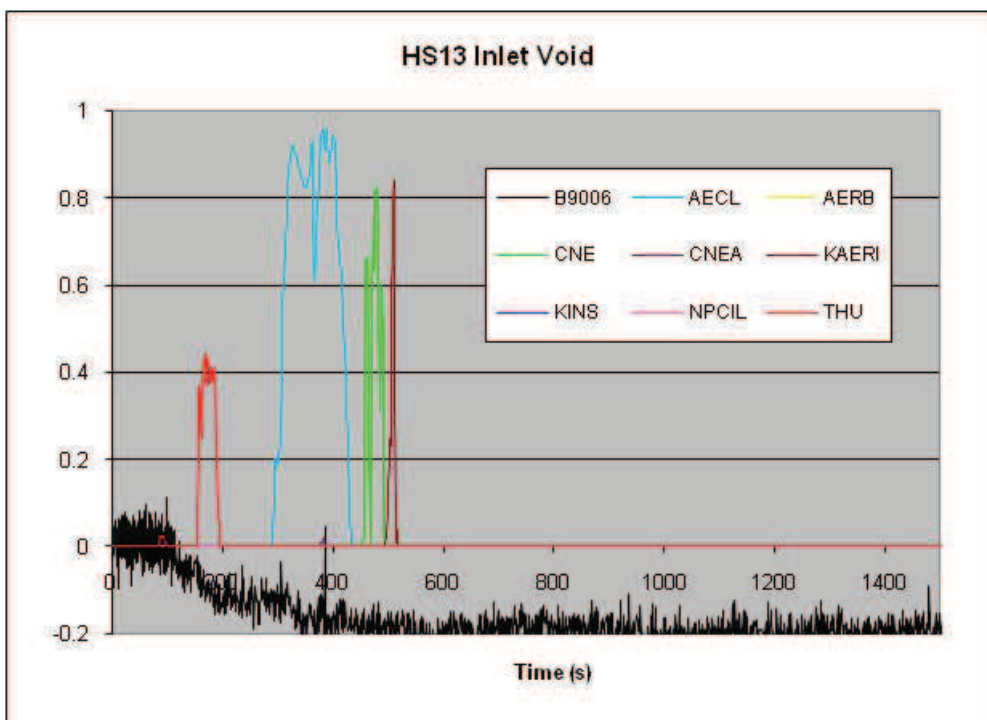


FIG. 4-96. Heated section HS13 inlet void.

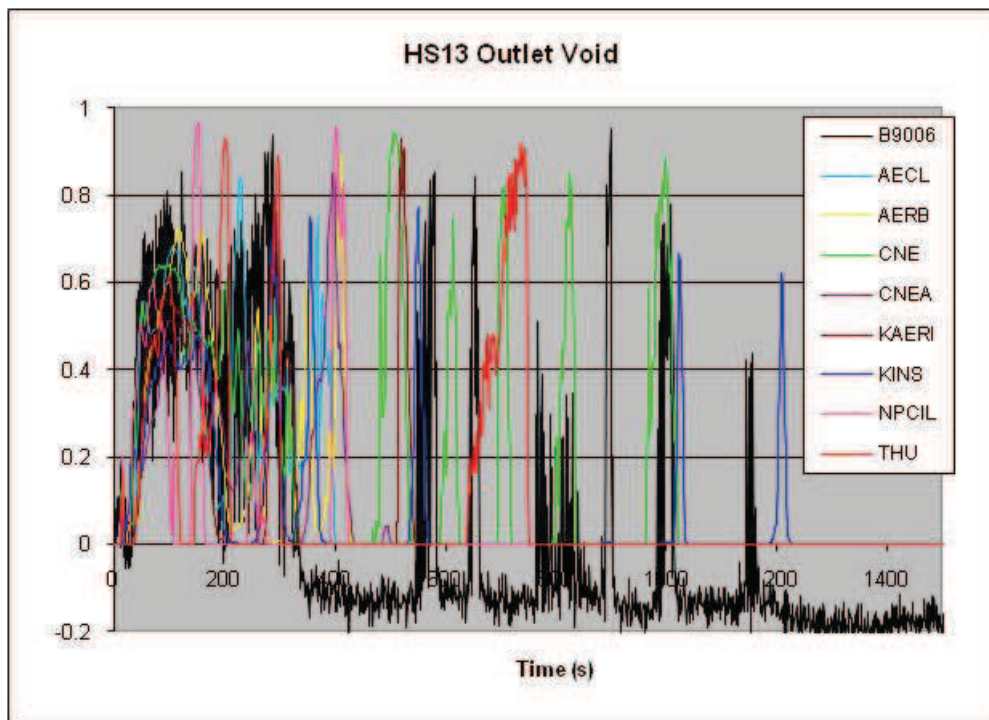


FIG. 4-97. Heated section HS13 outlet void.

4.3.13 Differential pressure along outlet feeder from HS13 to HDR5

Since flow rates are very low (nearly zero after ~400s) and predominantly single-phase, except for brief periods of time, the feeder pressure drop predictions follow experimental trends closely, as shown in Fig. 4-98. One exception is NPCIL, who predicts large pressure variations and a rather low average pressure drop after ~300s, compared to the experiment and other calculations, because they predict reverse flow through HS13 (see Section 4.2.11). Note, that due to the elevation difference, negative flow does not necessary result in a negative pressure drop (explained in detail in Section 4-5.8)

Pressure drop predictions in the 100-300-s timeframe are related to whether single- or two-phase flow is predicted, and the amount of void, in this particular outlet feeder (see previous section). In general, lower pressure drops are associated with higher void, due to the reduced density gravity head.

4.3.14 Snapshot of pressure, temperature and void fraction

In addition to assessing the computer model predictions against local data, some insight into the simulated loop behaviour may be gained from examining the pressure, temperature, and void distribution throughout the loop during key times of the transient. Some participants provided such time “snapshots”, which are presented below.

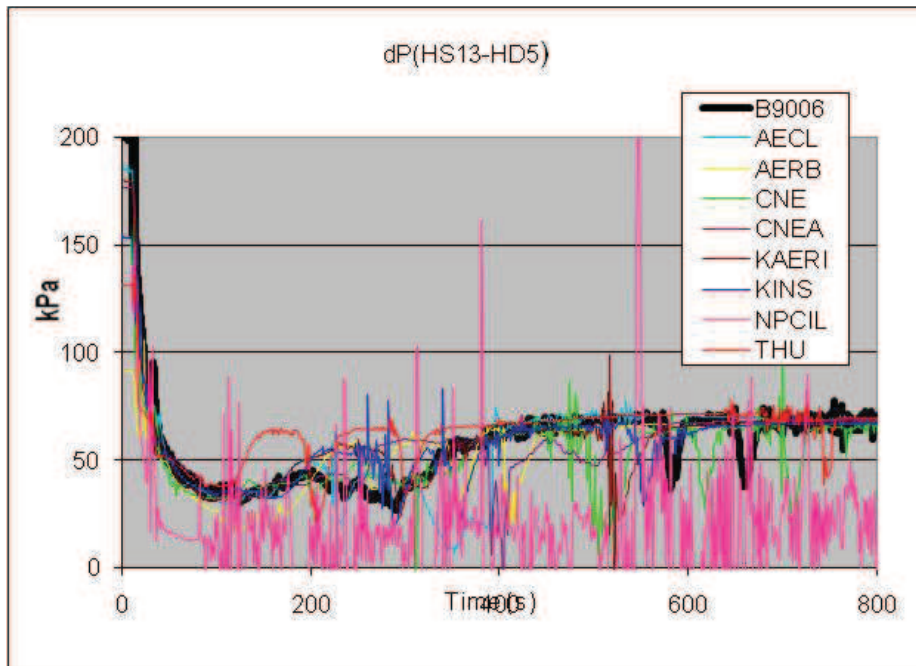


FIG. 4-98. Heated section HS13 to header HDR5 pressure drop.

Data of local pressure, temperature, and void are presented as a function of axial location around the figure-of-eight loop of the RD-14M facility, starting at the outlet of pump P1. The total loop length through the longest inlet-feeder/heater-section/outlet-feeder paths is 167m. Figures 4–99 to 4–101 show an example (AECL pressure, temperature and void calculation of test B9006 at time $t=70s$, just before opening of ECI injection valves) and illustrates the locations of major components, i.e. the pumps, headers and boilers. As can be seen, it clearly shows five parallel paths (of various lengths), representing the five channels in each pass. The effect of gravitational head is clearly evident (the highest pressures are in the lowest heated sections, and the lowest are in the top part of the boiler tubes), pressure drops are significant across the horizontal heated sections, and pressure losses along the loop balance the pressure difference across the pumps.

Figures 4–100 and 4–101 show the temperature increase in the heated sections and decrease in the boilers, and the corresponding void generation and collapse (Note: The high void between 0.8 and 0.9 are in the outlet end fittings, because of vapour trapped in the dead space).

Appendix II shows snapshots of pressure, temperature and void around the loop for four different times (in the test) from all participants.

4.4 DESCRIPTION OF TEST B9802

In this test, following a 3 mm inlet header break at 11.2 s (the break valve actually started to open at 12.2 s), coolant discharges at the rate of about 0.61 l/s, quickly dropping to 0.45 l/s, and causes initial sharp depressurization of primary loop. Heater power and pump speed remained constant in this test.

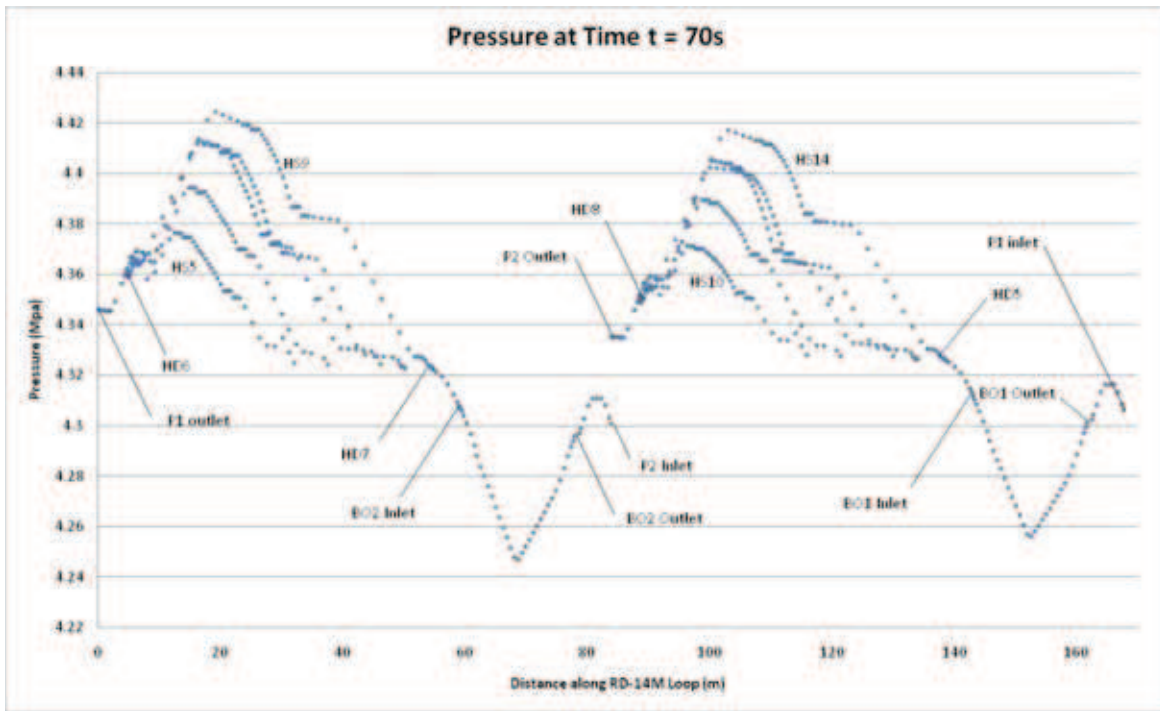


FIG. 4-99. Sample “Snapshot” illustrating locations of major components (AECL calculation of pressure during test B9006 at 70s).

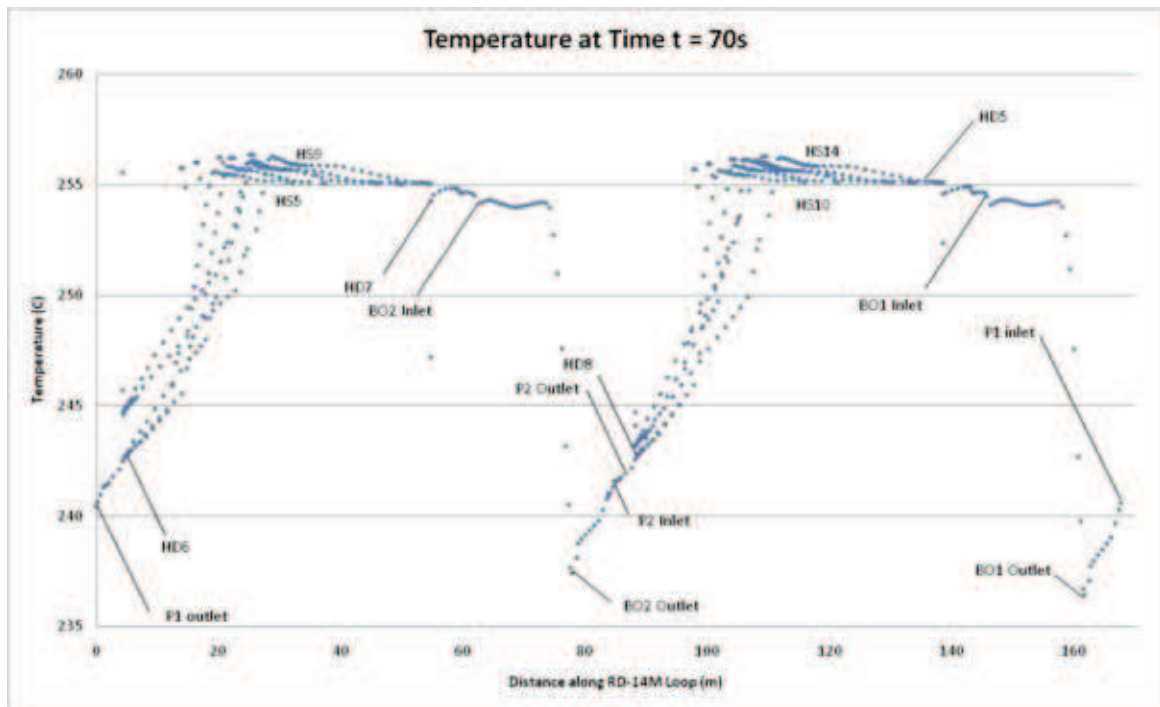


FIG. 4-100. Corresponding temperature “Snapshot” to Fig. 4-100.

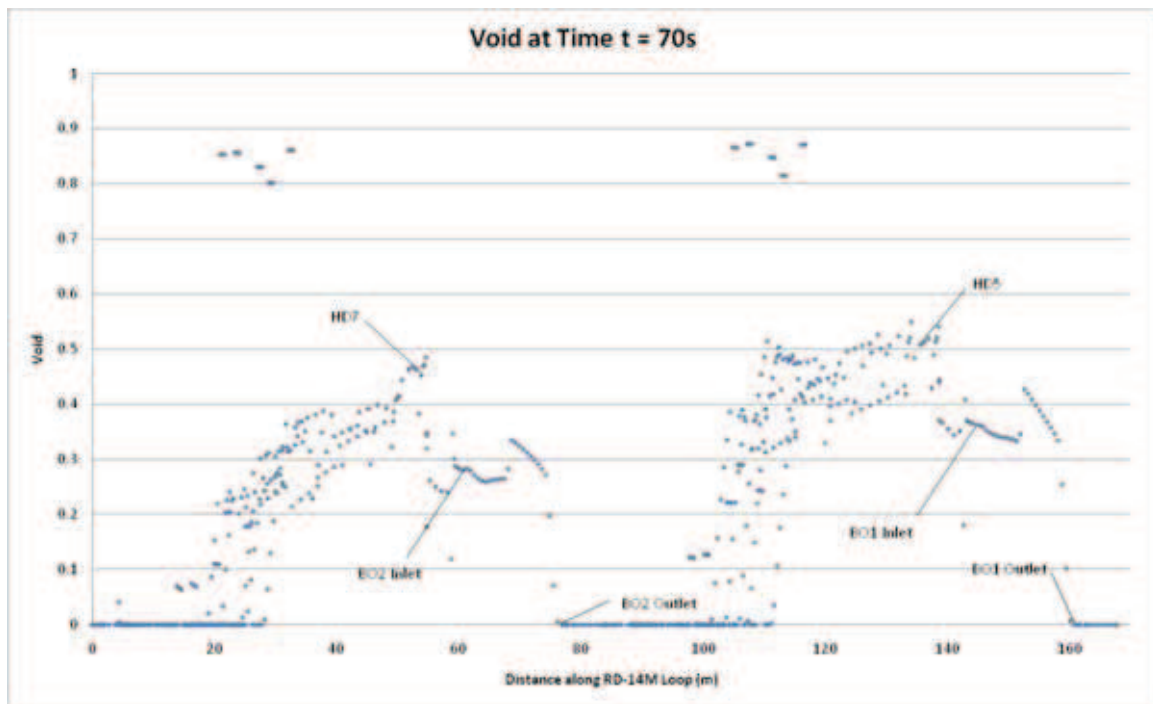


FIG. 4-101. Corresponding void “Snapshot” to Fig. 4-100.

Reduction in primary loop pressure causes generation of void at channel exit and boilers inlet, the high temperature and low pressure regions. Due to relatively lower temperature at boiler outlets and channel inlet sections, no voiding appears in these sections. Occurrence of void in the system results in gradual depressurization of the loop. Increase in void in the loop enhances system resistance which causes gradual reduction in the coolant flow in the loop and enhances the pump developed head.

Heat removal from FES occurs in nucleate boiling mode and void generated in channels gets condensed in boiler U-tubes. Due to continuous discharge, header pressure decreases. Voids are seen at boiler outlet at 650s. After about 900s, voids appear at pump outlet. When voiding starts at pump discharge, flow reduces which increases discharge pressure and results in void reduction at pump discharge. This phenomenon repeats and creates oscillations in the transient from 900 sec to 1150 sec. After 1150 sec pump P1 trips and its head ceases. Following pump P1 trip, coolant flow in the loop is maintained by pump P2, but its flow decreases and head increases.

At 1191.8 s., due to large void, pump P1 trips on over-voltage process protection trip. It is seen that following pump P1 trip, reduction in coolant flow results in deterioration of FES cooling in both passes and heat removal occurs in film boiling mode. At 1313 s, FES temperature in HS12 rises to above 600°C and heaters are tripped (in the test the power supplies are tripped when one pair of FES temperatures exceed 600°C (trip setpoint in this test); maximum measured FES temperature was ~640°C). It is observed that coolant flow rate is maintained in normal flow direction in all the channels during the transient.

4.5 BLIND CALCULATION RESULTS FOR TEST B9802

4.5.1 Sequence of major events

Test B9802 progresses in a monotone manner after the break, as a result of inventory loss out the break opening and the consequent voiding in the heated section and condensation of the steam in the boiler tubes. Therefore, timing of major events, such as start of boiler outlet void, oscillatory flow, and FES heatup, is driven mainly by the rate of break discharge, and secondarily by the boiler heat transfer modelling. All participants predict these phenomena, but at times somewhat earlier or later than in the experiment, due to differences in the break discharge rate, as summarized in Table 4-4.

Where the oscillatory flow is predicted to begin significantly earlier the FES heatup, the boiler tube heat transfer is insufficient, resulting in early incomplete condensation and void entering the pumps, thus causing oscillatory flow rates with only about 60–70% void in the boiler inlet plenum. In the experiment and those calculations with higher tube heat transfer, outlet void remains near zero (complete condensation) until about 80-90% boiler inlet void.

TABLE 4-4 SEQUENCE OF EVENTS FOR TEST B9802 (BLIND CALCULATION)

Events	Experiment (s) +/- 0.2	Code predictions (s)						
		AECL	AERB	CNE	KAERI	KINS	NPCIL	THU
Data gathering started/calculation starts	0.0	0.0	0.0	0.0	0.0	0.0	0.0	0.0
Surge tank isolated	8.2	8.2	8.2	8.2	8.2	8.2	8.2	8.2
Blowdown valve (MV17) opens	12.2	11.2	11.2	11.2	11.2	11.2	11.2	11.2
HD7 pressure drops to saturation	15.2	14.2		19.8	15.1		18.8	
Start of boiler outlet voiding (Void>0.1)	~900 (BO1&2)	730 (BO1) 750 (BO2)	713 (BO1) 733 (BO2)	760 (BO1) 790 (BO2)	850 (BO1) 900 (BO2)	984 (BO1) 950 (BO2)	668 (BO1) 689 (BO2)	960 (BO1) 1000 (BO2)
Start of oscillatory flow	~1050	860	540	880	650	680	920	700
Start of FES heatup	~1050	900	1210	900	1200	1050	1210	1280
Pump 1 trip (over-voltage process protection, boundary condition)	1192	1192	1192	1192	1192	1192	1192	1192
(Power supply trip – actual trip time occurred when HS12 bundle 1 top pin was at 640°C) FES sheath temperature first reaches 600C (HS12 bundle 1, B-1)	(1336) 1313 (HS12, B-1)		1236 (HS8 B-11)	945 (HS13 B-7)	1214	1216.2	1310	
End of test	1363	1370	1370	1360	1363	1400	1400	1362

4.5.2 Pump differential pressures and flow rates

Primary loop coolant circulation is provided by two high-head centrifugal pumps. In test B9802, the break occurred at inlet-header HD8 at 12.2 s (11.2 was used in the code calculations as per the ground rules), and the primary pumps were maintained at a constant speed of ~3000rpm. Thus the pump differential pressures and flow rates are a function of void at the pump and liquid density. Experimental volumetric pump flows, measured in l/s were converted to mass flows in kg/s by using liquid densities at the corresponding boiler outlet temperatures.

Figures 4–102 to 4–105 provide the code comparison of the primary pump differential pressures and flow rates to experimental measurements. All calculations show the proper trends, with a nearly constant differential pressure until the onset of void at the pump inlet, as indicated by oscillations in the differential pressure and flow rates. The timing of void arriving at the pump inlet and the degree of reduction in flow rate until then, however, vary greatly amongst the code simulations, due to different inventory loss through the break. A larger break discharge leads to a lower loop inventory, and thus higher void and earlier degradation in pump performance (see also Appendix I).

Pump P1 and pump P2 behaviour is very similar; however, P1 trips earlier as a result of a process trip, which is not related to the experiment.

The main differences between blind and open results are the timings of the onset of pump voiding, as indicated by oscillations in the pump differential pressure and flow rates. Most participants calculated a premature (earlier than measured) time of this phase for both pumps, except for AECL and NPCIL, in the blind simulations.

The overprediction of the pump dP during the fully-liquid phase is slightly higher in the blind NPCIL calculations, when compared to their open calculations, due to some adjustment in the loop flow resistances.

The header-to-header differential pressures follow the same trends, in terms of changes for each participant between blind and open results, as the pump differential pressures, and are therefore not shown here, but only for the open calculations in Section 4.6.

Header pressures predictions are also very similar between blind and open calculations, except for the timings of onset of the slight pressure oscillations and the final depressurisation, triggered by the power trip. Overall pressure levels and the amplitude of oscillations did not change significantly from blind to open results, and are therefore shown in Section 4.6 for the open calculations only.

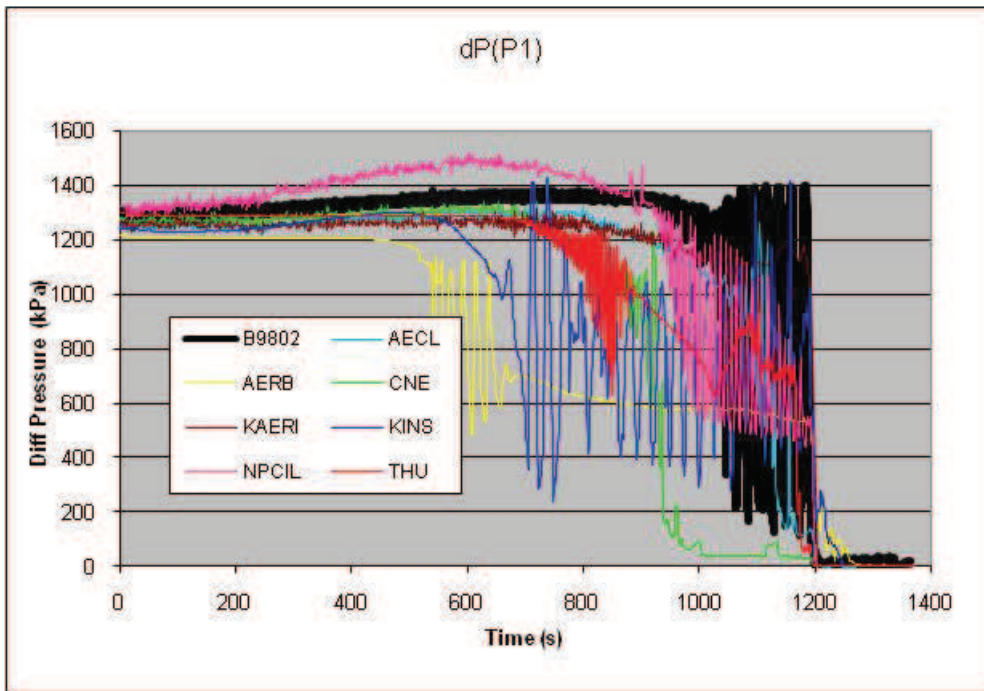


FIG. 4-102. Pump P1 differential pressure.

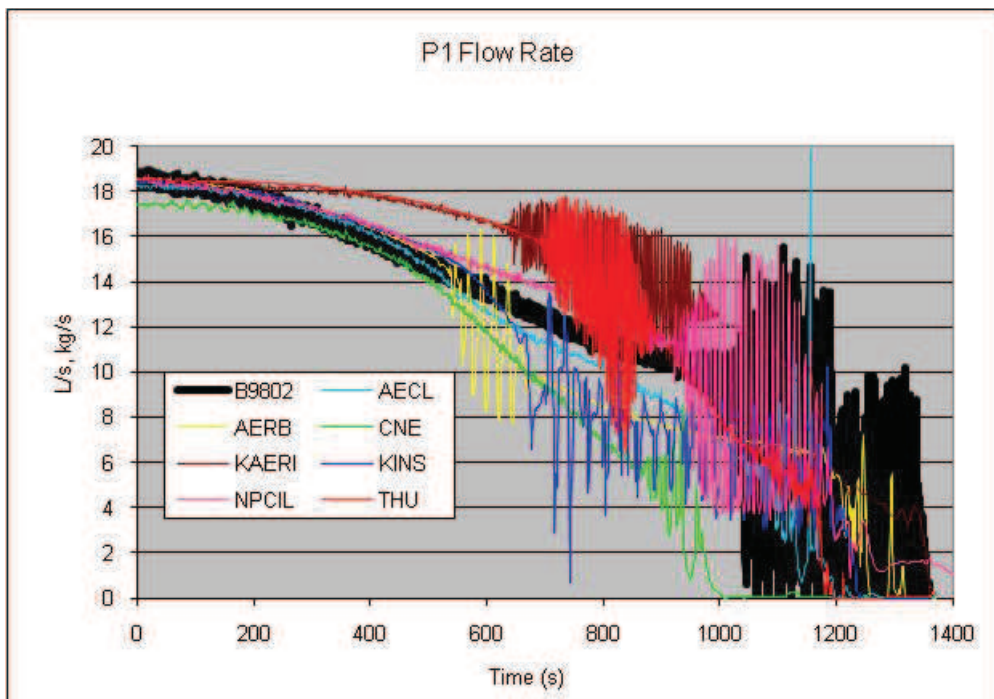


FIG. 4-103. Pump P1 flow rate.

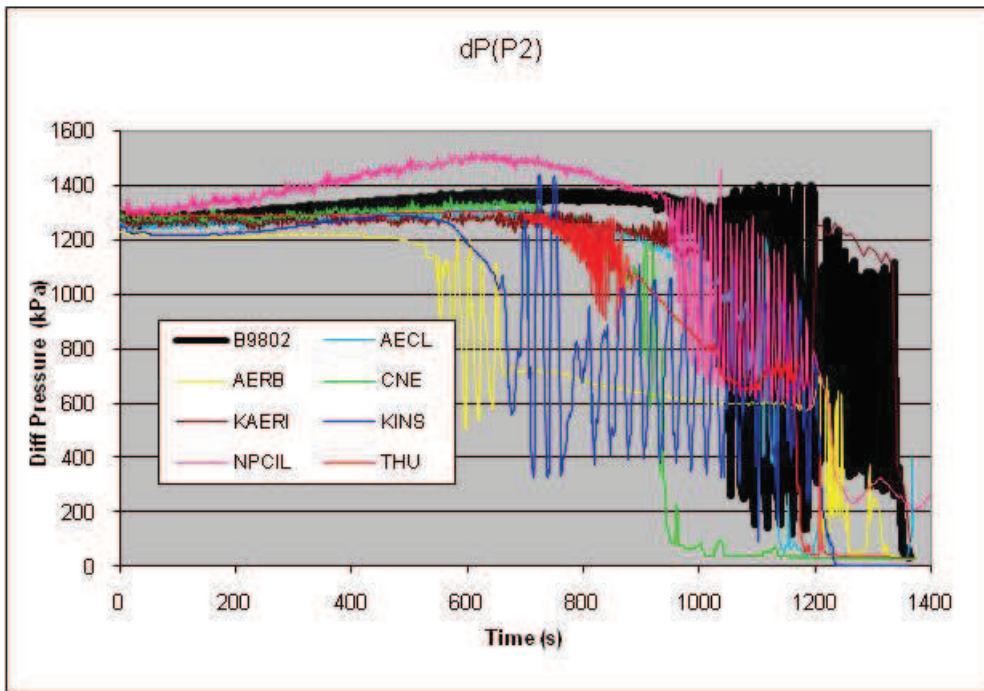


FIG. 4-104. Pump P2 differential pressure.

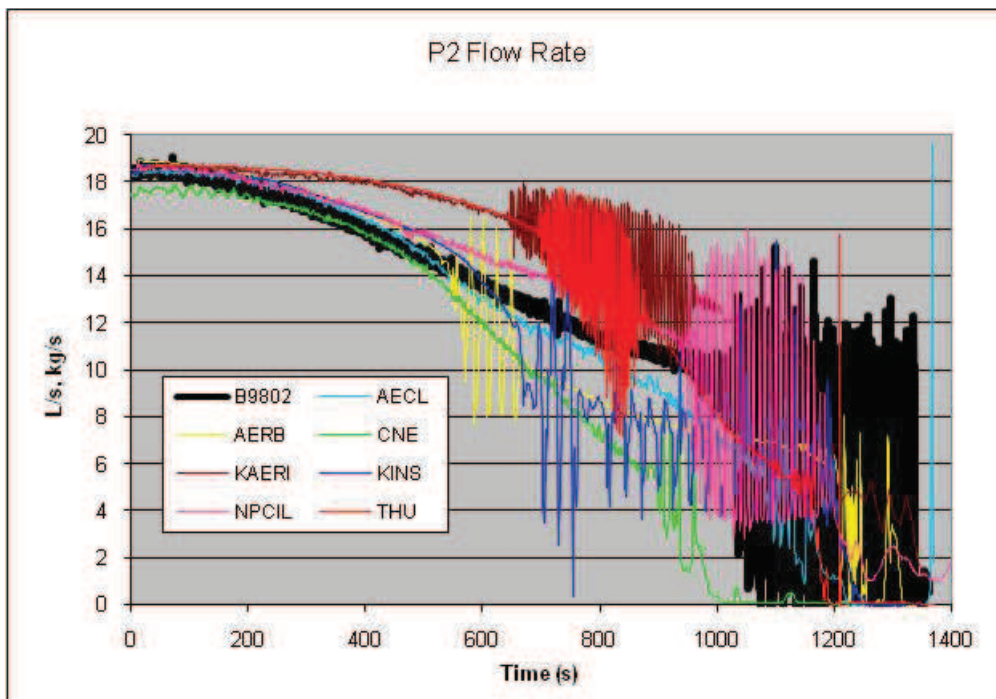


FIG. 4-105. Pump P2 flow rate.

4.5.3 Integral break flow and loop inventory

Since there was no ECI injection in test B9802, the mass lost through the break results in a continuous decrease in loop inventory. The transient loop inventory is shown in Fig. 4-106, with Figs 4-107 and 4-108 showing the measured and calculated break flow rate and cumulative break mass flows, respectively.

While the measured inventory loss reaches 460kg, in nearly linear fashion, at the end of the transient, code calculations vary from a low of 420kg (KAERI, KINS and THU) to a high of 580 kg (AECL). The changes in slope in the code calculations are due to the early termination of the heater power.

As shown in the sensitivity analysis in Appendix I, a change in the break flow rate (and thus in the inventory loss) has a significant effect on timing of events in this test. For example, the onset of pump degradation, oscillatory flow, and FES heatup are determined to a large degree by the loop inventory.

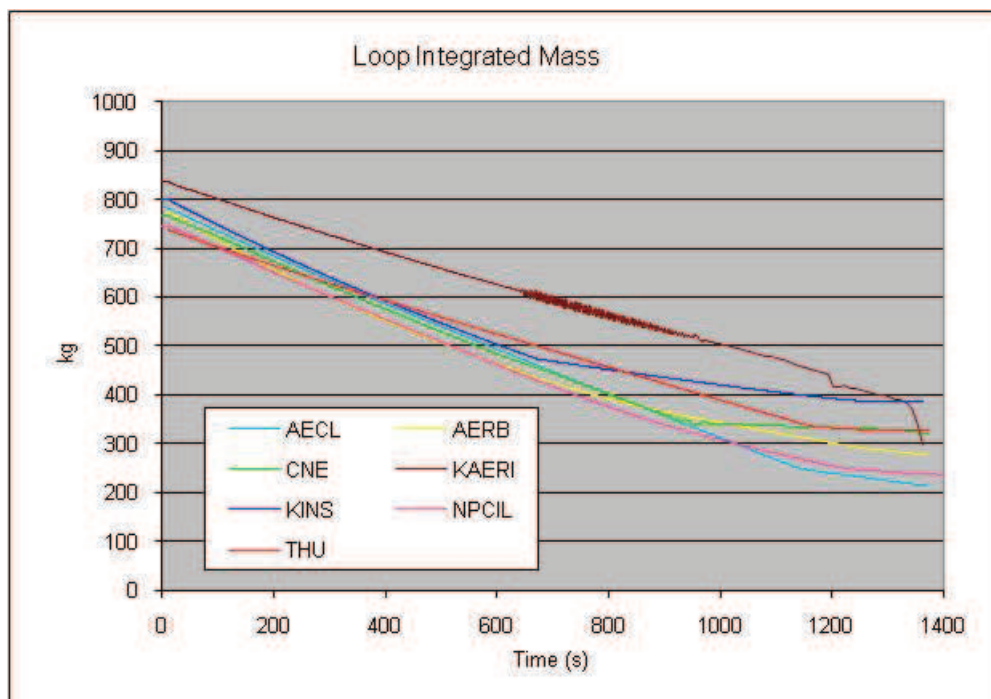


FIG. 4-106. Calculated loop mass.

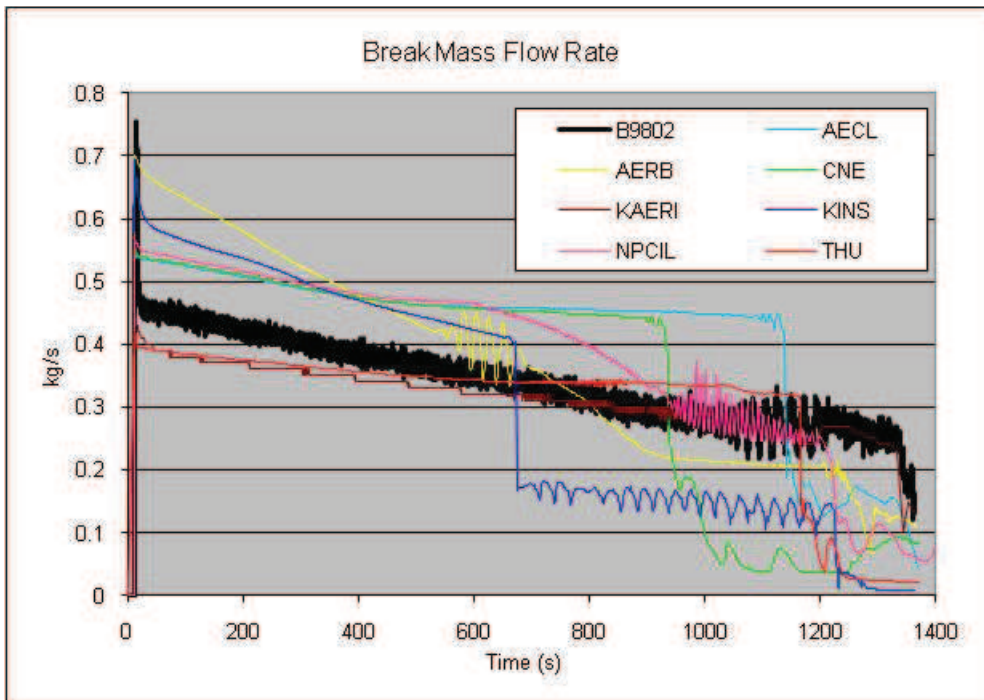


FIG. 4-107. Break flow rate.

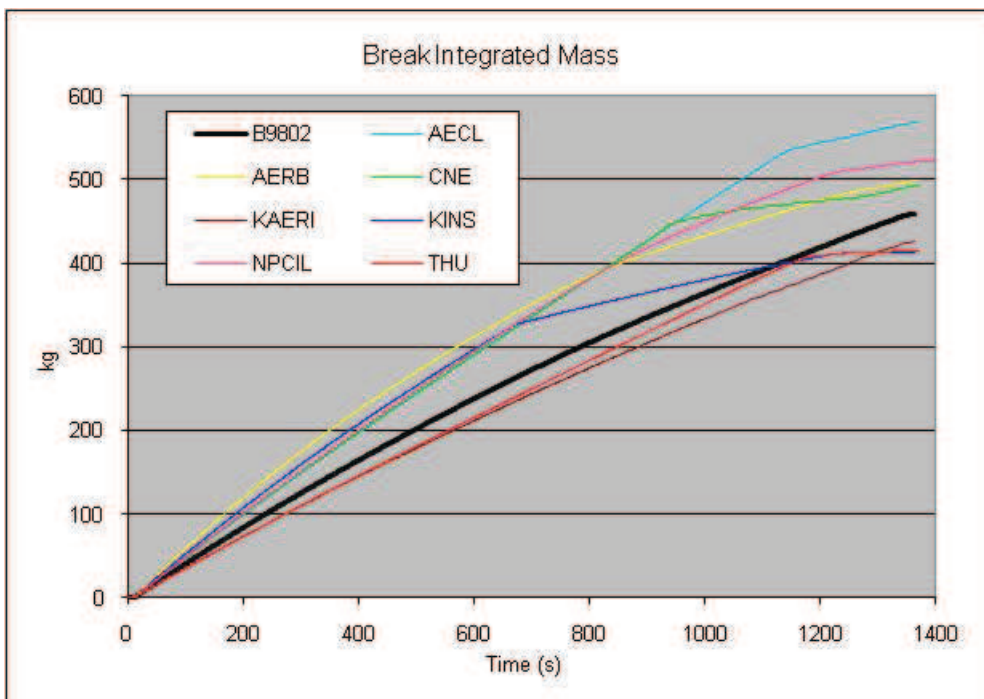


FIG. 4-108. Cumulative break flow.

4.5.4 Void fractions in boiler plenums and primary pumps

The inlet plenum voids represent the sum of the void generated in the heated sections of that loop pass, while the outlet plenum void are a reflection of the degree of condensation in the boiler tubes. With the exception of KAERI and THU, all participants follow the experimental trend of inlet boiler void quite well. The main differences, however, are in the outlet voids, which are a direct result of the effectiveness of condensation in the tubes. Thus different condensation heat transfer models will have an effect of overall loop behaviour and pump degradation in two-phase flow.

The boilers remained effective heat sinks throughout the transient (there was no secondary side depressurization) with a nearly constant thermal power, calculated as the flowrate times enthalpy change, of about 4MW in each boiler and constant steaming rate of about 2 kg/s. Basically, all the energy generated in the channels is removed in the boilers of the same loop, even during the later period of partial boiler outlet void (incomplete condensation). Boiler inlet voids are shown in Figs 4–109 and 4–111, while outlet voids are shown in Figs 4–110 and 4–112 for BO1 and BO2, respectively.

When pump P1 trips at 1192s due to an over-current condition, the flow reduces and the outlet void in boiler B1 drops back to zero. Only some of the participants correctly predict this drop in the blind calculations, as shown in Fig. 4–119. The outlet plenum of boiler BO2 does not drop to zero, probably because the flow is now only driven by pump P2, which creates a low pressure condition at its inlet and BO2 outlet. There is a large variation in predicted void at this location, seen in Fig. 4–112.

Those calculations that predict an early or excessive outlet void (i.e. less condensation than in the experiment) make up the extra heat removal through a higher sensible heat transfer, i.e. essentially the same flow rate, but higher inlet-to-outlet (liquid) temperature difference, as seen in the following section.

All participants predicted secondary side behaviour correctly, with various degrees of short-period oscillation in thermal power and steam production, but essentially the same average values as observed in the experiment right up to the point when a power trip is predicted. Therefore, no graphs of secondary side parameters are shown for this test, unlike B9006.

Both pumps do not void until they are shut off (P1 at $t=1192s$, P2 at the end of the test, see Figs 4–113 and 4–114). Most participants predict some small void at the pump outlets as shortly after there is void at the corresponding boiler outlet, which is expected. However, the experimental data suggests that the void, which arrives from the boilers at the pump inlets, is collapsed due to the increase in pressure in the pumps, while they are running. Experimental data for pump P2 between 12s and 62s is suspect (it showed an increase to full void during this time) and has been removed from Fig. 4–114.

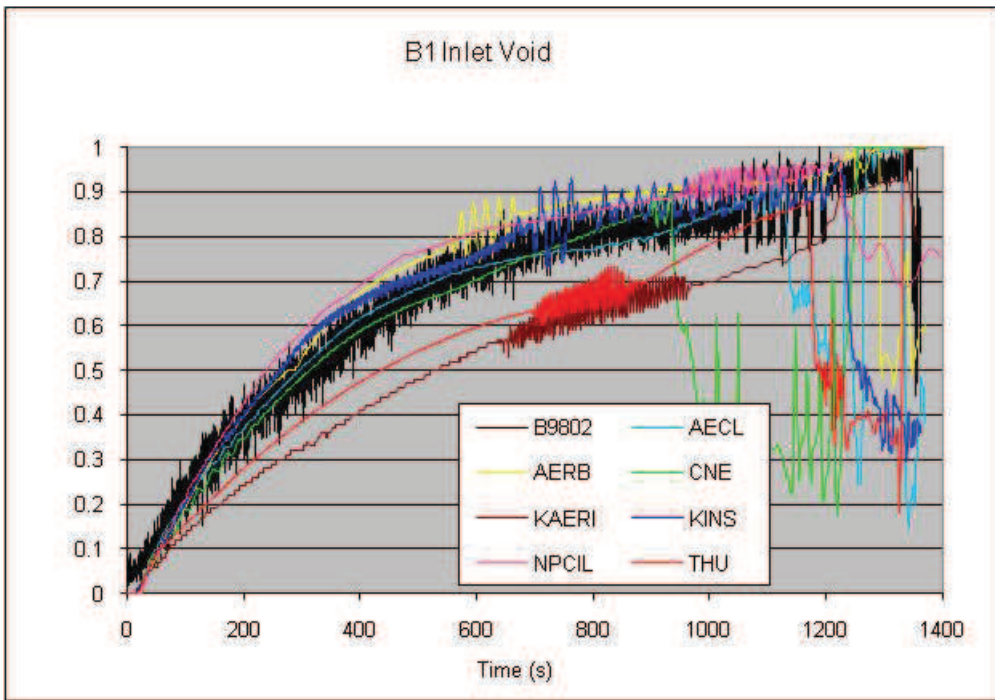


FIG. 4-109. Boiler BO1 inlet void.

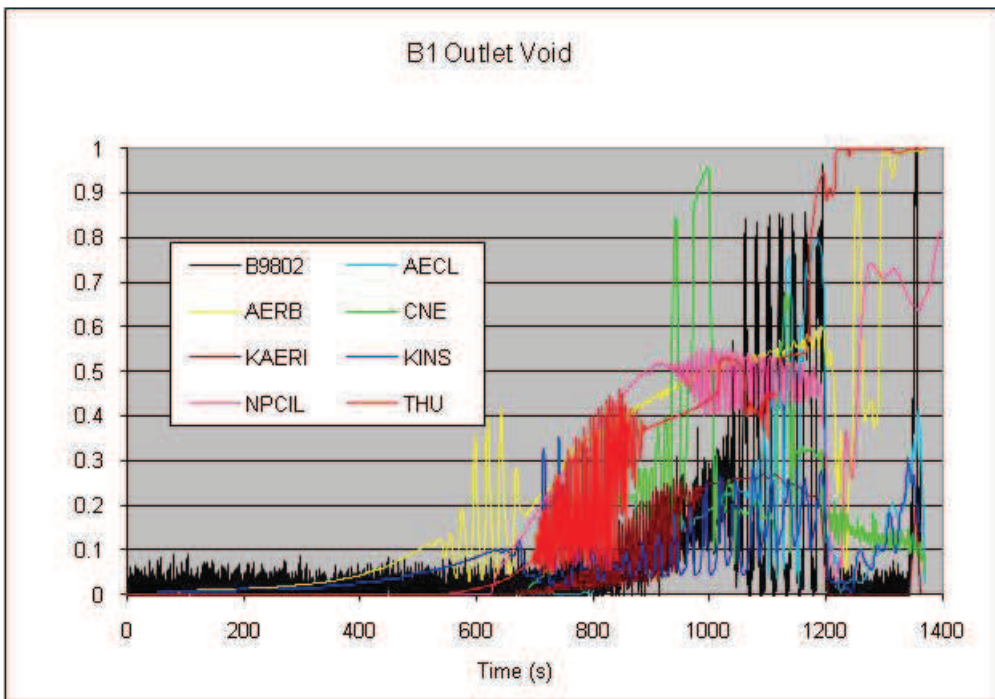


FIG. 4-110. Boiler BO1 outlet void.

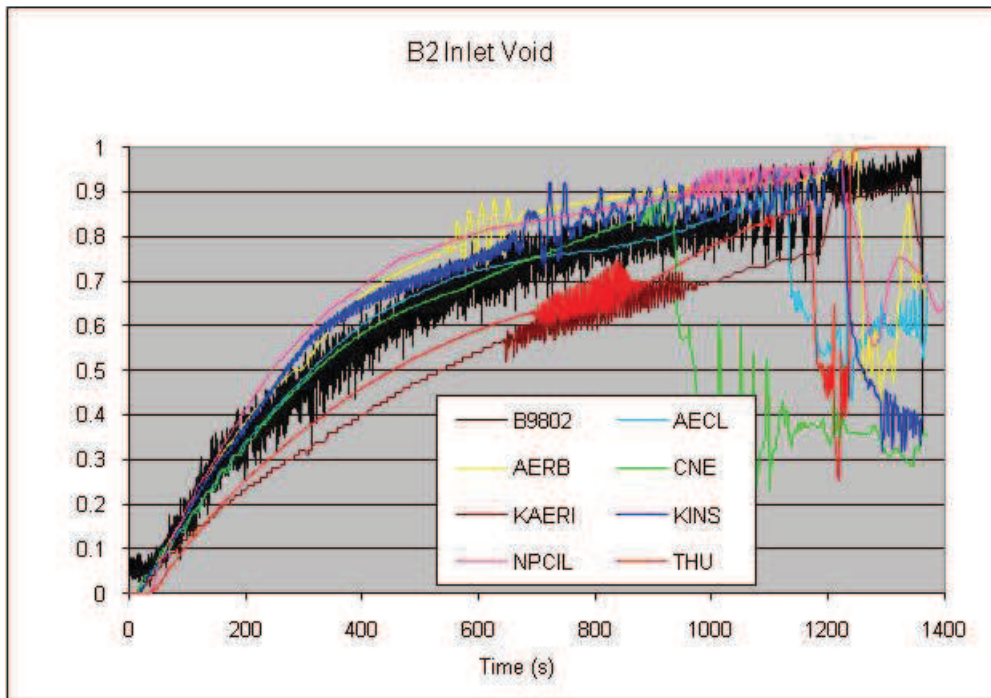


FIG. 4-111. Boiler BO2 inlet void.

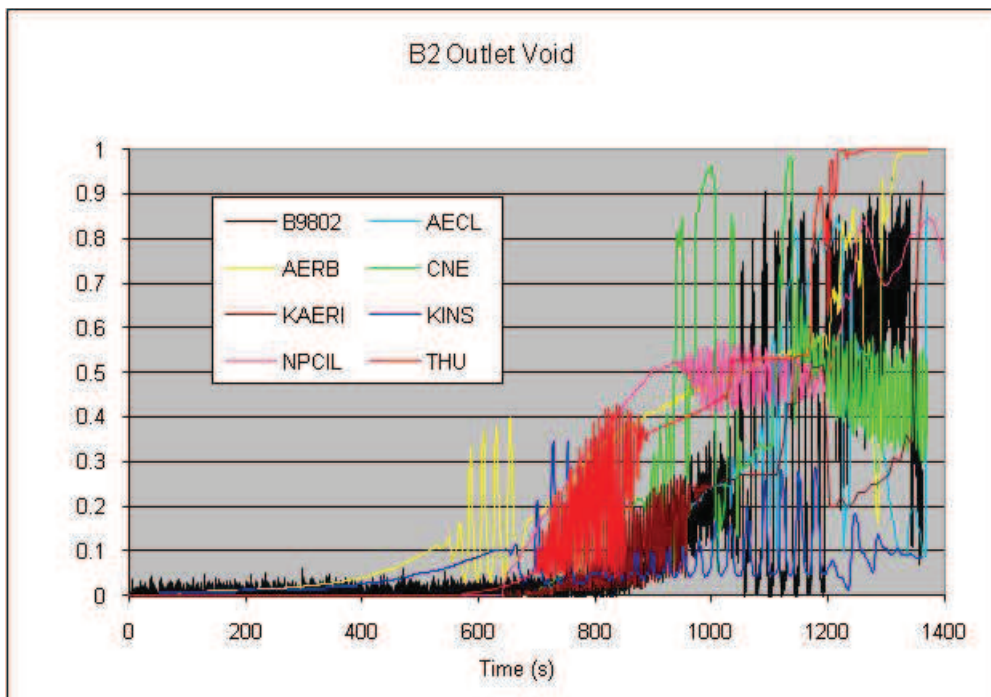


FIG. 4-112. Boiler BO2 outlet void.

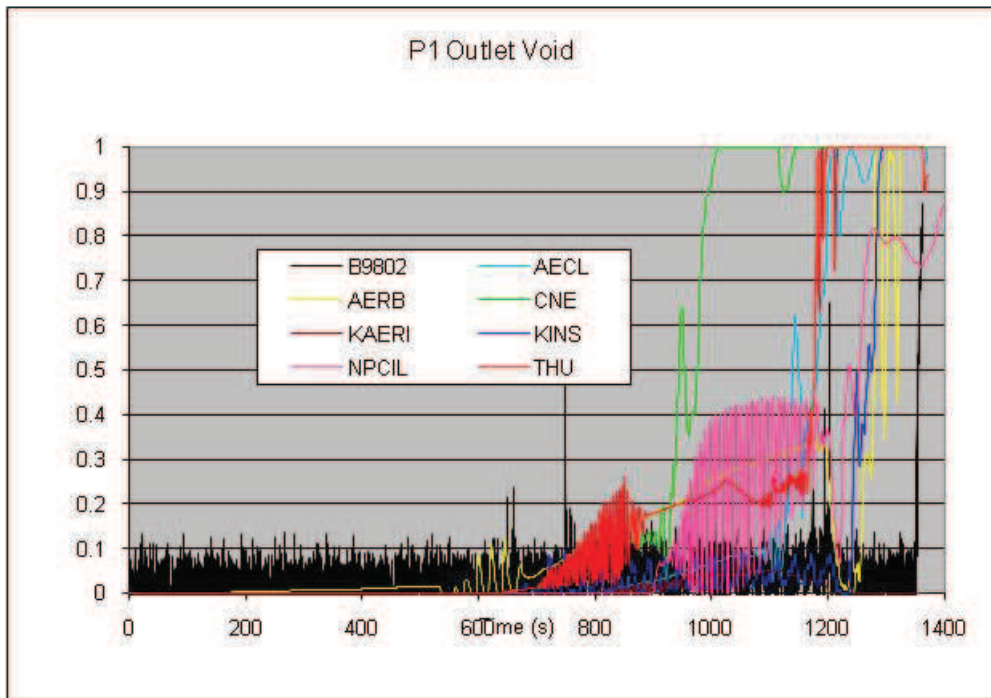


FIG. 4-113. Pump P1 outlet void.

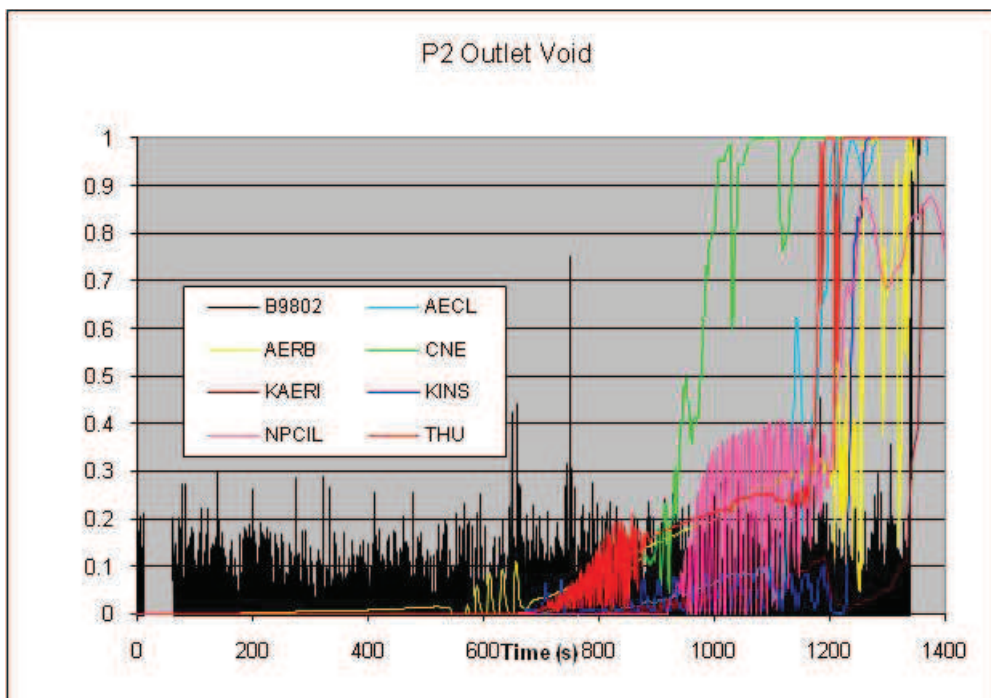


FIG. 4-114. Pump P2 outlet void.

4.5.5. Boiler inlet and outlet fluid temperatures

Measured and calculated temperatures in the inlet and outlet plenums of boilers BO1 and BO2 are shown in Figs 4–115 to 4–118.

In the experiment and all predictions the initially high temperature drop of $\sim 40^{\circ}\text{C}$ across the boilers slowly decreases to between 10 and 18°C as the heat removal changes from being dominated by single-phase convection to two-phase condensation. During the condensation phase, inlet and outlet temperatures remain essentially constant on average, except for oscillations, which result from oscillatory flow.

As discussed previously, the various inlet-to-outlet temperature differences are a result of the predicted condensation rate.

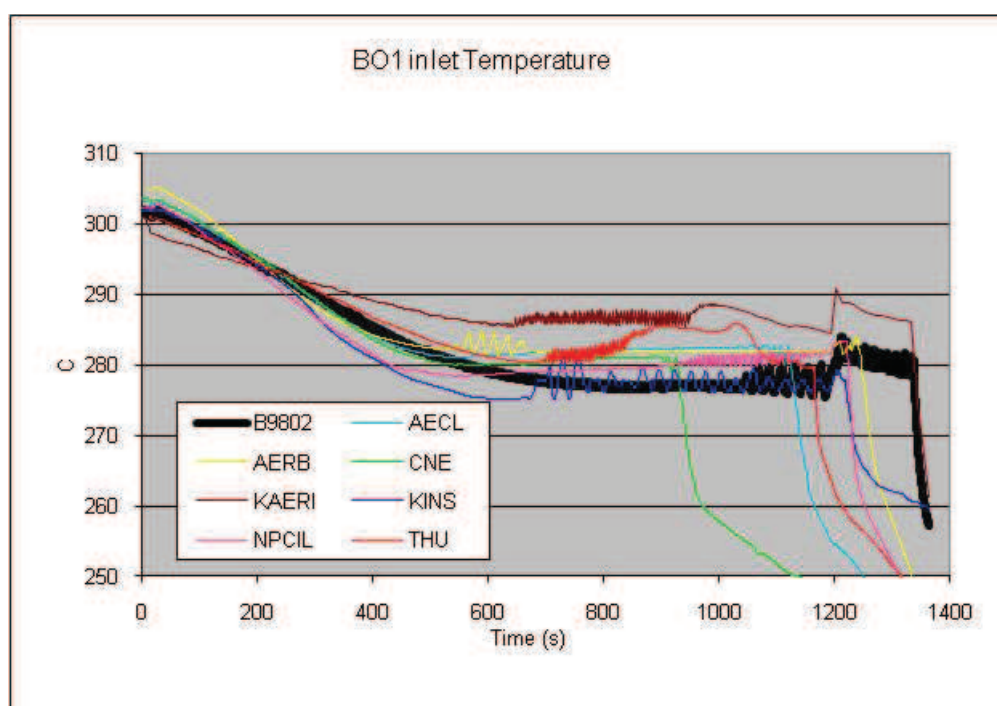


FIG. 4-115. Boiler BO1 inlet temperature.

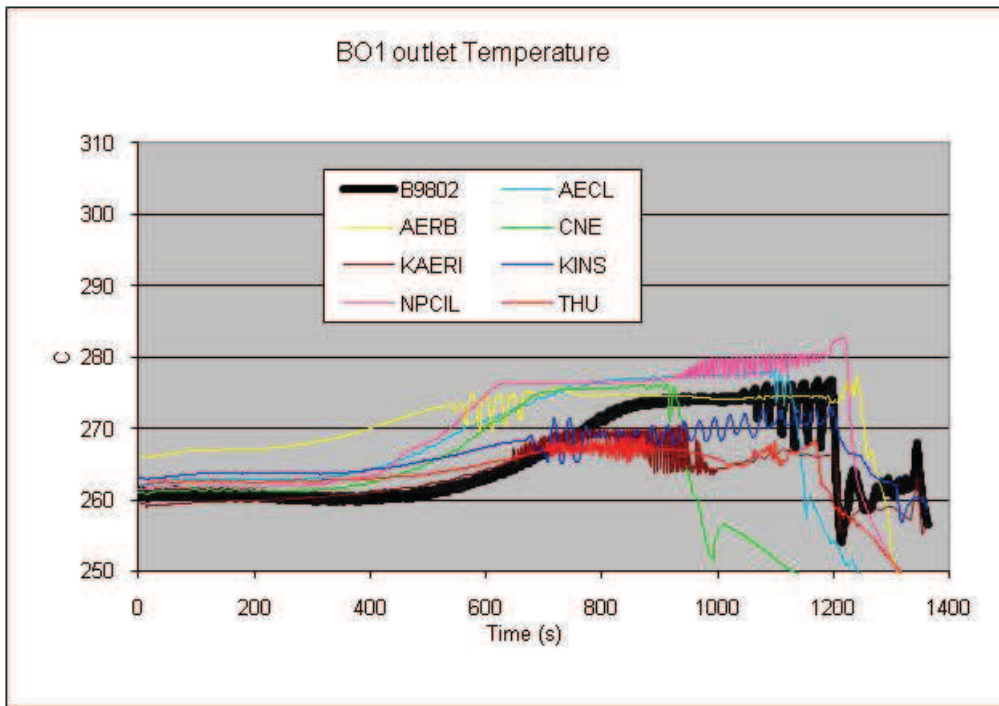


FIG. 4-116. Boiler BO1 outlet temperature.

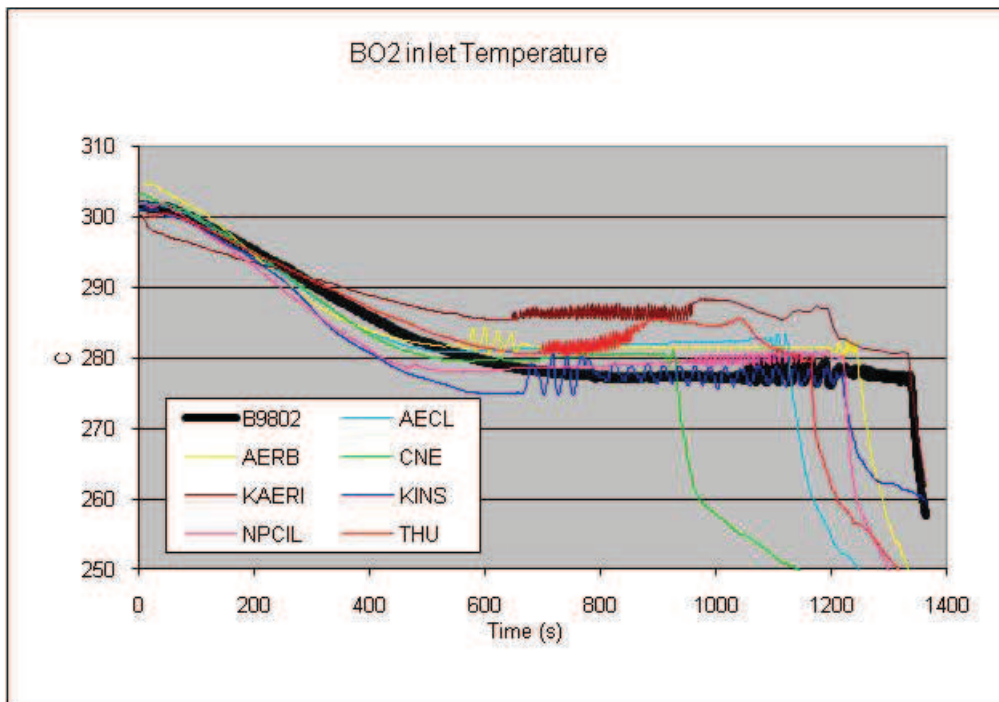


FIG. 4-117. Boiler BO2 inlet temperature.

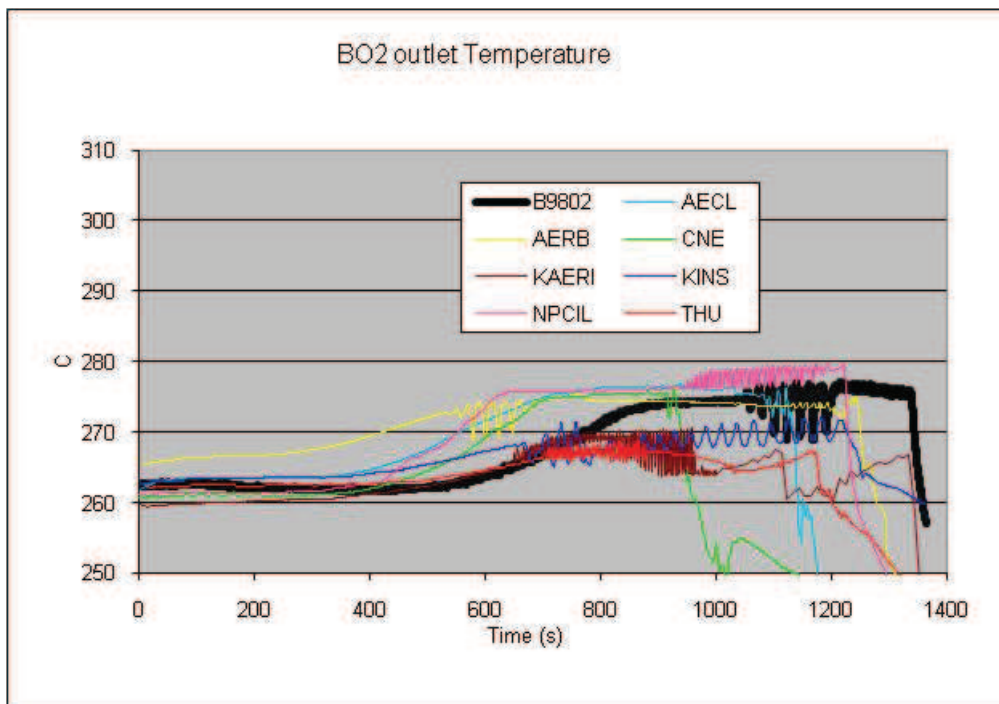


FIG. 4-118. Boiler BO2 outlet temperature.

4.5.6 FES sheath temperatures in heated sections HS8 and HS13

The maximum FES sheath temperature is often the most significant parameter in safety analyses. In test B9802, high FES sheath temperatures were measured in the high power channel of the broken pass, heated section HS13 and to a lesser degree in the high power channel of the intact pass, HS8; these are shown in Figs 4–119 to 4–123.

The following five graphs show temperatures of a top FES in the center of a high-powered channel of the unbroken pass, HS8, and near the inlet, center, and outlet of a high-powered channel, HS13, of the broken pass. The last figure is the bottom FES temperature near the outlet of HS13.

It is interesting to note that the initial inlet-to-outlet temperature gradient of about +25°C decreases gradually and reverses to a -10 C gradient (negative gradient), with all channel temperatures between 320 and 330°C prior to the FES dryout and heatup. During two-phase (mixed) flow through the channels there is a significant pressure drop, and thus saturation temperature drop in the fluid. This, in combination with a continuously increasing mixture/vapour velocity improves heat removal from the FES and a decreasing FES surface temperature along the channel. This behaviour is correctly predicted by all participants. As seen in the following section, and expected because the pumps continue to run in this test, the net flow is always in the forward direction in HS13. Since these flowrates qualitatively mimic the overall loop flowrates, discussed in Section 4.5.1 above, detailed figs and discussion are not presented here, but they are included for the open calculations in Section 4.6 below, for completeness.

Most participants predict a sharp and brief temperature excursion in HS 8 and HS13 once the critical heat flux is exceeded locally, followed by the temperature trip.

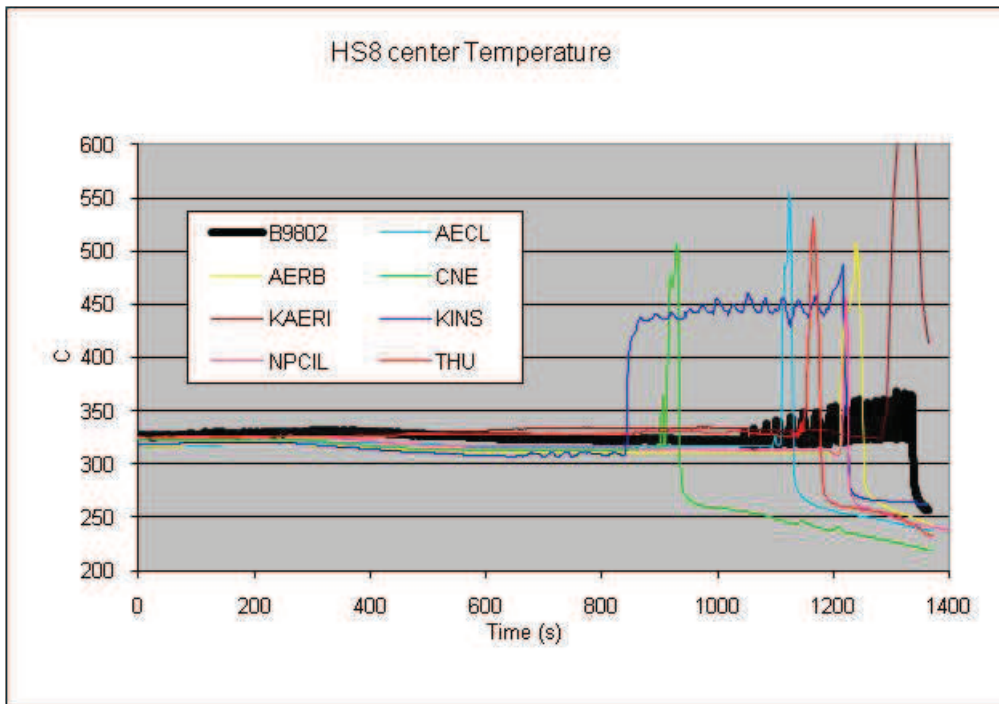


FIG. 4-119 Heated section HS8 center temperature.

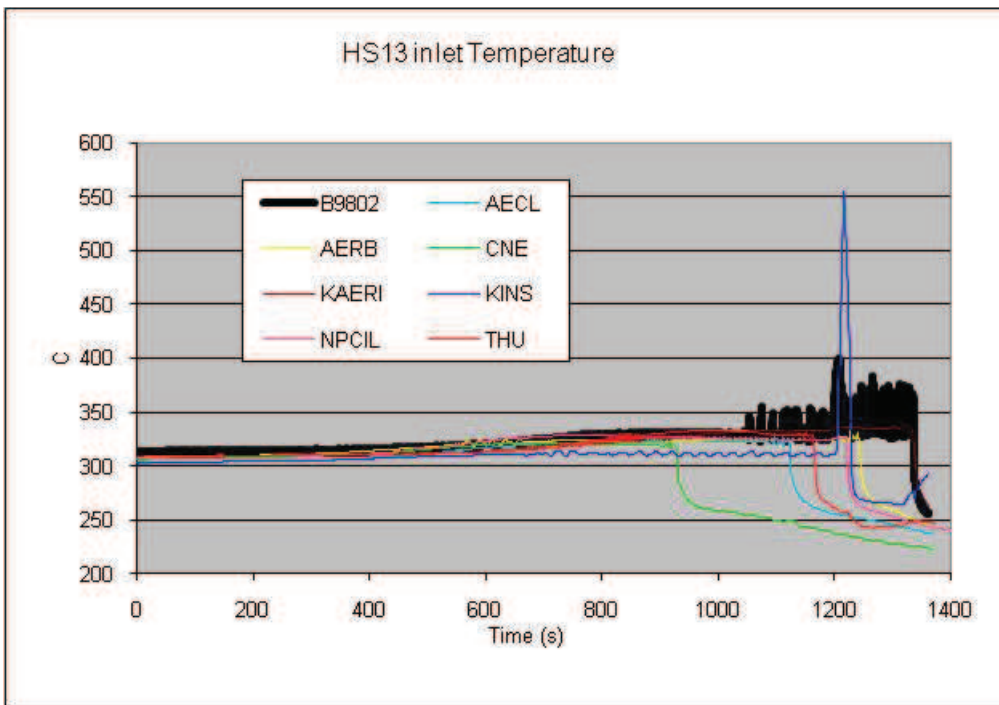


FIG. 4-120. Heated section HS13 inlet temperature.

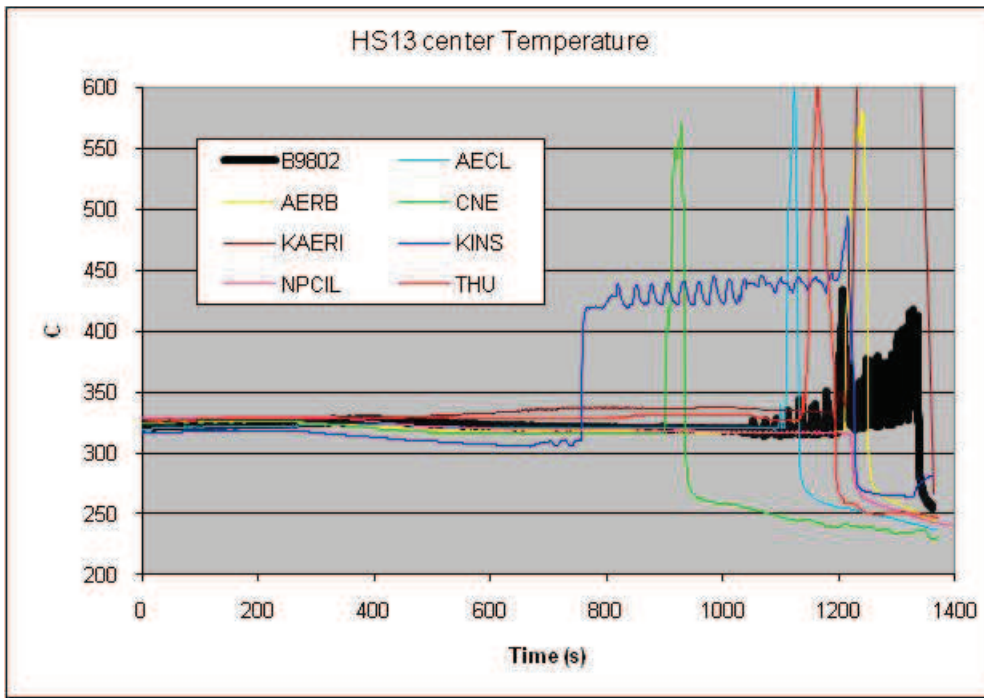


FIG. 4-121. Heated section HS13 center temperature.

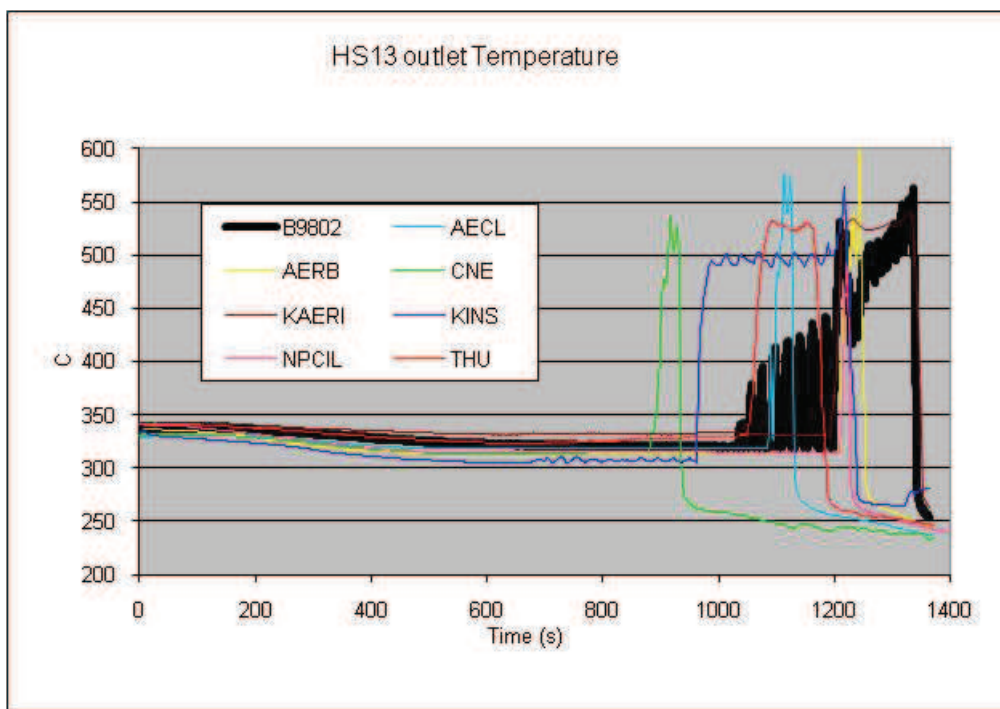


FIG. 4-122. Heated section HS13 outlet temperature.

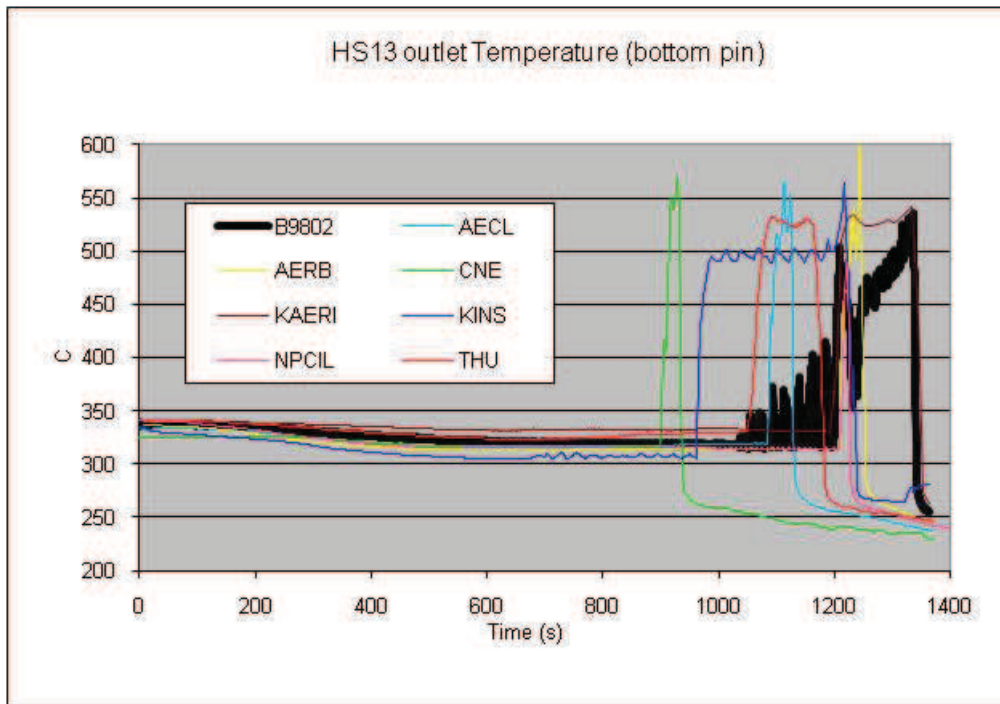


FIG. 4-123. Heated section HS13 outlet temperature (bottom FES).

4.5.7 Heated sections HS 5, 8, 10 and 13 inlet and outlet void

Channel inlet and outlet void fractions were measured approximately 2 m upstream and downstream of the heated section end in the inlet and outlet feeders and are shown, along with calculated voids from all participants, in Figs 4–124 to 4–131.

Voiding occurred in all outlet feeders almost immediately into the transient, slowly reaching 80-90% void and at the onset of the oscillations. The inlet feeders of channels in the intact pass remained liquid-filled throughout the transient. When pump P1 tripped, outlet void in both passes reaches almost 1 due to the decrease in overall loop flow rate. Outlet void drops in all channels immediately following the power trip at 1340s, as pump P2 remains operational.

Note, that the boiler secondary side depressurizes and feedwater is shut at the same time ($t = 1340s$) resulting in the boilers becoming ineffective in condensation. Therefore, the void is transported down the inlet feeders of the broken pass (HS10 and 13) by the pump P2, which is still operating.

Figures 4–124 to 4–131 show the experimental measurements and code predictions. Most simulations correctly calculate the void in the feeders, at least until the onset of significant FES heatup. Such good agreement can be expected due to the well-defined flow direction and slow progression of this transient test. THU calculates a significant delay in initial void generation in HS8, while KAERI shows a delay in HS13. Both participants predict a significantly lower initial break flow rate than measured and then calculated by others (see Fig. 4–107). These are also both low-elevation, high-powered channels, thus having a slightly higher pressure than the other channels.

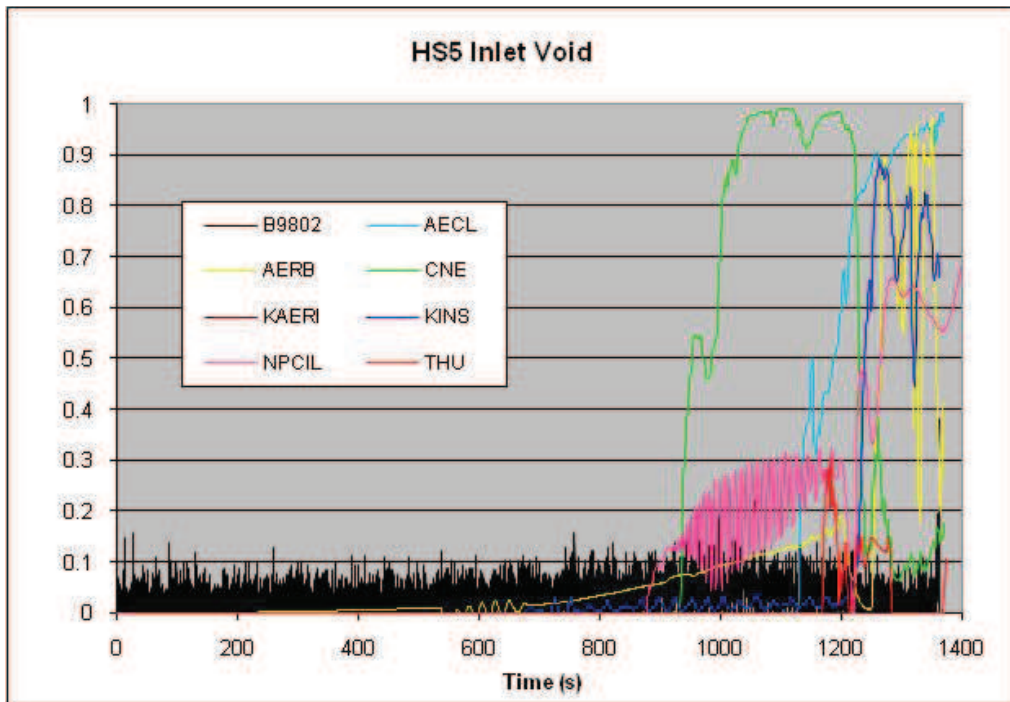


FIG. 4-124. Heated section HS5 inlet void.

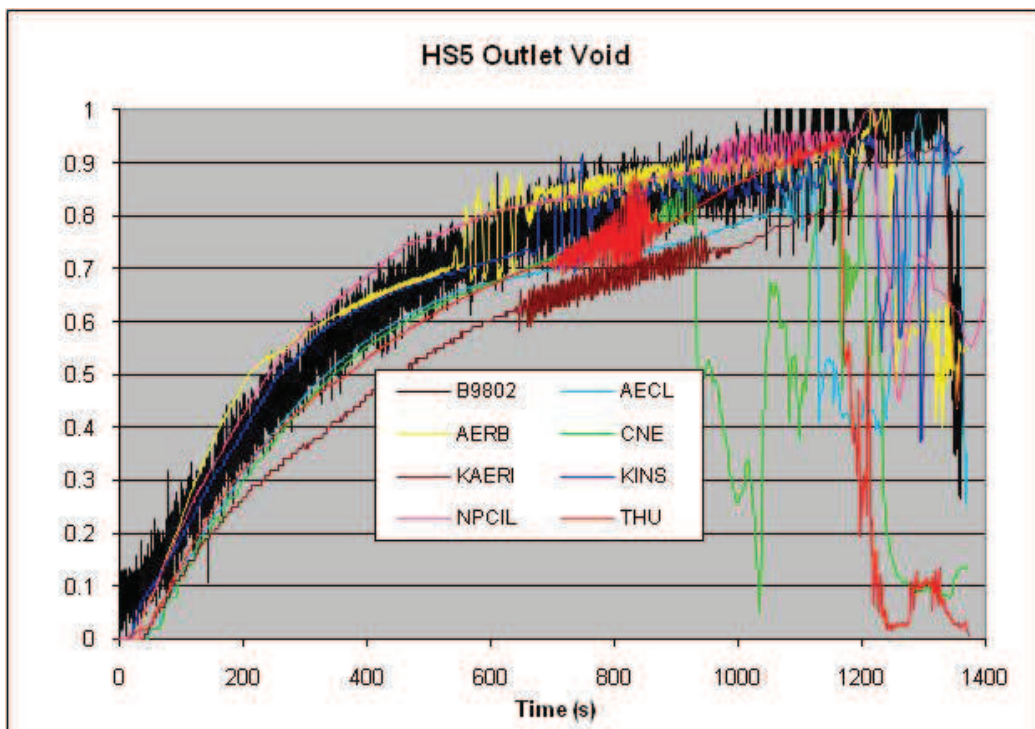


FIG. 4-125. Heated section HS5 outlet void.

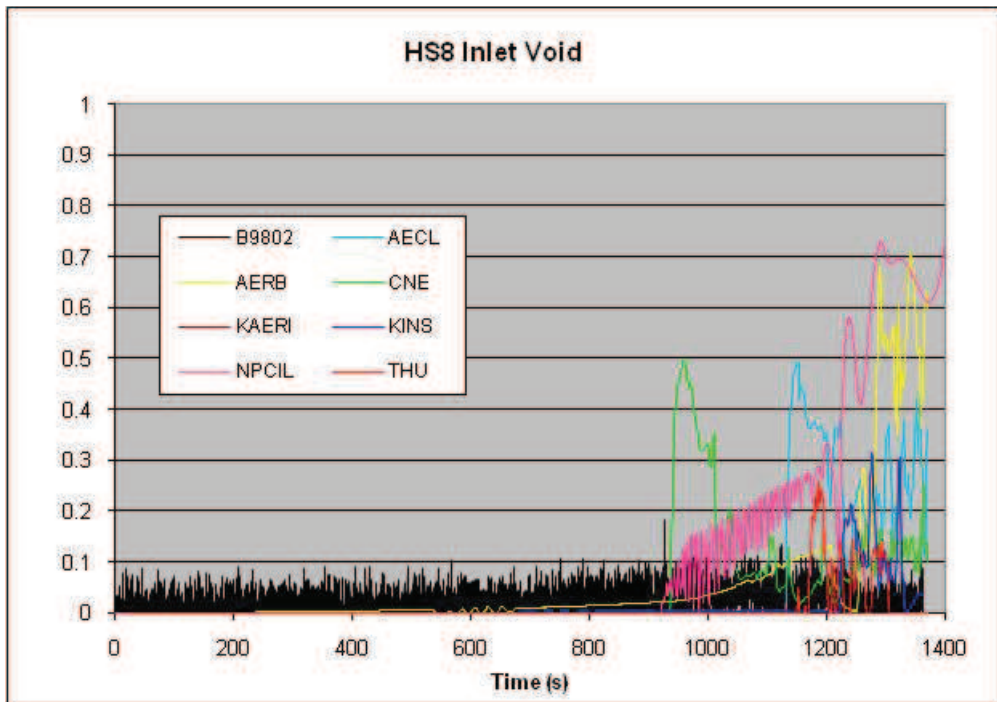


FIG. 4-126. Heated section HS8 inlet void.

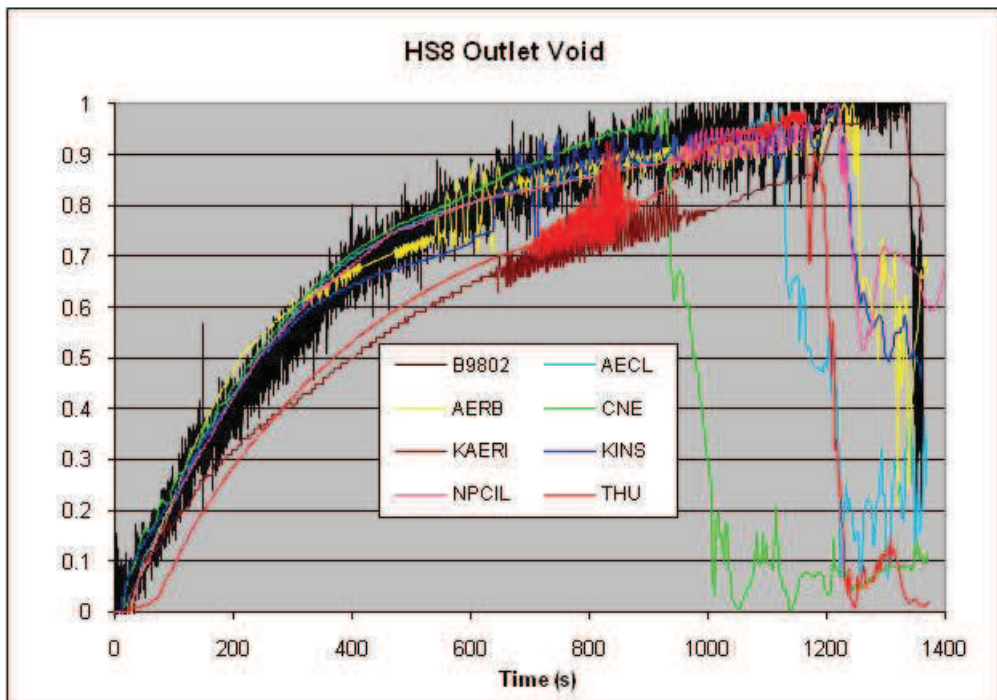


FIG. 4-127. Heated section HS8 outlet void.

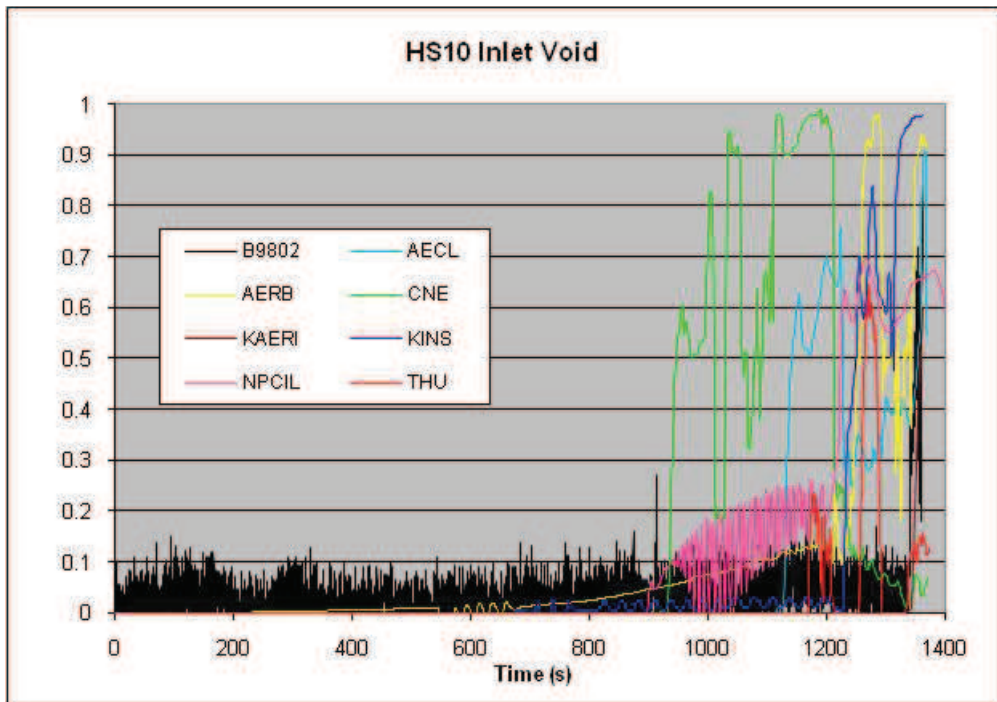


FIG. 4-128. Heated section HS10 inlet void.

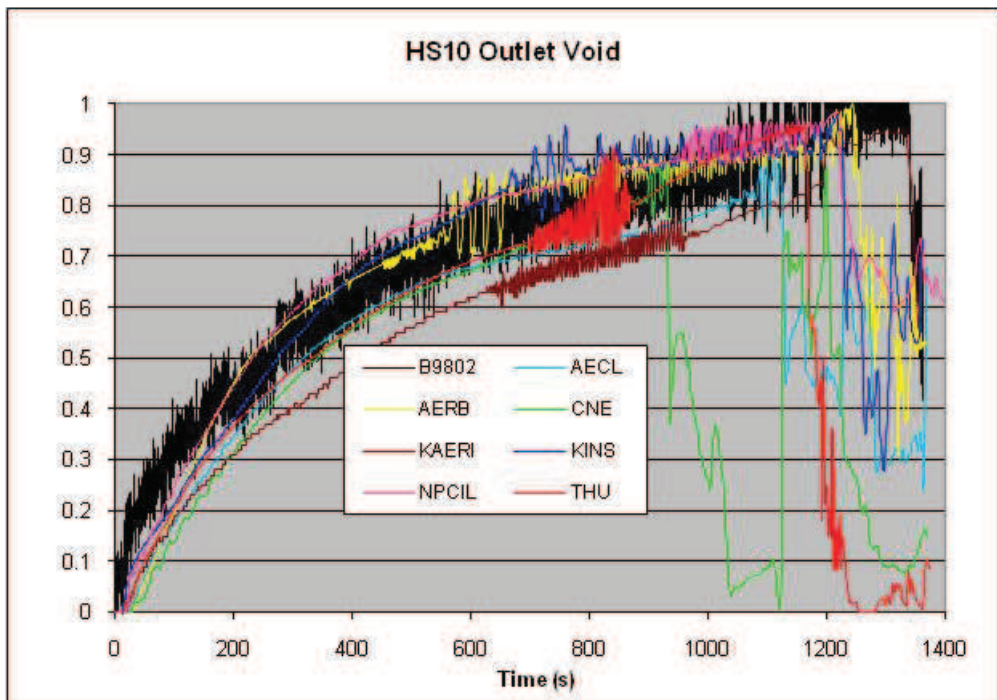


FIG. 4-129. Heated section HS10 outlet void.

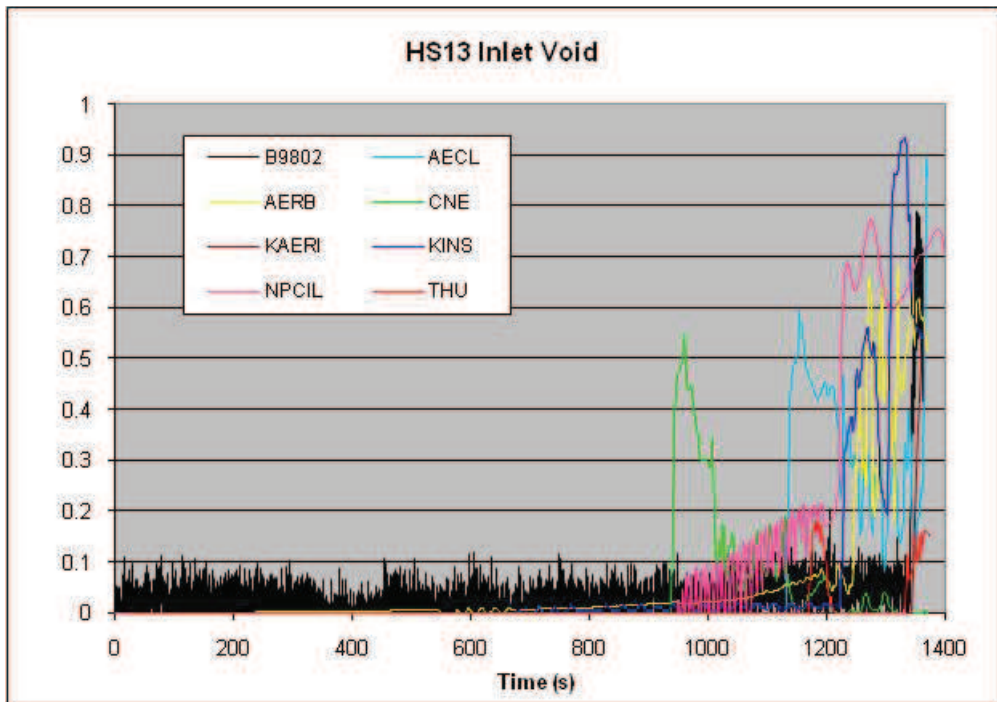


FIG. 4-130. Heated section HS13 inlet void.

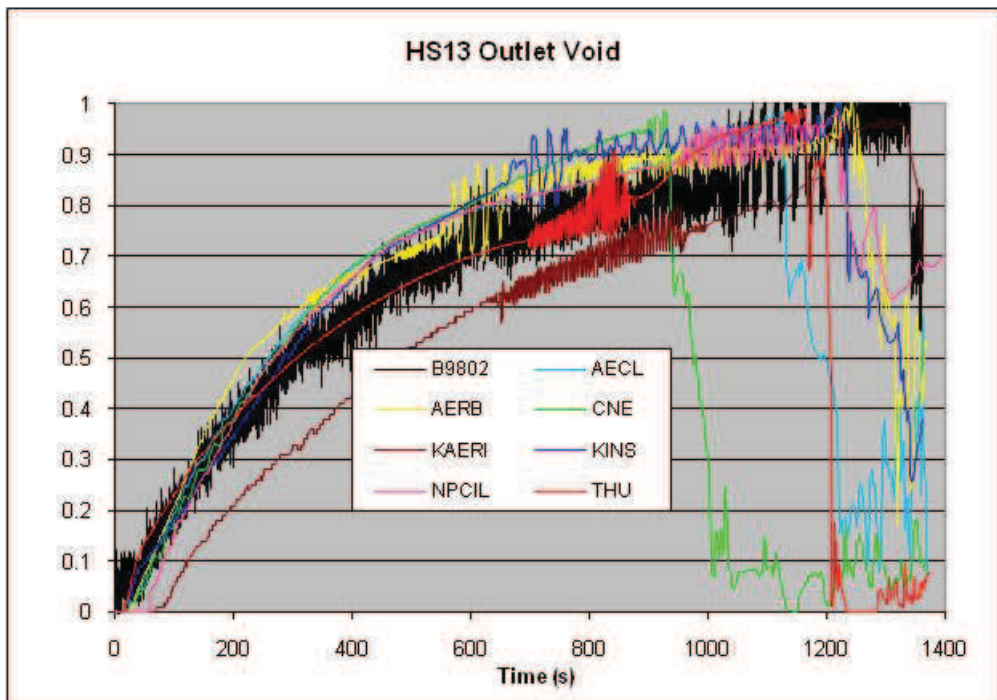


FIG. 4-131. Heated section HS13 outlet void.

4.5.8 Pressure drop along the outlet feeder from HS13 to HDR5

Experimental measurements of differential pressures across an elevation difference are corrected for the static head in the DP-cell sensing lines, as per Reference [2]. All differential pressure cells are zeroed under no flow, liquid filled, 2 MPa (g), ambient temperature conditions. In other words, differential pressure measurements where there is an elevation difference have the head component at 2 MPa (g) and ambient temperature zeroed out. The 7.57-m elevation difference thus results in a 73.8 kPa being added to the actual measurement. This corrected measurement is shown in Fig 4–132, along with the various code predictions.

The calculation of pressure drop along feeder lines strongly depends on the method chosen by each participant in assigning single-phase flow loss coefficients to the various feeder/end-fitting/channel components, and any adjustments/tuning made to match the steady-state flow distribution in the parallel channels. Since this is an outlet feeder, it operates in two-phase shortly after the start of the test; therefore, differences in the two-phase multiplier further contribute to variations in code predictions: While some participants (AECL, CNE, NPCIL) calculate a steeper increase in differential pressure as void increases, others (KAERI, KINS, THU) calculate a slower increase. AERB predicts and almost constant pressure difference for the entire transient, which indicates a deficiency in the two-phase friction multiplier.

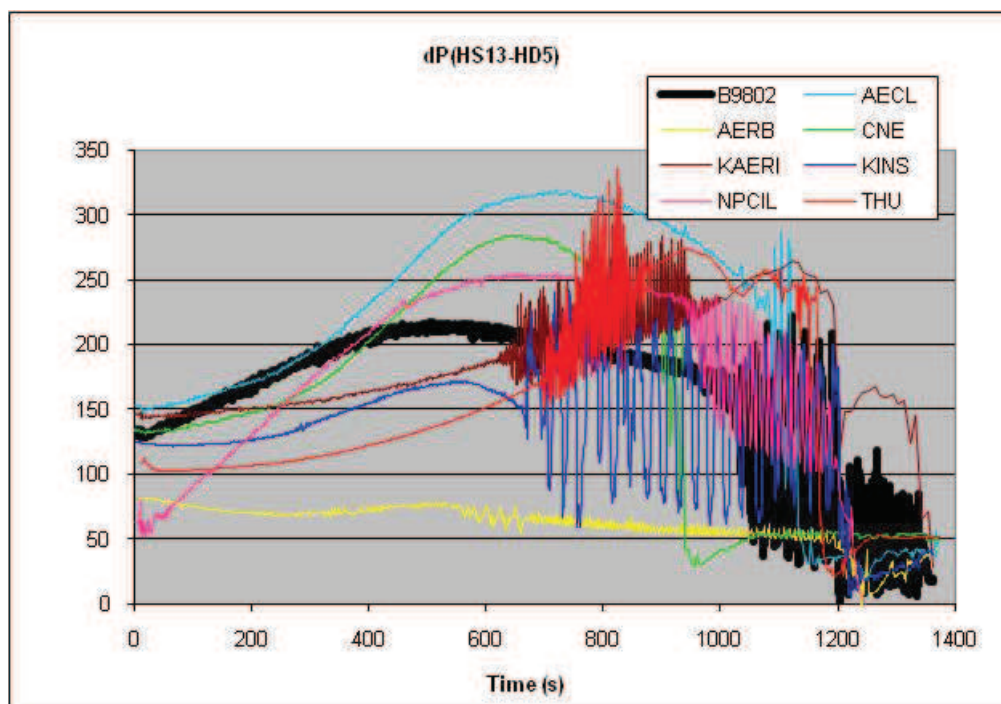


FIG. 4.132. Heated section HS13 to header HDR5 pressure drop.

4.6 OPEN CALCULATION RESULTS FOR TEST B9802

All participants who calculated this test, were able to replicate all important parameters with acceptable accuracy, but various timings, as shown in Table 4–5. The most important factor affecting the timing of events is the loop inventory, thus the modelling of the break flow is of primary importance. Compared to differences in break flow rates, no other modelling parameter, or differences between various codes or users, was significant.

Appendix I further investigates the impact of break flow modelling parameters and their quantitative effects on loop parameters, in particular timing of oscillatory flow and FES heatup.

4.6.1 Sequence of major events

Table 4-5 show the sequence of events collected from open calculations for Test B9802.

4.6.2 Primary pump differential pressures, ΔP_{P1} and ΔP_{P2} , and flow rates

Primary loop coolant circulation is provided by two high-head centrifugal pumps. In test B9802, the break occurred at inlet-header HD8 at 12.2 s (11.2 was used in the code calculations as per the ground rules), and the primary pumps were maintained at a constant speed of ~3000rpm. Thus the pump differential pressures and flow rates are a function of void at the pump and liquid density. Experimental volumetric pump flows, measured in l/s were converted to mass flows in kg/s by using liquid densities at the corresponding boiler outlet temperatures.

TABLE 4-5. SEQUENCE OF EVENTS FOR TEST B9802 (OPEN CALCULATION)

Events	Experiment (s) +/- 0.2	Code predictions (s)						
		AEC L	AER B	CNE	KAE RI	KINS	NPCI L	THU
Data gathering started/Calculation starts	0.0	0.0	0.0	0.0	0.0	0.0	0.0	0.0
Surge tank isolated	8.2	8.2	8.2	8.2	8.2	8.2	8.2	8.2
Blowdown valve (MV17) opens	12.2	11.2	11.2	11.2	11.2	11.2	11.2	11.2
HD7 pressure drops to saturation	15.2	14.2		19.8	15.1		18.8	
Start of Boiler Outlet Voiding (Void>0.1)	~900 (BO1&2)	730 (BO1) 750 (BO2)	713 (BO1) 733 (BO2)	760 (BO1) 790 (BO2)	850 (BO1) 900 (BO2)	984 (BO1) 950 (BO2)	668 (BO1) 689 (BO2)	960 (BO1) 1000 (BO2)
Start of oscillatory flow	~1050	860	780	880	650	980	920	1050
Start of FES heatup	~1050	900	1210	900	1200	1050	1210	1280
Pump 1 trip (over-voltage process protection, boundary condition)	1192	1192	1192	1192	1192	1192	1192	1192
(Power supply trip – actual trip time occurred when HS12 bundle 1 top pin was at 640°C) FES sheath temperature first reaches 600C (HS12 bundle 1, B-1)	(1336) 1313 (HS12, B-1)		1236 (HS8 B-11)	945 (HS1 3 B-7)	1338	1216. 2	1310	
End of test	1363	1370	1370	1360	1363	1400	1400	1362

Figures 4-133 to 4-136 provide the code comparison of the primary pump differential pressures and flow rates to experimental measurements. All calculations show the proper trends, with a nearly constant differential pressure until the onset of void at the pump inlet, as indicated by oscillations in the differential pressure and flow rates. The timing of void arriving at the pump inlet and the degree of reduction in flow rate until then, however, vary

greatly amongst the code simulations, due to different inventory loss through the break. A larger break discharge leads to a lower loop inventory, and thus higher void and earlier degradation in pump performance (see also Appendix I).

Pump P1 and pump P2 behaviour is very similar; however, P1 trips earlier as a result of a process trip, which is not related to the experiment.

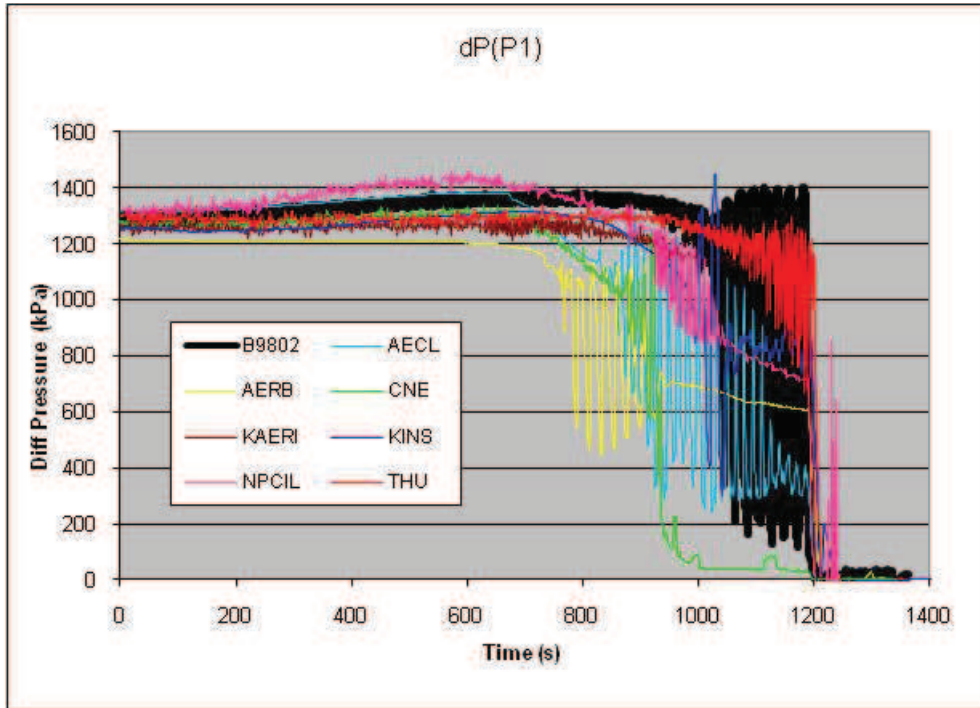


FIG. 4-133. Pump P1 differential pressure.

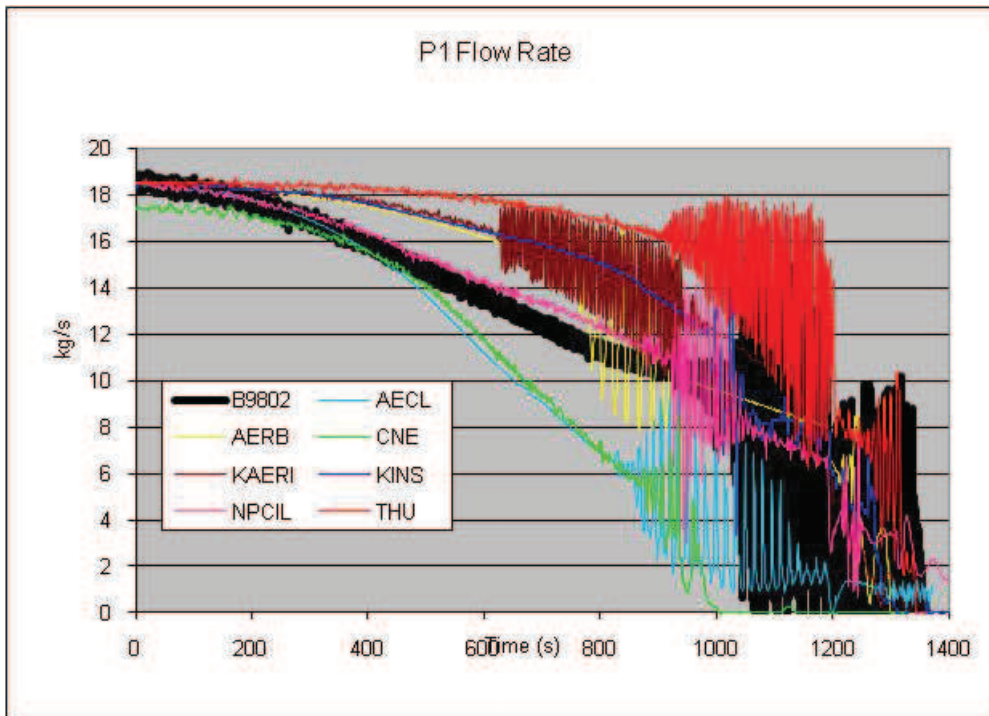


FIG. 4-134. Pump P1 flow rate.

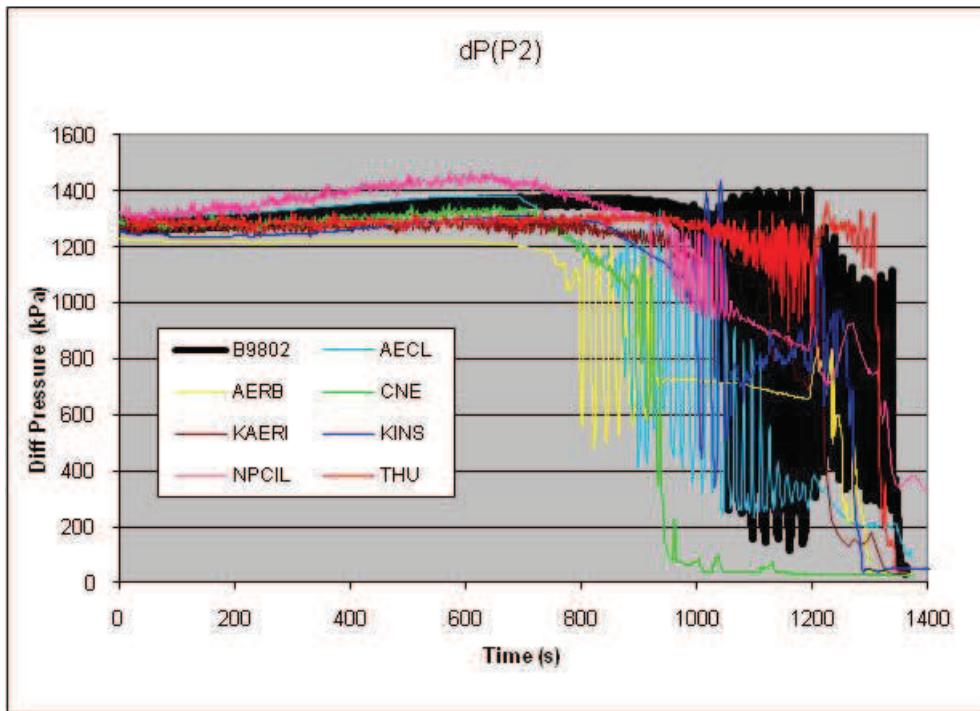


FIG. 4-135. Pump P2 differential pressure.

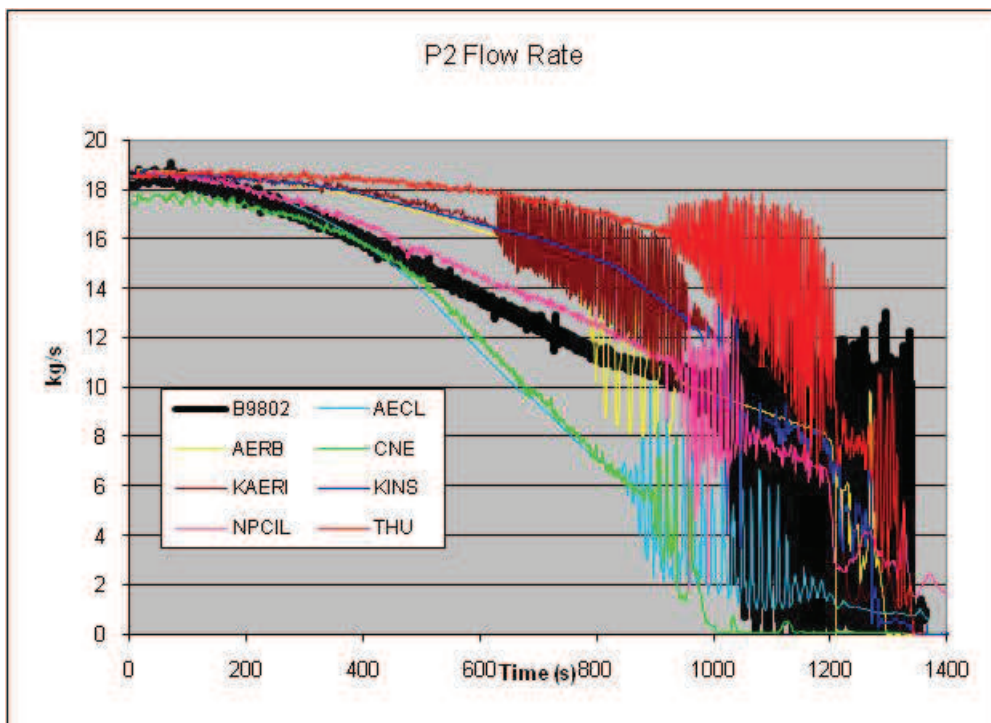


FIG. 4-136. Pump P2 flow rate.

4.6.3 Header differential pressures, $\Delta\text{PHD8-5}$ and $\Delta\text{PHD6-7}$

The header-to-header differential pressures follow a similar general trend as the pump differential pressures.

Figures 4–137 and 4–138 show the broken and unbroken-pass header-to-header differential pressures, respectively. This pressure drives the flow through below-header portion of the loop (inlet feeders, heated sections and outlet feeders) during the transient. Therefore, there are no periods of stagnation or reverse flow in individual channels, unlike in test B9006, except possible at the very end of the transient.

Most calculations show the correct trends, including the slight differential pressure increase from the break opening until about 600 s. The differential pressures are underpredicted by most participants.

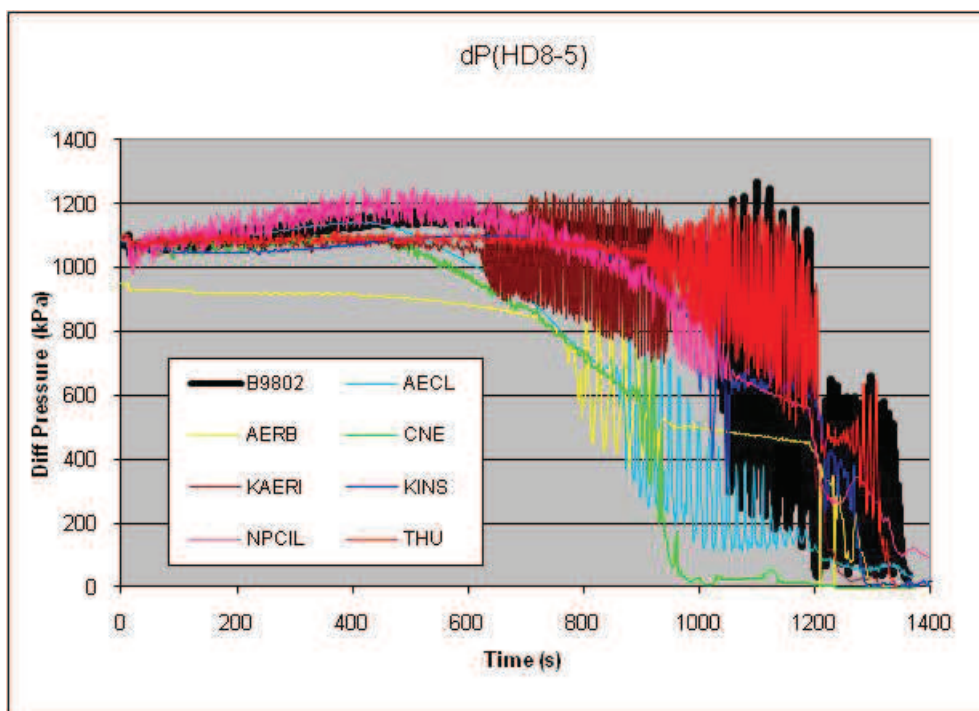


FIG. 4-137. Broken pass header-to-header differential pressure.

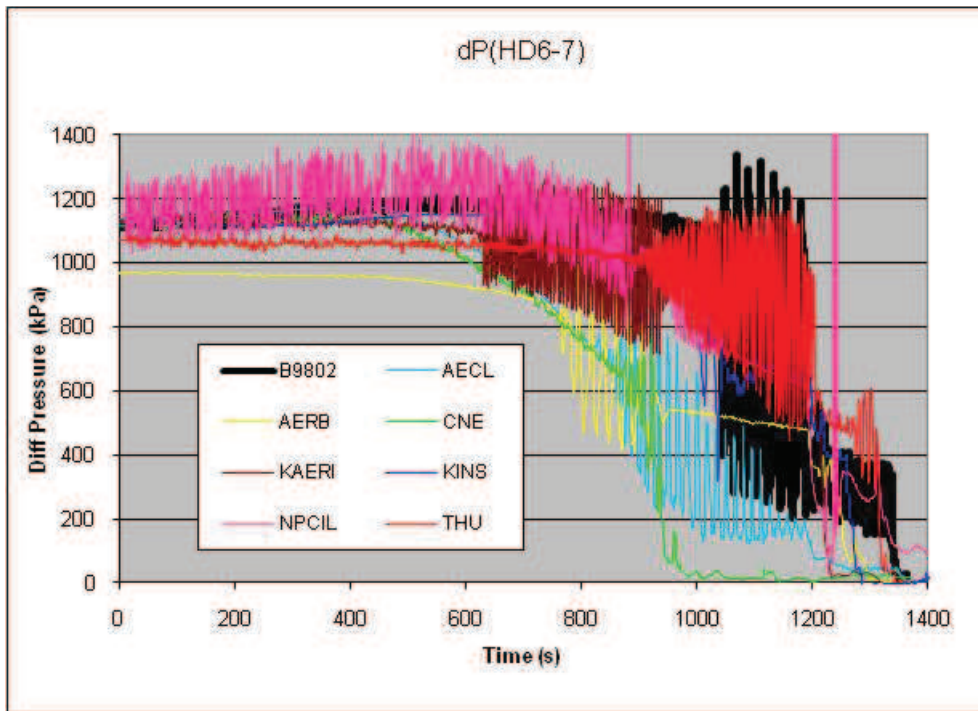


FIG. 4-138. Intact pass header-to-header differential pressure.

4.6.4 Header pressures, P(HD8), P(HD7) and P(HD6)

The entire loop depressurized relatively uniform during this SBLOCA, settling between 6 and 7 MPa prior to the pump trips. The initial depressurization to about 9 MPa in the outlet and 10 MPa in the inlet headers is the result of single-phase discharge from the break until saturation is reached and two-phase discharge starts. The depressurization is considerably slower during the two-phase discharge and slows down even further when significant boiling occurs in the heated channels.

Figures 4–139 to 4–141 show the pressure transient in headers HD8 (the broken header), HD7 and HD6 (the outlet and inlet headers of the intact pass). All participants replicate the correct trends with varying accuracy. KAERI predicts a “plateau” about 1 MPa over the measurement and the mean of the other code calculations with small oscillations, due to the steam generator condensation option in CATHENA not being selected (confirmed by sensitivity analysis in Appendix I). CNE predicts a much earlier final depressurization, due to their early FES heatup and consequent power reduction.

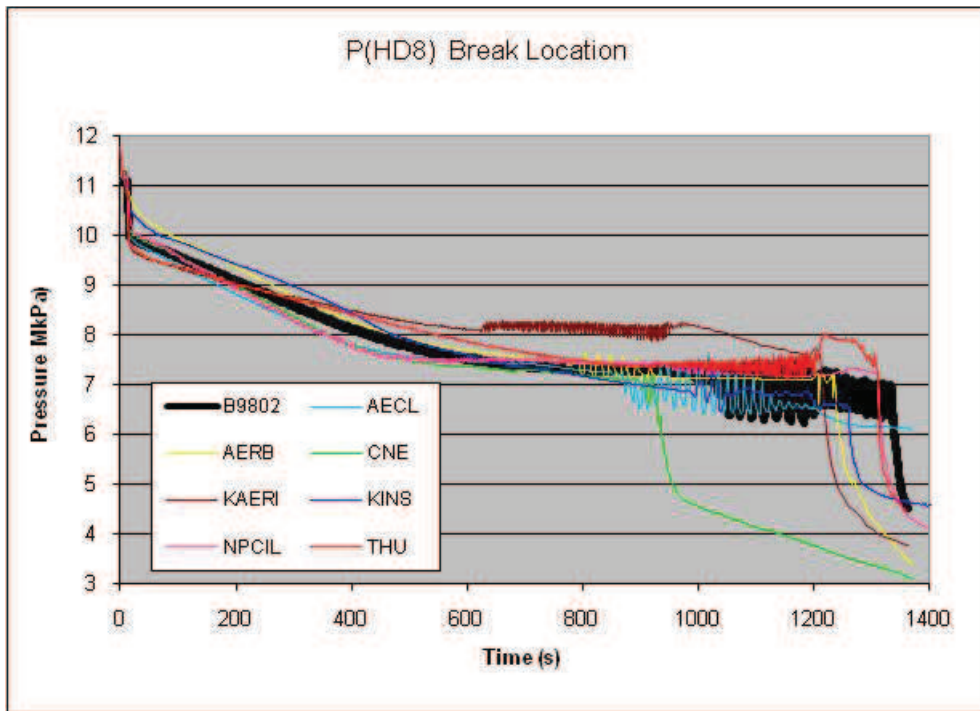


FIG. 4-139. Header HD8 pressure.

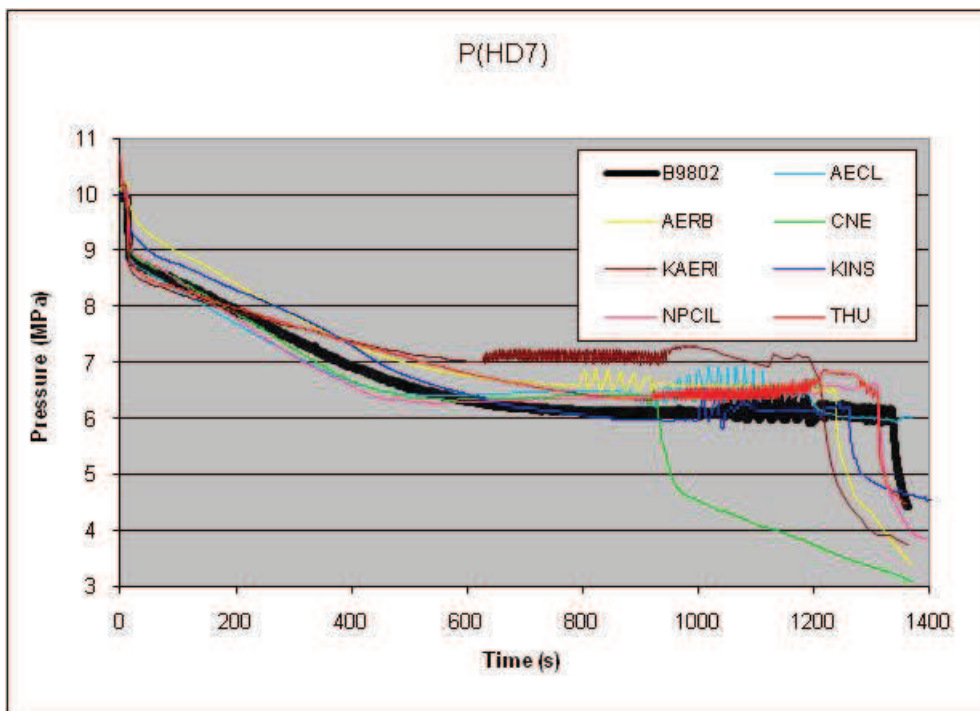


FIG. 4-140. Header HD7 pressure.

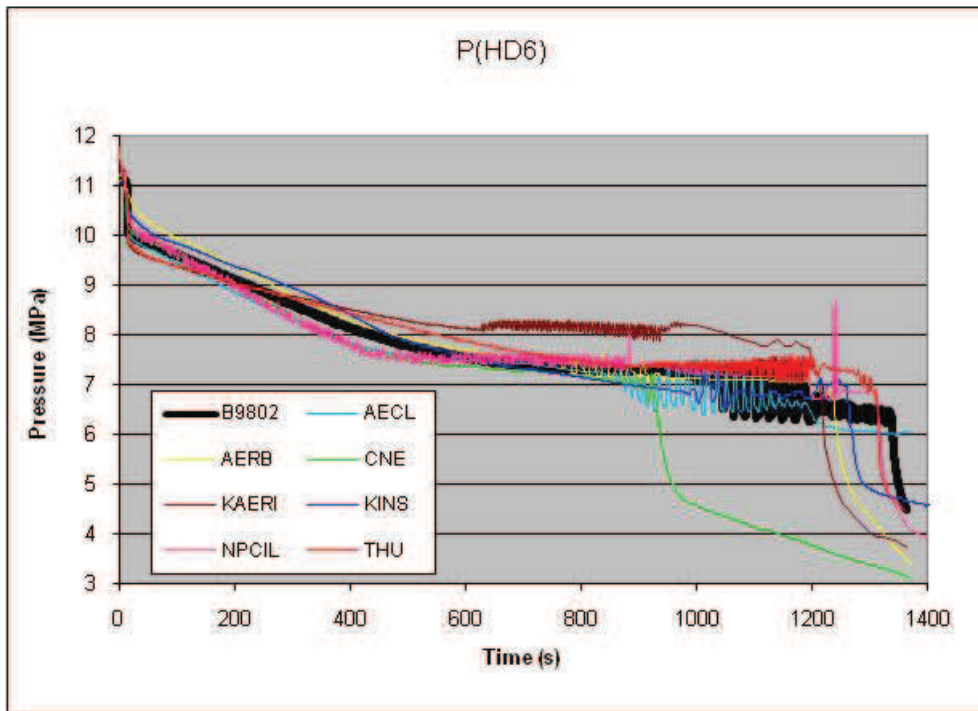


FIG. 4-141. Header HD6 pressure.

4.6.5 Integral break flow and loop inventory

Since there was no ECI injection in test B9802, the mass lost through the break results in a continuous decrease in loop inventory. This is shown in Fig. 4-142, with Fig. 4-143 showing the measured and calculated cumulative break mass flows.

While the measured inventory loss reaches 460kg, in nearly linear fashion, at the end of the transient, code calculations vary from a low of 330kg (THU) to a high of 580 kg (AECL). The change in slope in the CNE and KINS calculations are due to the early termination of the heater power.

There are significant differences in the AERB, KINS and THU blind and open predictions of the break flow rate, as reflected in the calculated loop inventory, and integral break flow plots below. While predictions improved for the submissions from AERB and KINS, they became worse for THU.

As shown in the sensitivity analysis in Appendix I, a change in the break flow rate (and thus in the inventory loss) has a significant effect on timing of events in this test. For example, the onset of pump degradation, oscillatory flow, and FES heatup are determined to a large degree by the loop inventory.

4.6.6. Void fractions in boiler plenums and primary pumps

The inlet plenum voids (Figs 4-144 and 4-146) represent the sum of the void generated in the heated sections of that loop pass, while the outlet plenum voids (Figs 4-145 and 4-47) are a reflection of the degree of condensation in the boiler tubes. With the exception of KAERI and THU, all participants follow the experimental trend of inlet boiler void quite well. These two calculations did not include the recommended condensation option (STM-GEN-COND) for the boiler tubes.

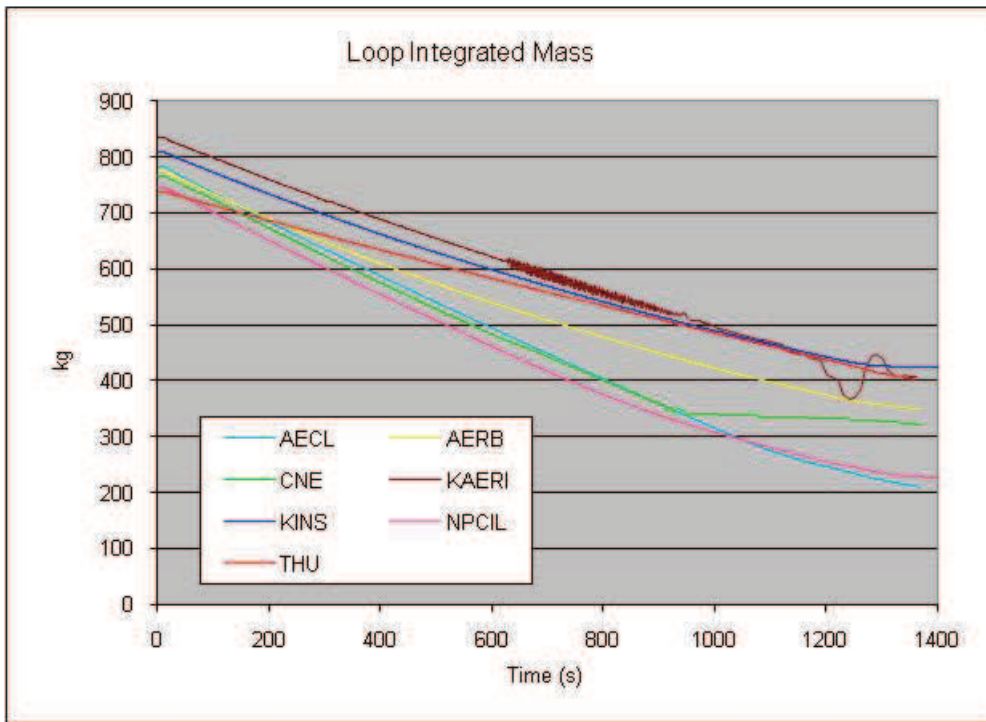


FIG. 4-142. Calculated loop mass.

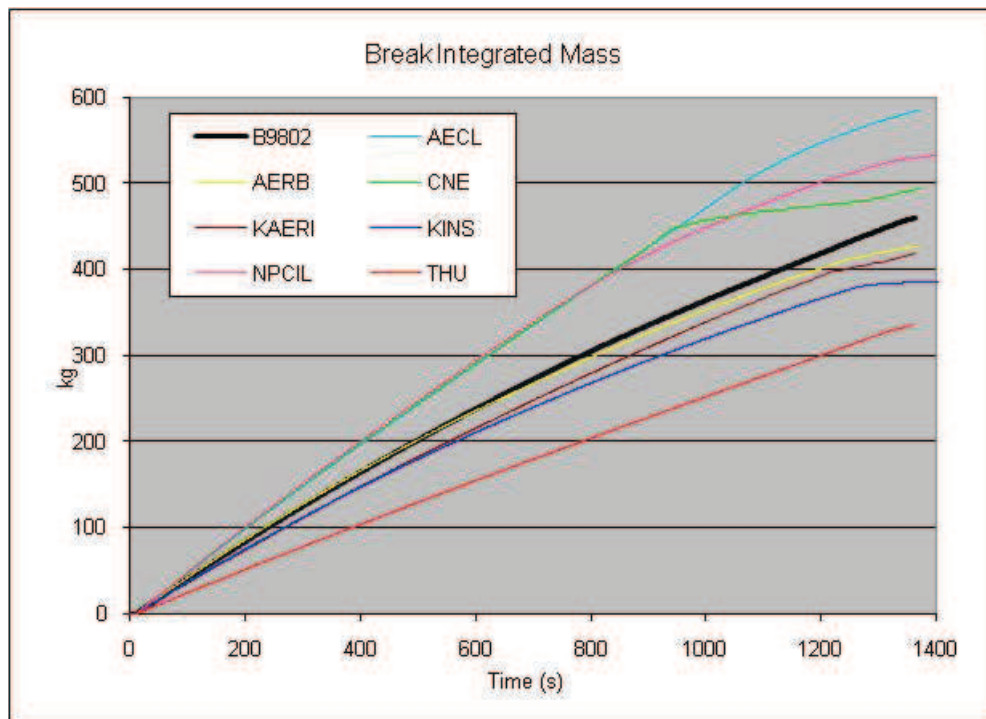


FIG. 4-143. Cumulative break flow.

The boilers remained effective heat sinks throughout the transient (there was no secondary side depressurization) with a nearly constant thermal power of about 4MW in each boiler and constant steaming rate of about 2 kg/s. Basically, all the energy generated in the channels is removed in the boilers of the same loop, even during the later period of partial boiler outlet void (incomplete condensation). When pump P1 trips the flow reduces and the outlet void in

boiler B1 drops back to zero. All participants correctly predict this drop in the open calculations, although most still show a subsequent temporary voiding. The outlet plenum of boiler BO2 does not drop to zero, probably because the flow is now only driven by pump P2, which creates a low pressure condition at its inlet and BO2 outlet. All participants, except KINS, correctly predict a sustained significant void in the boiler BO2 outlet.

All participants predicted secondary side behaviour correctly, with various degrees of short-period oscillation in thermal power and steam production, but essentially the same average values as observed in the experiment. Therefore, no graphs of secondary side parameters are shown for this test, unlike B9006.

Both pumps do not void until they are shut off (P1 at $t=1192s$, P2 at the end of the test, see figs 4-148 and 4-149). Most participants predict some small void at the pump outlets as shortly after there is void at the corresponding boiler outlet, which is expected. However, the experimental data suggests that the void, which arrives from the boilers at the pump inlets, is collapsed due to the increase in pressure in the pumps, while they are running. Experimental data for pump P2 between 12s and 62s is suspect (it showed an increase to full void during this time) and has been removed from Fig. 4-149.

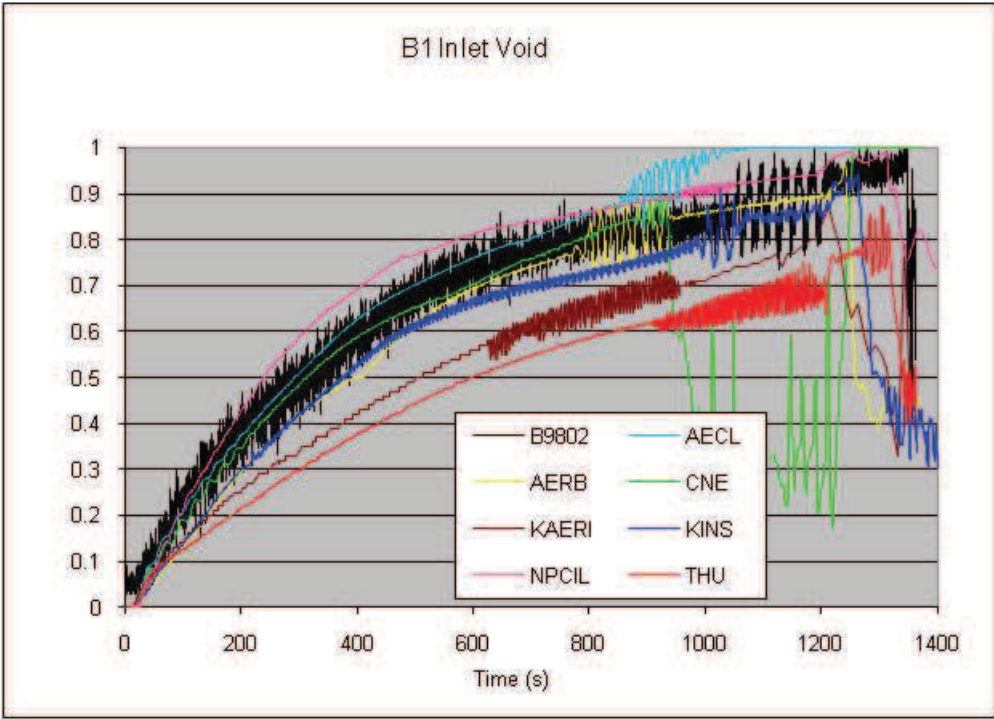


FIG. 4-144. Boiler BO1 inlet void.

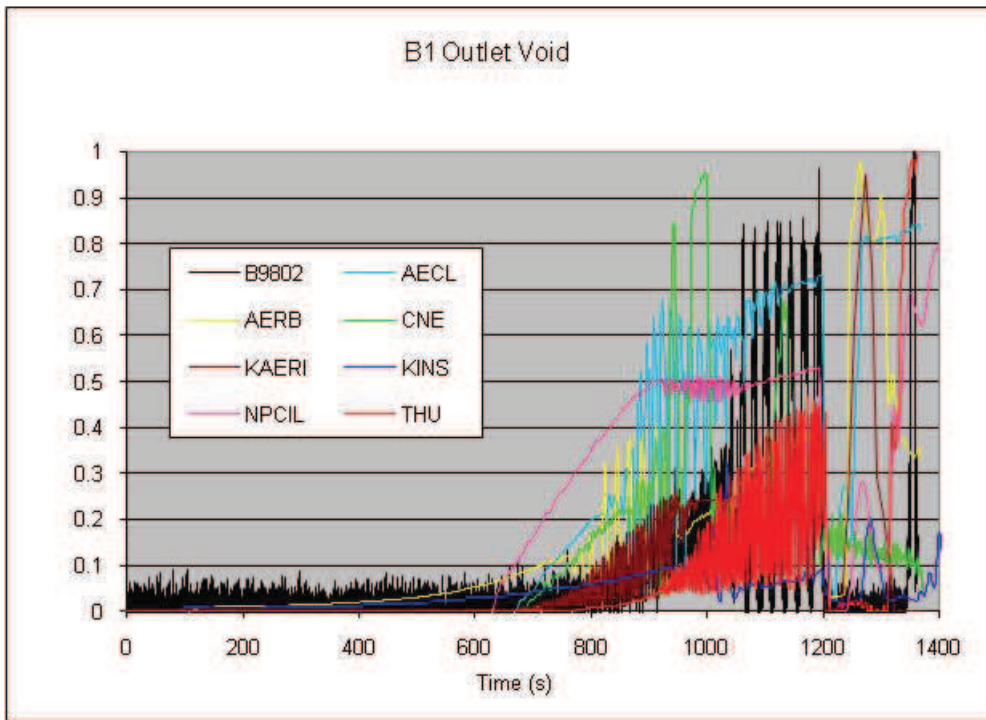


FIG. 4-145. Boiler BO1 outlet void.

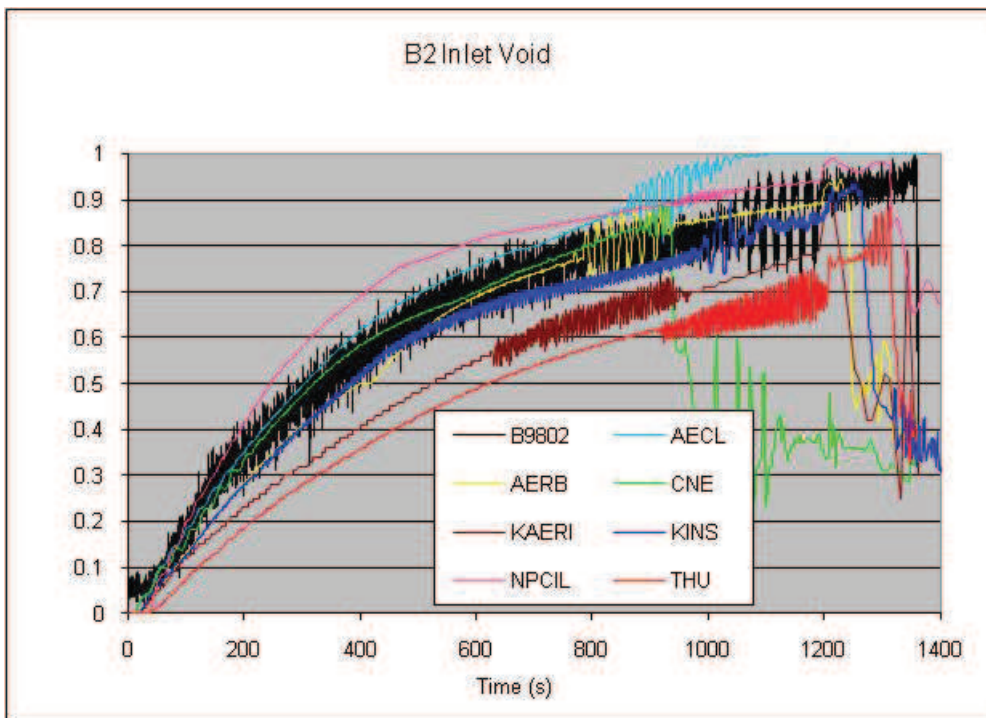


FIG. 4-146. Boiler BO2 inlet void.

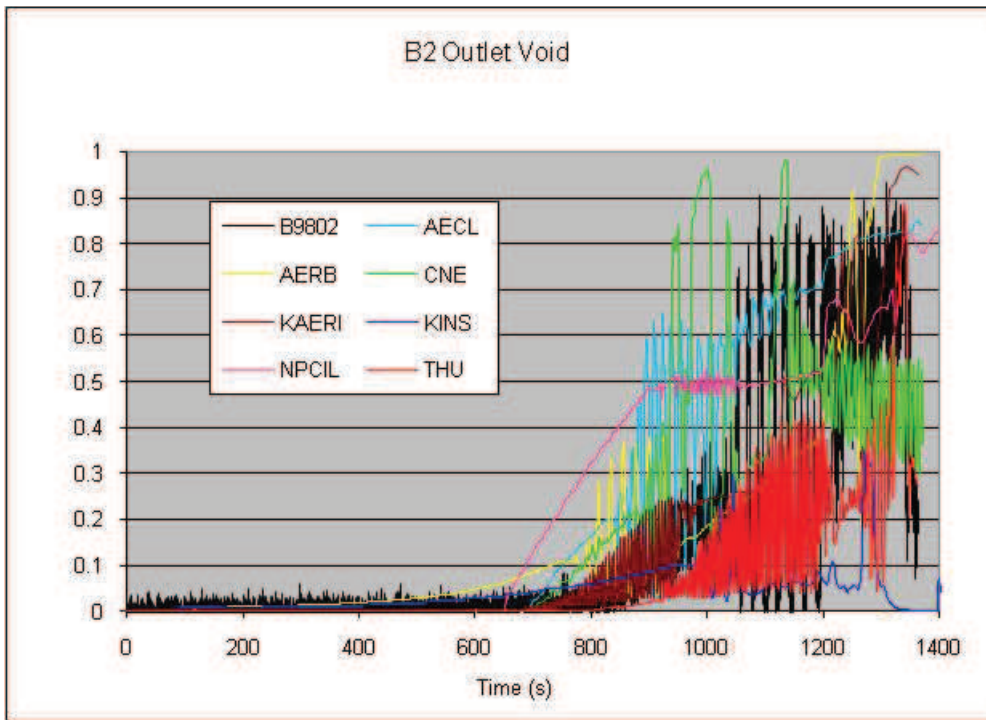


FIG. 4-147. Boiler BO2 outlet void.

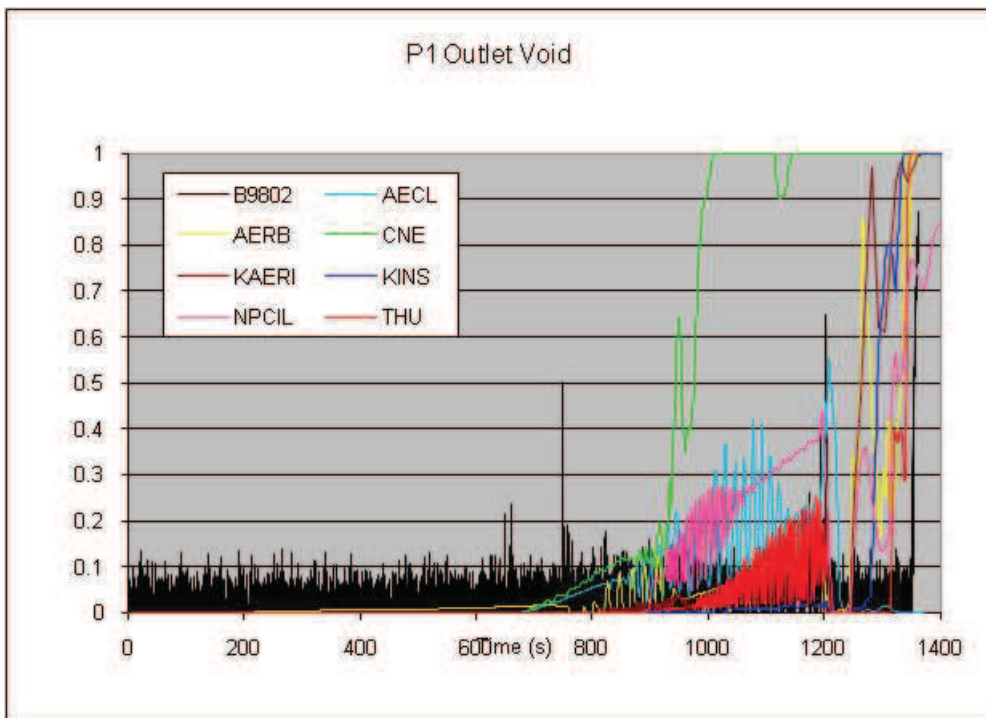


FIG. 4-148. Pump P1 outlet void.

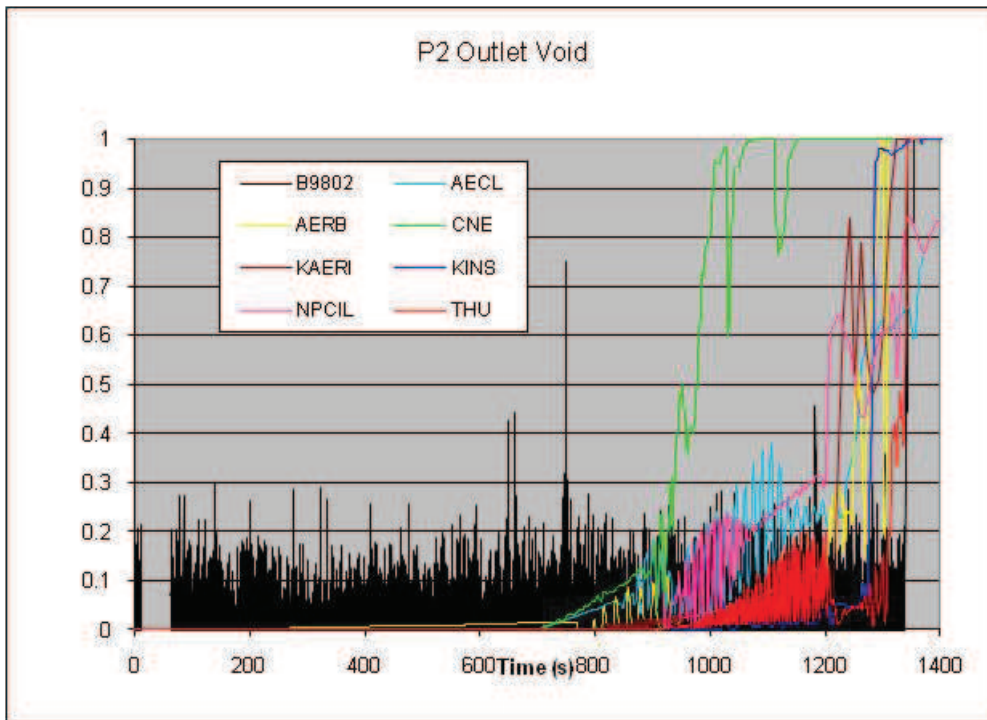


FIG. 4-149. Pump P2 outlet void.

4.6.7 Boiler inlet and outlet fluid temperatures

Boiler inlet and outlet fluid temperatures provide local fluid temperature measurements in the primary loop and can be used as confirmatory data for simulations. They provide information about heat removal capability of the boilers during the experiment.

Figures 4–150 to 4–153 provide the code comparison to experiment. All calculations show the correct experimental trend with different degrees of accuracy. Since the pumps continue to operate, forcing flow throughout the loop in the “forward” direction, the temperature difference from the boiler inlet to outlet indicates that both boilers continue to remove heat throughout the transient. The boiler inlet temperature closely follows the saturation temperature (which decreases with the slowly decreasing loop pressure), while the outlet temperatures reflect the boiler heat sink temperature, at least during the single-phase period. Oscillatory temperature behaviour is observed in the experiment and calculated by all participants during the time when the boilers no longer fully condense the steam in the boiler tubes.

In general, both boilers behave similar.

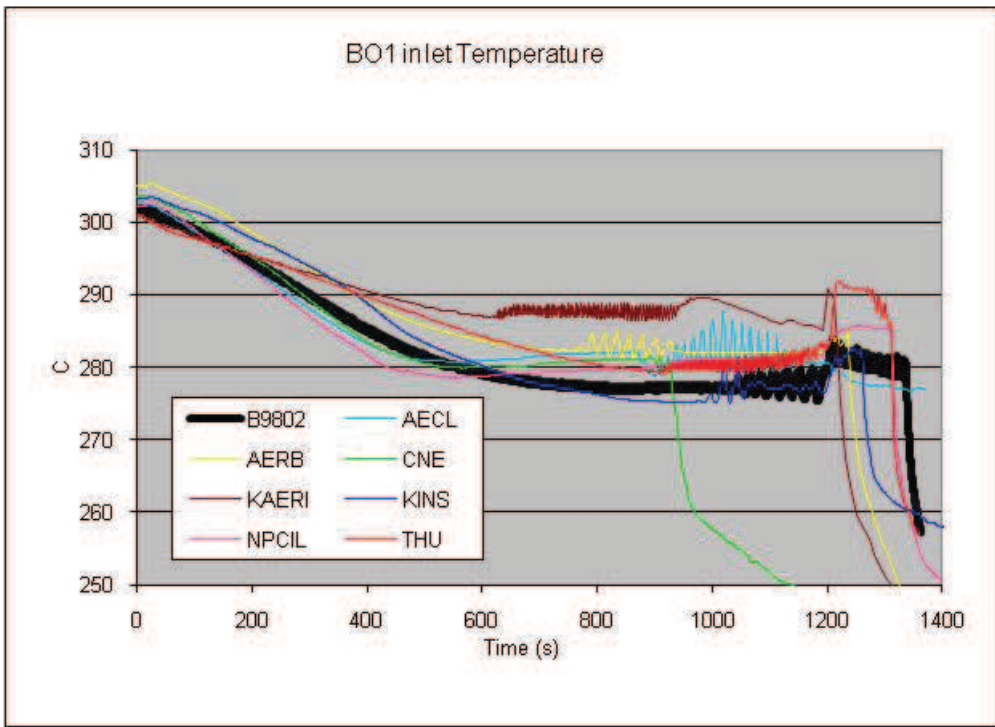


FIG. 4-150. Boiler BO1 Inlet temperature.

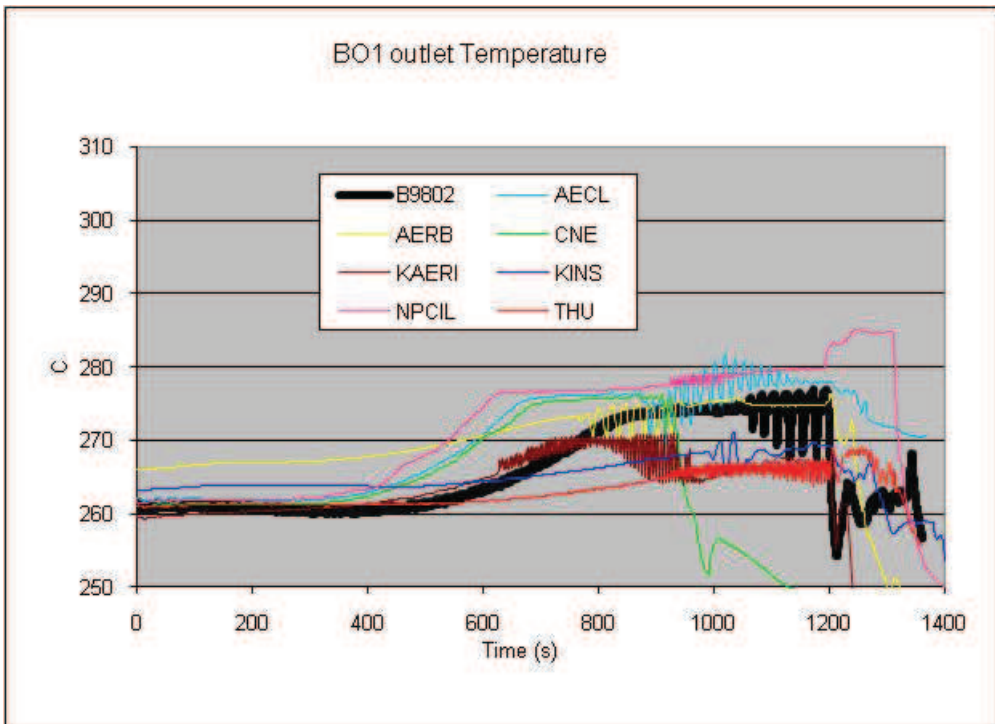


FIG. 4-151. Boiler BO1 outlet temperature.

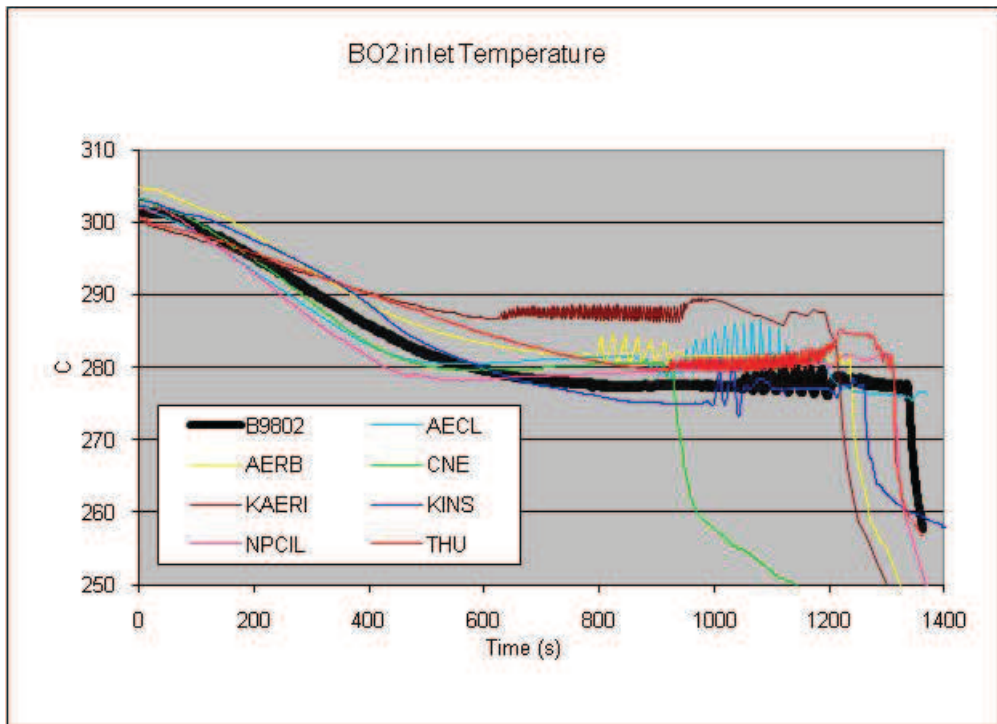


FIG. 4-152. Boiler BO2 inlet temperature.

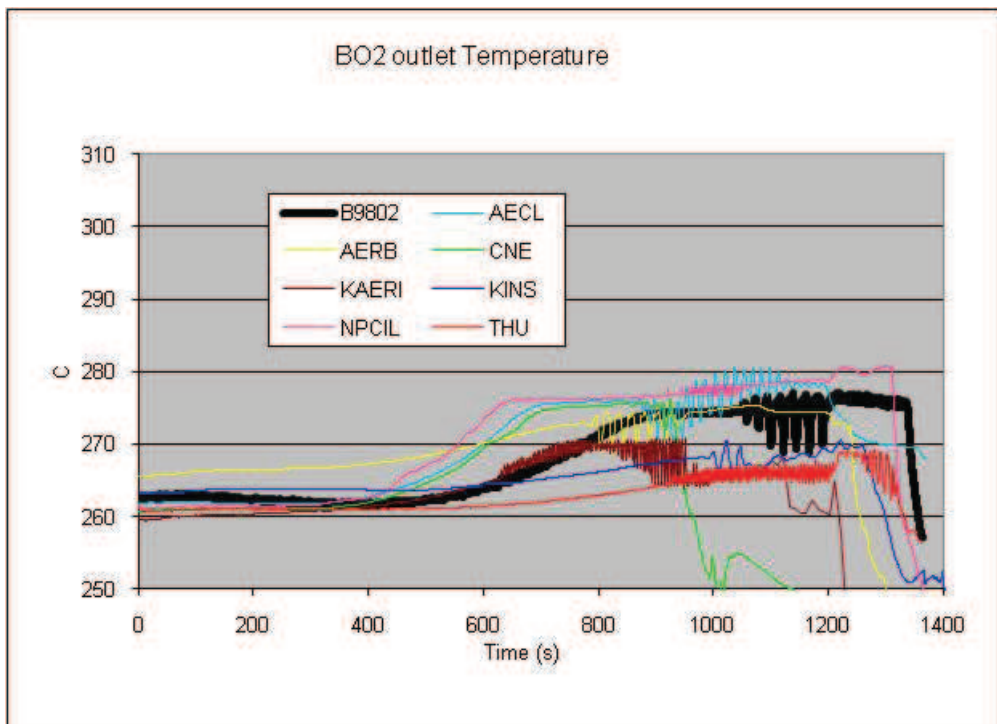


FIG. 4-153. Boiler BO2 outlet temperature.

4.6.8 FES sheath temperatures in heated sections HS8 and HS13

The maximum FES sheath temperature is often the most significant parameter in safety analyses. In test B9802, high FES sheath temperatures were measured in the high power channel of the broken pass, heated section HS13 and to a lesser degree in the high power channel of the intact pass. The maximum temperature actually occurred in heated section HS12, a slightly lower-powered channel at a higher elevation, which cause the power trip when it reached ~ 640 °C near the inlet end. Both the top and bottom FES near the outlet of HS13 experienced significant heatup, reaching almost 600°C during the test on the top. The center and inlet regions also showed temperature excursions, but with lower peaks.

Figure 4–154 shows the center temperature in HS8 (intact pass high-powered channel) while figs 4–155 to 4–158 show inlet, center, and outlet FES temperatures in HS13, a high-powered channel in the broken pass.

All participants predicted a significant sustained (i.e. not oscillating) heatup near the outlet of HS13 at approximately the right time, but AECL and CNE at about 300s prior. CNE and AECL predict the earlier power trip due to temperatures in HS13 center (CNE) and inlet (AECL) reaching 600 °C. In the test, the top FES near outlet heated up first and eventually was much hotter than the center or inlet.

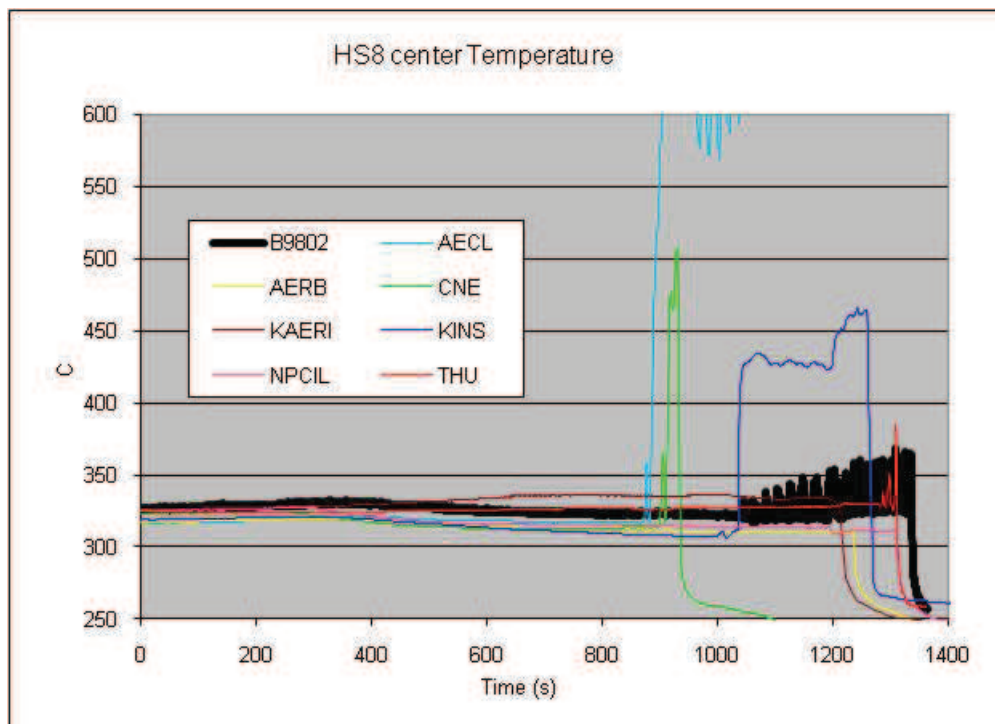


FIG. 4-154. Heated section HS8 center temperature.

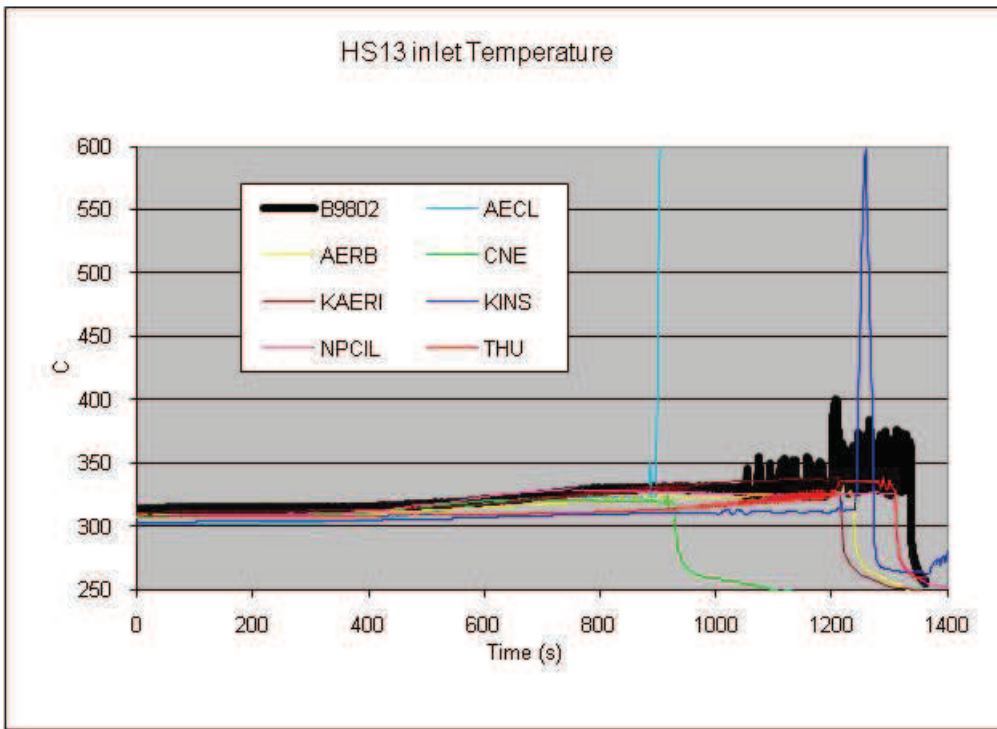


FIG 4-155. Heated section HS13 inlet temperature.

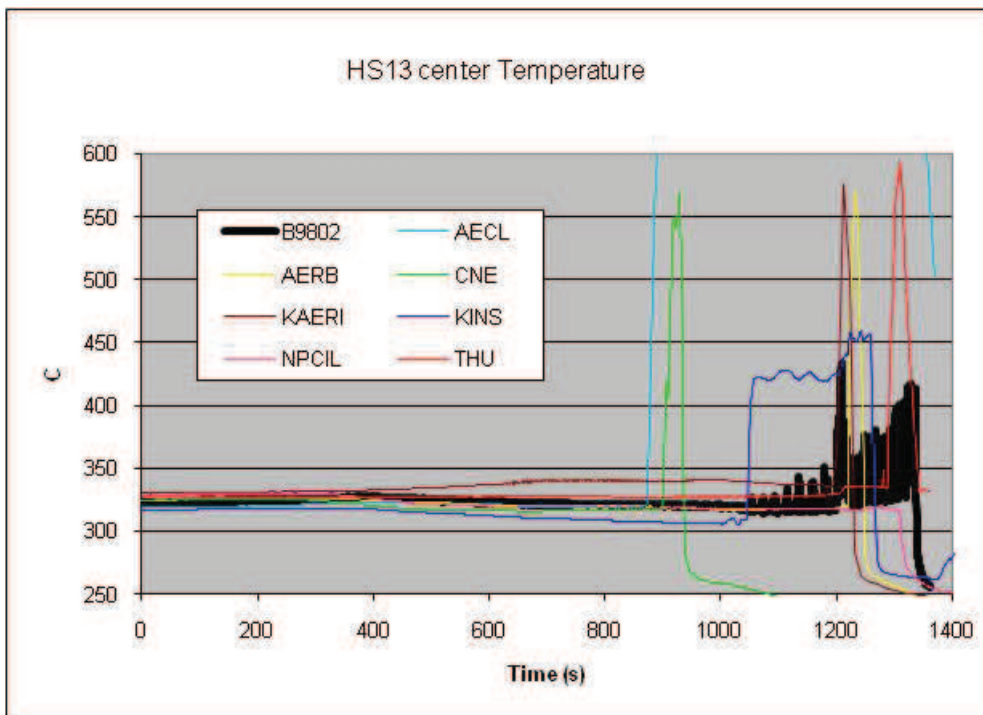


FIG. 4-156. Heated section HS13 center temperature.

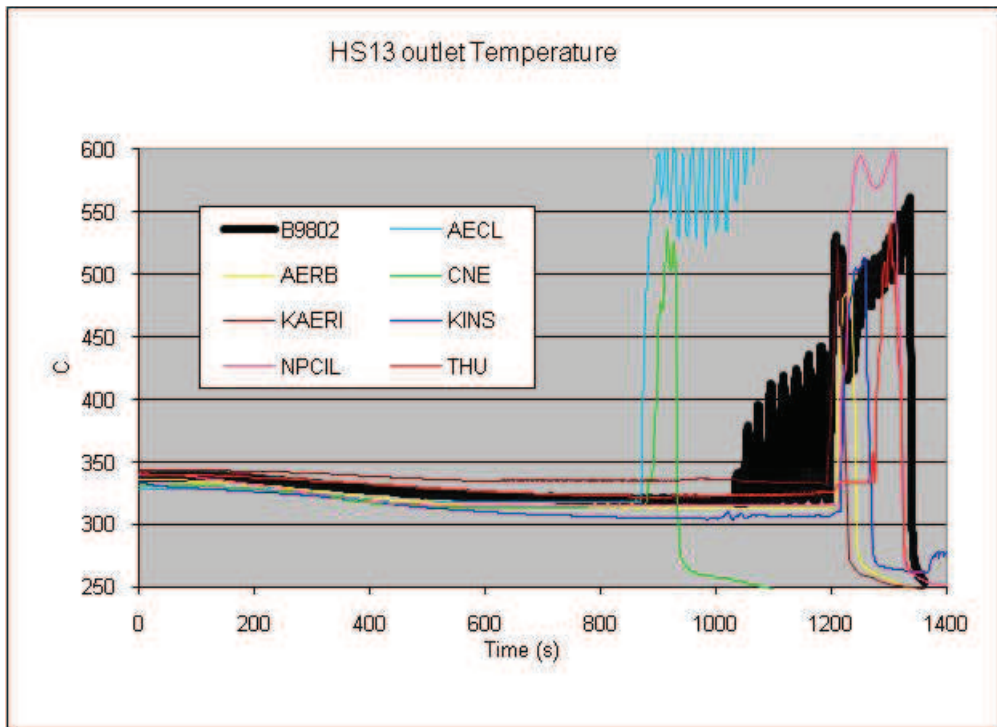


FIG. 4-157. Heated section HS13 outlet temperature (Top FES).

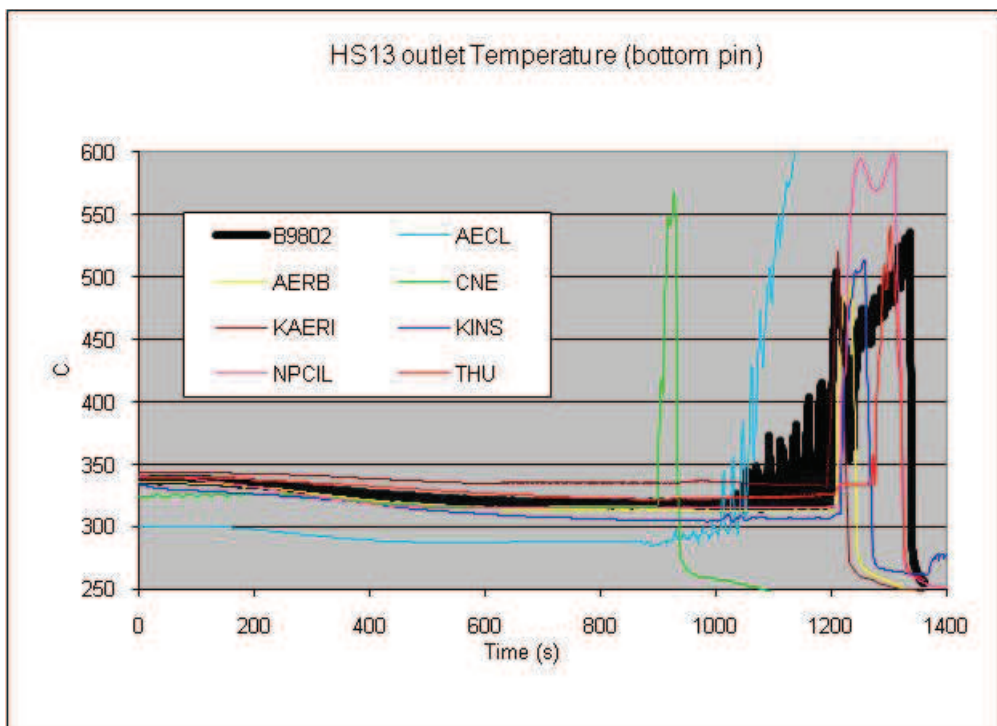


FIG.4-158. Heated section HS13 outlet temperature (Bottom FES).

4.6.9 Flow rates in heated section HS 5, 8, 10 and 13

All heated section flow rates follow the same trend as dictated by the header-to-header pressure differences, discussed earlier. They are shown below in Figs 4–159 to 4–162, for completeness.

Note that the experimentally measured volumetric flow rate has been converted to a mass flow rate by using the boiler outlet temperature to calculate the liquid density.

4.6.10 Inlet and outlet void in heated section HS 5, 8, 10 and 13

Channel inlet and outlet void fractions were measured approximately 2 m upstream and downstream of the heated section end in the inlet and outlet feeders.

Voiding occurred in all outlet feeders almost immediately into the transient, slowly reaching 80-90% void and at the onset of the oscillations. The inlet feeders of channels in the intact pass remained liquid-filled throughout the transient. When pump P1 tripped, outlet void in both passes reaches almost 1 due to the decrease in overall loop flow rate. Outlet void drops in all channels immediately following the power trip at 1340s, as pump P2 remains operational.

Note, that the boiler secondary side depressurizes and feedwater is shut at the same time ($t=1340s$) resulting in the boilers becoming ineffective in condensation. Therefore, the void is transported down the inlet feeders of the broken pass (HS10 and 13) by the pump P2, which is still operating.

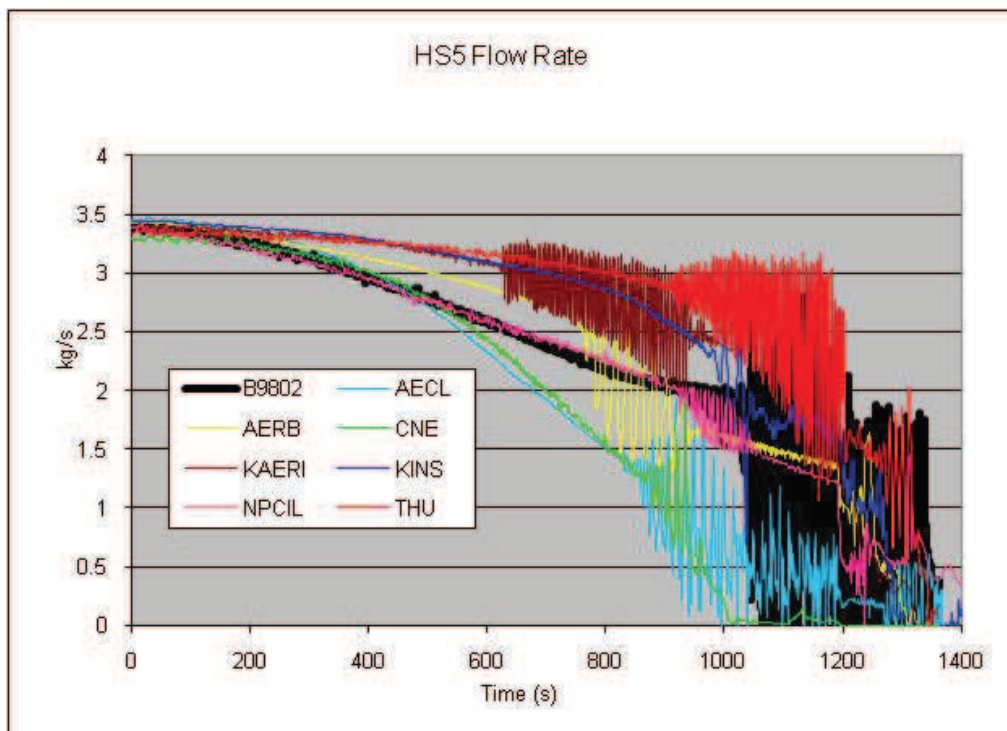


FIG. 4–159. Flow through heated section HS5 (low power, intact pass).

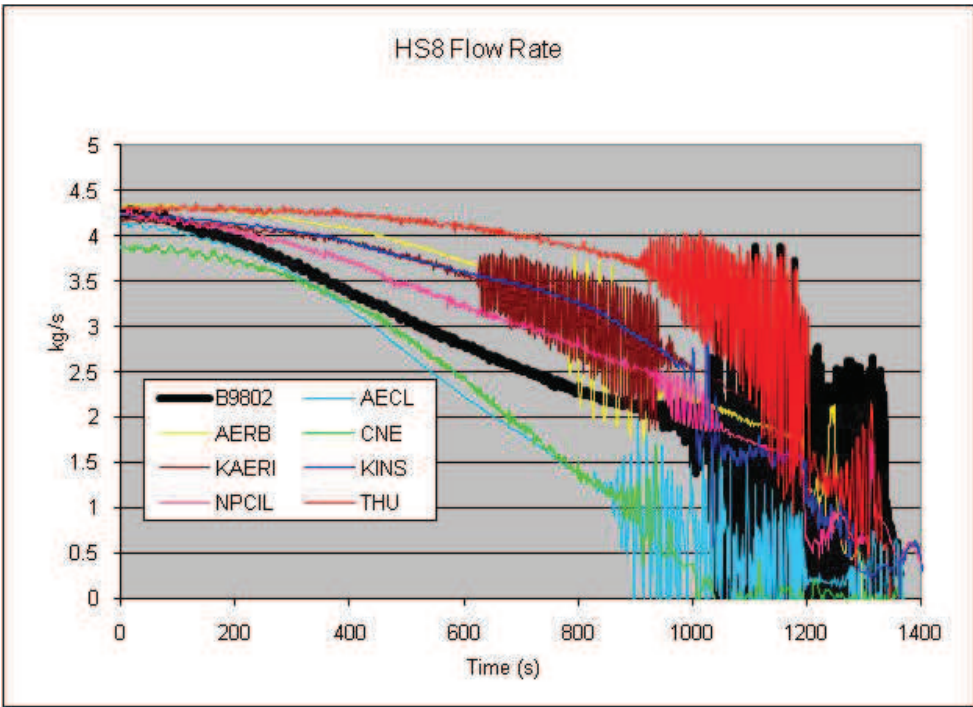


FIG. 4-160. Flow through heated section HS8 (high power, intact pass).

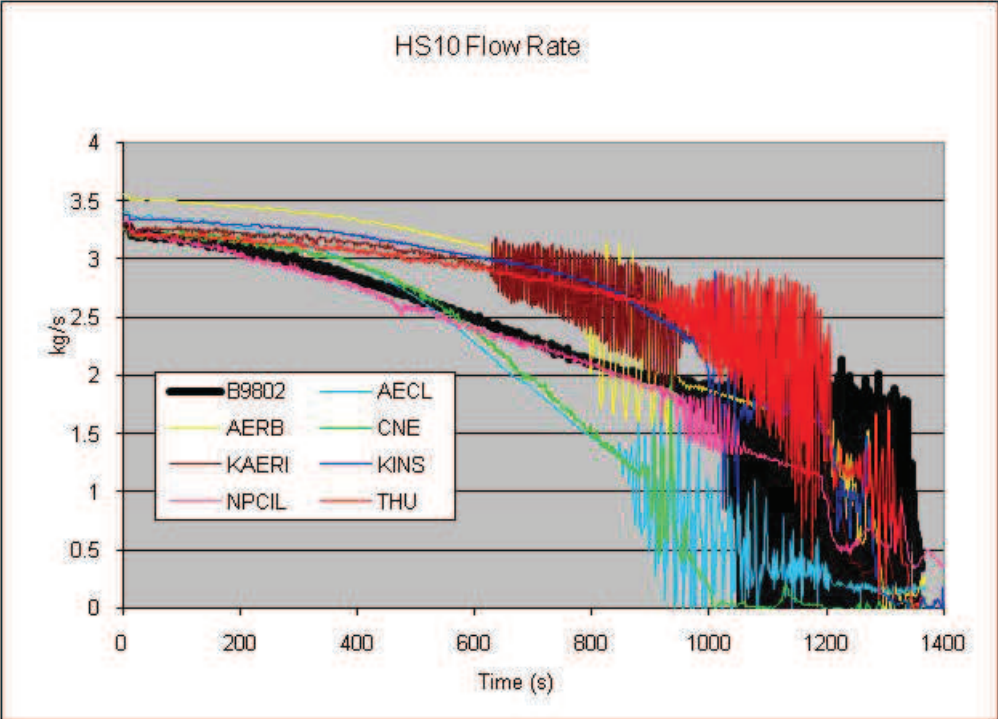


FIG. 4-161. Flow through heated section HS10 (low power, broken pass).

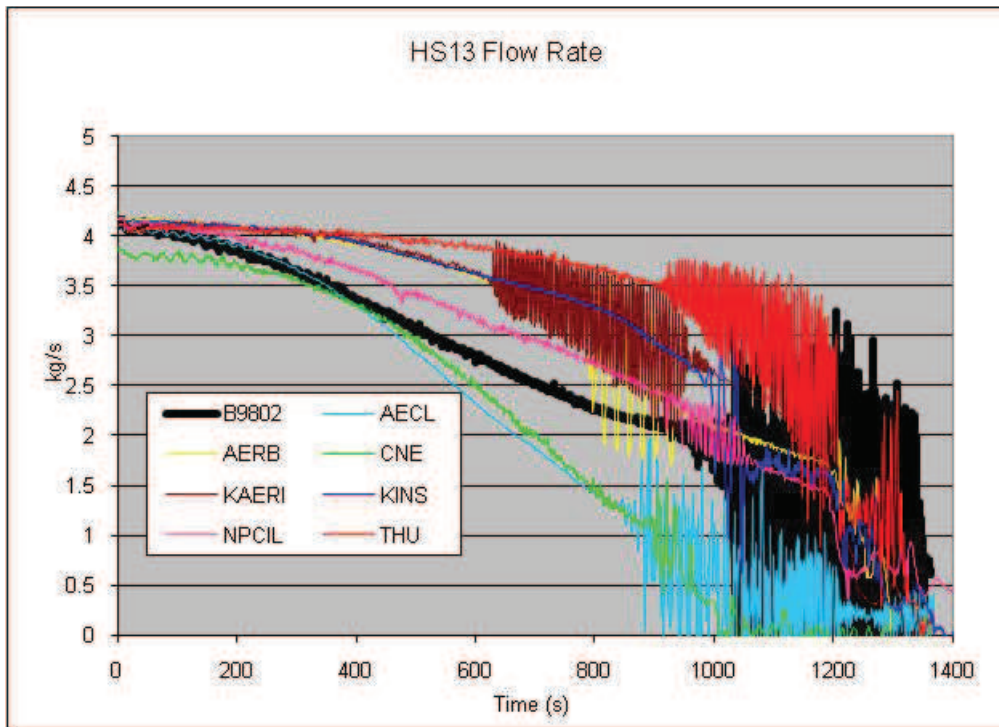


FIG. 4-162. Flow through heated section HS13 (high power, broken pass).

Figures 4-163 to 4-170 show the experimental measurements and code predictions. Most simulations correctly calculate the void in the feeders, at least until the onset of significant FES heatup.

Such good agreement can be expected due to the well-defined flow direction and slow progression of this transient test. THU calculates a significant delay in initial void generation in HS8, caused by the small discharge coefficient 0.23, which was selected to match the discharge flow. With a larger discharge coefficient of 0.51, there is no delay in the void of HS8 outlet.

Early prediction of inlet feeder void by CNE is caused by the early trip, which shuts off the FES power, thus allowing void to escape through the inlet feeders while the channels see a reversed refilling. In the case of NPCIL the void is coming from the boiler outlets.

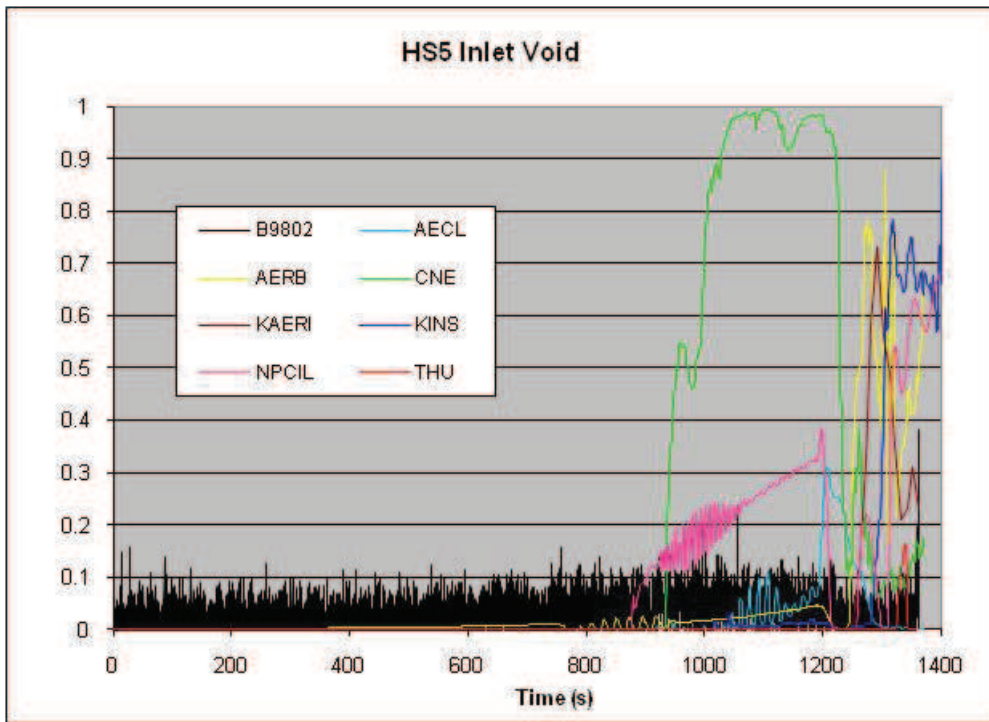


FIG. 4-163. Heated section HS5 inlet void.

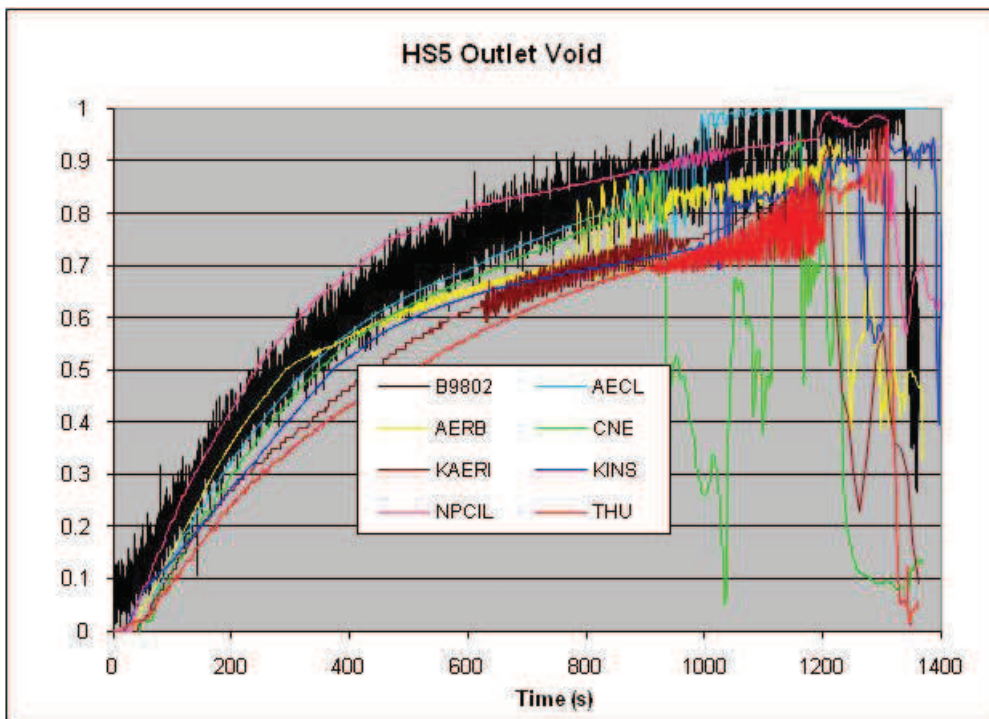


FIG. 4-164. Heated section HS5 outlet void.

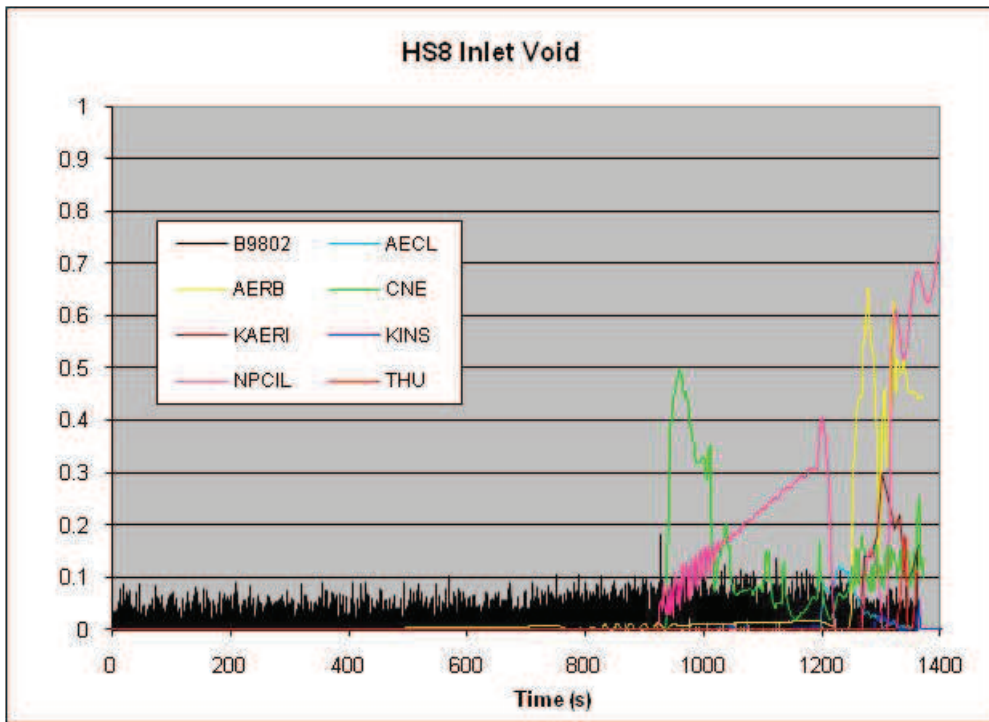


FIG. 4-165. Heated section HS8 inlet void.

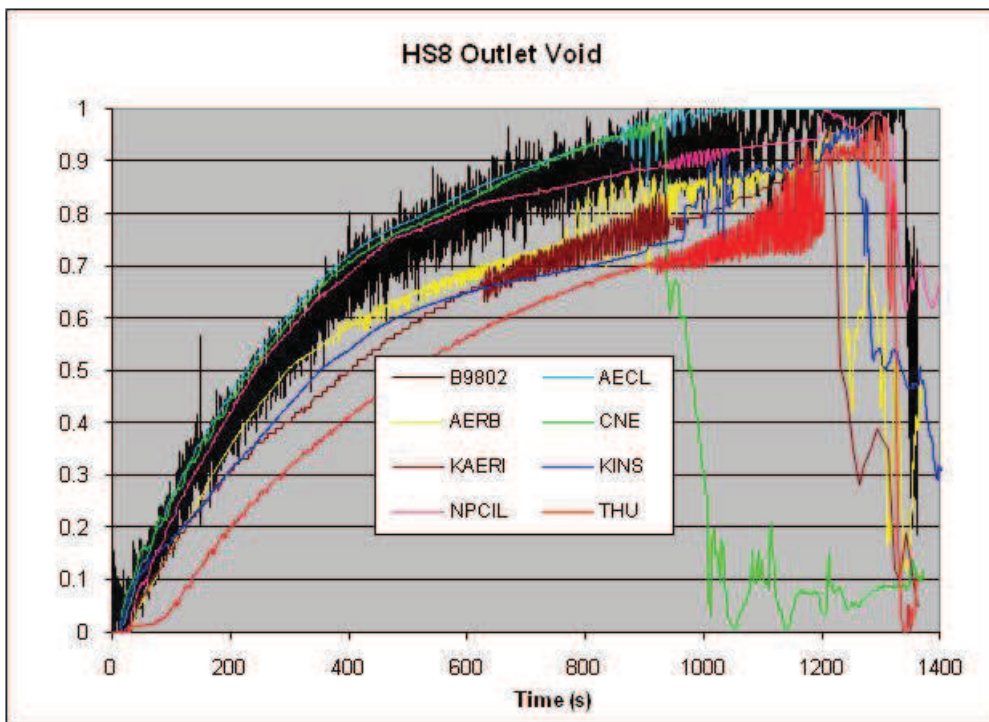


FIG. 4-166. Heated section HS8 outlet void.

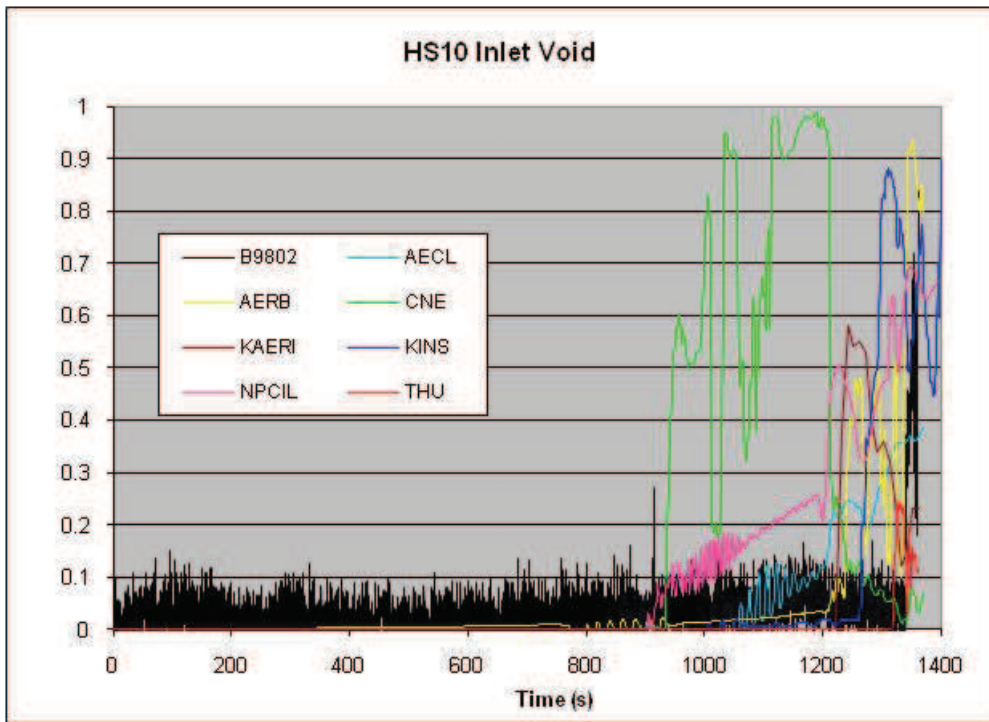


FIG. 4-167. Heated section HS10 inlet void.

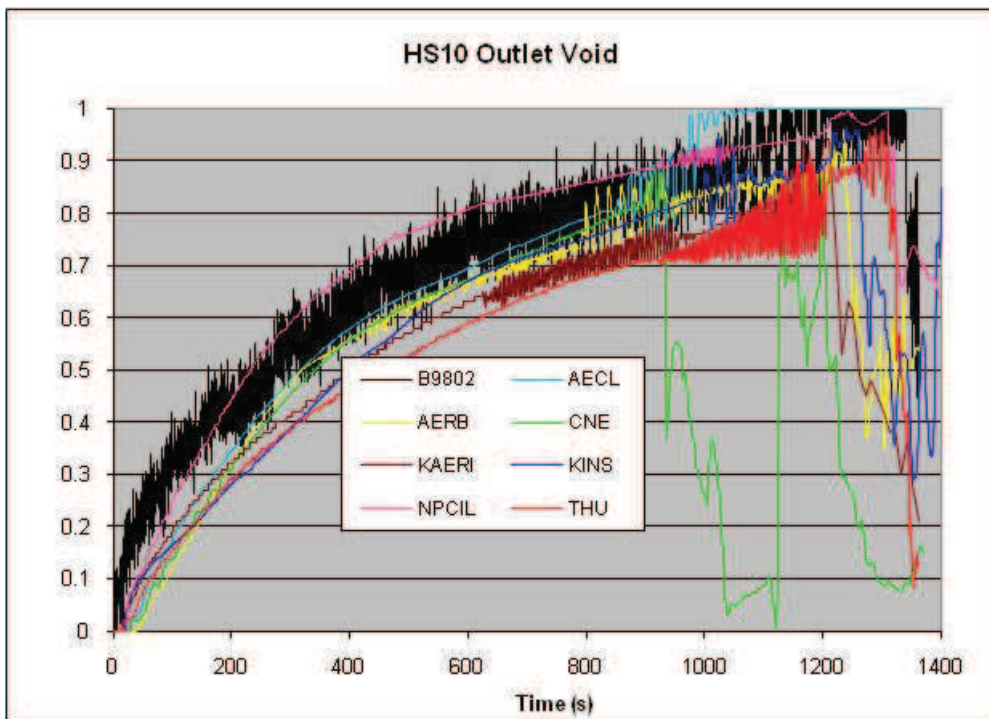


FIG. 4-168. Heated section HS10 outlet void.

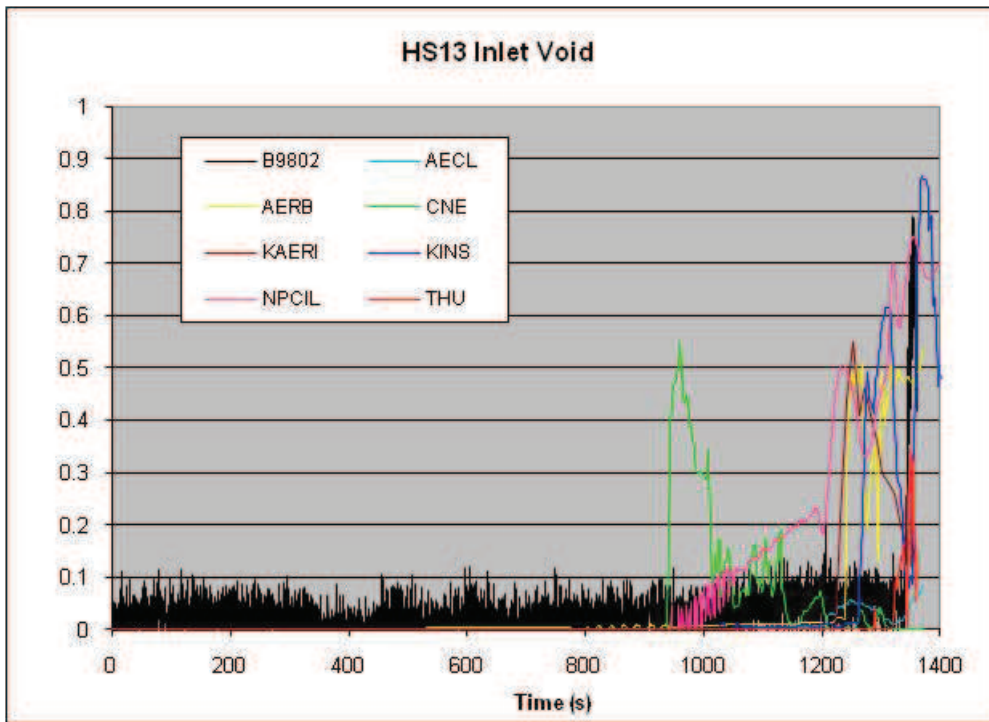


FIG. 4-169. Heated section HS13 inlet void.

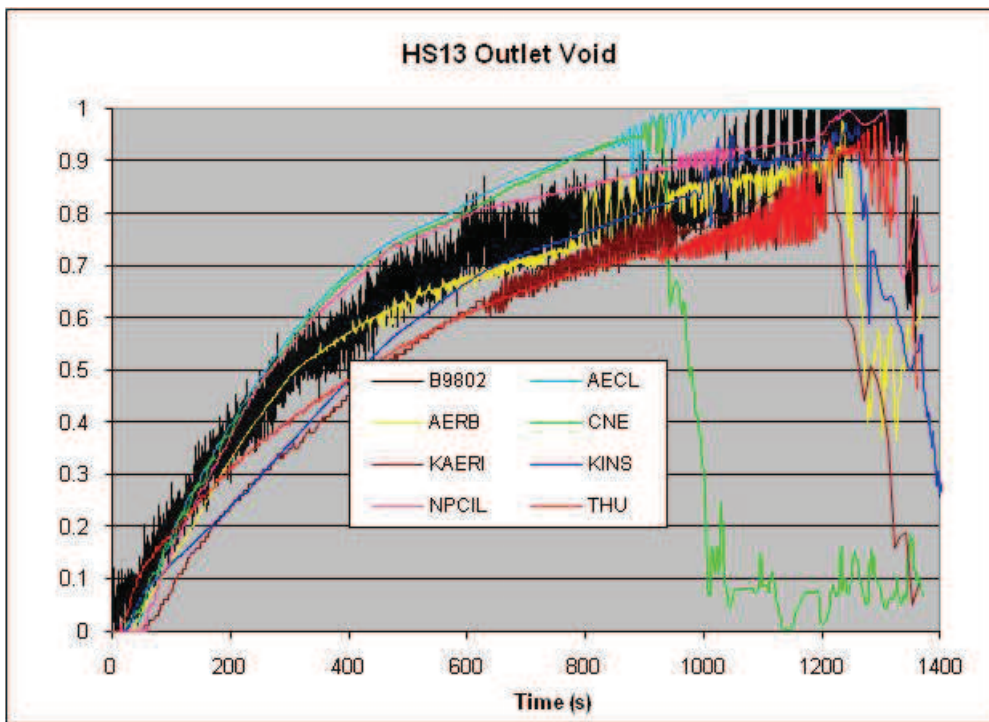


FIG. 4-170. Heated section HS13 outlet void.

4.6.11 Pressure drop along the outlet feeder from HS13 to HDR5

This parameter was discussed in detail in the blind calculation comparison earlier. Other than changes in timing of the maximum, or of oscillations, the open calculations did not improve in the prediction of the pressure difference between HS13 and HDR5, as shown in Fig.4-171.

THU predicts significantly lower initial and transient values than in their blind calculations, due to adjustments in the feeder losses.

4.6.12 Snapshot of pressure, temperature and void fraction

Data of local pressure, temperature, and void are presented as a function of axial location around the figure-of-eight loop of the RD-14M facility, starting at the outlet of pump P1. The total loop length through the longest inlet-feeder/header-section/outlet-feeder paths is 167m.

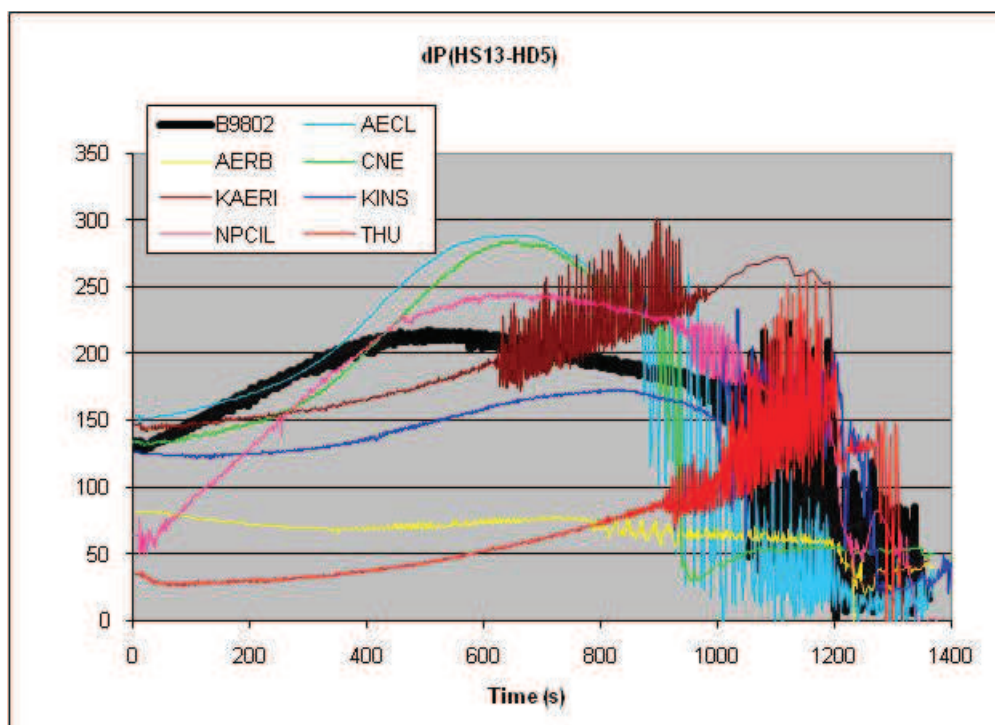


FIG. 4-171. Heated section HS13 to header HDR5 pressure drop.

Figures presented below show an example (AECL pressure, temperature and void calculation of test B9802 at time $t=400s$) and illustrates the locations of major components, i.e. the pumps, headers and boilers. As can be seen, the five parallel paths (of various lengths), representing the five channels in each pass are less defined than in the previous test. However, the effect of gravitational head is clearly evident (the highest pressures are in the lowest heated sections, and the lowest are in the top part of the boiler tubes), pressure drops are significant across the horizontal heated sections, and pressure losses along the loop balance the pressure difference across the pumps. Appendix II shows snapshots of pressure, temperature and void around the loop for three different times (in the test) from all participants.

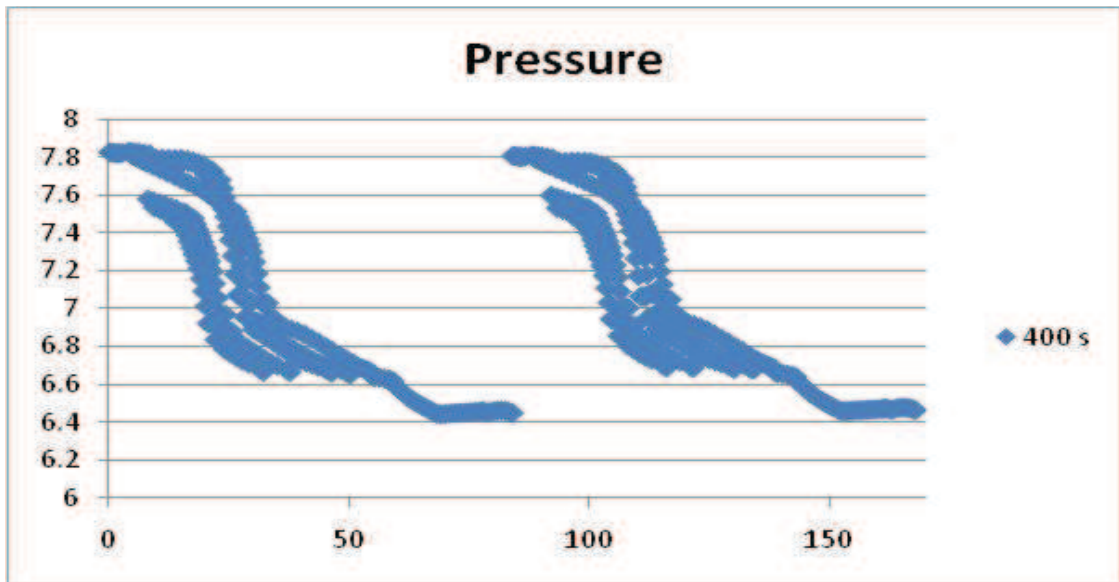


FIG. 4-172. Sample "Snapshot" illustrating locations of major components. (AECL calculation of pressure during test B9802 at 400s).

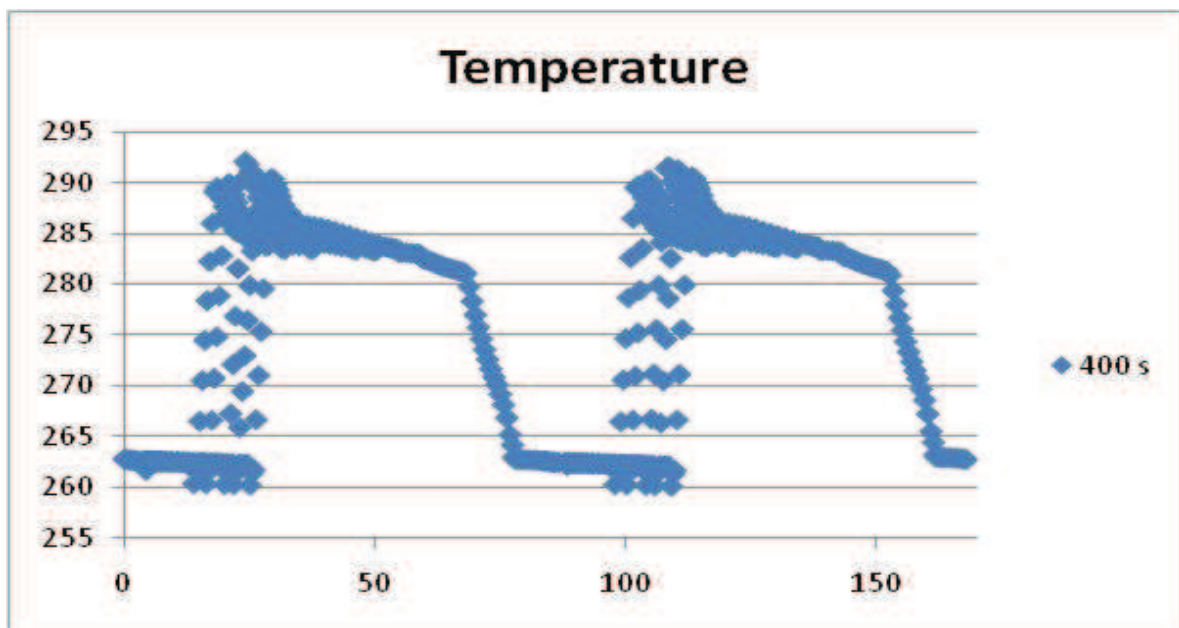


FIG. 4-173. Corresponding temperature "Snapshot" to Fig. 4-190.

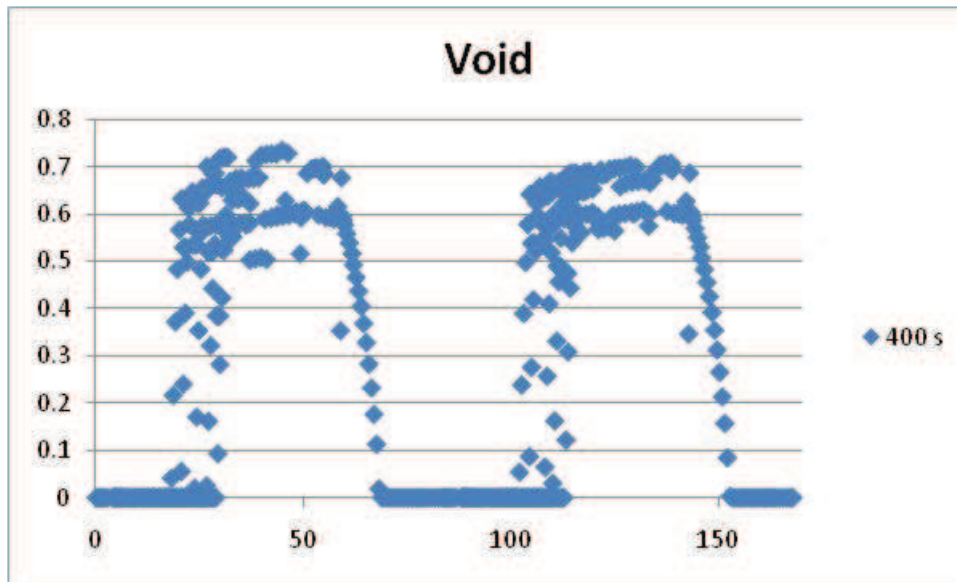


FIG.4-174 Corresponding void “Snapshot” to Fig. 4-190.

5 LESSONS LEARNED FROM ICSP

The Benchmark exercise “ICSP on code comparison for HWR” offered a constructive platform giving unique opportunity to code developers/experts and experimentalists to jointly verify and validate their thermal-hydraulic codes. The direct technical interaction among experts was helpful to improve/enhance understanding of important thermal hydraulic phenomena observed in a parallel channel facility under Small Break LOCA transients. The experience gained during participation has been fruitful in identifying code strength and areas requiring improvement. The lesson learned from participation in the IAEA-ICSP blind as well as open calculation in various important areas that are generic in nature, such as user effects, code deficiencies and need for capability improvement, experimental considerations and ICSP specification, are highlighted below.

5.1 USER EFFECTS

User effects were evident in a few isolated instances and explained some of the difference in the results obtained with the various codes. User qualification is necessary in the areas of modeling of experimental facilities and representation and interpretation of experimental data, which greatly influence the selection of a modeling scheme and subsequent simulation of the transient. There were no fundamental differences in the adopted nodalization schemes, except that some users employed rather coarse nodalizations. It is noted that the comparison between code results and test data is simplified and improved if instrument location is given due consideration in the nodalization of the entire facility. The following user options resulted in noticeable differences in predicted behaviour:

- Significant differences in ECC system modelling (valve logic, flow resistances, ECC tank model and/or pressure boundary condition), especially during the blind calculations, were responsible for significant differences in the code predictions of loop pressure and refill behaviour. An accurate representation of the ECI systems is necessary to correctly predict the coolant distribution among the various headers and subsequently the coolant distribution into the channels;

- PHTS pump characteristics play an important role and influence in the prediction of pump head under degraded conditions, affecting coolant flow and subsequent FES heatup;
- Significant differences in discharge modelling were responsible for significant differences in the code predictions of loop pressure and refill behaviour;
- Grouping of FES within channels, to allow temperature stratification, resulted in some participants replicating short periods of temperature stratification, although they were overpredicted. In fact, those that did not allow stratification (e.g. by lumping all heated FES into one group) predicted FES temperatures closer to those measured, because any stratification in the experiments were small and of short duration.

The following general areas were also deemed important in obtaining acceptable results:

- Experience in the application of the code to test facilities: All codes have numerous user-selectable options and the quality of the results strongly depends on the choice of the appropriate models and model parameters. Available documentation and guidelines for specific options should be followed;
- Familiarity with the facility: This was mostly helped by the facility visit during the second meeting, and the interaction with facility operations staff;
- Availability of a reference input file increased confidence that the nodalization was adequate (only CATHENA reference files were available to, and used by, AECL and KAERI). However, the use of a reference file discouraged fine-tuning of the feeder flow resistances and resulted in generally poorer agreement of the flow split among channels of the same pass during steady-state and transients.

5.2 CODE DEFICIENCIES AND NEED FOR CAPABILITY IMPROVEMENT

All codes were able to replicate important phenomena, which are generally considered challenging during simulation of Small Break Loss Of Coolant Accident (SBLOCA) scenarios, namely:

- Two-phase pressure drop, provided the pump degradation is well captured;
- Low flows and flow reversal in parallel channels, however, the quality of agreement is strongly dependent on matching steady-state flow distribution;
- Loop refill as a result of ECC injection (at varying times);
- Timing of LPECC start;
- Channel voiding;
- Condensation in boilers (steam generators), although using the appropriate condensation model is important;
- FES dryout.

All codes experienced difficulties in the following areas (B9802):

- Precise matching of break discharge flow rate, even with tuning of discharge models;
- Dryout/rewet cycles, prior to Post Dry-Out (PDO) heat transfer, in the channels;

- Slow heatup in PDO regime (only achieved by tuning the developing PDO model in one case).

Sensitivity cases for the blind calculation phase were well chosen for the two tests and generally showed expected trends and no surprises or very large changes in important code results. Some participants performed additional sensitivity cases on code models (e.g. liquid discharge coefficient) and test parameters (e.g. heater power, pump speed) as part of the open calculation phase and while results could be improved slightly, a perfect match to all measured parameters could not be obtained. This indicates that (1) the codes are robust and the “best-estimate” assumptions give acceptable results which can only be slightly improved by further tuning, however, also (2) that there still remain some code deficiencies.

TABLE 5-1. SUMMARY ON CODE DEFICIENCIES AND CAPABILITIES

Phenomena	Experiments		System codes			
	B9006	B9802	Cathena	Relap5	Mars	Atmika
Break discharge characteristics and critical flow	o	+	+	+	+	+
Coolant voiding	+	+	o	o	+	o
Phase separation	o	o	+	o	+	o
Single phase pressure drop	+	+	+	+	+	+
Two phase pressure drop	+	+	+	+	o	+
PHT Pump characteristics	o	o	+	+	+	+
Convective heat transfer	o	o	o	o	+	+
Nucleate boiling	o	o	+	o	+	+
Dryout behaviour	o	+	o	+	o	+
Condensation heat transfer	o	+	+	+	+	+
Core flow distribution	+	+	o	+	o	+
Natural circulation	+	-	+	+	+	+

Experiments:

- + well defined
- o occurring but not well characterized
- not occurring or not measured

System codes:

- + predicted with accuracy
- o qualitatively predicted
- not predicted
- x not applicable

5.3 EXPERIMENTAL CONSIDERATIONS AND ICSP SPECIFICATION

During the initial phase of this ICSP some facility parameters, test boundary conditions, and measurement techniques were unclear. Through discussion and code “experimentation” it became clear that the following are very important considerations when specifying such a SBLOCA comparison exercise:

- Exact physical description and operation of ECC system and secondary side;
- PHTS pump characteristics;

- Factors affecting differential pressure measurements, in particular those spanning a significant elevation difference;
- Unambiguous units for pressure measurements (MPa(a) or MPa(g)) and pressure-related trip setpoints and logic;
- Calibration, accuracy limits, and uncertainty of void meters and flow meters;
- Timing (including instrument delays) of power and pump rundowns and other trips, such as valve open and close times;
- Correct implementation of boundary conditions.

Sensitivity studies indicate that a significantly lower liquid discharge coefficient (compared to the default in all codes) is appropriate for this break geometry used in RD-14M SBLOCA tests. Critical flow model selection as well as 2-phase or gas discharge coefficients had small effects.

6 CONCLUSIONS AND RECOMMENDATIONS

The activity documented in this report deals with small break LOCA analysis in an HWR system. The reference experiments were performed in the RD-14M test loop located at the AECL Whiteshell Laboratories in Pinawa, Manitoba. This is the second international code to experiment comparison exercise of this type in an HWR system and was made possible, within the framework of an IAEA project, by the availability of experimental data from AECL. The activity required significant resources from all participants and from the host institution (AECL, Chalk River) and was carried out in a manner similar to an ISP (International Standard Problem within the OECD/CSNI framework).

Different insight into SBLOCA behaviour and code capabilities were gained from each of the two tests of this ICSP. All calculations were capable of achieving steady state conditions consistent with the experimental data apart from deviations in flow distribution among the individual parallel channels in each pass where no effort was made to tune the feeder hydraulic resistances. The transient pressure, temperature and void development in both tests were strongly influenced by the transient loop inventory.

The first test, B9006, included all phases of a typical SBLOCA scenario: blowdown through a 7 mm break (a scaled reactor feeder break), power and primary pump rundown, boiler depressurization, and high- and low-pressure ECC injection. In this test the modelling of the ECC system was the determining factor in calculating the correct loop temperatures and refill behaviour. Overprediction in ECC flowrates caused faster depressurization and early refill times. The experiment clearly showed ECC flowrates which slowly increased throughout the HPECC injection phase, while some calculations showed the opposite trend, namely an initially high injection rate, which slowly decreases with time. Different modelling strategies were evident in applying different boundary conditions to simulate the ECC system. Prediction of parameters in the loop could be improved by imposing the ECC flowrates as boundary conditions; however, this was not done as a sensitivity case, because modelling of the ECC system was part of the scope of this exercise. The need for accurate boundary and initial conditions became clear in the analysis of this experiment. An accurate representation of the ECI systems is necessary to correctly predict the fluid split among the various headers and consequently the fluid distribution into the system and subsequent establishment of bidirectional flow in the parallel channel geometry.

Correct void predictions throughout the loop were initially believed to be critical in predicting other safety- or trip-related parameters, such as header pressure and FES temperatures. However, this exercise showed that, while there was a very large scatter in the timing of voiding and refill in various loop locations (namely boiler plenums and pumps), as well as in the levels of void calculated at various phases of the transient, the overall pressure and temperature response was calculated quite accurately, with very few exceptions. Since there were no significant FES temperature excursions observed or calculated (due to the relatively low heater powers), even differences in the prediction of flow direction in the channels (including flow stagnation and reversal) did not generate large differences in overall loop behaviour. Short periods of mild temperature stratification within a channel (in the order of 10 s duration and 20-30°C magnitude) were observed and predicted (at different times and with different, usually higher, magnitude) by CATHENA simulations that allowed flow stratification and had different FES groups (upper, middle and bottom). Prediction of flow stratification is dependent on code capability, user options and nodalisation. Again, the void predictions at the channel ends showed a much higher scatter and deviation from measurements.

Flow reversal of significant flow rate and duration was observed predominantly in the high-elevation, low-powered channels in both passes (HS5/10), and also in the middle-elevation channels (HS12/13) of the broken pass. During significant reverse flow, heat removal is effective, but inlet header temperatures stabilize at a higher value, therefore, increasing inlet temperature of forward-flowing channels. This phenomenon accounted for some of the differences in FES temperature predictions. The significant differences in transient flowrates through the heated sections are noteworthy. It was evident in the code comparison that those participants, who tuned the steady-state feeder hydraulic resistances to match experimental flowrate distribution among channels, were better able to reproduce the observed flow reversal behaviour during the transient. Also, small changes in feeder resistance could result in different channels experiencing flow reversal. As compared to a LBLOCA simulation, however, FES temperatures are less sensitive to variations in the feeder loss coefficients.

Test B9802 was a smaller (3-mm) break without ECC injection or pump, power or boiler-pressure ramps and was not intended to be representative of any accident scenario, although it does represent qualitatively the expected behaviour in a “blind SBLOCA”. The test was an extreme case, simulating ignoring of reactor trips, which would have terminated it earlier, and therefore allowing almost full channel voiding. The key phenomena in this test were void generation through boiling in the channels (initially nucleate boiling, later PDO heat transfer) and steam condensation in the boiler tubes. An important feature of this test was the direct measurement of the break flow rate.

In this test the prediction of the break flow rate was the determining factor in calculating the correct loop behaviour, in particular the timing of flow oscillations and temperature excursions. All codes predicted overall loop pressure and flow oscillations to various degrees, resulting from boiling in the channels and condensation in the boiler tubes, and the resultant void generation/collapse cycles, but at different time and with slightly different amplitudes and frequencies. Prediction of pump head under degraded conditions, which influences coolant flow and subsequent FES heat up upon the loss of forced circulation, is influenced by the PHTS pump characteristics under two phase flow.

None of the codes predicted the FES temperature oscillations that occurred at channel voids above ~ 80% correctly or the relatively slow increase in temperature during the PDO heat transfer phase thereafter. All codes calculated a faster temperature increase without the initial

dryout/rewet oscillations, leading to generally early power trip times, due to the codes' inability to correctly model the post-dryout heat transfer and rewet behaviour observed in the test. One simulation was able to predict the relatively slow heatup once in dryout, by using a "developing PDO correlation with modified coefficients" (tuned correlation).

Axial temperature gradients in the channels were positive (increasing temperature in the flow direction) during the initial phase of the voiding transient (up to about 70% outlet void), while the FES's were covered by the liquid phase. In the later phase of nucleate boiling, the temperature gradient reversed, in particular for the top FES's, due to the decrease in saturation pressure and temperature of the coolant along the flow direction. This lower fluid temperature, combined with increased vapour velocity resulting from the rapidly increasing void, improved FES cooling towards the channel outlet. Whether this phenomenon was captured in the calculations depended on the PDO model, FES grouping, and whether stratification was allowed by the code and user options. It also affected whether subsequent FES temperature excursions into the PDO regime were predicted to be larger/earlier near the channel inlet or outlet.

The calculated break flow rates varied significantly among participants, primarily due to different critical flow models and coefficients used. Since there was no ECC injection, the break flow resulted in the slow but steady depletion of loop inventory, and different break flow rates caused different overall loop void generation rates and thus different times for FES dryout and heatup. Since the flow remained forced throughout the transient, the flow directions in the heated sections was fixed, and with a relatively high heating rate, the outlet void development was predicted with acceptable accuracy by all codes.

The above is also confirmed by sensitivity cases run by AECL and CNE. Reducing the break discharge coefficient had a similar effect as changing (reducing) the break area (as seen in the sensitivity cases, Appendix I). The break flow area sensitivity was correctly chosen to demonstrate a significant sensitivity in both tests (more so in B9802, without ECC). In B9006 the change in break flow area affected ECC timing only slightly, and thus a decrease in break flow rate (from a reduced break size) led to an increase in minimum loop inventory, and vice versa.

The inclusion of "snapshot" graphs, which show the pressure, temperature, and void profile throughout the loop, were considered by all participants as a useful tool to assess the code calculations. They showed that all code calculations were essentially self-consistent, and aided in the explanation of deviations from the test data during key times of the transient. They also pointed out differences in model nodalizations and differences in code calculations, in particular of temperature and void distribution throughout the loop. However, the comparison between codes must consider also the variation in the timing of key events by each code.

Significance to safety analysis

For SBLOCA, channel voiding is not a concern as much as for LBLOCA and code accuracy for void prediction is not essential. However, maximum FES temperatures are important, and therefore, improvements in PDO models and in the critical break discharge models are required. Also, ECC effectiveness for channel refilling and SG effectiveness for condensation are important phenomena that affect FES heatup. While in B9006 (ECC active) some FES temperature stratification was observed during low-flow periods, they were of very short duration and low magnitude, and occurred near the time when maximum loop void of about

35% was predicted. It can be concluded that up to that level of void in the loop, no significant stratification and sheath heatup periods (dryout) should be expected.

All main phenomena (e.g. break discharge, coolant voiding, pressure drop, boiling and condensation heat transfer, and temperature excursion in the heated sections) are qualitatively captured by the participants. Discrepancies in quantitative terms, in particular in void predictions, are observable and explainable but these do not significantly affect the prediction of the overall system performance or of those parameters that are critical in defining safety margins.

The application of codes developed outside the HWR technology did not show any special deficiency in the comparison with the present experimental database. Therefore, it can be concluded that HWR systems do not need special tools for the analysis of benchmark experiments of this type. However, the existence of parallel channels, and the potential of flow reversal in some of them, is untypical in other PWR reactor systems and requires special attention in the modeling. One dimensional thermal-hydraulic codes combined with an appropriate nodalization, accurate hydraulic resistances, and consistent set of assumptions are able to grossly predict the parallel channel effects as experienced during the simulation of current ICSP exercise.

The performed activity is relevant in assessing the capabilities of codes and permitted the quantification of the amount of discrepancy between measured and calculated values, however, it has not been immune from code user effect. The participants received great benefit from the analysis of this experiment having had the opportunity of direct contacts with developers of HWR technology and the transfer of information that is not available in open literature. Moreover, they increased the confidence in the prediction capabilities of system codes and achieved a better understanding of physical phenomena related to HWR SBLOCA transient scenarios.

The exercise confirmed the importance of having built and operated complex facilities like RD-14M and showed, within an international context, the quality level achieved by some computational tools developed within the HWR technology. In addition, this was an opportunity for the AECL to assist scientists of HWR owner countries in performing state of the art quality accident analyses and permit the quantification of code accuracies.

It is recommended to further extend the use of RD-14M or other large-scale data for the benefit of the scientific and engineering community engaged in carrying out safety analysis of HWRs. One area of interest is the prediction of multi-channel loop behavior under natural circulation (thermo-syphoning) conditions. Additionally, other interesting test data can be considered for the future ICSPs.

REFERENCES

- [1] INTERNATIONAL ATOMIC ENERGY AGENCY, The Intercomparison and Validation of Computer Codes for Thermalhydraulic Safety Analysis of Heavy Water Reactors, IAEA-TECDOC-1395, IAEA, Vienna (2004).
- [2] SWARTZ, R., RD-14M Facility Description, COG Report COG-00-034 (2003).
- [3] KRAUSE, M., RD-14M Small-Break LOCA Experiments for an IAEA International Collaborative Standard Problem AECL Report 153-108210-440-001 (2008).
- [4] INTERNATIONAL ATOMIC ENERGY AGENCY, Advances in Heavy Water Reactor Technology, IAEA-TECDOC-984, IAEA, Vienna (1997).
- [5] SINGHAL, M., LBLOCA Analysis for Retrofitted ECCS at MAPS using Modified Computer Code ATMKA. First National NRT Conference on Nuclear Reactor Safety, Mumbai, India , Nov 25-27 (2002).
- [6] INTERNATIONAL ATOMIC ENERGY AGENCY, Thermohydraulic Relationships for Advanced Water Cooled Reactors, IAEA-TECDOC-1203, IAEA, Vienna (2001).
- [7] HANNA, B.N., CATHENA: A Thermalhydraulic Code for CANDU Analysis, Nuclear Engineering and Design (180) 113-131 (1998).

Appendix I

SENSITIVITY CASES

I.1. INTRODUCTION

In parallel with the base cases analysis, a set of sensitivity cases were run in order to have a supplementary evaluation of the effects of different parameters. The sensitivity cases were included in the initial planning for the blind calculation phase. For the open calculation phase, some of the participants decided to run supplementary sensitivity cases in order to evaluate the effect of changing one single parameter at a time. The following sections present the sensitivity cases considered and some of the associated results. Results from CNE are shown here for both the blind and open calculation sensitivity cases.

I.2 BLIND CALCULATIONS SENSITIVITY CASES

Sensitivity cases were proposed for both tests involved in the International Comparative Standard Problem (ICSP). A list and a general presentation of each sensitivity case considered during the blind calculation phase are presented in Table A.1.

TABLE I.1. LIST OF CASES SIMULATED FOR BLIND CALCULATION PHASE

Case No.	Test	Case description
1	B9006	Break area increase by 10%
2	B9006	Break area decreased by 10%
3	B9006	Outside temperature 15 °C or heat loss increased by ~10%
4	B9006	Outside temperature 25 °C or heat loss decreased by ~10%
5	B9802	Break area increased by 10%
6	B9802	Break area decreased by 10%
7	B9802	Boiler heat transfer area (or heat transfer coefficient) increased by 10%
8	B9802	Boiler heat transfer area (or heat transfer coefficient) decreased by 10%

I.2.1 Test B9006

The sensitivity cases that were considered for this test were related to break area dimension and circuit outside temperature. The break area was changed within 10% of the nominal break area because it will have a direct effect on the flow rate discharged through the break and this could affect the overall test results. The heat loss from the loop was also considered important for the overall behaviours in the long term once the power is reduced to decay power levels. Depending on how each participant modeled the loop heat loss, two different temperatures, different heat flux, or heat transfer coefficients were considered for these sensitivity.

The steady state results for the first set of sensitivity cases (break area change) were identical to those obtained for the base case. For the second set of sensitivity cases (loop heat loss), the participants observed some small differences in the steady state conditions. The magnitude of the difference and local effects depended on the ways the heat transfer to the outside was included by each participant in the individual models.

Sensitivity cases results for break area change.

For the sensitivity cases related to break area, the overall transient loop responses were similar to the blind calculation base cases and most of the parameters showed the same general behavior as for the base cases. However, as a general remark, due to larger break area and larger break discharge, the moment the ECC injection is started and the moment for transfer to low pressure ECC stage were earlier than for the base case. The reverse effect was observed for the case when the break area was decreased (see Fig. I.1): a lower discharge, a later initiation of ECC high pressure and a later transfer to low pressure stage.

Although the test data did not show significant fuel sheath temperature excursions, some participants show larger fuel element sheath temperature increases. Regarding the sensitivity case presented, it was noted that increasing the break area led to earlier maximum sheath temperatures. In addition, they increased in magnitude. Similar, when the break dimension was decreased, the maximum fuel sheath temperature decreased (see Fig. I.2). This behavior was expected because a larger break will reduce the circuit inventory faster and more void is expected (or similar void is expected earlier) and some flow stagnation in the heated sections may occur. Since stagnation in the heated sections results in poor fuel cooling, increasing the amount of void or changing its distribution in the loop may induce larger or longer fuel sheath temperature excursions.

Sensitivity cases results for outside temperature

Loop heat losses impact the energy content and distribution within the loop, with more heat losses (lower outside temperature) leading to lower overall loop energy, and vice versa. This should result in generally lower FES temperatures and lower void. However, loop losses also affect the distribution of energy and therefore can affect driving forces and flow patterns in a parallel-channel arrangement under low-flow conditions as found in test B9006.

Figure I.3 shows that the highest peak FES temperatures at the center of HS13 are not predicted for the low-heat loss case ($T=25\text{C}$), but for the base case ($T=20\text{C}$), as a result of more severe flow stagnation in the base case in this particular channel. Figure I.4 plots the HS13 outlet FES temperatures and shows a mixture of the expected trend (highest FES temperatures for $T=25\text{C}$) and the trend shown in Fig. I.3, depending on the time during the transient.

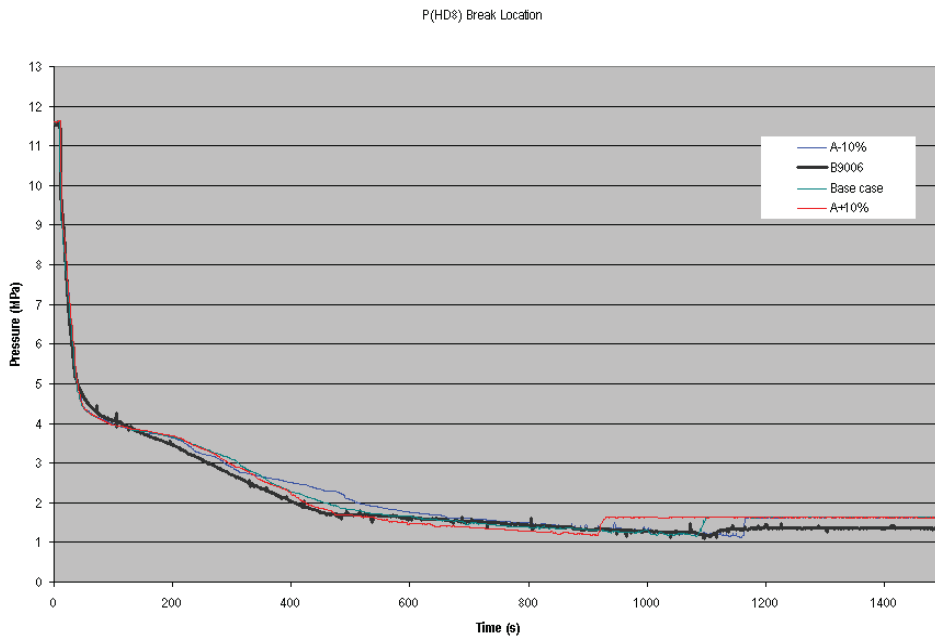


FIG. I.1. Header HD8 pressure - break area effect.

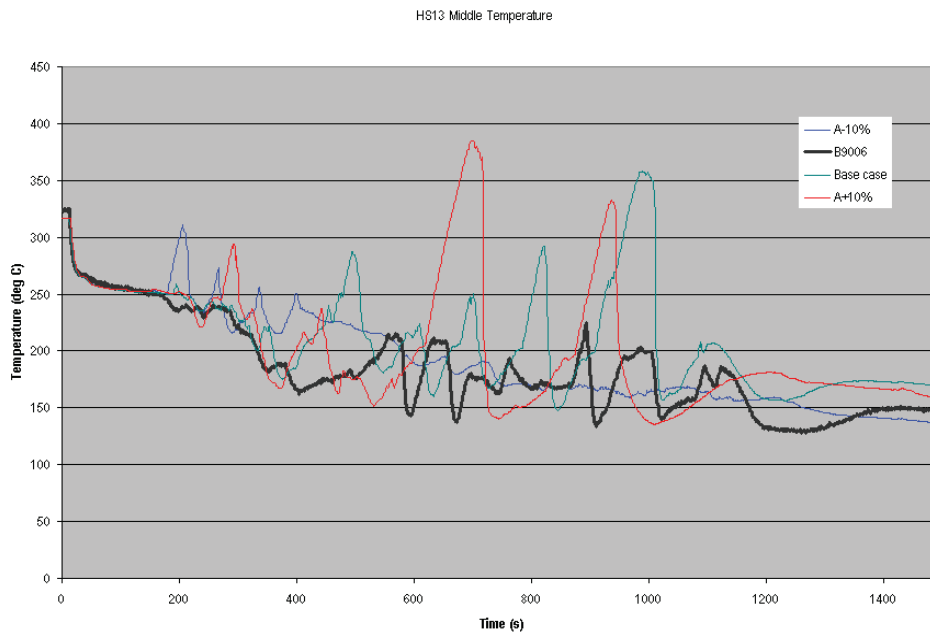


FIG. I.2. Heated section HS13 center temperature; break area effect.

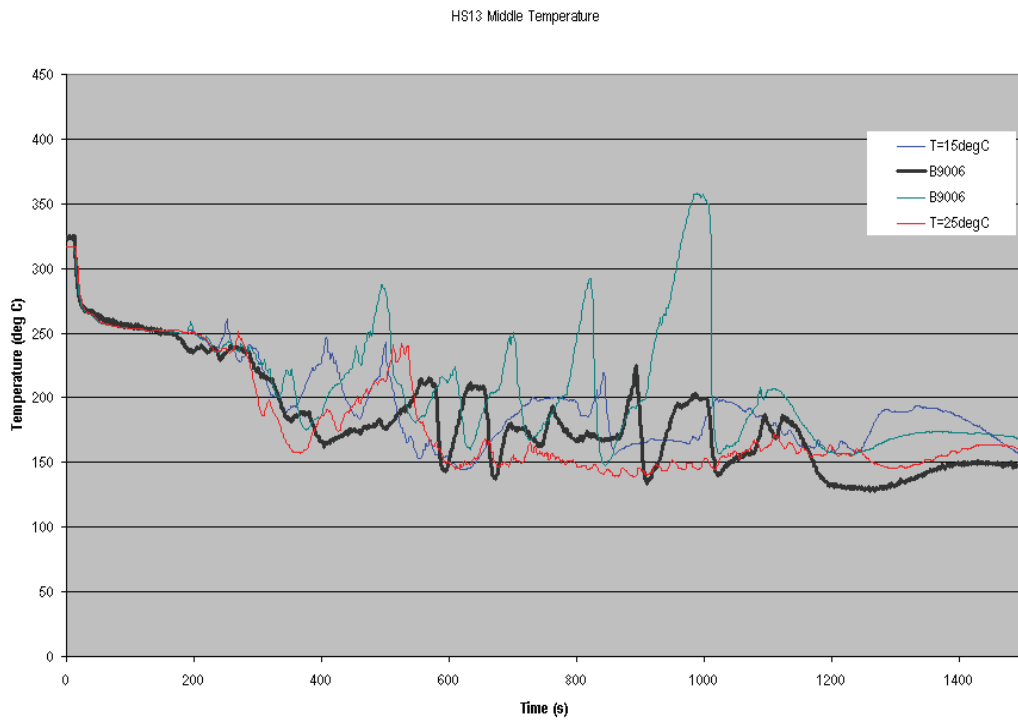


FIG. I.3. Heated section HS13 center temperature; outside temperature effect.

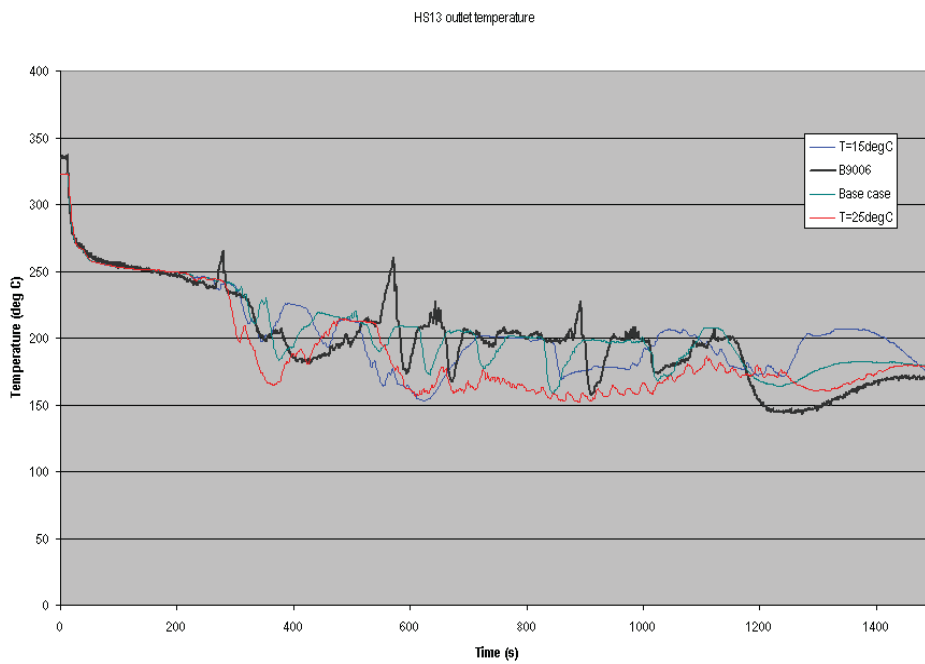


FIG. I.4. Heated section HS13 outlet temperature; outside temperature effect.

I.2.2. Test B9802

For the blind calculations phase, the sensitivity cases that were considered were related to break area dimension and boiler heat transfer area. The break area was changed within 10% for the sensitivity calculations for similar reasons as presented for test B9006. The boiler heat transfer area was also considered to have importance since it will affect the amount of energy transferred from the loop. This was the reason the area was changed within 10% versus the reference case.

The steady state results for the first set of sensitivity cases (area change) were identical to those obtained for the base case. Small differences were observed for the second set of sensitivity cases (boiler surface area change).

Sensitivity cases results for break area change

The break discharge area was found to have a significant effect on test B9802 results because the area itself is very small and the change induced a significant effect in the circuit. All parameters selected for comparison are affected by the changes in the break area.

Increasing the break discharge area results in a larger flow discharge and less inventory in the circuit. For the case of increased break discharge area, since there is no ECC flow to compensate and to collapse the void in the circuit, the flow oscillations occur earlier than for the base case (see Fig. I.5).

Decreasing the break area, less flow is discharged and the model predictions became closer to those recorded during the test. In the same time, more inventory will be maintained in the circuit. As a direct effect, less void and later oscillations are observed for this case compared to the base case.

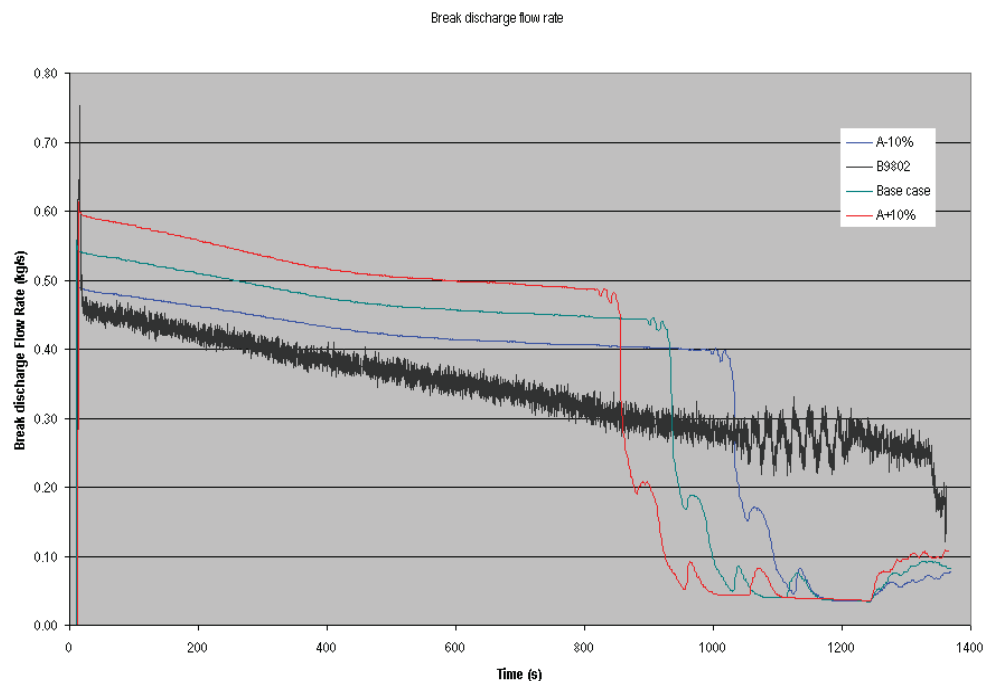


FIG. I.5. Break discharge flow rate; break area effect.

Fuel sheath temperature excursions occur earlier, the larger the break size, but have a similar heat-up rate (see Fig. I.6). The maximum temperature is maintained at similar values independent of the break area, because it is limited by the high temperature trip protection, (power trip occurs when fuel element sheath increases above 600°C).

Sensitivity cases for boiler surface area change

Change in the steam generator surface area was found to have an insignificant effect on circuit behavior, timing of significant events and fuel element maximum sheath temperature (see Figs I.7 and I.8.). The overall effect is small because the power is maintained constant throughout the transient and the boilers have sufficient heat removal capacity even with the lowest heat transfer coefficient.

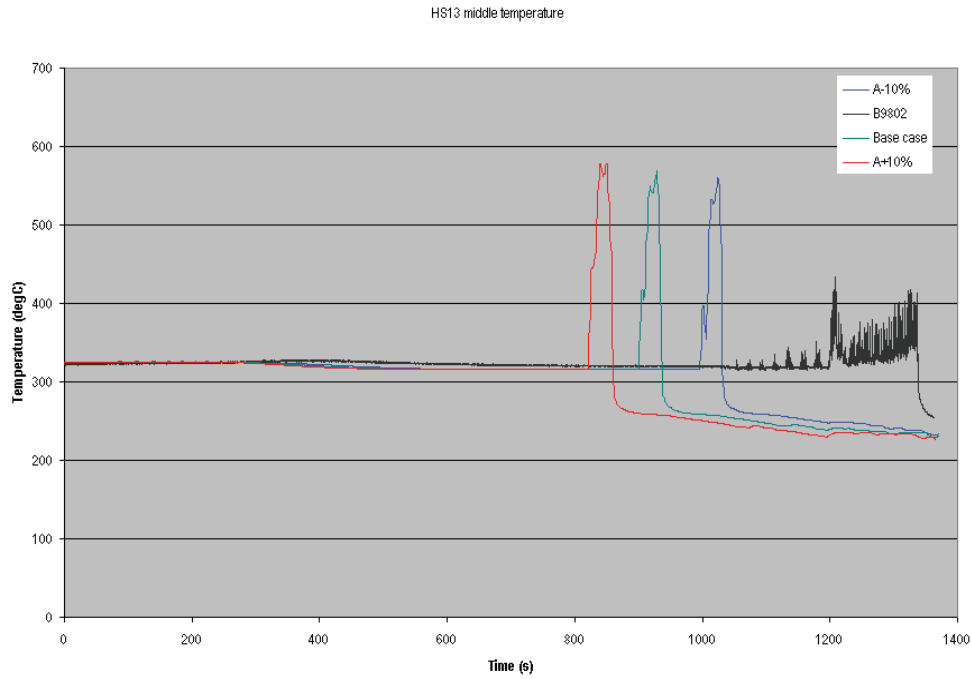


FIG. I.6. Heated section HS13 outlet temperature; break area effect.

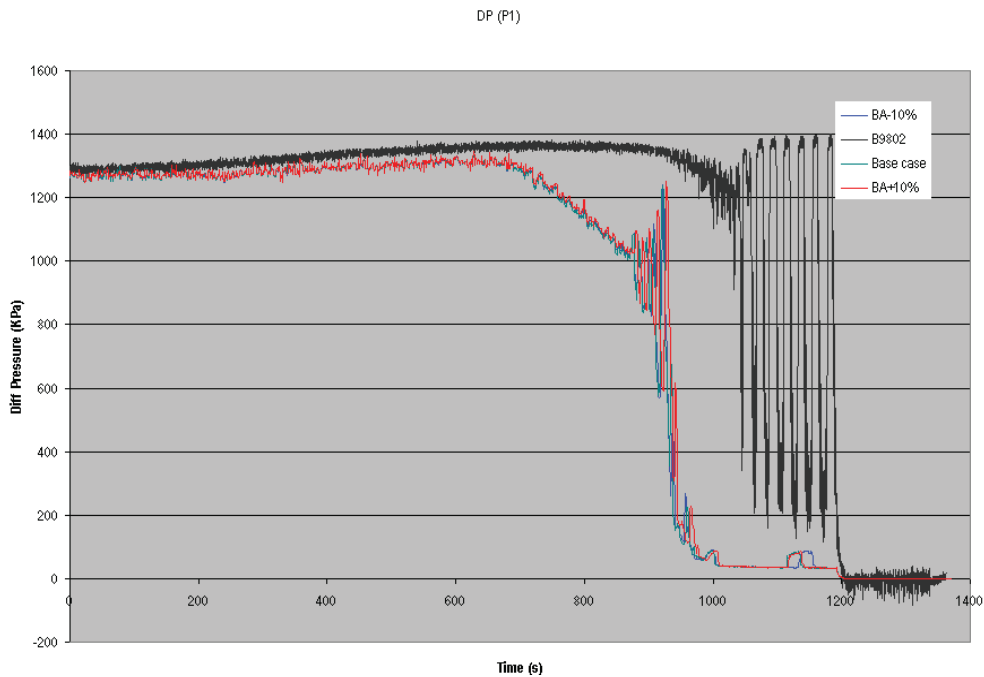


FIG. I.7 Pump P1 differential pressure; boiler surface area effect.

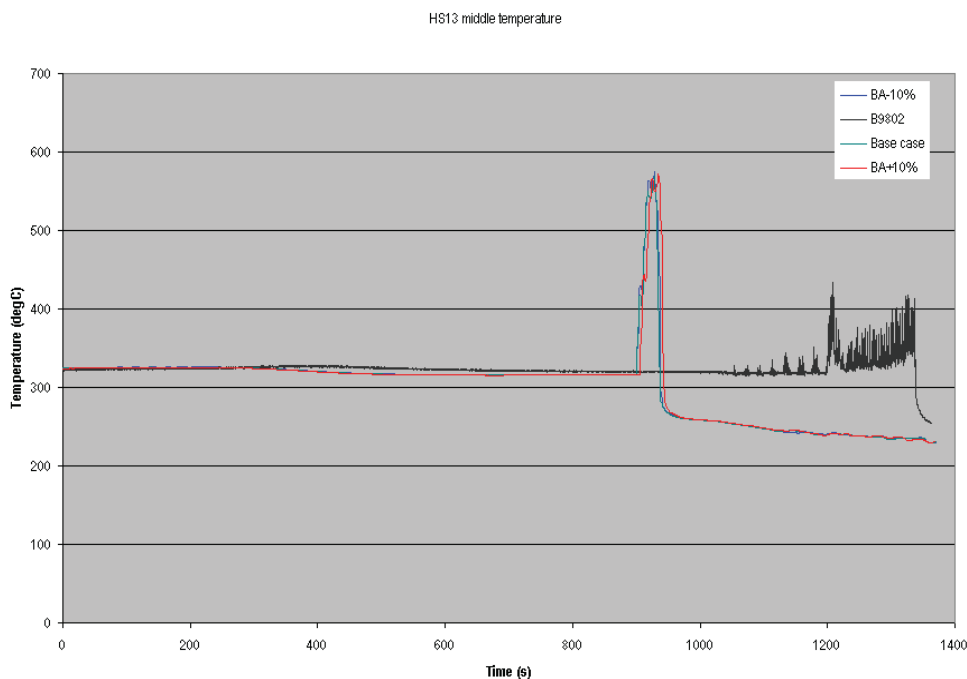


FIG. I.8. Heated section HS13 center temperature; boiler surface area effect.

I.3 OPEN CALCULATIONS SENSITIVITY CASES

No sensitivity cases were required for the open calculation phase. However, some of the participants decided and performed more sensitivity cases by changing one parameter at a time in order to evaluate the model response.

Based on the blind calculation sensitivity cases that were run for test B9802, a significant improvement was observed in the model predictions versus test recorded data in case when the break area was decreased by 10% versus the nominal value (base case). Most of the parameters followed the same behaviour as for the base cases but the oscillations and high temperature trip were reached closer to the time recorded during the test (as presented in Figs I.5 and I.6). The main difference between the calculations is believed to be generated by the break discharge flow rate.

Taking into consideration these aspects, the effects of the break discharge characteristics and of the break discharge area were further evaluated by some of the participants. The effect of void condensation in the boiler tubes was also evaluated because it was considered that the condensation is responsible for inducing oscillations and affecting their amplitude. These are discussed in the following sections.

Break discharge liquid coefficient

The break discharge flow was measured only for test B9802 and consequently, the focus was on the results for this test.

AECL and CNE performed a set of sensitivity cases related to the subcooled-liquid break discharge coefficient. In both cases, the default value was used for the base case open calculations. However, it was observed that the discharged flow is higher than that measured in the test. For this reason, the break discharge liquid coefficient was reduced from the default

in the test. For this reason, the break discharge liquid coefficient was reduced from the default value to lower values in order to match the measured break discharge flow. The calculated break discharge became closer to the measured flow for a liquid discharge coefficient of 0.51 but only for the first part of the transient (see Fig. I.9). For the second part of the transient, after about 400 seconds in the test, the discharged flow remains about 10% higher than the values recorded during the test. The same behavior is observed for the break integrated mass (Fig. I.10): considering a discharge liquid coefficient of 0.51 the integrated mass is very well predicted for the first 400 seconds of the test, prior to the development of significant void in the loop.

A general improvement was also observed for other parameters like onset of pump degradation and flow oscillations (Fig. I.11), header pressure evolution (Fig. I.12) or the timing of fuel sheath temperature excursions (Fig. I.13). In each case, the events occurred later in the transient closer to the time recorded during the test. However, the rate of FES temperature increase, once in dryout, continued to be overpredicted and the high temperature trip occurred earlier than recorded during the test.

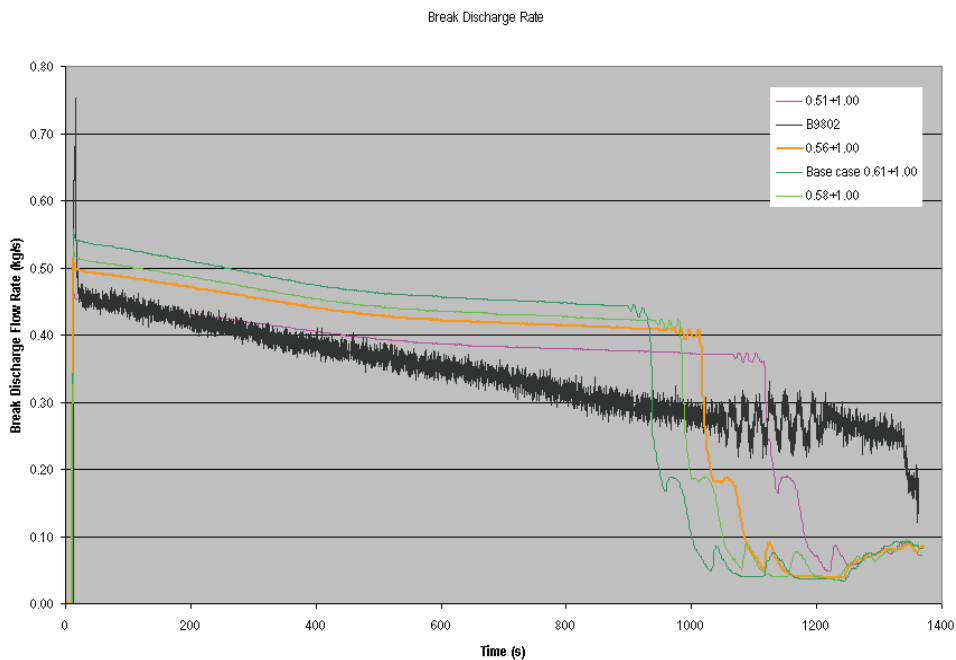


FIG. I.9. Break discharge flow rate; break discharge liquid coefficient effect.

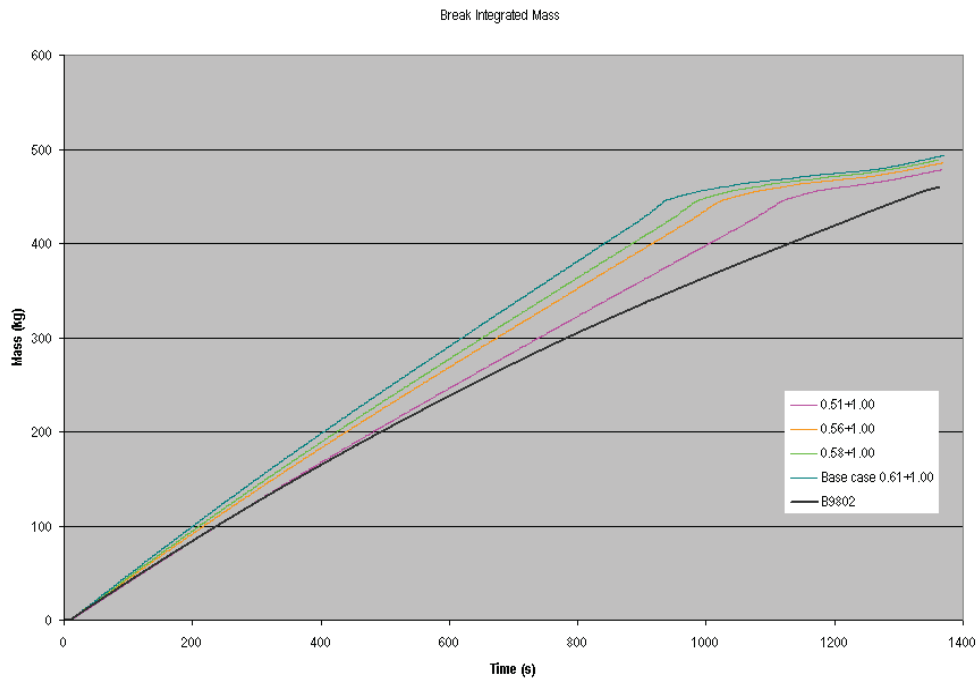


FIG. I.10. Break discharge integrated mass; break discharge liquid coefficient effect.

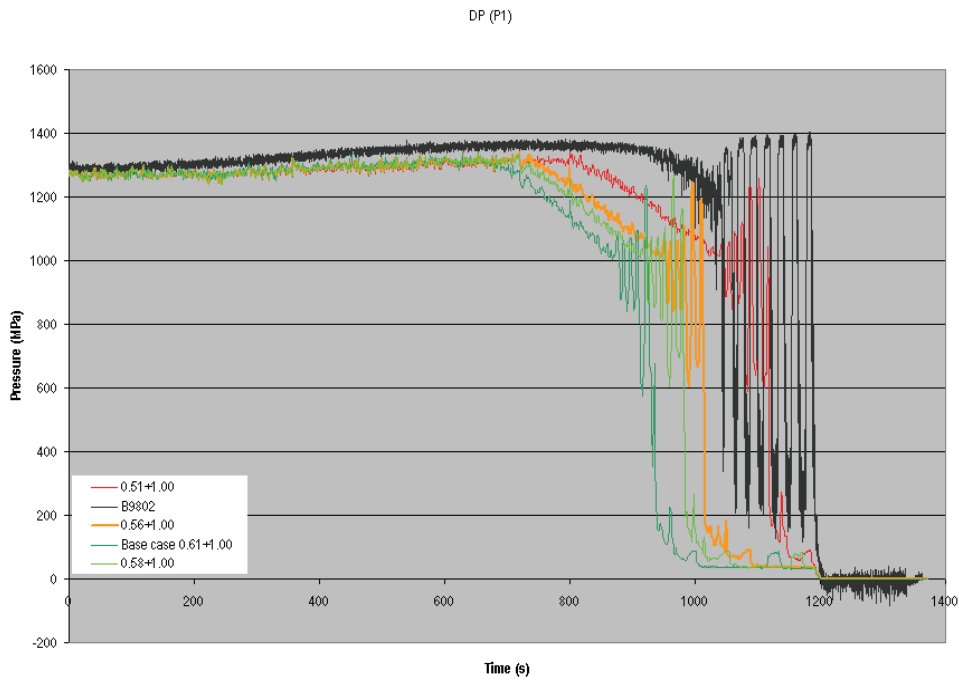


FIG. I.11. Pump 1 differential pressure – break discharge liquid coefficient.

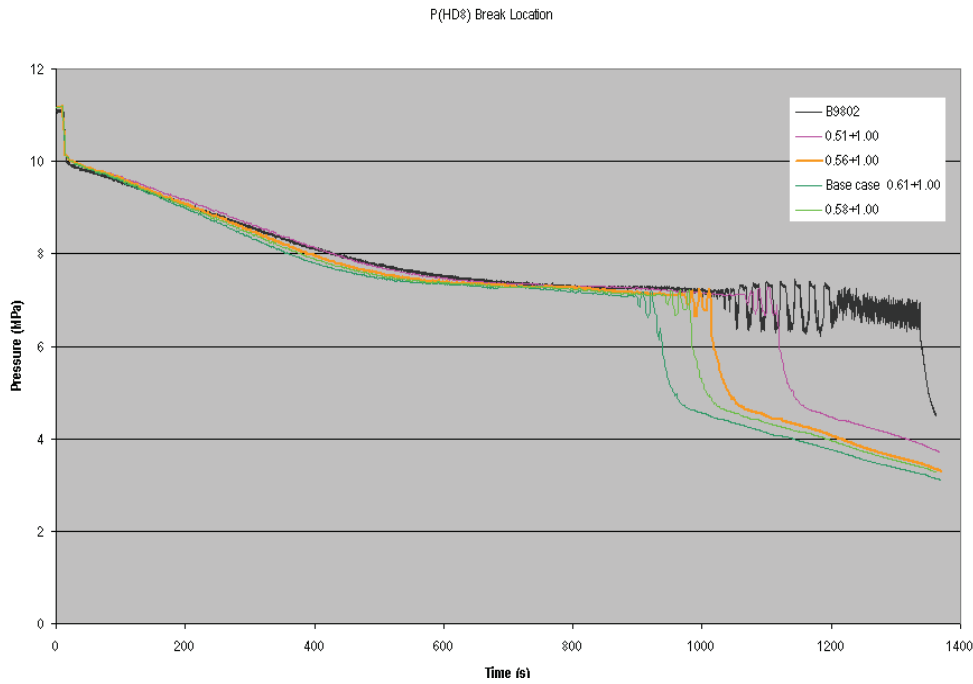


FIG. I.12. Pressure at broken header (IHD8); Break discharge liquid flow coefficient.

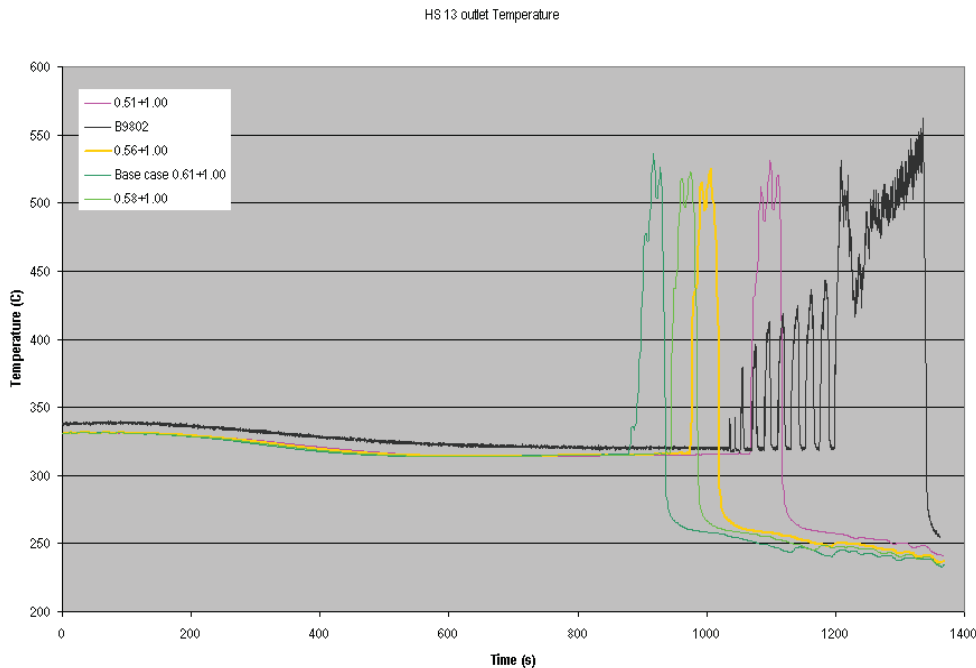


FIG. I.13. Temperature at HS 13 outlet; break discharge liquid flow coefficient.

Break discharge area and higher temperature trip setpoint effects

Based on the sensitivity cases performed for the blind calculation phase, it was found that the break area may have a significant effect on the break discharge and on the time the oscillations occur. It was also observed that the fuel element temperatures increase significantly before the time recorded in the test.

These were the reasons a sensitivity case was performed including the combined effect of reducing the break discharge area by 15% and increasing the high temperature trip set point from 600°C to 800°C.

The effect of reduced break area is directly observed as a lower inventory discharged. The higher mass in the circuit delays the moment the oscillations occur (Figure I.14). The increase in the high temperature trip increases the number of oscillations before the maximum temperature trip is reached.

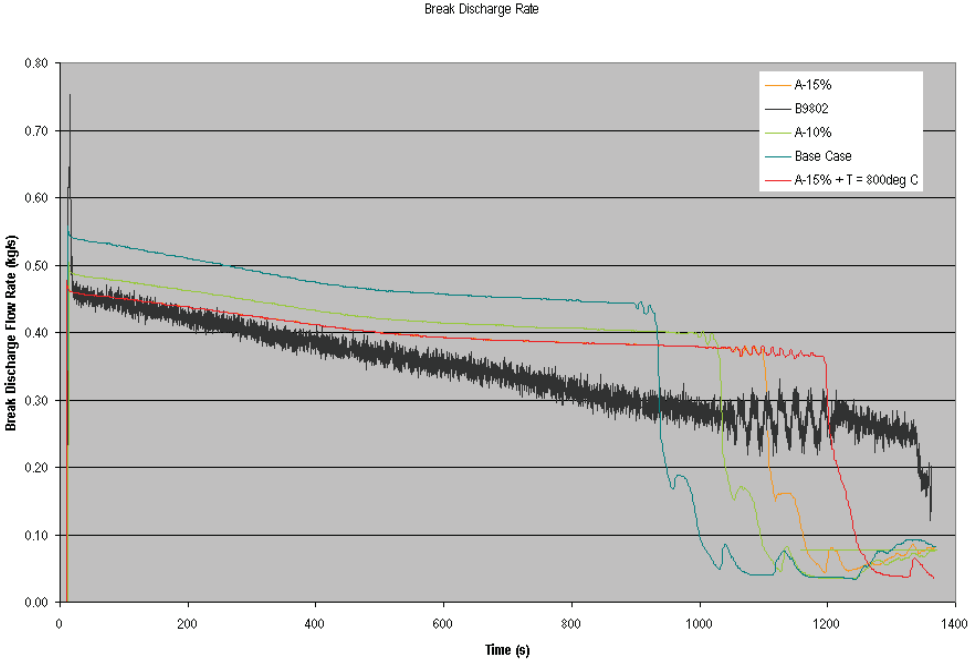


FIG. I.14. Break discharge flow rate; break discharge area/temperature effect.

The steady state conditions for this sensitivity case are identical to those obtained for the base case. The effect of reducing the flow area in the pump 1 differential pressure is presented in Fig.I.15. Decreasing the break area, the behaviours of the differential pressure for pump 1 was similar to that recorded during the test until about 800 seconds. Even if the pressure decreased earlier, the moment the oscillations started was closer to that recorded in the test. In addition, by increasing the temperature at which power trip occurs, the time interval for oscillations was extended becoming similar to that recorded during the test. A similar behaviour was noted for differential pressure on pump 2.

Even if the differential pressure across pumps shows a good agreement with the test data, other parameters did not entirely reproduce the behaviours recorded during the test. The pressure at the broken header is presented in Fig I.16. The pressures in the other headers show a similar behaviour to the pressure evolution in the broken header. The pressure evolution respected the trend recorded during the test (and oscillatory behaviour) until high temperature trip, which was reached earlier than recorded during the test.

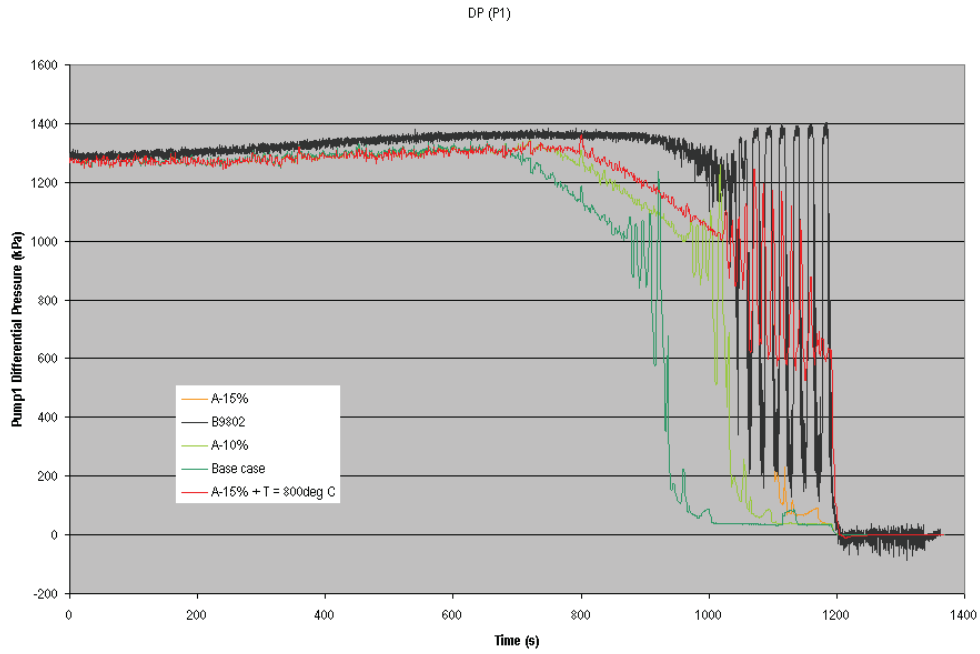


FIG. I.15 Pump 1 Differential pressure; break area and temperature effect.

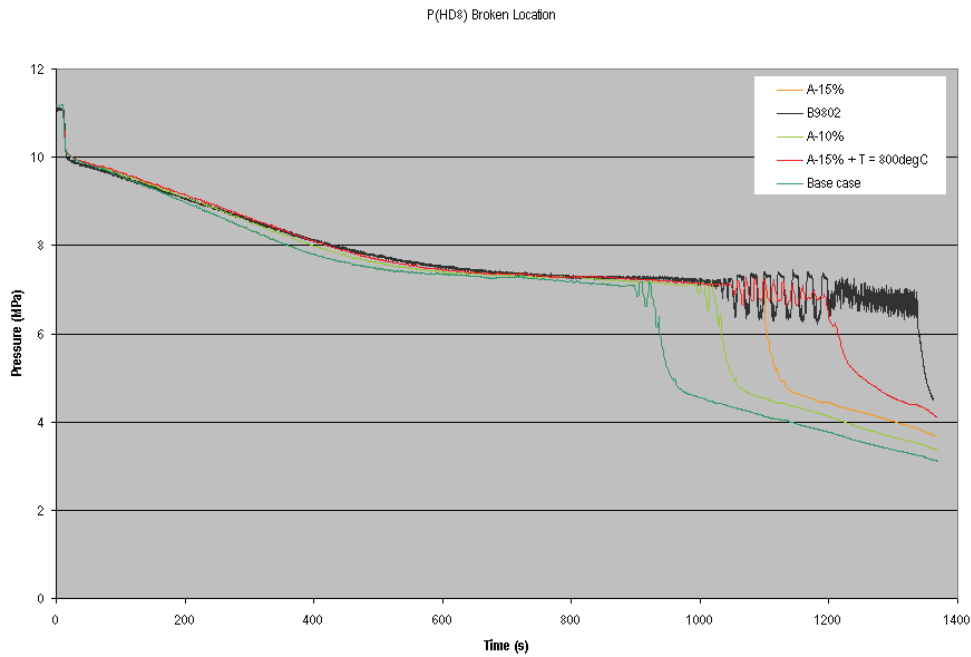


FIG. I.16. Pressure at the broken header – break area/temperature effect.

Void fraction at the inlet and outlet of the boiler 1 are presented in Figs. I.17. and I.18. While the timing of the start of the oscillations is similar to that recorded during the test, their amplitude is lower. A lower void fraction is predicted at the end of the simulation once the power is reduced (determined by fuel element sheath high temperature).

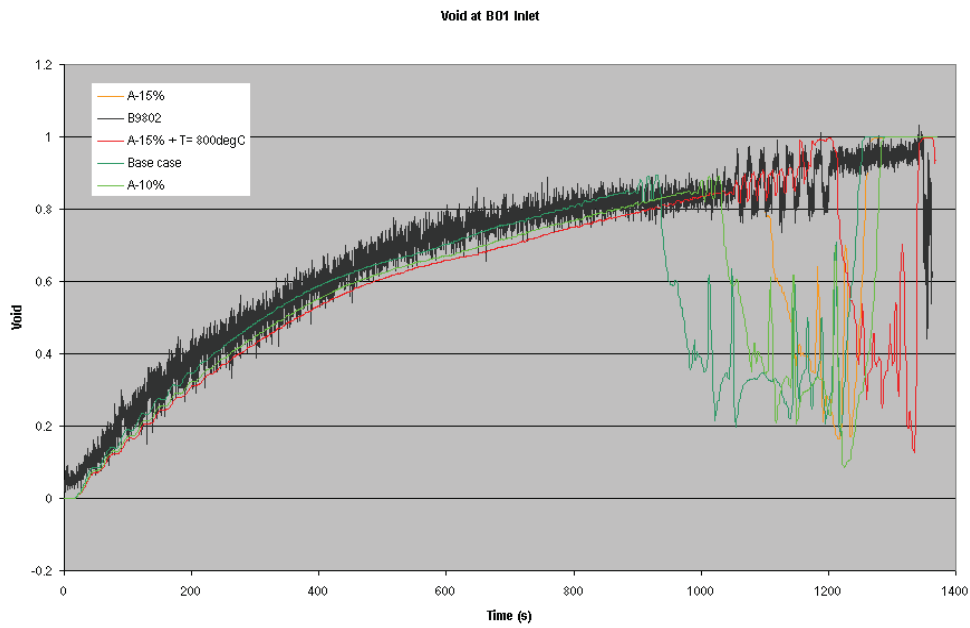


FIG. I.17. Void at boiler 1 Inlet; break area/temperature effect.

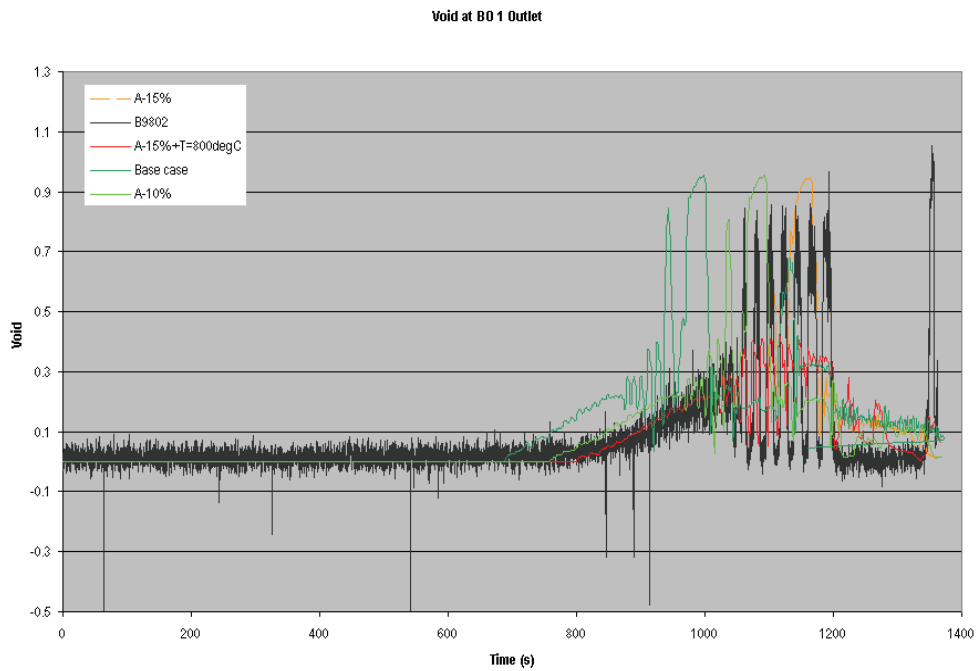


FIG. I.18. Void at boiler 1 outlet; break area/temperature effect.

The trip on high temperature is generated by the fuel element sheath temperature excursion. When the limit was artificially increased to 800°C, the temperatures in the other locations show a trend similar to the reference case (Figs I.19 and I.20), but with a longer duration at elevated, post-dryout, temperatures.

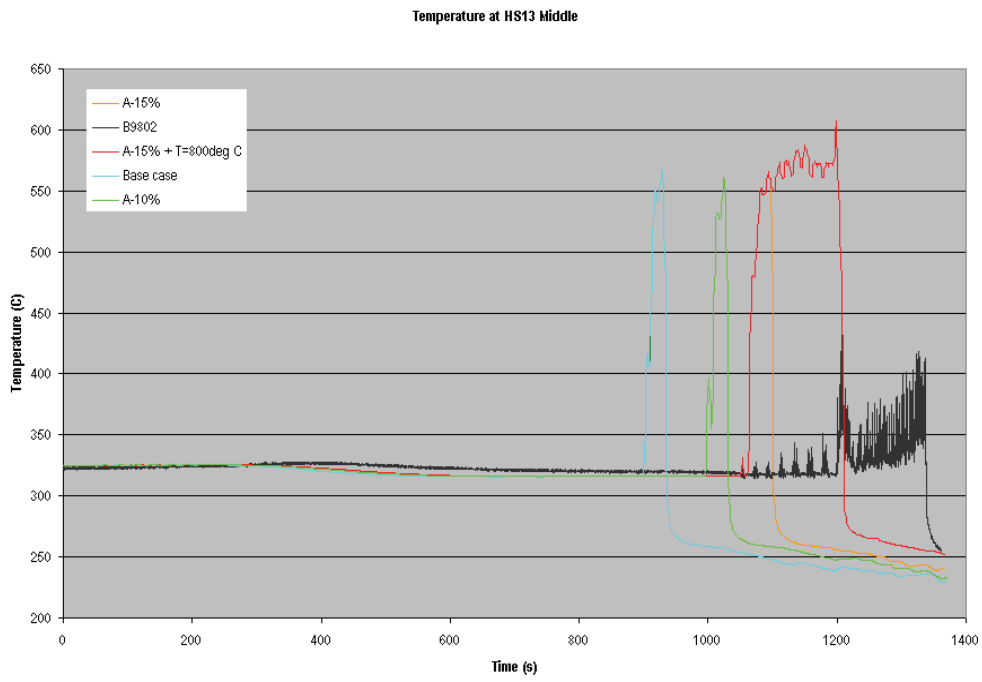


FIG. I.19. Heated section HS13 center temperature; break area/temperature effect.

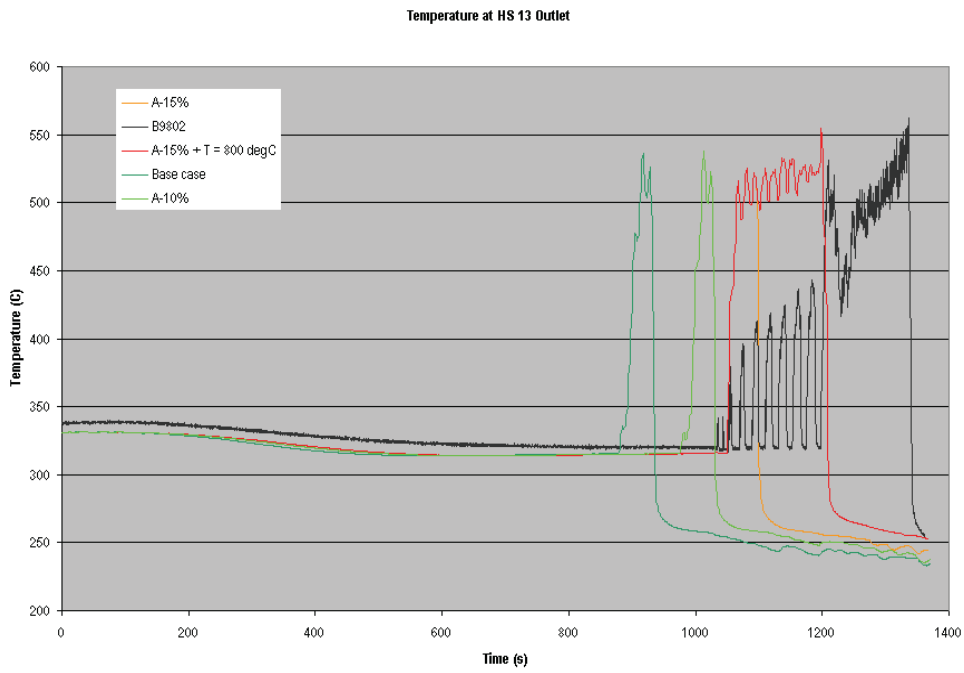


FIG. I.20. Heated section HS13 outlet temperature; break area/temperature effect.

Effect of using the STM-GEN-COND option

The FES temperature show significant oscillations (dry-out and rewet) during the last part of the test B9802. As part of the open calculation phase, KAERI performed a set of sensitivity cases using the developing PDO correlation for test B9802. The results shows an improved prediction in terms the timing of the maximum FES temperature.

Furthermore, the open calculation results, in conjunction with ‘STM-GEN-COND’ option selected for steam generator U-tubes, show even better results. From the comparison of the header pressure measurements with the CATHENA open calculation predictions (see Section 4.2.3), a “plateau” at about 1 MPa above the measurement was observed. However, this deviation from the test results disappears in the new sensitivity calculation applying the option ‘STM-GEN-COND’ to the primary side of steam generator tubes (see Figs I.21 and I.22). The CATHENA option for ‘STM-GEN-COND’ specifies that direct condensation of vapor as a result of heat removal at the wall surface is to take place. Without this option, condensation within the tubes may be underestimated.

The direct effect the “STM-GEN-COND” option is observed in the FES temperature. If we add the steam condensation option to the reference case, the PDO heat transfer coefficients must be tuned again to correct the slightly different timing of the FES temperature excursion. However, the new calculation with ‘STM-GEN-COND’ option shows a better FES temperature behaviour compared to the test results (see Figs I.23 and I.24).

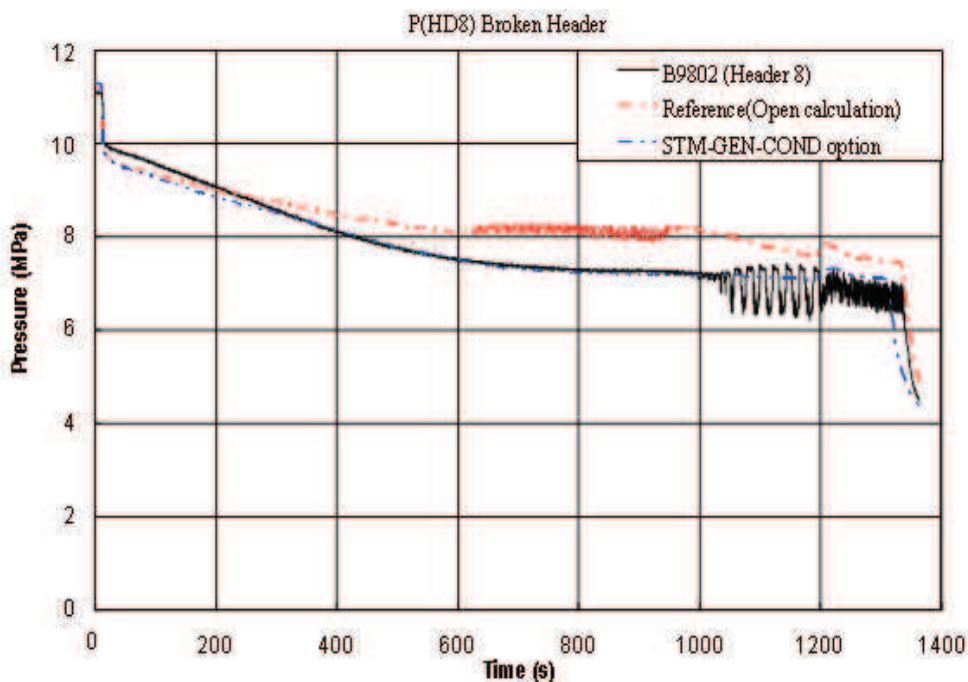


FIG. I.21. Pressure at the broken header – “STM-GEN-COND” option effect.

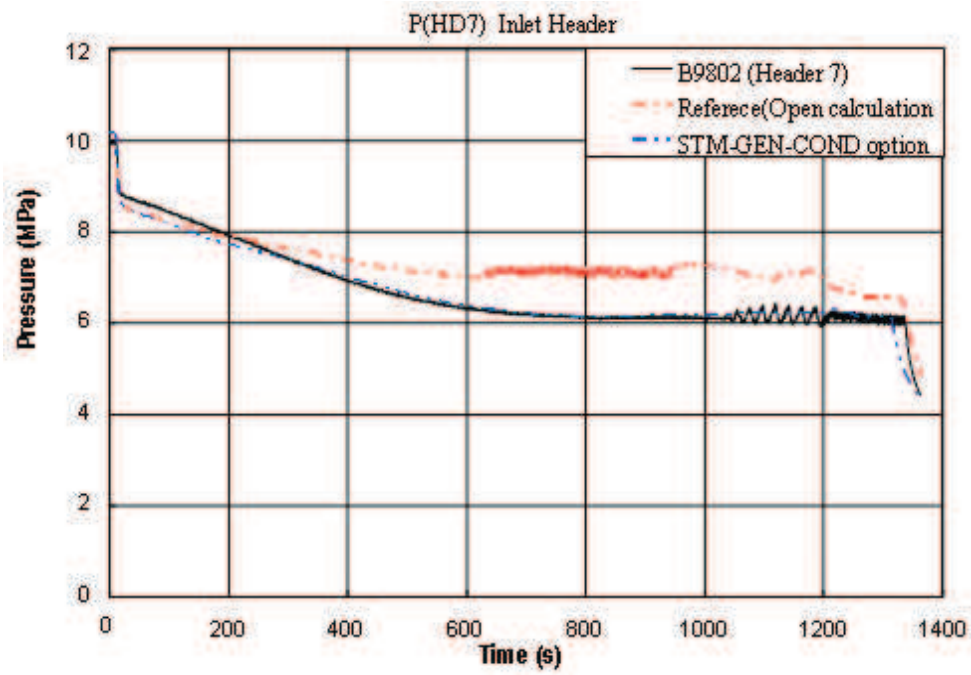


FIG. I.22. Pressure at header 7 – “STM-GEN-COND” Option effect.

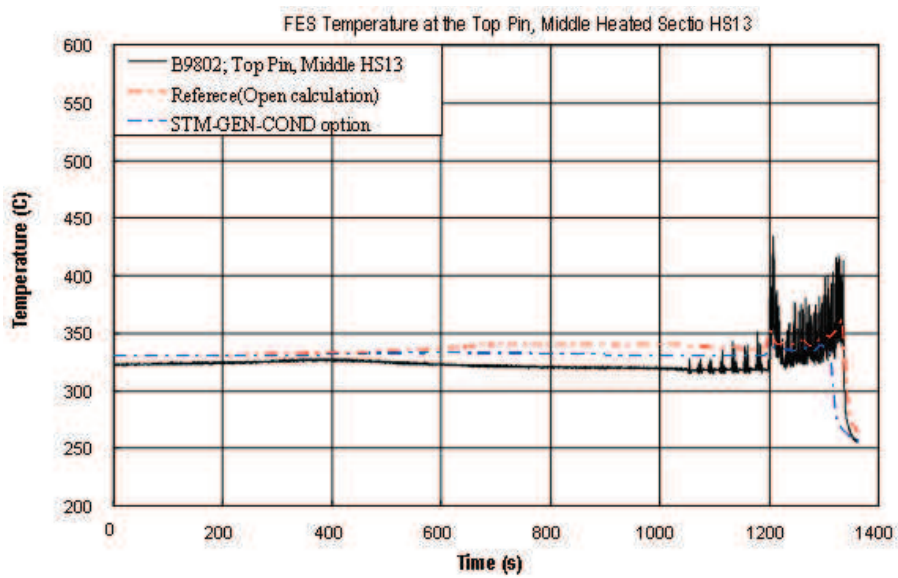


FIG. I.23. Heated section HS13 center temperature “STM-GEN-COND” option effect.

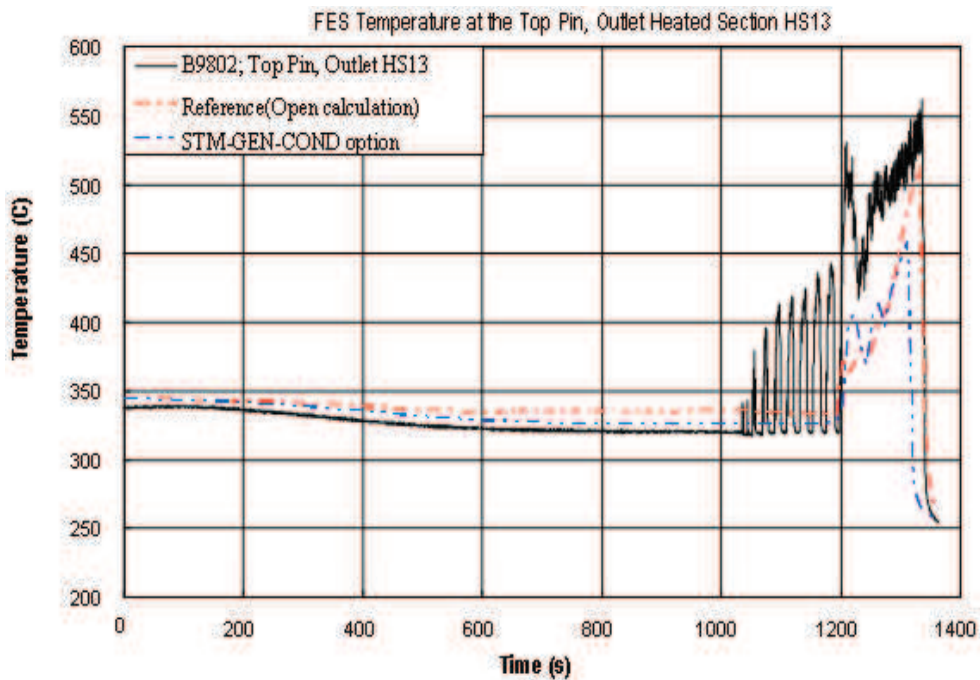


FIG. I.24. Heated section HS13 outlet temperature – “STM-GEN-COND” option effect.

I.4 CONCLUSIONS

Based on the results of sensitivity cases presented it was concluded that both the break discharge liquid coefficient and break discharge area have an important effect on the small LOCA events behavior.

Each of these parameters taken individually is affecting the discharged flow and for relatively long transients, they will affect the overall transient behavior and, consequently, the timing of the important effects like fuel sheath temperature increase.

Based on the single test result (test B9802), it was concluded that the effect of reducing the break discharge liquid coefficient by about 15% is equivalent in terms of circuit behaviour to a break area decrease by about 16%.

At this moment, the CATHENA code conservatively predicts these phenomena but some supplementary margins may be available during real events. Considering that the small LOCA events may be challenging for some plants during the lifetime, it may be of interest to evaluate the effects of these parameters through multiple tests performed in the same or similar experimental facilities.

The “STM-GEN-COND” option was found to have an important effect on pressure evolution but less so for the FES temperatures.

Appendix II

SNAP SHOT GRAPHS

II.1 INTRODUCTION

In addition to assessing the computer model predictions against identified selected transient variables, more insight into the simulated loop behaviour may be gained from examining the pressure, temperature, and void distribution throughout the loop during key selected times of the transient. All the participants provided such time “snapshots” for open calculations, which are presented below.

Snapshots of pressure, temperature and void around the loop were selected for four different times of test B9006:

- T1 = 70s, just before opening of ECI injection / accumulator valves;
- T2 = 320s, approximately in the middle of the period of reverse flow and P1 pump voiding;
- T3 = 1050s, just before the end of HPECI;
- T4 = 1500s, long after LPECI has started, quasi steady-state conditions;

Snapshots of pressure, temperature and void around the loop were selected for three different times of test B9802:

- T1 = 400s, during pressure decrease, quasi steady-state behaviour;
- T2 = 1000s, during degraded boiler condensation, just prior to oscillatory flow;
- T3 = 1300s, during FES heatup, after P1 trip, before FES temperature trip.

Data of local pressure, temperature, and void are presented as a function of axial location around the figure-of-eight loop of the RD-14M facility, starting at the outlet of pump P1. The total loop length through the longest inlet-feeder/heater-section/outlet-feeder paths is 167m.

From the inlet header to the outlet header, flow is divided in five parallel paths (of various lengths), representing the five channels in each pass. In the graphic representation of all the channels simultaneously, longest length has been considered on X-axis and pressure, temperature and void distribution is normalized to this length.

The inclusion of “snapshot” graphs, which show the pressure, temperature, and void profile throughout the loop, were considered by all participants as a useful tool to assess the inter comparison of code calculations.

It is seen that all code calculations were essentially self-consistent, and aided in the explanation of deviations from the test data during key times of the transient. It is also seen that minor differences exist in code calculations, in particular of temperature and void distribution in the loop. However, the comparison between codes must also consider the variation in the timing of key events by each code.

II.2 TEST B9006

In this test, following the 7 mm inlet header break at 11 s, the system pressure decreases rapidly until it reaches saturation pressure of the fluid at the hottest locations. System pressure falls to 8.8 MPa in HDR-7 at 11.3 s and the power of heated section reduces to decay level (5%). Pump ramp boundary conditions are imposed to represent a coincident loss of Class-IV power supply. At this time, a time varying secondary pressure (cool down) is imposed as a boundary condition representing the effect of opening of main steam safety valves.

Pressure reduction in the primary system continues and the pressure falls to 6.0 MPa at 28.5 s at which ECI injection valves open as per logic. No water from the HP ECI system enters the loop at that time as tank pressure (4.2 MPa (g)) is lower than the header pressure. ECI tank pressure is also imposed as a boundary condition with the time as specified in the test. Prior to the actual ECI injection from the accumulator, the opening of the header injection valves located at headers permitted a flow from inlet headers to outlet headers through ECI lines, bypassing the test sections. Entry of relatively cold fluid from inlet header to outlet header reduced the coolant temperature of outlet header and thereby primary coolant in outlet headers was at saturation condition.

Prior to ECI initiation at 70 s, all the participants have consistent pressure trends qualitatively in the entire RD-14M facility. Pressure in the loop ranges from 4.0–4.5 MPa except AERB and KINS have higher values. All pressure trends are as expected in a figure of eight geometry of RD-14M loop.

From the inlet of header 6, all figures clearly show five parallel paths presented on the same length, representing the five channels in each pass. As primary pumps are ramped, gravity plays an important role. The highest pressures are in the lowest heated sections, and the lowest are in the top part of the boiler tubes.

Forced convection flow provided by pump coast down brings the primary fluid temperature close to the secondary fluid temperature in the initial period of the transient. At 70s, all participants are in good agreement with regard to temperatures. Temperatures in the heated sections are in the range of 250°C to 260°C. Temperature trends confirm the positive flow direction in the heated sections.

Prior to ECI initiation at 70s, voids are seen in all the predictions consistently. Generally in heated sections, voids are in the range of 40% to 60%.

ECC flow into each header starts when a particular header pressure drops below the ECC tank pressure. Furthermore, when a header pressure reaches the ECC pressure of about 4.2 MPa, the depressurization rate slows down due to a near-balance in channel steaming and discharge from the small break. Therefore, significant net ECC inflow did not start until about 115 s. Even during ECC injection, the header pressures are very close to the ECC tank pressure, thus ECC injection does not significantly affect header pressures until establishment of sustained ECI injection. The depressurization is considerably slower during the two-phase discharge and slows down even further when flashing occurs in the heated channels. Once sustained ECI injection established, header pressure is determined by ECI pressure.

At around 320 s, all predictions are in good agreement. Pressure in the loop is generally varying from 2.4 MPa to 2.9 MPa except KINS and CNE have slightly higher value.

Temperature trends confirm the positive flow direction in the heated sections except in the top elevation channels in both passes i.e. HS5, HS10 and one of middle elevation channels in the broken pass i.e. HS12 at 320s. In heated sections HS8 and HS13, flow is maintained in its normal direction in experiment. In heated sections HS5 and HS10, which are the channels with the highest elevation, low to stagnant flow is observed in initial period of transient; subsequently reverse flow is maintained in experiment. In this test, it is found that usually, in broken pass, flow reversal occurs in two channels (either in HS-12 or HS13 and HS10) whereas in unbroken pass, flow reversal occurs in only one high elevation channel (mostly in HS5). It is clearly seen from temperature trends that AECL and NPCIL have flow reversal in the channels. THU has almost the same temperature in the entire loop.

At the same time, void predictions are in good agreement among the participants except NPCIL which shows early loop refilling as voiding is less in the loop. Other participants have the full void range in the entire loop.

Prior to isolation of HPECI at 1050s, pressure trends match well among the participants. Generally, the pressure varies from 0.85 MPa to 1.45 MPa except CNEA and AERB have higher values ranging from 1.45 MPa to 1.75 MPa. Temperature also shows good matching and depicts the flow reversal in some of the heated sections in all trends. THU has almost the same temperature in the entire loop.

Wide variations are seen in the void predictions from 1050s onwards. At 1050s, AECL, CNE and KAERI predicted significant voiding while NPCIL, AERB, CNEA and KINS predicted almost no void. THU predicted high voids near the HD-6 region and the rest of the system is filled with water. KAERI had also significant voids in the loop prior to the isolation of HPECI which clearly dictates that the loop is yet to be filled completely. In general, all the participants have almost complete loop refilling except some intermittent voids which could be trapped in some locations e.g. end fitting.

The net flow of ECI into the system, based on the depletion of the ECI tank, varied from 1.0 to 2.0 l/s in the initial stage. The high pressure accumulator tank ECI phase is terminated upon depletion of the accumulator ECI tank at 1110 s. The final loop pressure at the end of the high pressure ECI stage is around 1.4 MPa. At the same time, low pressure emergency coolant pump injection started. In the low pressure pumped ECI phase, constant ECI flow in all headers is observed which indicates that the void from the primary system is collapsed.

After the isolation of HPECI and initiation of LPECI at 1500s, system pressures are in very good agreement among the participants. The final loop pressure ranges from 1.3 MPa to 1.75 MPa. Temperature also shows the correct trends except THU; THU has almost the same temperature in the loop. At the same time, it is clearly seen from the predictions that the loop is completely filled except KAERI; KAERI has significant voids still in the loop as HPECI is isolated and LPECI is initiated. Some significant voids are also seen in THU predictions at nodes near HD-6.

II.3 TEST B9802

In this test, the break is initiated at inlet-header 8 at 11.2 s, the power of the heated sections kept constant and primary pumps operated at a constant speed of 3000 rpm. As a result of the small break, the primary circuit inventory kept depleting gradually. In this test, no ECI systems were actuated.

Loop depressurization is largely determined by break discharge rate and steaming formation rate. Following the break, pressure in all the headers reduces sharply during the initial period of transient. Following initial sharp pressure reduction and voiding in outlet headers, pressure reduces gradually in two-phase condition. Saturation pressure at ROH stabilizes primary circuit pressures. At around 400 s onwards, ΔT across the primary and secondary has stabilized. ROH temperature and pressure stabilizes. Steam formation rate at high power has restricted depressurization of inlet headers even with continuous two phase discharge.

Since the pumps continue to operate, forcing flow throughout the loop in the “forward” direction, the temperature difference from the boiler inlet to outlet indicates that both boilers continue to remove heat throughout the transient. The boiler inlet temperature closely follows the saturation temperature (which decreases with the slowly decreasing loop pressure), while the outlet temperatures reflect the boiler heat sink temperature, at least during the single-phase period. When the boilers are no longer able to fully condense the steam in the boiler tubes, voiding is started at the pump suction.

After the initiation of the break, coolant discharges and causes initial sharp depressurization of primary loop. At 400s, there are no voids in both the pumps and they are providing full head. From the pump to inlet header and up to inlet feeders, there is single phase flow and hence pressure drop is relatively small. As coolant passes through the heated sections, resulting rise in pressure drop has been predicted well by all the participants. As coolant passes through steam generator U-tubes, steam gets quenched after transferring heat to secondary system. Again in single phase, pressure losses are very low as predicted by all the participants. Loop pressures vary from 6.4 MPa to 7.8 MPa except for KAERI, KINS, THU and AERB who have higher initial values at this time. The entire loop depressurized relatively uniformly during this SBLOCA, settling between 6.0 and 7.0 MPa prior to the pump trips.

At 400s, temperatures are in good agreement among the participants. Temperatures are generally 260°C at the boiler outlet and 290°C at the boiler inlet for all the predictions except THU. THU has temperature values at slightly higher side.

At 400s, voids are matching well among the participants. All trends clearly show about the heat removal capacity of the boilers. At pump outlet, no voids are seen whereas significant voids are seen at the heated section outlets in all the trends.

At around 1000s, just prior to oscillatory flow, the loop pressure stabilizes. Pressure at the pump outlet is ~ 7.2 MPa and at the boiler inlet is ~ 6.4 MPa. CNE has almost the same pressure throughout the loop at this time.

Predictions of all the participants for temperature at 1000s are similar to temperature variation at 400s except CNE and NPCIL. Both of them have not predicted any temperature rise by the heat of heated section. This is due to the presence of voids at the inlet header. Two phase coolant enters into the heated sections and no sensible heating takes place as only the phase change is occurring.

At 1000s, voids variation is similar to 400s only their values have increased. In general, voids are uniformly distributed in the entire loop which is predicted by all the participants.

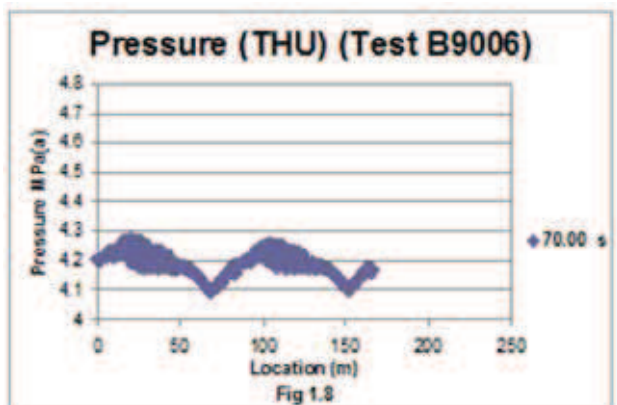
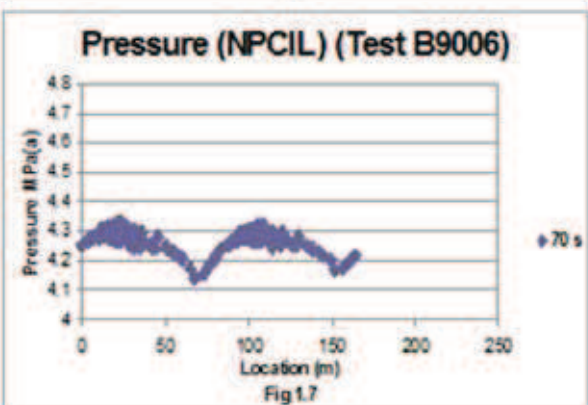
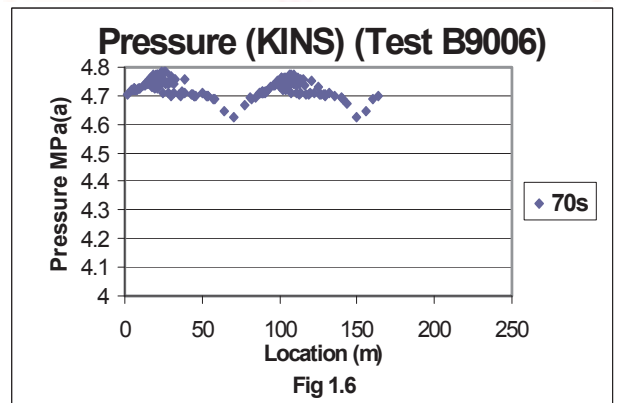
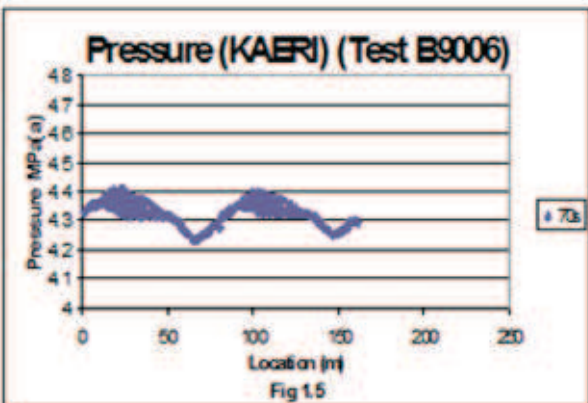
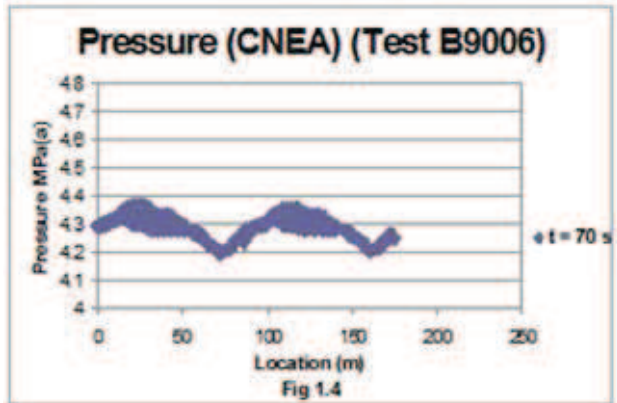
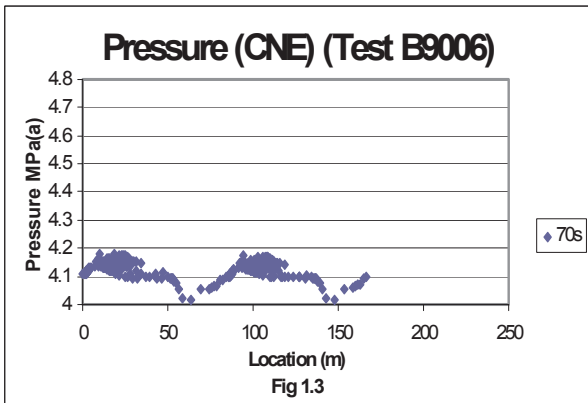
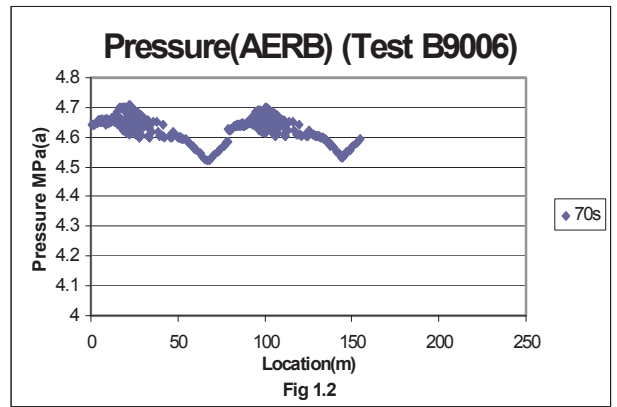
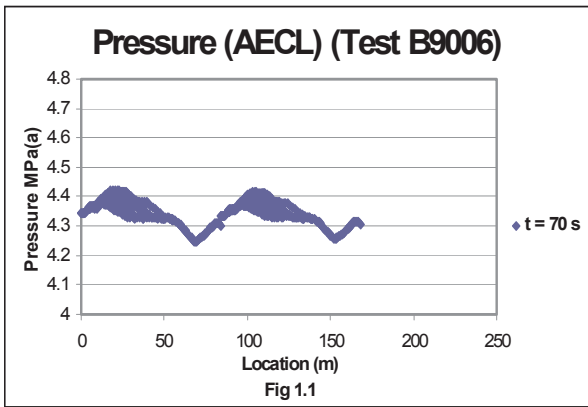
When voiding starts at pump discharge, flow reduces which increases discharge pressure and results in a void reduction at pump discharge. This phenomenon repeats and creates oscillations in the transient from 900 sec to 1200 sec. After 1200 sec pump-1 trips and its

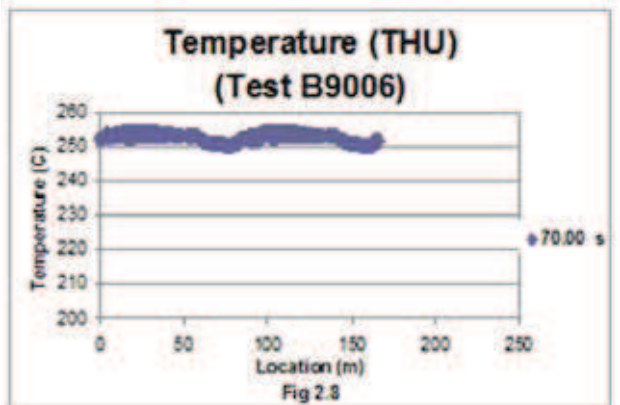
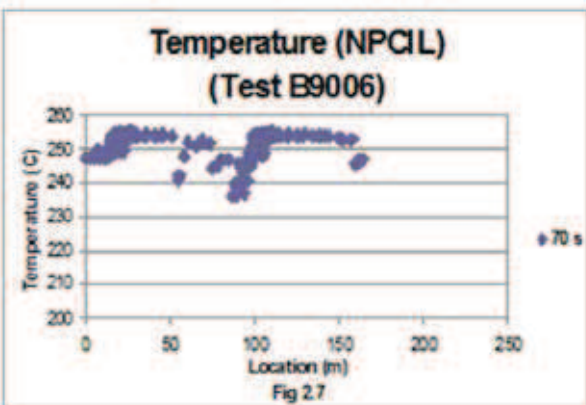
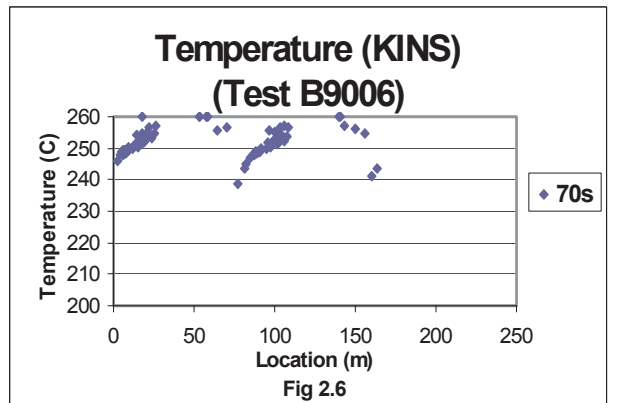
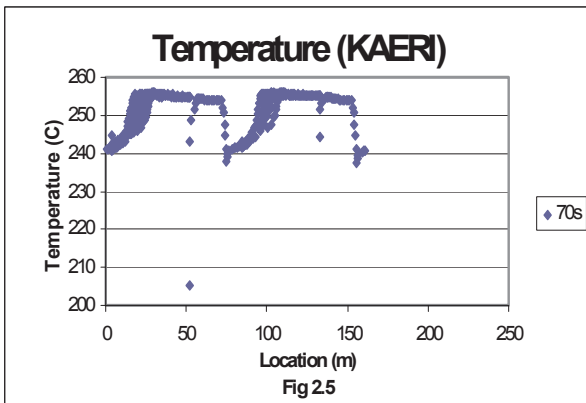
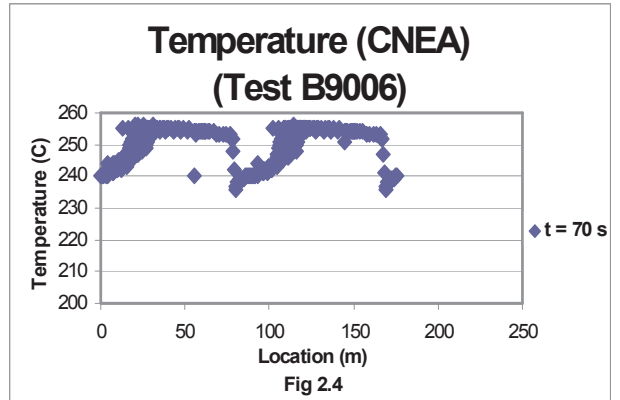
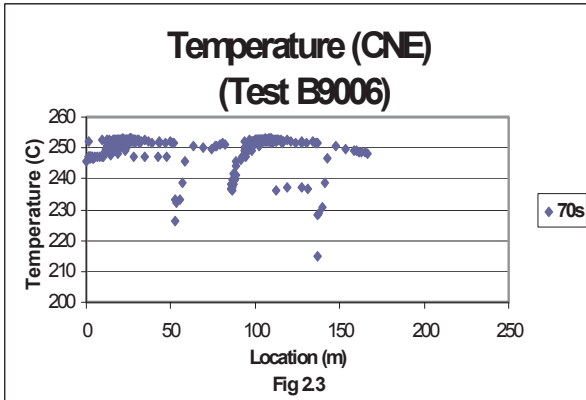
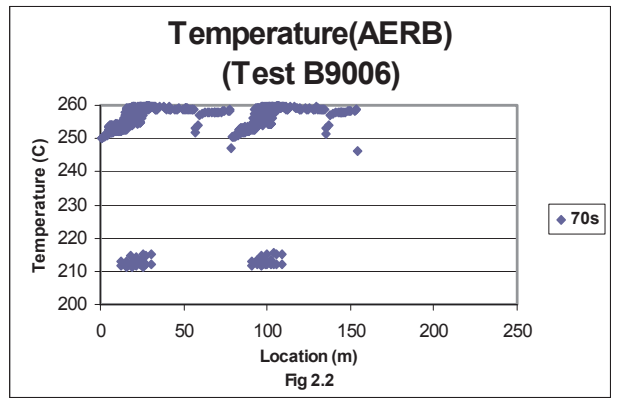
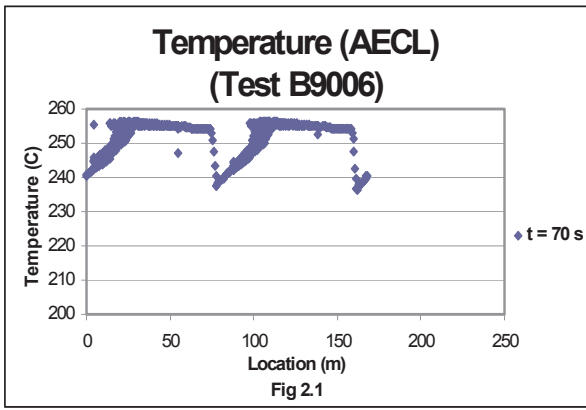
head ceases. Following the pump-1 trip, coolant flow in the loop is maintained by pump-2, its flow decreases and head increases.

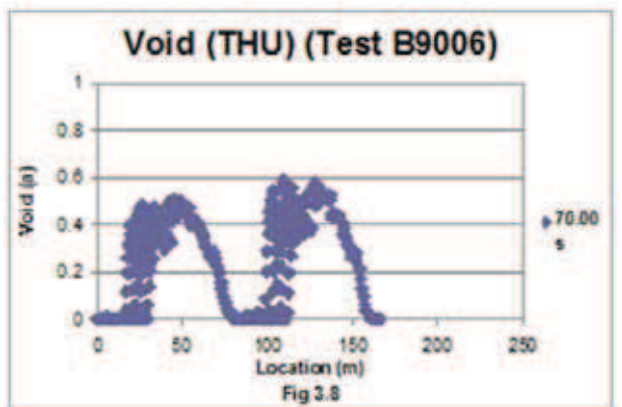
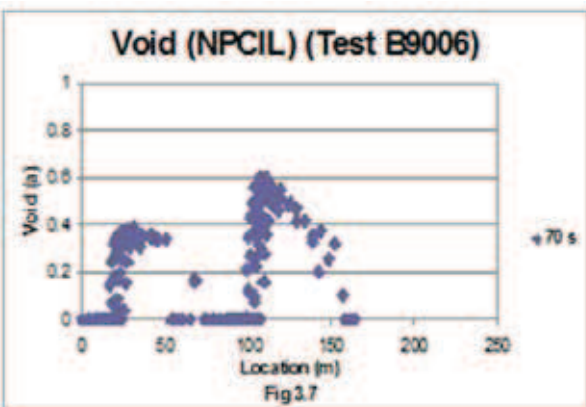
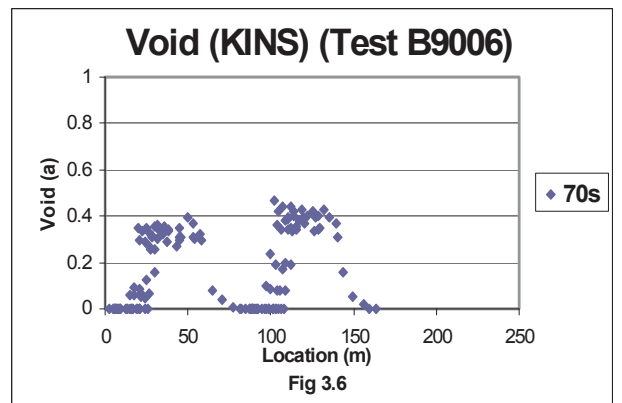
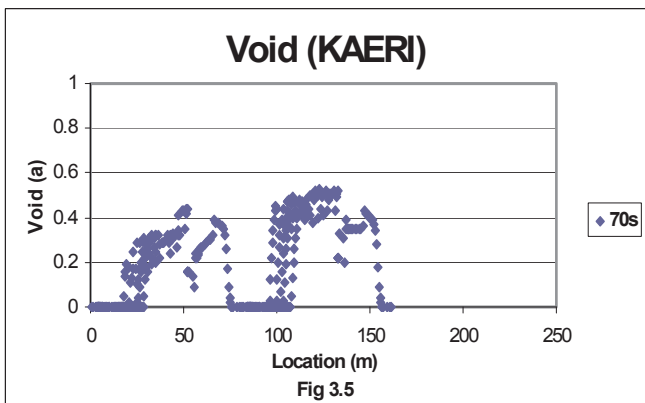
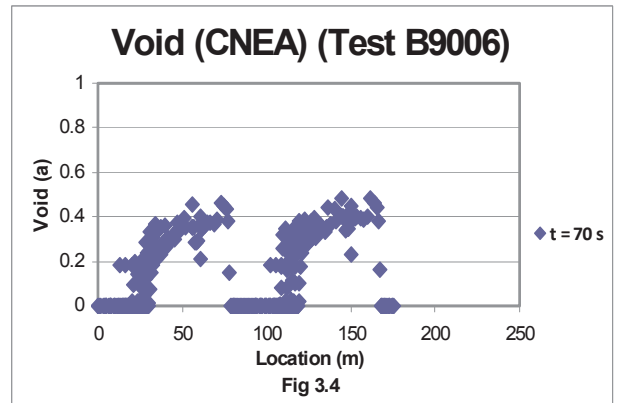
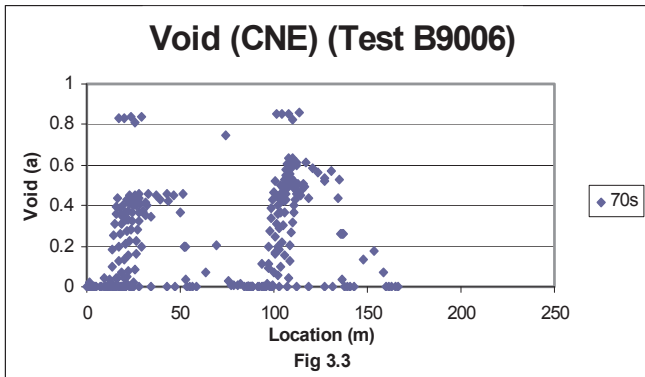
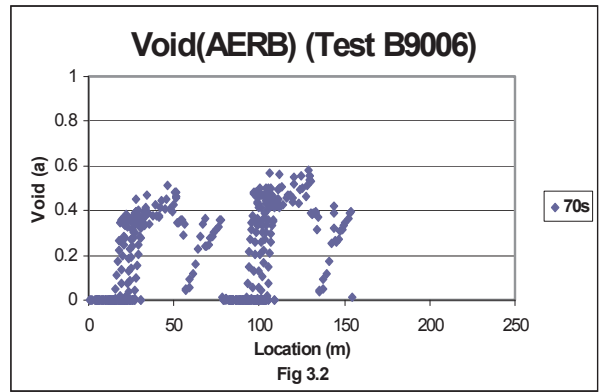
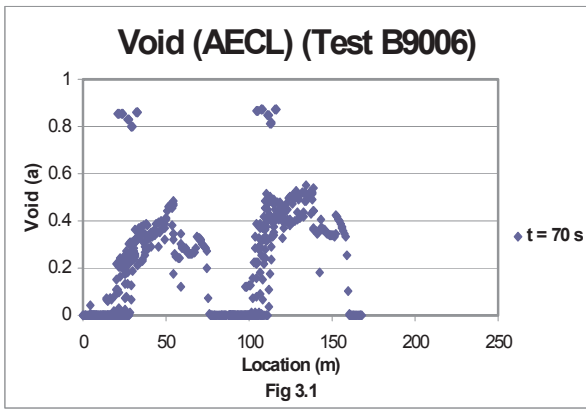
At around 1300s, loop pressure stabilizes at 6.0 to 7.0 MPa in the predictions except CNE and KINS. CNE has loop pressure at around 3.5 MPa and KINS at around 5.0 MPa.

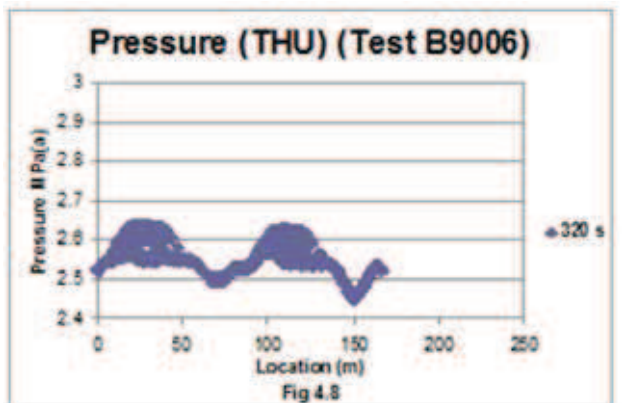
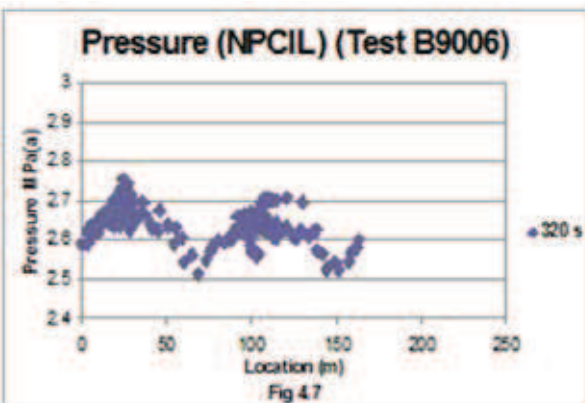
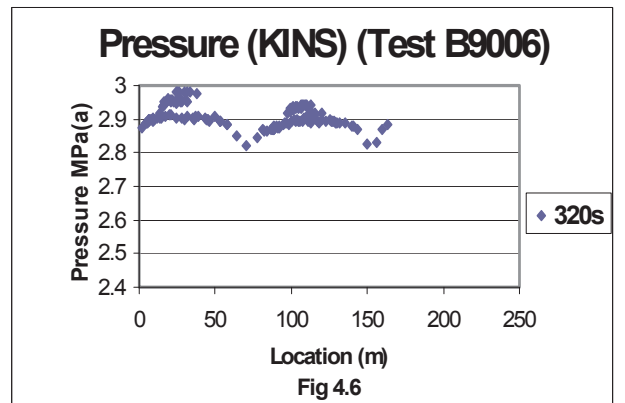
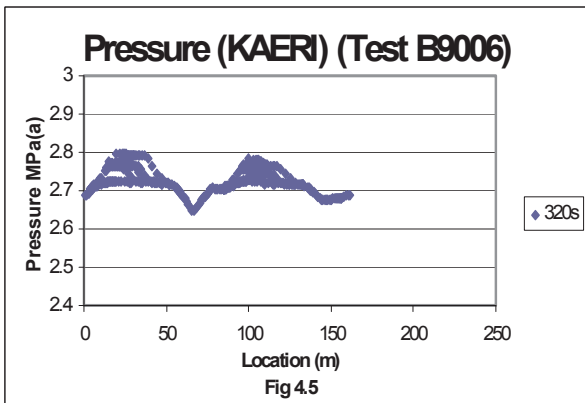
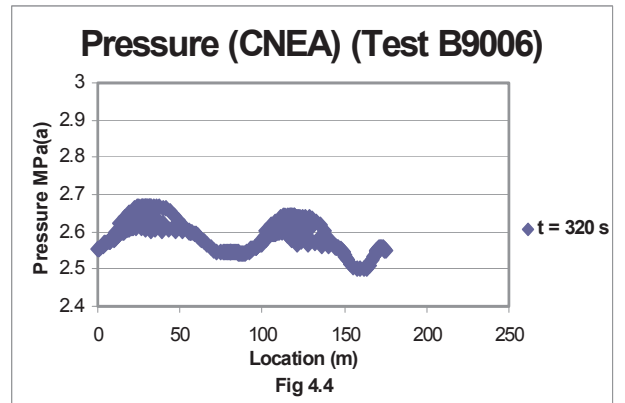
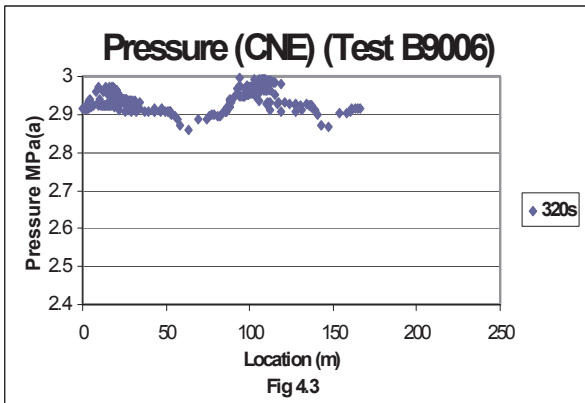
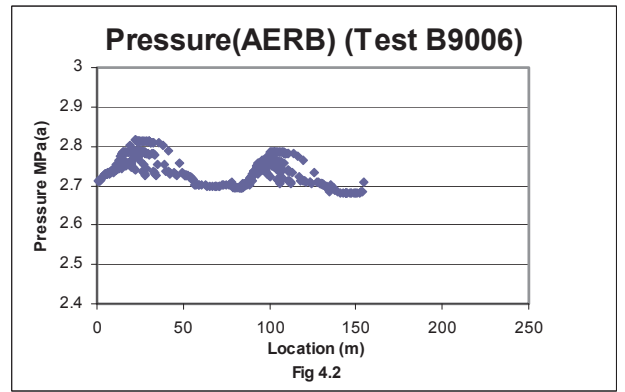
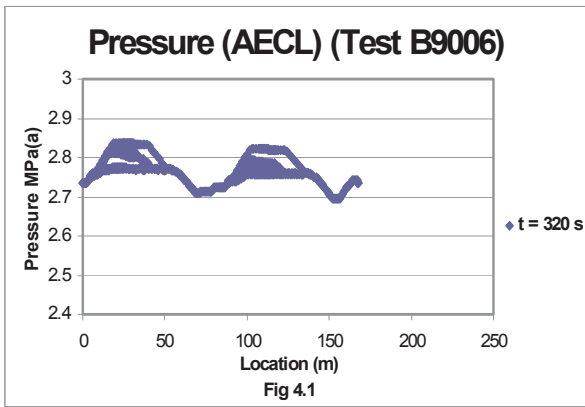
At the same time, temperatures are in good agreement among the participants. Almost 10°C Delta T is available across the boilers in the predictions except KAERI, THU and KINS.

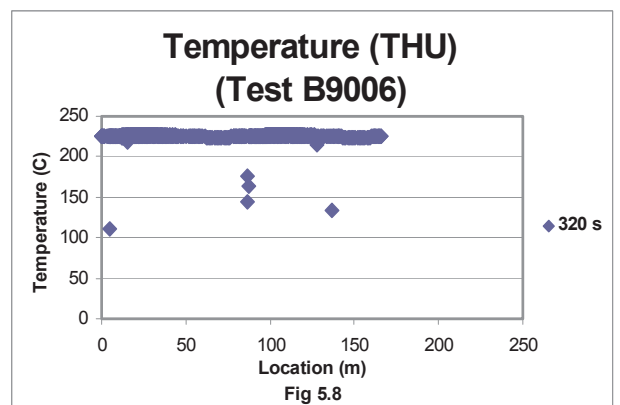
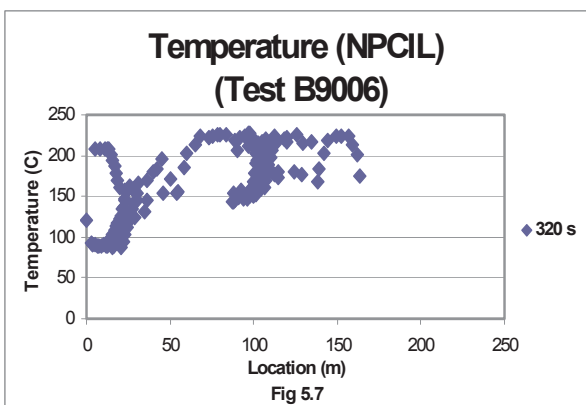
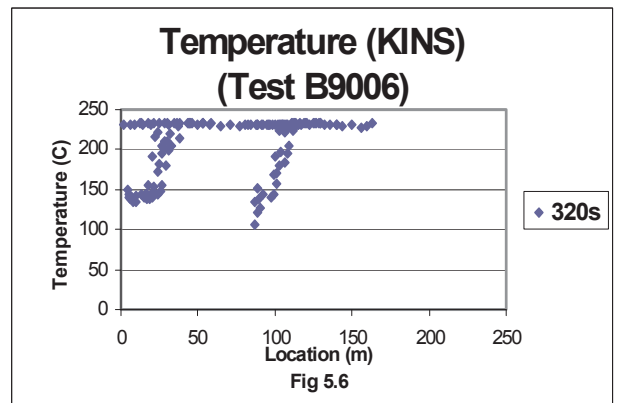
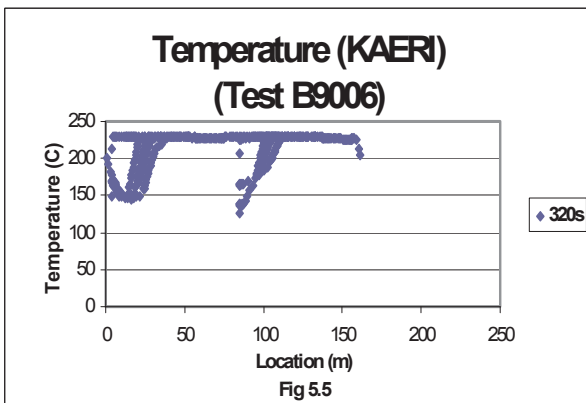
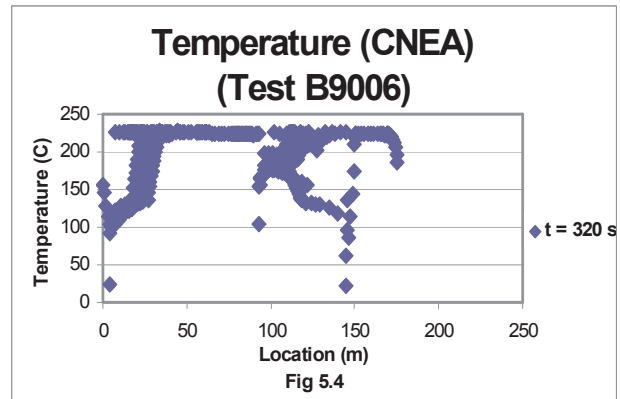
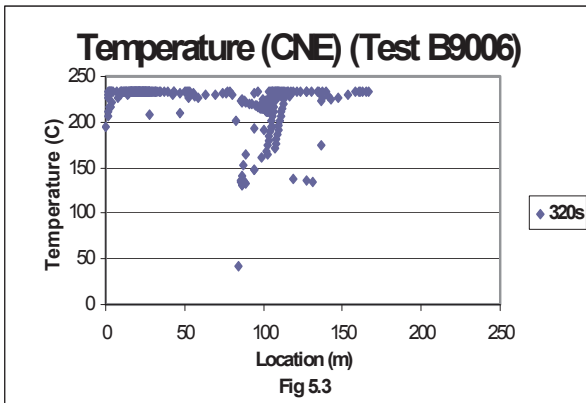
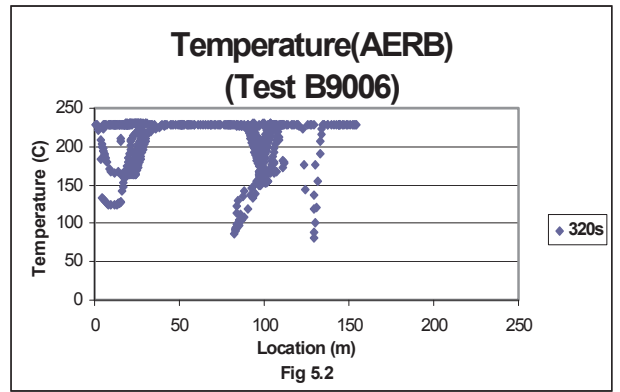
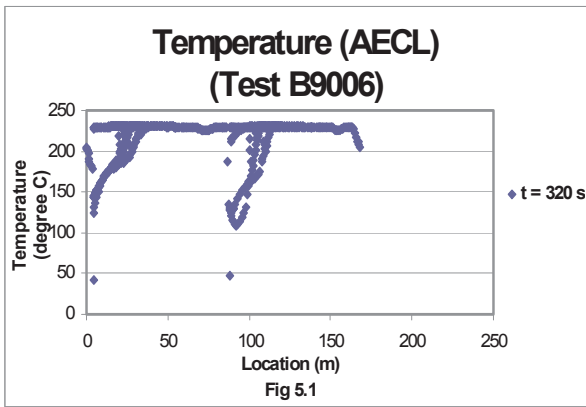
At this time, full voiding is seen at the heated sections outlet. This is well predicted by all the participants except KINS.

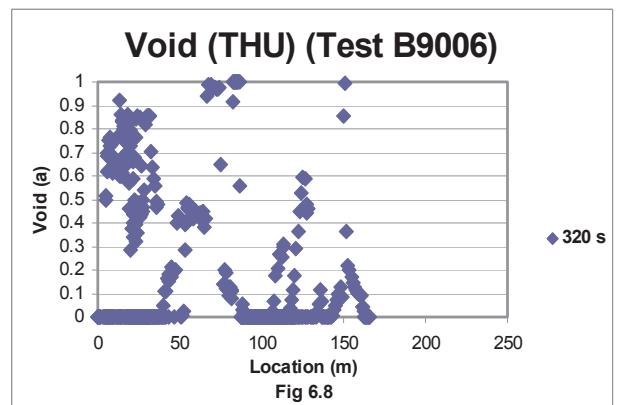
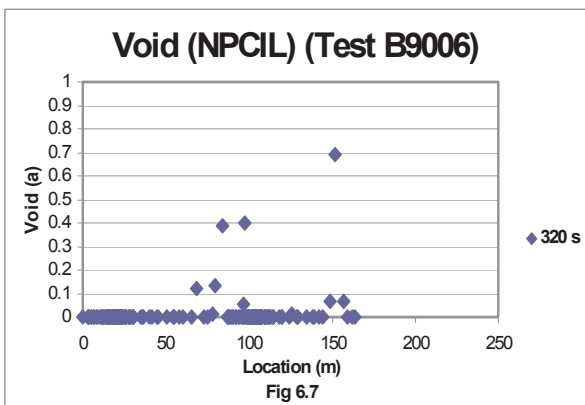
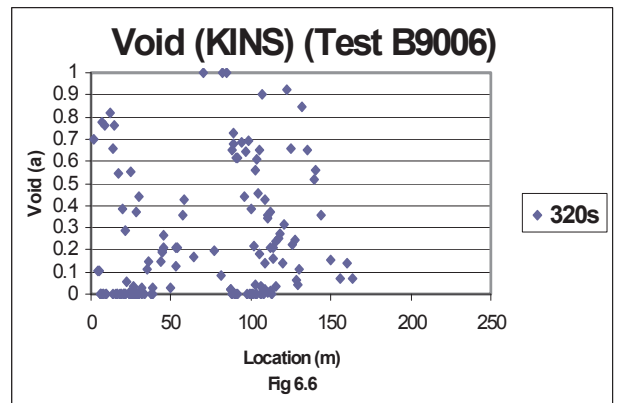
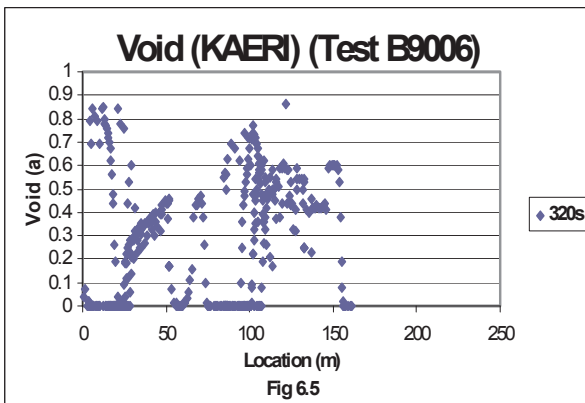
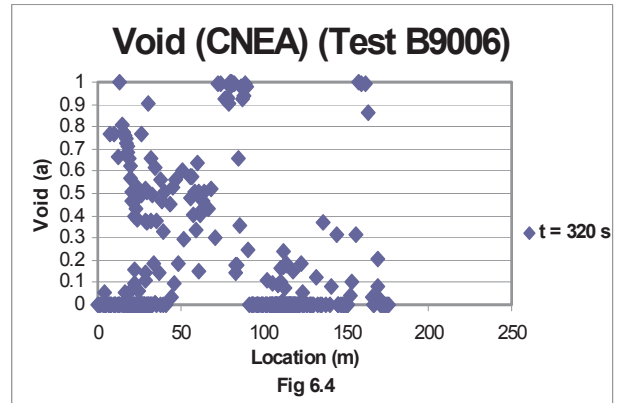
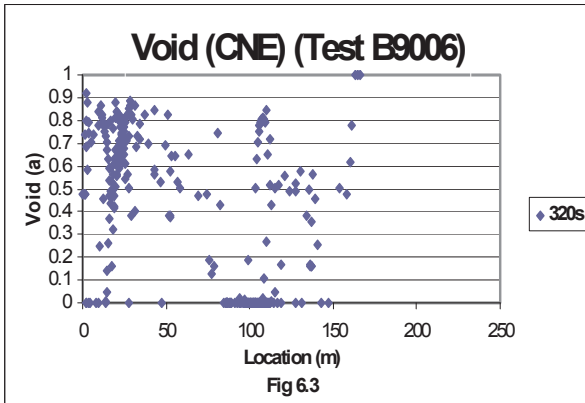
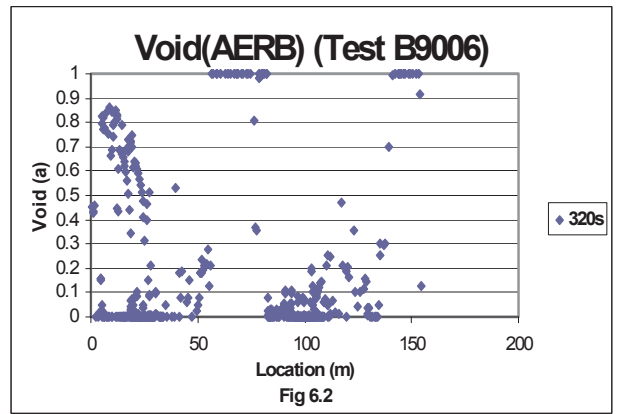
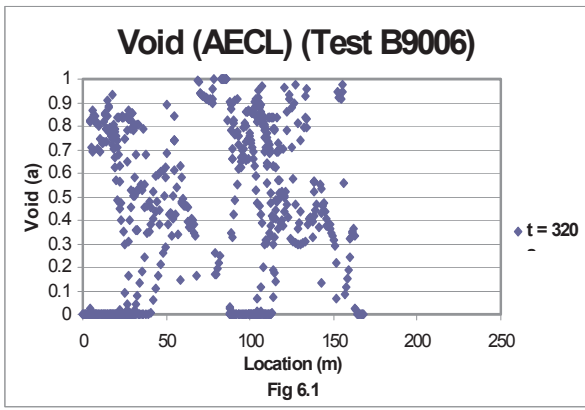


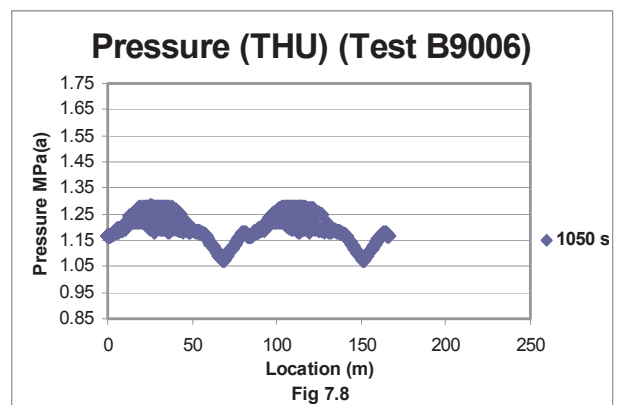
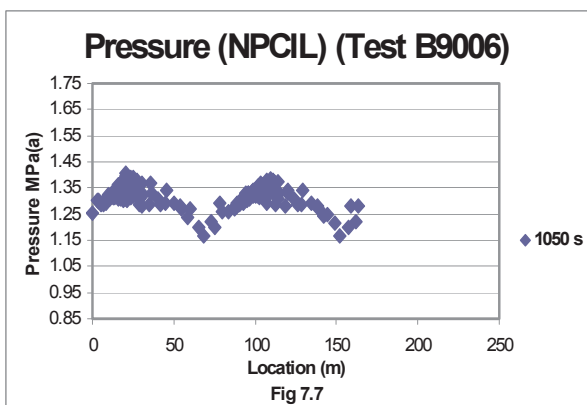
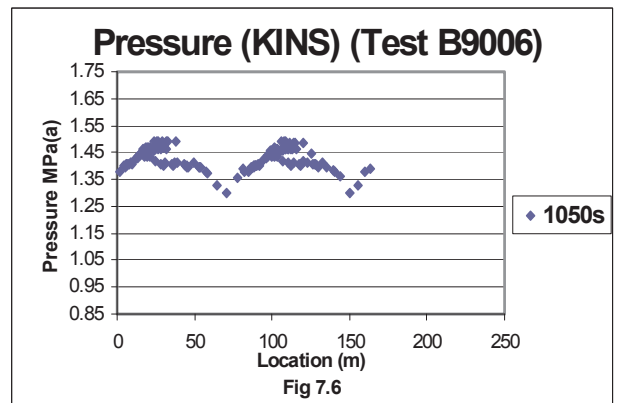
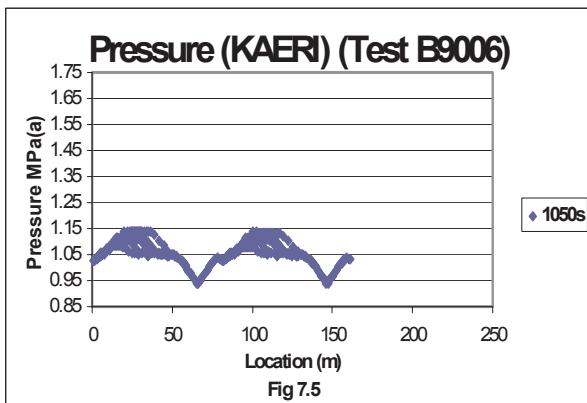
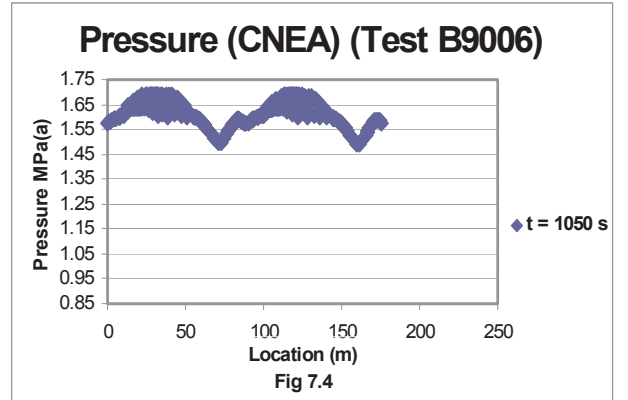
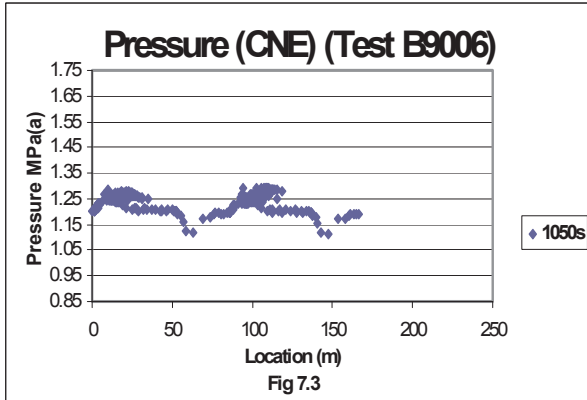
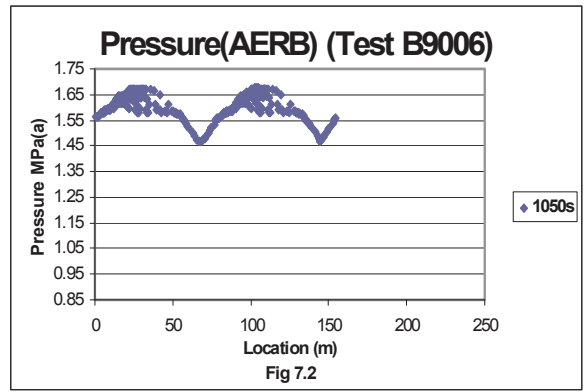
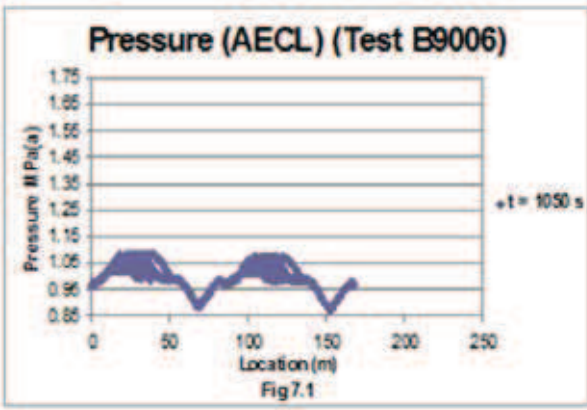


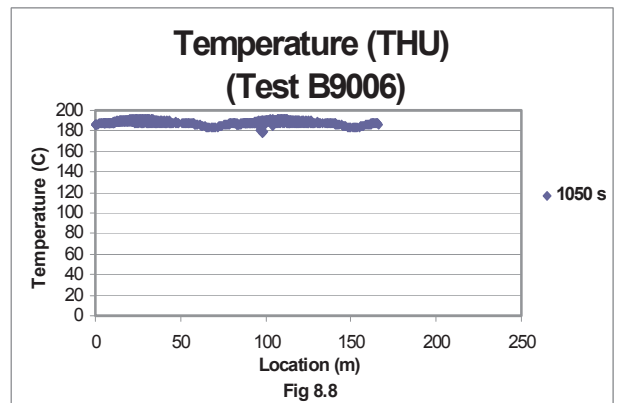
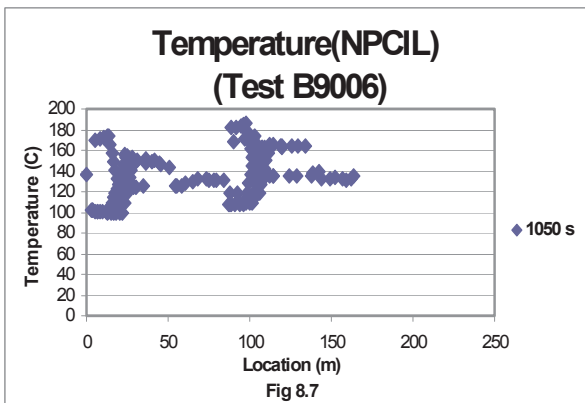
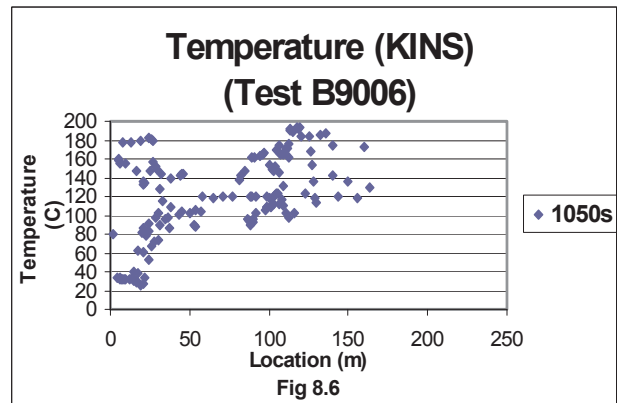
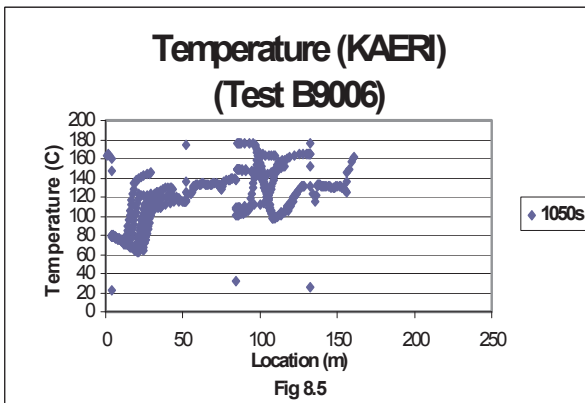
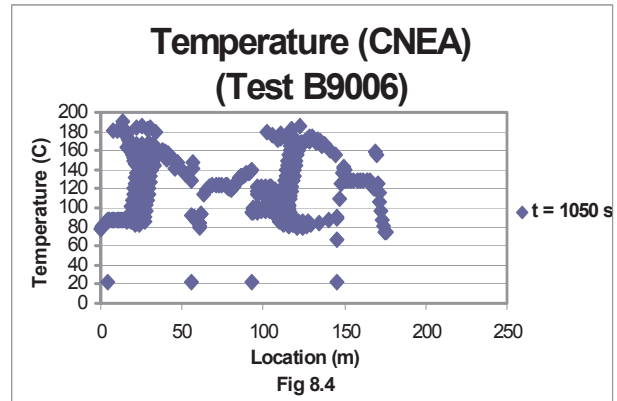
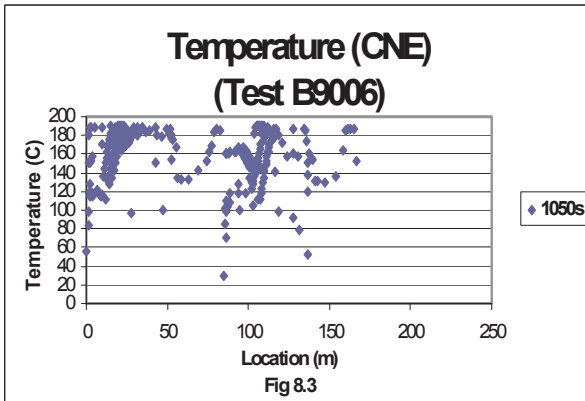
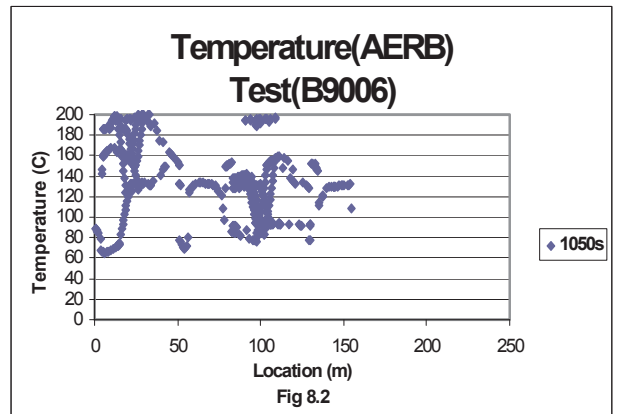
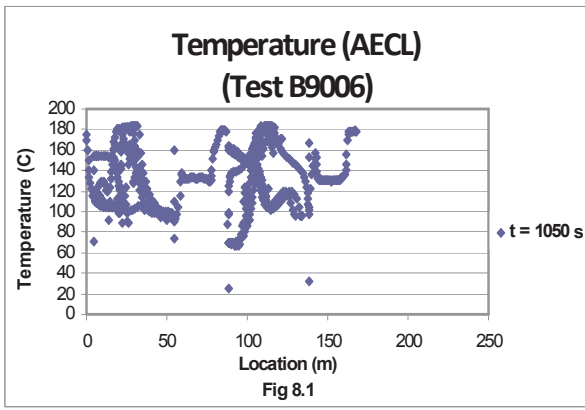


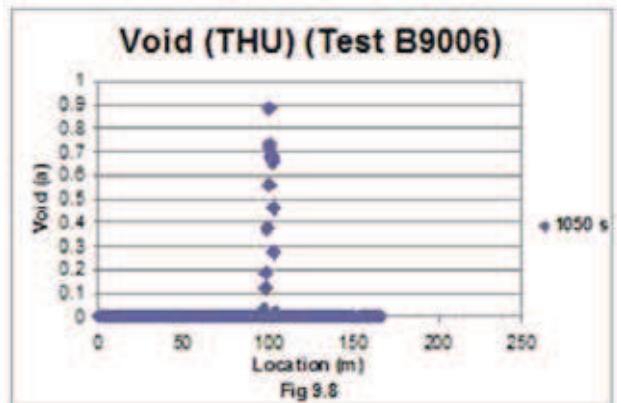
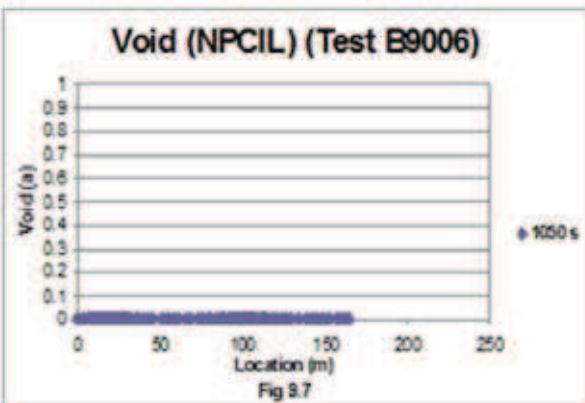
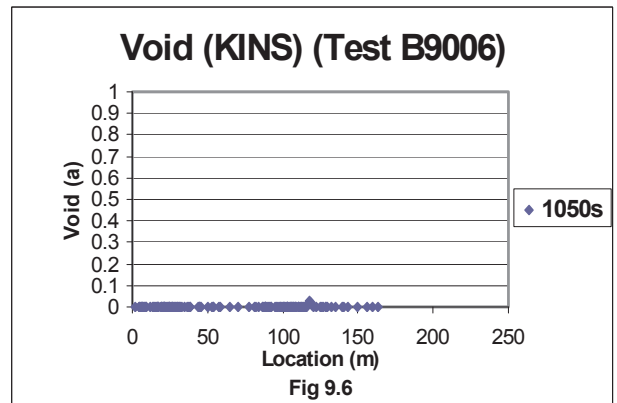
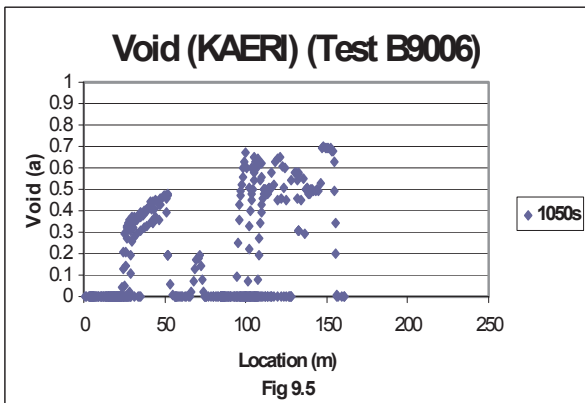
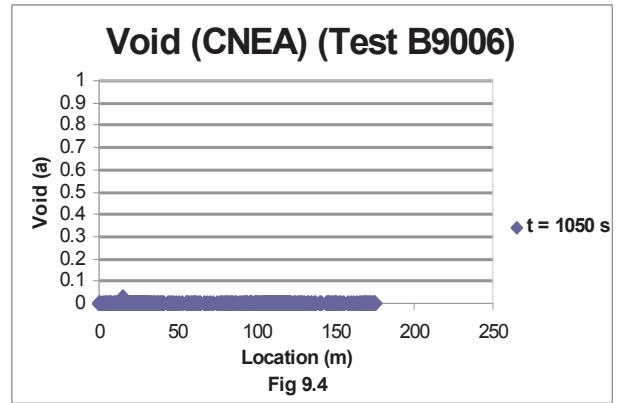
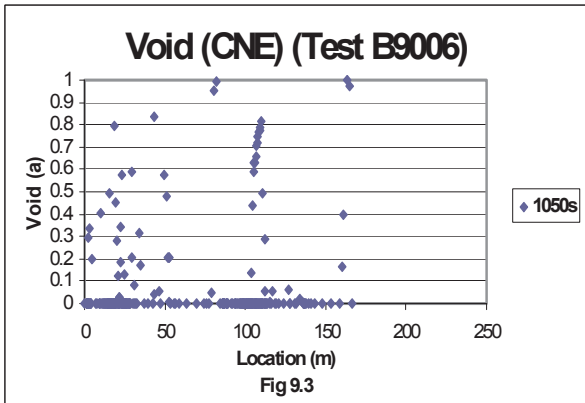
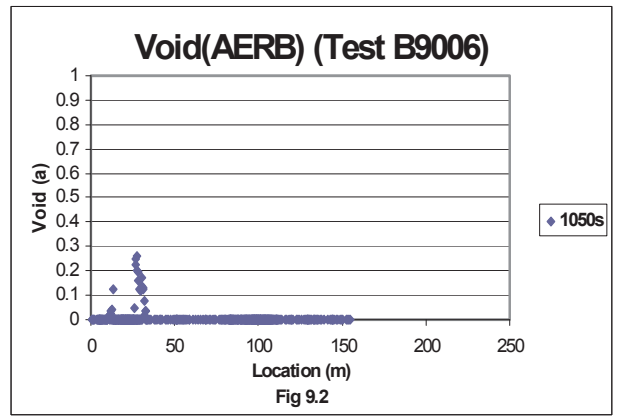
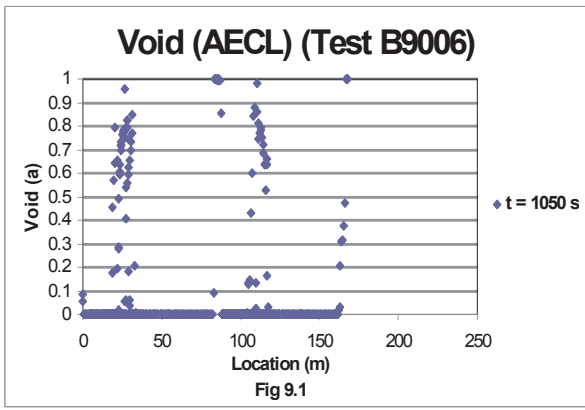


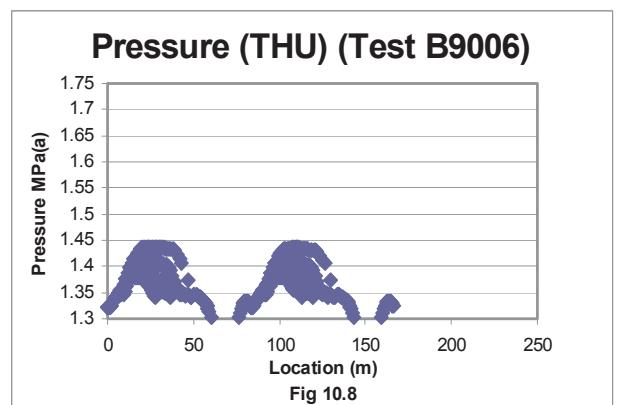
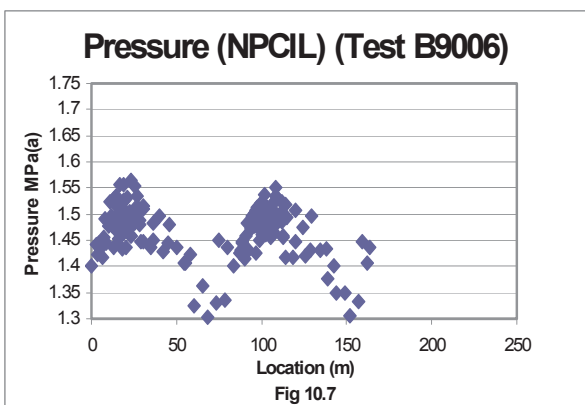
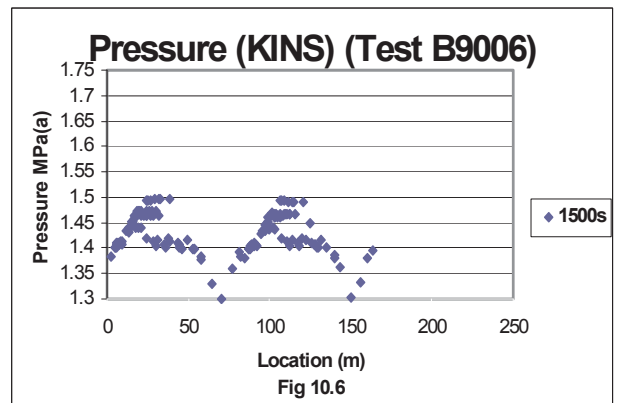
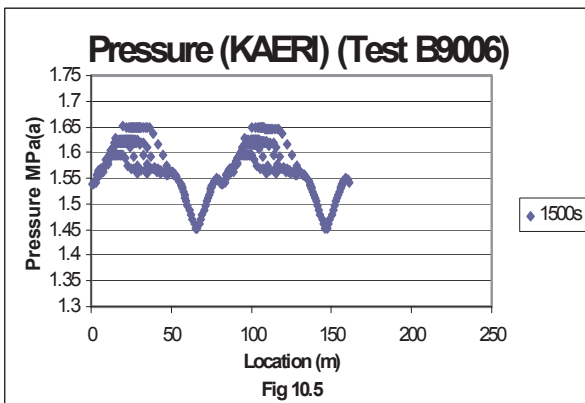
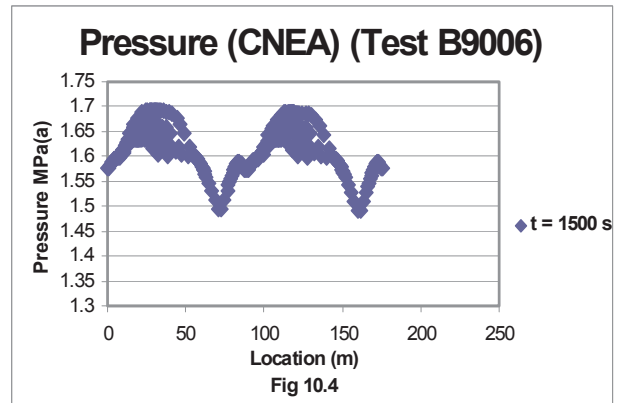
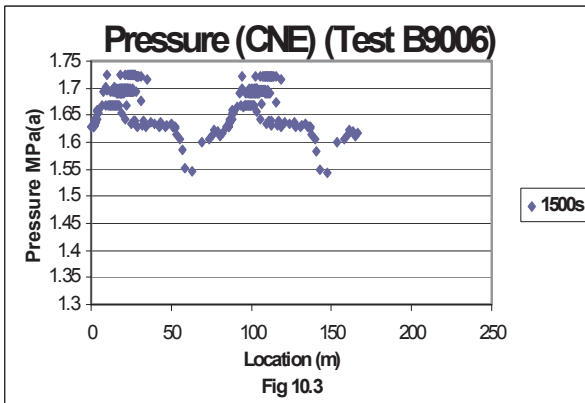
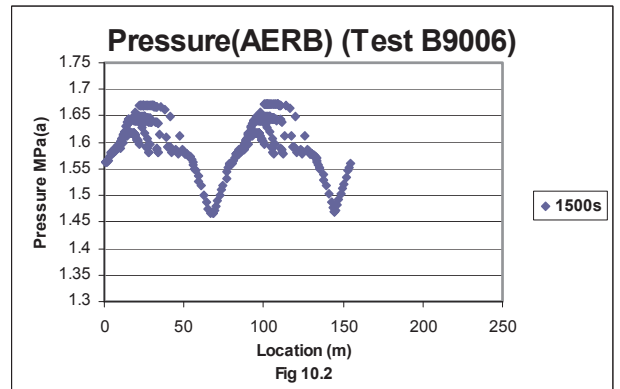
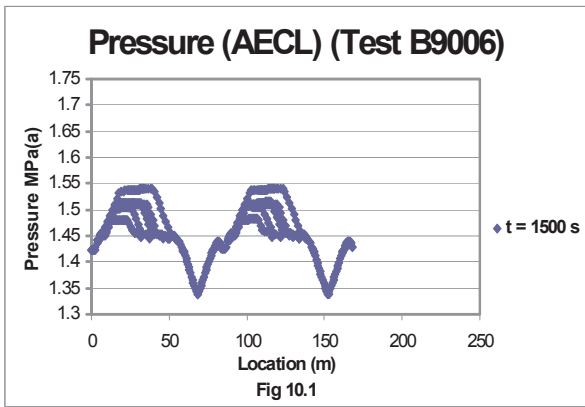


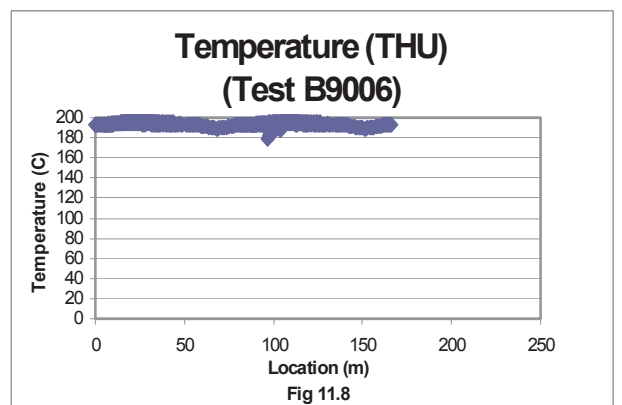
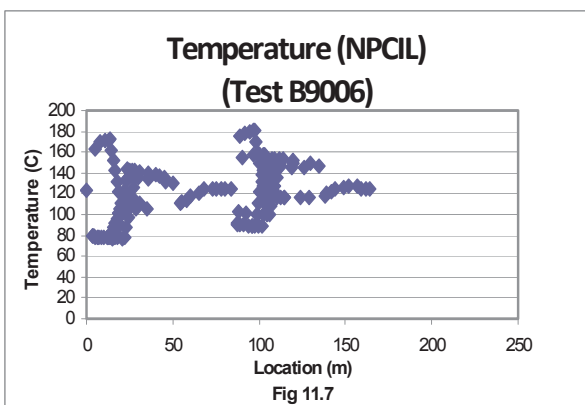
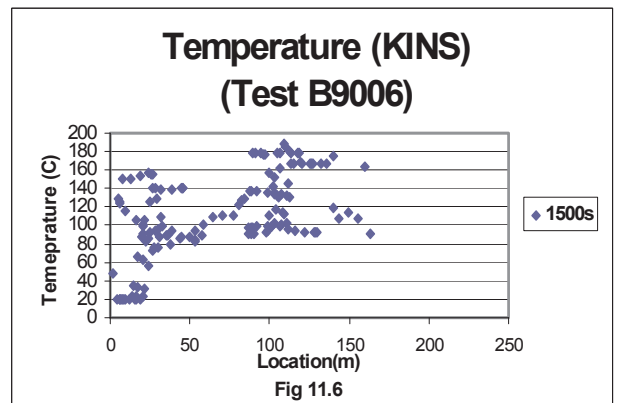
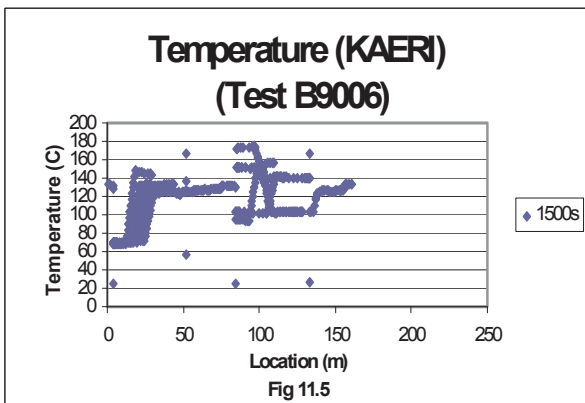
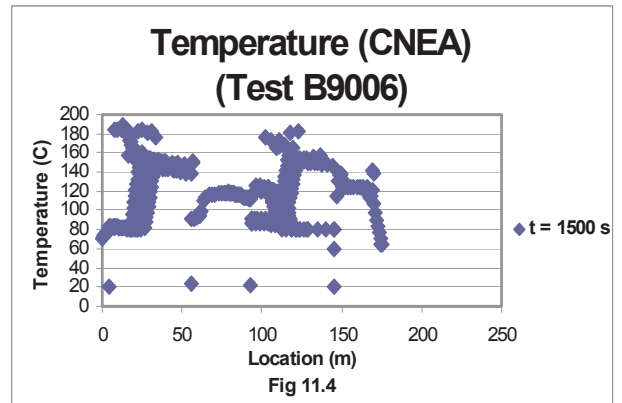
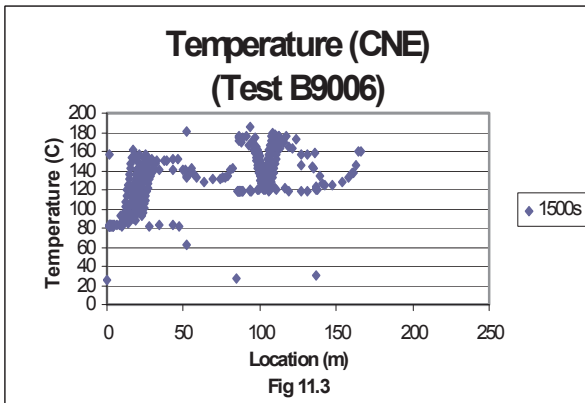
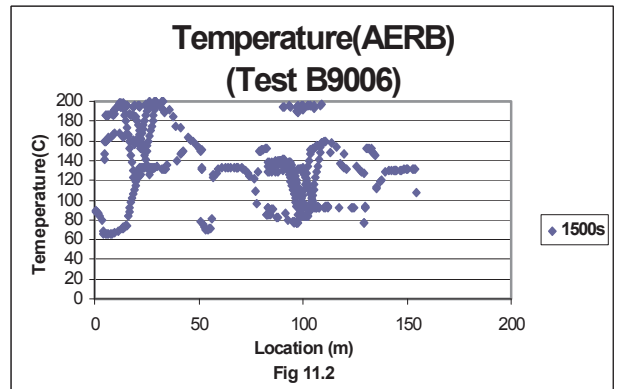
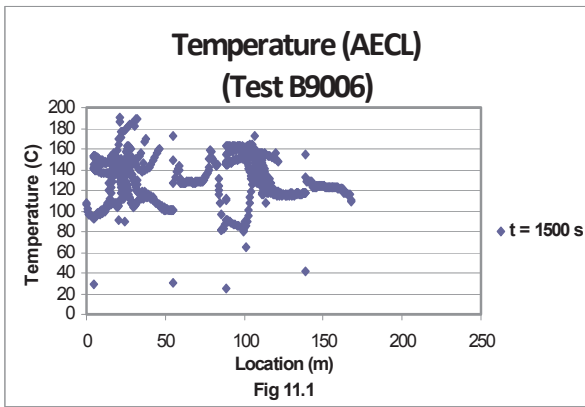


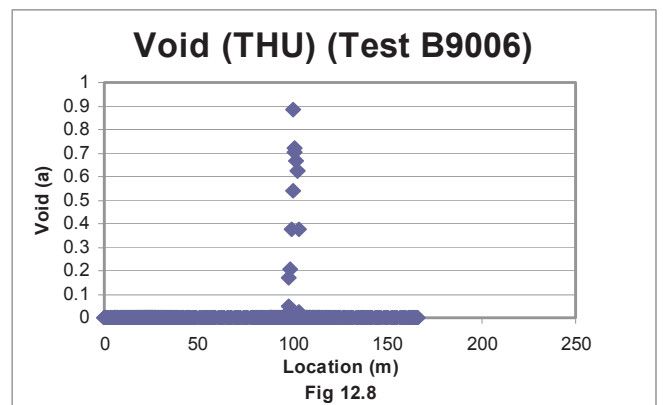
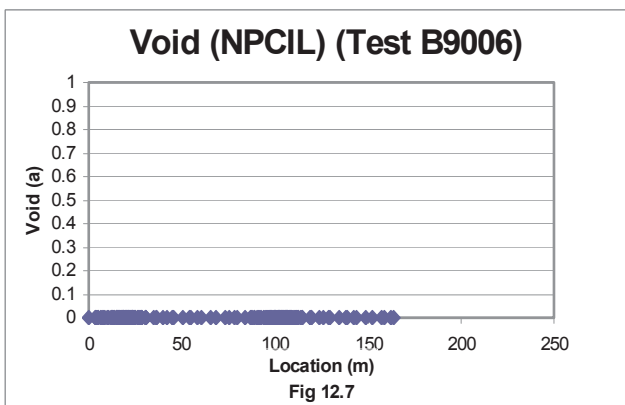
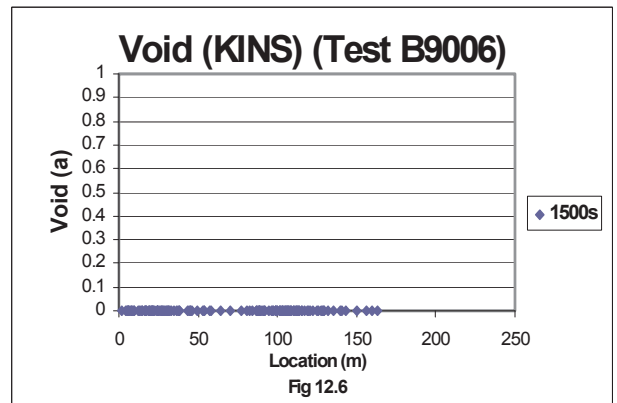
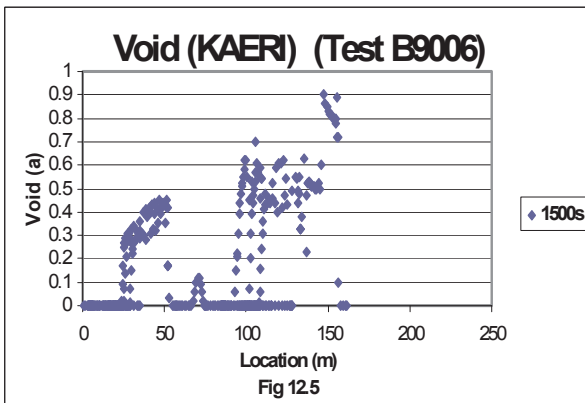
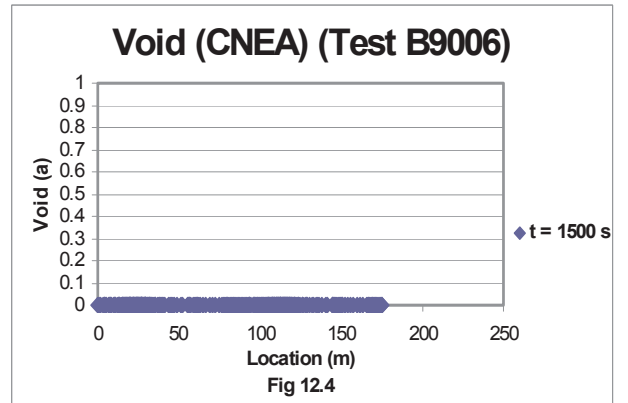
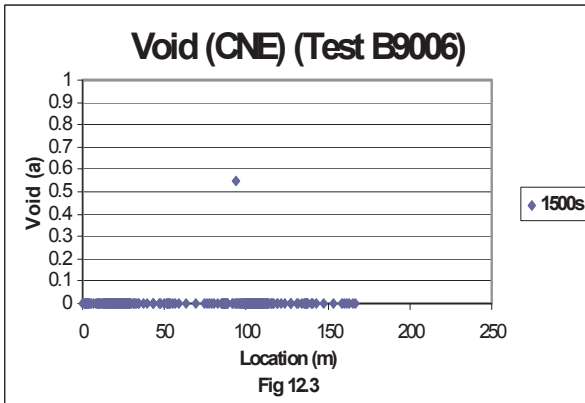
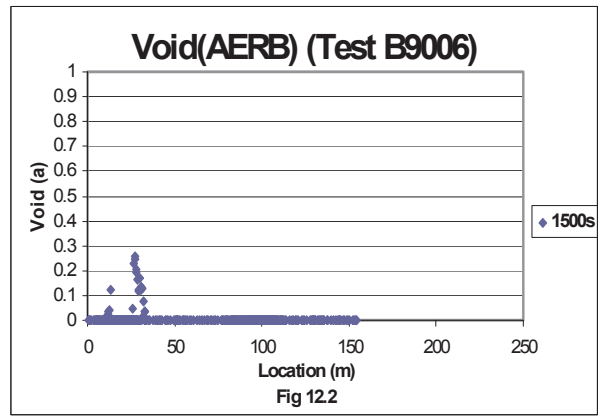
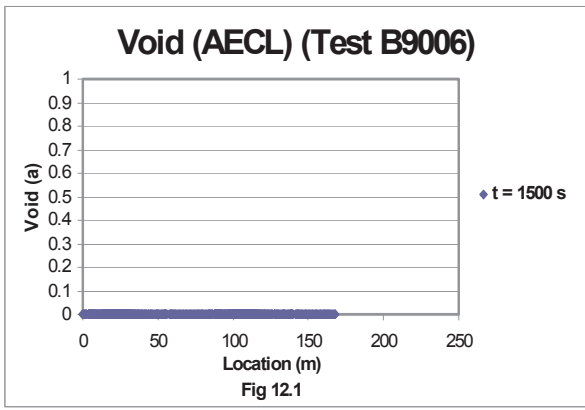


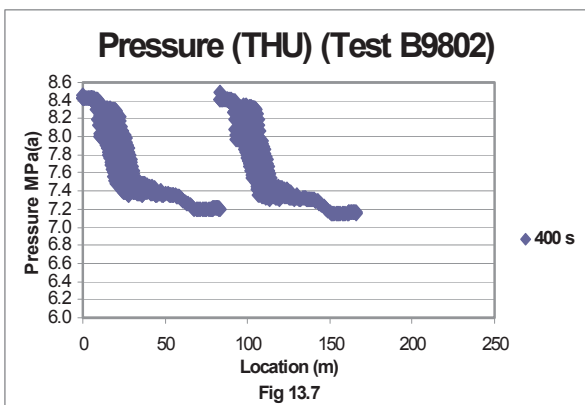
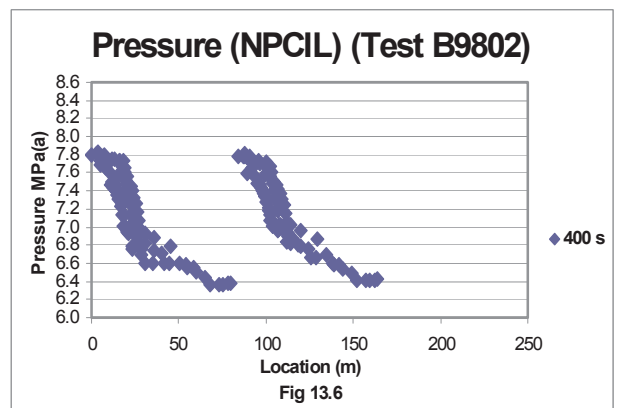
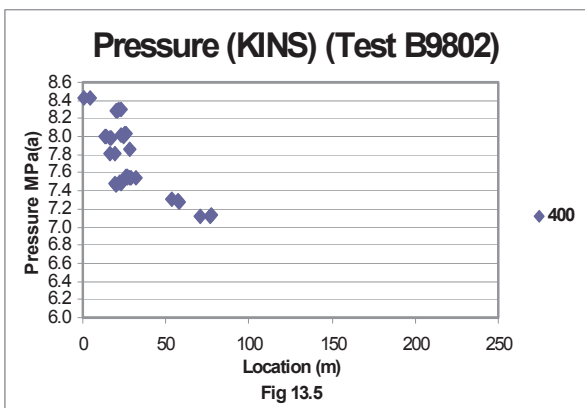
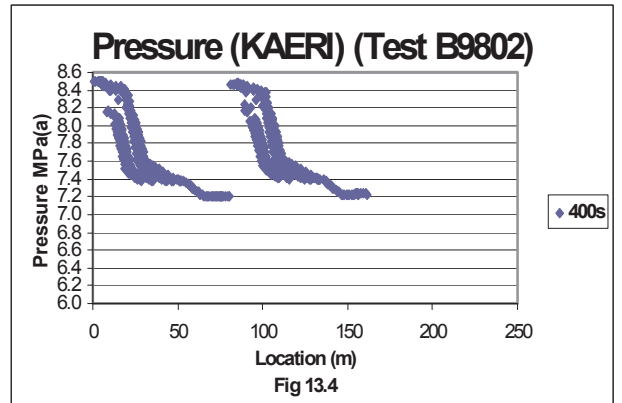
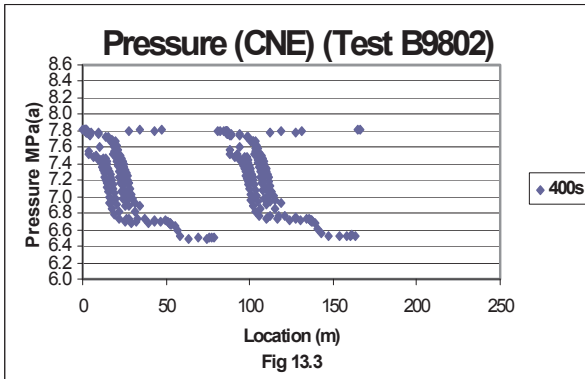
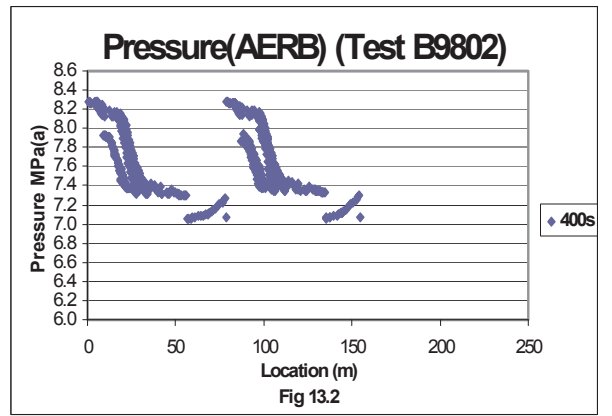
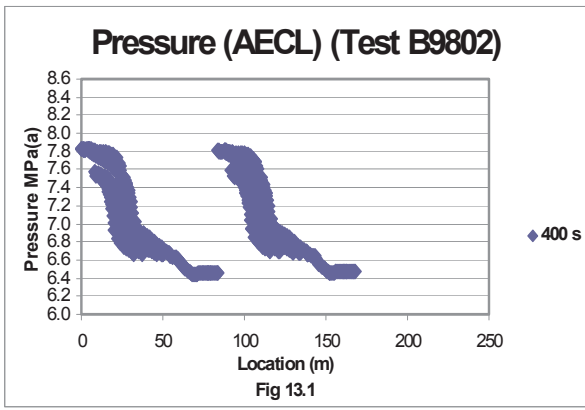


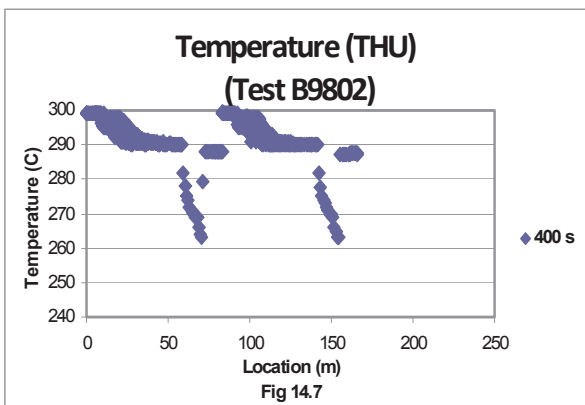
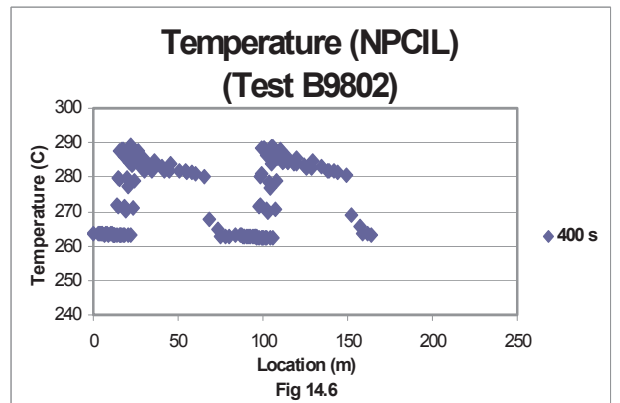
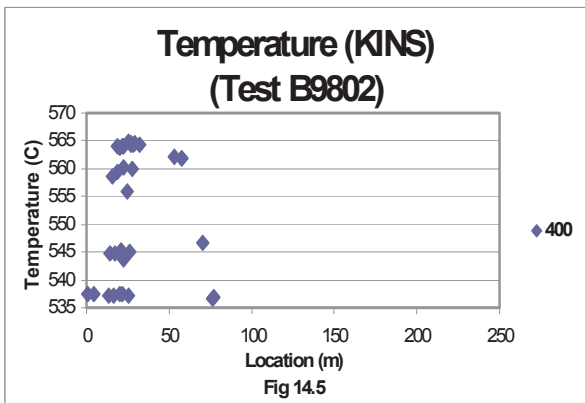
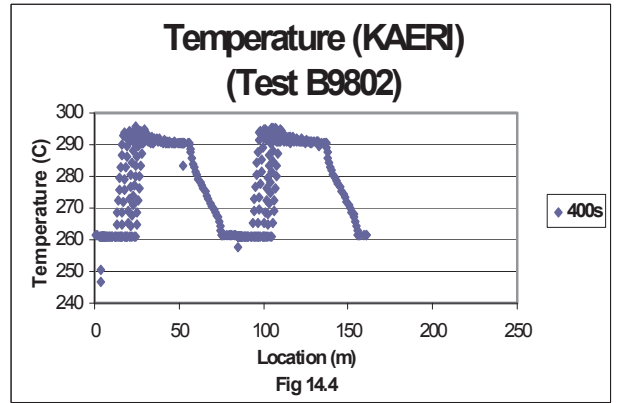
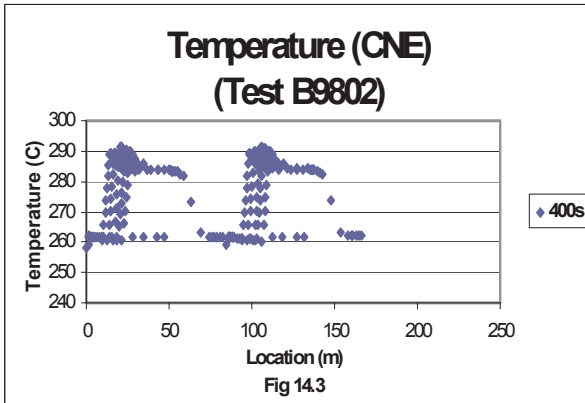
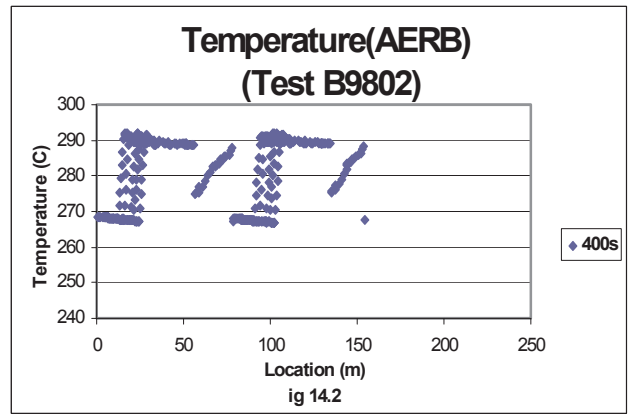
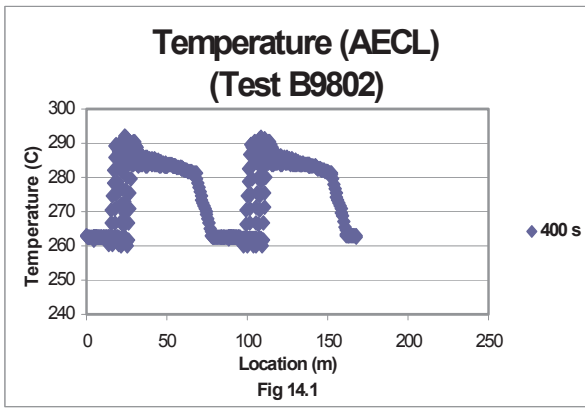


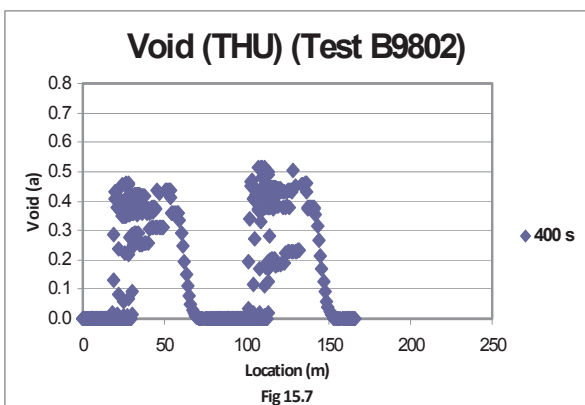
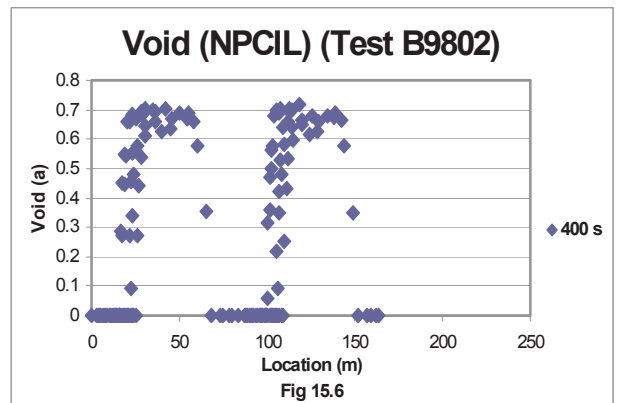
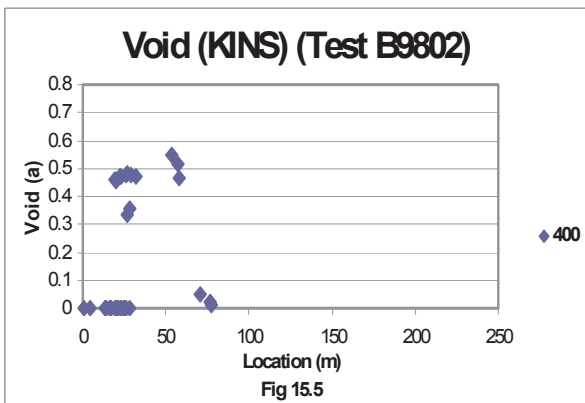
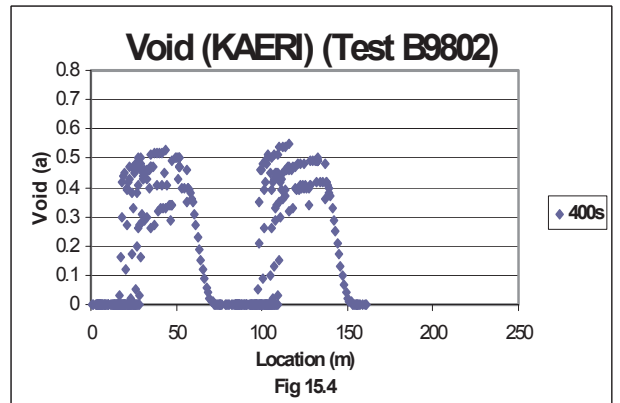
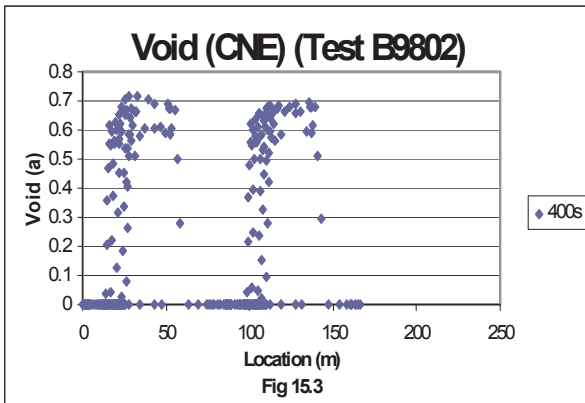
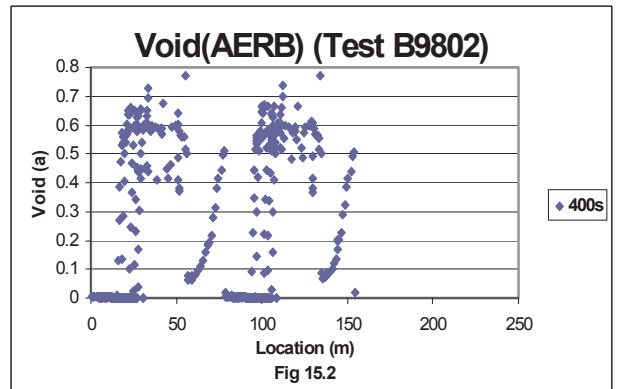
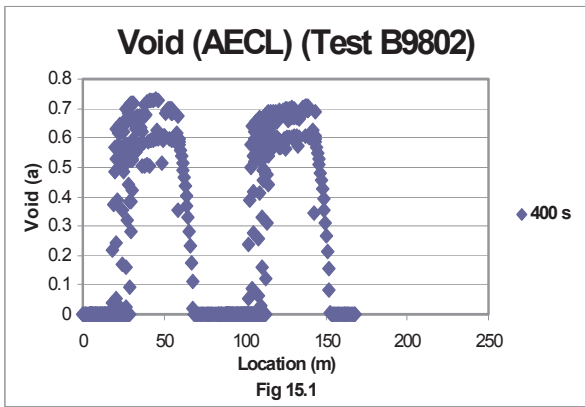


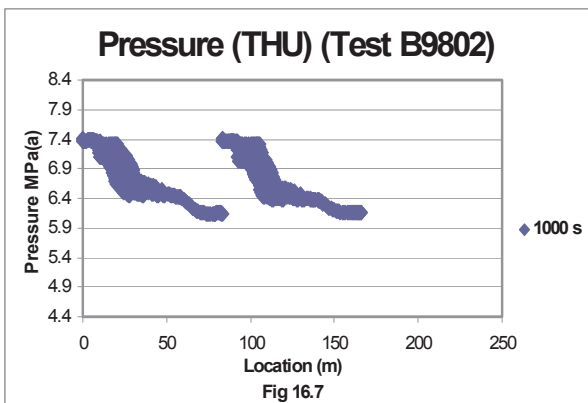
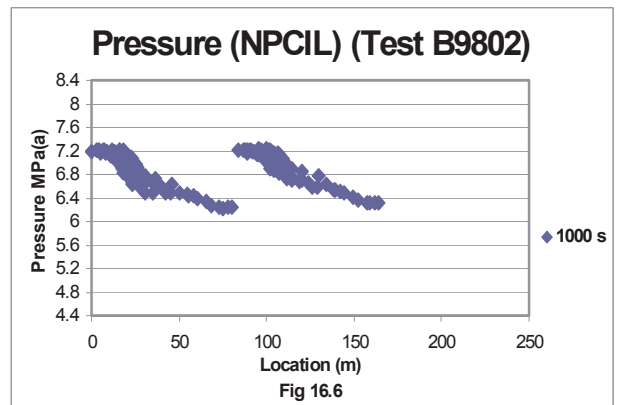
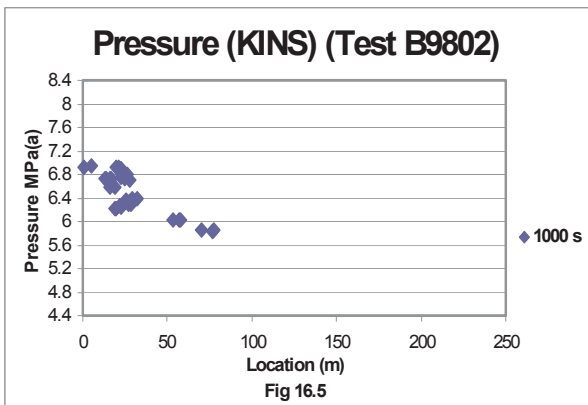
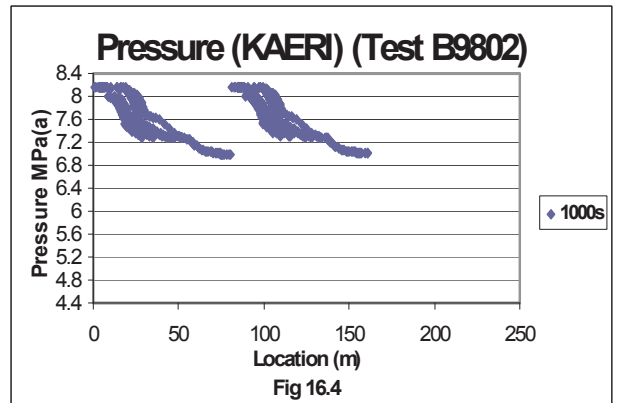
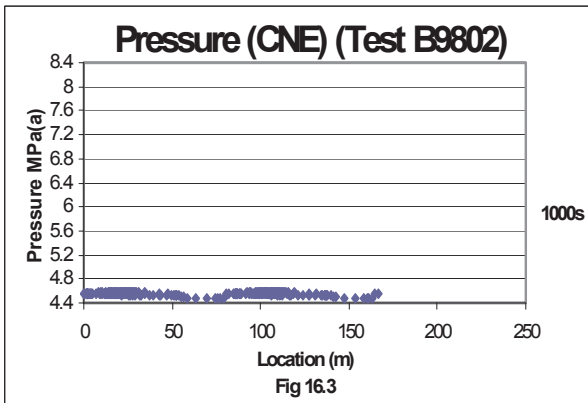
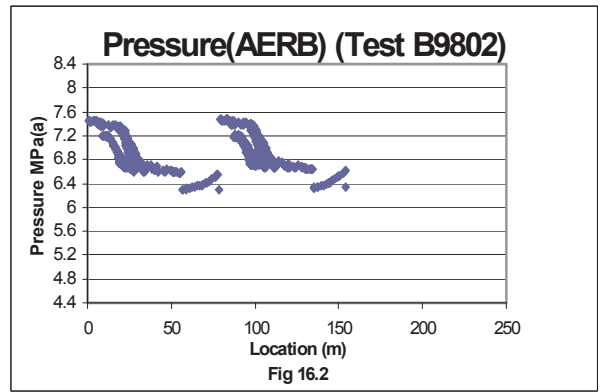
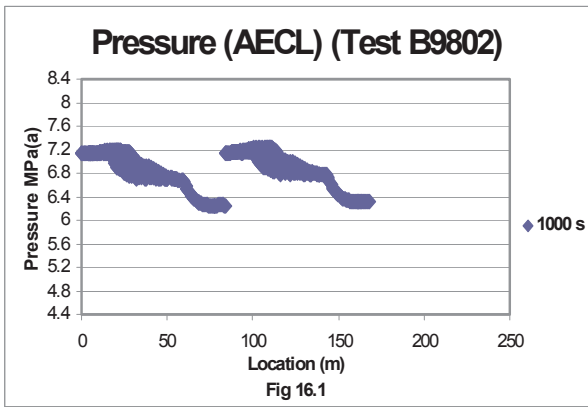


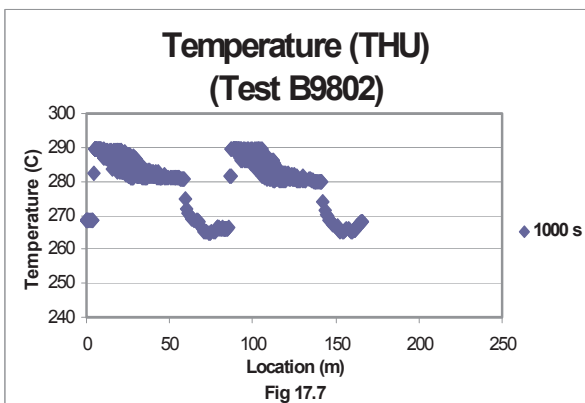
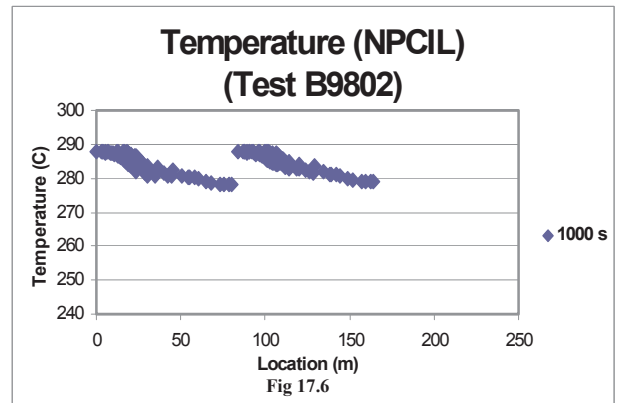
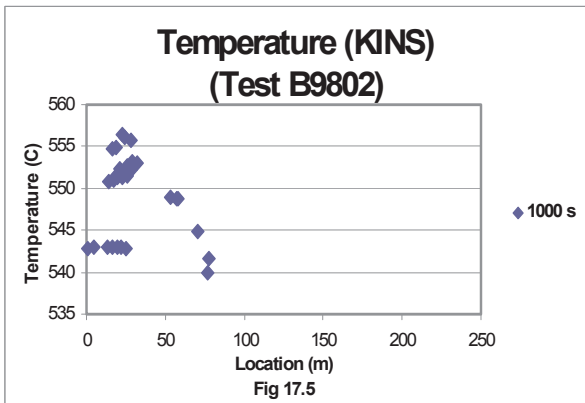
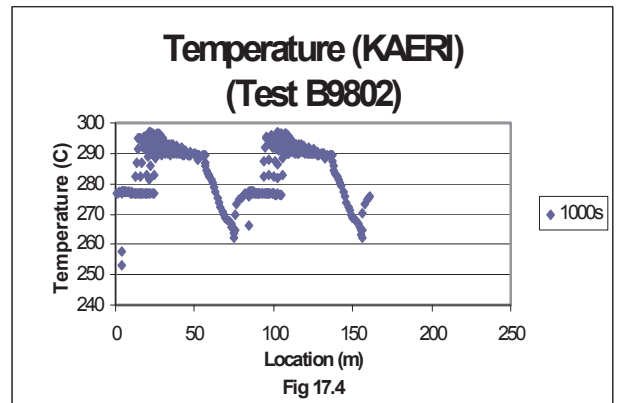
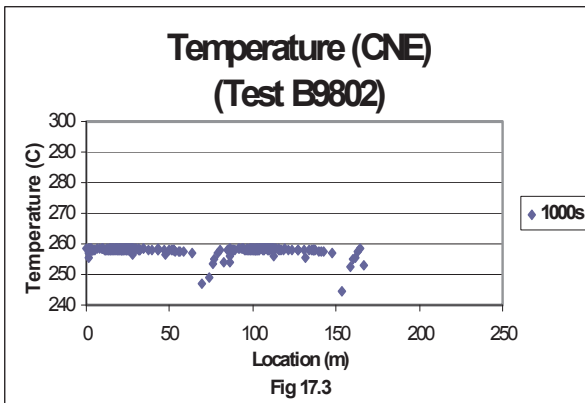
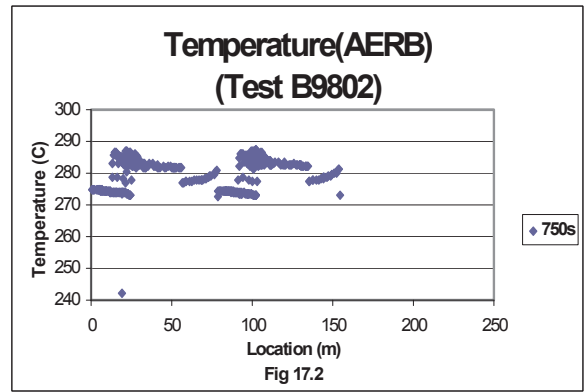
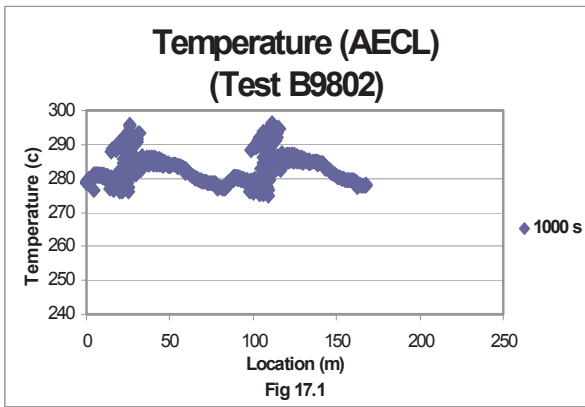


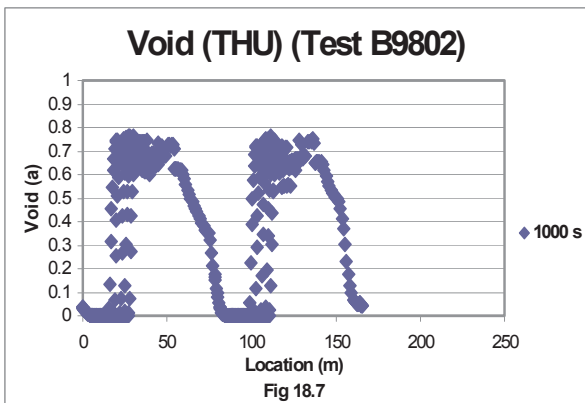
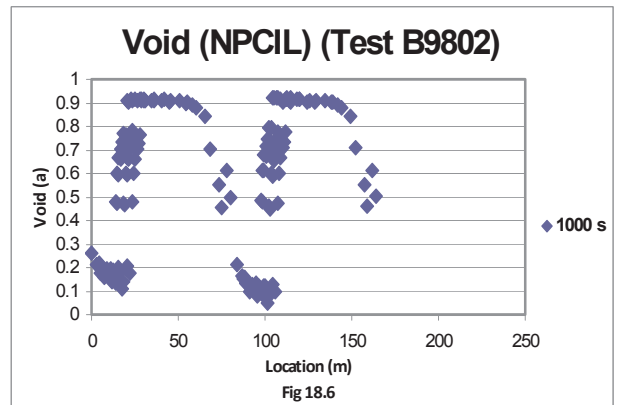
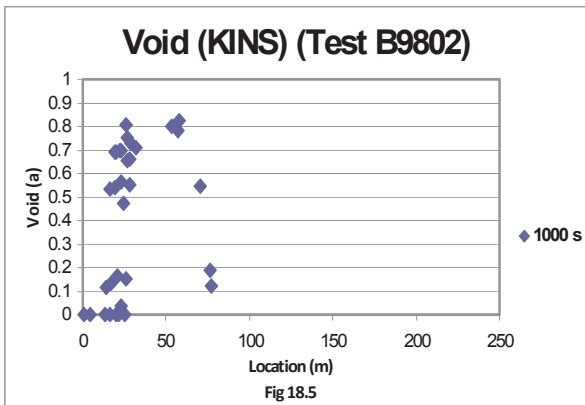
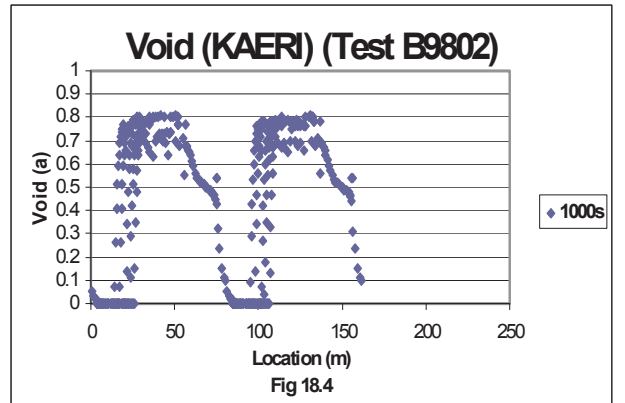
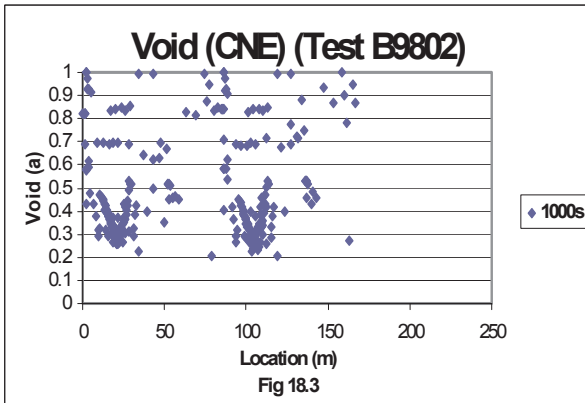
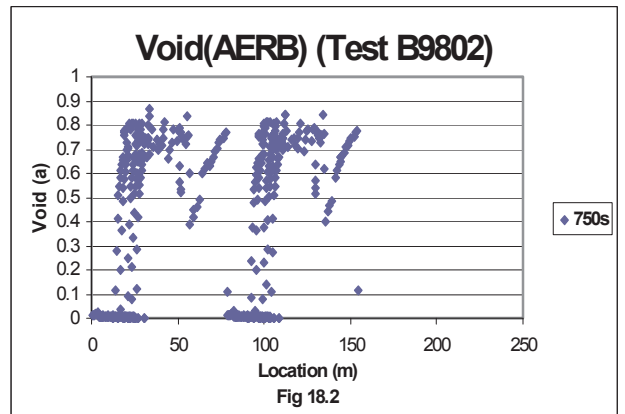
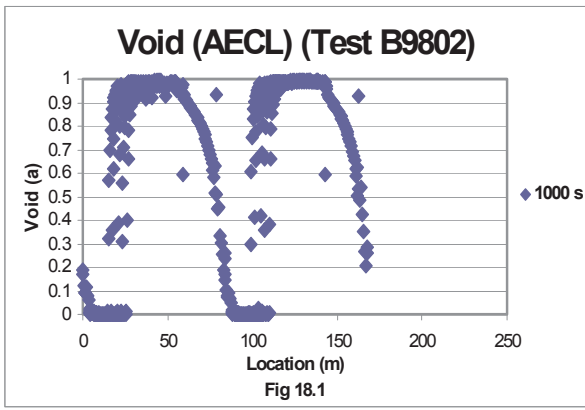


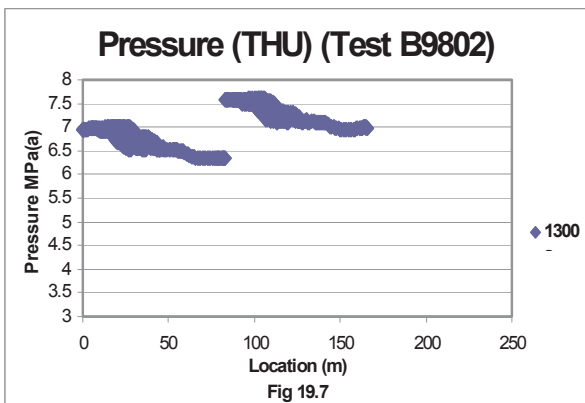
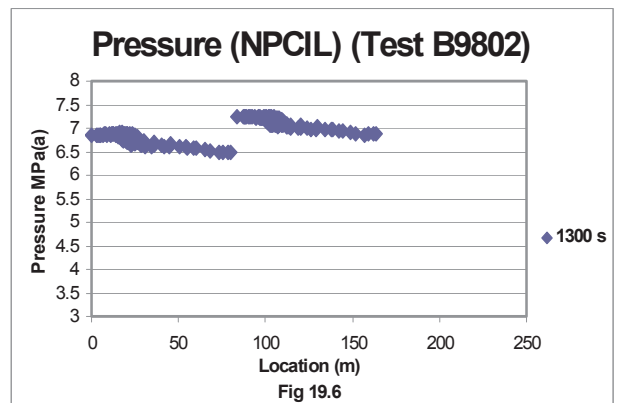
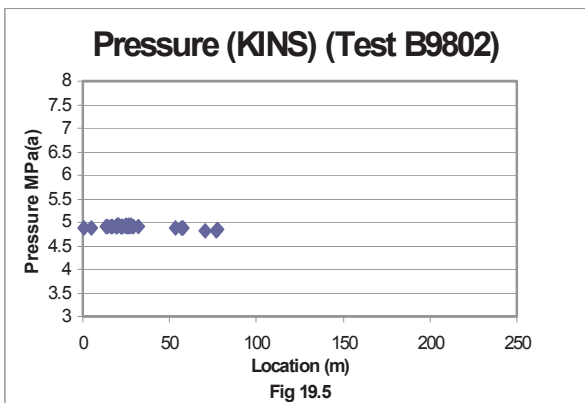
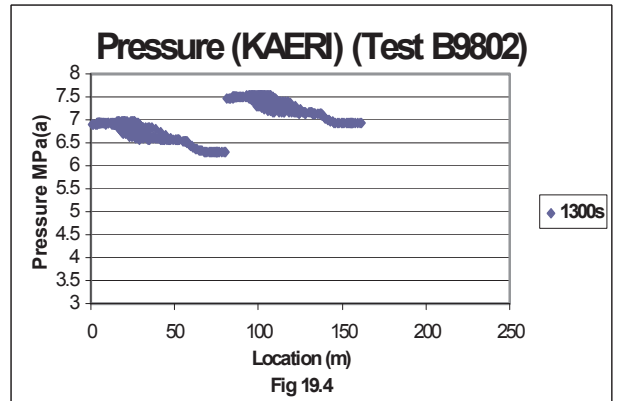
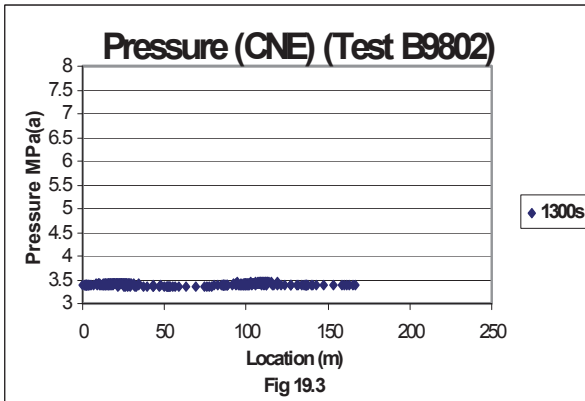
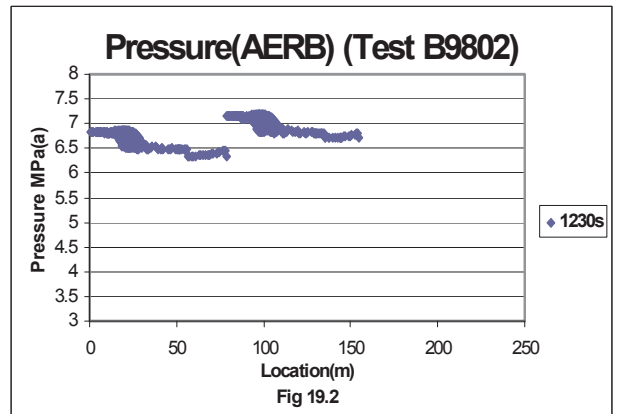
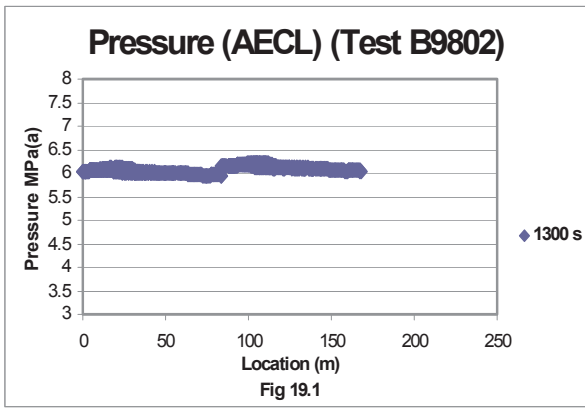


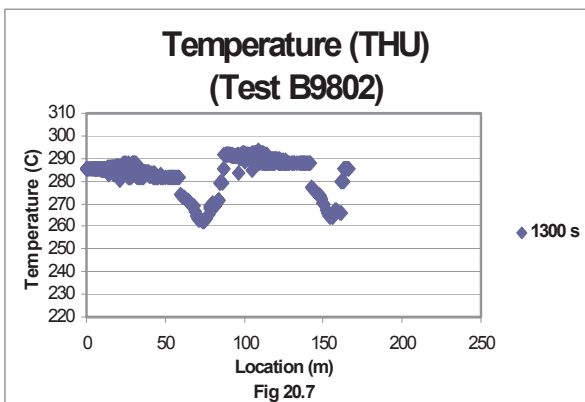
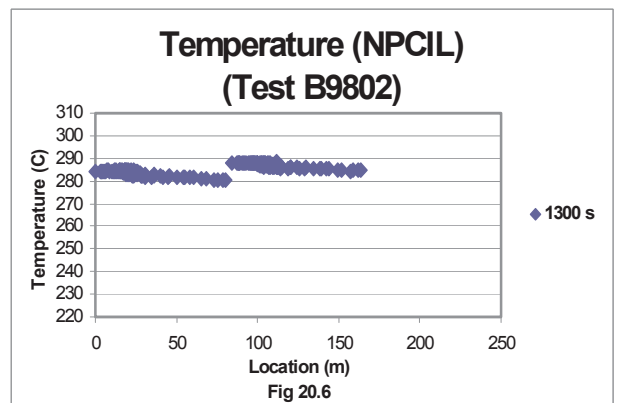
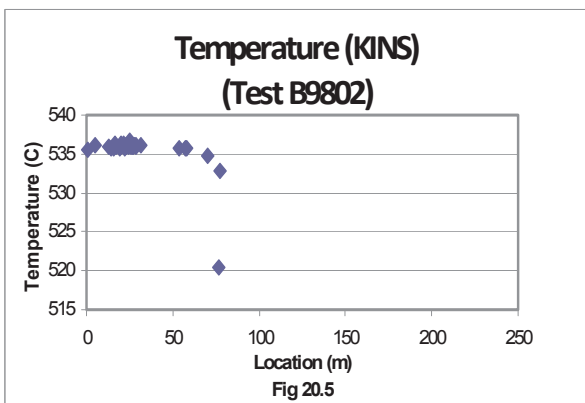
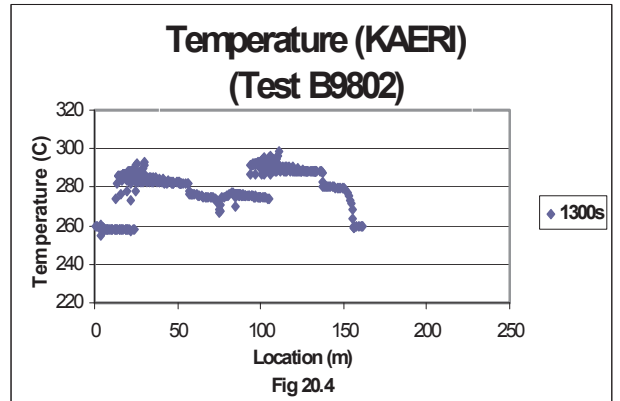
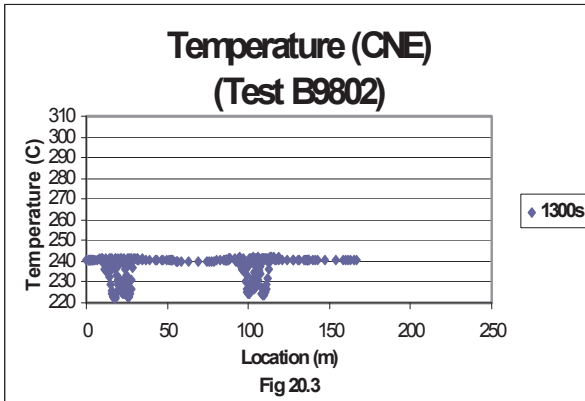
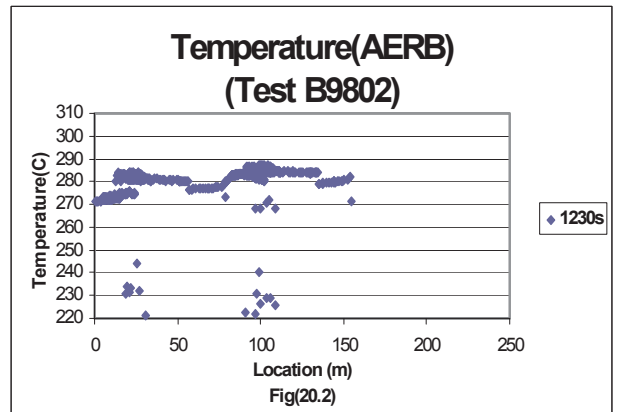
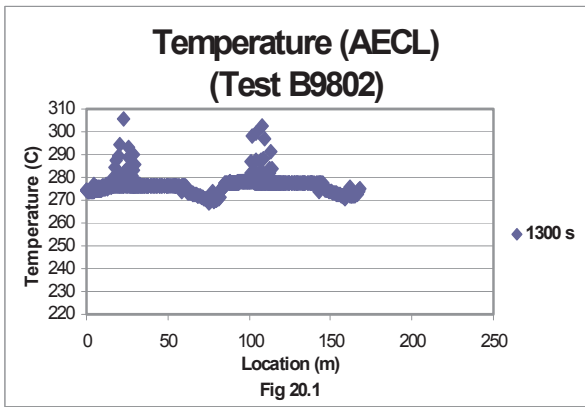


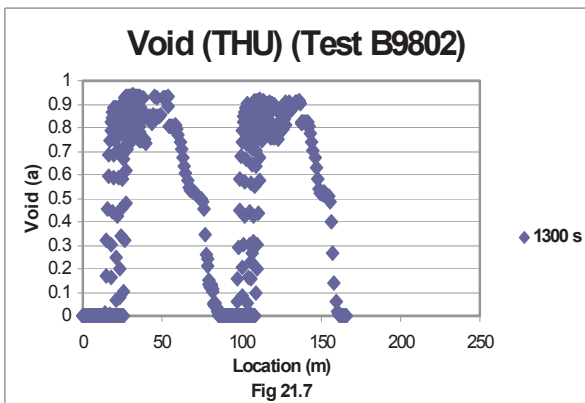
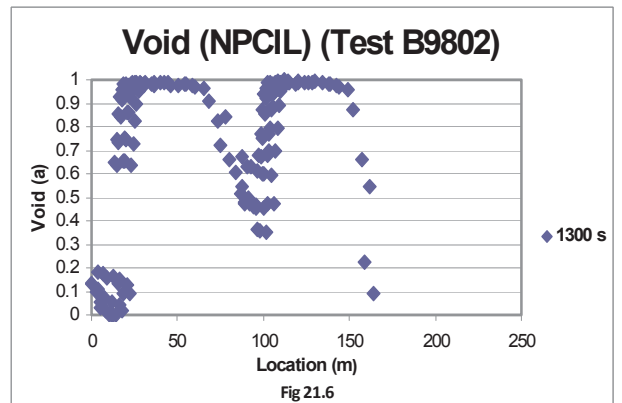
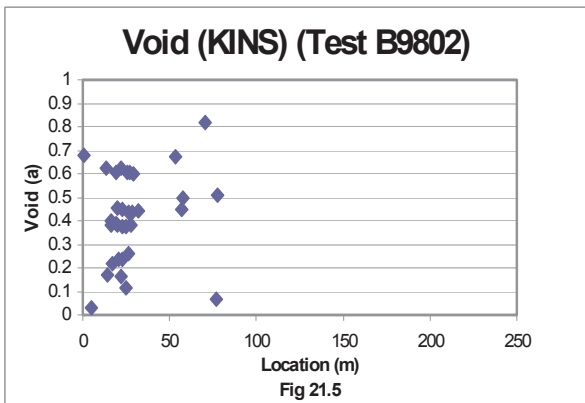
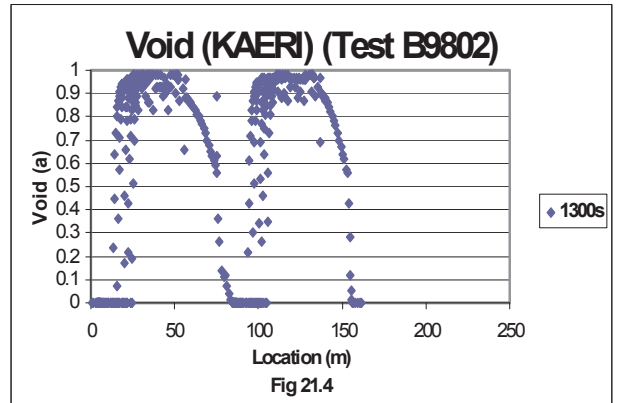
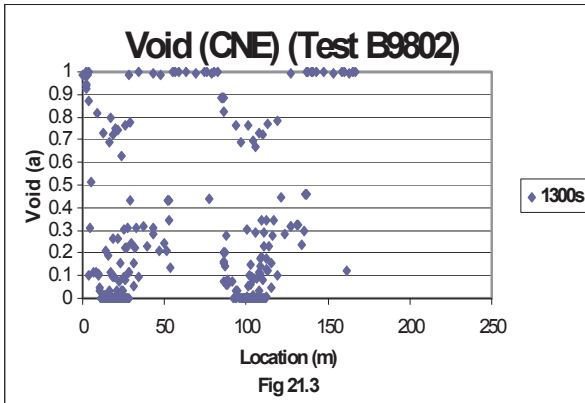
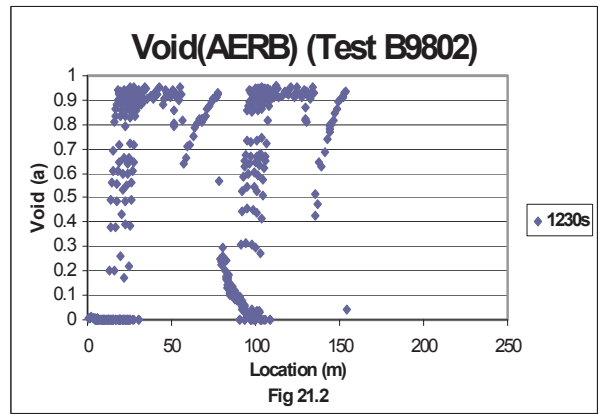
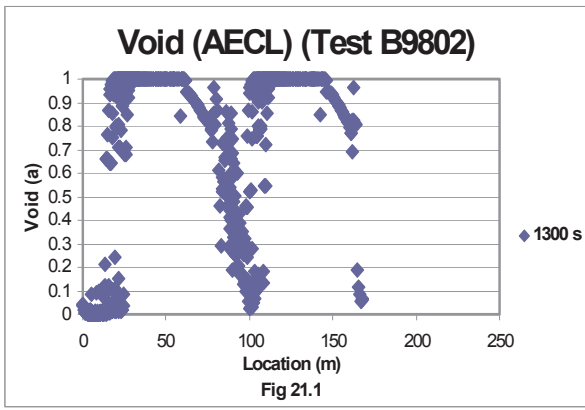












CONTRIBUTORS TO DRAFTING AND REVIEW

Choi, J.-H.	International Atomic Energy Agency
Gupta, S.K.	Atomic Energy Regulatory Board, India
Istrate, R.	Centrala Nucleara Electrica, Romania
Kim, H.-T.	Korea Atomic Energy Research Institute, Republic of Korea
Kim, K.	Korea Institute of Nuclear Safety, Republic of Korea
Krause, M.	Atomic Energy of Canada Limited, Canada
Ottaviani, A.	National Atomic Energy Commission, Argentina
Rao, R.S.	Atomic Energy Regulatory Board, India
Singhal, M.	Nuclear Power Corporation of India Limited, India
Yu, J.-Y.	Tsinghua University, China

Technical Meetings

Vienna, Austria: 14–16 November 2007; Winnipeg, Canada: 27–29 August 2008;
Vienna, Austria: 26–28 August 2009; Daejeon, Republic of Korea: 9–12 November 2010



IAEA

International Atomic Energy Agency

No. 22

Where to order IAEA publications

In the following countries IAEA publications may be purchased from the sources listed below, or from major local booksellers. Payment may be made in local currency or with UNESCO coupons.

AUSTRALIA

DA Information Services, 648 Whitehorse Road, MITCHAM 3132
Telephone: +61 3 9210 7777 • Fax: +61 3 9210 7788
Email: service@dadirect.com.au • Web site: <http://www.dadirect.com.au>

BELGIUM

Jean de Lannoy, avenue du Roi 202, B-1190 Brussels
Telephone: +32 2 538 43 08 • Fax: +32 2 538 08 41
Email: jean.de.lannoy@infoboard.be • Web site: <http://www.jean-de-lannoy.be>

CANADA

Bernan Associates, 4501 Forbes Blvd, Suite 200, Lanham, MD 20706-4346, USA
Telephone: 1-800-865-3457 • Fax: 1-800-865-3450
Email: customercare@bernan.com • Web site: <http://www.bernan.com>

Renouf Publishing Company Ltd., 1-5369 Canotek Rd., Ottawa, Ontario, K1J 9J3
Telephone: +613 745 2665 • Fax: +613 745 7660
Email: order.dept@renoufbooks.com • Web site: <http://www.renoufbooks.com>

CHINA

IAEA Publications in Chinese: China Nuclear Energy Industry Corporation, Translation Section, P.O. Box 2103, Beijing

CZECH REPUBLIC

Suweco CZ, S.R.O., Klecakova 347, 180 21 Praha 9
Telephone: +420 26603 5364 • Fax: +420 28482 1646
Email: nakup@suweco.cz • Web site: <http://www.suweco.cz>

FINLAND

Akateeminen Kirjakauppa, PO BOX 128 (Keskuskatu 1), FIN-00101 Helsinki
Telephone: +358 9 121 41 • Fax: +358 9 121 4450
Email: akatilauk@akateeminen.com • Web site: <http://www.akateeminen.com>

FRANCE

Form-Edit, 5, rue Janssen, P.O. Box 25, F-75921 Paris Cedex 19
Telephone: +33 1 42 01 49 49 • Fax: +33 1 42 01 90 90
Email: formedit@formedit.fr • Web site: <http://www.formedit.fr>

Lavoisier SAS, 145 rue de Provigny, 94236 Cachan Cedex
Telephone: + 33 1 47 40 67 02 • Fax +33 1 47 40 67 02
Email: romuald.verrier@lavoisier.fr • Web site: <http://www.lavoisier.fr>

GERMANY

UNO-Verlag, Vertriebs- und Verlags GmbH, Am Hofgarten 10, D-53113 Bonn
Telephone: + 49 228 94 90 20 • Fax: +49 228 94 90 20 or +49 228 94 90 222
Email: bestellung@uno-verlag.de • Web site: <http://www.uno-verlag.de>

HUNGARY

Librotrade Ltd., Book Import, P.O. Box 126, H-1656 Budapest
Telephone: +36 1 257 7777 • Fax: +36 1 257 7472 • Email: books@librotrade.hu

INDIA

Allied Publishers Group, 1st Floor, Dubash House, 15, J. N. Heredia Marg, Ballard Estate, Mumbai 400 001,
Telephone: +91 22 22617926/27 • Fax: +91 22 22617928
Email: alliedpl@vsnl.com • Web site: <http://www.alliedpublishers.com>

Bookwell, 2/72, Nirankari Colony, Delhi 110009
Telephone: +91 11 23268786, +91 11 23257264 • Fax: +91 11 23281315
Email: bookwell@vsnl.net

ITALY

Libreria Scientifica Dott. Lucio di Biasio "AEIOU", Via Coronelli 6, I-20146 Milan
Telephone: +39 02 48 95 45 52 or 48 95 45 62 • Fax: +39 02 48 95 45 48
Email: info@libreriaaeiou.eu • Website: www.libreriaaeiou.eu

JAPAN

Maruzen Company, Ltd., 13-6 Nihonbashi, 3 chome, Chuo-ku, Tokyo 103-0027
Telephone: +81 3 3275 8582 • Fax: +81 3 3275 9072
Email: journal@maruzen.co.jp • Web site: <http://www.maruzen.co.jp>

REPUBLIC OF KOREA

KINS Inc., Information Business Dept. Samho Bldg. 2nd Floor, 275-1 Yang Jae-dong SeoCho-G, Seoul 137-130
Telephone: +02 589 1740 • Fax: +02 589 1746 • Web site: <http://www.kins.re.kr>

NETHERLANDS

De Lindeboom Internationale Publicaties B.V., M.A. de Ruyterstraat 20A, NL-7482 BZ Haaksbergen
Telephone: +31 (0) 53 5740004 • Fax: +31 (0) 53 5729296
Email: books@delindeboom.com • Web site: <http://www.delindeboom.com>

Martinus Nijhoff International, Koraalrood 50, P.O. Box 1853, 2700 CZ Zoetermeer
Telephone: +31 793 684 400 • Fax: +31 793 615 698
Email: info@nijhoff.nl • Web site: <http://www.nijhoff.nl>

Swets and Zeitlinger b.v., P.O. Box 830, 2160 SZ Lisse
Telephone: +31 252 435 111 • Fax: +31 252 415 888
Email: info@swets.nl • Web site: <http://www.swets.nl>

NEW ZEALAND

DA Information Services, 648 Whitehorse Road, MITCHAM 3132, Australia
Telephone: +61 3 9210 7777 • Fax: +61 3 9210 7788
Email: service@dadirect.com.au • Web site: <http://www.dadirect.com.au>

SLOVENIA

Cankarjeva Založba d.d., Kopitarjeva 2, SI-1512 Ljubljana
Telephone: +386 1 432 31 44 • Fax: +386 1 230 14 35
Email: import.books@cankarjeva-z.si • Web site: <http://www.cankarjeva-z.si/uvvoz>

SPAIN

Díaz de Santos, S.A., c/ Juan Bravo, 3A, E-28006 Madrid
Telephone: +34 91 781 94 80 • Fax: +34 91 575 55 63
Email: compras@diazdesantos.es, carmela@diazdesantos.es, barcelona@diazdesantos.es, julio@diazdesantos.es
Web site: <http://www.diazdesantos.es>

UNITED KINGDOM

The Stationery Office Ltd, International Sales Agency, PO Box 29, Norwich, NR3 1 GN
Telephone (orders): +44 870 600 5552 • (enquiries): +44 207 873 8372 • Fax: +44 207 873 8203
Email (orders): book.orders@tso.co.uk • (enquiries): book.enquiries@tso.co.uk • Web site: <http://www.tso.co.uk>

On-line orders

DELTA Int. Book Wholesalers Ltd., 39 Alexandra Road, Addlestone, Surrey, KT15 2PQ
Email: info@profbooks.com • Web site: <http://www.profbooks.com>

Books on the Environment

Earthprint Ltd., P.O. Box 119, Stevenage SG1 4TP
Telephone: +44 1438748111 • Fax: +44 1438748844
Email: orders@earthprint.com • Web site: <http://www.earthprint.com>

UNITED NATIONS

Dept. I004, Room DC2-0853, First Avenue at 46th Street, New York, N.Y. 10017, USA
(UN) Telephone: +800 253-9646 or +212 963-8302 • Fax: +212 963-3489
Email: publications@un.org • Web site: <http://www.un.org>

UNITED STATES OF AMERICA

Bernan Associates, 4501 Forbes Blvd., Suite 200, Lanham, MD 20706-4346
Telephone: 1-800-865-3457 • Fax: 1-800-865-3450
Email: customercare@bernan.com • Web site: <http://www.bernan.com>

Renouf Publishing Company Ltd., 812 Proctor Ave., Ogdensburg, NY, 13669
Telephone: +888 551 7470 (toll-free) • Fax: +888 568 8546 (toll-free)
Email: order.dept@renoufbooks.com • Web site: <http://www.renoufbooks.com>

Orders and requests for information may also be addressed directly to:

Marketing and Sales Unit, International Atomic Energy Agency

Vienna International Centre, PO Box 100, 1400 Vienna, Austria
Telephone: +43 1 2600 22529 (or 22530) • Fax: +43 1 2600 29302
Email: sales.publications@iaea.org • Web site: <http://www.iaea.org/books>